Conference Proceedings of the Society for E

J.M. Caicedo · F.N. Catbas · A. C
K. Salyards *Editors*

Topics on

Conference Proceedings of the Society for Experimental Mechanics Series

Series Editor
Tom Proulx
Society for Experimental Mechanics, Inc.,
Bethel, CT, USA

For further volumes:
http://www.springer.com/series/8922

J.M. Caicedo • F.N. Catbas • A. Cunha • V. Racic
P. Reynolds • K. Salyards
Editors

Topics on the Dynamics of Civil Structures, Volume 1

Proceedings of the 30th IMAC, A Conference on Structural Dynamics, 2012

Springer

Editors
J.M. Caicedo
University of South Carolina
Columbia, SC, USA

F.N. Catbas
University of Central Florida
Orlando, FL, USA

A. Cunha
Universidade do Porto
Portugal

V. Racic
University of Sheffield
UK

P. Reynolds
University of Sheffield
UK

K. Salyards
Bucknell University
Lewisburg, PA, USA

ISSN 2191-5644 e-ISSN 2191-5652
ISBN 978-1-4614-2412-3 e-ISBN 978-1-4614-2413-0
DOI 10.1007/978-1-4614-2413-0
Springer New York Dordrecht Heidelberg London

Library of Congress Control Number: 2012933794

Preface

Topics on the Dynamics of Civil Structures represents one of six volumes of technical papers presented at the 30th IMAC, A Conference and Exposition on Structural Dynamics, 2012 organized by the Society for Experimental Mechanics, and held in Jacksonville, Florida, January 30–February 2, 2012. The full proceedings also include volumes on Substructuring and Wind Turbine Dynamics; Nonlinear Dynamics; Model Validation and Uncertainty Quantification; and Modal Analysis, I & II.

Each collection presents early findings from experimental and computational investigations on an important area within Structural Dynamics. The current volume on *Topics on the Dynamics of Civil Structures* centers on the testing, monitoring, and assessment of civil structures. Bridge dynamics and monitoring are two topics that are explored as part of a special focus on large civil structures. Damage detection, human loading, and vibration control address safety of civil structures.

The organizers would like to thank the authors, presenters, session organizers, and session chairs for their participation in this track.

Columbia, SC, USA — J.M. Caicedo
Orlando, FL, USA — F.N. Catbas
Porto, Portugal — A. Cunha
Sheffield, UK — V. Racic
Sheffield, UK — P. Reynolds
Lewisburg, PA, USA — K. Salyards

Contents

Chapter 1
Damping Effect of Humans

Lars Pedersen

Abstract Passive humans (sitting or standing) might well be present on flooring-systems, footbridges or other structures that carry humans. An active crowd of people might generate structural vibrations, and these might be problematic. The passive crowd of people, however, will interact with the structural system and change its dynamic behaviour and its dynamic characteristics. When predicting structural vibrations it is not common to account for the passive crowd, but the paper will illustrate effects of the presence of a passive crowd on structural behaviour. Numerical and experimental results are presented and discussed.

Keywords Human-structure interaction • Passive damping

Nomenclature

e	Ratio
f_i	Empty floor frequency
f_h	Human frequency
p	Load
ζ_i	Empty floor damping
ζ_h	Human damping
E_c	Young's modulus of concrete
m_i	Empty floor modal mass
m_h	Human modal mass

1.1 Introduction

Jumping, bouncing or other rhythmic activities of humans may generate vibrations in structures. The humans that perform these activities may be referred to as active humans. Passive humans, for instance, standing on the structure may also be present.

A number of tests have validated that it is reasonable to consider a floor occupied by passive humans as a combined human-floor system were the passive humans are modelled as auxiliary systems attached to the floor mass with the implication that passive humans add damping to the floor. The overall tendency of this behaviour has for instance been observed on full-scale real life structures [1–4], but tests validating the behaviour have also been performed on floors in laboratory environments [5–7], and some tests have suggested dynamic characteristics of a passive human. That a passive human may be modelled as a dynamic system is in agreement with findings in biomechanics [8].

L. Pedersen (✉)
Department of Civil Engineering, Aalborg University, Sohngaardsholmsvej 57, DK-9000 Aalborg, Denmark
e-mail: lp@civil.aau.dk

J.M. Caicedo et al. (eds.), *Topics on the Dynamics of Civil Structures, Volume 1*,
Conference Proceedings of the Society for Experimental Mechanics Series 26,
DOI 10.1007/978-1-4614-2413-0_1,

In a number of previously performed tests dealing with the interaction between floors and passive humans, the excitation has not been performed by a crowd of active humans asked to excite the floor resonance frequency. Often a mechanical device has been used to excite the floor or impact actions have been employed. This is useful, but on real life structures it would typically be the rhythmic activity of active humans that courses the structural vibrations. Hence, the idea of the investigations of this paper is to employ this type of excitation (rhythmic activity) in tests on a real life structure and to monitor floor acceleration levels with and without passive humans on the floor. This indirectly provides a measure of the amount of damping that the passive humans add to the floor, which can be compared with the theoretical predictions of added damping established from a dynamic model considering passive humans as auxiliary systems attached to the floor mass.

The real life structure employed in tests is a sports hall floor. The floor is introduced in Sect. 1.2, and the section also presents the empty floor dynamic characteristics as derived from finite element analyses and initial measurements. Assuming a theoretical model for the combined human-floor system, the expected damping ratios of the floor carrying passive humans are derived. The acceleration levels generated by a jumping crowd measured with and without passive humans on the floor are presented and the amount of added damping is compared with theoretical predictions. The results are discussed.

1.2 The Sports Hall Floor

The structure subjected to investigation and testing is a sports hall floor. It consists of nine TTD deck elements made of prestressed concrete placed next to each other. The TTD deck elements are supported by the walls of the story below the sports hall.

The length of the elements is 16.3 m and the width is 2.4 m; each element consisting of a horizontal concrete slab with two stiffening ribs below.

The total floor area is 16.3 × 21.6 m with a total of 18 ribs spanning 16.3 m. Furthermore, the deck consists of a reinforced concrete topping with a height of approximately 150 mm. On top of this comes the actual sports floor, which does not contribute with bending stiffness.

1.2.1 Dynamic Characteristics of the Empty Floor

Initially, and using best estimates of geometry, stiffness and material densities, a finite element model (FEM) was established to provide an understanding of the dynamic characteristics of the floor.

Frequency analysis determined the frequencies (f_i) for the first three bending modes and results are shown in Table 1.1.

The modelling considered both stiffness of reinforcement and stiffness of concrete, and all four edges of the orthotropic floor were modelled as simple supports.

Not surprisingly, the mode shape for the first mode showed a floor where all points moved in the same direction at the same time with maximum motion at midpoint of the floor. As the floor is orthotropic with a stiffness which is quite small in the direction perpendicular to the ribs compared with the stiffness in the direction of the ribs, the mode shape for the second mode resembled that of the second mode of a uniform pin-supported beam spanning 16.3 m. So did mode shapes up to the seventh mode.

Quite simplistic experimental tests were conducted to determine natural frequencies and damping ratios of floor vibration modes. The instrumentation comprised an accelerometer clamped to the ribs of the TTD deck measuring in the vertical direction. The accelerometer was moved around (placed on different ribs) so as to be able to monitor deformations of at least the first three bending modes of the deck to heel impact loads.

From the obtained free decays, floor natural frequencies and damping ratios were determined after bandpass filtering of the measured decays, and the results are seen in Table 1.2 for the three lowest modes.

As can be seen there is a difference between the frequency estimates obtained from the initial finite element modelling and the experiments.

An attempt was made to tune the finite element model by altering Young's modulus (E_c) for concrete, and it turned out that by shifting E_c from 40 to 48 GPa there was a good match between FEM results and results from experiments (EXP). This is seen in Table 1.3.

The magnitude $E_c = 48$ GPa is considered fairly realistic considering that the dynamic value of Young's modulus is higher than the static equivalent; the value initially assumed in the finite element modelling. Other tuning parameters could have been considered, but this was beyond the studies for the investigations.

Table 1.1 Floor natural frequencies

f_1 (Hz)	f_2 (Hz)	f_3 (Hz)
7.62	8.58	10.80

Table 1.2 Natural frequencies and damping ratios determined from experiments

f_1 (Hz)	f_2 (Hz)	f_3 (Hz)	ζ_1 (%)	ζ_2 (%)	ζ_3 (%)
8.30	9.40	11.00	1.24	2.06	1.60

Table 1.3 Floor natural frequencies

	f_1 (Hz)	f_2 (Hz)	f_3 (Hz)
EXP	8.30	9.40	11.00
FEM	8.30	9.36	11.76

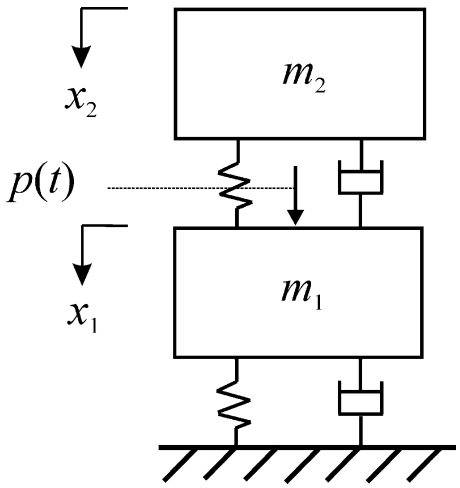

Fig. 1.1 Analytical model for the combined system

From Table 1.2, it can be noticed that the damping ratio of the first mode (ζ_1) is relatively low. Additionally that the first natural frequency of the floor (f_1) might be excited by rhythmic human activity on the sports floor in that the 4th harmonic of jumping action (8.3/4 Hz) would cause resonant excitation.

It would also be possible to excite the second and third natural frequency by rhythmic human activity, but the energy of the excitation would be lower than if caused by excitation at 8.3/4 Hz. Hence, in the following we shall only focus on the excitation at 8.3/4 Hz.

Even though the first and second mode have frequencies which are not that much apart, a standard criterion (also accounting for the damping ratios of the two modes) suggested that it would be reasonable to assume modal decoupling.

1.2.2 Dynamic Characteristics of the Floor Carrying Passive Humans

For situations where the floor carries a passive crowd of people, we will know make use of a model where the empty floor is modelled as an SDOF system, representing the first floor mode. Each passive human is modelled as an auxiliary SDOF system attached to the floor at the position where he or she is standing. For simplicity we shall assume that each and every passive human is standing at midpoint of the floor, as this fairly well represent conditions studied in subsequent experimental tests.

Hence, we shall assume a dynamic model of the combined human-floor system much like the one shown in Fig. 1.1.

Here the grounded SDOF subsystem represents the floor mode and the attached SDOF system represents the passive crowd of people.

On this basis, we shall calculate the damping ratio of the combined system (floor with a passive crowd of people atop the floor). For these calculations, the dynamic characteristics tabulated in Table 1.4 are assumed.

The dynamic characteristics for a passive person (f_h, ζ_h, and m_h) are those suggested in Ref. [7]. The dynamic characteristics of the empty floor (f_1, ζ_1, and m_1) are those presented in this paper, although the magnitude of the floor modal mass has not been mentioned previously.

Table 1.4 Natural frequency, damping ratio and modal mass

Floor			Humans		
f_1 (Hz)	ζ_1 (%)	m_1 (kg)	f_h (Hz)	ζ_h (%)	m_h (kg)
8.30	1.24	98,950	5.24	39	75

Table 1.5 Ratio e_a as a function of n

n	0	2	4	5	10	15
e_a	1	1.07	1.10	1.13	1.26	1.38

Table 1.6 Ratio e_e as a function of n

n	0	2	4	5
e_e	1	1.2	1.5	1.8

Based on these assumptions an analytical model was established (for situations with and without the presence of passive humans), and by assuming an impact acting on the floor mass, it was possible by Newmark time integration to determine a free decay of the floor mass. By employing the logarithmic-decrement technique a damping ratio was derived for the floor mode of the combined system. This was done for passive crowds of various sizes.

The damping ratio calculated with no passive persons on the floor is denoted $\zeta(0)$, and with n passive persons on the floor it is denoted $\zeta(n)$. For the presentation of results, the ratio e_a defined in (1.1) is introduced.

$$e_a = \zeta(n)/\zeta(0) \tag{1.1}$$

Thus, if e_a is equal to 1, there is no difference between the damping ratio calculated with and without passive persons on the floor, and if $e_a > 1$, the passive persons increase floor damping. The results in terms of e are tabulated in Table 1.5.

As can be seen, the theoretical calculations suggest that the damping increases with the number of passive people present on the floor mass.

1.2.3 Experiments: Floor Response to Actions of Jumping

A series of experiments with passive people on the floor were made to validate the theoretical findings. In the tests, the excitation was different from the theoretical investigations in that in tests the excitation was generated by at jumping crowd of people.

The jumping crowd consisted of five persons and was positioned at the midpoint of the floor. They surrounded five stationary people; so all ten persons were located in close proximity of the midpoint of the floor.

The jumpers were asked to jump to a piece of music with a beat frequency of 8.3/4 Hz hereby exciting the first natural frequency of the floor, f_1. First all passive persons were present on the floor, then one passive person left the floor leaving four passive persons. Then another passive person left the floor leaving three passive people, and finally only the five jumpers were present on the floor. During this sequence, vertical floor accelerations at midpoint of the floor were picked up by an accelerometer.

The acceleration signal was bandpass filtered leaving only the response of the first floor mode. From this signal the rms-value was derived after disregarding an initial period of resonance build up. The rms-value recorded with no passive persons on the floor is denoted $a_{rms}(0)$, and with n passive persons it is denoted $a_{rms}(n)$. For the presentation of results, the ratio e_e defined in (1.2) is introduced.

$$e_e = a_{rms}(0)/a_{rms}(n) \tag{1.2}$$

Thus, if e_e is equal to 1, there is no difference between the rms-accelerations recorded with and without passive persons on the floor, and if $e_e > 1$, the passive persons reduce rms-acceleration levels (add damping to the floor). The results in terms of e_e are shown in Table 1.6.

It can be noticed that the acceleration level of the floor steadily reduces as the number of passive persons increase. The results suggest that five passive persons positioned close to the midpoint of the floor are capable of reducing floor acceleration levels generated by the jumping action by 55% (by a factor $1/1.8 = 0.55$). In this context it is worth noting that the mass of the five passive persons amounts to about 400 kg, which is close to only 0.4% of the modal mass of the floor. Thus, the attenuating effect is quite considerable.

If the experimental results in terms of e_e (shown in Table 1.6) are compared with the theoretical results in terms of e_e (shown in Table 1.5), it can be found that the experimental results suggest a (much) higher damping effect of passive humans than the theoretical model predicts. The discrepancy between the results is discussed below.

In any prediction model there would be uncertainties. For instance, the input parameters for the model could be associated with uncertainty. In the present case, the modal characteristics of the floor serve as input parameters for predicting the damping added by passive humans. These properties are, of course, to some degree associated with uncertainty, and the calculated damping added by passive humans is sensitive to parameters such as the assumed empty floor frequency and empty floor damping as exemplified in Ref. [9]. However, these properties are derived from measurements on the specific sports hall floor, and unless gross errors have been made in their estimation, it is difficult to imagine that the uncertainty associated with these estimates can explain the observed discrepancy (between predicted and measured damping effect of humans). As for the floor modal mass, it is also somewhat uncertain, as for instance the height of the concrete topping might not be as drawings indicate. However, it would require a significantly misjudged modal mass to explain the observed discrepancy.

The assumed modal characteristics of passive humans are definitely uncertain, but yet again it would take gross errors to explain the observed discrepancy, and a number of references have indicated that the overall approach of modelling passive humans as auxiliary systems to the floor is generally valid.

Perhaps the most likely explanation to the observed discrepancy originates from the excitation. Jumping humans are not machines, and it is not unlikely that it has not been possible for the jumpers to maintain the same excitation during the test sequence. As the floor is lightly damped, a short period of off-resonant excitation would bring down acceleration levels, and optimal synchronization between jumpers might have failed during some sequences of the tests. In the initially part of the tests, the passive humans (positioned in the middle of the crowd of people present on the floor) perhaps prevented the jumpers from being fully coordinated as visual contact between jumpers was not optimal. The visual contact between jumpers gradually improved as passive humans left the floor, which might suggest improved coordination between jumpers, and higher acceleration levels. This partially can explain why the acceleration levels were observed to be quite low when five passive humans were present on the floor.

Having mentioned all this, it cannot be ruled out that the experimental results are the valid data and that the theoretical model underestimates damping added by passive humans.

The discussions underline that it can be quite difficult on real life structure to validate models for human damping effects from tests involving active persons and passive persons, even though this is the situation were human damping effects are of interest. In the present case it would have been useful to supplement the experimental findings by doing further tests, but practical circumstances made this impossible.

1.3 Conclusion

Experiments made on a sports hall floor with a combination of passive and active people present on the floor support that passive humans can add damping to a vibrating floor.

Even a small crowd of people were capable of markedly reducing floor accelerations induced by jumping loads. As the number of passive people increased, the floor accelerations reduced, which is in line with the assumption that the passive crowd of people and the floor should be considered as a combined system where the passive people are modelled as auxiliary systems attached to the floor.

Even though the experimental results support the overall mechanisms of the phenomenon suggested by a theoretical model, they do also suggest a damping effect, which is (much) higher than what the theoretical prediction model suggests. The paper discusses this observation in seek of explanations.

Acknowledgements The author would like to acknowledge students at Aalborg University, Denmark, for their contributions.

References

1. Ellis BR, Ji T (1997) Human-structure interaction in vertical vibrations. Proceedings of the ICE: structures and buildings, vol 122, pp 1–9
2. Brownjohn JMW (2001) Energy dissipation from vibrating floor slabs due to human-structure interaction. Shock Vib 8(6):315–323
3. Reynolds P, Pavic A, Ibrahim Z (2004) Changes of modal properties of a stadium structure occupied by a crowd. In: Proceedings of the 22nd international modal analysis conference, Dearborn

4. Pedersen L (2005) Updating of the dynamic model of floors carrying stationary humans. In: Brincker R, Møller N (eds) Proceedings of the 1st international operational modal analysis conference, Copenhagen, pp 421–428
5. Sachse R, Pavic A, Reynolds P (2002) The influence of a group of humans on modal properties of a structure. In: Proceedings of the 5th European conference on dynamics, Munich, pp 1241–1246
6. Pedersen L (2007) A contribution to documenting and validating dynamic interaction effects. In: Proceedings of the 25th international modal analysis conference, Orlando
7. Zheng X, Brownjohn JMW (2001) Modeling and simulation of human-floor system under vertical vibration. In: Proceedings of SPIE, smart structures and materials, vol 4326, Newport Beach, pp 513–520
8. Griffin MJ (1990) Handbook of human vibration. Academic, London
9. Pedersen L (2010) Interaction between structures and their occupants. In: Proceedings of the 29th international modal analysis conference, Jacksonville

Chapter 2
Development of a Laboratory Test Program to Examine Human-Structure Interaction

Nicholas C. Noss and Kelly A. Salyards

Abstract Vibration serviceability is a widely recognized design criterion for assembly-type structures likely subjected to rhythmic human-induced excitation. Current design guidance is based on the natural frequency of the structure. However, a phenomenon known as human-structure interaction suggests that there is a dynamic interaction between the structure and the occupants, altering the natural frequency of the system. It is unknown if this shift in natural frequency is significant enough to warrant consideration in the design process. Therefore, there is a need to identify the circumstances under which human-structure interaction should be considered because of its potential impact on serviceability assessment. Because the influence of the structural properties on human-structure interaction cannot be separated from the influence of the crowd characteristics, this study explores the interface of both factors through experimental testing. To do so, a laboratory test structure is designed, constructed, and operated based on particular design criteria selected with knowledge from previous human-structure interaction studies. This study provides a review of the design and construction of the test structure, methods used to validate a finite element computer model to the as-built structure, and the experimental testing procedure for testing with occupants.

Keywords Human-structure interaction • Experimental modal analysis • Crowd dynamics

2.1 Introduction

Assembly-type structures are subjected to dynamic loading generated by the crowd occupying the structure. Motion of the crowd has the potential to induce vibrations that may be of concern to the occupants. Structural engineers refer to this as vibration serviceability. Vibration serviceability is of particular concern when the crowd is synchronized in its movement creating a significant dynamic force on the structure. Because structural designs are utilizing higher-strength materials and advanced analysis methods, assembly-type structures are designed and constructed with longer and lighter spans which are more susceptible to excitation by such crowd motion. It is likely that these structures have a fundamental frequency in the range of 4–8 Hz [1] which corresponds to the frequency range over which humans are most sensitive to vibrations. Occupants of such structures can perceive and be disturbed by these vibrations and if vibrations are excessive [2], widespread panic can occur amongst the crowd, ultimately risking the safety of the occupants. For these reasons, it is important that research continues in the area of vibration serviceability to improve upon the design guidance currently available to structural engineers.

In the United States, the design guidance available for the vibration serviceability design of assembly-type structures subjected to rhythmic excitation is limited. Design for rhythmic excitation is addressed in guidance published by the American Institute of Steel Construction (AISC) for floor structures [2]. This guidance specifies a minimum natural frequency of the structure to be achieved such that resonance with the expected rhythmic excitation is avoided. It assumes that only a single mode of vibration contributes to the dynamic response of the structure and also requires the identification of an appropriate acceleration limit for the purpose of the space. Whilst these assumptions may be reasonable for floor structures, the application of such assumptions to other types of structures, such as stadium grandstands, can be

N.C. Noss (✉) • K.A. Salyards
Department of Civil and Environmental Engineering, Bucknell University, Lewisburg, PA 17837, USA
e-mail: nick.noss@bucknell.edu; kas046@bucknell.edu

J.M. Caicedo et al. (eds.), *Topics on the Dynamics of Civil Structures, Volume 1*,
Conference Proceedings of the Society for Experimental Mechanics Series 26,
DOI 10.1007/978-1-4614-2413-0_2,

inappropriate. In addition, this guidance, along with others, utilizes the natural frequency of the empty structure for its assessment of serviceability. Although this may be representative of the extreme condition where all occupants are actively engaged in the rhythmic loading, it may not address all possible scenarios where some occupants are not engaged in the motion.

In addition, it has been observed by several researchers that the natural frequency of a structural system is also affected by another phenomenon. This phenomenon is known as human-structure interaction and addresses how occupants act more as a spring-mass-damper system rather than mass alone, ultimately affecting the dynamic properties of the overall structural system. The majority of these observations indicate that the natural frequency of the system is decreased from that of the empty structure and the damping ratio is increased from that of the empty structure [3]. This is potentially problematic because the natural frequency could be lowered into a frequency range excitable by rhythmic loading. A short discussion of these observations, ensuing research, and the current guidance for incorporating such effects aims to provide the impetus for the research described in this paper.

2.2 Evidence of Human-Structure Interaction

The human-structure interaction phenomenon was first acknowledged in 1966 in a floor vibration study by Lenzen at the University of Kansas [4]. It was not further examined until 1991 when in-situ monitoring of a stadium grandstand structure provided further evidence of this interaction with a lower natural frequency when the structure is occupied along with an additional mode of vibration [5]. The natural frequency of another assembly structure was found to be reduced from 16 Hz to around 5 Hz when occupied by a crowd [5]. Littler [6] provided further evidence of human-structure interaction, including its dependence on posture, through the in-situ testing of several retractable grandstands. These results from in-situ testing prompted further investigation and laboratory testing.

Experimental testing was performed in the laboratory by several researchers on simple structures. Ellis [7] examined the effects of human-structure interaction on a simply supported concrete beam ($f_n = 18.68$ Hz) with a single individual. Similarly, Brownjohn [8] explored the effects of a single individual on a precast plank ($f_n = 3.16$ Hz) varying posture. Falati [9] advanced the previous studies by examining the effects of two people on a concrete structure. Yao et al. [10, 11] expanded the range of structural frequencies examined through the use of a testing rig with a single individual. These laboratory experiments provide additional evidence of the phenomenon but are limited in their direct application because they utilize only one or two people.

The experimental evidence indicates that the crowd behaves as a dynamic spring-mass-damper system attached to the supporting structure. Several analytical studies have been undertaken to provide guidance for modeling this type of combined system and to identify the appropriate dynamic properties of the system representing the crowd. Several numerical models have been developed to model the human body for civil engineering applications [9, 12, 13]. Dougill et al. [14] provides a detailed modeling theory that accounts for human-structure interaction for structures with a single dominant natural frequency. Yet, no guidance for incorporating the human-structure interaction into the design process had been presented prior to 2008.

In 2000, a Joint Working Group was formed with members from the Institution of Structural Engineers (IStructE), the Department for Transport, Local Government (DTLG), and the Regions and Department for Culture, Media and Sport (DCMS) in the United Kingdom. This Joint Working Group published comprehensive design guidance aimed specifically toward grandstands entitled “Dynamic Performance Requirements for Permanent Grandstands Subject to Crowd Action” [15]. Currently, this publication is the only to address the human-structure interaction phenomenon, recognizing that previous recommendations for grandstands with dense crowd loading and natural frequencies below 7 Hz gave “insufficient consideration to the nature of the loading or to the effects of the mechanical interaction between individuals and the structure” [15]. The recommendations for modeling are based on Dougill’s analytical results [14] which have been corroborated with experimental measurements from bobbing on a flexible test rig structure at the University of Manchester. Additional experimental results are desirable to further validate the modeling recommendations.

2.3 Overview of Experimental Study

The test structure described herein is critical to the planned experimental investigation of the effects of human-structure interaction. The test structure is specifically design to represent a range of dynamic properties representative of cantilevered grandstands. The planned study addresses how crowd characteristics, such as posture and location, combine with structural characteristics, such as frequency and mass, to influence the dynamic properties of the combined system. Several of the

limitations of previous experimental studies, as referenced above, are addressed in this study. One such limitation is the experimental consideration of a structure occupied by more than a single individual. In addition, this study is designed to investigate a wider range of natural frequencies of the structure as opposed to previous studies or experimental measurements which were limited to a single frequency of the constructed structure. The objectives of the experimental work are:

1. To experimentally identify the circumstances for which the effects of human-structure interaction should be considered because of its potential impact on serviceability assessment.
2. Provide experimental evidence of the influence of structure and crowd characteristics on the recommended dynamic parameters for an appropriate crowd model.

To accomplish these objectives, a cantilevered steel test structure was designed as shown in Fig. 2.1. The natural frequency of the empty structure can be varied between 4.35 and 6.25 Hz or higher through the relocation and addition of supports which fasten to the wide-flange shape support beams. The test structure accommodates a maximum of nine passive occupants in various postures and locations on a concrete plank decking surface. The constructed structure is shown in Fig. 2.2. Experimental testing is planned to determine the dynamic properties of the human-structure system and how it is influenced by the structural and crowd characteristics when the test structure is occupied.

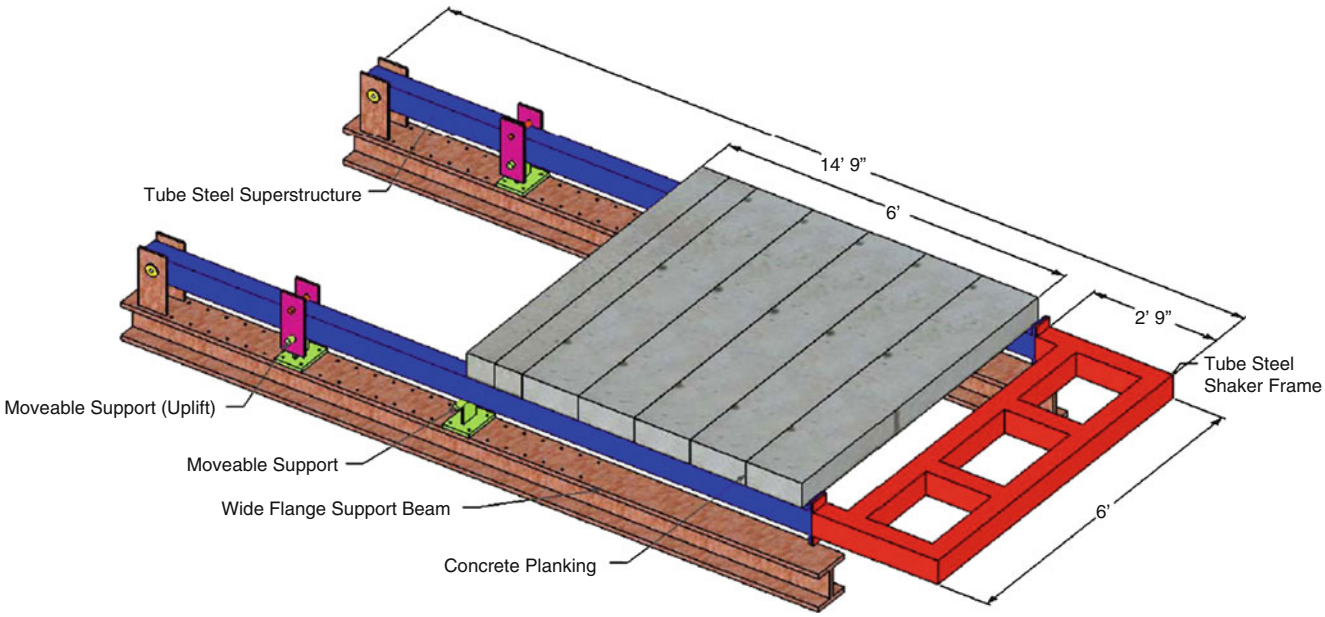

Fig. 2.1 Conceptual model of the cantilevered test structure

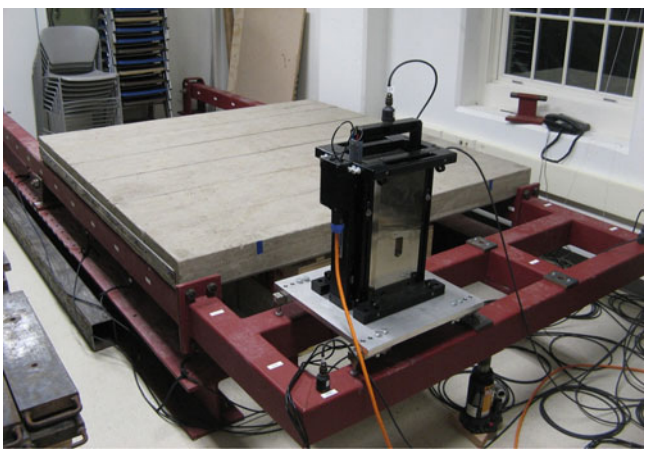

Fig. 2.2 As-built cantilevered test structure

This paper will describe how the conditions for the study are achieved through the design and construction of the test structure. A summary of the design and construction of a cantilevered test structure with a tunable fundamental natural frequency is presented first. The process of how experimental modal analysis, using shaker excitation and acceleration response, is employed to determine the dynamic properties and validate the finite element model of the structure is described.

2.4 Test Structure Design and Construction

This section describes how the required conditions for the experimental study are translated into design criteria implemented in the design and construction of the cantilevered test structure. The conditions to be met for the study include:

1. The test structure must safely accommodate small groups of individuals that have a combined mass which is in a desired proportional range to the mass of the empty structure.
2. The test structure must have dynamic properties that are representative of typical cantilevered grandstands.
3. The natural frequency of the test structure must be adjustable through the relocation and/or addition of supports.
4. Data collection techniques must yield reliable experimental data.

A detailed description of the geometry and layout of the test structure is given before addressing the specific design criteria.

2.4.1 Geometry and Layout

A cantilevered test structure is chosen for this study because cantilevers are widely used in assembly type structures, like stadiums, for the benefit of improved sightlines. However, they are often subject to vibration serviceability issues. The typical fundamental frequency range for cantilevered stadium sections is between 4 and 8 Hz [1], which can be achieved in a small scale experimental test structure. During the design phase a finite element model of the test structure was created in SAP2000 [16]. Initial design consisted of experimenting with various structural configurations, cantilever lengths, support conditions and material types. Controlling factors leading to the final design were the target frequency range, material stresses, and the deflection of the cantilever.

The final design resulted in a test structure with a fundamental frequency ranging from 4.35 to 6.25 Hz with only two supports and higher with the addition of a third support. The base dimensions of the structure measures 14.75′ long by 6′ wide. The structural configuration that results in a lower bound natural frequency of 4.35 Hz was achieved with a 6′ backspan and a 6′ concrete decking surface. The decking surface is constructed of reinforced concrete planks (12″W × 72″L × 5.25″D) spanning between the cantilevered sections. The last 2.75′ of the test structure's cantilever provides a mounting location for the electrodynamic shaker.

Increasing the natural frequency of the test structure from a range of 4.35–6.25 Hz is accomplished through shortening the length of the decking surface from 6′ to 4′ by moving a knife edge support in 4″ increments. The natural frequency of the test structure can be further increased though the addition of a support on the backspan of the structure as depicted in Fig. 2.3. The constructed connections are depicted in Fig. 2.4. A steel bushing connection in Fig. 2.4a was fabricated to represent an idealized pinned condition to restrain vertical, horizontal, and lateral movement. The pin was oiled to reduce friction and wear. The connection in Fig. 2.4b was designed and constructed to restrain vertical movement along the backspan of the test structure. A pin and eyebar connected to a knife edge support reduces deflection on the backspan of the test structure, increasing the natural frequency. The connection depicted in Fig. 2.4c is a knife edge support located at

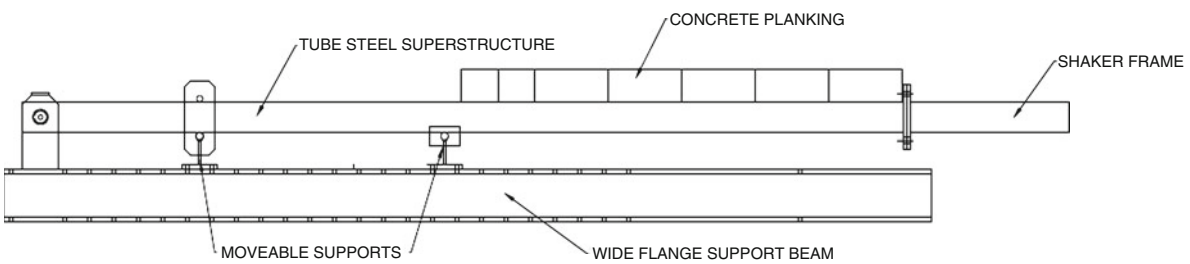

Fig. 2.3 Elevation view of the test structure

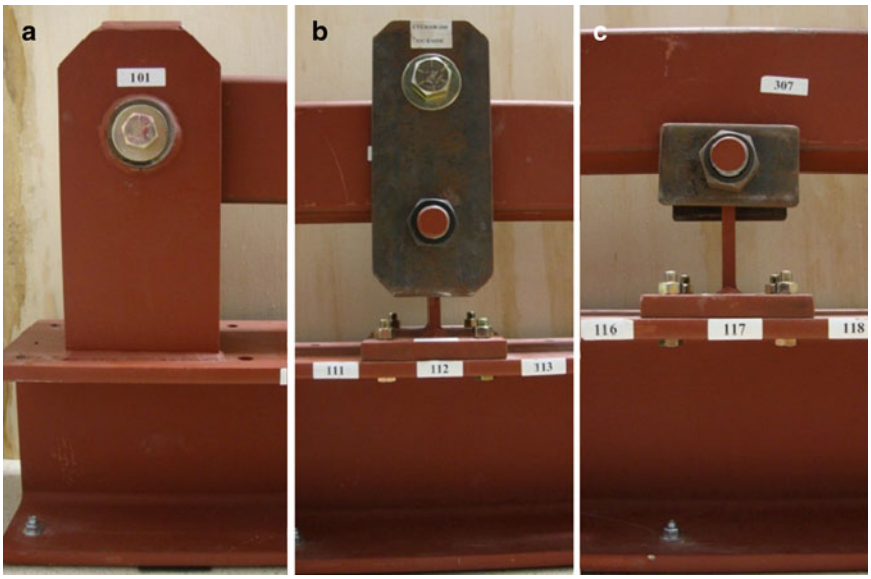

Fig. 2.4 (**a**) Pin support, (**b**) moveable backspan support, (**c**) moveable knife edge support

the transition between the backspan and the cantilever. This support will always remain in compression. Steel plates are attached to the knife support to reduce lateral movement of the tube steel superstructure.

The movable supports are bolted to wide-flange beams (W8 × 48) that have holes drilled along their top flange every 4″. The support beams were used for two main reasons. The support beams distribute the concentrated compressive and uplift forces from the supports along the length of the beam through the laboratory slab-on-grade. The support beams also provide a safe, consistent, and fast method for movement of the supports when adjusting the natural frequency of the test structure. The movable supports can be relocated and/or added by lifting the structure with a hydraulic bottle jack located under the tube steel frame at the end of the cantilevered decking surface, effectively removing the load from the supports temporarily.

2.4.2 Design and Materials

The test structure was designed using Load and Resistance Factor Design (LRFD) for static loading. ASCE 7–10: Minimum Design Loads for Buildings and Other Structures [17] recommends 100 psf live loading for stadium seating. This loading was compared to situations where nine individuals at 95th percentile weight (255 lb) were represented in the finite element model occupying the structure in loading scenarios that would be considered extreme for this type of experimental testing. An example of an extreme situation would be where all nine occupants are located within 3 ft of the end of the cantilevered decking surface; another would be unbalanced loading where all of the occupants would be located to one side of the structure. The ASCE 7–10 recommended static live loading of 100 psf on 36 ft^2 of the decking surface produced higher bending stresses and reaction forces than that of the "extreme" loading conditions described above.

The superstructure of the test structure was constructed of 5″ × 4″ × 3/16″ tube steel sections with a minimum yield stress of 46 ksi. These steel tubes provided the flexibility for a low fundamental frequency of the structure, yet still remained in the elastic bending range for the factored dead and live loads applied. However the deflection of the cantilever is quite noticeable when loaded to capacity. The deflection of the cantilever under design load condition is approximately 0.82 in., which is in the range of L/90 where L is the length of the cantilever. This is slightly more than the recommended cantilever deflection of L/140 [18]. The recommended deflection limit is not applicable as the structure is not attached to other systems which would be impacted and the deflection is not likely to be visually objectionable to the occupants as it is a test structure and not a regularly occupied structure. The 5″ × 4″ × 3/16″ tube steel sections are also considered compact eliminating the potential for local buckling; this is not the case for wide flange beams with a similar stiffness. The natural frequencies of vibration modes in the horizontal direction are increased with a higher moment of inertia in the lateral bending direction provided by the tube steel and the addition of the tube steel shaker frame attached to the end of the cantilevered decking surface.

Reinforced concrete planks (12″W × 72″L × 5.25″D) are designed to span from one tube steel cantilever to another, using a maximum of six planks to provide 36 ft^2 of decking surface for the occupants. The connection between the concrete

planks and the steel structure is a simple gravity connection. The decking surface was designed as reinforced concrete planking for the following reasons:

1. Additional mass was needed to achieve the lower bound of frequency at 4.35 Hz and the desired mass ratio range of 0.06–0.58.
2. Narrow planks without a mechanical connection to the steel structure limit the level of potential composite action of the cantilever.
3. Reinforced concrete planks are sufficiently rigid to resist excitation of local vibrations modes of the decking surface caused by occupants.
4. Planks can be added or removed to change the length of the cantilevered decking surface.

2.4.3 Occupancy and Mass Ratio

The test structure was designed to accommodate small groups of individuals in either standing postures or seated positions. It was determined that a test structure with an occupant capacity of nine people would provide additional insight into the human-structure interaction phenomenon when compared to previous experimental testing that used only one or two occupants on a structure. Previous research, along with the recommended modeling guidance, suggest that the relative size of the crowd compared with the size of the structure can be a factor in the level of interaction between the occupants and the structure [3, 15], this can be interpreted as a function of the crowd and structure mass.

Mass ratio is defined to be the ratio of the combined mass of the occupants to the mass of the empty structure [5]. A mass ratio of 0.25–0.75 is suggested for typical stadiums at full capacity [19]. Previous laboratory studies involving test structures used to investigate human-structure interaction had estimated mass ratios ranging from 0.067 to 0.431 [8, 20]. Further investigation of several in-service stadiums has shown that mass ratios vary between 0.27 and 0.63 at full occupancy based on ASCE 7–10 recommended live loading for stadium structures. For this study, the upper mass ratio was chosen to be roughly 0.60 when the test structure is at full capacity with nine occupants.

Knowing the desired mass ratio and number of occupants at full capacity, the weight of the empty structure is estimated by assuming an average weight of each occupant. Studies have indicated that the average weight of an adult is 180 lb [15]. Therefore, the weight of the empty test structure is designed to be 2,800 lb in order to achieve the desired mass ratio range. The platform size for the occupants is determined based on the space needed for an occupant to be in either a seated or standing position. An area of four square feet per occupant was deemed adequate.

2.5 Finite Element Model

The original finite element model used for the design of the test structure was created in SAP2000. The model was constructed of nodes and frame elements that represent the $5'' \times 4'' \times 3/16''$ tube steel members and $12'' \times 72'' \times 5.25''$ concrete planks as shown in Fig. 2.5. Nodes of the model are at locations of support conditions and accelerometer locations.

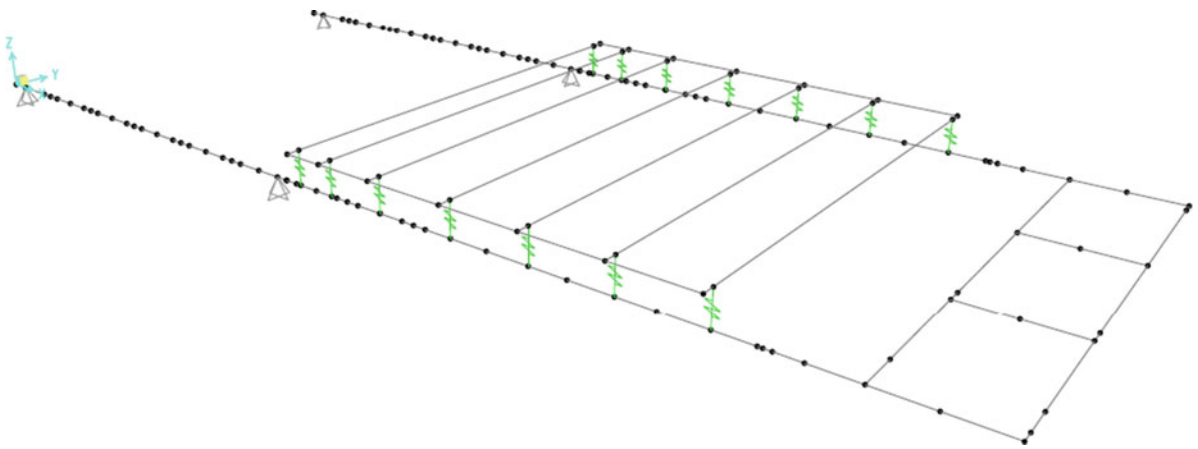

Fig. 2.5 SAP2000 finite element frame model

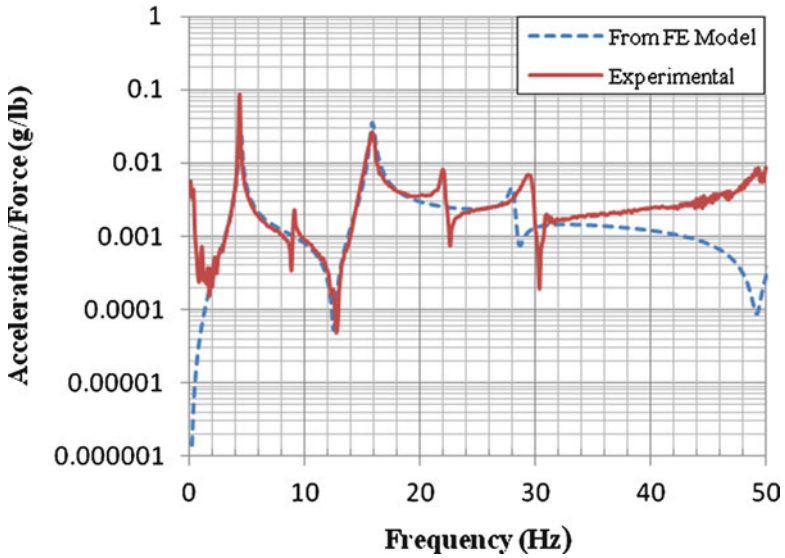

Fig. 2.6 Frequency response function (FRF) created from SAP2000 modal results and compared with the corresponding experimentally measured FRF

The wide flange support beams were not modeled in SAP2000 because they are a rigid base for the supports. During the modeling process, several assumptions were made when creating the original finite element model:

1. Pin connections of the as-built test structure are frictionless and allow free rotation.
2. The gravity connection between the concrete planks and the tube steel cantilever beams are best modeled as a pin connection.
3. Material properties from the AISC database in SAP2000 are representative of the materials used during actual construction.
4. The geometry of the as-built structure is identical to the geometry of the finite element model (no fabrication or installation errors).

The test structure was designed and constructed based on the finite element model and the above assumptions. Strength design of the structure is of the utmost concern for safety; however the dynamic properties such as natural frequency and modes shapes are also of particular interest in this study. SAP2000 is used to perform modal analysis to determine vibration modes of the modeled structure using Eigenvector analysis for undamped free-vibration modes and frequencies. The modal displacements at the accelerometer locations and natural frequencies of the modeled test structure are used to generate a series of analytical frequency response functions, illustrated in Fig. 2.6, to aid in the validation of the finite element model by comparison with experimentally measured frequency response functions from the as-built test structure.

2.6 Validation of Design

2.6.1 Experimental Testing

In order to better understand the behavior of the as-built test structure and validate the original finite element model created in SAP2000, dynamic properties of the empty test structure are determined using experimental modal analysis (EMA). EMA is based on the evaluation of the dynamic response of a structure due to a known excitation force. A swept-sine dynamic force is applied to the structure through the use of an electrodynamic shaker located on the end frame of the cantilever. The acceleration response of the structure is measured by accelerometers that are attached to the steel superstructure at various locations. The input force and the acceleration response are analytically combined to form a frequency response function in the eZ-Analyst data acquisition software [21]. From these response functions, modal properties such as natural frequencies, damping ratios, and mode shapes were estimated using curve-fitting techniques utilizing Vibrant Technology's ME'scopeVES 5.0 [22].

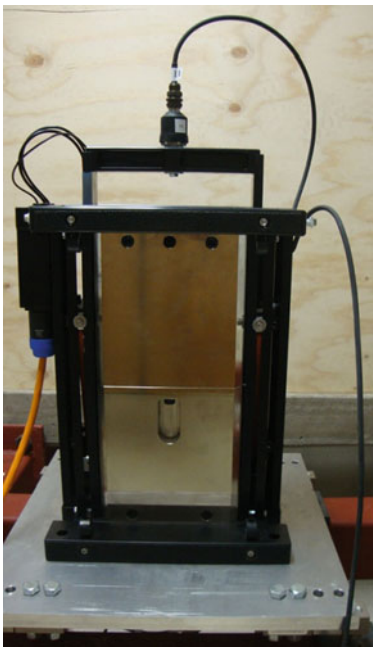

Fig. 2.7 Accelerometer attachment to the armature of the shaker

Ten PCB model 393A03 uniaxial seismic accelerometers are fastened using threaded steel studs at locations along the backspan and cantilever of the steel superstructure. The excitation source for cantilevered test structure is an APS Dynamics, Model 400 electrodynamic shaker. The sinusoidal input force from the shaker is calculated using the acceleration response and mass of the shaker armature. A PCB model 393A03 uniaxial accelerometer was attached to the armature to measure acceleration as shown in Fig. 2.7.

The data acquisition system for this study, an IOTech Wavebook 516E with WBK18 signal conditioning module, is connected to a computer and used in conjunction with eZ-Analyst software to output and collect real-time voltage signals. Amplified output voltages operate the shaker over a frequency range of 1–50 Hz in an 8 s time frame. The sampling rate for data collection is 128 samples/s corresponding to a frequency step of 0.125 Hz over a bandwidth of 50 Hz. The experimental data collection plan consists of collecting a minimum of three individual data sets for each experimental configuration of the empty test structure. Each of the data sets is a linear average of a minimum of three complete cycles of the electrodynamic shaker (24 s of data). The test structure was also loaded with steel weights to simulate an equivalent mass test from 500 to 2,000 lb in 500 lb increments. EMA was used to determine the modal properties associated with each configuration of the test structure and static deflections were measured along the backspan and cantilever.

2.7 Results

The modal parameters of the as-built test structure varied slightly from the analytical modal results of the original finite element model, despite the highest attention to detail and acceptable tolerances during the construction of the structure. The natural frequencies of the test structure determined from EMA were slightly higher than the natural frequencies predicted by the model. Two contributing factors to the inconsistency are the inappropriate modeling of the connections, and the slight imprecision in the cross-sectional properties of the structural steel sections.

The reinforced concrete planks were originally modeled as pin-connected to the tube steel since they bear directly on top of the cantilevered tube steel beams. However, an increase in frequency of the torsional mode of the structure indicates that the planks add stiffness to the second mode of vibration which is a torsional mode of the cantilevered section. The connection was adjusted in the FE model to a fixed connection as most modeling guidance suggests for vibration serviceability. However, the frequency of the torsional mode increased beyond that of the as-built structure. As a result, the plank connection to the cantilevered tube steel beam is modeled as a rotational spring to simulate the torsional behavior of the as-built test structure.

The finite element model was further modified by updating the cross sectional properties of the $5'' \times 4'' \times 3/16''$ tube steel to represent the actual dimensions of the tube steel that was used in the construction the test structure. The changes were

Table 2.1 Comparison of analytically predicted and experimentally measured natural frequencies

	6′ deck, 6′ cantilever		4′ deck, 5′ cantilever		4′ deck, 4′ cantilever	
Mode	FE model (Hz)	Experimental (Hz)	FE model (Hz)	Experimental (Hz)	FE model (Hz)	Experimental (Hz)
1	4.36	4.35	5.05	5.00	6.33	6.25
2	15.8	15.8	16.7	15.4	22.6	19.1
3	28.0	30.5	33.0	32.0	40.8	36.4

slight; resulting in deviations of a few thousandths of an inch from the AISC specified properties. This simple updating of cross sectional properties affected the natural frequency by approximately 0.1 Hz bringing it in line with the experimental results. The updated finite element model is able to satisfactorily represent the dynamic behavior of the structure for a range of support conditions for the empty structure and for each phase of the equivalent mass testing previously described. The FE model is also able to replicate the static deflection associated with the equivalent mass testing.

The natural frequencies identified in the FE model for the first three modes are compared to the experimentally determined natural frequencies in Table 2.1 for three configurations of the adjustable test structure. The comparison is reasonable for the first mode of vibration for all three configurations. The second and third modes are less critical for this study as the effect of human-structure interaction is likely to be more dominant in the first mode of vibration. In addition to the numerical comparison of natural frequencies, the frequency response functions analytically synthesized from the updated finite element model are compared to the experimentally measured frequency response functions. One such comparison is shown in Fig. 2.6. The initial comparison between the synthesized FRF and the experimental FRF is visual. Key features that should align are the location, magnitude, and slope leading to the peaks of the FRF. Further evaluation will be made by comparing the mode shapes of the finite element model to the experimental test data using the modal assurance criterion (MAC). Additional model updating is currently being pursued to further enhance the agreement of higher modes of vibration.

2.8 Summary

The design and construction of a cantilevered test structure has been described as it applied to the experimental investigation of the effects of human-structure interaction and its potential impact on serviceability assessment. The test structure is representative of a cantilevered grandstand with respect to its natural frequency and cantilever construction. This test structure has been specifically designed to allow for the relocation and/or addition of support conditions providing the ability to adjust the natural frequency. The design considerations pertaining to the planned experimental study and the associated design criteria have been presented. A FE model of the test structure has been created and updated. The dynamic properties of the test structure in its empty condition were determined using experimental modal analysis; this data was used in the preliminary validation of this finite element model. The test structure described herein is to be utilized in the experimental program currently underway investigating human-structure interaction.

References

1. Comer A, Blakeborough A, Williams MS (2010) Grandstand simulator for dynamic human-structure interaction experiments. Exp Mech 50 (6):825–834
2. Murray TM, Allen DE, Ungar EE (1997) Floor vibrations due to human activity, Steel design guide series, no. 11. American Institute of Steel Construction (AISC), Chicago
3. Sachse R, Pavic A, Reynolds P (2003) Human-structure dynamic interaction in civil engineering dynamics: a literature review. Shock Vib Digest 35:3–18
4. Lenzen KH (1966) Vibration of steel joist-concrete slab floors. AISC Eng J (6th Ser) 3:133
5. Ellis BR, Ji T (1997) Human-structure interaction in vertical vibrations. Proc Inst Civil Eng Struct B 122(1):1–9
6. Littler JD (1998) Full-scale testing of large cantilever grandstands to determine their dynamic response. In: Thompson PD, Tolloczko JJA, Clarke JN (eds) Stadia, arenas and grandstands. E and FN Spon, London, pp 123–134
7. Ellis BR, Ji T (1994) Floor vibration induced by dance-type loads: verification. Struct Eng 72(3):45–50
8. Brownjohn JMW (1999) Energy dissipation in one-way slabs with human participation. In: Proceedings of Asia-Pacific vibration conference, vol 1. Nanyang Technological University, Singapore
9. Falati S (1999) The contribution of non-structural components to the overall dynamic behavior of concrete floor slabs. Thesis, University of Oxford, Oxford

10. Yao S, Wright J, Pavic A, Reynolds P (2004) Experimental study of human-induced dynamic forces due to bouncing on a perceptibly moving structure. Can J Civil Eng 31(6):1109–1118
11. Yao S, Wright JR, Pavic A, Reynolds P (2006) Experimental study of human-induced dynamic forces due to jumping on a perceptibly moving structure. J Sound Vib 296:150–165
12. Sim JH (2006) Human-structure interaction in cantilever grandstands. Thesis, University of Oxford, Oxford
13. Ji T, Ellis BR (1995) Human actions on structures. Soc Earthquake Eng Civil Eng Dyn (SECED) Newsl (ICE) Autumn, 4–5
14. Dougill JW, Wright JR, Parkhouse JG, Harrison RE (2006) Human structure interaction during rhythmic bobbing. Struct Eng 84(22):32–39
15. Institution of Structural Engineers (2008) Dynamic performance requirements for permanent grandstands subject to crowd action, IStructE/DTLR/DCMS working group on dynamic performance and design of stadia structures and seating decks. Institution of Structural Engineers, London
16. SAP2000 (2011) Overview, Computers and Structures, Inc. http://www.csiberkeley.com/sap2000. Accessed 16 Sep 2011
17. American Society of Civil Engineers (2010) Minimum design loads for buildings and other structures. ASCE/SEI 7–10, Reston
18. American Institute of Steel Construction (2007) Steel construction manual, 13th edn. American Institute of Steel Construction, Chicago
19. Dougill JW (2005) Recommendations for design of grandstands subject to dynamic crowd excitation. In: Proceedings of the 6th European conference on structural dynamics (EURODYN 2005). European Association for Structural Dynamics (EASD), Munich, pp 491–496
20. Firman RJ III (2010) Investigating the effects of various crowd characteristics on the dynamic properties of an occupied structure. Thesis, Bucknell University, Lewisburg
21. IOtech eZ-Series (2011) Analysis software for IOtech devices – National instruments. http://sine.ni.com/nips/cds/view/p/lang/en/nid/208342. Accessed 13 Sep 2011
22. Vibrant Technology, Inc. (2011) Modal analysis, ODS, acoustic, and finite element analysis software (ME'scope). http://www.vibetech.com/go.cfm/enus/content/index. Accessed 13 Sep 2011

Chapter 3
Experimental and Numerical Studies of the People Effects on a Structure Modal Parameters

Anna Cappellini, Stefano Manzoni, and Marcello Vanali

Abstract In this paper the problem of human structure interaction is faced considering the case of a lightly damped steel staircase. People are a source of excitation forces and an added mass for structures but not only. It is well known human presence affects damping properties too.

The aspect authors are interested in is the dependency of structure modal parameters on people presence, just due to the abovementioned aspect. Experimental measurements on a steel stair walkway, which is a lowly damped civil structure, have shown that heavy damping ratio value changes are experienced due to the presence of people. Particularly, the higher people number is, the higher the damping ratio associated to the very first modes increases.

This aspect has been then studied by developing a numerical model, partly based on modal approach, able to describe people effect on this structure. Such a model is intended to show how the structure first eigenfrequencies and non-dimensional damping ratios are changed by people presence.

The model describes people as mass-damper-spring systems.

A model validation is provided by comparing its results to the experimental data collected thanks to the stair tests. Then such a model is exploited to fully investigate people influence on lowly damped structures.

Keywords Modal analysis • Human structure interaction • Vibration serviceability

3.1 Introduction

In the last years a great attention has been paid to all problems related to vibration serviceability issues of civil structures. The problem has come to great evidence in some famous cases like the millennium bridge [1] in London, but many other studies are reported. Stadia serviceability issues are deeply investigated [2–4] as long as pedestrian walking bridges and stairs [5]. International standards and codes (ISO 10137 [6], EUROCODE EN [7], etc.) exist to the purpose of both designing and evaluating the structure dynamics under the crowd action and they are the natural reference when vibration serviceability is assessed. Guidelines from British and Canadian engineering institution exist too.

At the design stage usually standard recommendations are given in terms of natural frequencies in order to avoid resonances in the frequency range mostly excited by the structure occupants (0.5–5 Hz), numerical models are given to foresee the people forcing on the structure and therefore to compute the vibrations levels that will be attained during the structure life.

Even if a reliable structural model is set-up in terms of resonance frequencies a large uncertainty is always present when damping coefficients are dealt with, making it very difficult to foresee the operational vibration levels due to people structure interaction at the design stage.

This is true even if an experimental modal analysis of the structure is performed to validate the numerical model. In effects it has been shown [8] that people presence on the structure greatly affects the damping coefficients according to the

A. Cappellini • S. Manzoni
Dipartimento di Meccanica, Politecnico di Milano, Milan, Italy

M. Vanali (✉)
Dipartimento di Ingegneria Industriale, Università degli studi di Parma, Parma, Italy
e-mail: marcello.vanali@polimi.it

J.M. Caicedo et al. (eds.), *Topics on the Dynamics of Civil Structures, Volume 1*,
Conference Proceedings of the Society for Experimental Mechanics Series 26,
DOI 10.1007/978-1-4614-2413-0_3,

number of people on the structure and according to people behaviour too. A simple experimental modal analysis test on the structure itself will provide an accurate estimate of the natural frequencies and structural damping, but will not take into account the added damping coming from the structure occupants.

In this paper the problems of people effects on structural dynamics are faced at first exploiting the experimental approach and then trying to develop a first numerical model to interpret the obtained results. A lowly damped steel structure is considered, this is a scultoric staircase installed in a new high rise building and linking the ground floor to the second floor restaurants. In order to evaluate the vibration serviceability issues a number of dynamic tests have been commissioned and carried out. At first a modal analysis of the structure itself has been carried out both by forcing the structure with an hydraulic actuator (Experimental modal Analysis (EMA) [9]) and by exploiting the ambient vibrations in an Operational Modal Analysis (OMA) approach [10, 11] allowing for a comparison and validation of the OMA results. Then tests have been carried out with people walking on the staircase and the same OMA approach could be exploited to assess the stair modal parameters with people on it, therefore quantifying the effect of humans on both proper frequencies and damping coefficients. A simple model describing the human structure interaction has then been set-up. In order to obtain a first model capable of describing the people effects, a preliminary stationary model was used. A brief description of the model and the first results are reported in Sect. 3.5.

In the next paragraph a description of the structure under test is presented together with the measurement set-up, then the modal analysis results referring to the structure alone are presented comparing OMA and EMA modal parameters. In the following sections the experimental results of the people structure interaction results are then shown and commented together with the developed model.

3.2 Structure Under Test

The structure under test is a cantilevered steel staircase installed in a recently built high rise building in the northern part of Spain. The lower part of the staircase is rigidly connected to the ground via bolts in the floor, while the upper part is connected to the second floor. At the moment tests were performed all the marble glass and carbon fibre finishing were not yet installed on the stair and their mass has been simulated using a number of steel plates and bars welded to the main structure.

Figure 3.1 shows a picture of the staircase with the installed added masses during the days of test. A FEM model of the structure was available and model results stated that the first resonant frequency should be around 7.7 Hz, with an associated modal shape showing mainly vertical displacements. Other resonant frequencies are located at 13.7 and 17.2 Hz always according to the model results. In order to validate model results and estimate the modal damping coefficients a proper measurement set-up has been designed.

Fig. 3.1 Picture of the considered staircase

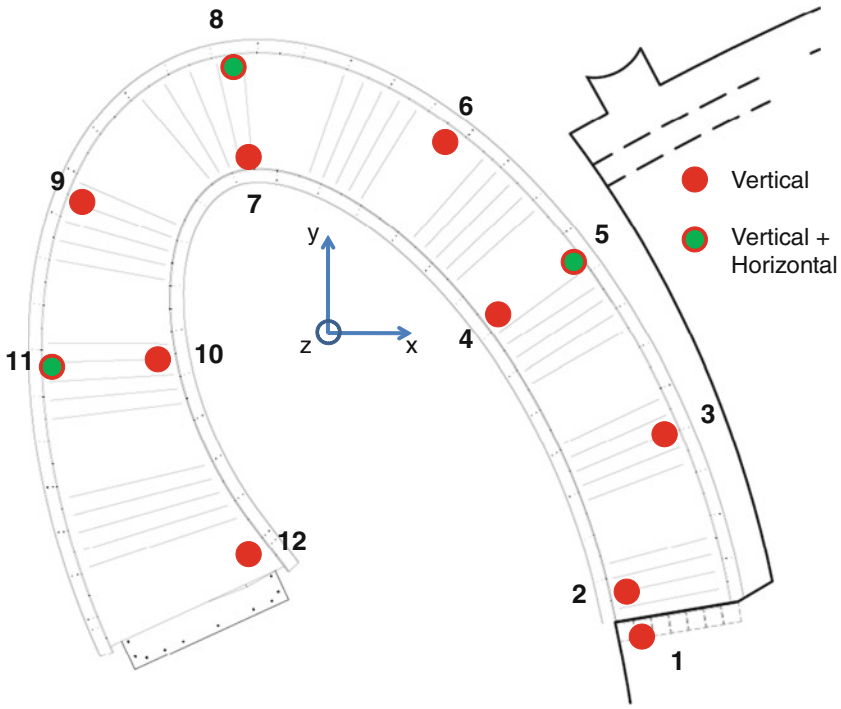

Fig. 3.2 Measurement points on the staircase

Table 3.1 Sensors main features

Sensor	Meas range (g)	Frequency range (Hz)	Sensitivity (V/g)
Piezo Acc PCB 393B12	0.5	0.1–500	10
Piezo Acc PCB 393A03	5	0.1–1,000	1

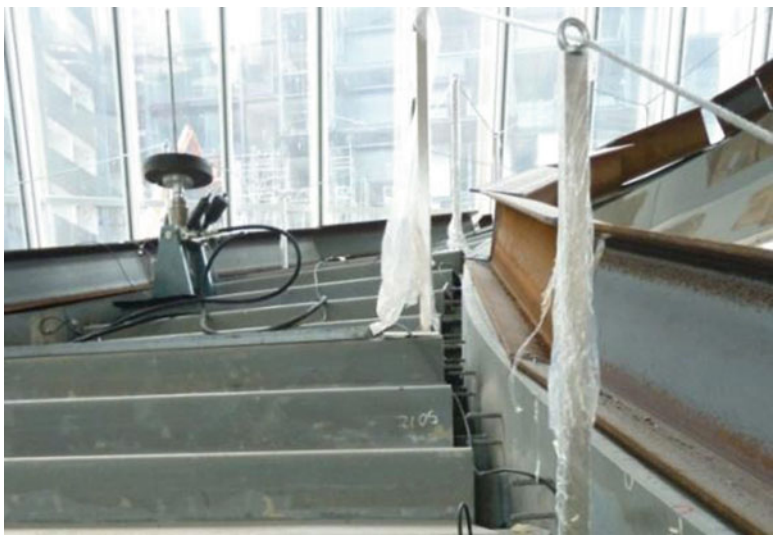

Fig. 3.3 Inertial forcing using hydraulic actuator

Figure 3.2 shows the measurement points installed on the staircase, each point was instrumented using high sensitivity low noise Piezo-accelerometers acquired with a 24 bit A/D system carrying built in anti aliasing filters. The accelerometers main features are reported in Table 3.1.

The selected sensor have proven to be adequate for both ambient and forced vibration testing having a very low noise floor and an adequate full scale value.

In order to provide meaningful forcing to the stair an hydraulic actuator has been used. The actuator has been placed on the stair in two different positions, moving an inertial mass of 70 kg (Fig. 3.3). As the expected damping values were not too high, this is mainly a steel structure, a band limited white noise has been selected as the forcing signal allowing to complete

all testing in a reasonable amount of time. In all cases the white noise signal was filtered in the band 4–35 Hz and 3,600 s time histories were acquired. The forcing band was chosen on the basis of some preliminary ambient vibration testing.

Figure 3.3 shows a picture of the hydraulic actuator installed on the staircase. Two different test set up have been used; in the first test set-up the actuator has been placed in point 8, referring to Fig. 3.2 while in the second the actuator has been placed in position 11, always referring to the same figure. The force transmitted to the structure has been estimated by measuring the inertial mass acceleration using a PCB capacitive accelerometer directly placed on the moving mass.

All acquired data have been processed in order to obtain the frequency response functions (FRF) between the forcing and the accelerations, and then the computed FRFs have been processed using the Polyreference least square frequency domain algorithm [10, 11] to estimate the principal modal parameters. Exploiting the same measurement set-up 3 h of ambient vibrations have been recorded and processed in order to estimate the modal parameters using an Operational Modal Analysis approach.

A resume of the modal parameter identified during the tests for the structure alone is given in the next paragraph.

3.3 Modal Analysis of the Structure Alone

Three different forced testing session have been carried out and analyzed together with 3 h of ambient vibration recordings. An example of the measured FRFs is given in Fig. 3.4, together with the estimated PSD from ambient vibration measurements.

The first three vibration modes are clearly identifiable. All the FRFs and PSDs have been processed using the polyreference least square method and the results are summarized in Table 3.2 in terms of frequencies.

The same results are summarized in Table 3.3 in terms of damping coefficients.

As can be seen in Tables 3.2 and 3.3 results between all forced testing are in good agreement; moreover the results obtained exploiting ambient vibrations are practically the same as the forced ones, even in terms of damping which is usually the most discordant value. The computed MAC values between homologous mode shapes in the different identifications are almost 100%.

These results serve as the reference value to both set-up the staircase numerical model and to assess people effects on the dynamic behaviour. The latter will be described in the next paragraph.

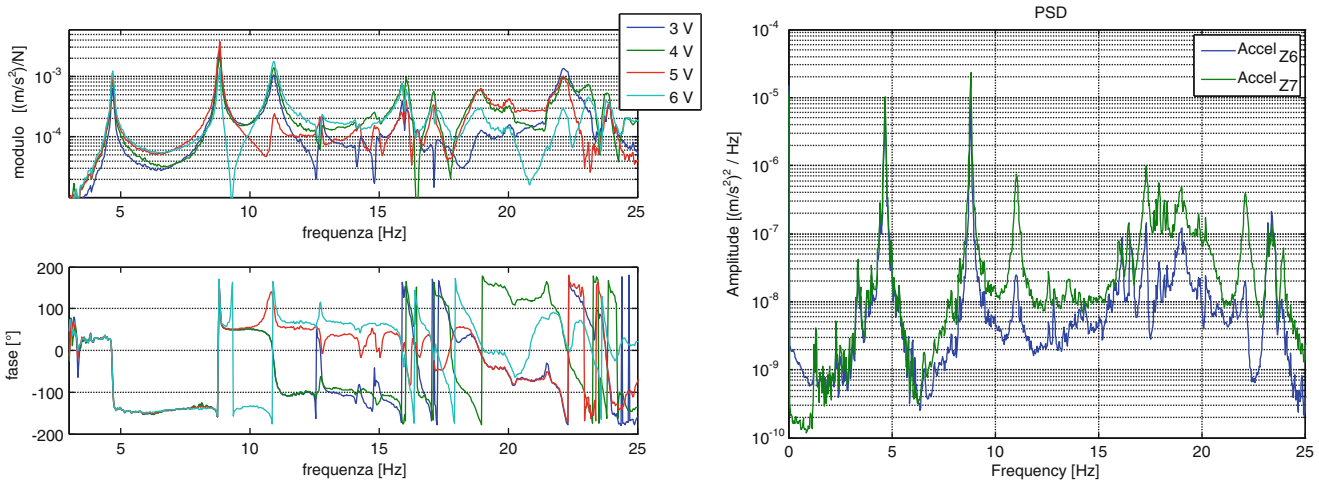

Fig. 3.4 Example of the measured FRFs, forcing in point 11, response in points 3,4,5,6 and the PSD estimated from ambient vibration in points 6 and 7

Table 3.2 Identified frequencies for the first three modes

Case Mode N	Forcing in 11 (Hz)	Forcing in 8 (Hz)	Forcing in 8 2° (Hz)	Operational (Hz)
1	4.69	4.69	4.68	4.68
2	8.82	8.82	8.80	8.82
3	10.94	10.91	10.95	11.03

Table 3.3 Identified damping for the first three modes

Case Mode N	Forcing in 11 %rc	Forcing in 8 %rc	Forcing in 8 2° %rc	Operational %rc
1	0.43	0.40	0.45	0.38
2	0.28	0.27	0.29	0.18
3	0.83	0.85	0.77	0.69

3.4 People Effects on the Modal Parameters

In order to asses vibration serviceability issues for the staircase a series of tests have been executed. The same data have then been used to estimate the modal parameters when the structure was occupied by people.

Test planning has been developed considering a maximum stair occupation of 1 person per square meter, as the staircase surface is approximately 40 m^2, the maximum load taken into account has been 44 people walking together on the staircase. In order to have an idea of the people number influence on the vibration levels and modal parameters a second set of test has been carried out having half of the people walking on the structure.

At first the PSD of the acceleration in the point showing maximum vibration level is shown in Fig. 3.5 for all the considered test cases (empty, 20 people, 40 people).

Looking at the curves in Fig. 3.5, it can be noticed that the identified peaks in the case of people occupancy (red and green lines) are slightly shifted to the left, probably due to the people added mass effects, moreover the peaks seem to be broader, indicating a change in the damping coefficients too.

The data have been processed using the Polyreference least square algorithm to extract the modal parameters and the obtained results are given in the following Table 3.4 in terms of frequencies.

Looking at all values in Table 3.4 the slight decrease in the frequency value is confirmed going from the empty situation to the 20 people one, if the 20 and 40 people cases are compared the identified frequencies are almost the same, moreover a slight increase in modes 2 and 3 frequencies is experienced in the 40 people case even of moderate entity. Results concerning the identified damping coefficients are reported in Table 3.5.

As it can be seen from the values in Table 3.5 a huge increase in the damping value identified is experienced when passing from empty stair conditions to occupied ones. First and second vibration mode damping coefficients are the ones experiencing the highest changes. Damping with 40 people is four times higher than the correspondent value with the empty stair; value with 20 people is two times the empty one.

In the next section the experimental results will be used to set-up a first model of the structure and people.

3.5 Numerical Model

To have a first model of the human-structure system, Krenk's approach [12] was used. In this model the people were considered to be stationary and integral to the structure. The model is therefore limited at the start and is only a starting point for the development of subsequent models. The same, however, was used to verify the compatibility between the experimental and numerical results in terms of change in natural frequency and damping.

According to Krenk's approach, the equation of motion (physical quantities) for the whole system can be expressed as:

$$M\ddot{u}(t) + C\dot{u}(t) + Ku(t) = f(t)$$

$$[-M\omega^2 + jC\omega + K]u = f$$

Using a modal representation,

$$u(t) = U\xi(t)$$

$$m\ddot{\xi}(t) + c\dot{\xi}(t) + k\xi(t) = q(t)$$

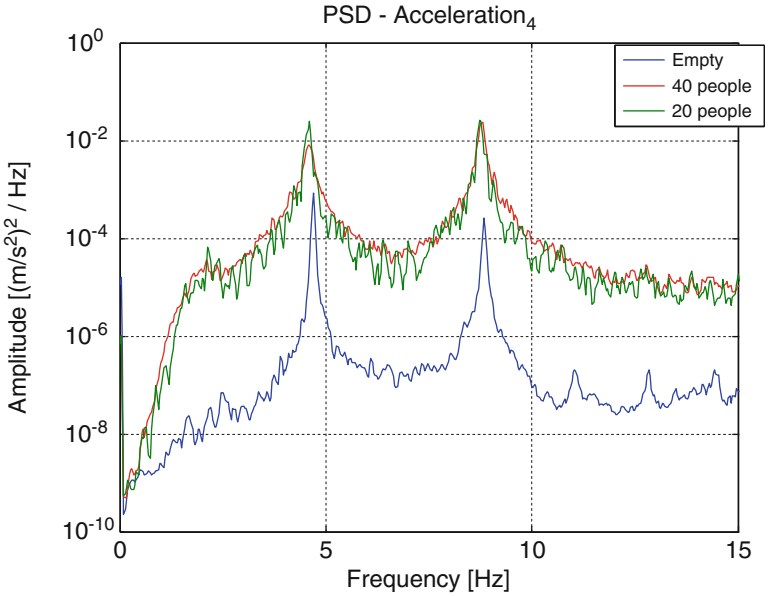

Fig. 3.5 Vertical acceleration PSD in all considered test cases

Table 3.4 Modal frequencies in all test cases

Case	First mode (Hz)	Second mode (Hz)	Third mode (Hz)
Empty stair	4.68	8.82	11.03
20 people	4.58	8.74	10.52
40 people	4.58	8.78	10.56

Table 3.5 Damping coefficients in all test cases

Case	First mode %rc	Second mode %rc	Third mode %rc
Empty stair	0.38	0.18	0.69
20 people	0.84	0.48	0.55
40 people	2.10	0.99	0.32

Where the modal system matrices are defined by,

$$m = U^T M U, \quad c = U^T C U, \quad k = U^T K U, \quad q = U^T f$$

normalizing the mode shape vectors to unit modal mass

$$m_j = u_j^T M u_j = 1, \quad k_j = u_j^T K u_j = \omega_j^2$$

And assuming $\boldsymbol{c}$ to be diagonal

$$c_j = u_j^T C u_j = 2\zeta_j \omega_j$$

It is possible to obtain n independent equations

$$[\omega_j^2 - \omega^2 + 2i\zeta_j \omega \omega_j]\xi_j = q_j$$

In terms of original variables

$$u = G(\omega) f$$

And

$$G(\omega) = U[\omega_j^2 - \omega^2 + 2i\zeta_j\omega\omega_j]^{-1}U^T = \sum_{j=1}^{n} \frac{u_j u_j^T}{\omega_j^2 - \omega^2 + 2i\zeta_j\omega\omega_j}$$

Introducing local elements each one able to introduce a force

$$f(\omega) = H(\omega)u(\omega)$$

The modified equation of motion becomes

$$\left[-M\omega^2 + jC\omega + K + WHW^T\right]u = [G^{-1}(\omega) + WHW^T]u = f$$

where $W = [w_1, \ldots, w_m]$ represents the connection of n elements and w_k identifies the connection of each element to the structure.

The new frequency response function can be expressed by the Woodbury matrix identity

$$(A + UCV)^{-1} = A^{-1} - A^{-1}U(C^{-1} + VA^{-1}U)^{-1}VA^{-1}$$

as

$$G_H = [G^{-1}(\omega) + WHW^T]^{-1} = G - GW(H^{-1} + W^TGW)^{-1}W^TG$$

The discrete elements (human bodies, $H(\omega)$) were modeled as apparent masses according to Matsumoto and Griffin [13] models:

$$H(\omega) = -M_a\omega^2$$

Two of the models used in Matsumoto and Griffin work were considered. Figure 3.6 shows the considered models

$$Model\ 1a : M_{1a}(i\omega)\frac{m_1(ic_1\omega + k_1)}{(-m_1\omega^2 + ic_1\omega + k_1)}$$

$$Model\ 2a : M_{2a}(i\omega)\frac{(ic_1\omega + k_1)\{m_1(-m_2\omega^2 + ic_2\omega + k_2) + m_2(ic_2\omega + k_2)\}}{\{-m_1\omega^2 + i(c_1 + c_2) + (k_1 + k_2)\}(-m_2\omega^2 + ic_2\omega + k_2) - (ic_2\omega + k_2)^2}$$

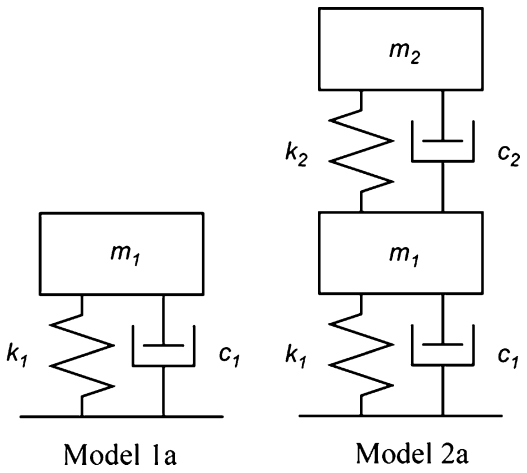

Fig. 3.6 Schematic expressions of models used in this study

Table 3.6 Optimized modal parameters for the mean normalized apparent masses

	Stiffness (Nm^{-1} kg^{-1})		Damping (Nsm^{-1} kg^{-1})		Mass (no unit)	
Case	k_1	k_2	c_1	c_2	m_1	m_2
Model 1a (standing)	1.34×10^3	–	5.16×10^1	–	1.03×10^0	–
Model 2a (standing)	4.39×10^3	5.53×10^2	3.71×10^1	1.18×10^1	5.74×10^{-1}	3.94×10^{-1}
Model 1a (one leg)	5.08×10^2	–	1.75×10^1	–	8.98×10^{-1}	–
Model 2a (one leg)	6.66×10^2	6.07×10^2	2.90×10^1	8.81×10^0	5.13×10^{-1}	4.22×10^{-1}

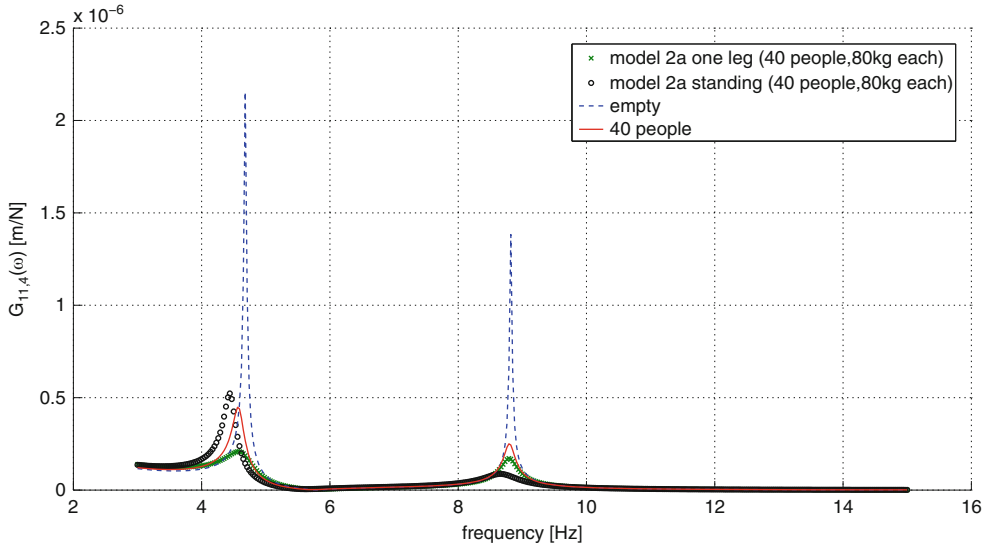

Fig. 3.7 Model-experimental comparison

The coefficients were chosen as the optimized model parameters determined by Matsumoto and Griffin for subjects in a normal standing posture and in a one leg posture and are reported in Table 3.6.

Figure 3.7 shows an example of the obtained results in terms of FRF. The figure shows the results for model 2a. The results of the model 1a are similar. As it can be seen from the figure, there is good agreement between numerical and experimental, especially for the low-frequency mode.

As it can be noted, the model, although developed assuming standing people, is able to give good results in terms of identification of the variation of modal parameters of a light and little damped structure. This is a good starting point for the development of a subsequent and more accurate model. A structure of this type, in fact, in operating conditions may be subject to problems of safety and comfort for people. So there is interest in the possibility of developing a simple model capable of predicting the effects of the human-structure interaction.

3.6 Concluding Remarks

In this paper the problem of people effects on the modal parameter of a lowly damped civil structure has been faced. The considered test case has been a steel staircase installed in a new building. The first part of the work dealt with the modal analysis of the structure itself. The problem has been approached by means of a number of forced vibration tests and also applying operational modal analysis techniques to a set of ambient vibration recordings. Results of both tests were in good agreement and allowed to extract the modal parameters of the first three resonant modes of the structure alone. Tests have then been carried out demonstrating that the people effect on structural damping is not neglectable and then the obtained results have been used to verify a numerical model of the people structure interaction. Even with the use of a model limited by the assumption of having people standing on the structure, good results were obtained in terms of identification of changes in modal parameters caused by the presence of people. The results obtained are therefore a good basis for the future development of a more accurate model.

References

1. Strogatz SH, Abrams DM, McRobie A, Eckhardt B, Ott E (2005) Theoretical mechanics: crowd synchrony on the Millennium Bridge. Nature (London) 4383:43–44
2. Caprioli A, Vanali M (2009) Comparison of different serviceability assessment measures for different events held in the G. Meazza Stadium in Milano. In: Proceedings of the 27th international modal analysis conference. 09/2/2009-12/2/2009, Orlando, pp 1–8
3. Caprioli A, Reynolds P, Vanali M (2007) Evaluation of serviceability assessment measures for different stadia structures and different live concert events. In: Proceedings of the 25th international modal analysis conference, Orlando
4. Reynolds P, Pavic A (2005) The dynamic performance of sports stadia under crowd dynamic loading at concert events. In: Structural dynamics EURODYN 2005. Millpress, Rotterdam, pp 473–479
5. Rebelo C et al (2010) Cable tensioning and modal identification of a circular cable-stayed footbridge. Exp Tech 34(4):62–68
6. ISO 10137(1992) Bases for design of structures – Serviceability of buildings against vibration
7. Eurocode EN(1990) Basis of structural design 1990, non c'è altro da aggiungere
8. Reynolds P, Pavic A, Ibrahim Z (2004) Changes of modal properties of a stadium structure occupied by a crowd. In: Proceedings of 22nd international modal analysis conference, Orlando
9. Ewins J (2001) Modal testing: theory, practice and application, 2nd edn. Taylor and Francis Group, London
10. Peeters et al (2004) The polyMAX frequency-domain method: a new standard for modal parameter estimation? Shock Vib 11(3–4):395–409, IOS Press, ISSN 1070-9622 (Print) 1875-9203 (Online)
11. Peeters B, Vanhollebeke F, Van der Auweraer H (2005) Operational PolyMAX for estimating the dynamic properties of a stadium structure during a football game. In: Proceedings of 23rd international modal analysis conference, Orlando
12. Krenk S (2007) Dampers on flexible structures. In: Proceedings of semi–active vibration suppression – The best from active and passive technologies. CISM, Udine
13. Matsumoto Y, Griffin MJ (2003) Mathematical models for the apparent masses of standing subjects exposed to vertical whole-body vibration. J Sound Vib 260(3):431–451

Chapter 4
A Refined Model for Human Induced Loads on Stairs

Michael Kasperski and Benjamin Czwikla

Abstract The tendency in modern architecture to lightweight and slender design of pedestrian structures is leading to an increased susceptibility to vibrations. Correspondingly, the evaluation of serviceability of pedestrian structures against vibrations due to human induced loads has gained more and more importance. Studies investigating corresponding action effects, usually focus on locomotion forms performed on a plane surface, e.g. jumping, running, walking. Information on the loads induced by ascending or descending stairs is scarce. In [1] a load model is presented which is based on a perfect repetitive single-foot load pattern leading to integer harmonic load contributions. Differences in the locomotion parameters for the left and the right foot are not considered leading to a loss of important information.

Based on experiments with a stair test section, this study investigates the load process due to descending and ascending stairs including the imperfections in the locomotion parameters. The dimension of stair rise and tread depth may have an influence on the harmonic load amplitudes. This is analyzed by experiments with different stair geometries. The paper discusses the random deviations in the locomotion process which may lead to additional intermediate harmonic load contributions. Furthermore, the randomness in the vertical load amplitudes in regard to the basic frequency content is analyzed.

Keywords Human-induced loads • Biodynamic • Staircases

Nomenclature

v_s	Walking speed
l_s	Step length
f_s	Step frequency
F(t)	Force depending on time
$F_1(t)$	Footfall trace induced by one foot
T_1	Contact period of one foot
t	Time
t_{dsp}	Duration of double stance phase
G	Body weight
T_s	Step period
s	Stair rise
a	Tread depth
a_0	Constant load share
a_n	Fourier coefficient for cosine contributions
b_n	Fourier coefficient for sine contributions
c_n	Harmonic load amplitude

M. Kasperski • B. Czwikla (✉)
Department of Civil and Environmental Engineering Science, Research Team EKIB,
Ruhr-University Bochum, Bochum 44780, Germany
e-mail: benjamin.czwikla@rub.de

J.M. Caicedo et al. (eds.), *Topics on the Dynamics of Civil Structures, Volume 1*,
Conference Proceedings of the Society for Experimental Mechanics Series 26,
DOI 10.1007/978-1-4614-2413-0_4,

n Harmonic
φ_n Phase
f_{ds} Step frequency of one double step
f_r Step frequency for the right foot
f_l Step frequency for the left foot

4.1 Introduction

The field of dynamic excitation of structures induced by walking or running persons has become a significant research topic during the last recent years. However, most of the research into walking or running deals with the locomotion in the plane. The research on loads induced by ascending or descending stairs is scarce, although in recent years problems with vibrating stair constructions have occurred.

The basic biomechanics for descending or ascending a stair differ from that for walking or running in the horizontal plane by two aspects. The first obvious aspect is the height difference between two consecutive steps, which influences the basic pattern of the load time history. The second aspect is the fixed step length forced by the geometry of the respective stair. Hence, the individual walking speed on a specific stair is only influenced by the step frequency:

$$v_s = l_s \cdot f_s \tag{4.1}$$

One of the few papers on human-induced loads on stairs has been published in 2001 by Bishop and Kerr [1]. The load time history of a single foot is measured for the fourth step of a stair with seven steps. The load time history of a single step and the corresponding step frequency are obtained applying the so-called biomechanical closure, i.e. by demanding that the integral of the force over the step period has to equal the body weight. Two basic patterns have to be distinguished, namely walking and running. The fundamental definition for walking is that at least one foot is in contact with the ground. Additionally, there is a shorter or longer phase where both feet are in contact with the ground. Correspondingly, these two phases can be named single stance and double stance phase. The characteristic feature for the locomotion form running is the existence of a flight phase, i.e. a phase where none of the 2 feet is in contact to the ground. The biomechanical closure for walking specifies the load time history during a single step as follows:

$$F(t) = \begin{cases} F_1(t) + F_1(T_1 - t_{dsp} + t) & t \le t_{dsp} \\ F_1(t) & t_{dsp} < t \le T_1 - t_{dsp} \end{cases} \tag{4.2}$$

The duration of the double stance phase is obtained by demanding that the integral over the period T_1-t_{dsp} equals the body weight G:

$$\int_{t=0}^{T_1 - t_{dsp}} F(t)\, dt \stackrel{!}{=} G \tag{4.3}$$

The corresponding step period and step frequency become:

$$\begin{aligned} T_s &= T_1 - t_{dsp} \\ f_s &= 1/T_s \end{aligned} \tag{4.4}$$

For running, F(t) simply equals $F_1(t)$ and t_{dsp} in (4.2) becomes negative and corresponds to the duration of the flight phase. It is important to note that a mixed form – as stated by Bishop and Kerr – does not exist, i.e. if there is no flight phase, the locomotion form is walking, if there is a flight phase, the locomotion form is running.

The biomechanical closure has to assume that there is no difference between the load time histories induced by the left and right leg. However, as has been shown for walking [2], almost every person has a stronger and a weaker leg which influences the walking parameters step length and step frequency.

The actual study exclusively aims in gathering the basic information for a probabilistic load model which later can be used in the scope of simulations. Therefore, three independent experiments have been performed. The first tests only monitor the loads induced by a single foot for walking a single step up or down. The second and main tests monitor the loads induced by walking on the extension of an existing stair. Basic information on these two tests is summarized in Sects. 4.2 and 4.3, respectively. The question arises, if the stair geometry will have an influence on the load amplitudes. Therefore, a third

experimental setup is created which is summarized in Sect. 4.4. Walking parameters and the differences between the left and the right foot are discussed in Sects. 4.5, 4.6, 4.7 and 4.8. In Sect. 4.9, the observed load amplitudes in the first three harmonics are presented and compared to the findings of Bishop and Kerr. The influence of the stair geometry on the harmonic load amplitudes for ascending a stair is discussed in Sect. 4.10.

4.2 Basic Biomechanics

The basic idea of the first series of experiments is it to measure the load time history of a single foot to identify the basic differences between ascending and descending. The forces are measured with a multicomponent force plate 9287 by Kistler (Fig. 4.1). This device consists of a stiff cover plate which is supported by four three-component force sensors. The resulting force F_R is separated into the three orthogonal force components F_x, F_y and F_z. Additionally, the position of the effective load in the x-y-plane can be obtained.

A wooden construction is placed on the force plate. The height of the construction plus the height of the force plate add up to 16 cm. The depth of the step is 32 cm. This geometry corresponds to the existing stair of the second test and appears on the edge of the German recommended values for stair geometries. The second step is obtained by a wooden frame with a height of 32 cm which is simply supported on the ground and has no contact to the force plate.

The first series of experiments is based on eight persons, males and females. A single run consists of five phases. During phase one, the subject climbs the force plate and remains there almost motionless for a few seconds. This phase allows measuring the body weight. The next four phases measure the left and the right foot for ascending and descending. All time series are normalized with the body weight.

Figure 4.2 shows the basic single foot load pattern for the locomotion form walking in the horizontal plane. This load pattern shows five characteristic points which can be explained by the chronology of a single step. The first characteristic point (A) shows the beginning of a single step where the heel is attached on the ground. The first maximum (B) marks the point of transferring the whole weight onto the leading leg. Then, the knees will be bended and the opposite leg swings to the front (C) before pushing oneself off with the toes which leads to the second maximum (D). The last characteristic point marks the end of the ground contact of the corresponding foot (E).

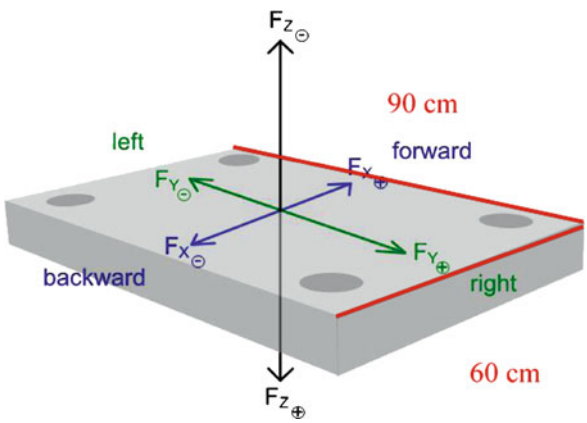

Fig. 4.1 Definition of the load components of the Kistler multicomponent force plate 9287 [4]

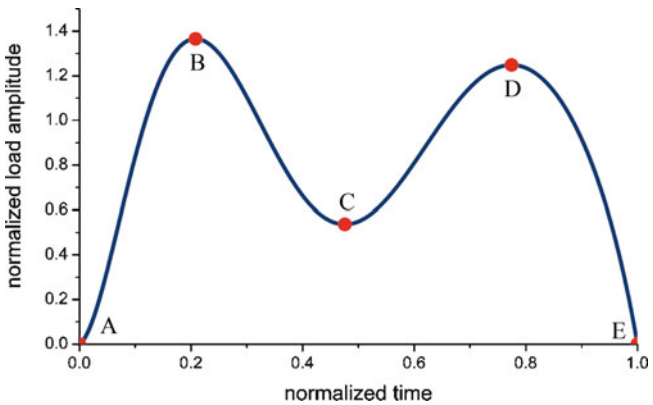

Fig. 4.2 Normalized single foot load pattern for walking in the horizontal plane

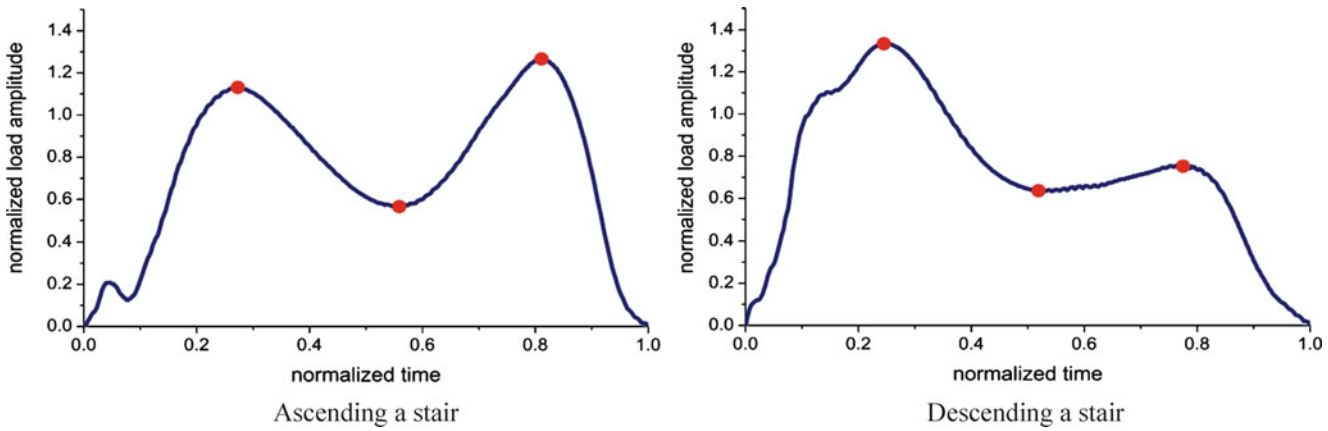

Fig. 4.3 Comparison of the single foot load patterns for ascending and descending a stair

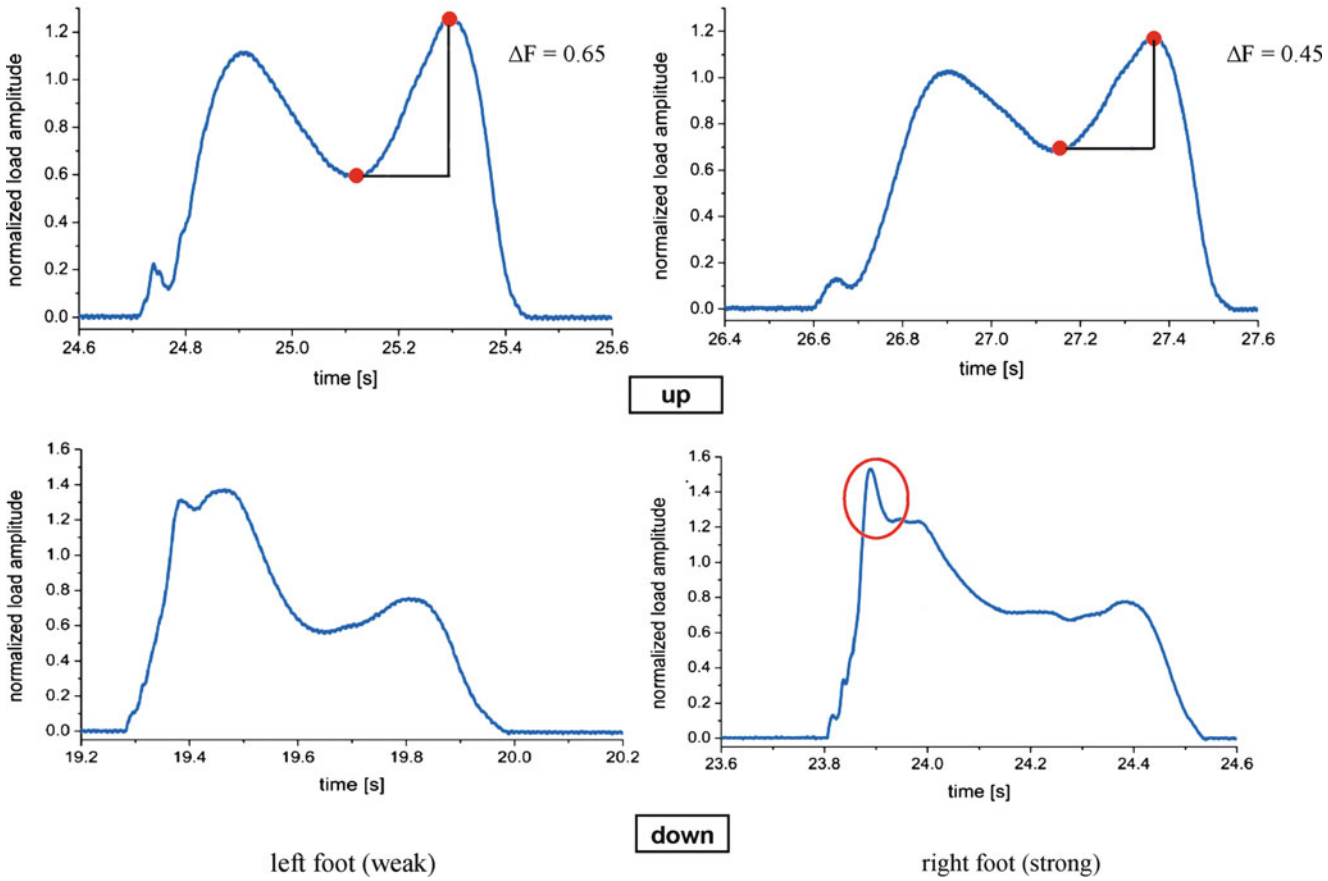

Fig. 4.4 Measured load pattern for ascending and descending a stair by the weak and strong leg

In Fig. 4.3, the basic single foot load patterns for the locomotion forms ascending and descending a stair are shown. Those patterns in Figs. 4.2 and 4.3 are obtained as an average of single foot traces from a single person. Compared to the load pattern for walking in the horizontal plane, which shows two maxima of almost the same amplitude, the load pattern for descending a stair has a considerably larger first maximum and the load pattern for ascending shows a shifted and more peaked second maximum. The differences between the left and the right foot for walking mainly are obtained in the walking parameters step length and step frequency [2].

For ascending and descending stairs these differences are obtained in the basic load patterns (Fig. 4.4). Generally, ascending a stair leads to a pattern of two local maxima and one local minima similar to walking in the horizontal plane.

However, during the initial phase, a small peak is added. This is due to the fact that the test person attaches his foot on the step and rolls it off before pushing the body off. A closer look on the load patterns of the left and right foot reveals that in this case the left foot induced larger load differences during the push-up phase, i.e. for the left foot the difference between the minimum and the second maximum is $\Delta F = 0.65$, while for the right foot a difference of only $\Delta F = 0.45$ is obtained. This indicates the more energy-efficient motion by the right foot. For descending a stair, another effect becomes apparent. At the beginning of the first local maximum for the right foot, the load amplitude reaches a sharp peak value, resulting from a strong impact. For the left foot, the initial impact is damped and the whole motion is more rounded.

The question arises, how the concept of distinguishing between the weak and the strong leg introduced for walking in the plane can be adopted for walking on stairs. For walking in the plane the strong leg is defined by the longer step length. Since the stair forces the step lengths to be almost the same, this criterion cannot be used. Instead, the strong leg is defined as that leg which induces for ascending the stair the more rounded pattern and which leads to the larger impact for descending.

4.3 Variability of Load Amplitudes

The second experiment deals with measuring the load time history of consecutive steps induced by ascending and descending. A wooden stair extension is placed on top of an existing stair. The parameters step height and step length of the extension are adopted from the existing stair to avoid a changing locomotion behavior before reaching or after leaving the stair extension. In Fig. 4.5, the experimental setup can be seen. The stair test section contains four active steps, so it is possible to measure the induced loads by at least one double step. The extension provides four passive steps above the active steps which serve as lead-in or lead-out section. The active steps are mounted on the force plate.

The test procedure for every person contained the following parts. Accordingly to the first measurements, every test person has to stand still on the test section. As explained already above, this phase is required to identify the weight of each person for the normalization. Then the test person has to walk upstairs step-by-step by starting with the right foot. The starting point lies eight steps down on the existing stair. When the test person reaches the upper end of the lead-out section, he or she turns around and descends the stair to the marked starting point. Then the same procedure is repeated for starting with the left foot. In the third and fourth sequence, the person climbs the stairs taking two steps at once, again first beginning with the left foot and then beginning with the right foot. Initially, the motion pattern of taking two steps at once was also intended for descending the stairs. However, first tests showed that this motion pattern is fairly unnatural for most persons.

The tests took place during the matriculation day; therefore, most of the volunteers are younger students. Altogether, the load time histories of 105 persons were measured, with 38 female and 67 male persons. The walking speed is freely chosen by each individual. However, the observed distribution of step frequencies may differ from a natural situation, since the extension of the stair ends up in the air at 1.28 m above the ground.

Fig. 4.5 Illustration of the experimental setup

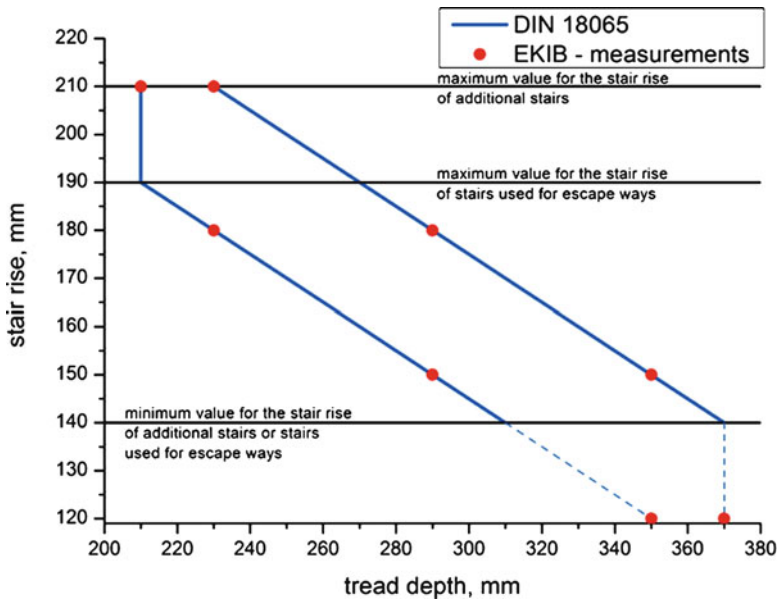

Fig. 4.6 DIN 18065 recommendations for stair rise and tread depth dimensions and EKIB measurements

4.4 Influence of the Stair Geometry

Most stairs are constructed by using an ergonomic relationship between tread and riser dimensions to guarantee a comfortable gait. The German standard DIN 18065 recommends that two times the stair rise plus the tread depth shall equal the mean step length of a person which is in a range of 590–660 mm [3]:

$$2 \cdot \mathrm{s} + a = 590 \div 660\,\mathrm{mm} \tag{4.5}$$

The differences in tread and riser dimensions may influence the load amplitude. To identify this influence, a stair construction is built with changeable tread depth and stair rise dimensions. This construction consists of one active step, one passive step in front and two passive steps afterwards. Figure 4.6 illustrates the possible range of combinations of tread and riser dimensions by using the recommendations of the German standard. The stair rise is limited to a minimum value of 140 mm for all stairs, and a maximum value of 190 mm for stairs used as escape ways, and 210 mm for additional stairs respectively. The red dots mark the analyzed stair rise and tread depth dimensions. For each stair rise, the maximum and minimum value for the tread depth is analyzed.

With the help of five volunteers, eight stair geometries are studied. The load patterns are monitored separately for the left and right foot for both walking directions, ascending and descending. Each test sequence is repeated ten times. The total number of individual load pattern then becomes 1,600.

4.5 Identification of Single Steps

The load time histories obtained for consecutive steps have to be subdivided into single steps. Analogue to the basic definition already used for walking in the horizontal plane, each single step starts with a double stance phase and ends with the next double stance phase. A useful criterion which works for ascending and descending uses the time derivative of the horizontal force F_y in walking direction which becomes large at the beginning of the double stance phase. Analogue to walking in the horizontal plane, the start of an individual step is obtained when F_y shows a local extreme (Fig. 4.7). The red lines indicate the starting point of the single steps. The load time history over four steps on the stair allows separating one left and one right step.

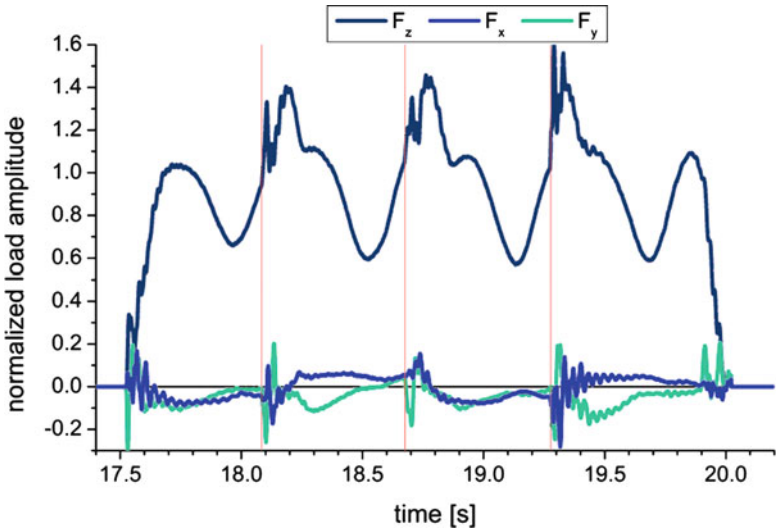

Fig. 4.7 Identification of single steps

4.6 Harmonic Analysis

Every periodic force F(t) can be decomposed into a constant part and an infinite number of harmonic waves using the Fourier analysis:

$$F(t) = a_0 + \sum_{n=1}^{\infty} a_n \cdot \cos\left(n \cdot \frac{2 \cdot \pi}{T} \cdot t\right) + b_n \cdot \sin\left(n \cdot \frac{2 \cdot \pi}{T} \cdot t\right) \tag{4.5}$$

The Fourier coefficients can be calculated by:

$$\begin{aligned} a_0 &= \frac{1}{T} \cdot \int_0^T F(t)dt \\ a_n &= \frac{2}{T} \cdot \int_0^T F(t) \cdot \cos\left(n \cdot \frac{2 \cdot \pi}{T} \cdot t\right) dt \\ b_n &= \frac{2}{T} \cdot \int_0^T F(t) \cdot \sin\left(n \cdot \frac{2 \cdot \pi}{T} \cdot t\right) dt \end{aligned} \tag{4.6}$$

Thereby, the Fourier coefficient a_0 describes the constant load share. The frequencies of the harmonic load contributions are integer multiples of the basic frequency $f_0 = 1/T$. The Fourier series can also be described by the effective load amplitude c_n and the phase shift φ_n of every harmonic:

$$F(t) = c_0 + \sum_{n=1}^{\infty} c_n \cdot \sin\left(n \cdot \frac{2 \cdot \pi}{T} \cdot t + \varphi_n\right) \tag{4.7}$$

With:

$$c_n = \sqrt{a_n^2 + b_n^2}, \ \varphi_n = \arctan\frac{a_n}{b_n}, c_0 = a_0 \tag{4.8}$$

In this analysis, the decomposition into a Fourier series is applied to each individual step, thus leading to the corresponding frequency content. While for an infinite time history of loads induced by consecutive steps the constant contribution has to equal the weight of the person, c_0 deviates slightly from unity, e.g. due to incomplete cycles of arm motions.

4.7 Observed Step Frequencies

Since the step length is given by the stair geometry, the only individual parameter which influences the walking speed is the step frequency f_S. Each basic locomotion pattern has its own frequency range. The lowest frequencies are obtained for ascending the stair taking two steps at once. The observed range extends from 0.8 to 1.9 Hz. For ascending the stair step by step, the corresponding range is obtained from 1.2 to 2.5 Hz. Descending leads to a frequency range from 1.6 to 3.6 Hz. All observed steps correspond to the basic locomotion form walking; running persons have not been observed. The observed step frequencies are different for male and female persons. This is shown in Fig. 4.8 on the example of ascending the stair taking one step at once. The mean step frequency of female volunteers is by 10% larger than the corresponding value for male volunteers, i.e. women climb the stairs faster than men. This finding is quiet astonishing since usually women are slower when walking in the horizontal plane.

In a next step, the differences in the observed consecutive step frequencies are analyzed. The results are shown in Fig. 4.9 for ascending and descending as traces of the non-exceedance probability. About 50% of the volunteers show relative

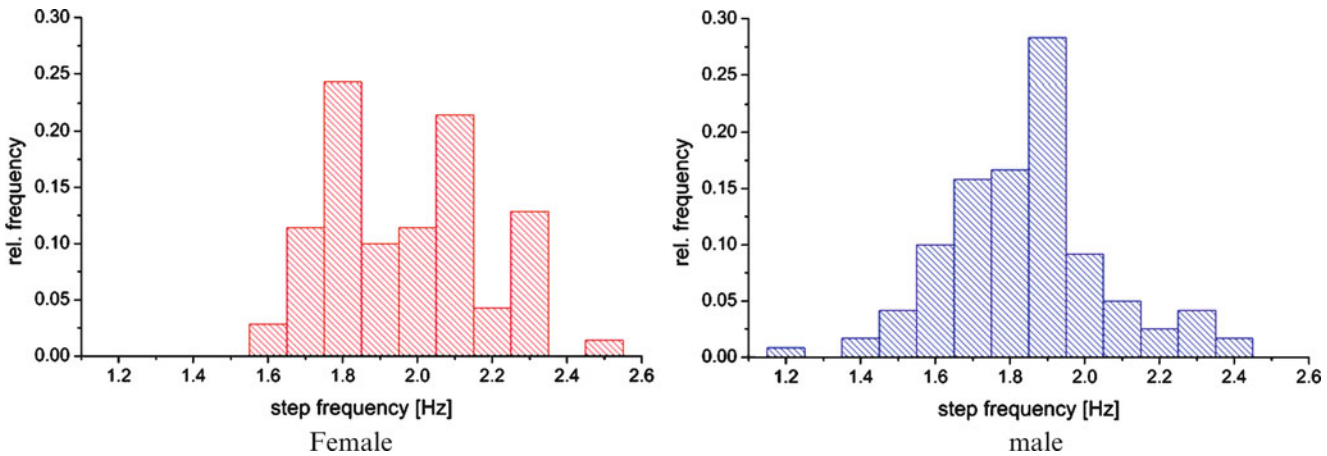

Fig. 4.8 Observed frequencies for ascending the stair taking one step at once

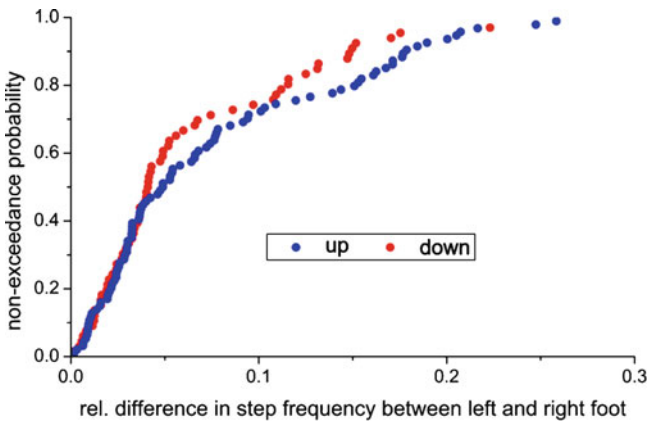

Fig. 4.9 Differences in the step frequencies of two consecutive steps

differences larger than 4%. Thereby, the relative difference is normalized by the mean value of the two consecutive step frequencies. It is worth mentioning that negligibly small differences of say smaller than 1% are observed for only 10% of the volunteers, i.e. measuring the force of only a single foot leads to incomplete information on the loading process.

4.8 Fourier Coefficients

In Figs. 4.10 and 4.11, the load amplitudes for the first harmonic are shown for descending and ascending a stair. The load amplitudes for all three locomotion patterns show a clear dependency of the step frequency. The loads induced by taking two steps at once are about 35% larger than those for taking single steps. The largest range of load amplitudes is obtained for descending.

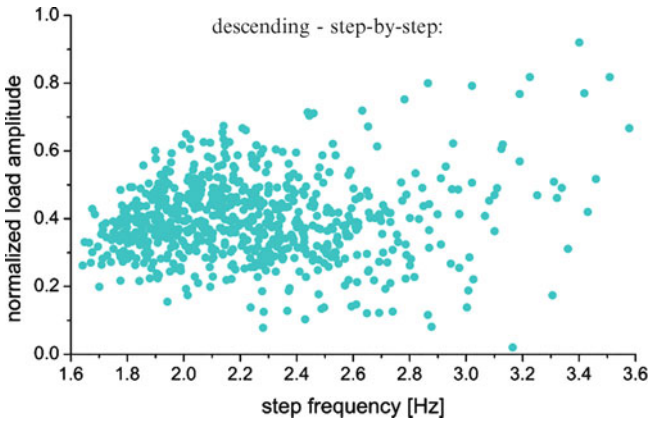

Fig. 4.10 First harmonic load amplitudes for descending a stair

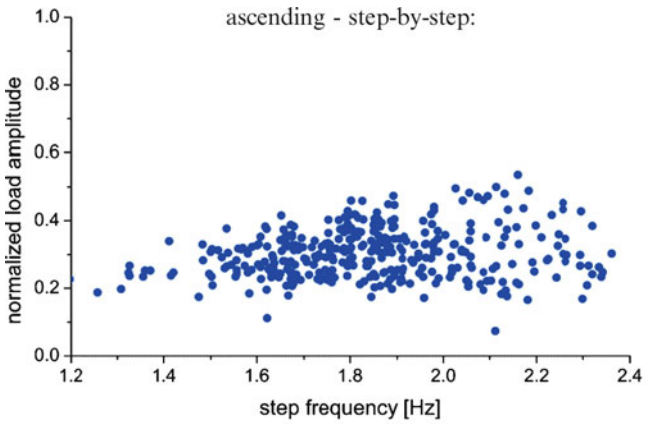

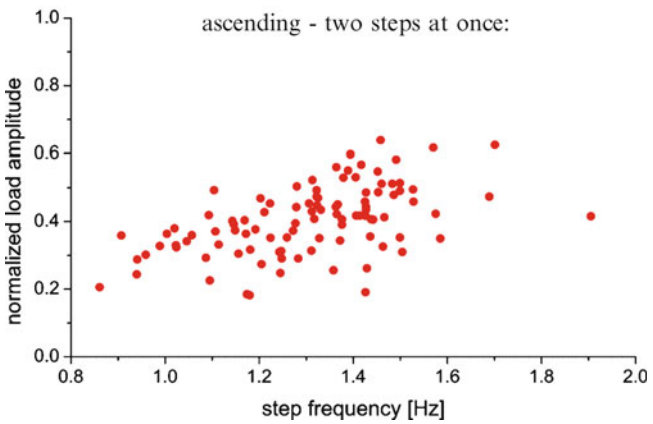

Fig. 4.11 First harmonic load amplitudes for ascending a stair

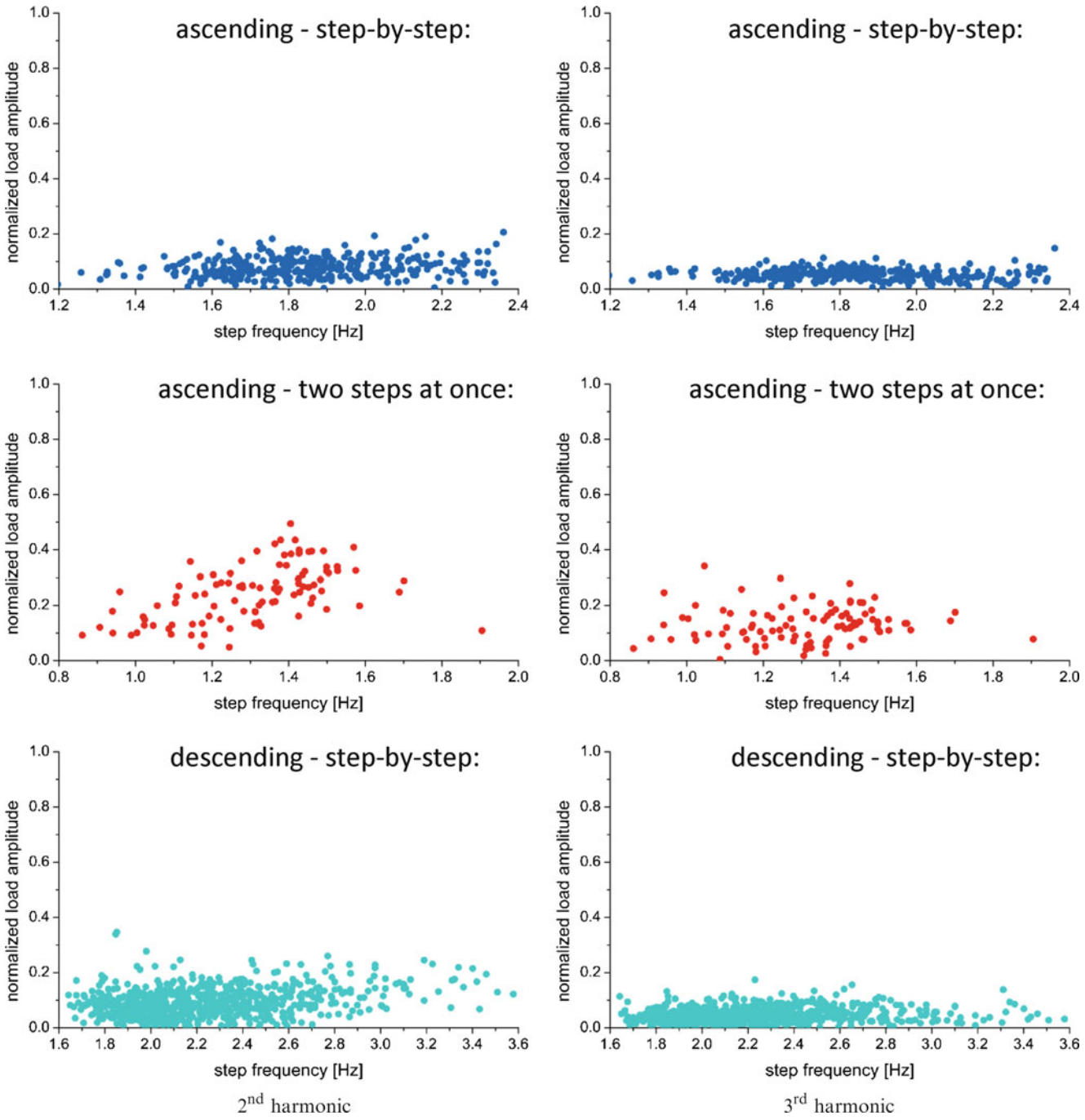

Fig. 4.12 Second and third harmonic load amplitudes for ascending and descending a stair

The second and third harmonic load amplitudes are shown in Fig. 4.12. For the single step motion pattern the higher harmonics keep below 0.2 and 0.1 for the second and third harmonic, respectively. Furthermore, they are more or less independent from the step frequency. For ascending the stair by taking two steps at once, the second harmonic increases with higher step frequencies, the values remain large and are in a similar range than the first harmonic for ascending in single steps.

The 'true' frequency content of a series of consecutive steps can be best evaluated by analyzing structural responses e.g. in terms of accelerations. The observed time series, however, are not long enough for such an analysis. Therefore, as a first step, the sub-harmonic and intermediate harmonic content is evaluated based on the differences between the integer

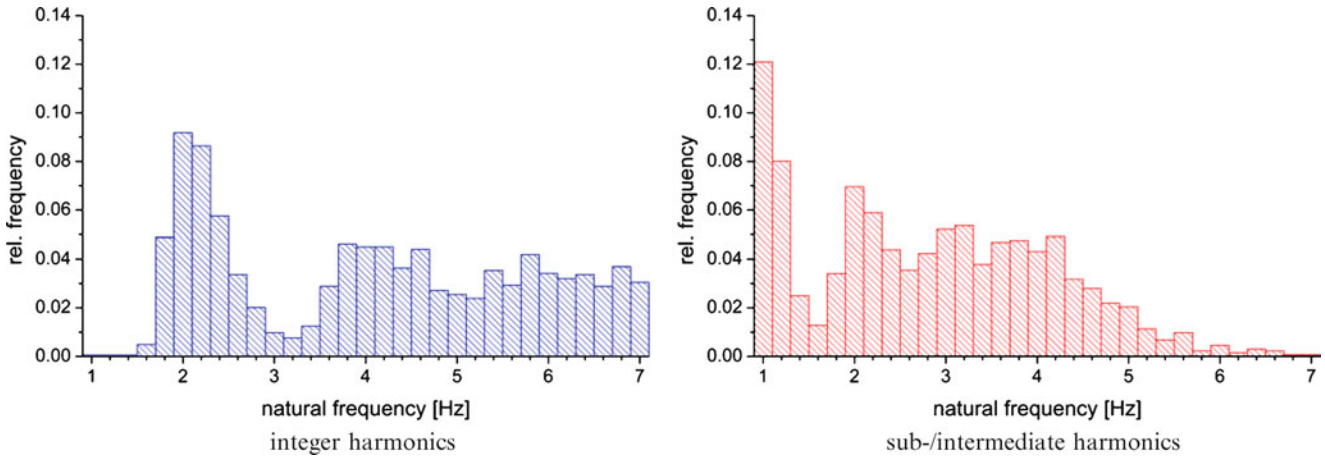

Fig. 4.13 Comparison of the frequency input of the integer harmonics and the sub- and intermediate harmonics for descending a stair

harmonic contributions for consecutive steps using only the first four harmonics. The differences between the harmonics c_n are assumed to occur at integer multiples of the double-step frequency f_{ds}:

$$f_{ds} = \frac{1}{1/f_r + 1/f_l} \tag{4.9}$$

The relative frequency of excitation for different natural frequencies from 1 to 7 Hz is shown in Fig. 4.13 for descending the stair. The integer harmonics show a clear and narrow peak around 2 Hz, a gap at 3.2 Hz, a second and broader maximum at 4 Hz, again a gap at 5 Hz and an unclear peak at 6 Hz. The sub- and interharmonic excitations especially show maxima at 1 and 3 Hz. It is important to note that an approach using only integer harmonics will fail to predict the corresponding excitations.

Using only the first four harmonics leads to an incomplete evaluation of the relative contributions to possible excitations for frequencies beyond two times the step frequency. Therefore, the contributions beyond say 4 Hz are incomplete for the evaluation of the intermediate harmonics.

4.9 Comparison to the Results of Bishop & Kerr

Bishop and Kerr measure a single step on a stair by putting a force plate under one of the steps. The chosen stair consists of seven steps with the active step in the middle. So, three steps are used as lead-in and lead-out section to guarantee a natural walking behavior. The measurement of Bishop and Kerr leads to 500 load time histories of single steps obtained for 23 male and 2 female persons. The volunteers are asked to change the step frequency for each run.

Before comparing the results of Bishop and Kerr with the results of the research team EKIB, the basic geometries of the tested stairs have to be compared. Bishop and Kerr use a stair test section which allows two different gradients. The corresponding values for stair rise and tread depths are listed in Table 4.1. Additionally, the EKIB-values are given. It can be seen, that the dimensions of the stair test section used by the EKIB Research Team are just between the two different geometries of Bishop and Kerr. So both measurements can be assumed to be sufficiently comparable.

Figure 4.14 shows the comparison of the Bishop and Kerr results to the EKIB-results for the first and second harmonic load amplitude for ascending step-by-step. The EKIB-results are in agreement with the Bishop and Kerr data, i.e. the incorrect assumption of equal loads for both feet does not lead to biased harmonic load amplitudes.

4.10 Influence of the Stair Geometry on the Harmonic Load Amplitudes

So far, it is possible to identify an influence of the step frequency on the load amplitudes, but as stated in Sect. 4.4, the tread depth and stair rise dimensions may influence the load amplitudes of the first harmonics, too. In Fig. 4.15, the first harmonic load amplitudes of a test person for ascending are illustrated for each stair geometry and foot. As seen for the results of

Table 4.1 Dimensions of the stair test sections

Test section	Tread depth [cm]	Stair rise [cm]
Bishop & Kerr 22° inclination	34.0	13.5
EKIB 27° inclination	32.0	16.0
Bishop & Kerr 33° inclination	28.0	18.0

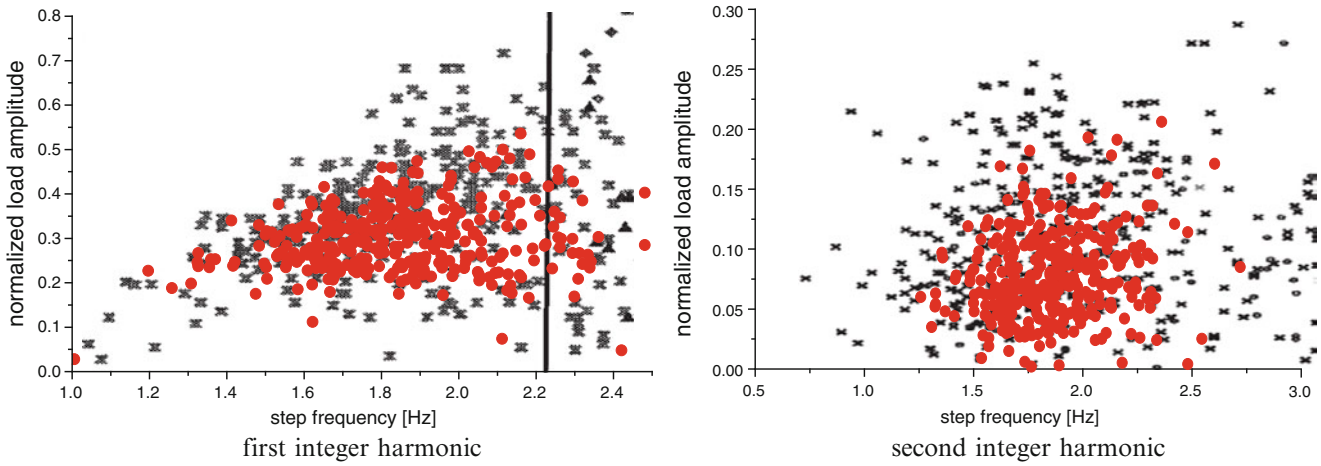

Fig. 4.14 Comparison of the first and second harmonic load amplitude for ascending a stair (• EKIB-data)

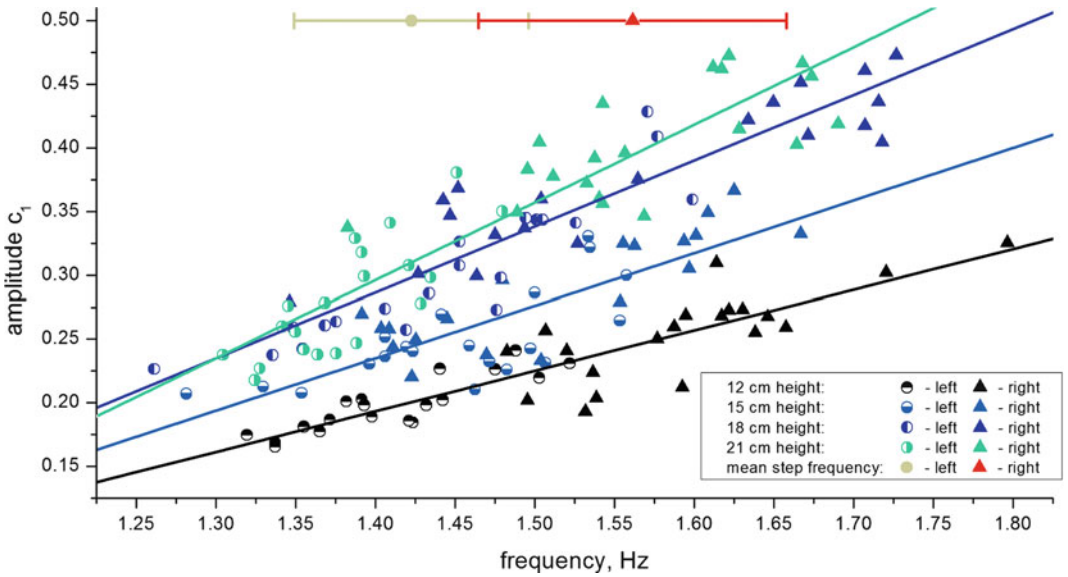

Fig. 4.15 First harmonic load amplitudes of a test person for ascending a stair with different stair geometries

Bishop and Kerr [1] and the EKIB data, the harmonic load amplitudes show a clear dependency on the step frequency. In a first approach, the results can be fitted by a straight line. Furthermore, the mean step frequency differs considerably for the left and right foot of the test person which underlines that the assumption of perfectly equal load patterns for both feet is incorrect and will lead to an underestimation of the sub- and intermediate harmonic content. But Fig. 4.15 also reveals that there is an influence of the stair geometry on the harmonic load amplitudes. Basically, it is expected that the higher the stair

rise, the higher should be the harmonic load amplitudes. Furthermore, the results for each geometry and foot seem to be clustered. This is due to the fact that for each stair rise, two different tread depths were analyzed. This has an influence on the step frequency of each person.

4.11 Summary and Conclusion

In recent years, the loads induced by walking in the horizontal plane have been in the focus of many researchers. However, studies on loads induced by ascending or descending stairs are scarce. The only paper [1] dealing with these loads uses the simplified technique of measuring the load trace of only a single foot to compose the loads induced by a complete step. A first set of experiments performed by the Research Team EKIB at Ruhr-University Bochum leads to the following conclusions:

- There are three motion patterns which have to be considered when predicting the possible excitations of a stair: ascending and descending step-by-step and ascending taking two steps at once.
- The motion pattern of taking two steps at once is analyzed for the first time in the actual paper.
- Taking two steps at once leads to much higher load amplitudes for the first two integer harmonics compared to taking only one step. Hence, this motion pattern might become decisive for the design of a stair structure.
- Taking two steps at once is a motion pattern which is almost exclusively used by male persons. On average, it is more than 40% faster than ascending the stair step-by-step.
- The results of Bishop and Kerr for the load amplitudes of the first and second harmonic are in reasonable agreement with the results of the measurement performed by the Research Team EKIB, i.e. the incorrect assumption of perfectly equal load patterns for both feet does not lead to biased harmonic load amplitudes.
- While the approach of measuring only the load trace of a single step to compose the loads may be sufficient for the prediction of excitations for integer multiples of the step frequency, the method fails to predict excitations at intermediate harmonics.
- In addition to the step frequency, the stair geometry has an influence on the harmonic load amplitudes.

Acknowledgements Part of this work has been sponsored by the German Research Foundation under the contract number KA675/13-1. This support is gratefully acknowledged.

References

1. Kerr SC, Bishop NWM (2001) Human induced loading on flexible staircases. Eng Struct 23:37–45
2. Sahnaci C, Kasperski M (2005) Random loads induced by walking. In: Proceedings of the 6th European conference on structural dynamics 2005, Paris, pp 441–446
3. DIN 18065 (2011) Gebäudetreppen – Begriffe, Messregeln, Hauptmaße
4. Agu E, Kasperski M (2011) A statistical approach to horizontal loads due to human rhythmic activity. In: Proceedings of the 8th international conference on structural dynamics 2011, Leuven, pp 994–1001

Chapter 5
Comparative Evaluation of Current Pedestrian Traffic Models on Structures

Erfan Shahabpoor and Aleksandar Pavic

Abstract Recent vibration serviceability problems of many structures have drawn researchers' attention to the walking-induced vibration modelling and assessment of floors and footbridges. Stochastic nature of human-induced vibration and its dependency on numerous conditions significantly reduce the accuracy of the current non-stochastic design procedures and consequently the level of confidence on them.

This paper tends to study the performance of two of the most recent design guidelines, UK National Annex to Eurocode 1 (2008) [1] and French Sétra guideline (2006) [2], on real structures and to highlight their advantages and disadvantages. These methods are used to calculate dynamic reactions of a slender and lightly damped pre-stressed concrete slab strip and an as-built footbridge using various loading scenarios such as group loading, spatially unrestricted flow of pedestrians, and crowd loading. The calculated structural responses under first and second harmonics of walking load are further compared with their corresponding experimentally acquired reactions to examine their accuracy and efficiency. Various potential sources of discrepancy in the results of these procedures in comparison with the experimental data, such as missing human-structure interaction effects (e.g. damping), invalid 'perfect periodicity' assumption, limited applicability and unrealistic people correlation are then discussed. Finally the effects of using stationary pedestrians' added damping on performance of considered design models are investigated and briefly discussed.

The results of this analysis can provide a comprehensive insight into current design procedures' accuracy and shall be taken as a good starting point for future researches in this area.

Keywords Footbridge • Vibration serviceability • Spatially unrestricted pedestrian traffic • Modal testing • Codified vertical load models • Human-structure interaction • Stationary damping

Nomenclature

f_p	Pacing frequency (Hz)
f_n	Natural frequency (Hz)
Q	Static load of one pedestrian (N)
$a_{max,95\%}$	Characteristic peak acceleration (m/s^2)
ζ	Modal damping ratio
L	Bridge length (m)
b	Bridge width (m)
q	Pedestrian stream density (Ps/m^2)
m_i	Modal mass of bridge span (kg)
λ	Flow rate (Ps/s)
t_s	Simulation duration (s)
a_N	Acceleration (m/s^2)

E. Shahabpoor (✉) • A. Pavic
Department of Civil and Structural Engineering, The University of Sheffield, Sir Frederick Mappin Building, Mappin Street, Sheffield S1 3JD, UK
e-mail: e.shahabpoor@sheffield.ac.uk

J.M. Caicedo et al. (eds.), *Topics on the Dynamics of Civil Structures, Volume 1*,
Conference Proceedings of the Society for Experimental Mechanics Series 26,
DOI 10.1007/978-1-4614-2413-0_5,

n	Number of harmonics
ψ	Load reduction factor
γ	Synchronization factor
k	Load reduction factor
λ	Span reduction factor
F_0	Reference dynamic load of one pedestrian (280 N)
A	Net area of the span (m^2)
$\phi(x)$	Mode shape
N, n_p	Number of uncoordinated pedestrians
d	Pedestrian traffic density (peds/m^2)
ρ	Crowd density (peds/m^2)
f_v	Vertical bridge natural frequency (Hz)

5.1 Introduction

Traditionally, the design guidelines for vibration serviceability of footbridges in the vertical direction use a single person dynamic walking load to predict the dynamic load of pedestrian traffic. In these guidelines, walking load is assumed to be periodic and is used to build the resonance in the structure, while in real-life cases it has been proven unrealistic. Recent approaches are more realistic and use the statistics to define the diverse features of pedestrians' traffic.

Some high profile serviceability failures of footbridges since 2000 have proven that human-structure interactions have significant effect on structural response while their nature is still unknown, to a high extent. This paper presents two of currently available design guidelines on vibration serviceability assessment of footbridges and tries to analyse their performance in different cases. Further, the scope is narrowed down to spatially unrestricted walking loads in the vertical direction. Three sets of tests have been done on the University of Sheffield laboratory post-tensioned slab strip and Podgorica footbridge located in Montenegro and performance of selected design models have been analysed under both first and second harmonics of walking. In the next step, possibility of using stationary pedestrians' added damping to improve the accuracy of design models has been investigated and finally a brief discussion of performance of selected methods is presented.

5.2 Current Design Guidelines

5.2.1 Sétra Guideline (2006)

The design guideline of Technical Department for Transport, Roads and Bridges Engineering and Road Safety (Service d'études techniques des routes et autoroutes – Sétra) on footbridges has presented two primary load cases for vertical pedestrian walking loads as; Case 1 sparse and dense crowd with densities between 0.5 and 0.8 peds/m^2; Case 2 very dense crowd; and a complement case for an evenly distributed crowd (second harmonic effect) based on the assumption that the probability distribution of the pacing rate within traffic follows Gaussian distribution. These load cases are developed based on four classes of footbridges (based on the level of traffic they are expected to experience, Class I: very heavy traffic, Class II: heavy traffic, Class III: moderate traffic and Class IV: low level of traffic) and four classes of frequency ranges (base on the expected risk of resonance, Range 1: maximum risk of resonance, Range 2: medium risk of resonance, Range 3: low risk of resonance for standard loading situations and Range 4: negligible risk of resonance). Case 1 model which is more relevant to the cases of this paper, presents the vertical dynamic load as [2]:

$$f_n(t) = 10.8 \times 280d\sqrt{\zeta/n}\psi Cos(2\pi f_v t) \tag{5.1}$$

Where, d is density 0.5/0.8 peds/m^2 for footbridges class III and II, respectively, n is the number of people in the crowd, 280 (N) is the dynamic load amplitude of a single pedestrian (0.4 × 700 N for the first and 0.1 × 700 N for the second harmonic), f_v is the natural frequency of relevant vibration mode, ζ is the damping ratio of that mode and ψ is a reduction factor that reduces the load for frequencies away from the average pacing rate. Although comprehensive set of simulations (500) have been used for developing this model and the effects of presence of pedestrians on modal masses is considered, the

model does not take into account the effects of pedestrians on damping of structure which reduces considerably the accuracy of the results. The model also, takes into account one harmonic at a time which is problematic in the case of footbridges with more than one susceptible mode in the range [2, 3].

5.2.2 UK National Annex to Eurocode 1 (2008)

UK National Annex to Eurocode 1 [1] defines two action models for pedestrian-induced vertical dynamic loading; one for single pedestrians and pedestrian groups and one for pedestrians in crowded conditions (with density of 0.4 peds/m^2 or above) using four classes of footbridges (based on the level of traffic they expect to experience, Class I: very heavy traffic, Class II: heavy traffic, Class III: moderate traffic and Class IV: low level of traffic). The crowd load model which will be used later in this paper is defined as load per unit area, with the load sign matching that of the mode shape:

$$w = 1.8\left(\frac{F_0}{A}\right) \cdot k(f_v) \cdot \sqrt{\gamma \cdot \frac{\rho \cdot A}{\lambda}} \cdot Sin(2\pi f_v t) \tag{5.2}$$

Where, F_0 is the reference dynamic load of one pedestrian (280 N), k is a factor that incorporates the excitation potential of the relevant forcing harmonic and probability of walking at the given resonant frequency in the model, ρ is the required crowd density with a maximum value of 1.0 persons/m^2, A is the net area of the span, γ is a factor to allow for the unsynchronized combination of actions in a crowd and λ is a factor that reduces the effective number of pedestrians, when loading from only part of the span contributes to the mode of interest [3]:

$$\lambda = \frac{\int_0^L |\emptyset(x)|/\emptyset_{max} dx}{L} \tag{5.3}$$

where L is the length of the loaded area, and $\phi(x)$ and $\emptyset_{max}$ are the mode shape along the bridge and its maximum ordinate, respectively. For a sinusoidal mode shape, $\lambda = 0.634$ and the equation becomes very similar to the Sétra equation with the multiplying constant equal to approximately 6.1 instead of 10.8, and k instead of ψ. This shows that the results of UK NA method in this case is 44% less conservative than Sétra method which is chosen with logical reasoning that some exceedance of the predicted response should be allowed in real life [3].

Similar to Sétra, UK NA method takes into account one harmonic at a time and does not take into account the effects of pedestrians on damping of structure which reduce considerably the accuracy of the results.

5.3 Description of Tested Footbridges

5.3.1 The University of Sheffield Post-Tensioned Slab Strip

The slab strip used in the following analytical and experimental tests is a simply supported in-situ cast post-tensioned slab strip of net span 10.8 m (Fig. 5.1) constructed in the light structure laboratory of The University of Sheffield for research purposes. Its total length is 11.2 m, including 200 mm overhangs over the supports. Its width and depth are 2.0 m and 275 mm respectively, and it weighs approximately 15 tones [4].

5.3.2 Podgorica Footbridge

The investigated footbridge spans 104 m over the Moraĉa River and is constructed in Podgorica, capital of Montenegro (Fig. 5.2) in early 1970s. The structural system of the footbridge is composed of a steel box girder with 78 m main span length between two inclined column supports and two side spans of 13 m each. The top flange of main girder is 3 m wide and forms the clear deck of the footbridge. Depth of the girder varies from 1.4 m in the mid span to 2.8 m over the inclined supports. The structure was stiffened with several stiffeners along the main girder and at the support connection points.

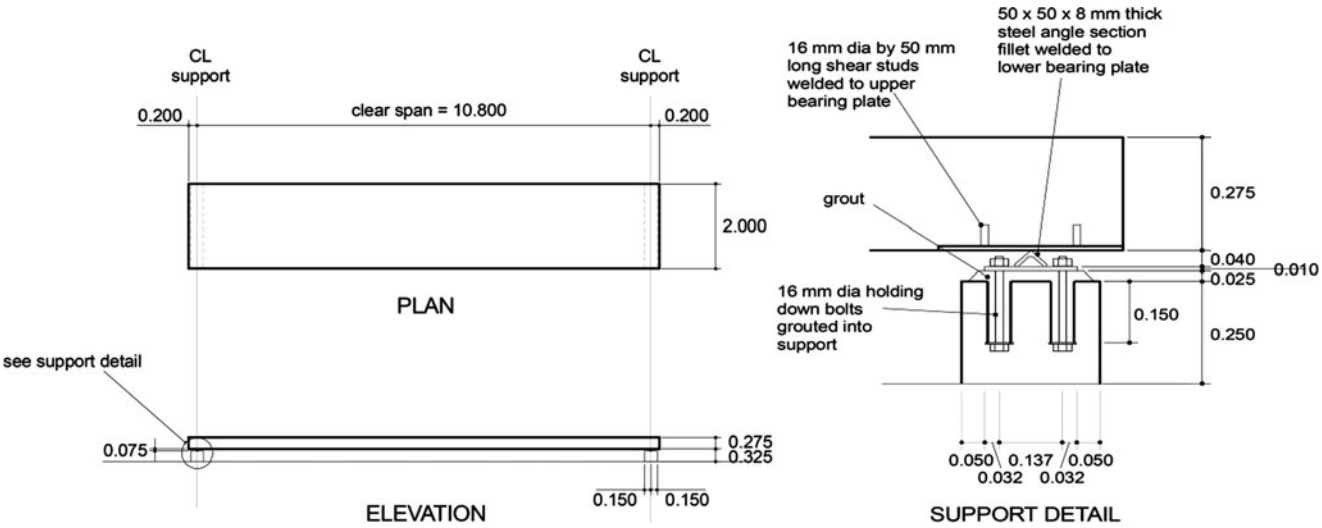

Fig. 5.1 Plan of slab strip and a typical support detail [4]

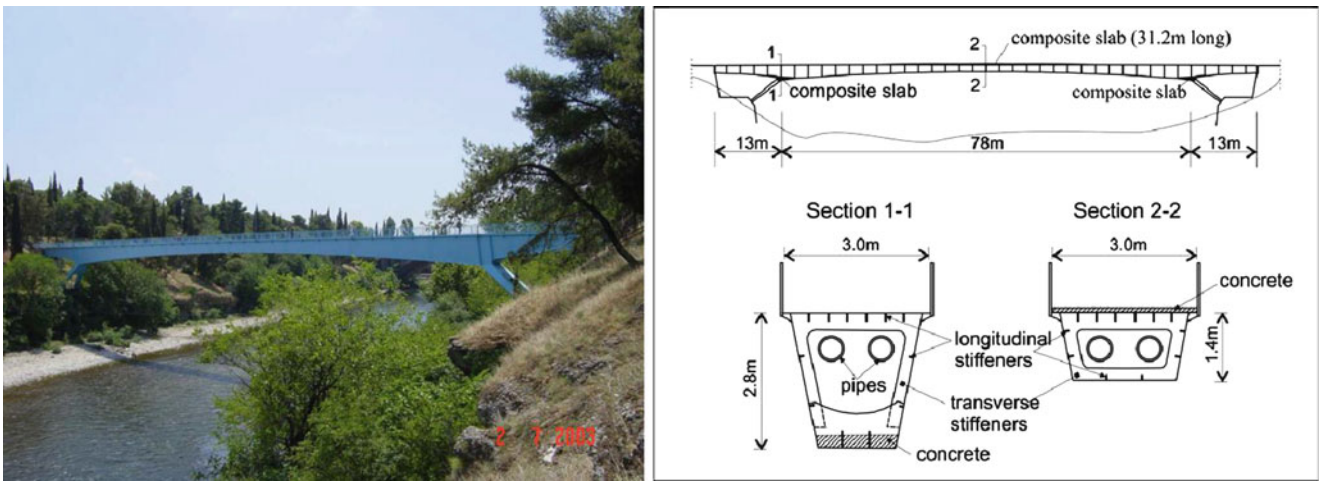

Fig. 5.2 Podgorica footbridge view (*left*) and general arrangement drawing (*right*) [5]

Two water supply and drainage pipes pass through the steel box section and are suspended from the top flange of the main girder [5]. The PG footbridge was found to be very susceptible to walking induced vibration. The structure later was strengthened by casting a concrete slab over the top steel flange in the mid-span and over the bottom flange in support areas, but it couldn't shift its natural frequency out of excitable region by the human walking.

5.4 Test Methodology

5.4.1 General Overview

The primary goals of this research are first to evaluate the performance of two of existing codified models of pedestrian walking, under first and second harmonics of walking, and second to evaluate the effects of human-structure interactions, specifically walking-induced damping, on the results and possibility of using added damping of stationary pedestrians to enhance the accuracy of design models. For these purposes, two sets of monitoring tests have been designed for PT laboratory slab and Podgorica footbridge. In the case of PT laboratory slab, a sub set of FRF-based modal tests for identification of modal properties of structure and a set of response monitoring tests under various traffic conditions have been considered. For each monitoring

test, full set of pedestrian traffic statistical data have also been recorded. Zivanovic [5] did few monitoring tests on the Podgorica footbridge in 2005, which results are used for analysis in this paper. In next step, calculated modal properties and pedestrian traffic statistical data have been used to build the design model for each case and to calculate the response based on selected guidelines. Finally, the experimentally acquired responses are used to examine the accuracy of the results of each built design model and to observe the effects of using stationary pedestrians' added damping on results.

5.4.2 Human-Structure Interactions: Damping

Human body, because of its biological structure and biodynamical actions, is found to be very sensitive vibration receiver [6] and this leads to its interaction with the structure. High level of vibration fluctuations due to HSI, in both vertical and lateral directions, has been observed in several structures but there is still not much about its effect in vertical direction.

To observe these effects and examine the capability of design guidelines to address human-structure interaction effects (damping in this case), every set of tests has been modelled in two conditions: (1) considering the modal properties of clear structure (structure without pedestrians on it) and (2) considering modal properties of occupied structure (structure with pedestrians standing still on it). These values are further used to examine accuracy of existing design guidelines. For the case of PT laboratory slab, an FRF-based modal test is conducted to calculate the modal properties of structure while people are on the slab, and these values are further used for modelling Human effects on structure. In the case of Podgorica footbridge, increased damping value recommended by Zivanovic [3] for this footbridge, has been used to introduce Human effects in the design model.

5.4.3 Test Structure

Two major test sets have been considered for each of structures in this research, (1) FRF-based modal tests and (2) Response monitoring tests. For PT laboratory slab, FRF-based modal test carried out in two situations: (1) clear structure and (2) structure while participants are standing-still and uniformly distributed all over the structure. Dynamic response of the PT slab is recorded in two response monitoring tests: (1) normal walking of six people on the slab and (2) synchronized walking of five people tuned to half of natural frequency of slab, 4.5 Hz, to build the resonance. Pedestrians' statistical data have been recorded during the test.

For the case of Podgorica footbridge, results of modal testing reported by Zivanovic [3] for both clear and occupied structure (structure with people walking on it) have been used. Dynamic response of structure have been monitored using three sets of measurements, each lasting about 45 minutes, and their corresponding pedestrian data, derived by post analysis of video recordings of bridge during the tests by Zivanovic, have been used as input in design models.

5.5 Full Scale Measurements

5.5.1 Modal Parameters Estimation

FRF-based modal testing was conducted on PT laboratory using 18 force balanced QA accelerometers placed parallel to the longer edges of slab, as shown in Fig. 5.3, to capture both vertical and torsional modes. An APS electro-dynamic shaker model 400, operated in the inertial mode was used to shake the structure. It was placed at TP 13 to be able to excite first three vertical mode shapes. The shaker was fed by random excitation with 0–50 Hz frequency band to capture all the modes in this frequency band, and the induced force was measured indirectly by a piezoelectric ENDEVCO accelerometer, attached to shaker's moving mass. The shaker, accelerometers and wires were placed in such a way that pedestrians could walk on the slab freely in both directions. The test setup is shown in Fig. 5.3.

The modal properties of the structure (Modal frequencies, damping values, masses and mode shapes) are obtained by curve fitting the resulted FRFs in ME'Scope software, for both clear and occupied structure. The results are presented in Tables 5.1 and 5.2 and Fig. 5.4. Based on the results, first mode of vibration, with 4.5 Hz natural frequency, is the only mode

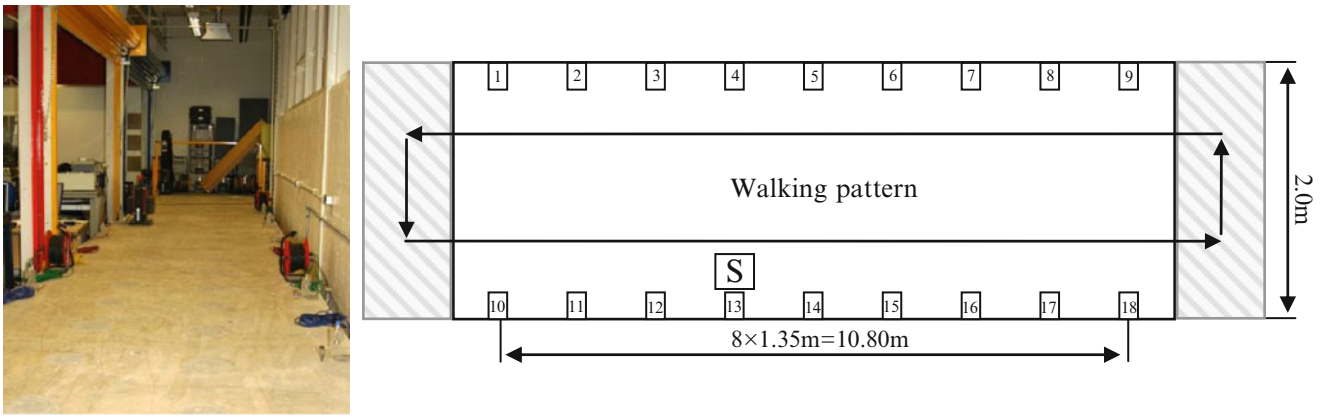

Fig. 5.3 Test setup photo (*left*) and walking patern of pedestrians (*right*)

Table 5.1 Estimated modal parameters of PT slab (empty structure) using both analytical and experimental methods

Mode	FE model	FRF based				
#	f (Hz)	f (Hz)	ζ (%)	M_i	C_i	K_i
1	4.55 (V)	4.5 (V)	0.98	6,000	3,315	4,796,628
2	17.02 (V)	16.8 (V)	0.61	6,000	7,739	66,854,332
3	–	25.9 (T)	0.95	6,000	18,103	158,895,104
4	28.92 (T)	28.3 (T)	1.22	23,000	99,789	727,211,007
5	37.71 (V)	37.8 (V)	1.20	6,000	34,201	338,450,053

Table 5.2 Estimated modal parameters of PT slab (occupied structure) using FRF-based methods

Mode	FRF based				
#	f (Hz)	ζ (%)	M_i	C_i	K_i
1	4.37 (V)	1.71	7,500	7,043	5,654,365
2	16.8 (V)	1.17	6,700	16,549	74,654,004
3	26.1 (T)	1.00	5,500	17,967	147,912,011
4	28.6 (T)	1.38	34,500	171,109	1,114,065,943
5	37.8 (V)	1.34	5,500	35,008	310,245,882

with major excitation possibility and will be investigated in this research. These results show almost two times increase in first and second modes damping due to presence of pedestrians on structure (also see Fig. 5.4).

Mode shapes of PT slab are illustrated in Fig. 5.5.

For the case of Podgorica footbridge, both FRF-based test and Ambient vibration survey was done by Zivanovic [5] for modal properties identification. Fourteen points along the longer edges of footbridge were chosen for the response to be monitored using Endevco 7754-1000 piezoelectric accelerometers. An APS (model 113) electro-dynamic shaker, placed at the quarter of the mid-span, was used to excite the structure. Detailed description of test and modal parameters estimation procedure has been presented elsewhere [5]. The derived modal properties of Podgorico footbridge are presented in Table 5.3.

5.5.2 *Properties of Pedestrian Traffic*

PT laboratory slab has been tested using two loading scenarios, (1) normal walking of six people on the slab and (2) synchronized walking of five people to half of first mode natural frequency to excite the slab to resonance. Using a specifically designed laser system for collecting pedestrian data, it was found that mean pacing frequency of pedestrians were 1.9 and 2.25 Hz, the stream densities were 0.278 and 0.235 p/m^2 and the average speed of pedestrians were 1.35 m/s^2 in both scenarios, respectively.

In the case of Podgorica footbridge, Zivanovic by analysis of video records of tests has reported that mean pacing frequency of pedestrians was 1.87 Hz, the stream density was 0.05 p/m^2 and the average speed of pedestrians was 1.4 m/s^2. The obtained results of both structures are further used as input for design methods to calculate the dynamic walking load of pedestrian. The complete list of these inputs is presented in Table 5.4.

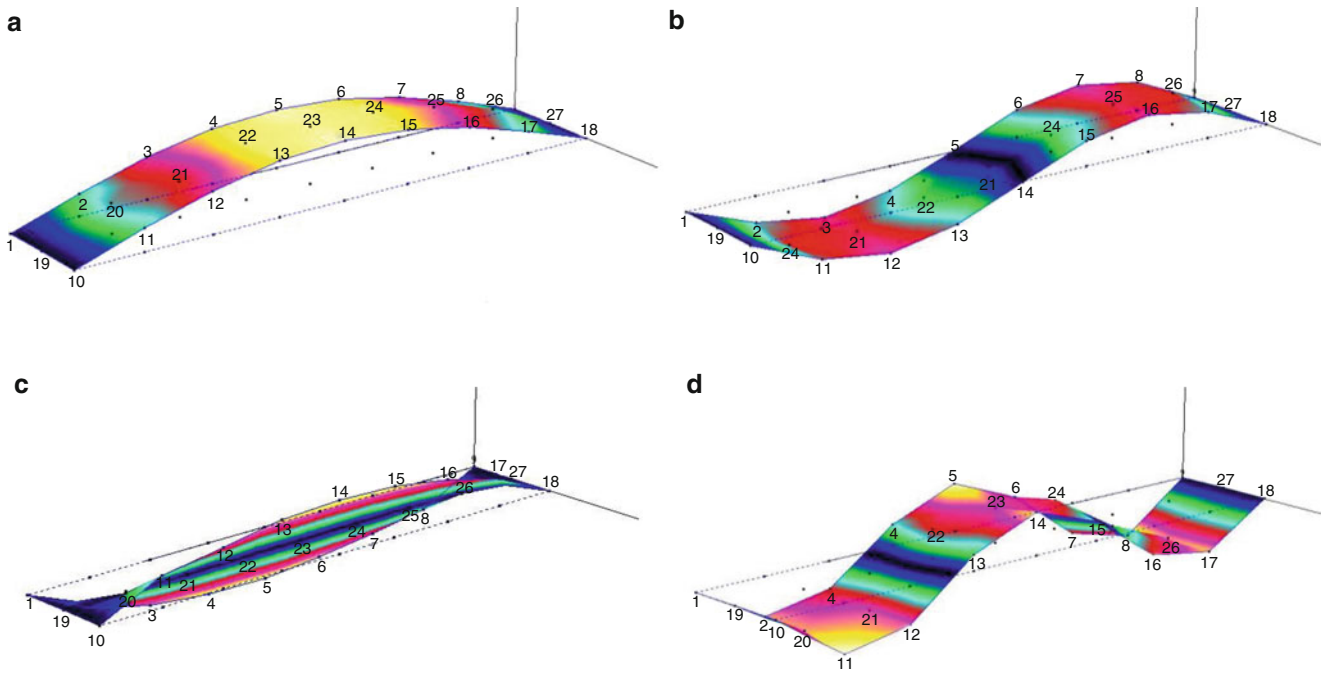

Fig. 5.4 Experimentally acquired mode shapes of PT slab: (**a**) first vertical mode shape @ 4.5 Hz, (**b**) second vertical mode shape @ 16.8 Hz, (**c**) first torsional mode shape @ 25.9 Hz, (**d**) third vertical mode shape @ 37.8 Hz

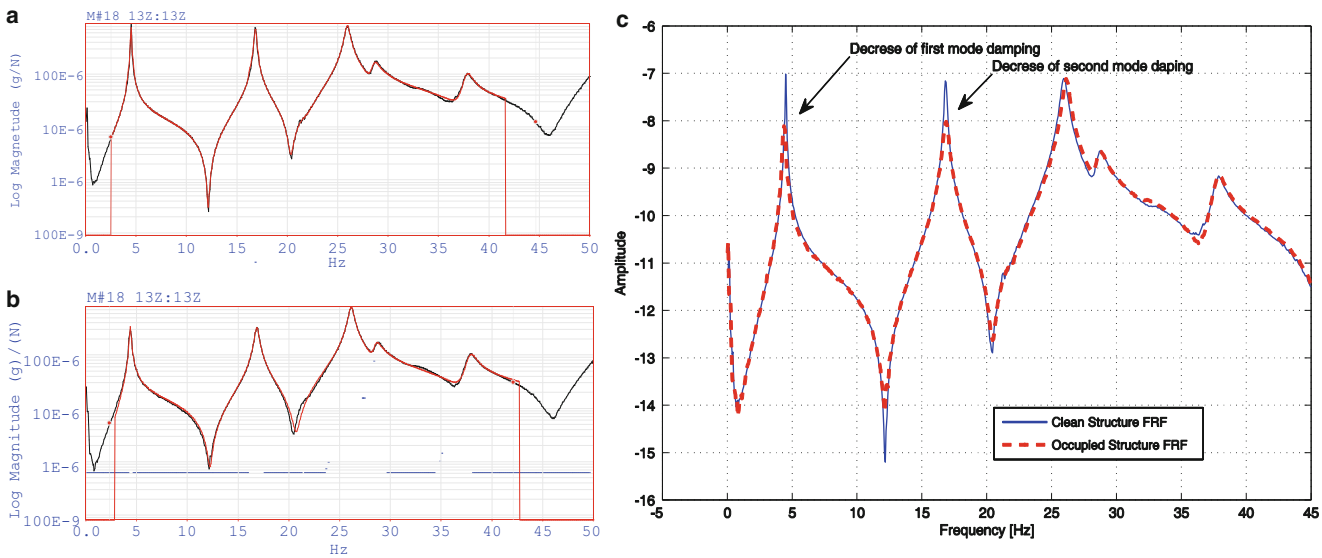

Fig. 5.5 Experimentally acquired FRFs of clean and occupied PT slab and their corresponding *fitted curves* (*left*): (**a**) FRF of PT slab and corresponding fitted curve (*red curve*) – Clean structure, (**b**) FRF of PT slab and corresponding fitted curve (*red curve*) – Occupied str. (**c**) Comparison of clean/occupied PT slab FRFs

5.5.3 Monitoring Tests

To measure the response of PT slab, as only the first mode is prone to be excited by walking forces, acceleration responses were measured at the mid-span, using two force balanced QA accelerometers located at both edges of the slab. Each test lasted 2 minutes. The results of these accelerometers are further averaged to remove the effects of torsional modes from the

Table 5.3 Estimated modal parameters of Podgorica footbridge using both analytical and experimental methods [5]

Mode #	FE model	FRF based		Ambient vibration survey (AVS)	
	f (Hz)	f (Hz)	ζ (%)	f (Hz)	ζ (%)
1	1.82 (1HS)	1.83 (1HS)	0.26	–	–
2	2.02 (1VS)	2.04 (1VS)	0.22	2.05 (1VS)	0.29
3	3.47 (1VA)	3.36 (1VA)	1.86	3.42 (1VA)	1.04
4	4.36 (1HA)	4.54 (1HA)	0.98	–	–
5	7.15 (2HS)	7.35 (2HS)	2.68	–	–
6	7.34 (2VA)	7.56 (2VA)	0.76	7.55 (2VA)	0.76
7	7.74 (2VS)	7.98 (2VS)	0.60	8.00 (2VS)	0.44

Table 5.4 Input parameters used in selected design methods

Parameters used in considered design methods											
		Value									
Item	Parameter/description	PT slab empty	PT slab occupied	PT slab empty harmonized	PT slab occupied har.	PG footbridge	PG footbridge occupied	Unit	French sétra guideline	UK NA to EC1 (Group)	UK NA to EC1 (Stream)
1	Pacing frequency (f_p)	1.90	1.90	2.25	2.185	1.87	1.87	Hz			
2	Natural frequency (f_n)	4.50	**4.37**	4.50	4.37	2.00	**2.00**	Hz			
3	Static load of one pedestrian (Q)	700	700	700	700	700	700	N			
4	Number of uncoordinated peds.	6	6	5	5	15	15	–			
5	Modal damping ratio (ζ)	0.0098	**0.0171**	0.0098	**0.0160**	0.0026	**0.0067**	–			
6	Bridge length (L)	10.8	10.8	10.8	10.8	78	78	m			
7	Bridge width (b)	2	2	2	2	3	3	m			
8	Simulation duration (t)	120	120	120	120	2,700	2,700	s			
Factors											
1	Load reduction factor (ψ)	0.625	**0.8**	0.625	**0.8**	1	1	–			
2	Synchronization factor (γ) (crowd)	0.0725	**0.1265**	1.00	1.00	0.0192	**0.0496**	–			
3	Synchronization factor (γ) (group)	0.69	**0.72**	1.00	1.00	0.17	**0.23**	–			
4	Load reduction factor (k)	0.25	**0.29**	0.25	**0.29**	1	1	–			
5	span reduction factor (λ)	0.634	0.634	0.634	0.634	0.634	0.634	–			

Right hand side panel shows which parameters are used in each specific code

obtained responses. Simultaneously, Pedestrian traffic is monitored using a specifically designed laser system, installed above pathway on both ends of slab. Similarly, on the Podgorica footbridge, the vibration and pedestrian traffic were monitored using two video cameras and an accelerometer placed at the mid-span. Each of monitoring tests lasted 45 minutes. For analysis purposes, two of Podgorica footbridge measurements, one with moderate traffic and the other with slightly heavier traffic, are combined, tail to head, to get a more realistic statistical results.

To be able to compare the acquired responses, statistical treatment is required. For this purpose, cumulative distributions of absolute value of local peak (i.e. peak acceleration per cycle), interval peak (5 s intervals for PT slab that correspond to single crossing time and 100 s intervals for Podgorica footbridge that correspond to two average crossing times) and instantaneous acceleration, together with their corresponding response time histories are presented in Fig. 5.6.

5.6 Results of Design Models

5.6.1 Overview

Earlier studies of behaviour of structures under human walking loads have suggested that there are some interactions between human body and structure. Recent attempts towards description and quantification of such interactions are still in initial stages and not yet mature. This section aims at investigation of the effects of using stationary pedestrian added damping for calculation of walking-induced response of same pedestrians on that structure.

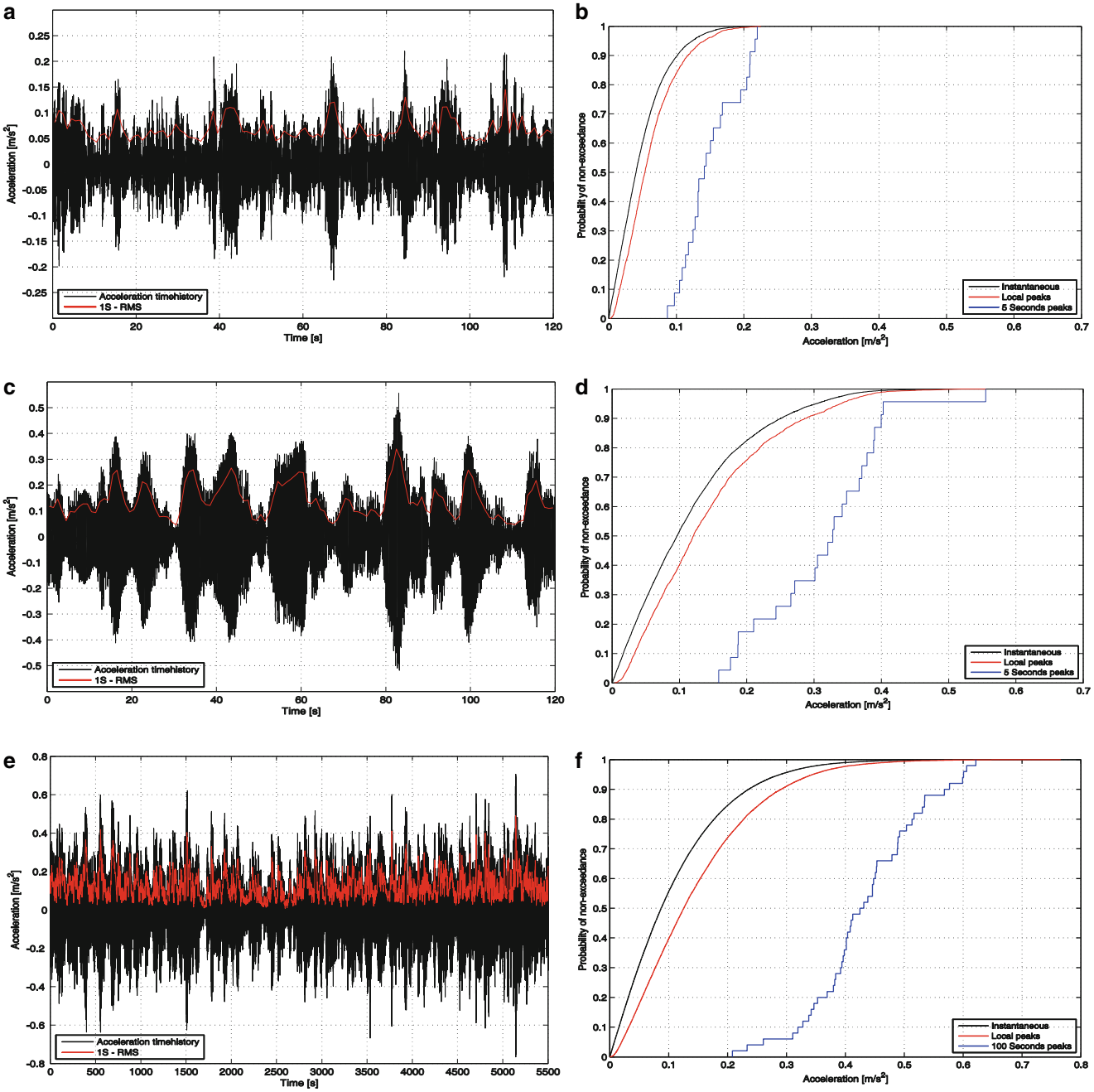

Fig. 5.6 Measured acceleration response (*at mid-span*) (*left*) and CDFs of test 1, 2 and 3 (*right*): (**a**) Test 1 – measured acceleration response (*at mid-span*), (**b**) Test 1 – CDFs of *mid-span* acceleration response, (**c**) Test 2 – measured acceleration response (*at mid-span*), (**d**) Test 2 – CDFs of *mid-span* acceleration response, (**e**) Test 3 – measured acceleration response (*at mid-span*), (**f**) Test 3 – CDFs of *mid-span* acceleration response

The results of previously discussed tests and corresponding calculated responses are presented in Table 5.5 with the following order:

Test 1: Test structure: PT laboratory slab – Pedestrian traffic: six pedestrians walking with their own normal pacing frequency

Case 1: Results of design models using damping ratio of empty structure ($\zeta = 0.0098$)
Case 2: Results of design models using damping ratio of occupied structure (higher damping values obtained from FRF-based modal test of structure while same pedestrians were standing-still on it) ($\zeta = 0.0171$)

Table 5.5 Results of test 1, 2 and 3

Guideline	Criterion	Experimental results (m/s^2)	PG footbridge clean (m/s^2)	Difference (%)	PG footbridge occupied (m/s^2)	Difference (%)
Test 1: PT slab – normal walking			$\zeta = 0.0098$		$\zeta = 0.0171$	
French Sétra	$a_{95\%}$	0.13	1.27	877	0.28	115
	$a_{max,1SRMS}$	0.15	1.00	567	0.20	33
UK NA to Eurocode 1 (Group)	$a_{2.5\sigma}$	0.15	1.31	773	0.47	213
	$a_{max,1SRMS}$	0.15	0.70	367	0.33	120
UK NA to Eurocode 1 (Stream)	$a_{2.5\sigma}$	0.15	1.28	753	0.28	87
	$a_{max,1SRMS}$	0.15	0.90	500	0.16	7
Test 2: PT slab – synchronized walking			$\zeta = 0.0098$		$\zeta = 0.0160$	
French Sétra	$a_{95\%}$	0.32	1.16	263	0.22	−31
	$a_{max,1SRMS}$	0.34	0.90	165	0.18	−47
UK NA to Eurocode 1 (Group)	$a_{2.5\sigma}$	0.37	1.39	276	0.49	32
	$a_{max,1SRMS}$	0.34	0.74	118	0.35	3
UK NA to Eurocode 1 (Stream)	$a_{2.5\sigma}$	0.37	4.33	1,070	0.54	46
	$a_{max,1SRMS}$	0.34	3.06	800	0.43	26
Test 3: Podgorica footbridge			$\zeta = 0.0026$		$\zeta = 0.0067$	
French Sétra	$a_{95\%}$	0.55	0.80	45	0.52	−5
	$a_{max,1SRMS}$	0.42	0.80	90	0.40	−5
UK NA to Eurocode 1 (Group)	$a_{2.5\sigma}$	0.34	1.00	194	0.56	65
	$a_{max,1SRMS}$	0.42	0.70	67	0.39	−7
UK NA to Eurocode 1 (Stream)	$a_{2.5\sigma}$	0.34	0.65	91	0.42	24
	$a_{max,1SRMS}$	0.42	0.46	10	0.30	−29

Test 2: Test structure: PT Laboratory slab – Pedestrian traffic: five synchronized pedestrians, walking with half of first vertical mode natural frequency (4.5/2 = 2.25 Hz)

Case 1: Results of design models using damping ratio of empty structure ($\zeta = 0.0098$)
Case 2: Results of design models using damping ratio of occupied structure ($\zeta = 0.0160$ - Note that in this case only five pedestrians are present on the structure and therefore corresponding damping ratio is slightly smaller than previous case with 6 people on the structure)

Test 3: Test structure: Podgorica footbridge – Pedestrian traffic: real-life situation, moderate to high traffic

Case 1: Results of design models using damping ratio of empty structure ($\zeta = 0.0026$)
Case 2: Results of design models using damping ratio of occupied structure (higher damping value suggested by Zivanovic based on Monte Carlo simulation of pedestrian stream [3]) ($\zeta = 0.0067$)

The graphical representation of the results is illustrated in Fig. 5.7.

5.6.2 Discussion on Results

In this section, the calculated responses of PT slab and Podgorica footbridge under proposed loading scenarios are discussed in comparison with the actual measured data. In should be mentioned that in each case, the contribution of corresponding pedestrians to the modal mass of the considered mode was taken into account. For stream of pedestrians, their masses were assumed to be uniformly distributed over the structure and further scaled by the square of the mode shape ordinates. For groups, their mass was considered as a mean value (static component) of dynamic force and exerted on the structure as a force, moving along the walking path.

Results show that Sétra guideline overestimates the results in case 1 of all the tests, but it gives a fairly good estimation of actual response in Podgorica footbridge in comparison with other two cases. Considerable improvement in accuracy of this method's results is noticeable using SP added damping (case 2 of tests).

Although UK National Annex to Eurocode 1 overestimates the results in case 1 of all the tests, it gives a fairly good estimation in test 3. Use of SP added damping ratio has greatly enhanced the results especially the results of test 2 and 3. Even though performance of 'stream' and 'group' load models of UK NA to EC1 were not consistent in all tests but 'stream' load model shows slightly better results.

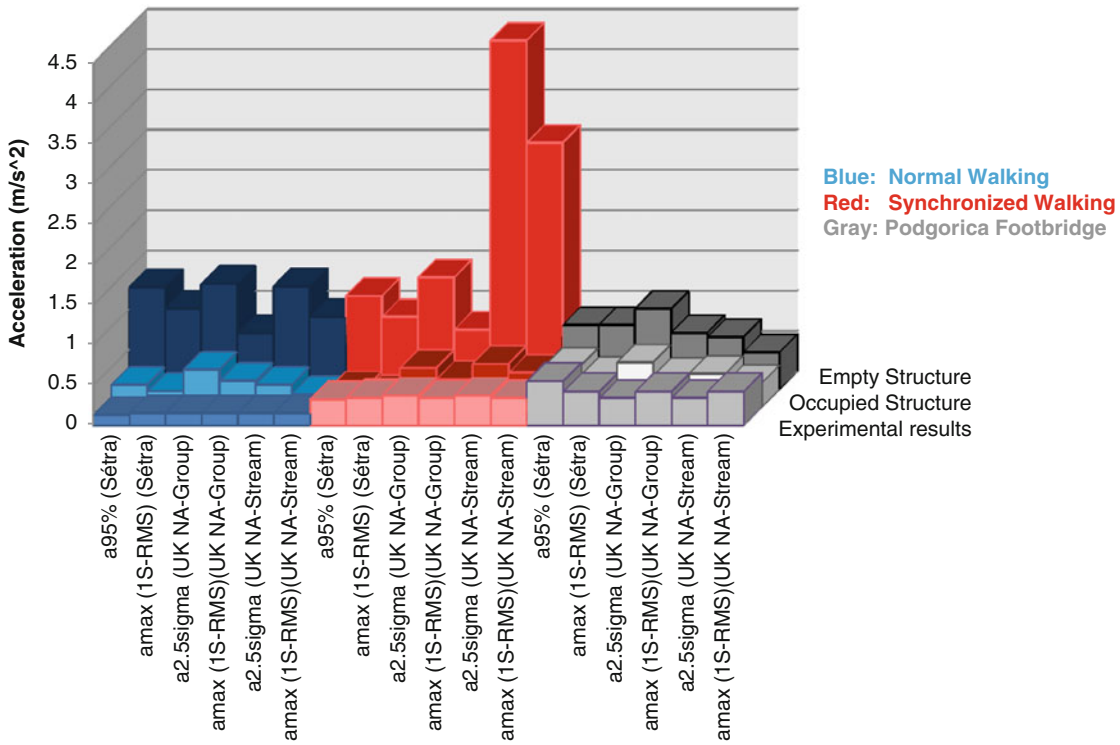

Fig. 5.7 Results of test 1, 2 and 3

Finally, the observed trend that both Sétra and UK NA to EC1 perform much better in test 2 and 3 is due to the fact that pacing frequency of pedestrians are closer to the natural frequency of structure and therefore closer to the initial assumption of these guidelines. It should also be noted that both codes refer to much denser traffics than are considered in this paper and therefore they need to be studied in more details in such cases.

5.7 Conclusion

This paper has reviewed two of the most recent and widespread guidelines which are used for vibration serviceability assessment of footbridges exposed to multi-person traffic and has analysed their performance under first and second harmonics of various types of walking loads. Results show that these design models are mostly tend to overestimate the response due to their conservative pre assumptions such as considering single amplitude and deterministic walking load, neglecting inter-subject (different people generate different loads) and intra-subject (nobody make two exactly identical step) variability [7], taking pedestrians pacing frequency equal to natural frequency of one of excitable modes and overestimation of traffic synchronization.

The studied guidelines have shown to be able to predict response of structures due to second harmonic of walking with more or less same accuracy of first harmonic; but none of them take into account the human structure interactions.

To investigate the effects of HIS on response of structures, SP added damping value (Damping of the excitable mode while pedestrians are standing-still on the structure) is used to improve the performance of design models which was successful in majority of the cases. The results prove that human-structure interactions have significant effects on response of structures in vertical direction due to walking and emphasize on an urgent need for further research on quantification of human effects on the structures.

Effects of walking pedestrians on structures are still to a high extent unknown and their quantification needs more comprehensive sets of real-life measurements and more detailed statistical analysis of pedestrian effects on structural response.

Acknowledgements The first author would like to express his deep gratitude to Mrs. Legha Momtazian for her supports.

References

1. NA to BS EN 1991-2:2003 (2008) BSI UK national annex to eurocode 1: actions on structures - part 2: traffic loads on bridges. s.l. British standards institution, London
2. Setra (2006) Footbridges, assessment of vibrational behaviour of footbridges under pedestrian loading, technical guide. Service d'Etudes Techniques des Routes et Autoroutes, Paris
3. Zivanovic S, Pavic A, Ingolfsson ET, ASCE (2010) Modelling spatially unrestricted pedestrian traffic on footbridges. J Struct Eng 136:1296–1308
4. Nyawako D, Reynolds P (2000) Active control of human induced floor vibrations. In: IMAC conference, Society for Experimental Mechanics (SEM), Jaksonville
5. Zivanovic S, Pavic A, Reynolds P (2006) Modal testing and FE model tuning of a lively footbridge structure. Eng Struct 28:857–868
6. Zivanovic S, Dıaz IM, Pavic A (2009) Influence of walking and standing crowds on structural dynamic performance. In: Proceedings of 27th international modal analysis conference (IMAC XXVII), Orlando
7. Brownjohn JMW, Pavic A, Omenzetter P (2004) A spectral density approach for modelling continuous vertical forces on pedestrian structures due to walking. Can J Civil Eng 31:65–77

Chapter 6
Sensitivity of Footbridge Response to Load Modeling

Lars Pedersen and Christian Frier

Abstract The paper considers a stochastic approach to modeling the actions of walking and has focus on the vibration serviceability limit state of footbridges. The use of a stochastic approach is novel, but useful, as it is more advanced than the quite simplistic deterministic load models seen in many design codes. Using a stochastic approach, however, requires a number of decisions to be made (statistical distributions and associated parameters) for walking parameters. These decisions might have an impact on the outcome of serviceability evaluations (bridge acceleration levels), but it is often not a simple matter to foresee their impact. The paper contributes by examining how some of these decisions influence the outcome of serviceability evaluations. The sensitivity study is made focusing on vertical footbridge response to single person loading.

Keywords Walking loads • Vibration serviceability • Footbridge vibrations

Nomenclature

f_0	Bridge frequency
l_s	Stride length
q	Modal load
e	Response ratio
ζ	Bridge damping ratio
f_s	Step frequency
m	Weight of pedestrian
L	Bridge length
a	Bridge acceleration
μ	Mean value
f	Walking load
p	Prob. density function
M	Bridge modal mass
α	Dynamic load factor
σ	Standard deviation

L. Pedersen (✉) • C. Frier
Department of Civil Engineering, Aalborg University, Sohngaardsholmsvej 57, DK-9000 Aalborg, Denmark
e-mail: lp@civil.aau.dk

J.M. Caicedo et al. (eds.), *Topics on the Dynamics of Civil Structures, Volume 1*,
Conference Proceedings of the Society for Experimental Mechanics Series 26,
DOI 10.1007/978-1-4614-2413-0_6,

6.1 Introduction

Walking-induced vibrations in footbridges are of concern because the vibrations may render bridges unfit for their intended use, as levels of bridge vibration may not comply with serviceability limit state requirements. The walking-induced vibrations in the London Millennium Bridge [1] serve as an example. In terms of serviceability evaluations of footbridges there are different ways of approaching the issue. One approach is to rely on simplistic deterministic load models when predicting bridge acceleration levels. Another approach, and a more advanced approach, is to use stochastic models for the walking parameters as offset for computing bridge response to actions of walking.

Many codes of practise (such as [2, 3]) rely on the deterministic load model. For a specific bridge this approach gives a deterministic value of bridge accelerations, which can be compared with a threshold value. The approach is reasonably simple to operate, but it does not account for the stochastic nature of the walking load (walking parameters). For instance, it does not consider that the walking velocity, stride length and step frequency is likely to vary between pedestrians crossing the bridge. Nor that the pedestrian weight and dynamic load amplification vary between pedestrians. Measurements and research have made stochastic models for a number of the walking parameters available [4–6], and [5] introduced an approach accounting for the stochastic nature of walking parameters when seeking to estimate probability distribution functions for bridge accelerations to action of single person traffic.

Even though the new approach is considered useful it is more difficult to operate than the fully deterministic approach, because it requires more input data and assumptions. For instance decisions need to be made with respect to distribution types, mean values and standard deviations for the walking parameters.

In the paper focus is on implications of different assumptions as concerns the standard deviation of walking parameters. Both realistic non-zero standard deviations and zero standard deviation assumptions are considered for a probability-based estimate of bridge accelerations, allowing comparisons of results.

This approach is useful as it explores how sensitive probability-based estimates of bridge accelerations are to standard deviation assumptions for the walking parameters (and standard deviation assumptions need to be made for a probability-based estimate of bridge accelerations).

Separate sensitivity studies (A, B, and C) are made focusing on different walking parameters. Study A addresses walking velocity assumptions, which can be related to assumptions made for stride length and step frequency and their standard deviations. Study B addresses standard deviation assumptions for pedestrian weight, and study C addresses standard deviation assumptions for the dynamic load factor.

Selected characteristics (quantiles) of the probability distribution function for footbridge response are considered for the evaluations. To facilitate the investigations, a footbridge model is required, and to this end a pin-supported footbridge (idealised as a single-degree-of-freedom system, SDOF-system) is employed. The bridge response characteristic given focus is the midspan peak acceleration (the parameter often used for judging bridge serviceability), and accelerations are predicted using numerical simulations.

Characteristics of the bridge and walking loads are introduced in Sect. 6.2. Section 6.3 presents the sensitivity studies and Sect. 6.4 summarizes the results.

6.2 Characteristics of Bridge and Walking Loads

6.2.1 Bridge Dynamic Characteristics

The dynamic characteristics of the bridge considered for the studies of this paper are shown in Table 6.1.

Having a natural frequency (f_0) of 2.00 Hz, the bridge has a high probability of resonating as a result of pedestrian traffic, as the mean value of step frequency assumed for the studies of this paper will be 1.99 Hz.

The magnitude of the modal mass (M) is considered to be fairly realistic for a bridge with a frequency of 2.00 Hz, and so is the length of the bridge, L, which is assumed to be 43 m.

The damping ratio,ζ, of 0.3% of critical damping means that the bridge is lightly damped.

Table 6.1 Bridge dynamic characteristics

f_0	M	ζ
2.00 Hz	$39.5{\cdot}10^3$ kg	0.3%

6.2.2 Model for Walking Loads

Focus is on walking loads in the vertical direction. A pedestrian with a weight of m is assumed to generate the load described by (6.1):

$$f(t) = mg\alpha \cos(2\pi f_s t) \tag{6.1}$$

in which t is time [7–9]. When on the bridge, the pedestrian is assumed to walk with a constant step frequency, f_s, but for the later studies of this paper it is modelled that the value of f_s might change from one pedestrian to the next by treating f_s as a random variable. How the dynamic load factor, α (non-dimensional), and the pedestrian weight, m (in kg), are modelled will be presented later. The parameter g represents acceleration of gravity (for simplicity $g = 10$ N/kg is assumed).

Super-harmonic load components (nf_s, $n = 2, 3,..$) would exist, but for the SDOF bridge considered for the study, it would be the first load harmonic ($n = 1$) that would cause the potentially problematic resonant response of the bridge. Hence, the studies do not consider super-harmonic load components.

It can be shown that the modal load on the bridge, $q(t)$, may be computed using (6.2):

$$q(t) = mg\alpha \sin(2\pi f_s t)\, \Phi(t) \tag{6.2}$$

where $\Phi(t)$ is the value of the mode shape function for the first vertical bending mode of the footbridge at the current position of the pedestrian. This value may be computed using either (6.3) or (6.4):

$$\Phi(t) = \sin\left(\frac{\pi v}{L} t\right) \tag{6.3}$$

$$\Phi(t) = \sin\left(\frac{\pi f_s l_s}{L} t\right) \tag{6.4}$$

as the walking velocity v may be derived from the following relationship:

$$v = f_s\, l_s. \tag{6.5}$$

For later computations, it is assumed that any pedestrian traverses the bridge using a constant stride length, l_s, (step length), and a constant step frequency, f_s, and thus with a constant walking speed v. However, it is also considered for later computations that stride length and step frequency may vary between pedestrians.

6.2.3 Model for the Dynamic Load Factor

The dynamic load factor is modelled to depend on step frequency, f_s, according to the relationship given in (6.6) [6]:

$$\alpha = c_1 f_s^3 + c_2 f_s^2 + c_3 f_s + c_4 \tag{6.6}$$

where

$$c_1 = -0.2649 \quad c_2 = 1.306 \quad c_3 = -1.7597 \quad c_4 = 0.7613. \tag{6.7}$$

In (6.6), α represents the mean value of the dynamic load factor (also denoted μ_α) for a given step frequency, f_s (inserted in Hz in (6.6)). According to [6], the standard deviation of the dynamic load factor (denoted σ_α) may be computed using (6.8):

$$\sigma_\alpha = 0.16\ \mu_\alpha \tag{6.8}$$

For the studies of this paper, the dynamic load factor is assumed to follow a Gaussian distribution.

This approach of modelling the dynamic load factor (as a random variable) is more advanced than the models used in many current codes of practise. For instance [2, 3] do not recognise that the dynamic load factor is a random variable nor that it depends on step frequency.

6.3 Sensitivity Studies

6.3.1 Study A

6.3.1.1 Approach and Study Assumptions

In this study, two different ways of modelling the walking load is considered. The difference is whether the mode shape function is calculated using (6.3) or (6.4). Basically, there should be no difference in the result, but it would depend on whether the walking velocity v is modelled deterministically (as a constant entering in (6.3)) or as a product of the outcome of two stochastic variables (step frequency (f_s), and stride length (l_s) entering in (6.4)).

In both cases it is relevant to consider the stochastic nature of step frequency (f_s), and stride length (l_s). In [4, 5] it is suggested to model these parameters as random variables following Gaussian distributions. The assumed mean values (μ) and standard deviations (σ) are shown in Table 6.2.

In the first study approach, A1, the walking velocity is calculated as:

$$v = f_s\, l_s \tag{6.9}$$

where step frequency (f_s) and stride length (l_s) represent the outcomes of the two stochastic variables; outcomes which can be obtained employing MonteCarlo simulations.

In the second study approach, A2, the walking velocity is calculated as:

$$v = 1.99\,\text{Hz} \cdot 0.71\text{m} = 1.413\,\text{m/s} \tag{6.10}$$

which is a result obtained entering the mean values for step frequency (f_s) and stride length (l_s) shown in Table 6.2 in (6.9).

In approach A2, the value of 1.413 m/s is assumed for any pedestrian, even though the product given in (6.9) would not be the same for every pedestrian. Hence, approach A2 is a simplification of matters. The interesting part is whether the probability distribution function for the bridge response is sensitive to whether approach A1 or A2 is used for the computation of walking loads.

For the pedestrian weight (m) a deterministic value of 75 kg is assumed.

6.3.1.2 Computations

In terms of bridge response, the midspan peak accelerations are considered. Probability distribution functions of bridge accelerations were computed using MonteCarlo simulations. These account for the modelled stochastic nature of the parameters of the load model. As many as 500,000 single person bridge crossings were simulated to provide estimates of probability distribution functions of bridge accelerations (assuming approach A1 and A2, respectively), and in the process Newmark time integration was employed to determine structural vibrations. In the paper, focus will only be on selected characteristics (quantiles) of the computed probability distribution functions. The quantile a_{95} is of interest as this quantile has been in focus in a number of other publications dealing with bridge response in a stochastic manner [5, 10, 11], and because it is believed that a high quantile would be useful for serviceability assessments. The value of a_{95} is expected to be exceeded in 1 out 20 bridge crossings. For completeness, some other quantiles were also derived from the computed probability distribution functions of bridge accelerations.

Table 6.2 Mean values and standard deviations

Variable	Unit	μ	σ
f_s	Hz	1.99	0.173
l_s	m	0.71	0.071

Table 6.3 Response ratios

e_{95}	e_{90}	e_{75}
− 0.02	0.00	0.00

Table 6.4 Mean values and standard deviations

	Variable	Unit	μ	σ
Approach B1	m	kg	75	15
Approach B2	m	kg	75	0

6.3.1.3 Results

For the presentation of results, the ratios defined in (6.11) are employed, where the subscript refers to the quantile being evaluated.

$$e_{95} = \frac{a_{95}(\mathrm{A2}) - a_{95}(\mathrm{A1})}{a_{95}(\mathrm{A1})} \quad e_{90} = \frac{a_{90}(\mathrm{A2}) - a_{90}(\mathrm{A1})}{a_{90}(\mathrm{A1})} \quad e_{75} = \frac{a_{75}(\mathrm{A2}) - a_{75}(\mathrm{A1})}{a_{75}(\mathrm{A1})} \tag{6.11}$$

The ratios define the relative difference between selected acceleration quantiles obtained using approach A1 and approach A2.

Table 6.3 gives results in terms of e using two digits.

It can be seen that the probability distribution function for bridge accelerations is relatively insensitive to whether approach A1 or approach A2 is employed for modelling walking loads. This has the effect that the probability distribution of bridge accelerations is insensitive to the stochastic nature of stride length (l_s). The stride length could be modelled deterministically (using its mean value), and almost similar results in terms of the probability distribution function for bridge acceleration would be obtained.

The same cannot be said for the step frequency (f_s), as this parameter enters the load equation not only in the expression for $\Phi(t)$. However, for the calculation of $\Phi(t)$, it appears to be sufficient to use the mean value for step frequency in combination with the mean value for stride length. In order words, the results suggest that it is not necessary to model walking velocity as a variable changing value between pedestrians.

It can be noted that the walking velocity of $v = 1.413$ m/s obtained using approach A2, is not that different from the walking velocity of 1.5 m/s, being the value often referred to as the typical walking velocity. For some reason, the design code [3] assumes the walking velocity to equal $0.9\, f_0$, thus relating the walking speed to the bridge frequency.

6.3.2 Study B

6.3.2.1 Approach and Study Assumptions

For these studies, the bridge characteristics are similar to those assumed for study A. The walking load is described using approach A1 in study A, so both step frequency and stride length are treated as random variables being the most advanced approach for modelling these parameters. For the parameters describing the stochastic nature of these parameters, reference is given to Table 6.2.

Focus of the study is on how sensitive the probability distribution function of midspan bridge accelerations is to whether the pedestrian weight m is modelled as a random variable with non-zero standard deviation (approach B1) or as a deterministic value (approach B2). For the studies, two different assumptions with respect to m are considered, and they are presented in Table 6.4.

Table 6.5 Response ratios

e_{95}	e_{90}	e_{75}
0.00	0.01	0.03

Table 6.6 Mean values and standard deviations

	Variable	μ	σ
Approach C1	α	Equation 6.6	Equation 6.8
Approach C2	α	Equation 6.6	0

In approach B1, m is assumed to follow a Gaussian distribution. The standard deviation of 15 kg is considered to be fairly realistic although, surprisingly, it is difficult to find literature focusing on the scatter of weights of humans.

6.3.2.2 Computations

The computations followed the scheme outlined in study A, and probability distribution functions for midspan accelerations were identified for approach B1 and approach B2. From these functions, bridge acceleration quantiles were extracted.

6.3.2.3 Results

Employing ratios as defined in study A, the relative difference between selected quantiles of the probability distribution function using approach B1 and B2 was identified. The results in terms of e are shown in Table 6.5.

As can be seen, the derived quantiles of the probability distribution function of midspan bridge accelerations are fairly insensitive to whether approach B1 or B2 is assumed. A plot of the probability distribution would reveal that this is not only the case for the selected quantiles, but that the entire probability distribution is fairly insensitive to whether a deterministic or a stochastic model is assumed for pedestrian weight.

The results suggest that it might not be that necessary to account for the stochastic nature of pedestrian weight (standard deviation of pedestrian weight), when the task is to predict the quantiles of midspan peak accelerations. More detailed investigations reported in [11] (considering a number of different statistical distributions for pedestrian weight) support this recognition.

6.3.3 Study C

6.3.3.1 Approach and Study Assumptions

For these investigations the walking load was determined in the same way as in approach B1 (modelling pedestrian weight and step frequency and stride length as random variables).

The central focus of study C is to explore how sensitive the probability distribution function of midspan bridge accelerations is to whether the dynamic load factor (α) is modelled as a random variable with non-zero standard deviation (approach C1) or as a deterministic value (approach C2). Hence, for the investigations, two different assumptions are considered taking offset in equations for mean value and standard deviation of the dynamic load factor, α, presented in Sect. 6.2.3. The two different assumptions are given in Table 6.6.

In approach C1, α is assumed to follow a Gaussian distribution. In approach C2, the scatter known to exist is disregarded for the computations. For these investigations, a bridge with slightly different modal characteristics than those given in Table 6.1 was investigated. Hence, it would not be reasonable to present results in the same way as done in study A and B.

It shall only be mentioned that it turned out that for the quantile a_{95}, the result obtained using approach C1 and C2 deviated by less than 3%, suggesting that it is not that relevant to account for the stochastic nature of the dynamic load factor when seeking to estimate the quantile a_{95}.

6.4 Conclusion

A number of the parameters of the load model (walking parameters) are by nature stochastic, leaving a number of decisions to be made prior to lunching a probability-based computation of bridge response; for instance decisions with respect to values of the standard deviations for the walking parameters. However, the results of sensitive studies imply that probability distribution functions of bridge accelerations are relatively insensitive to whether the considered walking parameters are treated as random variables (with non-zero standard deviation) or as deterministic values.

Without the sensitivity studies, this would be difficult to foresee, and the recognitions are useful, as they have the immediate effect that it is simpler to operate a probability-based approach to estimating bridge response. The complexity of the problem is markedly reduced by knowing which properties (input data) not to be that concerned with.

However, it must be recalled that the sensitivity studies only considered the response of a single bridge, and that multi-person pedestrian traffic was not addressed in the studies.

References

1. Dallard P, Fitzpatrick AJ, Flint A, Le Bourva S, Low A, Ridsdill-Smith RM, Wilford M (2001) The London millennium bridge. Struct Eng 79:17–33
2. Ontario Highway Engineering Division (1983) Ontario highway bridge design code, highway engineering division. Ministry of Transportation and Communication, Ontario
3. British Standard Institution (1978) Steel, concrete and composite bridges. Specification for loads, BS 5400: Part 2. BSI: London
4. Matsumoto Y, Nishioka T, Shiojiri H, Matsuzaki K (1978) Dynamic design of footbridges. In: Proceedings of IABSE, No. P-17/78: pp 1–15
5. Živanovic S (2006) Probability-based estimation of vibration for pedestrian structures due to walking. Ph.D thesis, Department of Civil and Structural Engineering, University of Sheffield, UK
6. Kerr SC, Bishop NWM (2001) Human induced loading on flexible staircases. Eng Struct 23:37–45
7. Ellis BR (2000) On the response of long-span floors to walking loads generated by individuals and crowds. Struct Eng 78:1–25
8. Bachmann H, Ammann W (1987) Vibrations in structures – induced by man and machines. IABSE Structural Engineering Documents 3e, Zürich
9. Rainer JH, Pernica G, Allen DE (1998) Dynamic loading and response of footbridges. Can J Civil Eng 15:66–78
10. Pedersen L, Frier C (2009) Sensitivity of footbridge vibrations to stochastic walking parameters. J Sound Vib. doi:10.1016/j.jsv.2009.12.022
11. Pedersen, L, Frier C (2009) Sensitivity study of stochastic walking load models. In: Proceedings of the 28th international modal analysis conference (IMAC XXVIII), Jacksonville

Chapter 7
Crowd-Induced Vibrations of a Steel Footbridge in Reykjavík

E.T. Ingólfsson, G.V. Gudmundsson, S. Živanović, and A. Pavic

Abstract Vibration serviceability of structures for human occupancy has become an important part of the design of slender civil engineering structures such as footbridges. In the past decades, a considerable amount of research has been carried out within the field and international codes of practice and state-of-the-art design guidelines been improved considerably. However, there are several important questions that remain unanswered. In particular the response of pedestrians to footbridge vibrations is severely under-researched. This is primarily due to lack of data from real-life footbridges subject to in-service traffic. In addition, the lack of a generally accepted way to quantify measured vibration response on footbridges makes it difficult to interpret data from already published experiments. In this paper, various methods to quantify human-response to vibrations are reviewed and put in relation to the results obtained from a controlled crowd test on a steel footbridge in Reykjavik, Iceland. A systematic quantification of the measured vibration response is carried out and the results are presented statistically through their probability distributions. Finally, testimonies from participants in a controlled perception tests are used in conjunction with measured responses, to obtain valuable information about human response to footbridge vibration. It is shown that there is only a small correlation between the subjective rating and the vibration felt by the pedestrians.

Keywords Footbridges • Human-induced vibration • Full-scale testing • Human-perception

7.1 Introduction

The work presented in this study is a part of a larger research campaign funded by the Icelandic Road Administration, within the framework of improving current national guidelines dealing with dynamic loads on footbridges and the associated response of pedestrians. The project was lead by Línuhönnun Consulting Engineers (now Efla) and carried out in collaboration with the Technical University of Denmark, the University of Iceland and the University of Sheffield. Within the project, an extensive experimental campaign has been undertaken to characterise the vibration serviceability of several footbridges, all of which are a part of the main foot- and bicycle-path system in the city of Reykjavik, Iceland. The most recently built bridges are three post-tensioned concrete bridges, two of which are susceptible to human-induced vibrations [1, 2]. Herewith, the results of an experimental investigation into the dynamic performance of the first footbridge on this path system (built in 1995) are presented. The footbridge under investigation features a complicated dynamic performance, with

E.T. Ingólfsson (✉)
Civil Engineering Structural Dynamics Group, Department of Civil Engineering, Technical University of Denmark, Bygning 118, Brovej, 2800 Kgs Lyngby, Denmark
e-mail: eti@byg.dtu.dk

G.V. Gudmundsson
Efla Consulting Engineers, Höfðabakki 9, 110 Reykjavík, Iceland

S. Živanović
Civil Research Group, School of Engineering, University of Warwick, Coventry CV4 7AL, UK

A. Pavic
Vibration Engineering Section, Department of Civil and Structural Engineering, University of Sheffield, Sir Frederick Mappin Building, Mappin Street, Sheffield S1 3JD, UK

J.M. Caicedo et al. (eds.), *Topics on the Dynamics of Civil Structures, Volume 1*,
Conference Proceedings of the Society for Experimental Mechanics Series 26,
DOI 10.1007/978-1-4614-2413-0_7,

multi-frequency and multi-axis vibrations when subject to loading from pedestrians. As such, a short review of available assessment methods capable of taking this into account is presented. An in-depth analysis of the measured response during a random crowd test is carried out, both using a simple single-mode, single-axis analysis and also by utilizing the concepts of both the ISO and the British standards. These methods are selected because they are compatible with other areas of engineering dealing with human response to vibration and also because they take into account the duration of the vibration exposure as well as the effect of combined multi-axis, multi-frequency vibration. In addition, most of the measured quantities are presented probabilistically, e.g. in terms of their probability distribution or return period dependency. The paper therefore moves beyond the scope of current footbridge design guidelines in an attempt to establish a well-reasoned and general methodology of presenting measured vibration responses on footbridges. In the final part of this paper, a controlled human perception test is carried out, in which a subjective rating of the vibration felt by the participants is analysed to investigate the serviceability of the bridge.

7.2 Human-Response to Whole-Body Vibration

7.2.1 Current Guidelines for Footbridges

With few exceptions, most research into vibration serviceability of footbridges has been focused on unidirectional load and response, whereas less is known about the reaction of pedestrians to combined vertical and lateral motion. In particular, modes which feature horizontal components may be more critical in relation to the serviceability of the bridge as human comfort tolerances are generally lower for lateral vibrations than their vertical counterpart for low frequency motion (below approximately 3 Hz).

Human response to a vibratory environment depends on a large number of variables. Of particular importance are the vibration characteristics (type, magnitude, frequency content, direction and duration), posture and activity (sitting, standing or walking), as well as the subject characteristics (number of people exposed to the vibration, gender, age, experience and expectation) [3]. The frequency dependency of the human response to vibration was acknowledged in the first code of practice that dealt with serviceability design of footbridges (BS 5440:1978 [4]). Here the limit between acceptable and unacceptable vibrations was defined as the limiting peak acceleration:

$$a_{\lim} = 0.5\sqrt{f} \tag{7.1}$$

Current state-of-the-art design guidelines for footbridge vibrations [5–7] do not take into account this frequency dependency. Instead various comfort limits are expressed in terms of maximum allowable peak acceleration, which is constant over the entire frequency range. In the international standard ISO 2631-2:1989 [8], *baseline curves* were introduced, which represent equal perception of vibration over the frequency range (Fig. 7.1a). For vibration magnitudes

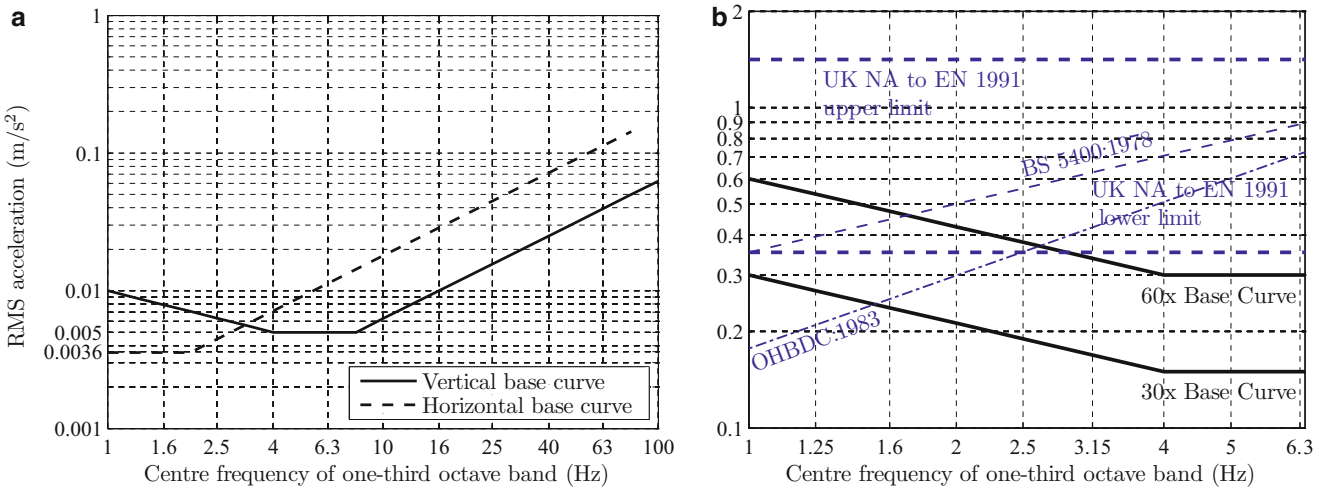

Fig. 7.1 (**a**) Base curve for human exposure to whole body vibrations in the vertical and horizontal (*medio-lateral*) direction according to ISO 2631-2:1989 [8] and (**b**) comparison between common (*vertical*) vibration criteria for footbridges

below the baseline curve, the probability of adverse comments was deemed low, hence these curve can be interpreted as approximations to the limit between perceptible and non-perceptible vibration. The allowable vibration magnitude, expressed in terms of the root-mean-square (RMS) acceleration is provided as a simple base curve multiplier (or response factor R). For verification of footbridge serviceability, a response factor $R = 30$ for standing and R = 60 for walking persons has been recommended [9] (with $\tau = 1$ s as averaging time). In Fig. 7.1b, a comparison between some common guidelines for vertical footbridge vibrations are shown. Criteria that rely on peak acceleration have been transformed to RMS using a multiplication factor $1/\sqrt{2}$. As illustrated in Fig. 7.1b there is a considerable difference between various vibration assessment methods for footbridge, both in terms of vibration quantity (peak or RMS), allowable magnitude and frequency dependency. The criterion proposed in BS 5400:1978 [4] is based on research studies using persons walking on a vertically moving surface whereas the ISO curves are primarily based on stationary human beings [3]. Kasperski [10] analysed the subjective rating of 84 pedestrians (and a number of joggers and cyclists) to vibrations on a "lively" footbridge and concluded that the ISO 10137 [9] criterion agreed qualitative with the observations made on the bridge. However, it was suggested that a limit value of $R = 24$ is more appropriate comfort criteria than R = 60 (and R = 30 for passive people).

Barker [11] argues that a method similar to that of BS 6472 [12] (i.e. vibration dose value obtained from frequency weighted acceleration) should be used as it is capable of integrating the net discomfort over frequency and vibration exposure. The fourth-power vibration dose value (VDV) is defined as

$$\mathrm{VDV} = \left[\int_0^T a^4(t)\,\mathrm{d}t\right]^{\frac{1}{4}} \tag{7.2}$$

The VDV is more sensitive to peaks in the time history that the RMS averaging and it is a cumulative quantity with the unit [m/s$^{1.75}$]. Thereby, it can potentially be used to compare the response of pedestrians on various bridges with varying vibration exposure time. Zivanovic and Pavic [13] analyzed the response felt by about 100 pedestrians during crossing of a 'lively' footbridge in Podgorica. It was shown that there is a strong linear correlation between the peak and the peak 1 s RMS acceleration felt by a pedestrian and also between the peak and the overall RMS and VDV value. Therefore, it was argued that these quantities are equally suitable for analysis of the human response to vibration on this particular footbridge experiencing narrow band vibrations at frequency around 2 Hz.

7.2.2 *Multi-axis and Multi-frequency Whole-Body Vibration*

In the original ISO 2631:1974 standard [14], the preferred vibration assessment method was the so-called *rating method*, which is based on the assumption that the human sensitivity (or vibration tolerance) is determined by the third octave band having the highest magnitude and thereby neglecting the effect of other frequencies. According to Griffin [3], this method may underestimate the response of human-beings if the vibration is not dominated by a single-axis, single-frequency sinusoidal vibration. A more general method is the *weighting method*, where the acceleration response is weighted by inverse baseline curve so to normalize the net effect of vibration on the human body in the form of vibration at a single frequency. In fact, the base curves are not an exact inverse of the frequency weighting functions, defined in ISO 2631-1:1985 [15], but simplified bi-linear approximations. The frequency weighting functions are shown in Fig. 7.2. The RMS acceleration or the VDV value is calculated for the weighted acceleration in each of the three axes. For the RMS acceleration, the effective response is obtained as the SRSS (Square-Root of the Sum of the Squares) of the individual components. Since the human-perception threshold may be different in the three directions (x, y and z), the effective acceleration is expressed through additional (optional) weights:

$$\mathrm{a}_{RMS,\tau} = \sqrt{k_x^2 a_{RMS,\tau,x}^2 + k_y^2 a_{RMS,\tau,y}^2 + k_z^2 a_{RMS,\tau,z}^2} \tag{7.3}$$

where $a_{\mathrm{RMS},\tau j}$ ($j = x, y, z$) is a frequency-weighted RMS acceleration with averaging time τ. The weighting factors for longitudinal (k_x), lateral (k_y) and vertical (k_z) directions take into account variations in the perception (or comfort) threshold for different directions, e.g. the lower threshold of the ISO base curve in Fig. 7.1a (ISO 2631-2:1989 [8]) is different for the horizontal and vertical direction. In this case, weighting factors $k_x = k_y = 1.4$ and $k_z = 1$ are appropriate (i.e. 0.005/0.00357).

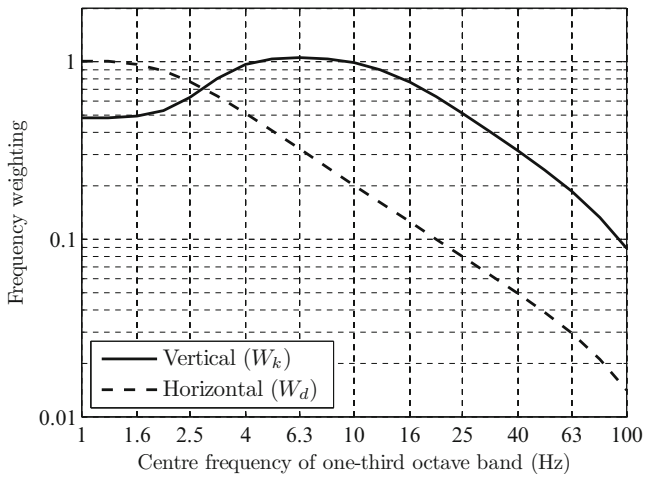

Fig. 7.2 Frequency weighting functions for human exposure to whole body vibrations in the vertical and horizontal directions according to ISO 2631-1:1985 [15]

More intuitively, the vibration exposure can be expressed in terms of the response factor (R), which is defined as the frequency-weighted acceleration normalized by the base curve acceleration in the appropriate direction:

$$R_x = \frac{a_{\mathrm{RMS},\tau,x}}{0.00357\,\mathrm{m/s^2}}, \quad R_y = \frac{a_{\mathrm{RMS},\tau,y}}{0.00357\,\mathrm{m/s^2}}, \quad R_z = \frac{a_{\mathrm{RMS},\tau,z}}{0.005\,\mathrm{m/s^2}}, \quad R = \sqrt{R_x^2 + R_y^2 + R_z^2} \leq R_{\mathrm{lim}} \tag{7.4}$$

Thereby, the limit acceleration can be expressed as an effective response factor, which should be less than a certain limit R_{lim}. This methodology is used in newly published recommendations for serviceability assessment of floor structures [16].

For the VDV acceleration value, BS 6472-1:2008 [12] states that assessment of the VDV in the most significant directions should be made separately and no combination rule is provided. Thereby, the limits for the vibration dose values are direction-independent, provided that the correct frequency-weighting has been applied. However, acknowledging that human-perception threshold is different in the vertical and horizontal directions, it seems reasonable to apply a similar combination rule as used for the RMS acceleration. This could be written as:

$$\mathrm{VDV}_{eff} = \left[k_x^4 \mathrm{VDV}_x^4 + k_y^4 \mathrm{VDV}_y^4 + k_z^4 \mathrm{VDV}_z^4\right]^{\frac{1}{4}} \tag{7.5}$$

where the weighting factors $k_x = k_y = 1.4$ and $k_z = 1$ can be used to take into account the difference between the lower horizontal and vertical base curve accelerations. However, this method is currently not advocated in the standards.

7.3 Description of Fossvogur Footbridge

This steel footbridge was built in 1995 and is a part of the main foot- and bicycle-path system in the city of Reykjavik, Iceland. The bridge crosses Kringlumýrarbraut, which is the main traffic artery between the city centre and southern parts of the Icelandic capital, Kópavogur and Hafnarfjördur. The bridge is slightly curved, both in plan and elevation and has an overall length of 96.5 m divided into four main spans (17 m) and two shorter side spans (15 and 13.5 m). The bridge deck is made of wooden boards (100 × 200 mm), supported on two steel rectangular hollow section edge beams, which are interconnected with cross beams every 3–4 m. This very light superstructure is supported on a single row of eccentrically placed, tapered and inclined (15° from a vertical axis) steel columns, making the bridge sensitive to both vertical and lateral dynamic loads (Fig. 7.3).

Since its opening, the footbridge presented herewith has been known as lively and noticeable lateral vibrations have been reported on few occasions, e.g. during the opening ceremony. However, to the authors' knowledge, no formal complaints have been reported, although the bridge is frequently used by leisure commuters and joggers. The bridge connects a recreational area with suburban dwellings and as it is located close to the city centre and comprises a part of the main path system in Reykjavik, future urban growth is likely to cause an increased pedestrian traffic on the bridge.

Although the bridge is essentially a continuous beam bridge, its dynamic behavior is complicated. This is primarily caused by its relatively light superstructure (of steel and timber) combined with the inclined columns and cantilevered deck, creating a laterally and torsionally flexible structure. An experimental modal identification was carried out on the bridge using an electrodynamic shaker (model APS 113). The shaker was placed in one position of the bridge, whilst three accelerometers (model QA, 6.5 V/g) were moved to 19 different test sections (S1–S19 in Fig. 7.4). The shaker generates a

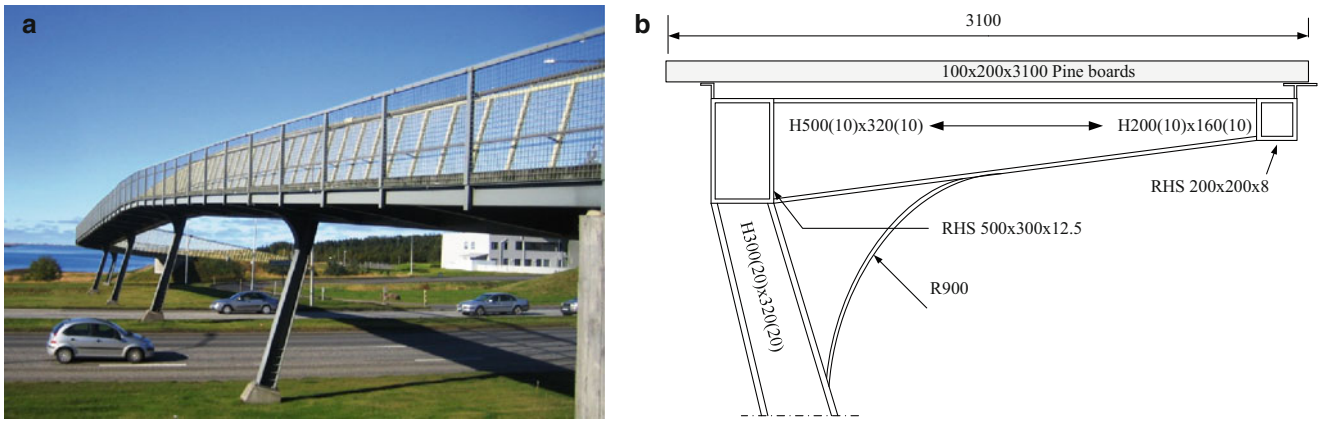

Fig. 7.3 Fossvogur steel footbridge (**a**) seen from the eastern end and (**b**) at a cross section at one of the columns

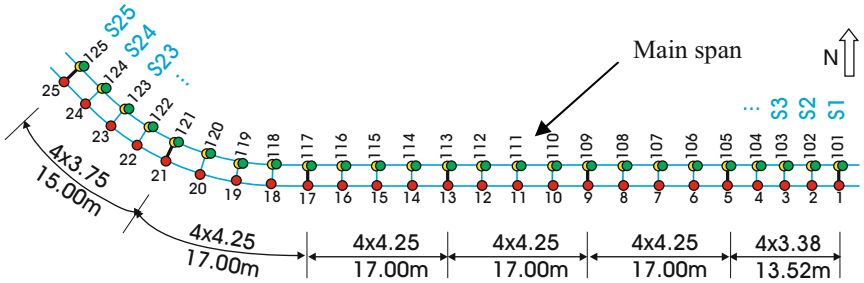

Fig. 7.4 Test-grid showing the test points used during the forced vibration tests

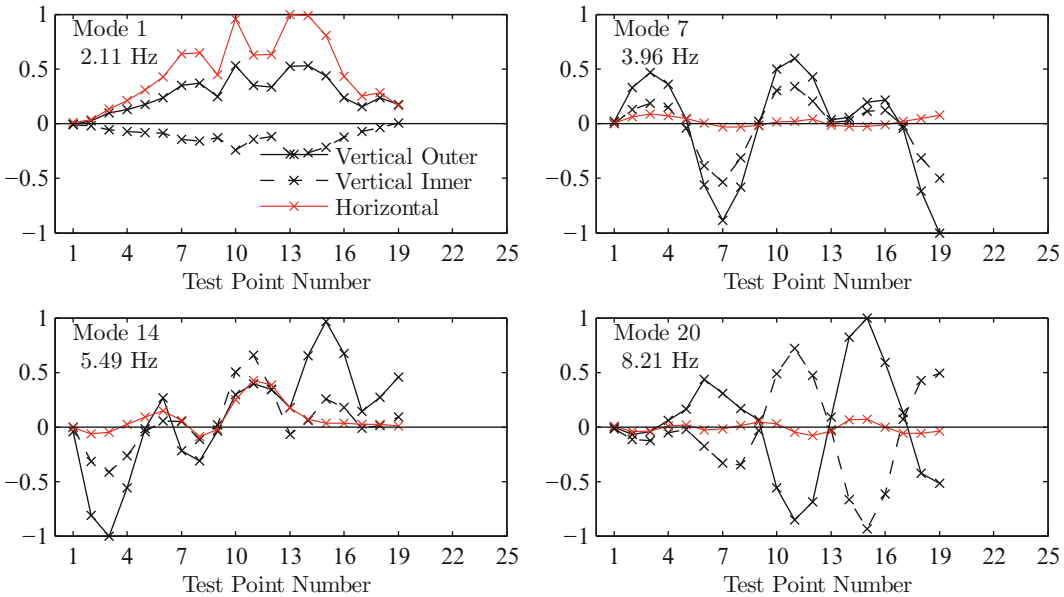

Fig. 7.5 Examples of experimentally determined vibration modes

pseudo-random vertical load with constant spectral density in the frequency range 0–20 Hz. A total of 22 modes with frequencies less than 9 Hz were identified, some of which are shown in Fig. 7.5. During the modal ID, the ambient wind load produced considerable vibrations in the bridge, which affected the quality of the modal estimates. Therefore, some of the mode shapes and modal masses as obtained experimentally should be calibrated with an updated FE-model. However, this process is beyond the scope of this paper.

7.4 Random Crowd Tests

A number of crowd tests were carried out on the bridge, utilizing more than 40 volunteering students from the University of Iceland. During all tests, the acceleration response of the structure was measured with four accelerometers (model QA, 1.3 V/g), three in the horizontal lateral direction and one in the vertical direction (Fig. 7.6). All acceleration signals were acquired with a sampling frequency 200 Hz. A large number of pedestrian tests were carried out with walking and jogging groups of various sizes to investigate the bridge vibrations under a number of realistic load cases. In this paper, only the results from the "random crowd" test and those dealing specifically with human-perception to vibration are presented.

7.4.1 Description of Random Crowd Test

Two groups of pedestrian were formed, one on each side of the test area shown in Fig. 7.6. The pedestrians were asked to enter the bridge, at a randomly generated time instant. The arrival time instance was generated from a uniform distribution, such that the arrival of the pedestrians resembles a Poisson process with a uniform flow rate. When the pedestrians had crossed the test area, they would wait at the other side for a signal to re-enter. The overall duration of this test was about 15 min. The participants were asked to walk normally across the bridge at their own comfortable walking speed. The pedestrian flow rate was selected as $\lambda = 0.3$ persons/s arriving from each side of the bridge. This means that the average crowd density in this test was around 0.13–0.19 persons/m^2 which corresponds to an average of around 20 people on the deck at any one time. In Fig. 7.7, the Power Spectral Density (PSD) of the measured response is shown.

From the spectral density, it is clear that several vibration modes at different frequencies are excited considerably during the crowd tests. Also, there is a difference between the response characteristics of the horizontal channels and the vertical one, which increases the complexity of the data analysis. However, it is noted that for the horizontal lateral direction (TP111,

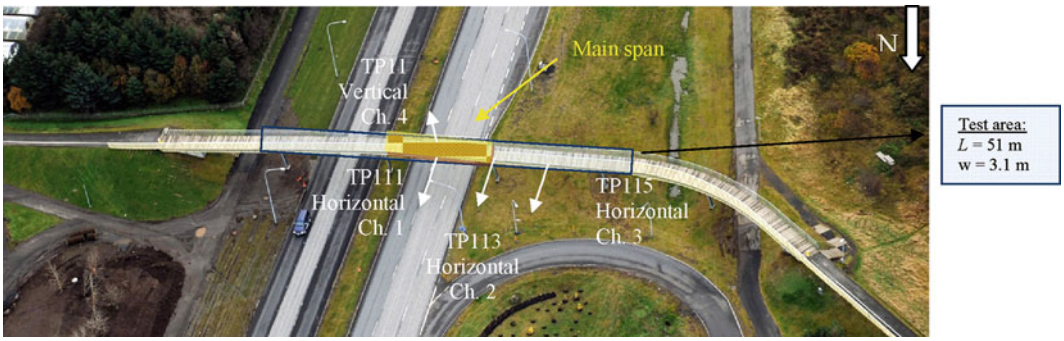

Fig. 7.6 Location of accelerometers during crowd tests

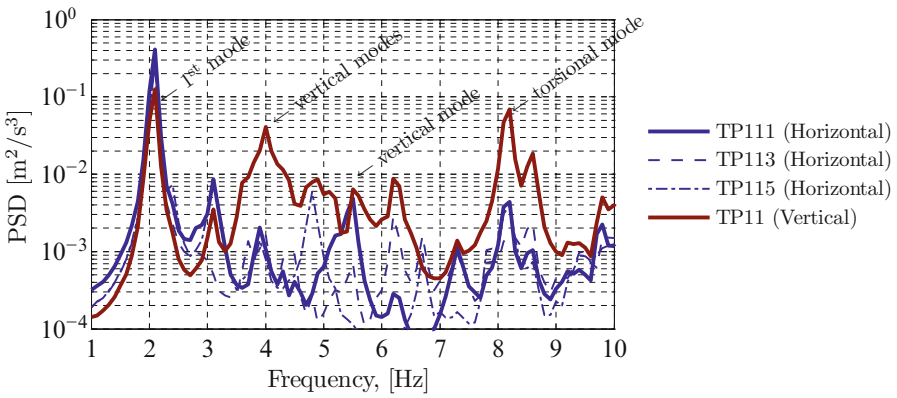

Fig. 7.7 PSD of the acceleration response measured during the crowd test

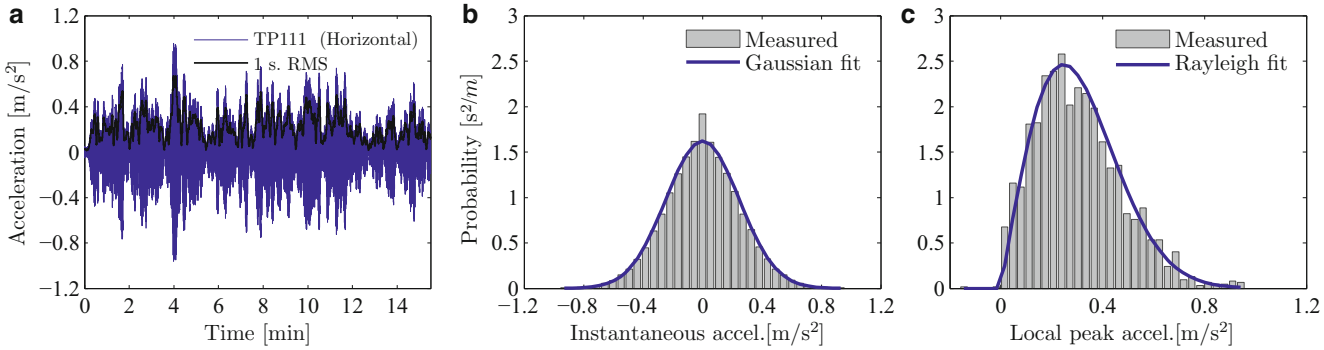

Fig. 7.8 (**a**) Modal acceleration response of fundamental vibration mode, (**b**) probability distributions of instantaneous accelerations and (**c**) local maxima as measured during crowd test

TP113 and TP115), there is a large vibration peak at the frequency of the fundamental mode (at 2.11 Hz) and three smaller peaks at around 3.1, 4.8 and around 5.5 Hz. The latter two responses appear to be caused by a horizontal component of predominantly vertical vibration modes (Fig. 7.5).

However, it is worth noting that the maximum response (in all four channels) occurs in the fundamental global vibration mode (first mode) and in the horizontal lateral direction (TP111, TP113 and TP115), only this mode is significantly excited. For the vertical vibration response, the largest response peak occurs at the frequency of the fundamental mode, but the spectral density also features a considerable number of peaks at different frequencies. This is caused by a large number vibration modes (local vertical, global vertical and torsional) with a low modal mass. In particular, the global vertical mode at around 4 Hz and the global torsional mode at around 8 Hz seem to contribute significantly to the overall response.

7.4.2 Modal Acceleration of Fundamental Vibration Mode

The dominant bridge vibration is that of the fundamental vibration mode (at 2.11 Hz), featuring a combined vertical and lateral motion of the bridge deck. The low-pass filtered horizontal lateral acceleration time-history (with a cutoff-frequency of 2.5 Hz) is shown in Fig. 7.8a, representing the modal response of the fundamental vibration mode. In addition, the running 1 s RMS acceleration is shown as recommended by the ISO 10137 standard [9]. Due to the mode shape, there is a linear relationship between the vertical and the horizontal acceleration amplitudes (1:1.79 coupling) and therefore only the results measured in the horizontal direction are presented in the following.

In Fig. 7.8b, the probability distribution of instantaneous acceleration values (the parent distribution) is shown together with a fitted Gaussian distribution (S.D. 0.246 m/s^2). For narrow-band stationary Gaussian processes with zero-mean, it can be shown that the distribution of local maxima in the time history approaches the Rayleigh distribution [17]. In Fig. 7.8b, the distribution of local peak accelerations is shown with the fitted Rayleigh distribution. In both cases a reasonably good fit is obtained. In Fig. 7.9a, the measured extreme accelerations, defined as the absolute peak within non-overlapping windows of 60 s, is shown together with the corresponding overall RMS acceleration. In addition, both the extreme peaks and the peak factor, k_p, (defined as the ratio between the absolute peak (a_p), and the RMS acceleration (a_{RMS}) within each window) are shown as functions of the return period in Fig. 7.9b and 7.9c respectively. The distribution of extreme responses can be predicted using the classical wind-engineering approach:

$$k_p(T) = \frac{a_p(T)}{a_{RMS}} \cong \sqrt{2\ln \nu T} + \frac{0.5772}{\sqrt{2\ln \nu T}} \tag{7.6}$$

where $\nu \approx 2.1$ Hz is the average up-crossing frequency and T is the return period. This approximation is valid for Gaussian zero-mean processes and is based on a simplified expression for the extreme value distribution [17]. Following the approach of Ingólfsson et al. [18] (which is based on the Response Spectrum Methodology [19]), a Generalized Extreme Value (GEV)

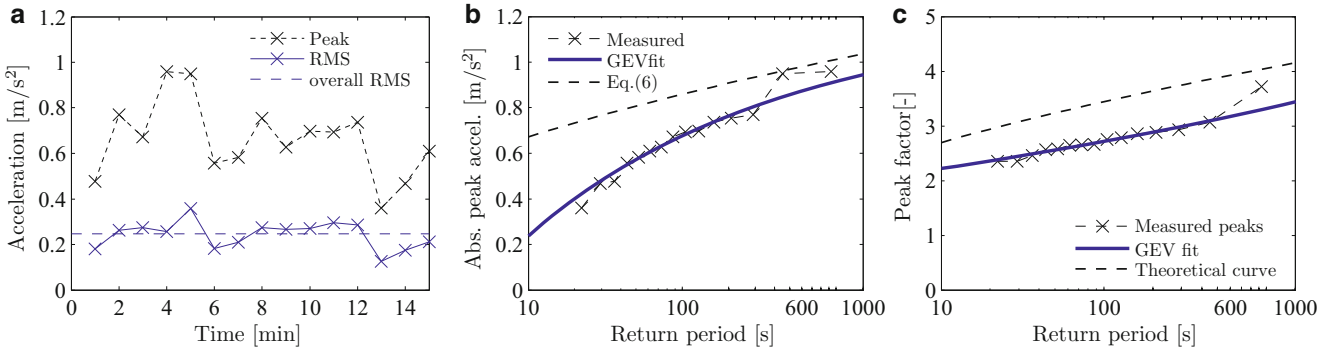

Fig. 7.9 (**a**) Measured extreme peak and RMS acceleration in 60 s non-overlapping windows, (**b**) the corresponding response factor and (**c**) the peak factor shown as functions of time and return period respectively

distribution can be used to fit the measured extreme responses. The cumulative density function depends on the shape, location and scale parameters (ξ, μ and ψ respectively) of the distribution in the following way:

$$H(x) = \exp\left\{-\left[1 + \xi\frac{x-\mu}{\psi}\right]^{-\frac{1}{\xi}}\right\} \tag{7.7}$$

The function is defined in the region where $1 + \xi\,(x–\mu)/\psi > 0$, else $H(x) = 1$ or 0. This expression can be used inversely to express the peak acceleration as a function of the return period. In Fig. 7.9b and 7.9c, the fitted GEV distribution is shown for the peak acceleration and the peak factor, respectively. The fit was obtained using a maximum likelihood estimate: $\{\xi = 0.366, \mu = 0.101, \psi = -0.334\}$ for the peak response and $\{\xi = 0.314, \mu = 2.635, \psi = -0.024\}$ for the peak factor. In Fig. 7.9b and 7.9c, the capability of the theoretical expression from (7.6) to predict the peak response is shown. For short duration crowd events it appears that the use of (7.6) to predict the peak factor will yield overly conservative results.

It is interesting to note that the comfort criteria in Annex 2 of Eurocode EN 1990 [20] for normal bridge traffic ($a_p \leq 0.2$ m/s^2) is exceeded in all of the 15 windows whereas the criteria for exceptional crowd events ($a_p \leq 0.4$ m/s^2) is exceeded in all except one windows. When using the fitted GEV distribution (Fig. 7.9b), these exceedances correspond to return periods of less than 10 s (normal traffic) and approximately 20 s (exceptional crowd events). According to the Sétra guideline [6], the bridge (under the given load intensity) is generally classified in the minimum comfort category (0.3 m/s^2 $\leq a_p \leq$ 0.8 m/s^2). In order to estimate the return period which will cause the bridge to fall outside the minimum comfort category, the fitted GEV distribution can be used to determine a return period of approximately 5 min associated with a horizontal peak acceleration of 0.8 m/s^2. Similarly, the simplified expression in (7.6) can be used to predict a return period of approximately 1 min for a peak acceleration of 0.80 m/s^2.

According to the rating method in the ISO 10137 [9], the base curve (RMS) acceleration (at frequency 2.1 Hz) is 3.77 mm/s^2 for the horizontal direction and 6.91 mm/s^2 for the vertical direction. For footbridges, an averaging time of 1 s is recommended for the calculation of the RMS value. With an up-crossing frequency of 2.1 Hz, there is a near-linear relationship between the local peak acceleration and the 1 s RMS acceleration ($a_p = \sqrt{2}\sigma_a$) [13]. Therefore, the results from Fig. 7.8 to Fig. 7.9 can still be used for comparison with the rating method of the ISO standard. It is straight-forward to find that both the criteria for passive persons (R = 30 ~ $a_p \leq 0.16$ m/s^2) and for active persons (R = 60 ~ $a_p \leq 0.32$ m/s^2) are exceeded in all of the 15 windows.

7.4.3 Analysis of Multi-modal, Multi-axis Response

Instead of treating the response on a mode-by-mode basis, the weighting method (as explained in Sect. 7.2.2) can be used to quantify the vibration response. Here the measured response is pre-filtered and the running 1 s RMS is calculated in each one-third octave band, both in the vertical and the horizontal direction. By normalizing with the base-curve acceleration (7.4), the response factor (for 1 s RMS averaging) in each band is obtained. The overall response factor is calculated according to (7.4), where the RMS acceleration is obtained in a moving 1 s window (i.e. $\tau = 1$ s). Therefore, the response factor is shown in Fig. 7.10a as a function of time. In Fig. 7.10b the probability distribution of this response factor is shown

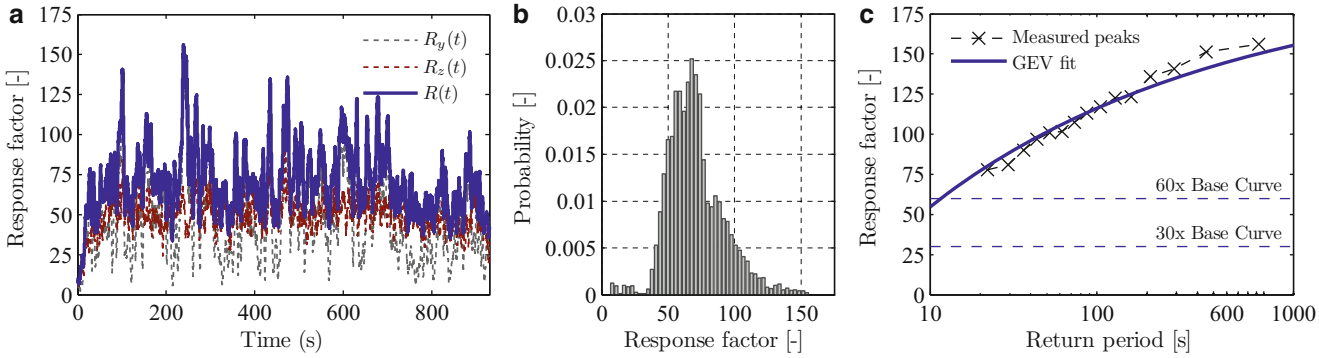

Fig. 7.10 Overall response factor: (**a**) shown as a function of time, (**b**) as a probability distribution and (**c**) as a function of the return period

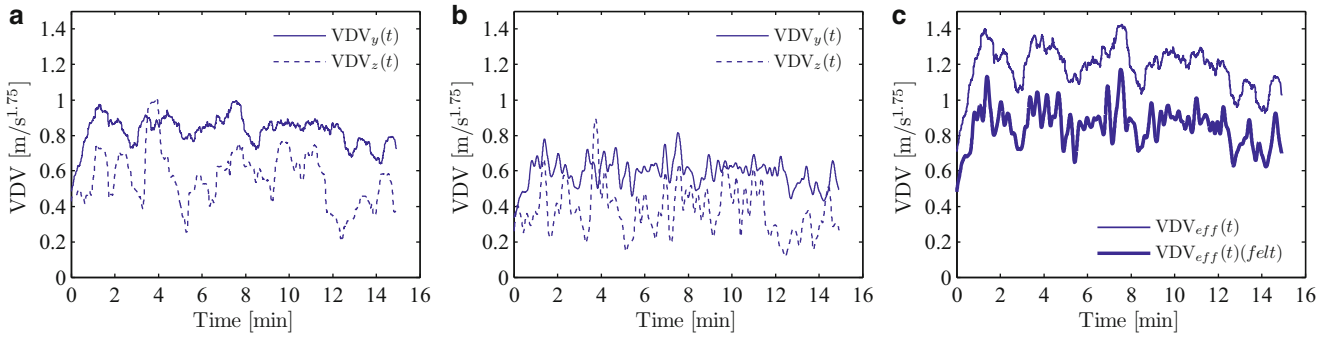

Fig. 7.11 Moving VDV (35 s exposure time) of (**a**) modal acceleration at TP11/111, (**b**) mode-shape weighted modal acceleration and (**c**) effective VDV calculated according to 7.5 with and without mode-shape weighting

and in Fig. 7.10c its return period dependency, obtained as the maximum value in 60 s non-overlapping windows is depicted. Again, a GEV distribution has been used to fit the extreme values of the response factor $\{\xi = 22.05,\ \mu = 105.7,\ \psi = -0.236\}$. When comparing the results of Fig. 7.10c with the ISO criteria for passive and active persons, it is obvious that for very low return periods (<20 s), both criteria are exceeded.

It should be mentioned, that the analysis shown here is based on the measured acceleration at a single point on the bridge (TP11/TP111) at which the maximum acceleration of the fundamental horizontal mode occurs. As the pedestrians move across the structure, they are exposed to various levels of acceleration during a limited time. The overall vibration dose value (VDV_y or VDV_z) felt by the pedestrian during a single crossing can therefore be determined from the mode-shape weighted modal acceleration. This means, that a frequency-dependent mode-shape weighting should be applied to take into account the differences between the mode shapes. However, as an initial conservative approximation, the mode shape weighting is taken as a uniform scaling of unity over the entire bridge span and the vibration dose value is calculated in a sliding window of length 35 s, corresponding to a typical crossing time (walking speed of 1.5 m/s = 5.2 km/h). In Fig. 7.11a, the calculated VDV accelerations are shown as functions of time for both the horizontal and vertical acceleration response in TP111.

A first approximation to take the mode shape into account is to consider only the effect of the fundamental vibration mode. As a further approximation, the shape is assumed to follow a half-sine with a wavelength of 81.52 m (between TP1 and TP21). The frequency-weighted acceleration is thereby weighted by the half-sine, prior to calculating the VDV. In Fig. 7.11b, the mode shape weighted VDV is shown and in Fig. 7.11c, the effective VDV, as calculated according to (7.5), is shown, both with and without mode-shape weighting (using directional weights $k_y = 1.4$ and $k_z = 1.0$). Currently, there exist no criteria for the maximum allowable VDV for active persons, but according to BS 6472-1:2008 [12] (and ISO 10137:2007 [9]), adverse comments are probable for building occupants for VDV in the range between 0.8 and 1.6 m/s$^{1.75}$ (calculated for a 16 h daytime vibration exposure). For VDV in the range 0.4–0.8, adverse comments are possible. As shown in Fig. 7.11, the vibrations are clearly perceptible during a large portion of the crowd test, with a possibility of adverse comments. In particular, when using the proposed combination rule in (7.5), the VDV felt by the pedestrian during a single crossing is within the range where adverse comments are possible.

After completion of the random crowd tests, all tests subjects were asked to rate the vibration felt during the test. Five options were given and interestingly, most people rated the vibrations as 1: “Non-perceptible” (11 people) or 2: “Only barely

perceptible" (12 people). A total of 6 persons rated the vibration as 3: "Clearly perceptible, but not unpleasant", whereas only 1 (of 30 answers) rated the vibration as 5: "Very unpleasant". None of the test subjects used the rating option 4: "Unpleasant". This result is well in line with the estimated vibration dose values shown in Fig. 7.11 and the BS 6462-1:2008 [12] ratings.

7.5 Preliminary Assessment of Human Comfort

To investigate the subjective assessment of pedestrians to vibration, a controlled experiment was undertaken, in which the structure was manually excited into vibrations in the first mode. A total of 34 test subjects were asked to cross the bridge, and rate the vibration felt. Four ratings were possible: (0) no vibration felt, (1) vibrations are acceptable (i.e. not considered important), (2) vibrations are unpleasant (i.e. would cross the bridge in the future, but would prefer if vibration were not present) and (3) vibrations are unacceptable (i.e. would not like to cross the bridge again). A total of 13 pedestrians did not feel the vibrations, 18 rated the vibrations acceptable, three persons rated them unpleasant, but none of the persons felt them being unacceptable. In Fig. 7.12, the results from the questionnaire are correlated with the frequency-weighted acceleration which is additionally weighted by the mode shape of the fundamental mode (approximated as a half-sine). For comparison, different methods of quantifying the vibrations are presented. The effective response factors are obtained from the component RMS accelerations (i.e. moving 1 s RMS and overall RMS in both horizontal and vertical directions) and combined using (7.4). Similarly, the VDV is obtained from (7.5) (using $k_y = 1.4$ and $k_z = 1$).

As shown in Fig. 7.12, there is not a strong correlation between the vibration felt and the subjective rating. The mean and median values of the vibration response show some increase from "non-perceptible" to "perceptible, but acceptable," vibration magnitudes. Vibration magnitudes which are rated as uncomfortable are lower than those rated acceptable. The lack of obvious correlation between the rating and the vibration magnitude may partly be caused by the limited number of test persons interviewed and the bias associated with their participation in the earlier test campaign. However, a similar degree of inter-subject variability was observed by Zivanovic and Pavic [13], who interviewed 100 randomly selected users of a lively footbridge in Podgorica. The vibration magnitude (defined as peak acceleration) felt by these unhappy pedestrians varied from around 0.1–0.6 m/s^2 with no significant correlation between the vibration magnitude and the subjective vibration rating.

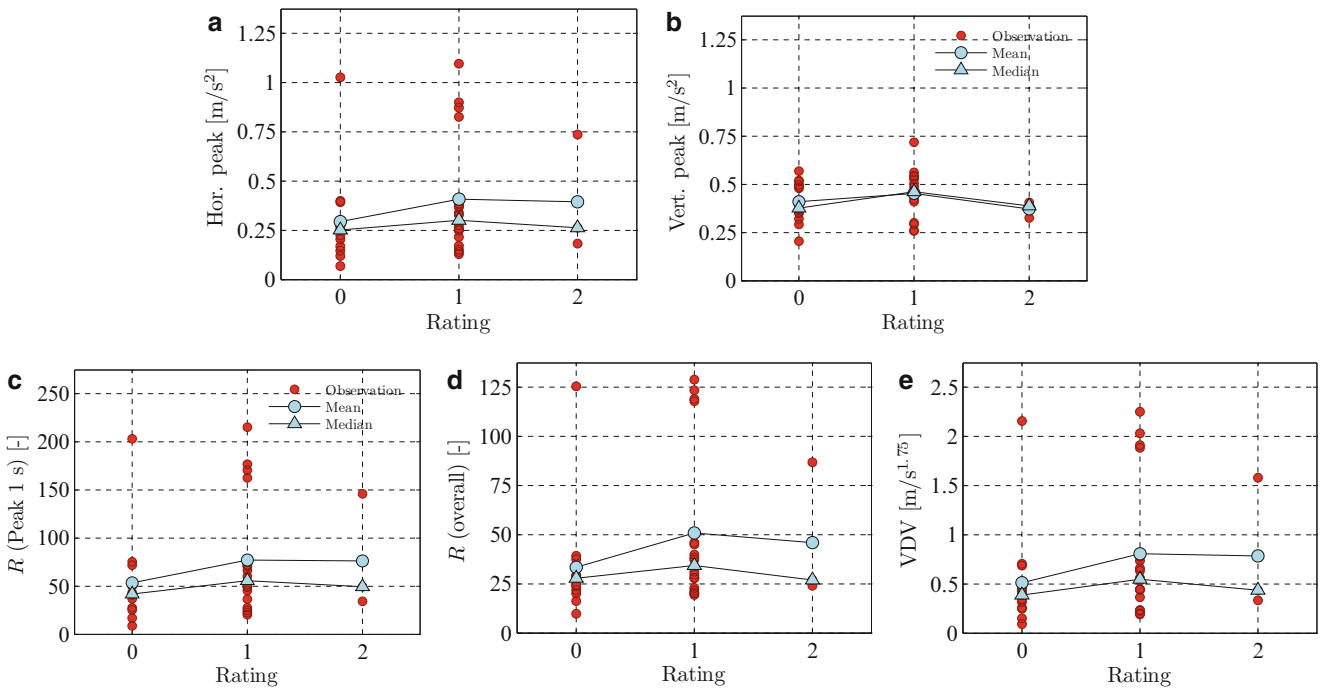

Fig. 7.12 Subjective rating of vibration, quantified as (**a**) peak horizontal, (**b**) peak vertical, (**c**) maximum 1 s RMS, (**d**) overall RMS, and (**e**) overall VDV felt during the crossing

In the study of Zivanovic and Pavic [13], the vibration magnitudes were generally lower (both peak, RMS and VDV) than those presented herewith, but the total of 31 (of 100) persons rated the vibration as either unpleasant or intolerable.

Although a direct comparison between the two studies is not possible, the difference between the subjective ratings is interesting. It suggests that soft issues, such that earlier experience with vibration, the expectation of the individual and the specific bridge type may influence the subjective rating. In particular, the fact that the test persons used in this study had already witnessed large vibrations and/or expected the bridge to vibrate perceptibly, may have altered their subjective rating. It should also be noted that the direction of vibration is predominantly vertical on the Podgorica bridge which also features a larger modal mass. Finally, it is worth noting that a number of test persons stated that the wind (a fresh to strong breeze during the tests) was more uncomfortable than the vibration.

7.6 Conclusions

In this paper, the results from an experimental investigation of a steel footbridge in Reykjavik (Iceland) are presented. It is shown that there exists no broadly accepted method of quantifying the vibration exposure of pedestrians and current guidelines for the design of footbridge adopt a particularly simplified method. As human-induced loads and their response to vibration are governed by randomness the need for introducing probabilistic methods in the serviceability assessment is evident. It is shown that the measured modal response from a random pedestrian crowd is approximately a narrow-band zero-mean Gaussian process and that the distribution of local maxima follows a Rayleigh distribution. However, a GEV distribution provides a better fit to measured extreme values than the simplified expression in (7.6), which seems to provide overly conservative estimates. In cases where the structure is subject to multi-axis and/or multi-frequency vibrations, a general assessment method is proposed which is based on the calculation of the effective RMS response (written in terms of a response factor) or the effective VDV, based on the frequency weighted acceleration measurement. A subjective assessment of the vibration felt by a number of pedestrians did not show a strong correlation between the vibration felt and the subjective rating. This is partly caused by the large inter-subject variability associated with human response to vibration. Interestingly, the acceleration levels which were rated as acceptable were considerably larger than the limits in current footbridge guidelines. However, there is a general need for more data on both the response of footbridges under normal pedestrian traffic and the subjective rating of its user.

Acknowledgements The authors kindly acknowledge Efla Consulting Engineers and the Icelandic Road Administration for their financial support and students from the University of Iceland for participating in the pedestrian tests.

References

1. Gudmundsson GV, Ingólfsson ET, Einarsson B, Bessason B (2008) Vibration serviceability of three lively footbridges in Reykjavik. In: Proceedings of 3rd international conference on footbridge 2008, Porto, 2–4 July 2008
2. Zivanovic S, Ingólfsson ET, Pavic A, Gudmundsson GV (2010) Experimental investigation of Reykjavik City Footbridge. In: Proceedings of the 28th IMAC conference, Florida, 1–4 Feb 2010
3. Griffin MJ (1996) Handbook of human vibration. Academic, London
4. BS 5440:1978 (1978) Steel, concrete and composite bridges, part 2: specifications for loads; appendix C: vibration serviceability requirements for foot and cycle track bridges. British Standards Institute, UK
5. UK NA to EN 1991-2:2003 (2003) UK national annex to Eurocode 1: actions of structures – part 2: traffic loads on bridges. British Standard Institute, UK
6. Sétra, Footbridges (2006) Assessment of vibrational behavior of footbridges under pedestrian loading. The Technical Department for Transport, Roads and Bridges Engineering and Road Safety, France
7. HIVOSS (2007) Design of footbridges – guidelines and background document, RFS2-CT-2007-00033
8. ISO 2631-2:1989 (1989) Mechanical vibration and shock – evaluation of human exposure to whole-body vibration – part 2: vibration in buildings (1 Hz to 80 Hz). International Organization for Standardization, Genèva
9. ISO 10137:2007 (2007) Bases for design of structures – serviceability of buildings and walkways against vibration. International Organization for Standardization, Genèva
10. Kasperski M (2006) Vibration serviceability for pedestrian structures. In: Proceedings of the ICE: structures and buildings, vol 159(5), pp 273–282
11. Barker C (2007) Footbridge pedestrian vibration limits background to response calculations. Int J Space Struct 22(1):35–43
12. BS 6472-1:2008 (2008) Guide to evaluation of human exposure to vibration in buildings. Part 1: vibration sources other than blasting. British Standard Institution, UK

13. Zivanovic S, Pavic A (2009) Probabilistic assessment of human response to footbridge vibration. J Low Freq Noise Vib Active Control 28(4):255–268
14. ISO 2631:1974 (1974) Guide for the evaluation of human exposure to whole-body vibration, 1st edn. International Organization for Standardization, Genéva
15. ISO 2631/1:1985 (1985) Evaluation of human exposure to whole-body vibration – part 1: general requirements. International Organization for Standardization, Genéva
16. Willford MR, Young P (2006) A design guide for footfall induced vibration of structures. The Concrete Centre, CCIP-016, Camberley
17. Sólnes J (1997) Stochastic processes and random vibration, theory and practice. Wiley, Chichester
18. Ingólfsson ET, Georgakis CT, Svendsen MN (2008) Vertical footbridge vibrations: details regarding experimental validation of the Response Spectrum Methodology. In: Proceedings of 3rd international conference on footbridge 2008, Porto, 2–4 July 2008
19. Georgakis CT, Ingólfsson ET (2008) Vertical footbridge vibrations: the Response Spectrum Methodology. In: Proceedings of 3rd international conference on footbridge 2008, Porto, 2–4 July 2008
20. EN 1990:2002/A1:2005 (2005) Ammendment 1 to eurocode – basis of structural design. European Committee for Standardization, Brussels

Chapter 8
Random Model of Vertical Walking Force Signals

Vitomir Racic, James M.W. Brownjohn, and Aleksandar Pavic

Abstract This paper presents a mathematical model to generate synthetic narrow band vertical force signals due to individuals walking. The model is fitted to a unique database comprising many directly measured vertical walking force time histories due to diverse population of human test subjects walking on an instrumented treadmill at a range of speeds, yielding a random approach to generating their artificial - yet realistic counterparts. Integrated in computer software, the modelling strategy presented offers a radical departure from traditional hand-based calculations of human-induced vibrations towards more realistic and more reliable assessment of dynamic performance of pedestrian structures that could be adopted in modern design practice.

8.1 Introduction

The lateral sway of the London Millennium Bridge and dozens of similar examples of excessive human-induced vibrations reported in the last decade have increased research interests in vibration serviceability design of pedestrian structures such as footbridges and floors [1]. However, due to the sheer complexity of the problem, there is still a firm requirement for better understanding of walking loads and developing of realistic mathematical models which can be used in more reliable vibration performance assessment.

Measured continuous force time histories are invariably near-periodic (Fig. 8.1a), indicating their narrow-band nature (Fig. 8.1b, c). However, to simplify analysis and utilisation of the measured forcing time histories in design, they have usually been assumed to be perfectly periodic. This means that actual forces due to continuous walking can be re-created or synthesised, by adding a sequence of identical single footfall traces, temporally displaced by integer multiples of an exact footfall interval. Based on this assumption, walking force time histories are presentable via Fourier series sinusoids (see [1, 2] for more details). However, numerous studies have shown the Fourier approach to be inappropriate for real situations of single and multiple occupants because it leads to significant loss of information and introduction of inaccuracies during the data reduction process [2–4].

Brownjohn et al. [3] showed that there were significant differences between the resonant responses due to the imperfect real forces and the equivalent perfectly periodic simulation. These differences are most significant (1) for higher Fourier harmonics where the simulated vibration response is regularly overestimated and (2) for resonant vibrations of lightly damped structures where the simulated response is often underestimated. In the former case the differences are caused by unnaturally high amplitudes of periodic force representation, whereas the latter case is a direct result of neglecting energy of the actual walking excitation around dominant harmonics (Fig. 8.1b). However, excessive structural vibrations due to walking are not necessarily resonant. For instance, in the case of high-frequency floors (i.e. when the natural frequency of the fundamental mode of vibration is far above pacing rate), strong vibration response due to people walking typically shows a transient character [5]. Such response is induced by high-frequency components of pedestrian dynamic loading generated when the heel strikes the walking surface [1]. As each following heel strike is made, another transient decay is generated, but no build-up of vibrations can be developed over several oscillations between footfalls due to the damping [6].

V. Racic (✉) • J.M.W. Brownjohn • A. Pavic
Department of Civil and Structural Engineering, The University of Sheffield,
Sir Frederick Mappin Building, Mappin Street, Sheffield S1 3JD, UK
e-mail: v.racic@sheffield.ac.uk

J.M. Caicedo et al. (eds.), *Topics on the Dynamics of Civil Structures, Volume 1*,
Conference Proceedings of the Society for Experimental Mechanics Series 26,
DOI 10.1007/978-1-4614-2413-0_8,

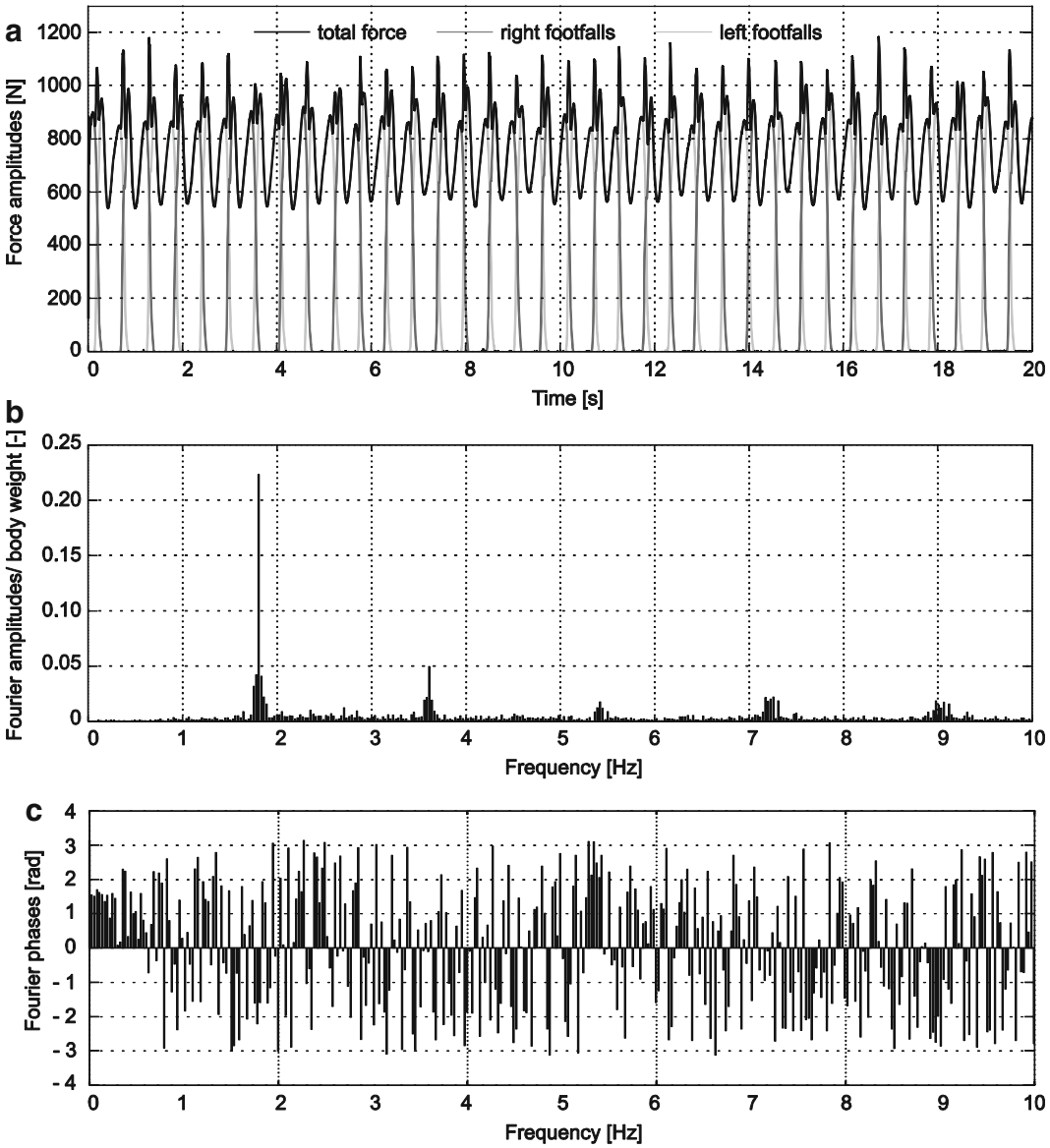

Fig. 8.1 (**a**) An example of continuously measured walking force signal and (**b–c**) the corresponding Fourier amplitudes and phases derived from a window comprising 64 successive footfalls

The difference in the nature of resonant and transient vibration responses has led to a requirement for two conceptually distinct walking force models used in design guidelines of low and high frequency structures. For floors, the most up to date guidance is available in Appendix G [5] of the Concrete Society Technical Report 43 (CSTR43). It provides design values of harmonic force amplitudes for single pedestrians for low frequency floors (i.e. if natural frequency of the fundamental mode is below 10 Hz) and equivalent impulse values for high frequency floors (i.e. if the fundamental natural frequency is above 10 Hz). However, this artificial division proves unreliable when a floor has strong responses in both the low and high frequency region, which clearly indicates the need for a uniform model capable of taking into account the complete frequency content of walking forces [6]. In an attempt to overcome this problem, Zivanovic and Pavic [7] merged together the Appendix G impulses and their previously published low-frequency force model based on the Fourier approach [8]. The new model takes into account the differences in the walking force induced by different people and, as a result, can estimate the probability distribution of vibration responses generated by a pedestrian population. However, Middleton showed that inter-subject variations do not affect the dynamic response as much as variations in an individual's pace rate for successive steps [9]. In the case of high-frequency floors, a lack of these variations can overestimate response up to 40%, indicating a need for a more reliable and more realistic footfall model.

This paper advances the field by bringing together: (1) an extensive database of continuously measured vertical walking forces generated by individuals, and (2) a unique stochastic model of these forces. This includes modelling of near-periodic features of actual forces, such as variations in timing, shape and amplitudes, as well as the complete frequency spectrum.

8.2 Experimental Data Acquisition

A database comprising many high-quality walking force records is an essential component for the development of a stochastic model of individual walking loads. Section 8.2.1 is a brief description of the experimental setup while Sect. 8.2.2 explains the test protocol.

8.2.1 Experimental Setup

All walking tests were carried out in the Light Structures Laboratory in the University of Sheffield. Continuously measured force records were collected of one person walking at a time on the state-of-the-art instrumented treadmill ADAL3D-F [10]. The treadmill is installed in a recessed pit and flush with the laboratory floor, as illustrated in Fig. 8.2.

To measure independently the left and right footfalls, ADAL3D-F design includes two identical belts, one for the left and one for the right side of the walking area (Fig. 8.2). All components (including a motor, belt and secondary elements) of each treadmill are mounted on a single metal frame and mechanically connected to the supporting ground only through a pair of Kistler 9077B three-axial piezoelectric force sensors [11]. Therefore, assuming the rigidity of the above mentioned ensemble, the entire treadmill is mechanically isolated. This means that the forces due to belt friction and belt rotation can be considered as internal forces and are not detected by the sensors [12]. The stiffness constants for the force sensors are large enough that natural frequencies of the supported treadmill frame are very high compared to the bandwidth of significant walking forces. Thus, the sensors measure only external forces, i.e. actual three-axial forces exerted by the feet on the treadmill belts. Only the vertical time series are considered here (Fig. 8.1a), while lateral and longitudinal components are beyond the scope of this paper.

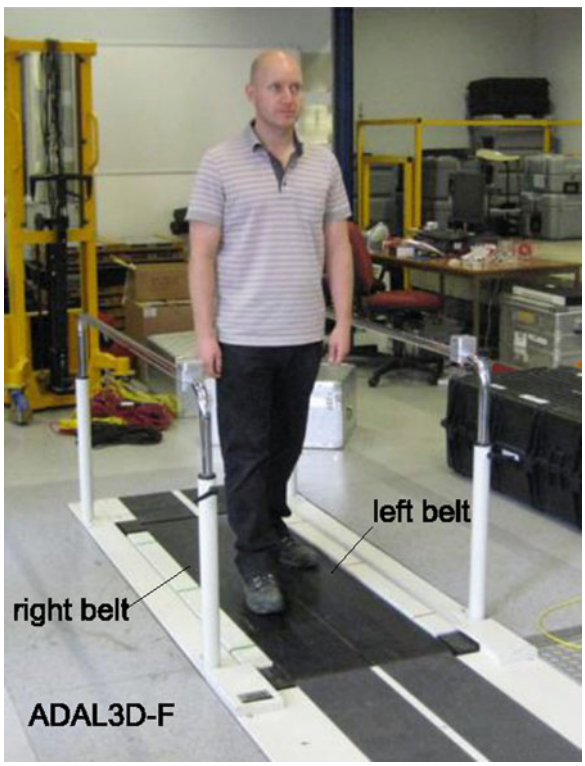

Fig. 8.2 Experimental setup

Each treadmill belt is driven by a brushless servomotor equipped with internal velocity controllers to maintain the speed as constant as possible. Velocity of treadmill belts in the range 0.1–10 km/h can be controlled and monitored remotely either with a control panel or with ADAL3D-F software, Adisoft2000 [10], run from the data acquisition PC. Similar to fitness treadmills, the remote control panel and the treadmill itself are equipped with a safety stop switch.

8.2.2 Test Protocol

Participants who had no experience with treadmill walking were given a brief training prior to the measurements supervised by a qualified instructor. All test subjects did approximately 10 min long warming up, which included walking on the treadmill while the walking speed was varied randomly and controlled by the speed of rotation of the treadmill belts. This interval was reported as long enough for pre-test habituation to treadmill walking, when differences between treadmill and overground walking vanish even for inexperienced test subjects [13].

The acquisition of walking forces started at a speed of 2 km/h and continued in increments of 0.5 km/h up to the maximum comfortable walking speed, which was determined by each test subject individually. This speed differs between people and depends primarily on the length of a test subject's legs and therefore their overall height [14]. Pacing rate was not prompted by any stimuli such as a metronome, and it was determined only from subsequent analysis of the generated force signals.

In total, 80 volunteers (55 males and 25 females, body mass 76.1 $\pm$ 15.3 kg, height 174.8 $\pm$ 8.1 cm, age 29.7 $\pm$ 9.3 years) were drawn from students, academics and technical staff of the University of Sheffield. On average, forces corresponding to ten different walking speeds were collected for each test subject depending on their maximum comfortable walking speed. All together they generated 824 vertical walking force time series of kind illustrated in Fig. 8.1a. Each walking time series was sampled at 200 Hz.

8.3 Modelling Individual Force Signals

This section describes the concept of the model development, from analysis of continuous walking parameters of a single force record to its synthetic counterpart, so the reader can follow the rationale for the remaining parts of the paper. In Sect. 8.4 it will be applied to each force record in the database presented in Sect. 8.2 yielding a mathematical generator of stochastic near-periodic walking time series.

8.3.1 Basic Processing of Measured Force Records

Figure 8.3 illustrates a portion of a continuously measured force-time history generated by a single person walking at 5 km/h and 1.81 Hz pacing rate. The force signal was filtered using a fourth-order low-pass Butterworth digital filter having cut-off frequency at 60 Hz.

It is apparent that there is some variation in shape of footfall forces (i.e. pulses), intervals and force amplitudes on a step-by-step basis. Instrumented treadmills are normally used in biomechanics of human gait to provide a series of statistics or gait parameters describing footfalls [1]. However, data relevant for structural analysis concerning intra-subject variations in timing of the individual footfalls and their amplitudes are not readily available from the literature.

Closer inspection also reveals differences between the left and right footfalls. For instance, the left footfalls have greater first peak of the characteristic 'M' shape. Sahnachi and Kasperski [15] showed that this asymmetry in walking induces intermediate harmonic load amplitudes (so called 'sub-harmonics' which are illustrated in Fig. 8.1b) which may lead to larger vibration responses than higher integer harmonics for some test subjects. Therefore, in this study the total vertical force will be modelled on a stride-by-stride basis, where a stride (i.e. walking cycle) consists of two successive footfalls, left and right (Fig. 8.3).

A walking cycle can be defined between any two nominally identical events of the total force signal. Since the amplitudes of the total vertical forces oscillate around body weight of the test subject, the point close to the beginning of the left footfall where amplitude of the total force is equal to body weight was selected as starting (and completing) event (Fig. 8.3).

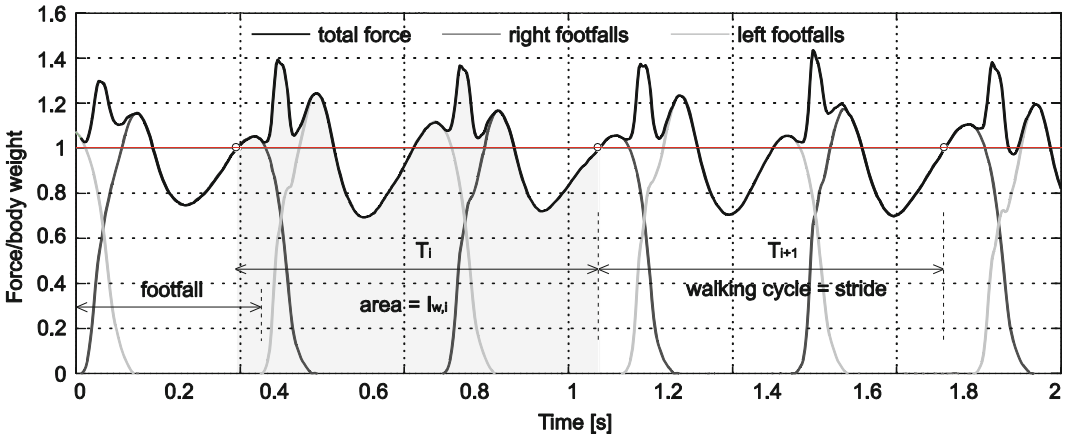

Fig. 8.3 A portion of a continuously measured GRF due to walking. The total duration of the signal is 40 s

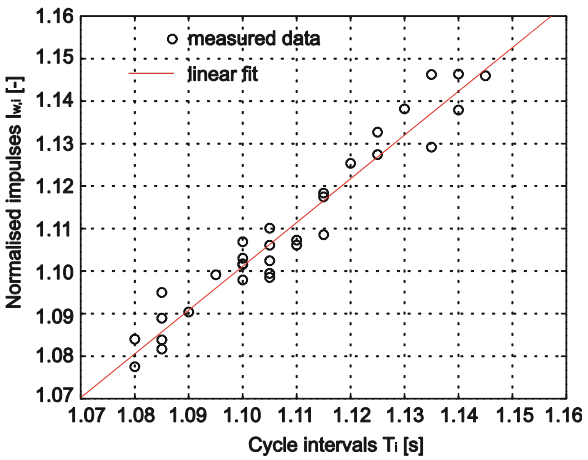

Fig. 8.4 Linear trend between periods T_i and weight normalised impulses $I_{w,i}$

From the 40 s long force signal illustrated in Fig. 8.3 yielding about 72 footfalls, a window comprising 32 successive cycles (64 footfalls) was extracted from the middle of the signal for further analysis.

Figure 8.4 shows values of normalised impulses $I_{w,i}$ as a function of the cycle intervals T_i. The normalised impulse is defined as the cycle impulse (i.e. the integral of the force over T_i) divided by test subject body weight. The apparent linear trend between these two parameters makes it possible to describe weight normalised impulses as a function of the cycle intervals.

8.3.2 Variability of Cycle Intervals

Variations of intervals T_i ($i = 1, \ldots, 32$) can be represented by a sequence of dimensionless numbers τ_i calculated as:

$$\tau_i = \frac{T_i - \mu_T}{\mu_T} \qquad \mu_T = mean(T_i) \tag{8.1}$$

As variance σ_τ^2 of τ_i can be obtained as the total area under its Auto Spectral Density (ASD) [16], the aim is to use ASD of actual τ_i series to generate synthetic τ_i' series with the same statistical properties, such as standard deviation and 'structure' of variation between successive τ_i values. Under assumption that the variation of τ_i does not change for the given test subject, pacing rate and duration of walking (e.g. caused by fatigue and physical discomfort), this applies regardless of the number of discrete data points in the measured and artificial data sets, which will be demonstrated later in this section.

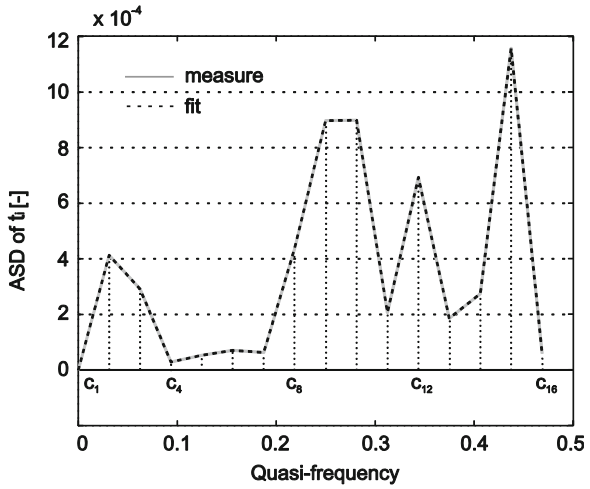

Fig. 8.5 Single-sided ASD of τ_i values

The ASD of τ_i can be calculated as:

$$S_\tau(f_m) = \frac{A_\tau^2(f_m)}{2\Delta f}, \quad f_m = \frac{m}{32}, \quad m = 0, \ ..., \ 15 \tag{8.2}$$

where $A_\tau(f_m)$is a single-sided discrete Fourier amplitude spectra having spectral line spacing $\Delta f = 1/32$ (Fig. 8.5).

The ASD ordinates do not depend on the number of discrete data points τ_i used for the calculation of A_τ (f_m) via Fast Fourier Transform (FFT) but it is coarse due to the limited number of points (16 single-sided FFT). More points might reveal a much richer structure but this requires a longer walking force signal. However, concerning ethics in research, the duration was limited to avoid fatigue and discomfort, which can also influence natural variability of the force records.

The ASD $S_\tau(f_m)$ can be analytically represented by a series of Gaussian functions (Fig. 8.5):

$$S_\tau'(f) = \sum_{j=1}^{16} W_j e^{-\frac{\left(f-c_j\right)^2}{2b_j^2}} \tag{8.3}$$

Here, parameter W_j is the height of the j-th Gaussian peak, c_j is the position of the centre of the peak, and b_j controls the width (i.e. time duration) of the corresponding Gaussian function. The Gaussian centres c_j, $j = 1, \ldots, 16$, are placed in each sample on the quasi-frequency axis in order to fit exactly the measured ASD (Fig. 8.5). For such fixed positions of c_j and predefined widths $b_j = \Delta f$, Gaussian heights W_j (also called weights) can be computed using the non-linear least-square method [17].

Representation of the discrete ASD $S_\tau(f_m)$ in the form of the continuous function $S_\tau'(f)$ enables generation of synthetic series τ_i' (i = 1, . . ., N) of arbitrary length (e.g. N> > 32), which will have statistically the same properties of variations on the sample-by-sample basis as the measured set of 32 actual τ_i data points. This is done by calculating a new set of ASD amplitudes for a sequence of discretely spaced frequency points $f_n = \Delta f_n'$ using (8.5), where n = 0, . . ., N/2-1 and $\Delta f_n' = 1/N$. The new set of ASD amplitudes $S_\tau'(f_n)$ and (8.3) are then used to generate a new set of Fourier amplitudes $A_\tau'(f_n) = \sqrt{2\Delta f_n' S_\tau'(f_n)}$. Finally, assuming random distribution of phase angles in the range [-π, π], these amplitudes are used in inverse FFT algorithm to generate a synthetic set of N variations τ_i'. Different realisations of the random phases may be specified by varying the seed of the random number generator, hence many different series τ_i' may be generated with the same spectral properties (Fig. 8.6).

8.3.3 Variability of Normalised Impulses

The measured weight normalised impulses $I_{w,i}$ can be expressed as a function of the cycle intervals T_i (Fig. 8.4) using the following linear regression model [18]:

$$I_{w,i} = \rho_1 T_i + \rho_0 + \Delta I_{w,i} \tag{8.4}$$

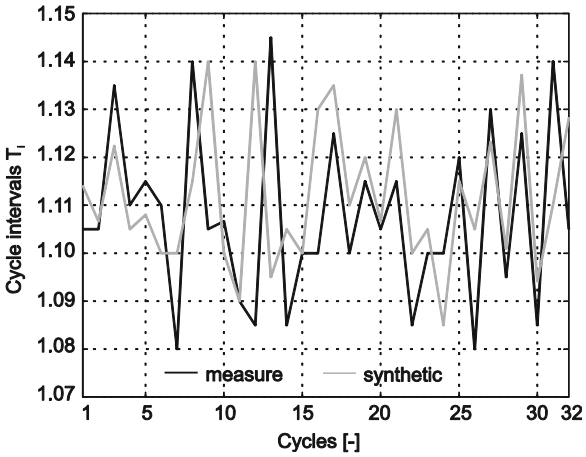

Fig. 8.6 Measured τ_i and an example of synthetic $\tau_i^{'}$ series

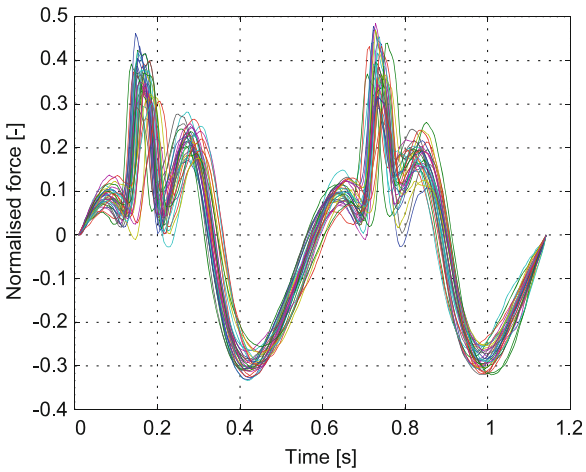

Fig. 8.7 Normalised walking cycles

Here, $\rho_1 = 1.05$ $\rho_1 = 1.05$and $\rho_0 = -0.05$ are regression coefficients and $\Delta I_{w,i}$ is the subsequent error (also known as a disturbance term), which is a random variable. Given the regression coefficients $\rho_1$and ρ_0, $\Delta I_{w,i}$ can be calculated as:

$$\Delta I_{w,i} = I_{w,i} - \rho_1 T_i - \rho_0 \tag{8.5}$$

It is common to model $\Delta I_{w,i}$ as a random noise having a Gaussian distribution [18].

Given a set of synthetic cycle intervals $T_i^{'}$ generated as explained in Sect. 8.3.2, a series of the corresponding synthetic normalised impulses $I_{w,i}^{'}$ can be calculated using (8.4). These are used in the next section to scale amplitudes of successive strides, thus make a smooth transition of walking energy between successive cycles.

8.3.4 Template Waveform of Walking Force Signals

The 32 normalised walking cycles have been detrended (body weight has been removed), resampled to the maximum length of all the cycles and aligned with respect to the common time axis, as shown in Fig. 8.7. Visual inspection suggests that there is a common waveform of the walking force which distorts along time and amplitude axes on a cycle-by-cycle basis. The key challenge here is to extract this waveform and provide its reliable mathematical representation which can be used to generate synthetic time series.

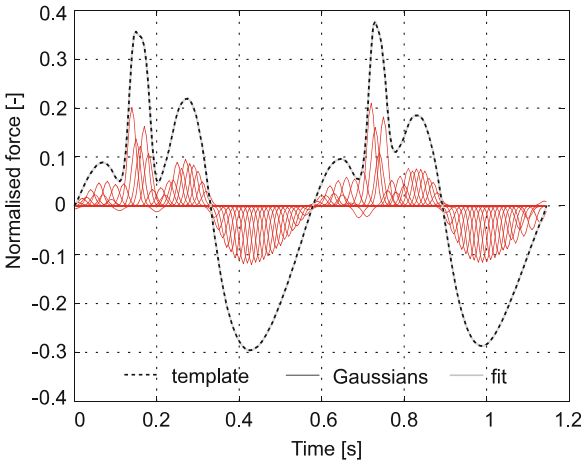

Fig. 8.8 Fitting the template cycle with a series of Gaussian basis functions

The average cycle is considered unreliable representative due to misalignments and shifts of the common events, such as positions of the local extreme values. To correct for these slight variations, a procedure called dynamic time warping (DTW) is applied to the measured cycles before their average is calculated. When the warping has been completed and the common events in the cycles aligned, the template cycle is formed as average of the warped cycles, as illustrated in Fig. 8.8. More details about the procedure can be found in [2].

For $f_s = 200$ Hz sampling rate and interval of 1.15 s, the underlying shape of the template cycle (Fig. 8.8) can be modelled mathematically as a sum of 115 Gaussian functions Z(t):

$$Z(t) = \sum_{j}^{115} A_j e^{-\frac{(t-t_j)^2}{2\delta_j^2}} \tag{8.6}$$

where the parameter A_j is the height of the j-th Gaussian peak, t_j t_j is the position of the centre of the peak, and δ_j is the width of the corresponding Gaussian functions in the sum (Fig. 8.8).

The Gaussian centres $t_j = n\Delta t$ ($n = 1, \ldots, 115$, $\Delta t = 1/f_s$) are placed in every second sample on the time axis to fit accurately the normalised force amplitudes, thus to reflect completely the corresponding Fourier amplitude spectrum. A less dense distribution of Gaussian functions (e.g. centres are placed in every third or fourth sample) makes the fit smoother causing the high frequency components to vanish. For such fixed positions of Gaussian centres and predefined widths $\delta_j = 2\Delta t$, Gaussian heights A_j can be optimised using non-linear least-square curve fit [17].

Scaled in the vertical and horizontal direction, analytical functions Z(t) can be used to generate artificial force signals which reflect the variations of impulses $I'_{w,i}$ and time intervals T'_i for successive walking cycles (Fig. 8.9, 8.10). The process is explained in more detail in [2].

8.4 Development of Stochastic Walking Model

This section integrates everything presented so far to create a numerical generator of stochastic near-periodic walking force signals. Section 8.4.1 deals with organisation of the modelling parameters extracted (as explained in Sect. 8.3) from the numerous database of the individual force records collected in Sect. 8.2. This is followed by a brief description of the mechanism underlying generation of random walking loads in Sect. 8.4.2.

8.4.1 Utilisation of Existing Database

The 824 force signals measured in Sect. 8.2 were classified into 20 categories (clusters) with respect to the actual pacing rate, as shown in the histogram in Fig. 8.11. Each bar in the histogram is approximately 0.1 Hz wide. For example, all force records with the pacing rate in the range 1.58–1.68 Hz are gathered into one cluster. Such fine resolution is a key feature for development of a stochastic model outlined in the next section.

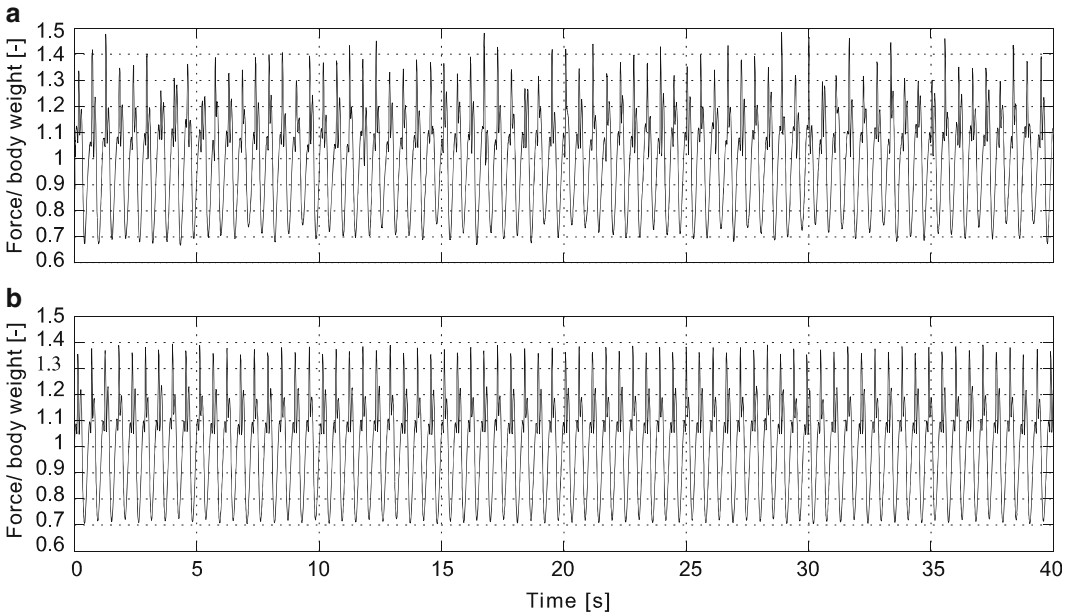

Fig. 8.9 (**a**) Measured and (**b**) an example of synthetic walking time series generated using the template cycle

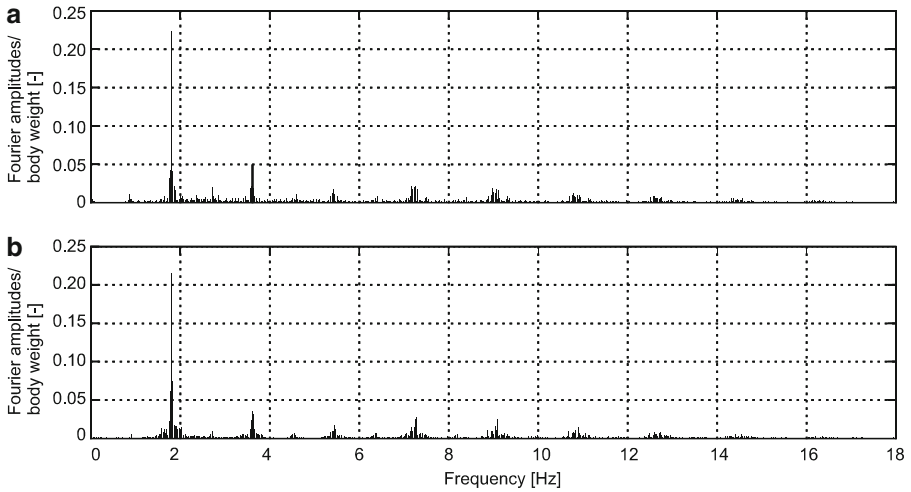

Fig. 8.10 Discrete Fourier amplitudes of (**a**) measured and (**b**) synthetic walking time series. Figures 8.9 and 8.10 represent the same data

Note that walking at different speeds does not necessarily yield different pacing rates. This is because people unconsciously control their step length to walk at their most comfortable pacing rate [19]. In the present study, the cluster for the rates between 1.88 and 1.98 Hz is the most numerous comprising 101 different walking force records. This might be an indicator that this is the range of the most comfortable pacing rates for the majority of participants in this study.

Each force history within a cluster was processed using the concept described in Sect. 8.3. Multiple sets of information (parameters of the Gaussian fits and the ASD, autoregression coefficients and the parameters of the Gaussian random noise) were extracted and stored within the cluster as MATLAB structure files [20].

8.4.2 Procedure for Generating Synthetic Forces

The stochastic approach adopted in this paper rests on the assumption that a set of the modelling parameters selected randomly and equally likely from a cluster can be used to synthesise walking time series at any pacing rate which falls within

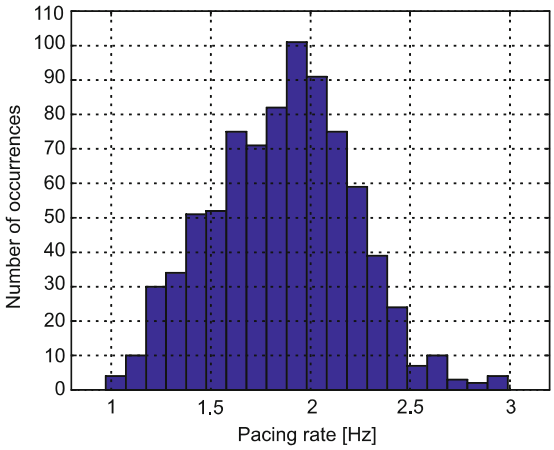

Fig. 8.11 Histogram of pacing rates yielding 20 clusters

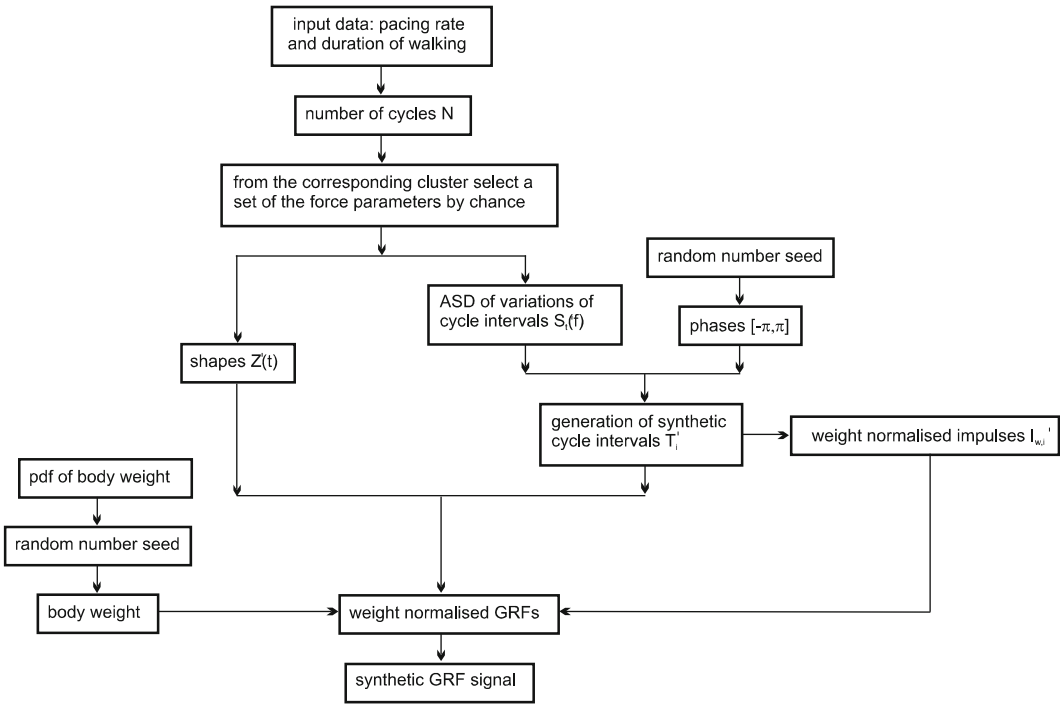

Fig. 8.12 Algorithm for generating synthetic time series

the cluster's narrow frequency range. This means that the modelling parameters extracted from real walking at particular rate can be used to generate synthetic walking forces at rates which are close enough.

The flow chart in Fig. 8.12 illustrates the complete process (algorithm) of creating synthetic GRF signals. For a specified pacing rate and duration of walking, the algorithm first estimates the total number of walking cycles N. Then, from a frequency cluster corresponding to the pacing rate, it selects by chance a set of multiple modelling parameters. At this point, the algorithm splits into two actions. First, it creates intervals T_i' using the ASD $S_\tau'(f)$ (Sect. 8.3.2) and then calculates normalised impulses $I_{w,i}'$ using the regressive model given by (8.6). The algorithm then assigns functions Z(t) to each of the N walking cycles.

The next step integrates everything generated so far to generate synthetic forces of a kind shown in Fig. 8.9b. More details and examples of artificial forces can be found in [2].

8.5 Conclusions

A data-driven mathematical concept has been developed for modelling dynamic loads generated by pedestrians walking. The ability to replicate temporal and spectral features of real walking loads gives this model a definite advantage over the existing walking models which can be found in the current UK and worldwide design guidelines for pedestrian structures, such as footbridges and floors. Therefore, the model presented in this paper can serve as a framework for a more realistic dynamic performance assessment which can be adopted in the design practice. The modelling strategy takes a complex numerical approach, thus can be distributed to designers as a user-friendly software. For example, it can be a graphical user interface which will allow designers to change pacing rate, duration of force signals and walking path through direct manipulation of graphical elements such as windows, menus, check boxes and icons. Automated structural design would help reduce its costs and improve the efficiency with which structural engineers can handle it.

The first refinement of the current design procedures would account for innate variability of individual walking excitation. To simplify dynamic analysis, this excitation is conventionally assumed in guidelines to be perfectly periodic and therefore presentable as a series of identical footfalls replicated at precise intervals. However, this leads to significant loss of information and introduction of inaccuracies in predicted dynamic response. As demonstrated in this paper, the proposed model accounts for variations of intervals, impulses and shapes of successive strides (walking cycles).

The second refinement addresses the artificial division in the current design guidelines between low and high frequency structures. This is due to the lack of a mathematical concept which can associate all frequency components of real walking excitation within a single model. Assumed perfect periodicity allows walking forces to be presentable as a Fourier series for low frequency structures prone to resonant vibration under pedestrian excitation, whereas the same loads are modelled as a series of equivalent impulses in the case the human walking causes a transient response to the successive heel strikes. However, problems typically occur for a structure that has strong responses in both the high and low frequency region. This paper presents a uniform model which can account for all energy levels of walking excitation, thus can simulate dynamic response for a structure having an arbitrary fundamental frequency.

Contrary to conventional approach to their modelling, walking forces are not deterministic but are a random phenomenon. Hence, the third refinement of the current design procedures would follow principles used in experimental and analytical treatment of other random forces dynamically exciting civil engineering structures, such as wind, waves or earthquakes. Therefore, the steps taken in this paper, such as gathering a large number of time-varying loading records of walking, establishing a viable database of them and using it to develop a new generation of walking models for stochastic-based dynamic calculations of real-life structures, present a timely opportunity to advance the whole field of vibration serviceability assessment of structures carrying pedestrians, such as footbridges and long-span floors.

The model is based on straight line horizontal walking data but ought to apply for walking paths that are mildly curved in the horizontal plane. For vertical curves (e.g. for significantly cambered footbridges) a databases of forces for ascent and descent would be required. Finally, the mathematical framework presented can be extended further to stochastic walking loads due to groups and crowds. At the moment, individual forces can be summed with random phase lags as suggested elsewhere [21]. However, there are indications that this is not what is happening in reality [1] and more research into synchronisation between people walking is needed.

Acknowledgements The authors would like to acknowledge the financial support provided by the UK Engineering and Physical Sciences Research Council (EPSRC) for grant reference EP/E018734/1 (‘Human Walking and Running Forces: Novel Experimental Characterisation and Application in Civil Engineering Dynamics’).

References

1. Racic V, Pavic A, Brownjohn JMW (2009) Experimental identification and analytical modelling of human walking forces: literature review. J Sound Vib 326:1–49
2. Racic V, Brownjohn JMW (2011) Stochastic model of near-periodic vertical loads due to humans walking. Adv Eng Inform 25(2):259–275
3. Brownjohn JMW, Pavic A, Omenzetter P (2004) A spectral density approach for modelling continuous vertical forces on pedestrian structures due to walking. Can J Civil Eng 31:65–77
4. Zivanovic S, Pavic A, Reynolds P (2005) Human-structure dynamic interaction in footbridges. Bridge Eng 158(BE4):165–177
5. Pavic A, Willford MR (2005) Appendix G: vibration serviceability of post-tensioned concrete floors. In: Post-tensioned concrete floors design handbook, 2nd edn. Concrete Society, Slough, pp 99–107
6. Middleton CJ, Brownjohn JMW (2009) Response of high frequency floors: a literature review. Eng Struct 32(2):337–352
7. Zivanovic S, Pavic A (2009) Probabilistic modelling of walking excitation for building floors. J Perform Constr Fac 23(3):132–143

8. Zivanovic S, Pavic A, Reynolds P (2007) Probability based prediction of multi mode vibration response to walking excitation. Eng Struct 29(6):942–954
9. Middleton CJ (2009) Dynamic performance of high frequency floors. Ph.D. thesis, University of Sheffield, UK
10. HEF Medical Development (2009) User manuals. HEF Groupe, Lion
11. Kistler (2011) Kistler user manuals. www.kistler.com
12. Belli A, Bui P, Berger A, Geyssant A, Lacour JR (2001) A treadmill ergometer for three-dimensional ground reaction forces measurement during walking. J Biomech 34(1):105–112
13. van de Putte M, Hagemeister N, St-Onge N, Parent G, de Guise JA (2006) Habituation to treadmill walking. Bio-Med Mater Eng 16:43–52
14. Rose J, Gamble JG (1994) Human walking, 2nd edn. Williams & Wilkins, Baltimore
15. Sahnaci C, Kasperski M (2005) Random loads induced by walking. In: Proceedings of the 6th European conference on structural dynamics (EURODYN), Millpress, Rotterdam, pp 441–446
16. Newland DE (1993) An introduction to random vibrations, spectral and wavelet analysis, 3rd edn. Pearson Education, Harlow
17. Bates DM, Watts DG (1998) Nonlinear regression and its applications. Wiley, New York
18. Bishop CM (2006) Pattern recognition and machine learning. Springer, New York
19. Sekiya N, Nagasaki H, Ito H, Furuna T (1997) Optimal walking in terms of variability in step length. J Orthop Sports Phys Ther 26:266–272
20. MathWorks (2011) Matlab user guides. www.mathworks.com
21. Matsumoto Y, Nishioka T, Shiojiri H, Matsuzaki K (1978) Dynamic design of footbridges. In: Proceedings of IABSE, Zürich, pp 1–15

Chapter 9
Towards Modelling In-Service Pedestrian Loading of Floor Structures

S. Živanović, A. Pavic, and V. Racic

Abstract With increasing importance of vibration serviceability limit state in floor design, especially in relation to human induced dynamic loading, there is a need for defining reliable models of pedestrians that reflect normal usage of the structure. Modelling the walking loading for individual pedestrians has rapidly advanced over the past decade. However, there is a serious lack of information about realistic loading scenarios (e.g. walking habits of people using the floor, their walking patterns and the number of active people at any one time) and the corresponding vibration response. This paper aims to improve our understating of the issues by presenting the results of a 3-day monitoring of in-service vibration at a "hot spot" in an office floor. In addition, it is not known how well the single person loading scenario, advocated in the current design guidelines, reflects the actual in-service vibration of the structure normally exposed to multi-person excitation. The data acquired for this study are analysed statistically to evaluate the key vibration measures relevant for the vibration serviceability state of the floor. Then possibility for modelling human loading in the form of virtual pedestrian(s) representing the floor occupants is analysed. It was found that the single person model results in conservative estimates of the actual vibration on this particular floor.

Keywords Floors • Vibrations • Pedestrian loading • Multi-person traffic

9.1 Introduction

Floor structures are increasingly slender and therefore could be susceptible to excessive vibration due to human-induced loading, such as walking. To predict accurately in-service vibration response of a floor, it is necessary to make reliable estimates of dynamic properties of the structure, expected loading scenarios and the corresponding dynamic force induced by human activities.

This study aims to investigate in-service vibration behaviour of an office floor structure exposed to normal multi-person walking during normal working hours (9 am–5 pm). Current design guidelines in the UK, such as Technical Report 43 published by the Concrete Society [1], SCI Publication No. P354 by the UK Steel Construction Institute [2], and Guideline by Concrete Centre [3] require vibration serviceability checks for a single person walking scenario only. They require performing simulations of walking at feasible pacing frequencies, with particular attention to those frequencies that can excite resonance in low-frequency vibration modes. The predicted vibration response to walking at any particular walking frequency is said to have 25% probability of exceedance. The current guidelines do not consider the multi-person loading scenarios that are most likely in normal use of floors. It is not clear what is the relationship between responses to the multi-person excitation and the single person excitation of the floor, and if the single person excitation at critical frequencies is

S. Živanović (✉)
Civil Research Group, School of Engineering, The University of Warwick, Coventry CV4 7AL, UK
e-mail: s.zivanovic@warwick.ac.uk

A. Pavic • V. Racic
Vibration Engineering Section, Department of Civil and Structural Engineering, The University of Sheffield, Sir Frederick Mappin Building, Mappin Street, Sheffield S1 3JD, UK

J.M. Caicedo et al. (eds.), *Topics on the Dynamics of Civil Structures, Volume 1*,
Conference Proceedings of the Society for Experimental Mechanics Series 26,
DOI 10.1007/978-1-4614-2413-0_9,

the most relevant for vibration performance of the floors, as implied by the current design guidelines. The main reason for this status quo is the lack of experimental data that could be used to learn about correlation (or lack of it) between the two loading scenarios.

This study presents experimental data acquired during 3-day monitoring of in-service vibration of a floor structure, as well as the vibration data acquired in controlled walking tests involving a single person. The data of this kind are very rare and they are analysed here with the aim to answer the following questions:

- What are statistical properties of in-service vibration response on the floor investigated?
- How is in-service response correlated with the usual code-defined scenario of a single person walking at a controlled pacing rate to excite maximum response of the structure?

The analysis aims to inform development of a model for predicting in-service vibrations.

9.2 Description of the Structure

The floor structure investigated in this paper is on Level 4 of a seven-storey steel frame building. The floor is fully furnished. Structurally, it features composite steel beams supporting slabs cast of lightweight concrete poured over profiled decking. Figure 9.1 shows a plan of the structural steel layout. The typical bay size is 9 m by 7.5 m with primary beams spanning 9 m between columns and cellular secondary beams running parallel with primary beams at 3 m centres. A 120 mm thick concrete slab made of lightweight concrete over metal decking acts compositely with cellular beams. The South part of the floor is an open plan office space while the North part is more partitioned and features more irregular and slightly shorter end span.

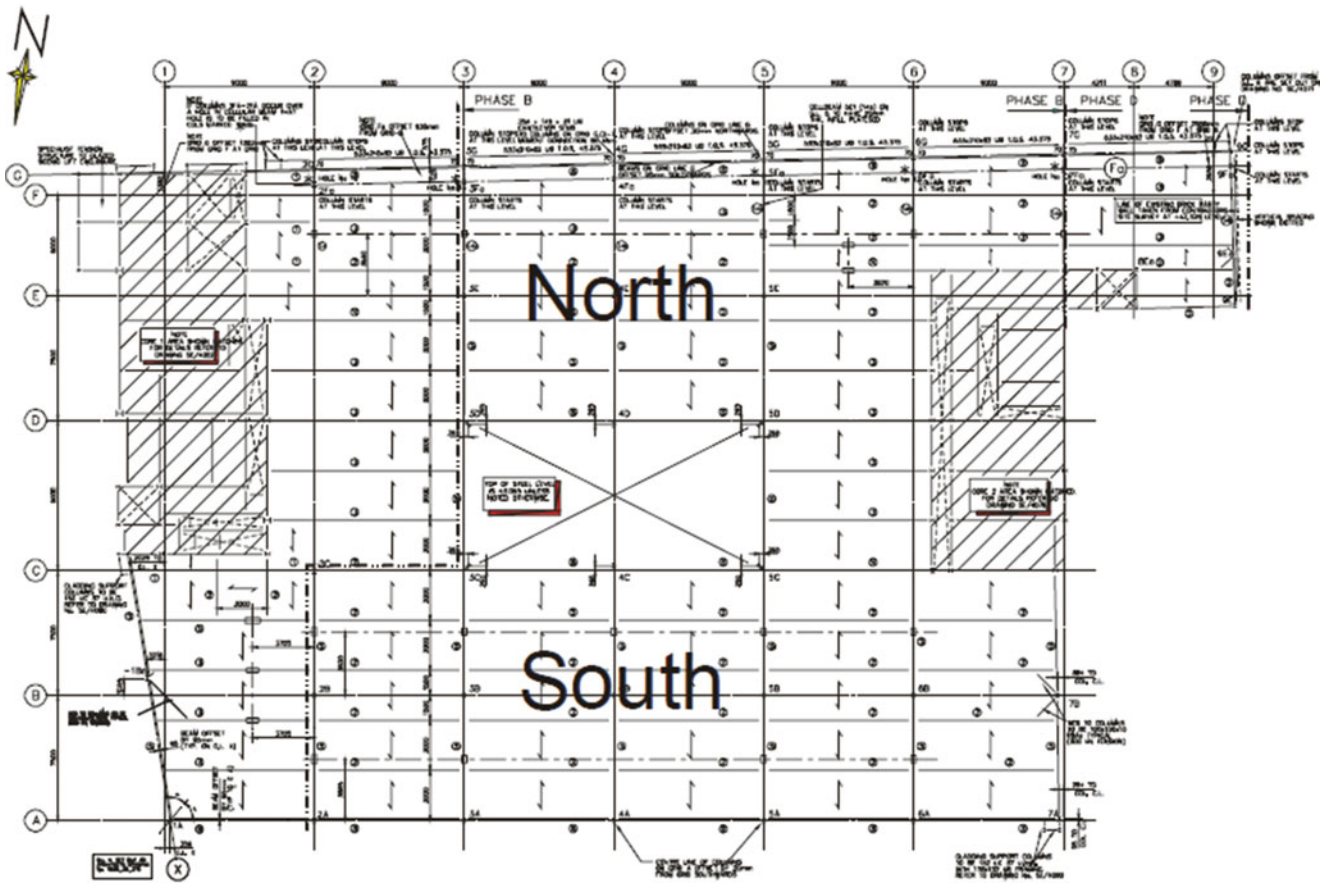

Fig. 9.1 The Level 4 floor

9.3 Experimental Programme

The experimental programme consisted of three types of tests: (1) modal testing, (2) in-service vibration monitoring and (3) response measurements to single person excitation. The grid of test points (TPs) used during testing is shown in Fig. 9.2. A work station close to TPs 10 and 11 was reported to be a particularly sensitive location with some perceptible vibrations caused by walking.

9.3.1 Modal Testing

Frequency response function (FRF) based modal testing of the floor was performed using continuous random excitation by four electrodynamic shakers. Two of the shakers were APS Dynamics Model 113 shakers (with a peak harmonic force capacity of either 133 N or 180 N) while remaining two shakers were APS Dynamics Model 400 (peak harmonic force capacity of 400 N). A test grid of 79 points was marked on the floor, as shown in Fig. 9.2. The four shakers were placed at test points (TPs) 12, 37, 61 and 71 (Fig. 9.2). They were driven by uncorrelated random signal allowing to spread the excitation energy around the floor. By measuring the response in 79 TPs it was possible to determine FRFs between each excitation and response point. The excitation was provided in the frequency range 0–20 Hz, since the modes in this frequency range were most significant contributors to the structural vibration. The sampling rate was 51.2 Hz. The responses were measured using Endevco Model 7754-1000 piezoelectric accelerometers, with nominal sensitivity of 1,000 mV/g. The FRF measurements were collected after 40 averages with an overlap of 75%. Hanning window was applied to each average.

Typical point mobility FRF at TP12 is shown in Fig. 9.3. Two major peaks at 5.7 and 6.4 Hz correspond to two dominant modes engaging TP12.

ME'scope software was used for modal parameter estimation using the Global Polynomial method. All FRFs were analysed simultaneously. The nine mode shapes identified are shown in Fig. 9.4.

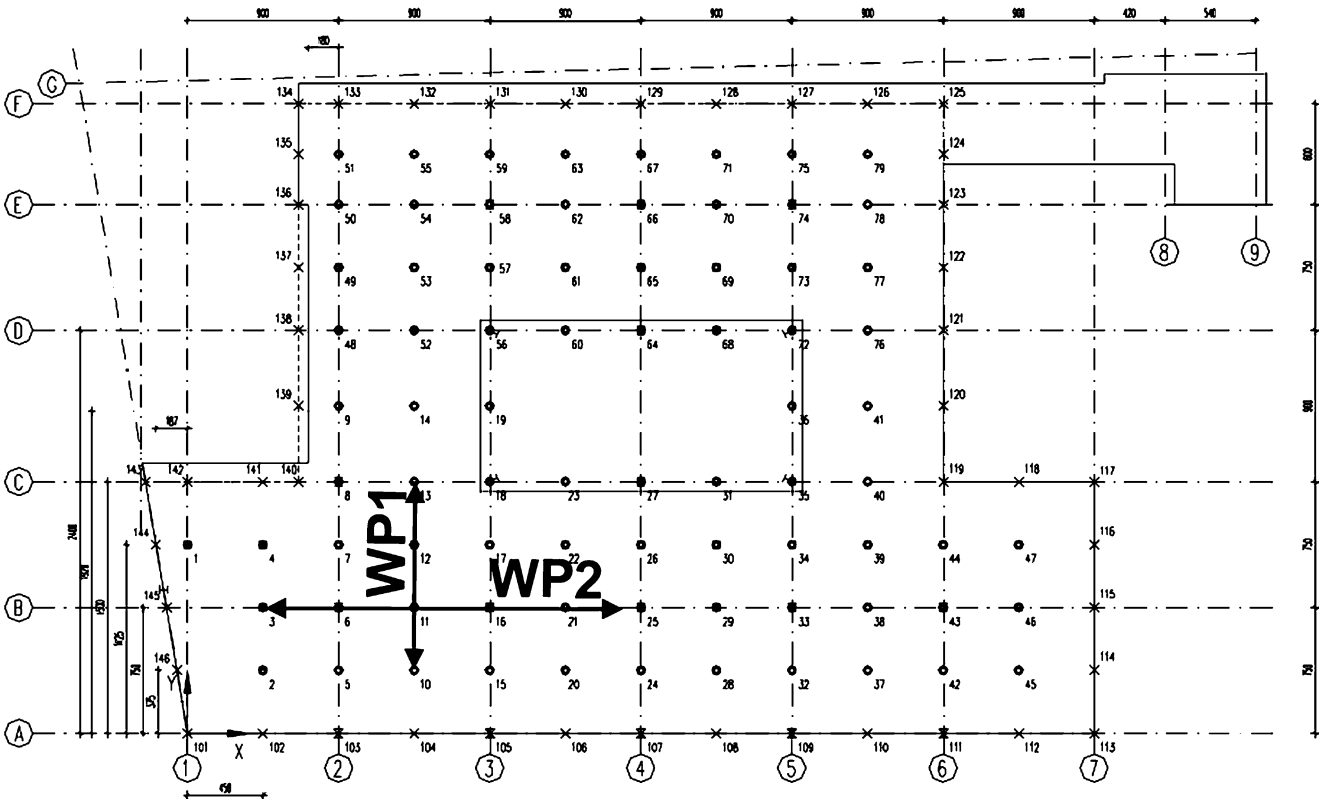

Fig. 9.2 Test grid and walking paths in single pedestrian tests

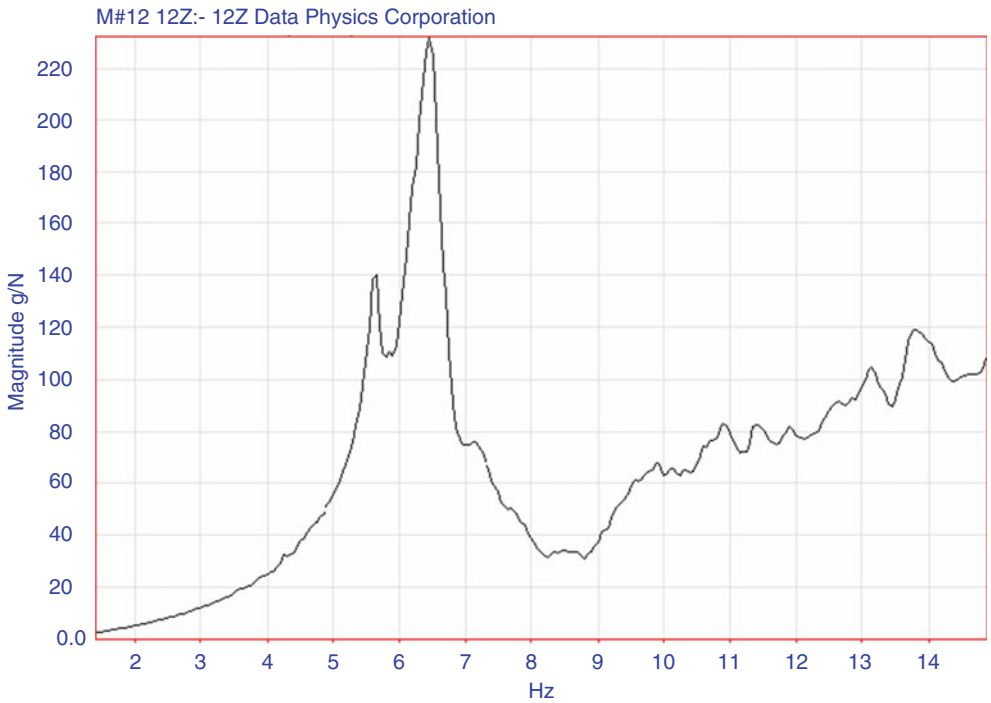

Fig. 9.3 Point mobility at TP12

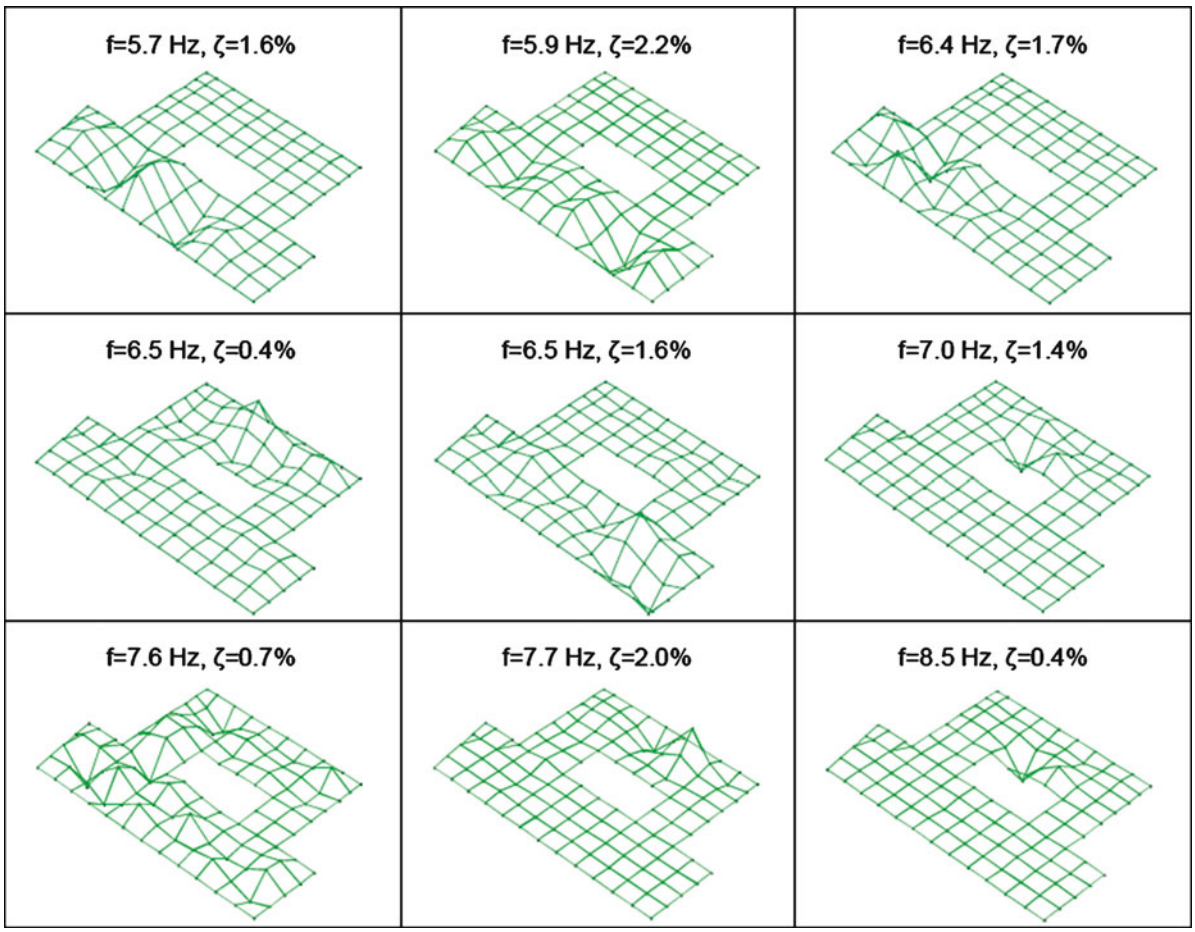

Fig. 9.4 Modes of vibration of the floor

Table 9.1 Description of test subjects

TS #	Sex (F/M)	Mass (kg)
1	M	80
2	F	60
3	M	64
4	M	75

It can be noticed that the lowest three modes occurred mainly in less stiff South part of the floor. Some modes occurring in the North part are more localised, possibly due to effects of partitions. One example is mode at 7.0 Hz which was localised to one of the conference rooms.

9.3.2 In-Service Vibration Monitoring

The in-service vibration monitoring was carried out during normal working hours during three working days. A single accelerometer was placed on the concrete slab below the false floor, as close as possible to the workstation at which noticeable vibrations were reported. Since the accelerometer was hidden in the floor, walking over the floor could take place as normal and without any impediment. Data acquisition system (analyser and a notebook PC) were placed beneath a desk close to the accelerometer location. A cable connecting the accelerometer with the data acquisition system ran through the false floor, and therefore was not visible to floor users. Wireless communication with the notebook PC was enabled during the acquisition, and therefore users of the building were not interrupted in any way during the data collection. This test setup allowed for usual walking patterns to take place on the floor as they would occur on a normal working day.

After an initial investigation of sensitivity of measured vibration to sampling rate (initially set at 204.8 Hz), it was found that reduced sample rate of 60 Hz was appropriate to genuinely represent frequency content of the vibration record. Therefore the sampling rate adopted was 60 Hz.

9.3.3 Response to Single Person Excitation

The aim of controlled walking tests to single person excitation was to excite one of first three modes of vibration presented in Fig. 9.4 and generate maximum vibration response under a single pedestrian. This is a common loading scenario adopted in the current design guidelines [1–3].

Four test subjects, whose basic data are shown in Table 9.1, took part in the testing programme. They walked forth and back along a pre-specified walking path (WP) and with a pacing rate controlled by a metronome. The two WPs utilised are shown in Fig. 9.2. WP1 connected TPs 10, 11, 12 and 13, while WP2 was along TPs 3, 6, 11, 16, 21 and 25. Along WP1, test subjects walked at walking frequency of 1.88 Hz (so that the third harmonic matches the natural frequency of the first mode), and 2.15 Hz (third harmonic matching the third mode). Walking along WP2 was at 1.98 Hz so that third harmonic would match the second mode of vibration. Each walking test was repeated twice. Summary of the tests performed is shown in Table 9.2.

During these tests, the acceleration was measured at TPs 10, 11, 12 and 13. The data were sampled at 204.8 Hz, with each record lasting 40 s.

9.4 Analysis of Vibration Behaviour

9.4.1 In-Service Vibrations

The time history of in-service vibration recorded on Day 1 during eight working hours (9:00–17:00) is shown in Fig. 9.5a. Similar records were acquired in other two tests. The frequency spectrum (averaged using time window of 100s) is shown in Fig. 9.5b. Several peaks were clearly visible in the spectrum, and they belong to two distinct frequency ranges. First range is between 0 and 15 Hz, with peaks clearly labelled in the figure. This range includes the responses in the vibration modes

Table 9.2 Description of the tests conducted

Test #	TS	WP	Pacing frequency (Hz)
1	1	1	1.88
2	1	1	1.88
3	2	1	1.88
4	2	1	1.88
5	3	1	1.88
6	3	1	1.88
7	4	1	1.88
8	4	1	1.88
9	1	1	2.15
10	1	1	2.15
11	2	1	2.15
12	2	1	2.15
13	3	1	2.15
14	3	1	2.15
15	4	1	2.15
16	4	1	2.15
17	1	2	1.98
18	1	2	1.98
19	2	2	1.98
20	2	2	1.98
21	3	2	1.98
22	3	2	1.98
23	4	2	1.98
24	4	2	1.98

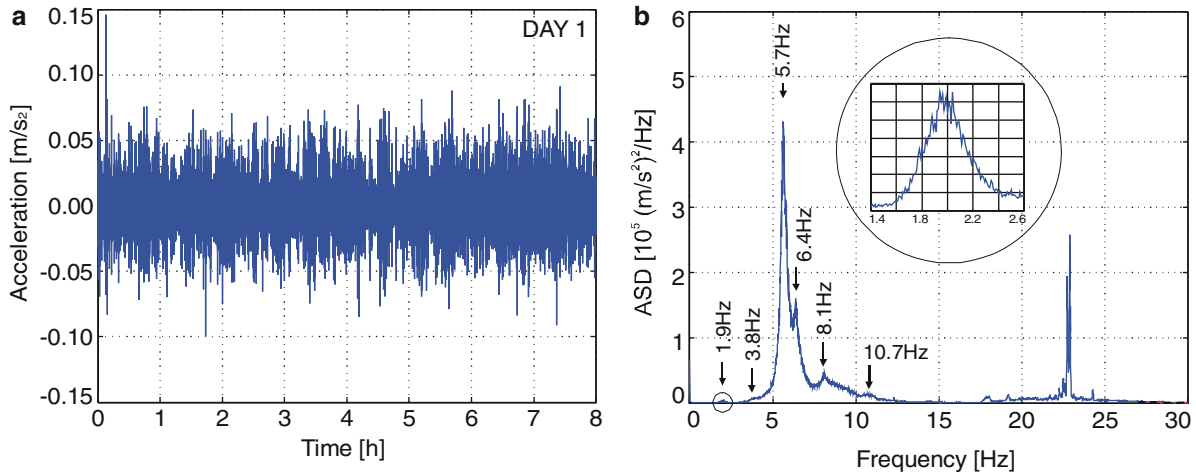

Fig. 9.5 (**a**) In-service vibrations during a working day and (**b**) spectrum of the measured vibration

identified during testing as well as harmonic components of the excitation (walking) force. Second range between 15 and 30 Hz is probably due to higher vibration modes that were not identified during modal testing. The vibration modes below 15 Hz dominated the vibration response of the floor. Their contribution to the total vibration energy was 82% on Day 1, 83% on Day 2 and 76% on Day 3. An enlarged display of the vibration spectrum in the frequency range 1.4–2.6 Hz is also shown in Fig. 9.5b. This part of the spectrum reveals that the distribution of walking frequency in this office has the mean value in the range 1.9–2.0 Hz. Similar conclusions were reached for measurements on Day 2 and Day 3.

Statistical properties of the instantaneous and 1s root-mean-square (1sRMS) accelerations measured during the 3 days are shown in Table 9.3. It can be seen that the skewness for the instantaneous acceleration is close to zero while it is positive value for 1sRMS. This means that the distribution of the response is symmetric for the instantaneous acceleration and skewed to the right for the 1sRMS. In addition, both variables have kurtosis larger than three, meaning that their "degree of peakedness" is larger (i.e. the peak is narrower) than in case of a normally distributed variable. These observations are confirmed by plotting the relevant distributions on the graphs shown in Fig. 9.6.

Table 9.3 Statistical properties of 8 h long acceleration records

Day #	Statistical property	Instantaneous acceleration	1sRMS
Day 1	Mean (m/s^2)	0	0.0063
	Standard deviation (m/s^2)	0.0072	0.0034
	(Min, Max) (m/s^2)	(−0.0997, 0.1458)	(0.0017, 0.0350)
	Skewness	0.023	1.98
	Kurtosis	8.02	7.99
Day 2	Mean (m/s^2)	0	0.0060
	Standard deviation (m/s^2)	0.0069	0.0034
	(Min, Max) (m/s^2)	(−0.1210, 0.1505)	(0.0015, 0.0385)
	Skewness	0.036	2.21
	Kurtosis	8.90	9.54
Day 3	Mean (m/s^2)	0	0.0063
	Standard deviation (m/s^2)	0.0070	0.0032
	(Min, Max) (m/s^2)	(−0.0880, 0.1024)	(0.0014, 0.0412)
	Skewness	0.014	2.08
	Kurtosis	7.63	9.22

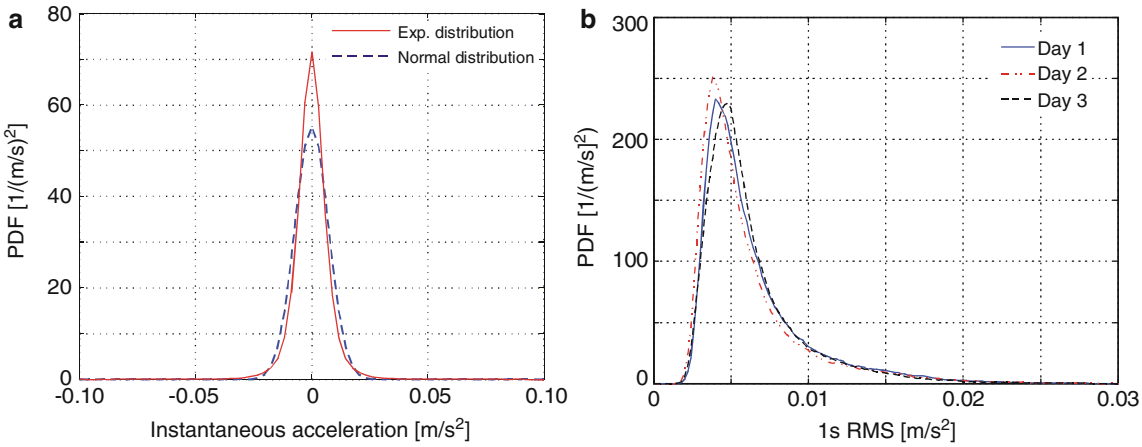

Fig. 9.6 (**a**) PDF of acceleration measured on Day 1 (*solid line*) and the corresponding normal distribution (*dashed line*) and (**b**) PDFs for 1sRMS acquired during 3 days of measurements

1sRMS acceleration normalised by the RMS acceleration that is just perceptible by an "average" human being is called the response factor (R-factor), and it is this vibration measure which is most often used when evaluating vibration serviceability of the floors. This quantity is required not to exceed a pre-defined limiting value (which is either 4 or 8 depending on the guideline) so that the office floor is deemed serviceable. The difficulty with this concept is that the 1sRMS is a stochastic variable which significantly varies in time. Figure 9.7a shows the variation of RMS value as a function of the time window over which the RMS value is calculated, starting with time window of 1s and going up to 60 min. The 1sRMS varies by factor 21, from 0.002 to 0.042 m/s^2. In this situation it is difficult to justify choosing a single value of 1sRMS for vibration serviceability assessment of a floor.

With increasing length of the time window, the variability in RMS reduces significantly. On this floor, it stabilises in the region 0.005–0.010 m/s^2 for time windows of 10 min or longer. This suggests that longer time window than currently used 1s could be more appropriate for accessing in-service vibration serviceability of floors. This would require using same length of time for assessing human response to vibrations they were exposed. It is interesting that crest factor (the peak acceleration divided by the RMS value over the same time window) is quite high for this floor (Fig. 9.7b). If the extreme (maximum) values are removed from the graph, it can be noticed that the crest factor varies in the range 10–15 for longest time windows. This is more than two times larger value of the crest factor than values recorded on a low frequency footbridge [4].

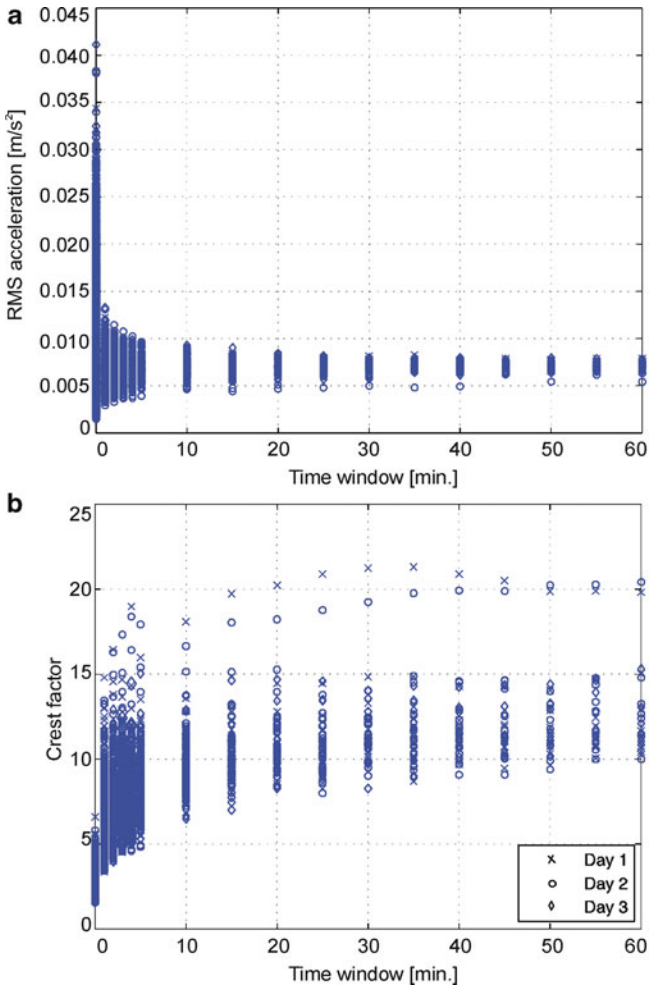

Fig. 9.7 (**a**) RMS acceleration and (**b**) crest factor as functions of time window used for calculations

9.4.2 Vibration Response to a Single Person Walking Excitation

During controlled walking tests the largest vibration response was most often recorded at TP11. This is the reason to choose TP11 for analysis in this section. Before the analysis, the measured time histories were filtered using Butterworth low pass filter of the fourth order, with cut-off frequency set at 75 Hz. This allowed for all frequency content below 60 Hz to go through, and stopped most of the frequency content above 60 Hz (it should be noted that the frequency content above 60 Hz had negligible contribution to the total energy of the signal). The filtering allowed to compare the vibration response to single person excitation to that measured during in-service monitoring.

Since each walking test was repeated twice (Table 9.2), the data collected in nominally identical tests were merged before being analysed. Statistical properties of the vibration response to single person excitation for each test subject and each pacing rate are shown in Table 9.4.

Comparing the skewness and kurtosis in Tables 9.3 and 9.4, it can be concluded that the statistical properties of the responses to single person excitation and in normal in-service conditions are different. On average, higher level vibrations are preserved in metronome controlled single person tests. This is expected given that the single person excitation is localised in the problematic zone of the structure, and that it is closed to the measurement points.

Results in Table 9.4 show that most extreme acceleration was achieved in tests involving walking at fastest pacing rate of 2.15 Hz. TS1 proved to be most efficient dynamic exciter, inducing maximum vibration levels that were higher than those recorded during in-service monitoring.

As pointed out earlier, the 1sRMS acceleration is a vibration measure on which the vibration serviceability check of floor structures is normally based. Figure 9.8 shows the cumulative probability of 1sRMS value as acquired during 3 days of in-service measurements. In the same figure, the peak 1sRMS measured in each single person test is also labelled.

Table 9.4 Statistical properties of vibration response to single person excitation

TS	Statistical property	Instantaneous acceleration 1.88 Hz/2.15 Hz/1.98 Hz	1sRMS 1.88 Hz/2.15 Hz/1.98 Hz
1	Mean (m/s^2)	0/0/0	0.0153/0.0225/0.0140
	Standard deviation (m/s^2)	0.0161/0.02491/0.0164	0.0052/0.0107/0.0085
	(Min, Max) (m/s^2)	(−0.0875,0.1101)/(−0.2012,0.2902)/(−0.1042,0.1727)	(0.0060,0.0290)/(0.0077,0.0553)/(0.0066, 0.0361)
	Skewness	0.1430/0.5087/0.6948	0.3696/1.1984/1.2620
	Kurtosis	5.0142/14.6594/12.8106	2.6012/4.0757/3.2991
2	Mean (m/s^2)	0/0/0	0.0113/0.0115/0.0103
	Standard deviation (m/s^2)	0.0118/0.0121/0.0111	0.0033/0.0039/0.0039
	(Min, Max) (m/s^2)	(−0.0582, 0.0863)/(−0.1065,0.1178)/(−0.0718,0.0780)	(0.0062, 0.0203)/(0.0063,0.0253)/(0.0060, 0.0204)
	Skewness	0.0593/−0.0624/0.1272	0.7589/1.2180/1.2127
	Kurtosis	4.3213/7.1114/6.2427	3.0134/4.2986/3.1850
3	Mean (m/s^2)	0/0/0	0.0180/0.0170/0.0146
	Standard deviation (m/s^2)	0.0194/0.0185/0.0160	0.0075/0.0074/0.0067
	(Min, Max) (m/s^2)	(−0.0916 0.1311)/(−0.1168,0.1863)/(−0.0856,0.1568)	(0.0065, 0.0354)/(0.0058,0.0423)/(0.0063, 0.0336)
	Skewness	0.0419/0.5800/0.7609	0.5123/0.8720/1.0725
	Kurtosis	4.6264/9.5045/9.9807	2.3056/3.4373/3.2922
4	Mean (m/s^2)	0/0/0	0.0138/0.0132/0.0126
	Standard deviation (m/s^2)	0.0145/0.0143/0.0142	0.0045/0.0055/0.0066
	(Min, Max) (m/s^2)	(−0.0975,0.1136)/(−0.1005,0.1265)/(−0.0939,0.1374)	(0.0067, 0.0252)/(0.0070,0.0324)/(0.0063, 0.0321)
	Skewness	0.2010/0.2997/0.5167	0.8862/1.5084/1.5718
	Kurtosis	5.3016/9.5959/10.2062	3.1505/4.7631/4.2801

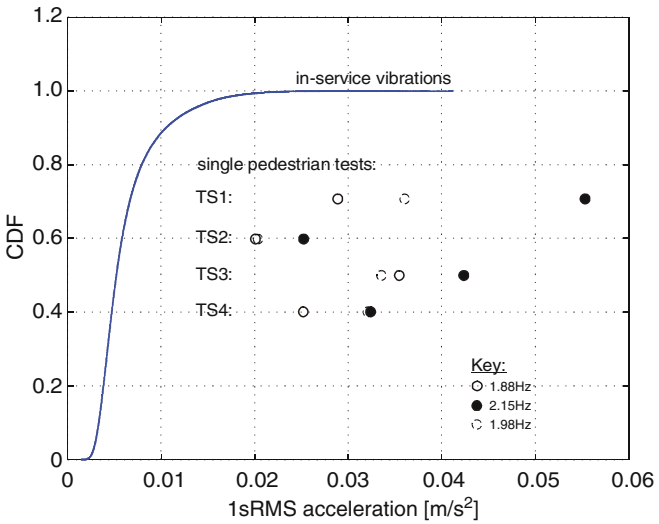

Fig. 9.8 CDF of 1sRMS acceleration measured during in-service monitoring, with addition of peak 1sRMS values recorded in single person tests

It can be seen that the peak 1sRMS varies between different test subjects, with TS1 generating largest and TS2 lowest vibration levels. Regardless of the large differences in dynamic excitation potential between four test subjects, it is clear that the maximum 1sRMS values they generated in different tests were extremely rarely (or never, in case of TS1 and TS3 walking at 2.15 Hz) exceeded during in-service monitoring. It is striking that all responses measured during single person walking tests had considerably less than 1% chance of being exceeded during normal use of the floor. Therefore, the single person loading scenario might not be best way to estimate vibration serviceability of floor structures. A possible way forward could be defining the properties of a virtual pedestrian that would be able to replicate the 1sRMS values achieved during in-service conditions. For this, simulations to establish the significance of different walking paths on the vibration response are required. In addition, acquiring experimental data about floor responses via similar monitoring exercises together with occupants' activities and actual walking paths during a normal working day are of crucial importance to establish reliable and non-conservative models.

9.5 Conclusions

Monitoring of in-service vibrations of an office floor during normal working hours on three successive days revealed a similar vibration pattern on any single day. It was shown that the occupants of the floor are exposed to lower vibration levels during normal occupancy than in single pedestrian walking tests along the most critical walking paths, even at the most responsive location on the floor. This suggests that frequently used single person model walking at a pre-specified walking frequency might be too conservative for vibration serviceability design of the floors. To improve the predictability of in-service vibrations, and at the same time to keep the model simple, a pedestrian model capable of replicating the 1sRMS values achieved during in-service conditions is needed. This model might need to be defined for various probability of exceedance and would need to include relative importance of walking along different walking paths. To help development of such a model, more experimental data on occupants' activities and actual walking paths during normal working hours are required.

References

1. Pavic A, (2005) Willford M Vibration serviceability of post-tensioned concrete floors. Appendix G in Post-tensioned concrete floors design handbook, 2nd edn. Technical report 43. Concrete Society, Slough, pp 99–107
2. Smith AL, Hicks SJ, Devine PJ (2009) Design of floors for vibration: a new approach (revised edition). The Steel Construction Institute, London
3. Willford M, Young P (2006) A design guide for footfall induced vibration of structures. The Concrete Center, Camberley
4. Zivanovic S (2011) Statistical description of pedestrian loading and vibration response of a footbridge. In: Proceedings of the 8th international conference on structural dynamics, Leuven, 4–6 July

Chapter 10
Discomfort Evaluation on Lively Footbridges with Soft-Rubber Pavement

M. Istrate, N. Ibán, A. Vasallo, A. Lorenzana, and I.M. Diaz

Abstract This paper deals with the measurement of the pedestrian perception of the movement of lively footbridges. Several tests on a 80 m single span stress-ribbon footbridge are presented. This footbridge is very slender and has a very low structural damping and several modes under 3 Hz, resulting in sensible vertical movements. Despite of that, general users do not complain too much, probably because its pavement is made of a thick pour-in-place soft-rubber material.

When a pedestrian walks on a flexible pavement, in every step he notices how first the heel, then the toe, sinks and rises, and probably that feeling makes the pedestrian, unconsciously, no to be so demanding regarding the movement of the walkway. To verify this effect, we compare the recordings of three accelerometers installed on the pedestrian when he walks on four different scenarios. Two of the accelerometers are located on one of the pedestrian's shoes (one at the heel and the other one at the toe) and the third is placed on his hip (all of then in the right side of the body).

The walking scenarios are: rigid and thick soft pavement on solid soil and thin and thick soft pavement on the footbridge walkway. Comparing the acceleration levels in these four scenarios, some conclusions are reached.

Keywords Footbridges • Soft-rubber pavement • Perception • Discomfort • Serviceability

10.1 Introduction

Pedestrian loads are low intensity quasi-periodic loads. Applied to very stiff and massive structures this loads could hardly make them vibrate significantly. However, aesthetic, technical and technological developments lead to ever more slender and flexible footbridges and, as a consequence, they can vibrate significantly even under a single person and frequently require a thorough dynamic analysis.

In some footbridges, probably in project stages, using numerical techniques, or after a dynamic assessment, once built, through experimental techniques, different alternatives have to be proposed in order to avoid relevant vertical acceleration levels. Those alternatives tend to change the dynamic response by adding mass, or stiffness, or damping.

In this paper a novel alternative is analyzed: by adding a thick soft-rubber pavement, pour-in-place, softer than the one used in athletic training tracks, several effects are introduced. Although for standard footbridges, the additional mass (with no addition in stiffness) is irrelevant in changing natural frequencies or natural modes, for light footbridges, as steel or composite stress-ribbon ones, the effect could be appreciable. Also the rubber pavement improves the structural damping, being this effect very desirable for this kind of lively structures. But the main factor, analyzed in this paper, is its influence in

M. Istrate (✉) • N. Ibán • A. Vasallo
CARTIF Centro Tecnológico, Parque Tecnológico de Boecilllo, 47151 Valladolid, Spain
e-mail: melist@cartif.es

A. Lorenzana
ITAP, University of Valladolid, 47011 Valladolid, Spain

I.M. Diaz
ETSI Industriales, University of Castilla-La Mancha, Ciudad Real, Spain

J.M. Caicedo et al. (eds.), *Topics on the Dynamics of Civil Structures, Volume 1*,
Conference Proceedings of the Society for Experimental Mechanics Series 26,
DOI 10.1007/978-1-4614-2413-0_10,

two important aspects of the human-structure interaction process. The first one is that the flexibility of the pavement affects the way the load is exerted to the structure. The second one, and more important in the perception of the discomfort, is that the pavement also affects the way the pedestrian senses the acceleration of the structure. The following sections are devoted to quantify this second effect.

10.2 Evaluation of Footbridge Comfort According to Standards and Guidelines

Modern pedestrian bridges are very often slender very flexible structures, where the first natural frequencies of vibration may fall close to dominant frequencies of the dynamic excitation due to walking or running. It is caused by technologically advanced materials used for their construction, with better strength parameters from those used before, together with the architectural trend for designing atypical and daring structures which quite often contradicts the classic principles of designing footbridges. The designer must take into account the phenomena of the man-bridge interaction and its vibration perception by human beings. Although such vibrations don't cause usually structural problems, they can induce some uncomfortable sensations. Vibrations of high amplitudes can cause a feeling of anxiety and fear, and even panic among pedestrians, affecting the functionality of the footbridge. Exceptionally, continuous vibration under standard service conditions, such as normal pedestrian use, may also cause fatigue that could damage the bearing structure and consequently affect structural safety. In addition, if the frequency of the actions is very close to the natural frequency of the structure itself and damping weak, resonance could occur if the actions are continuous, widening the vibration amplitude and raising the risk of structural collapse.

Some codes, standards or guidelines (ISO10137, EUROCODES 1 and 5, DIN4150, BS5400-6472, SBA1982, ENV1995, AISC1997, SETRA, HIVOSS, . . .) establish maximum acceptable values of acceleration, normally expressed as function of the fundamental frequency of the footbridge. A detailed literature review on human-induced dynamic loading of footbridges is given by Zivanovic et al. [14]. In many of those codes [2–4, 6, 8, 12], dynamic problems are addressed by defining limits for the natural frequencies of the structures or for the accelerations associated with pedestrian-induced vibrations. Such approaches are usually conservative and fail to deal with all the parameters relevant to human sensitivity to vibrations, which is highly subjective. This, together with the fact that the natural frequencies and accelerations calculated by analytical or numerical methods are subject to uncertainties, may hinder pedestrian bridge design.

The dynamic behaviour of footbridges depends on many parameters [5] whose impact on vibrations is uncertain. These include material properties and mass, structural stiffness, including the boundary conditions, *deck surfacing*, guard rails, contribution of non-bearing elements, total damping, ...

Numerical simulation should be as realistic as possible with regard to all the parameters relevant to dynamic behaviour. Moreover, modelling the excitation (moving footfalls) is not easy [1, 7, 10, 11, 15] and it is usually assumed to be a stationary harmonic force, i.e. the walking path is not taken into consideration. In general, the location of the stationary excitation and hence the location of the response are selected where the largest vibration amplitudes are expected (usually in the middle of the span). As a result, calculated responses can differ from one code to another in more than four times (has pointed out in Ref. [13]) and use to be considerable overestimated.

Once the response is obtained, the acceptance criterion is applied. Although some criteria are established not just in terms of RMS values of acceleration response at deck's midspan, usual recommended acceleration limits for footbridges are between 0.5 and 0.7 m/s^2 in the usual range of footbridges frequencies.

Note that for all those calculations, local properties cannot be considered, so, i.e., in the same footbridge with two lanes (bicycle and pedestrian) with different pavements, computed RMS acceleration is unique, affecting to both lanes.

10.3 Human Perception

In general, the perception and the individual judgement, whether vibrations are disturbing or not, are based on the psychological parameters and can lead to different limits, as certain persons can detect vibrations without being discomforted by them. Some of these parameters are difficult to quantify or are highly subjective. They include the number of simultaneous users; frequency of use; pedestrians' activity (walking, jogging, standing or sitting on the bridge);

characteristics of the excitation forces (harmonic or transient); time of exposure; deck and guard rail transparency; height over ground level; footbridge appearance, if vibration is expected or not, etc.

It is considered that the vertical motion of the human body while walking is characterized by a relative motion between the center of gravity of the body ($\mathbf{u_b}$) and the deck ($\mathbf{u_g}$). This is the result of a cyclic sequence of vertical movements caused by the movement (flexing) of the lower limbs. In each cycle, the body moves down due to the bending of each leg and restores its position with the tightening of the respective leg. This vertical motion induces forces un the deck (**F(t)**) and is also influenced by the stiffness, damping, mass and other properties of the structure. Based on this, simple biodynamic models can be conceived, although its application to evaluation of the comfort of the pedestrian is still to come. Note that **F(t)** contains all the complexity of human being and the applied forces are governed by a very sophisticated control system: the human brain.

Among other effects, in this paper we focus on walking on flexible pavement. When a pedestrian walks on a softy soil, in every step he notices how first the heel, then the toe, sinks and rises, and probably that feeling makes the pedestrian, unconsciously, no to be so demanding regarding the movement of the walkway. To verify this effect, we compare the recordings of three accelerometers installed on the pedestrian when he walks on four different scenarios. Two of the accelerometers are located on one of the pedestrian's shoes (one at the heel and the other one at the toe) and the third is placed on his hip (all of then in the right side of the body).

10.4 Methodology

To record the accelerations during normal walking, three uniaxial accelerometers (PCB Piezotronics, model 352C65, high sensitivity, miniature ceramic shear ICP® accel. 100 mV/g, 0.5–10k Hz) have been installed on the pedestrian (75 kg weight). As shown in Fig. 10.1, one is placed on his hip (C), other on his heel (T) and the third one on his toe (P). All of them are in the vertical axis when the pedestrian is at rest. Accelerometer (C) almost remains in the vertical direction over the whole walking cycle but (T) and (P) can change in more than 80°. The three signals are recorded synchronously at a sample rate of 100 Hz.

Several tests were conducted with same pedestrian (male, 1.80 m height, 80 kg weight) in similar conditions (clothes, rubber-soled shoes, . . .) wearing the three accelerometers and walking with a standard pacing rate (105 bpm) using a metronome.

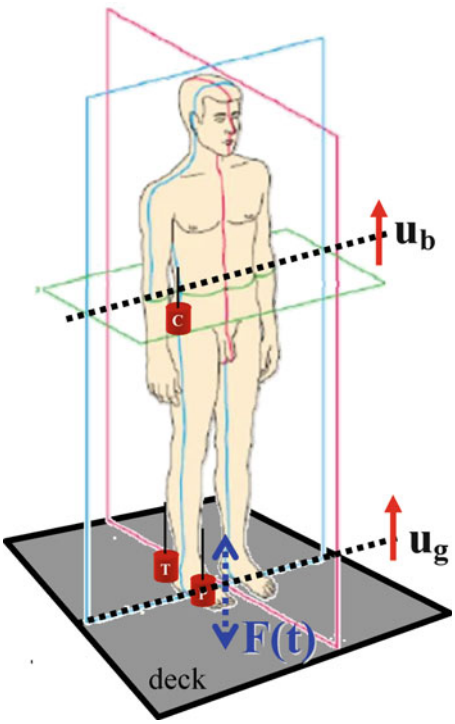

Fig. 10.1 Accelerometers placed at pedestrian's *right* hip, toe and heel

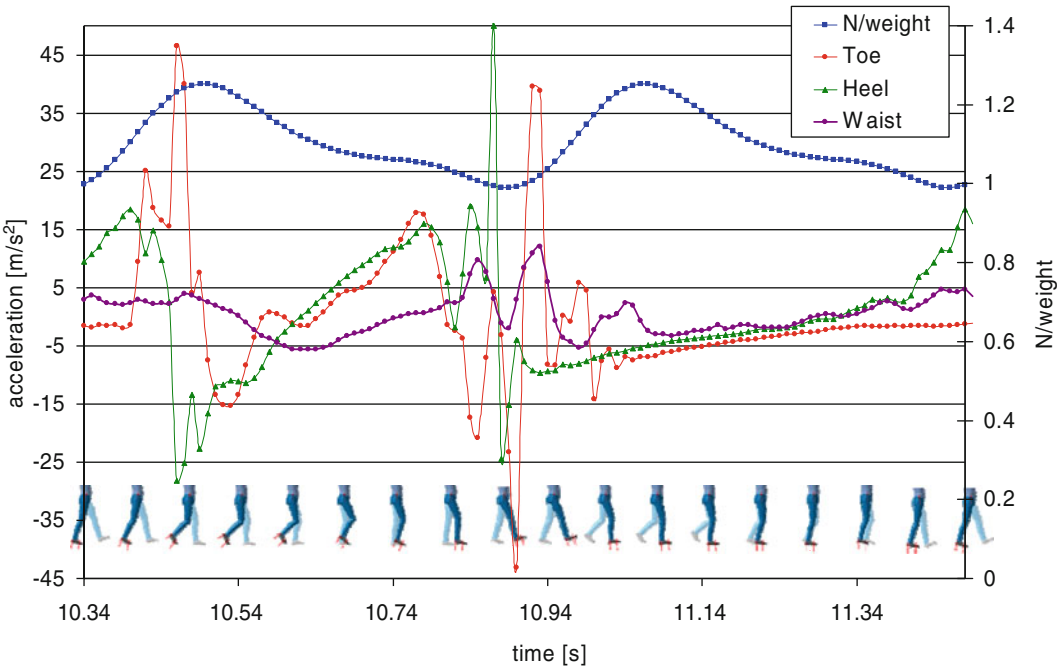

Fig. 10.2 One cycle accelerometer recordings for hip, toe and heel

Typical pacing frequencies for a person walking generally lie between 1.6 and 2.4 Hz. Fifty percent of pedestrians walk at rates between 1.9 and 2.1 Hz and 95% of pedestrians walk at rates between 1.65 and 2.35 Hz [10]. The scenarios to be compared are:

- (S) standard rigid pavement out of the footbridge
- (R) rubber pavement before entering in the footbridge (thickness about 40 mm)
- (F1) rubber pavement on bicycle lane of the footbridge (thickness about 10 mm)
- (F2) rubber pavement on pedestrian lane of the footbridge (thickness about 40 mm)

In Fig. 10.2, 18 selected instants of the walking cycle on (S) are shown in a schematic way (ground contact, stretching, rocking and swing) focusing in the right leg. Measured accelerations for the three accelerometers are plotted for a representative step, together with the estimated contact force when walking on rigid pavement. For 105 bpm the duration of the cycle is 1.14 s. Accelerations in toe P and heel T are obviously greater than in the hip C and also more sharpy and "noisy". The contact force (two legs) is estimated after Petersen [9] (for a pacing frequency of 1.75 Hz, for which the corresponding parameters for the first, second and third harmonics are 0.240, 0.108 and 0.018 and phase lag are $\pi/5$, amplitude normalized by relating them to the body weight of the pedestrian) and included in Fig. 10.2 for the sake of completeness.

In Fig. 10.3, not only accelerations for the hip are presented, but also velocities and displacements (computed by numerical integration) and also jerks (numerical differentiation from the acceleration). All of these magnitudes (RMS and amplitudes during 100s recordings) are going to be compared for the four different scenarios.

For each location (P, T or C), ten representative cycles (steps) are shown in Fig. 10.4. All of then are matched in the instant when the toe lifts off the ground. For each step, also the following one is shown. Trying to get relevant information for understanding why walking on F2 is more comfortable than walking on F1, parameters Δa_0, Δa_1, $\bar{a}$ and Δt are going to be evaluated for the four different scenarios. Δa_0 is the amplitude of the impact when the heel reach the ground (between mean values for the ten selected cycles), Δa_1 is the acceleration interval in the next step, with mean value is $\bar{a}$, and Δt is the corresponding time interval.

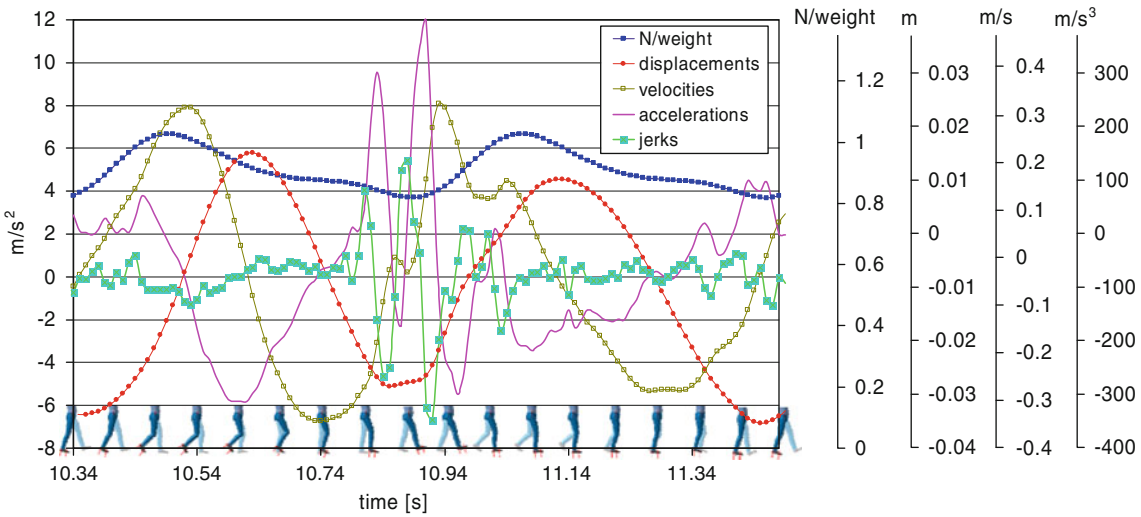

Fig. 10.3 Hip acceleration and corresponding velocity, displacement and jerk

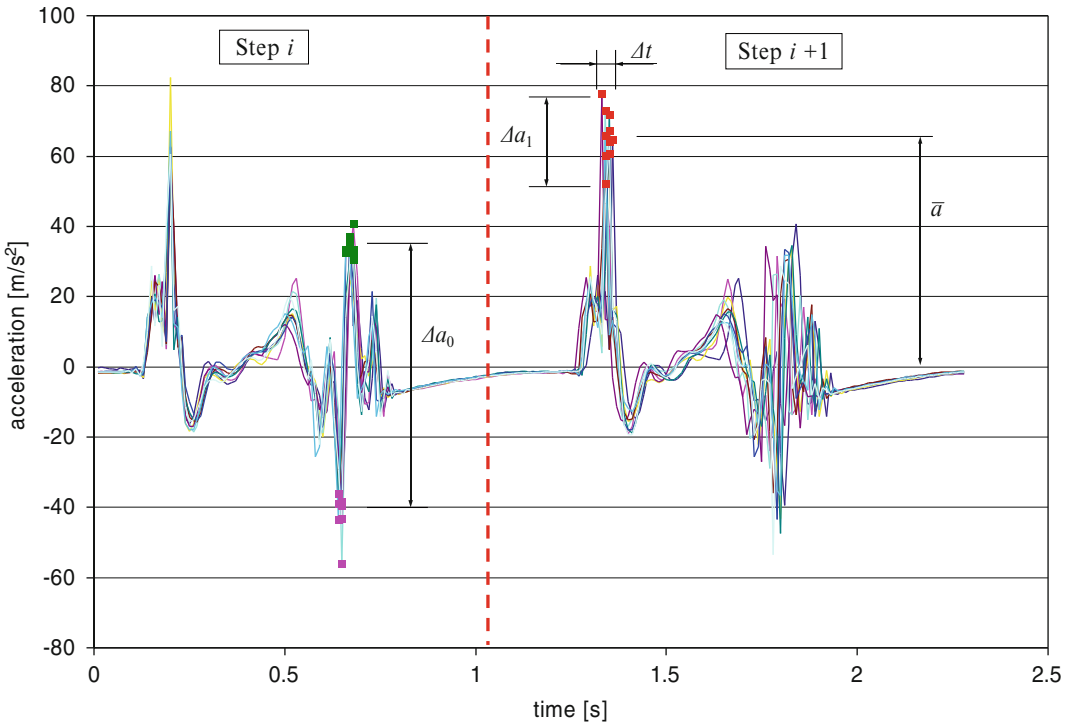

Fig. 10.4 Toe accelerations during two cycles

10.5 Results

Numerical results are shown in the following tables. RMS values and maximum values of accelerations for 100s recordings are presented for toe (Table 10.1), heel (Table 10.2) and hip (Tables 10.3 and 10.4) for the four scenarios. Also corresponding jerks are computed and resented, and for the hip, also velocities and displacements.

Table 10.1 Results for 100s recording at toe

	a_{RMS}	a_{max}	j_{RMS}	j_{max}
(S)	11.31	82.14	1001.04	7133.6
(F1)	12.73	91.36	1148.04	8463.7
(R)	10.03	78.52	864.43	7136.3
(F2)	11.5	85.31	978.99	7840.6

Table 10.2 Results for 100s recording at heel

	a_{RMS}	a_{max}	j_{RMS}	j_{max}
(S)	9.56	68.36	775.45	6151.6
(F1)	10.07	64.57	827.45	8449.2
(R)	8.96	62.36	707.06	6776.2
(F2)	9.71	66.82	731.30	7697.8

Table 10.3 Results for 100s recording at hip

	a_{RMS}	a_{max}	j_{RMS}	j_{max}
(S)	3.23	14.33	141.08	736.5
(F1)	3.17	13.30	170.56	622.3
(R)	2.89	12.5	122.47	1851.6
(F2)	3.33	17.11	136.80	1159.0

Table 10.4 Results for 100s recording at hip

	v_{RMS}	d_{max}	d_{RMS}	d_{max}
(S)	0.219	0.469	0.0151	0.0387
(F1)	0.217	0.509	0.0199	0.0428
(R)	0.201	0.49	0.0183	0.0365
(F2)	0.233	0.546	0.0207	0.0398

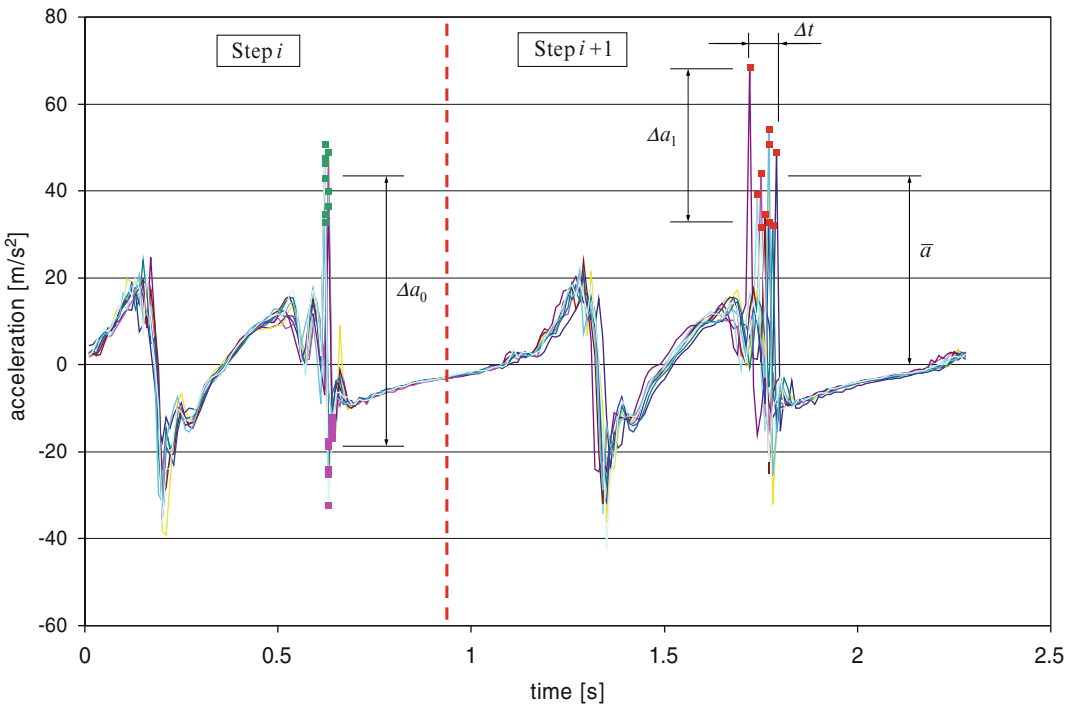

Fig. 10.5 Heel accelerations during two cycles

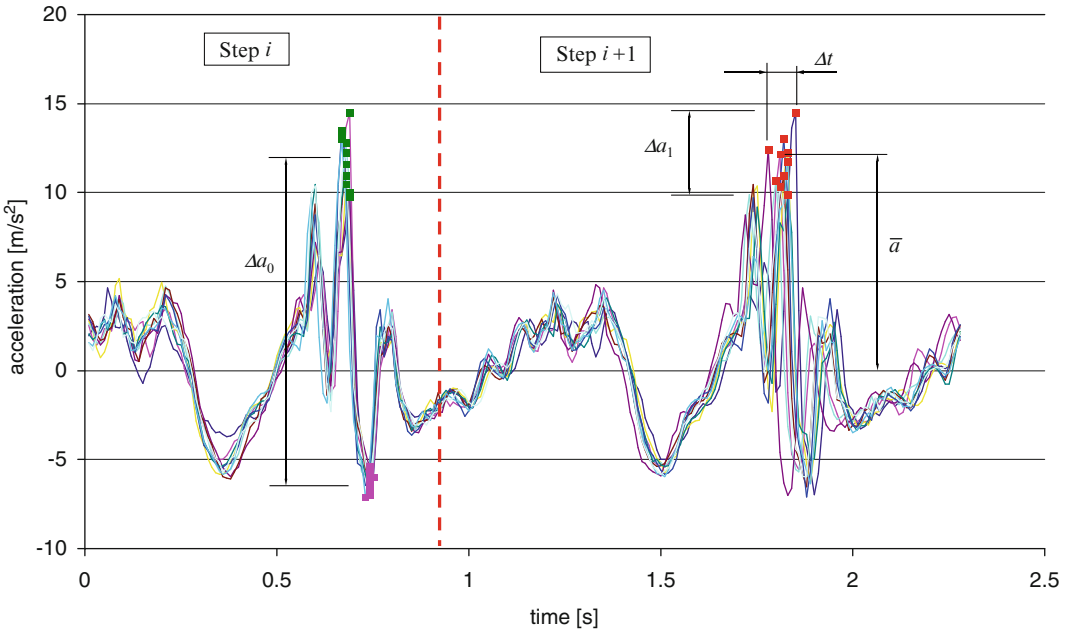

Fig. 10.6 Hip accelerations during two cycles

Table 10.5 Parameters for two cycle: toe

	Δa_0	Δt	Δa_1	$\bar{a}$
(S)	76.39	0.03	25.53	65.76
(F1)	66.28	0.06	23.69	72.43
(R)	53.26	0.07	28.04	57.12
(F2)	51.47	0.07	36.48	65.95

Table 10.6 Parameters for two cycle: Heel

	Δa_0	Δt	Δa_1	$\bar{a}$
(S)	61.05	0.07	36.86	43.72
(F1)	45.21	0.15	38.28	35.65
(R)	52.03	0.19	23.78	34.66
(F2)	46.34	0.21	43.98	34.13

Table 10.7 Parameters for two cycle: hip

	Δa_0	Δt	Δa_1	$\bar{a}$
(S)	18.19	**0.06**	5.58	11.79
(F1)	14.87	**0.15**	7.27	11.50
(R)	15.59	**0.17**	5.55	11.41
(F2)	11.65	**0.20**	6.95	10.38

In a similar way, all the parameters defined in Figs. 10.4, 10.5, and 10.6 are presented in Tables 10.5, 10.6 and 10.7 for ten selected double cycles. Among all these data, the more relevant conclusion is that Δt increase when pavement is more flexible.

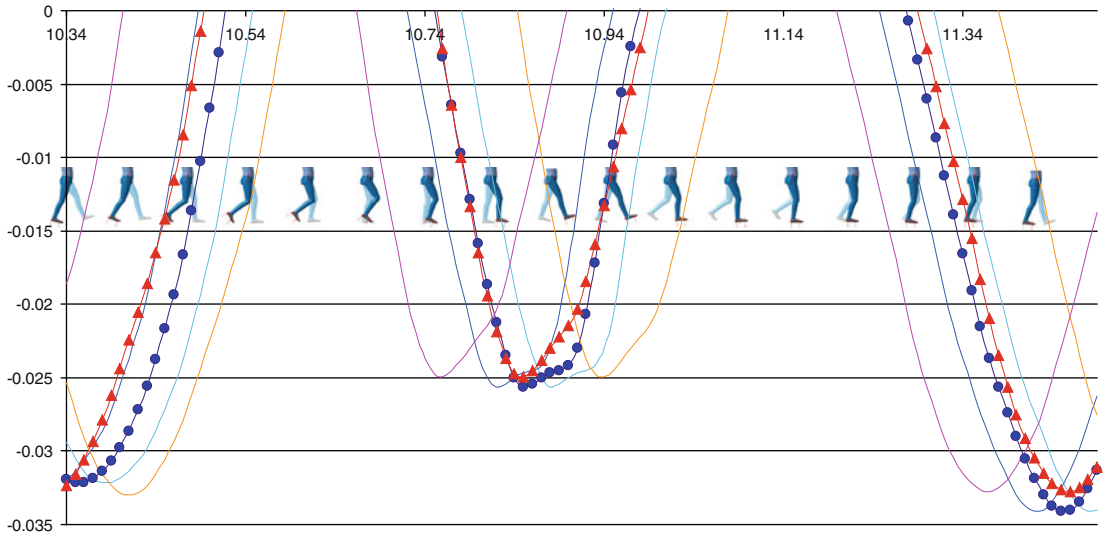

Fig. 10.7 Expected hip displacements (*circled line* for (S) and *triangled line* for (F2)) and corresponding displacements for possible faster or slower steps

10.6 Conclusions

The shape of recordings in the representative walking cycles is similar. Some differences can be found in acceleration amplitudes, but more statistic analysis is required to get decisive conclusions. Although jerk is often used to measure the comfort of rides (elevators, trams, roller coasters, etc.), no relevant results can be obtained from the attempt done in this study of evaluate the jerk in toe, heel or hip.

Analyzing the timing and dispersion of walking cycles, a relevant conclusion can be found: when walking on soft pavement the cycles are not as similar, between themselves, as when walking on rigid pavement. The dispersion Δt is much greater for (R) and (F2), as expected.

Accelerations recorded in the deck during F1 and F2 events were very similar, with RMS values about 0.064 m/s^2 and maximum values about 0.52 m/s^2. The corresponding FFT reveals dominant contribution at the frequencies 1.07, 1.73 and 2.24 Hz. Corresponding numerical computed displacements were about 2.78 mm maximum, with RMS about 1.17 mm. Modal masses and modal dampings are yet to be determined. During those recordings, no more that five people (less than 0.02 person/m^2) were crossing the footbridge. In those conditions, according to usual acceptance criteria, the dynamical behaviour of the footbridge is adequate ($<$0.7 m/s^2). But another source of discomfort could be that the ground is or not in the expected position. Bearing in mind the values for Δt given in Table 10.7, one step can be $\Delta t/2$ faster or slower than the previous ones. In that time, according to Fig. 10.7, expected vertical displacement in the hip can be around 1.8 mm for (S) and around 15 mm for F2, even though, it is not difficult neither uncomfortable to walk on the rubbered footbridge (F2). Movements of the deck are more strongly perceived in (F1), although Δt, and is less than for (F2). Due to the sensation of softy pavement, it could be that the pedestrian mind was not as challenging to keep pace and therefore not as sensitive to ground motion perception, as vibrations are expected after walking on (R).

Acknowledgment The results of this paper are partly obtained within the framework of a current research project, BIA2011-28493-C02-02, financed by the "Ministerio de Ciencia e Innovación", Spanish government.

References

1. Cheng JC, Moura JMF (1997) Tracking human walking in dynamic scenes. In: Proceedings of the IEEE international conference on image processing, ICIP'97, vol 1, Santa Barbara, pp 137–140
2. European Committee for Standardization CEN:EN1991-2, UK National Annex to Eurocode 1-actions on structures, Part 2: traffic load on bridges, 2003
3. European Committee for Standardization CEN:EN1995-2, Eurocode 5 – design of timber structures, Part 2: traffic load on bridges, 2003

4. Federation international du beton, Guidelines for the design of footbridges, FIB Bulletin No. 32, Lausenne, 2006
5. Figueiredo FP, Silva JGS, Lima LRO, Vellasco PCG, Andradec SAL (2008) A parametric study of composite footbridges under pedestrian walking loads. Eng Struct 30(3):605–615
6. HIVOSS, Design of footbridge guidelines, human induced vibrations of steel structures, 2008
7. Hogan N (1990) Mechanical impedance of single- and multi-articular systems. In: Multiple muscle systems: biomechanics and movement organization. Springer, New York
8. International Standards Organization, ISO 10137:2004, Bases for design of structure, serviceability of buildings and pedestrian walkways against vibration, Geneva, 2005
9. Petersen C (1996) Dynamik der Baukonstruktionen. Vieweg, Braunchweig/Wiesbaden
10. Racic V, Pavic A, Brownjohn JMW (2009) Experimental identification and analytical modelling of human walking forces: literature review. J Sound Vib 326(1–2):1–49
11. Sánchez J, Instituto de biomecánica de Valencia (1999) Biomecánica de la marcha humana normal y patológica (in Spanish). Instituto de biomecánica de Valencia, Valencia, ISBN-13.9788495448125
12. Setra. Technical guide footbridge: assessment of vibration behavior of footbridges under pedestrian loading, Paris, 2006
13. Zivanovic S, Pavic A, Ingolfsson ET (2010) Modelling spatially unrestricted pedestrian traffic on footbridges. J Struct Eng-ASCE 136 (10):1296–1308
14. Zivanovic S, Pavic A, Reynolds P (2005) Vibration serviceability of footbridges under human-induced excitation: a literature review. J Sound Vib 279(1–2):1–74
15. Whittingtonm BR, Thelen DG (2009) A simple mass-spring model with roller feet can induce the ground reactions observed in human walking. J Biomech Eng 131:011013

Chapter 11
Direct Output Feedback and Model-Based Control Approaches for Mitigation of Human-Induced Vibrations in Floors

D.S. Nyawako, P. Reynolds, and M. Hudson

Abstract In recent years, there has been a considerable amount of research effort devoted to the development and application of active vibration control (AVC) techniques for mitigation of human-induced vibrations in floors. Through analytical studies and some field trials, it has been demonstrated that, as well as improving the vibration serviceability performance of problem floors considerably, this technology could potentially be used as a retrofit to problem floors prone to human-induced vibrations.

Most of these past researches have focused on direct-output feedback AVC approaches, the traditional approach that has been investigated extensively and used for floor vibration control, and there is on-going progress towards model-based vibration control approaches, which are quite new technologies being investigated for controlling human-induced vibrations in floors and that show considerable promise. This paper reviews each of these approaches and explores the potential benefits that may be realised from their implementation in 'problematic floors', by using a laboratory structure for this case study. This research study demonstrates potential improvements in vibration mitigation performances with model-based controllers by isolating and controlling target modes of vibration.

Keywords Active vibration control (AVC) • Human-induced vibration

11.1 Introduction

Vibration serviceability problems in floors have been exacerbated by advancements in materials, design and construction technologies that are leading to progressively longer, structurally more efficient and slender floor structures with fewer internal partitions [1–3]. They possess low and close natural frequencies, sometimes falling within the range of frequencies produced by human activities as well as low internal damping characteristics. A tendency for developers to require floor structures suitable for a variety of types of occupation in order to increase flexibility of their usage and thus their economic viability does have clear consequences on its vibration serviceability [4]. An overview of some technologies for mitigation of human induced vibrations in civil engineering structures is presented in Ref. [5].

In the recent few years, there has been considerable promise demonstrated by the use of active vibration control (AVC) technologies for mitigation of human-induced vibrations in problem floors both in analytical studies and field trials. Direct output feedback (DOFB) AVC technologies, in particular Direct Velocity Feedback (DVF) have been investigated and implemented in field trials and show considerable augmentation of damping in problem floors and thereby improving their vibration serviceability performances [6, 7]. Other direct-output feedback schemes that have been investigated include compensated acceleration feedback, response-dependent velocity feedback, integral resonant control scheme, and DVF with enhanced actuator compensators [8–12]. Direct output feedback approaches have a global effect in controlling all vibration modes and there is always the potential of spillover instability or destabilization of higher modes that are not of interest. Most of these studies have comprised of collocated actuator and sensor pairs.

Model-based control approaches, for example, the Linear Quadratic Controller (LQR), Independent Modal Space Control (IMSC), Pole Placement (PP), and H-infinity controllers are quite new technologies for the on-going research work on AVC

D.S. Nyawako (✉) • P. Reynolds • M. Hudson
Vibration Engineering Section, Department of Civil and Structural Engineering, The University of Sheffield,
Sir Frederick Mappin Building, Mappin Street, Sheffield S1 3JD, UK
e-mail: d.nyawako@sheffield.ac.uk

J.M. Caicedo et al. (eds.), *Topics on the Dynamics of Civil Structures, Volume 1*,
Conference Proceedings of the Society for Experimental Mechanics Series 26,
DOI 10.1007/978-1-4614-2413-0_11,

of human-induced vibrations in problem floors. These technologies have been extensively investigated in some applications, for example, in earthquake hazard, wave and wind mitigation applications in tall buildings, long-span bridges and offshore structures [13–16], as well as in the marine industry for developing isolation systems that improve passenger and crew comfort [17]. The principles of some of these approaches are outlined by Soong [18] and Inman [19]. The potential advantage that can be derived from some of these approaches in the present research work, for example, the IMSC and PP approaches is the possibility of isolation and control of target/problematic modes of vibration.

The research work presented in this paper is a comparative study of vibration mitigation performances between the DVF scheme (with an inner-loop actuator compensator to enhance its stability margins as derived in Ref. [11, 12]) and Pole-Placement and IMSC controllers. DVF and Pole-Placement controllers are designed and implemented in a SISO scheme while the IMSC controller is derived and implemented in a MIMO scheme. The Pole-Placement and IMSC controllers are designed to target specific modes of vibration of the test structure, while the DVF control law has a global influence in controlling all vibration modes. The experimental studies carried out to evaluate the performances of these control strategies comprise of uncontrolled and controlled point accelerance frequency response function (FRF) tests and uncontrolled and controlled responses to walking at a pacing frequency of 2.25 Hz. In Sect. 11.2, the test structure and actuator dynamics are introduced, and Sect. 11.3 provides an overview of the control strategies used in this research work. Section 11.4 provides a summary of results from the experimental studies and some conclusions are outlined in Sect. 11.5.

11.2 Test Structure and Actuator Dynamics

The test structure used in this research work is a simply-supported in-situ cast post-tensioned slab strip with a span of 10.8 m, width of 2.0 m and depth of 275 mm as shown in Fig. 11.1. The first and second bending modes are 4.5 and 17.0 Hz. It weighs approximately 15 t. The two locations selected for the SISO and MIMO AVC studies presented in this work are shown as A1, S1 and A2, S2, in which the former represent the actuator and sensor at location 1, whereas the latter represent the actuator and sensor at location 2. An experimental modal analysis exercise was carried out to determine the structural dynamic properties at these locations. Artificial excitation was provided by two electrodynamic shakers (APS Dynamics Model 113) that were driven by continuous uncorrelated random excitation signals with a frequency span 0–100 Hz. Responses were measured by accelerometers placed at these two locations. The point accelerance frequency response functions (FRFs) are shown in Fig. 11.2.

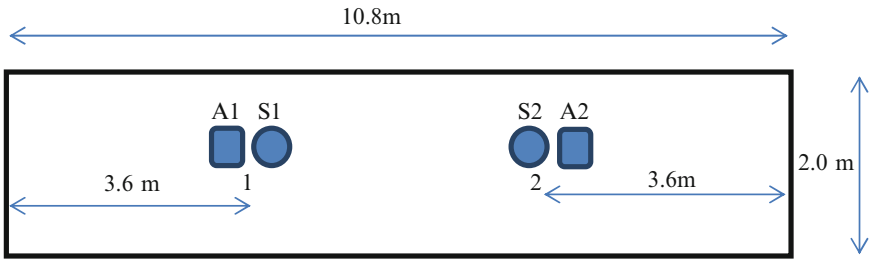

Fig. 11.1 Laboratory structure plan view and location of actuators (A1, A2) and sensors (S1, S2)

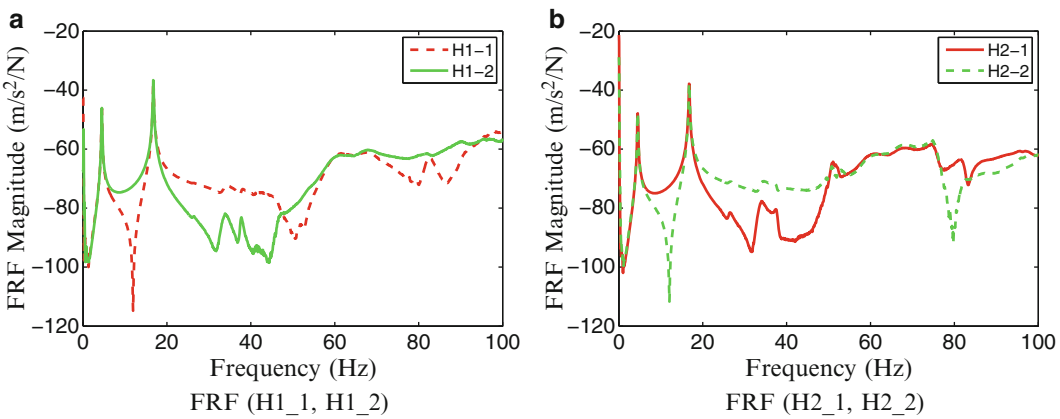

Fig. 11.2 Point accelerance FRFs with excitation force and sensor measurements at locations 1 and 2. (**a**) H1_1 – actuator 1, sensor 1, H1_2 – actuator 1, sensor 2. (**b**) H2_1 – actuator 2, sensor 1, H2_2 – actuator 2, sensor 2

Two APS dynamics model 400 shakers (actuators), each with an inertial mass of 30.4 kg and peak stroke of 6.25 in. were used in the AVC studies presented in this paper. They were operated in the current drive mode, in which the actuator dynamics can closely be described by a linear second order model in (11.1). This shows the relationship between the force applied to the structure, $f(t)$, and the input voltage to the actuator amplifier $v(t)$. A system identification procedure was used to estimate their dynamic properties. These comprise of a resonant frequency of 1.33 Hz and damping ratio of 0.07.

$$G_{act}(s) = \frac{F(s)}{V(s)} = \frac{340s^2}{s^2 + 1.17s + 69.83} \tag{11.1}$$

11.3 Control Schemes

The controller schemes investigated in this research work comprise of

(a) Direct output feedback: Direct velocity feedback (DVF) plus inner loop actuator compensator [11, 12]
(b) Model-based controllers: Pole-placement approach and Independent Modal Space Control (IMSC) approach

The key components of the control scheme for the DVF with the inner loop actuator compensator are illustrated in Fig. 11.3. $G_s(s)$ is the structural model shown in (11.2) based on the point accelerance FRF at location 2 in Fig. 11.1, $G_{bp}(s)$ a bandpass filter, and $G_{act}(s)$ the actuator model in (11.1). The outer loop, $C_o(s)$ in (11.3) is a velocity feedback scheme that is designed to impart significant damping to the structural modes of vibration. The inner loop compensator $C_I(s)$ in (11.4) is designed to achieve a closed-loop transfer function of the actuator inner loop with a frequency 1.50 Hz and damping ratio of 0.60 thereby enhancing the stability margins of the closed-loop system. $\gamma_{dc} = 300$ is the velocity feedback gain used in the studies presented that ensures a gain margin (GM) of 11.5 dB, phase margin (PM) greater than 30° and realises a target damping in the dominant mode of vibration of the test structure of 0.25. DVF is implemented in a SISO scheme with the collocated actuator and sensor pair at location 2 in Fig. 11.1.
Where:

$v_e(t)$	Initial control voltage signal	$\ddot{y}(t)$	Structural acceleration response
$x_a(t)$	Displacement of actuator moving mass	$\dot{y}(t)$	Structural velocity response
$f(t)$	Actuator force	$r(t)$	Reference signal
$e(t)$	Error signal	$v(t)$	Final control voltage signal
$g(v_e)$	Saturation nonlinearity	$d_i(t)$	Input disturbance
$r(t)$	Reference signal		

$$G_s(s) = \sum_{i=1}^{4} \frac{\alpha_i s^2}{s^2 + 2\zeta_i \omega_i s + \omega_i^2} \tag{11.2}$$

$$C_o(s) = \frac{\gamma_{dc}}{s + \beta} \tag{11.3}$$

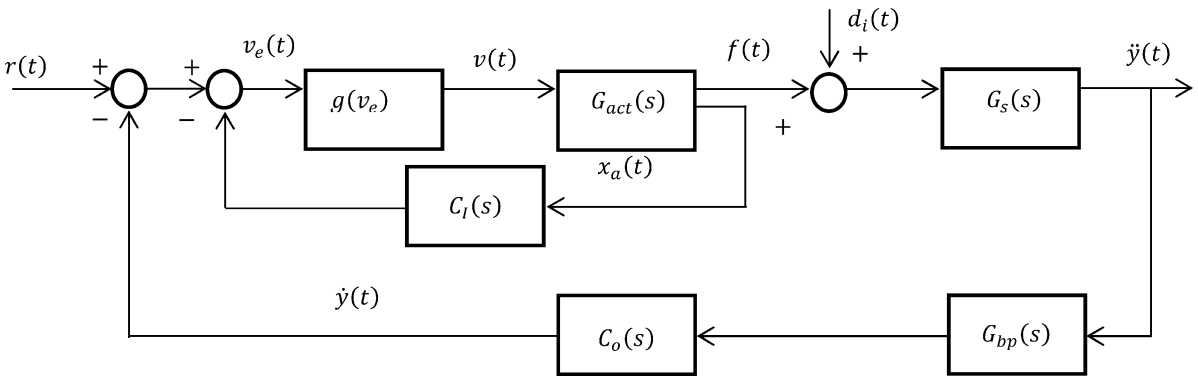

Fig. 11.3 Control scheme for DVF with inner loop actuator compensator

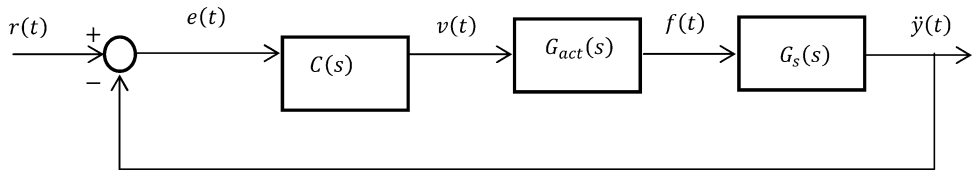

Fig. 11.4 Control scheme for pole-placement controller

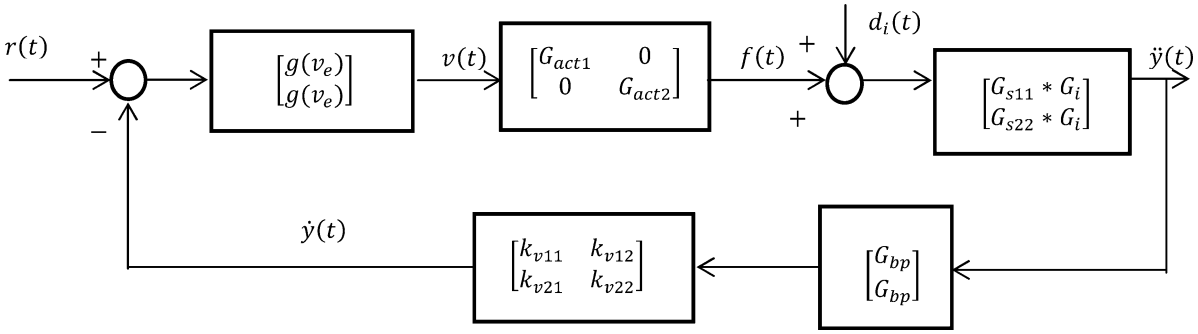

Fig. 11.5 Control scheme for IMSC controller

$$C_I(s) = \frac{s^2 + 1.14s + 66.72}{s^2 + 11.31s + 88.83} \tag{11.4}$$

Where:

α_i Inverse of modal mass for mode i ω_i Natural frequency of mode i
ζ_i Damping ratio of mode i

The components of the control scheme for the pole-placement design take the form of Fig. 11.4. $C(s)$, a proper compensator, is designed to achieve desired closed-loop characteristics of the poles of the structural model and the actuator. With $C \times (s)$, $G_{act}(s)$, $G_s(s)$ taking the forms of (11.5), the overall transfer function from r to y takes the form of (11.6). Thus, given a desired set of poles e.g. of test structure and/or actuator, a polynomial $F(s)$ that has the desired poles as its roots can be formed. The coefficients of $C(s)$ thus become the solution to (11.7) [20]. The pole-placement controller is also implemented in a SISO scheme with the collocated actuator and sensor pair at location 2 in Fig. 11.1. The results of two pole-placement controllers are presented: controller 1 in (11.8a) aims to achieve a damping ratio of 0.25 and 0.007 in modes 1 and 2 (i.e. virtually leaving mode 2 unchanged), while controller 2 in (11.8b) aims to achieve damping ratios of 0.25 and 0.10 in modes 1 and 2.

$$C(s) = \frac{B(s)}{A(s)}, \quad G_{act}(s) = \frac{N_{act}(s)}{D_{act}(s)}, \quad G_s(s) = \frac{N_s(s)}{D_s(s)} \tag{11.5}$$

$$G_T(s) = \frac{B(s)N_{act}(s)N_s(s)}{A(s)D_{act}(s)D_s(s) + B(s)N_{act}(s)N_s(s)} \tag{11.6}$$

$$A(s)D_{act}(s)D_s(s) + B(s)N_{act}(s)N_s(s) = F(s) \tag{11.7}$$

$$C_1(s) = \frac{1.09s^5 - 25.11s^4 + 1.26e004s^3 - 3.08e005s^2 + 2.57e006s + 1.85e007}{0.93s^5 + 40.67s^4 + 138.60s^3 + 280.50s^2 + 437.30s + 268.90} \tag{11.8a}$$

$$C_2(s) = \frac{-0.50s^5 + 418.80s^4 + 1.23e004s^3 + 1.13e005s^2 + 2.97e006s + 7.53e006}{1.03s^5 + 24.80s^4 + 139.00s^3 + 281.10s^2 + 437.60s + 268.90} \tag{11.8b}$$

The IMSC scheme is realised by modal filtering [21] with two sensor arrays at locations 1 and 2 in Fig. 11.1. Both actuators at locations 1 and 2 are used in the AVC studies. Figure 11.5 shows the IMSC controller scheme. A single actuator

at either of the locations can be used provided it is implemented with the two sensor arrays. The derived weighting coefficients of the modal filter that isolates mode 2 is shown in (11.9a). Equation (11.9b) shows the feedback gains derived to achieve a target damping ratio of 0.3 in mode 1 whilst leaving mode 2 unchanged. G_i is an integrator. The inner loop compensator $C_I(s)$ outlined in (11.4) is also incorporated in the IMSC scheme.

$$\alpha_k = \begin{bmatrix} \alpha_{11} & \alpha_{12} \\ \alpha_{21} & \alpha_{22} \end{bmatrix} = \begin{bmatrix} 1 & 1 \\ 1 & 1 \end{bmatrix} \tag{11.9a}$$

$$K_v = \begin{bmatrix} k_{v11} & k_{v12} \\ k_{v21} & k_{v22} \end{bmatrix} = \begin{bmatrix} 120 & 120 \\ 120 & 120 \end{bmatrix} \tag{11.9b}$$

11.4 Experimental Studies

Two sets of experimental studies were carried out to evaluate the vibration mitigation performances of the controller schemes described in the previous section.

(a) Uncontrolled and controlled point accelerance FRF tests to a random excitation force with frequency span $0 - 100$ Hz.
(b) Uncontrolled and controlled responses to walking excitation at a pacing frequency of 2.25 Hz

Figure 11.6 shows the uncontrolled and controlled point accelerance FRFs to the random excitation input force described within a frequency span of 0–30 Hz for clarity. The attenuations in the target modes of vibration for each of the controller schemes are presented in Table 11.1.

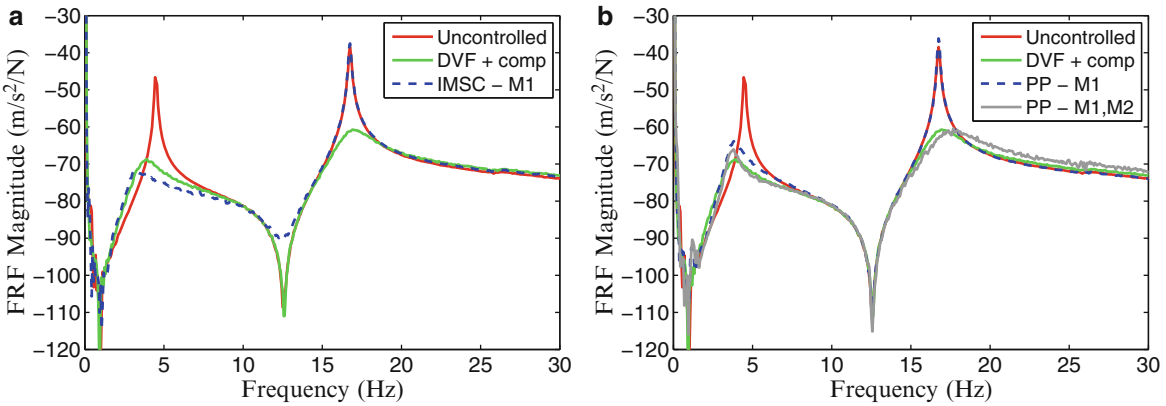

Fig. 11.6 Point accelerance FRFs from experimental implementation of the direct output feedback (DVF + comp) and model-based (pole-placement, IMSC) controller structures

Table 11.1 Attenuations in target modes of vibration for direct output feedback and model-based controllers

AVC design	Mode 1 – E (dB)	Mode 2 – E (dB)
DVF		
Compensator (1.50 Hz, 0.60)	−22.5	−23.6
Pole-placement		
PP controller 1	−17.5	+0.5
PP controller 2	−20.5	−23.5
IMSC		
IMSC controller	−26.0	0.0

E experimental, *PP* pole placement

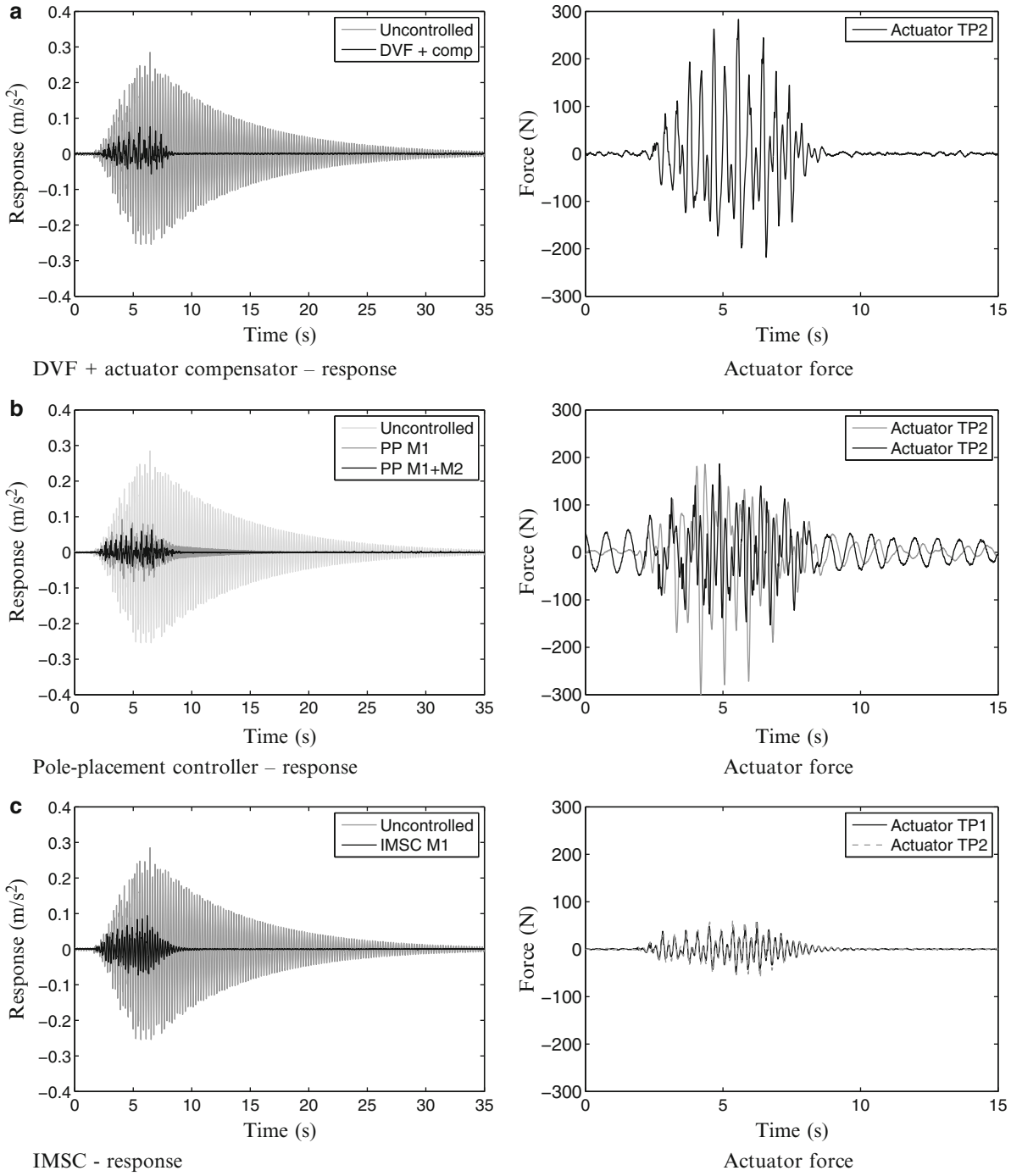

Fig. 11.7 Uncontrolled and controlled responses to walking excitation at a pacing frequency of 2.25 Hz for direct output feedback and model-based controllers. (**a**) DVF + actuator compensator – response, (**b**) Pole-placement controller – response, (**c**) IMSC – response

These experimental studies highlight the flexibility offered by pole-placement and IMSC control approaches to isolate and control only target modes of vibration. By focusing energy on only problematic resonances, there is potential for improvement in the vibration mitigation as can be seen from Table 11.1, for example, in which the IMSC strategy is tuned to tackle only the first mode of vibration of the test structure that is prone to excitation by human pacing frequencies.

Figure 11.7 shows the uncontrolled and controlled responses to walking excitation tests for a pacing frequency of 2.25 Hz as well as the actuator effort for each of the controllers. The peak 1sRMS acceleration responses (MTVV) for uncontrolled and controlled walking studies are shown in Table 11.2.

Table 11.2 MTTV for uncontrolled and controlled responses to walking excitation for direct output feedback and model-based controllers

AVC design	W2.25 Hz – E (m/s^2)	Reduction (%)
Uncontrolled	0.2463	
DVF		
Compensator (1.50 Hz, 0.60)	0.0422	82.8
Pole-placement		
PP controller 1	0.0380	84.6
PP controller 2	0.0146	94.0
IMSC		
IMSC controller	0.0486	80.3

W2.25 Hz walking at 2.25 Hz, *E* experimental

The experimental results from the uncontrolled and controlled responses to walking excitation in Fig. 11.7 and Table 11.2 demonstrate potential advantages of using model-based controller schemes, for example, pole-placement and IMSC for mitigation of human induced vibrations. They isolate and tackle only specific problematic frequencies or combinations thereof as opposed to direct output feedback techniques which have a global effect on controlling multiple modes and could have potential to destabilise some higher modes. In these studies, the DVF and pole placement controllers are implemented in a SISO scheme while the IMSC is implemented in a MIMO scheme.

11.5 Conclusions

Model-based control approaches are relatively new approaches towards active vibration control of human-induced vibrations in problem floors. These studies demonstrate the considerable promise of these technologies for this application. They offer flexibility for isolating and controlling only specific problematic frequencies with substantial savings in computational efforts. Floors are often characterised by a troublesome mode or groups of modes and model-based control approaches offer a potential practical solution to isolating and controlling them without influencing or even destabilising other modes. The ready availability of multiple sensors and actuators ensures that the control spillover problem experienced earlier, for example, with IMSC is manageable.

Acknowledgement The authors would like to acknowledge the financial assistance provided by the UK Engineering and Physical Sciences Research Council (EPSRC) through a responsive grant mode grant entitled "Active Control of Human-Induced Vibration" (Ref. EP/H009825/1). The assistance of PhD student Mr. Robert Westgate with the walking tests is highly appreciated.

References

1. Bachmann H (1992) Case studies of structures with man-induced vibrations. J Struct Eng 118(3):631
2. Setareh M, Hanson RD (1992) Tuned mass dampers to control floor vibration from humans. J Struct Eng 118(3):741–762
3. Murray TM (1998) Floor vibration and the electronic office. Mod Steel Constr 38:24–28
4. Webster AC, Levy MP (1992) A case of the shakes. Civil Eng J, Feb 2002, US 0885-7024/92-0002-058
5. Nyawako D, Reynolds P (2007) Technologies for mitigation of human-induced vibrations in civil engineering structures. Shock Vib Dig 39 (6):465–493
6. Hanagan LM, Murray TM (1997) Active control approach for reducing floor vibrations. J Struct Eng 123(11):1497–1505
7. Hanagan LM, Murray TM, Premaratne K (2003) Controlling floor vibration with active and passive devices. Shock Vib Dig 35(5):347–365
8. Diaz IM, Reynolds P (2010) Acceleration feedback control of human-induced floor vibrations. Eng Struct 32:163–173
9. Diaz IM, Pereira E, Reynolds P (2010) Integral resonant control scheme for cancelling human-induced vibrations in light-weight pedestrian structures. Struct Control Health Monit. doi:10.1002/stc.423
10. Nyawako D, Reynolds P (2009) Response-dependent velocity feedback control for mitigation of human-induced floor vibrations. Smart Mater Struct 18:1–14
11. Diaz IM, Pereira E, Reynolds P, Casado CM (2011) Human-induced vibration cancellation using an active mass damper modified by an inner loop. In: Proceedings of the 8th international conference on structural dynamics, EURODYN 2011, Leuven, 4–6 July
12. Nyawako D, Diaz IM, Reynolds P, Hudson M (2011) Enhancing velocity feedback with inner loop compensators for the actuators. In: SMART conference 2011, Germany, pp 629–639
13. Agrawal AK, Yang JN (1999) Design of passive energy dissipation systems based on LQR methods. J Intell Mater Syst Struct 10:933–944
14. Loh CH, Lin PY, Chung NH (2000) Design of dampers for structures based on optimal control theory. Earthquake Eng Struc 29:1307–1323

15. Smith HA, Chase JG (1996) Comparison of LQR and H-infinity algorithms for vibration control of structures in seismic zones. In: Proceedings of the ASCE structures congress XIV, Chicago, Apr 1996
16. Wu JC, Yang JN, Schmitendorf WE (1998) Reduced-order H-infinity and LQR control for wind excited tall buildings. Eng Struct 20(3):222–236
17. Daley S, Johnson FA, Pearson JB, Dixon R (2004) Active vibration control for marine applications. Control Eng Pract 12:465–474
18. Soong TT (1990) Active structural control: theory and practice, Longman Scientific & Technical, Harlow, ISBN 0-470-21670-0
19. Inman DJ (2001) Active modal control for smart structures. Phil Trans Roy Soc London 359:205–219
20. Chen CT (1999) Linear system theory and design. Oxford University Press, New York, ISBN 0-19-511777-8
21. Preumont A, Francois P, De Man P, Pierfort V (2003) Spatial filters in structural control. J Sound Vib 265:61–79

Chapter 12
Frequency Domain Optimization of Dry Friction Dampers on Buildings Under Harmonic Excitation

Z. Eren Erisen and Ender Cigeroglu

Abstract Friction mechanism has an extensive usage in many different fields for energy dissipation. It is also used at buildings to reduce the displacement that is caused by ground acceleration during an earthquake. Despite friction damper is a simple device to use on structures, due to its nonlinear characteristic, analysis and design of a structure equipped with a friction damper is difficult. In this paper, Harmonic Balance Method (HBM) is employed to represent the frictional contact as a nonlinear complex stiffness in order to find the steady state displacement of each story of a multi-story building under harmonic ground acceleration. Application of HBM results in a set of nonlinear algebraic equations in frequency domain which can be solved by an iterative method. As a result of this, the solution method presented reduces the computational effort compared to time integration methods; therefore, optimization of friction dampers can be performed in a reasonable time. Accuracy and validation of the presented method is demonstrated on a single-story shear building model equipped with a single friction damper by comparing the frequency domain solution with time marching results. A multi-story building is considered as a case study where the slip force of each dry friction damper is optimized in order to minimize the relative displacement between the stories.

Keywords Dry friction damper • Optimization of slip force • Earthquake vibration damping • Damper optimization • Harmonic balance method

12.1 Introduction

As a result of structural vibrations that occur during an earthquake, structural damage or even failure may occur at buildings. In order to minimize the effects of earthquakes on buildings, passive or active control systems can be utilized. The ways to accomplish a seismic response control are [1]:

- Decreasing the energy transmission of the earthquake ground motion to the structure.
- Isolating the natural frequency of the building from the dominant frequency of the earthquake.
- Achieving the non-stationary and non-resonant state by providing nonlinear characteristics.
- Applying control forces to the building.
- Utilizing energy absorption mechanisms.

Friction can be defined as the resistance to motion during sliding or rolling when one body is in tangentially contact with another body [2]. Since there is no requirement of an external power supply or a sensor, usage of dry friction dampers on buildings is a passive vibration control method and an energy absorption mechanism. Analysis of buildings equipped with dry friction dampers is complicated and requires high computational effort due to the nonlinear characteristic of dry friction. Frequency domain and time domain solution methods are utilized for structures with dry friction dampers; however, for the solution of buildings equipped with dry friction dampers, time domain methods based on time integration have been frequently used in the literature which require more computation effort and significant computation times compared to

Z.E. Erisen • E. Cigeroglu (✉)
Mechanical Engineering Department, Middle East Technical University, 06800 Ankara, Turkey
e-mail: ender@metu.edu.tr

J.M. Caicedo et al. (eds.), *Topics on the Dynamics of Civil Structures, Volume 1*,
Conference Proceedings of the Society for Experimental Mechanics Series 26,
DOI 10.1007/978-1-4614-2413-0_12,

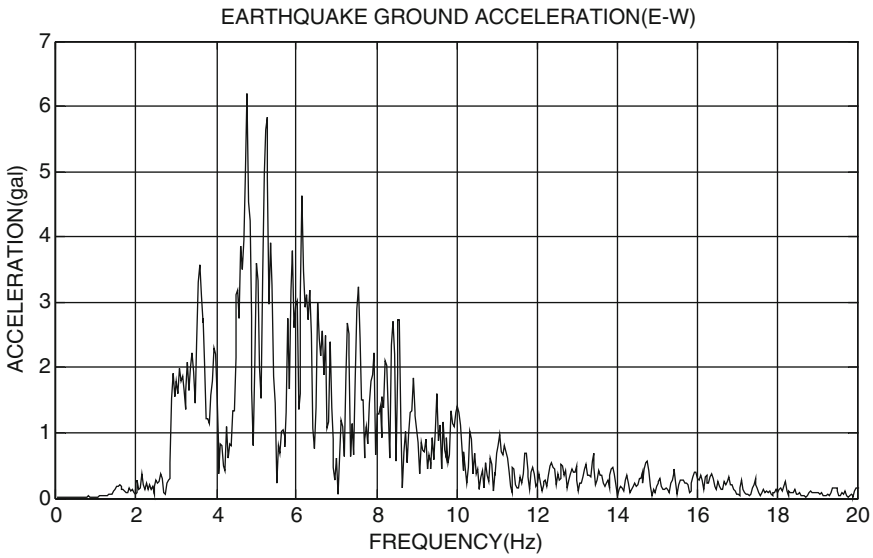

Fig. 12.1 Frequency response function of 1992 ERZINCAN earthquake

frequency domain methods. Moreover, by utilizing time domain analysis, it is hard to guess the most unfavorable ground motion for a building that may occur at the specified site and this brings another difficulty for the analysis [3].

There are many factors which effect the building performance and they depend on both earthquake characteristics such as amplitude and frequency of the ground motion and also building properties such as mass, stiffness, damping and ductility of the building. Since passive control systems are not adaptive to changes in the excitation, an optimum damping ratio and damping distribution along the building is very important.

As can be seen from Fig. 12.1, ground motion at a site is superposition of different frequencies with different amplitudes. If one of the dominant frequencies of an earthquake is far from the natural frequency of the building, then the vibration amplitude of the building will be low; however, it is not always possible to isolate the natural frequency of the building from these dominant frequencies due to constructive challenges and due to the fact that most of the earthquakes are dominant in the frequency range of 0–15 Hz.

12.2 Modelling of the System

In this paper, orientation of the dampers will not be investigated and at each floor, response will be studied only in one direction for optimization purposes; hence, using shear building model will be sufficient. Placement of the dampers also play an important role in modeling of the building. In this study, shear building model given in Fig. 12.2 is used where the dampers are placed between the successive floors; however, different damper configurations are as well possible.

12.2.1 Shear Building Model

Schematic representation of a n-story building model used for the simulations is given in Fig. 12.2. Equation of motion of the system can be given as follows:

$$\begin{aligned} &[M]\{\ddot{x}\} + [C]\{\dot{x}\} + [K]\{x\} + \{f_{NL}\} = \{f_{exc}\} \\ &\{f_{exc}\} = -[M]\ddot{x}_g \end{aligned} \tag{12.1}$$

In this equation, $[M]$, $[C]$ and $[K]$ represent mass, damping and stiffness matrices of the building and $\{x\}$, $\{\dot{x}\}$, $\{\ddot{x}\}$ are displacement, velocity and acceleration vectors of the stories, respectively, $\{f_{NL}\}$is the nonlinear forcing vector consisting of the nonlinear forces due to friction dampers, $\{f_{exc}\}$is the excitation vector, and $\ddot{x}_g$is ground acceleration due to earthquake. The details of these matrices and vectors are given as:

$$[M] = diag(m_1, m_2, m_3 \cdots m_{n-1}, m_n) \tag{12.2}$$

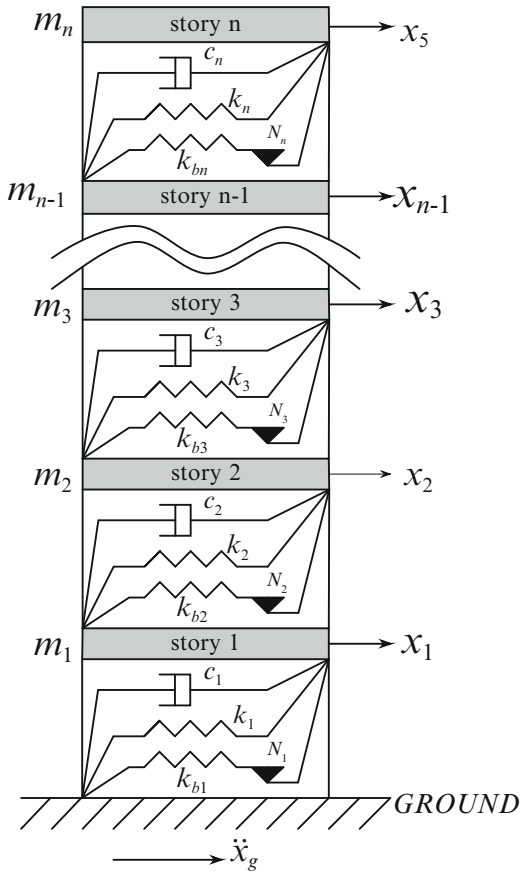

Fig. 12.2 MDOF shear building model

$$[C] = \begin{bmatrix} c_1 + c_2 & -c_2 & 0 & \dots & \dots & \dots & 0 \\ -c_2 & c_2 + c_3 & -c_3 & \dots & \dots & \dots & \vdots \\ 0 & -c_3 & c_3 + c_4 & \dots & \dots & \dots & \vdots \\ \vdots & \dots & -c_4 & \ddots & \dots & \dots & 0 \\ \vdots & \dots & \dots & 0 & -c_{n-1} & c_{n-1} + c_n & -c_n \\ 0 & \dots & \dots & \dots & 0 & -c_n & c_n \end{bmatrix} \tag{12.3}$$

$$[K] = \begin{bmatrix} k_1 + k_2 & -k_2 & 0 & \dots & \dots & \dots & 0 \\ -k_2 & k_2 + k_3 & -k_3 & \dots & \dots & \dots & \vdots \\ 0 & -k_3 & k_3 + k_4 & \dots & \dots & \dots & \vdots \\ \vdots & \dots & -k_4 & \ddots & \dots & \dots & 0 \\ \vdots & \dots & \dots & 0 & -k_{n-1} & k_{n-1} + k_n & -k_n \\ 0 & \dots & \dots & \dots & 0 & -k_n & k_n \end{bmatrix} \tag{12.4}$$

$$\{x\} = [x_1, x_2, x_3 \cdots x_{n-1}, x_n]^T. \tag{12.5}$$

Details of $\{f_{NL}\}$ vector is given in Sect. 12.3.1.

12.2.2 Modeling of Dry Friction

In this paper, macro-slip friction model which is composed of a spring and a frictional contact with a slip load μN as shown in Fig. 12.3, is used. In this model, k_f, μ, N and x represent the stiffness of the friction damper, coefficient of friction, normal

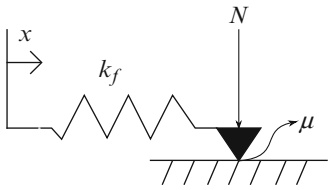

Fig. 12.3 Macro-slip friction model

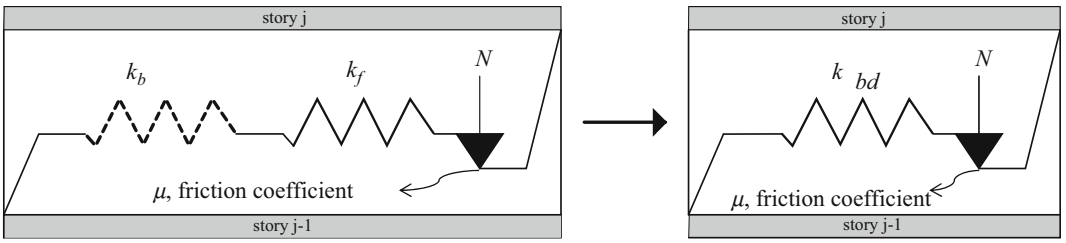

Fig. 12.4 Modeling of dry friction damper connection to the building

load acting across the contact surface and relative motion across the damper, respectively. When the force on the spring is less than the slip load (force), μN, the damper is in stick state and the friction force is defined as:

$$F_f = k_f x. \tag{12.6}$$

Damper remains in stick state until the friction force reaches to the slip force where further increase of the relative motion results in slip state. During the slip state, friction force equals to the slip force which can be expressed as:

$$F_f = \mu N. \tag{12.7}$$

The damper continues to slip until the relative velocity becomes zero (i.e. $\dot{x} = 0$) and at this point damper sticks again.

In the literature, friction is idealized by rigid perfectly plastic models and modeled as a fictitious spring having infinite stiffness.

$$k_f \longrightarrow \infty. \tag{12.8}$$

While modeling the dry friction damper, flexibility of the elements that are used to support and connect the damper to the main structure should also be introduced as shown in Fig. 12.4, where k_b represents the stiffness of the bracing. Stiffness of the damper assemblage, k_{bd}, can be given as follows:

$$\frac{1}{k_{bd}} = \frac{1}{\frac{1}{k_b} + \frac{1}{k_f}}. \tag{12.9}$$

From (12.8), (12.9) reduces to

$$k_{bd} = k_b. \tag{12.10}$$

Therefore, dry friction damper is modeled with a spring of stiffness k_b, for which the hysteresis diagram for a simple harmonic motion is given in Fig. 12.5 and the corresponding equation for the friction force is given in (12.13).

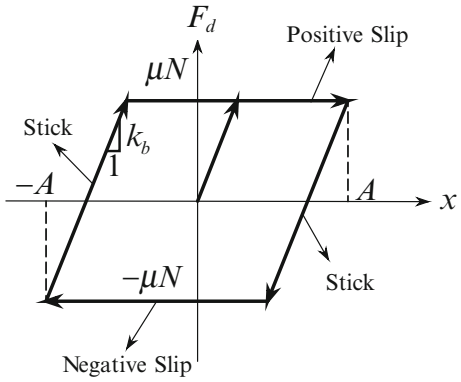

Fig. 12.5 Hysteresis diagram of dry friction damper

12.3 Solution Method

For frequency domain solution, $\{f_{exc}\}$ is assumed to be sinusoidal in the form of:

$$\{f_{exc}\} = \mathrm{Im}\left(\{F\}e^{i\varphi}\right), \tag{12.11}$$

where $\varphi = \omega t$, $\{F\}$ and $\{\omega\}$ are the complex vector of amplitudes of external forces and excitation frequency, respectively. Assuming that the structure vibrates harmonically the response can be expressed as follows:

$$\{x\} = \mathrm{Im}\left(\{X\}e^{i\varphi}\right), \tag{12.12}$$

where $\{X\}$ is the complex vector of displacement amplitudes.

$$F_d = \begin{cases} \mu N & \text{Positive slip} \\ \mu N + k_b(x - A) & \text{Stick} \\ -\mu N & \text{Negative slip} \\ -\mu N + k_b(x + A) & \text{Stick} \end{cases} \tag{12.13}$$

12.3.1 Harmonic Balance Method

Sanliturk et al. [4], used harmonic balance method (HBM) for vibration analysis of turbine blades with friction dampers. In this part, short information about HBM will be given.

HBM is based on finding linearized coefficients which, in general, depend on both the frequency and the amplitude of the oscillations. For the given harmonic displacement in (12.12), linearized stiffness coefficient for the friction damper is expressed as:

$$k^*_{eq}(A) = k^r_{eq}(A) + ik^i_{eq}(A), \tag{12.14}$$

where (A) is the displacement amplitude of the relative motion across the damper as shown in Fig. 12.5, k^r_{eq}, k^i_{eq} are the real and imaginary parts of amplitude-dependent equivalent stiffness, respectively.

In this paper, only the fundamental harmonic term is considered as suggested by Chen and Menq [5] and Cigeroglu et al. [6]. Then, equivalent stiffness coefficients can be calculated as follows:

$$\begin{aligned} k^r_{eq}(A) &= \frac{1}{\pi A}\int_0^{2\pi} F_d(A\sin\varphi)\cos\varphi d\varphi, \\ k^i_{eq}(A) &= \frac{1}{\pi A}\int_0^{2\pi} F_d(A\sin\varphi)\sin\varphi d\varphi. \end{aligned} \tag{12.15}$$

Up to now, general information about defining a nonlinear force as a complex stiffness is given. For the macro-slip friction model having the hysteresis curve shown in Fig. 12.5, the nonlinear stiffnesses expressed in (12.15) are given as follows:

$$
\begin{aligned}
k^r{}_{eq}(A) &= \left\{ \begin{array}{ll} \dfrac{1}{\pi}\left(\dfrac{2\mu N}{A} - k_b\right)\sqrt{1-\left(\dfrac{k_bA-2\mu N}{k_bA}\right)^2} + k_b\dfrac{\gamma}{\pi} - \dfrac{k_b}{2} & \text{if} \quad k_bA > \mu N \\ k_b \quad \text{if} \quad k_bA \le \mu N & \end{array} \right\} \\
k^i{}_{eq}(A) &= \left\{ \begin{array}{ll} -\dfrac{4\mu N(\mu N - Ak_b)}{\pi k_b A^2} & \text{if} \quad k_bA > \mu N \\ 0 \quad \text{if} \quad k_bA \le \mu N & \end{array} \right\} \\
\gamma &= \pi - \sin^{-1}\left(\frac{\mu N}{Ak_b} - 1\right).
\end{aligned}
\tag{12.16}
$$

From (12.16), the nonlinear friction forces on each damper can be obtained as follows:

$$
F_{d_j} = k_{eq}{}^*\left(Y_j\right) \cdot Y_j, \tag{12.17}
$$

where,

$$
\begin{aligned}
Y_j &= X_j \qquad \text{for} \quad j = 1 \\
Y_j &= X_j - X_{j-1} \quad \text{for} \quad j \ge 2.
\end{aligned}
\tag{12.18}
$$

Using (12.17), nonlinear forcing vector, $\{f_{NL}\}$, can be defined as follows:

$$
\{f_{NL}\} = \mathrm{Im}\left(\{F_{NL}(\{X\})\}e^{i\varphi}\right). \tag{12.19}
$$

where $\{F_{NL}(\{X\})\}$ is expressed as

$$
\{F_{NL}(\{X\})\} = [F_{d_1} - F_{d_2}, F_{d_2} - F_{d_3}, F_{d_3} - F_{d_4}, \cdots, F_{d_{n-1}} - F_{d_n}, F_{d_n}]^T. \tag{12.20}
$$

Then, (12.1) can be re-written for harmonic motion as follows:

$$
\left[[K] - \omega^2[M] + i\omega[C]\right] * \{X\} + \{F_{NL}(\{X\})\} = \{F\}. \tag{12.21}
$$

12.3.2 Solution of Resulting Nonlinear Equations

Since the nonlinear force given in (12.21) is displacement dependent, an iterative method is required for the solution. Equation 12.21 can be expressed as a residual vector as follows:

$$
\{R(\{X\},\omega)\} = \left[[K] - \omega^2[M] + i\omega[C]\right] * \{X\} + \{F_{NL}(\{X\})\} - \{F\} = \{0\}. \tag{12.22}
$$

Solution of (12.22) can be obtained for values of $\{X\}$ that result in $\{R(\{X\},\omega)\} = 0$. Using Newton's method the following iterative formula can be written for the solution of (12.22):

$$
\{X\}_{k+1} = \{X\}_k - \left[\frac{\partial\{R(\{X\},\omega)\}}{\partial\{X\}}\right]^{-1}\Bigg|_{\{X\}_k,\omega} \{R(\{X\}_k,\omega)\}, \tag{12.23}
$$

where k is the iteration number and$[\partial\{R(\{X\},\omega)\}/\partial\{X\}]$ is the Jacobian matrix and should be calculated either analytically or numerically. This iteration for $\{X\}$continues until a pre-defined error tolerance, either on the relative difference between$\{X\}_{k+1}$ and $\{X\}_k$ or on $\{R(\{X\},\omega)\}$ or on both, is satisfied.

12.4 Results

12.4.1 Validation of the Method

The validation of the solution method suggested is demonstrated by comparing the results obtained from frequency domain and time domain solutions. For this reason, a single story building equipped with a dry friction damper connected between ground and the floor is investigated under a harmonic ground acceleration. In order to have a scale for the parameter values used in the study, the stiffness and the slip load of the damper is normalized as follows:

$$SR = \frac{k_{b1}}{k_1}, \quad PS = \frac{F_s}{m_1 g}100, \tag{12.24}$$

where SR and PS demonstrates stiffness ratio and percentage slip load, respectively and g is gravitational acceleration. The response of the 1-dof system is studied by keeping the amplitude of ground acceleration, $\ddot{x}_g$, and SR constant at 0.2 m/s^2 and 0.2 respectively and PS is changed between 0.7 and 6. The investigated 1-dof system is modeled such that; its mass, stiffness and viscous damping coefficient are equal to 5,000 kg, 805,000 N/m and 1280 N/m, respectively. In this analysis, $PS = 0$ is the case corresponding to no damper.

Figure 12.6 shows the comparison of displacement values of the building calculated by using the frequency domain solution and time domain simulation. When the results are compared, it is seen that the values are in excellent agreement although single harmonics is used at harmonic balance method.

12.4.2 Effect of Damper Parameters on Displacement

In this section, the effect of brace stiffness and slip load on building displacement response will be demonstrated with a simple analysis. For this reason, the same system studied in Sect. 12.4.1 is investigated under a constant harmonic ground acceleration which has a magnitude of 0.2 m/s^2.

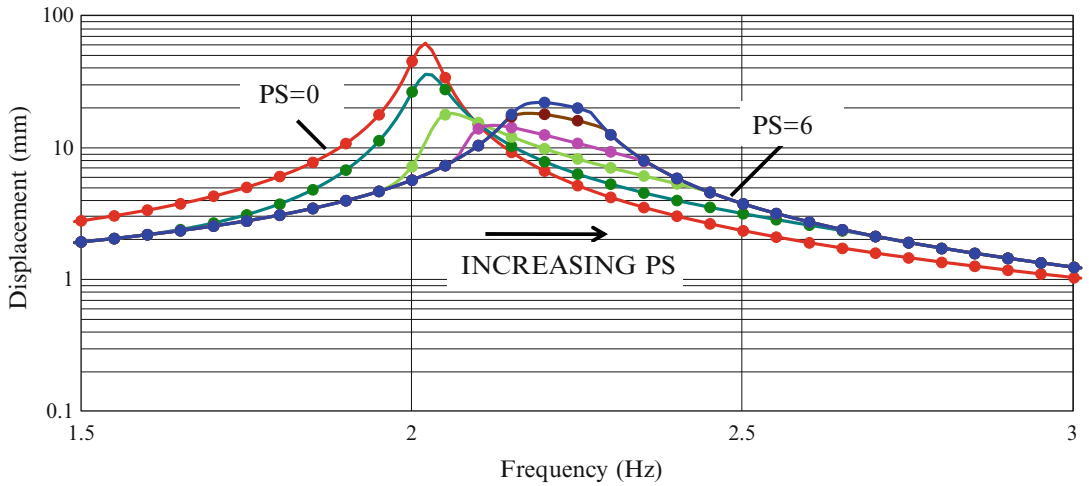

Fig. 12.6 Displacement versus frequency curve for time and frequency domain solutions comparison and PS values as 0, 0.7, 1.5, 2.5, 4.5 and 6. *Full lines* are frequency domain solutions and *discrete points* are time domain simulations

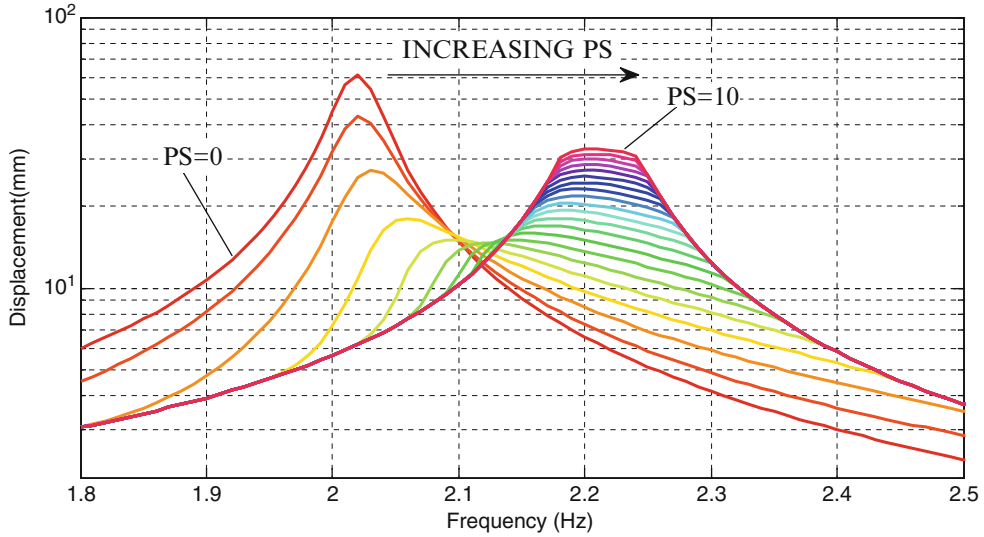

Fig. 12.7 Frequency-displacement curve for SR = 0.2 and PS values as 0, 0.5, 1, 1.5,. . .,10

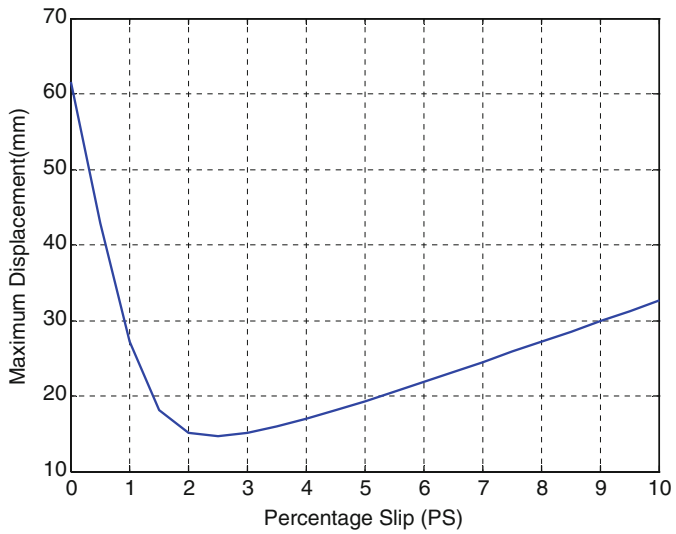

Fig. 12.8 Maximum displacement versus PS curve for SR = 0.2

The response of the 1-dof system is studied by varying *PS* and *SR* from 0 to 10. It should be noted that, in real life, it is difficult to achieve values of *SR* much greater than 1 as Tabeshpour and Ebrahimian [7] mentioned; however, there exists several studies in the literature where values of *SR* are much larger than 1 are considered for bracing systems [8–10].

Figures 12.7, 12.8 and 12.9 show the effect of *PS* on the displacement amplitude and resonance frequency of the building when *SR* is kept constant at 0.2. As already mentioned before, $PS = 0$ is the case corresponding to no damper. As can be seen from Fig. 12.8, there is an optimum point of *PS* which results in minimum displacement amplitude. It should also be noted that, for high values of *PS*, damper cannot slip and the system behaves like a linear one with an equivalent stiffness of $k_1 + k_{b_1}$ and the resonance frequency of the building becomes identical to the stuck case resonance frequency.

Figures 12.10, 12.11 and 12.12 show the effect of *SR* on the displacement amplitude and the resonance frequency of the building when *PS* is kept constant at 2. In this analysis, $SR = 0$ is the case corresponding to no damper. From these graphs, it is observed that, the maximum displacement amplitude decreases and the resonance frequency increases with increasing SR.

Effect of *SR* and *PS* on the maximum displacement is as well demonstrated on a 3D graph given in Fig. 12.13. From this figure, it can be seen that optimum *PS* is a function of *SR*.

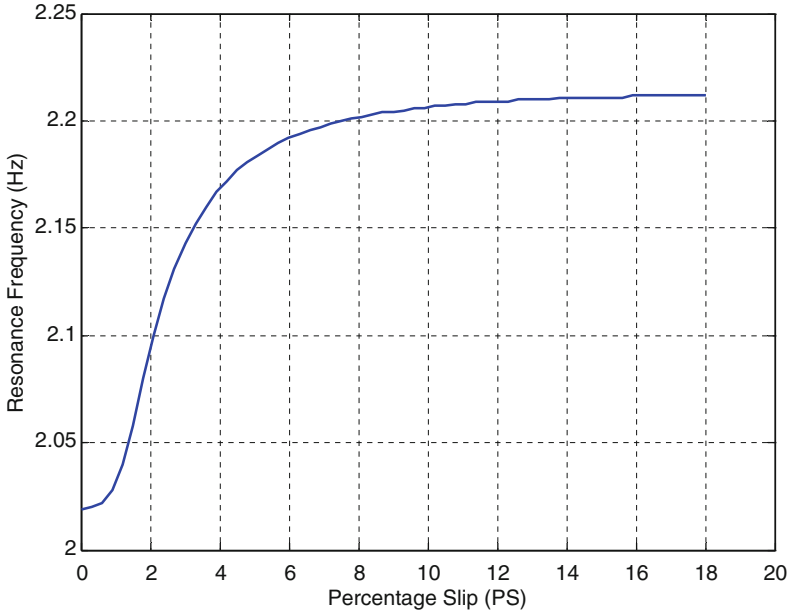

Fig. 12.9 Resonance frequency versus PS curve for SR = 0.2

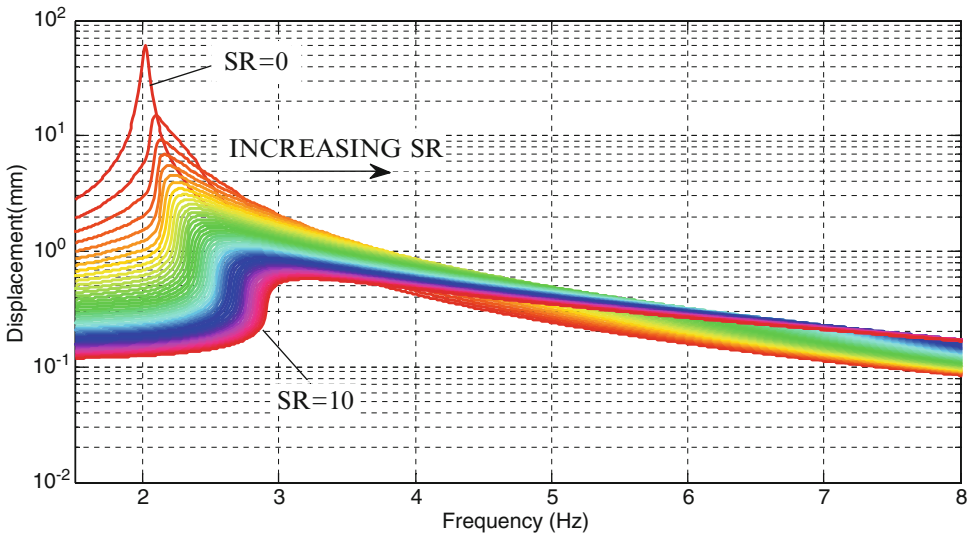

Fig. 12.10 Frequency-displacement curve for PS = 0.2 and SR values as 0, 0.5, 1, 1.5,. . .,10

12.4.3 Optimization Studies

In this section a six-story building with the following properties is studied:

$m_j = 50000$ kg for $j = 1, 2, 3 \cdots 6$
$k_1 = 74000$ kN/m, $k_2 = 66000$ kN/m, $k_3 = 56000$ kN/m, $k_4 = 44000$ kN/m, $k_5 = 31000$ kN/m, $k_6 = 16000$ kN/m
$c_1 = 120$ kNs/m, $c_2 = 90$ kNs/m, $c_3 = 75$ kNs/m, $c_4 = 65$ kNs/m, $c_5 = 45$ kNs/m, $c_6 = 32$ kNs/m.

The six-story building is analyzed by adding dry friction dampers between each story and between the first story and the ground. *SR* is kept constant at 0.2 for all dampers and ground acceleration is kept constant at 0.067 m/s^2 which is the maximum frequency response value of the 1999 Bolu earthquake in east–west direction. In order to obtain the global

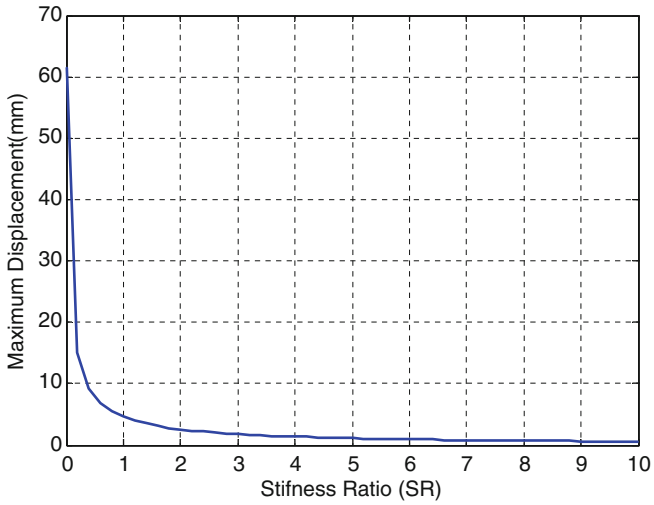

Fig. 12.11 Maximum displacement versus SR curve for PS = 2

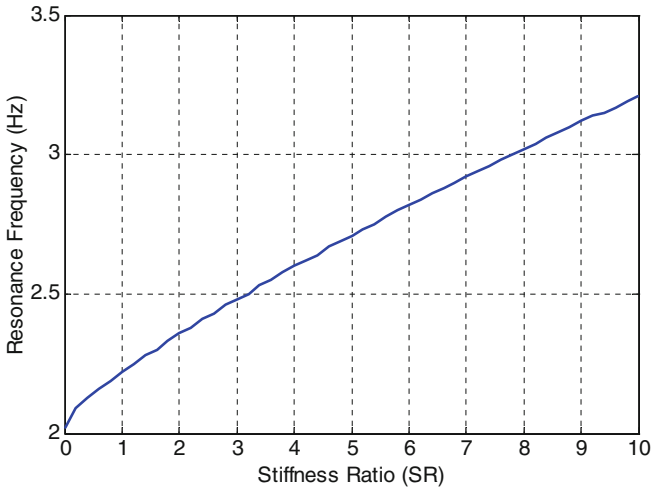

Fig. 12.12 Resonance frequency versus SR curve for PS = 2

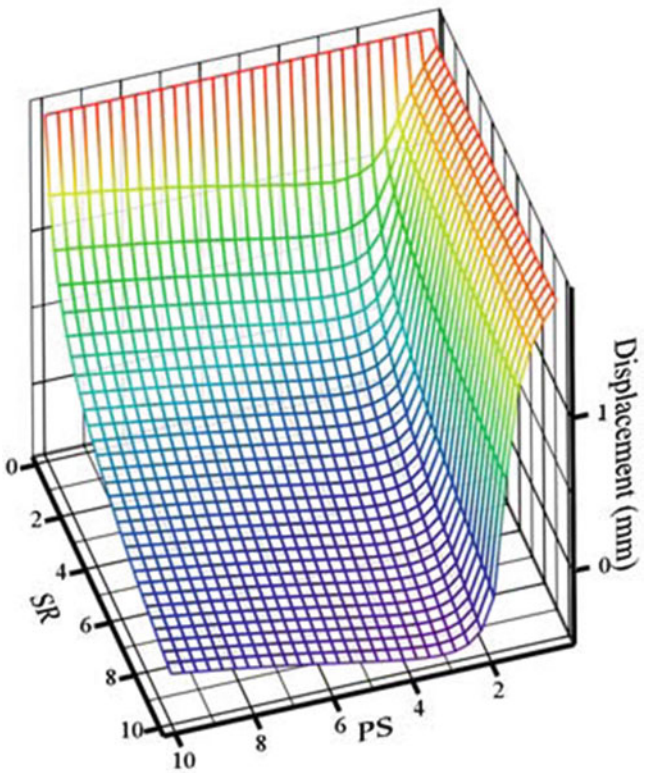

Fig. 12.13 Effect of PS and SR on maximum displacement

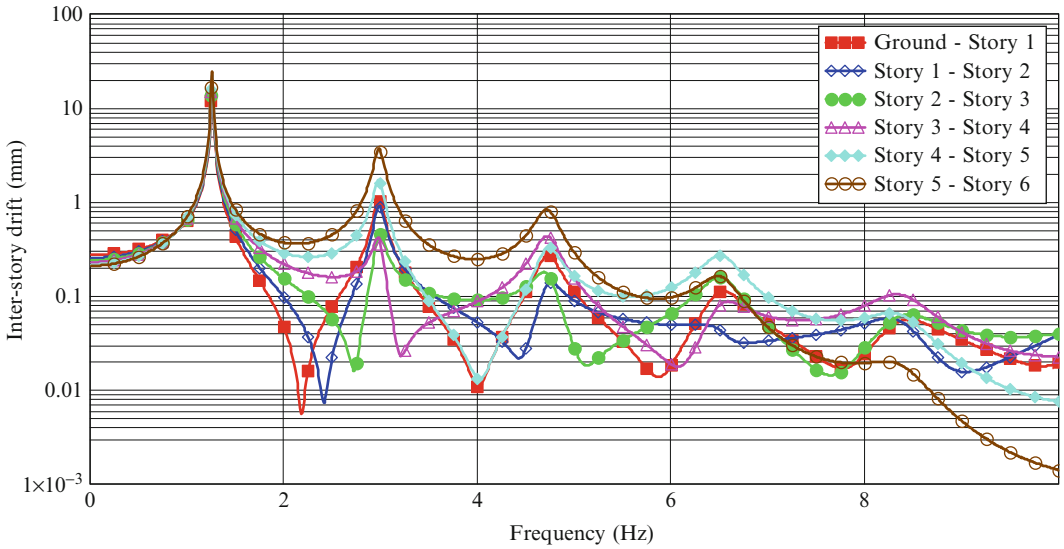

Fig. 12.14 Inter-story drift plot (no damper)

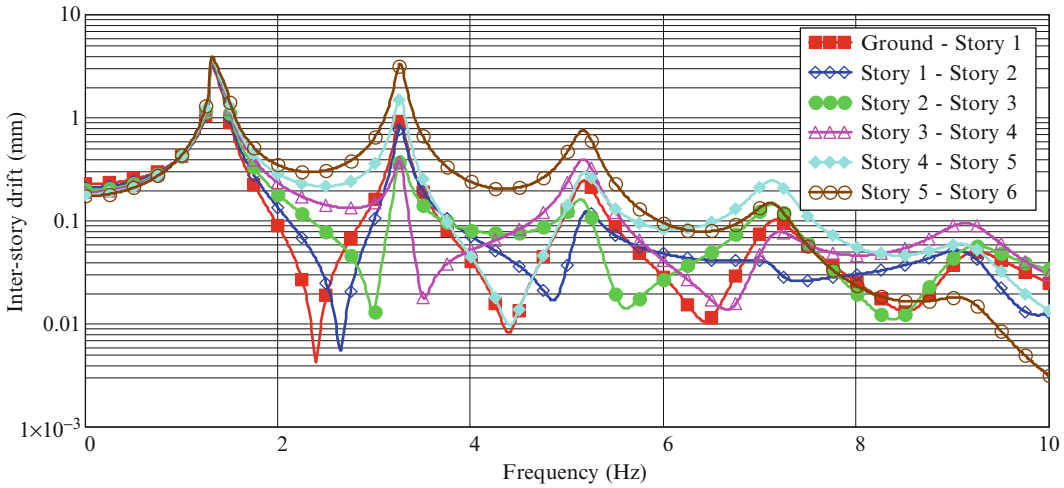

Fig. 12.15 Inter-story drift plot (PS = 0.5631 for all dampers)

optimum value of *PS*, a hybrid optimization method is utilized in MATLAB which applies Genetic Algorithm at first and then uses fmincon, a gradient based optimization, in order to enhance the results further. The cost function used in the optimization problem is defined as the minimization of the relative displacement between two successive floors i.e. inter-story drift and the design variables are the slip forces of each damper. As can be seen from Fig. 12.14, maximum inter-story drift value for the building without any damper is 24.4 mm at 1.25 Hz and it is between fifth and sixth story.

In the first part of the study, it is assumed that the slip load on each damper is identical and it is optimized. The optimum value for *PS* is obtained as 0.5631 and the maximum inter-story drift at 1.26 Hz is reduced to 3.92 mm as seen in Fig. 12.15.

In the second part of the study, slip loads on the dampers are considered to be independent from each other and all of these values are optimized. The optimum *PS*values are obtained as follows:

$$PS_1 = 0.6767,\ PS_2 = 0.6443,\ PS_3 = 0.5832,\ PS_4 = 0.4922,\ PS_5 = 0.3912,\ PS_6 = 0.3279$$

and the maximum inter-story drift at 1.3 Hz is reduced to 3.71 mm as shown in Fig. 12.16.

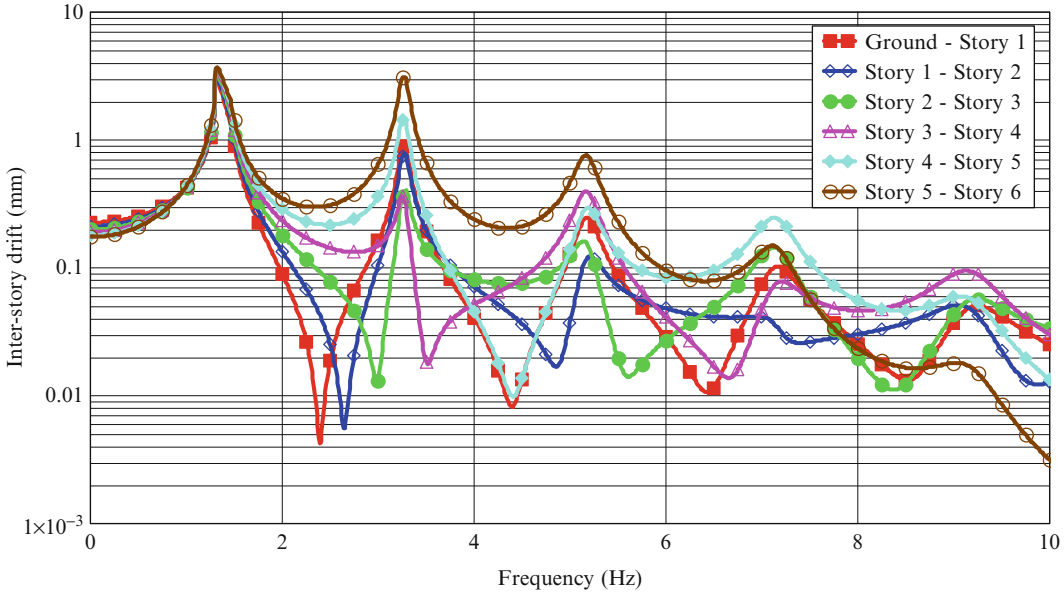

Fig. 12.16 Inter-story drift plot (optimum PS values)

12.5 Conclusion

In this paper, a multi story building equipped with dry friction dampers is studied under harmonic acceleration. Shear building and macro-slip friction model is used to mathematically model the building and dampers, respectively. In order to overcome the difficulties of time domain methods used in the literature and also decrease the computational expense, a frequency domain solution method is used utilizing Harmonic Balance Method. Although, earthquake motion is totally random and cannot be expressed with harmonic components completely, for optimization purposes this method is very advantageous compared to time domain optimizations, since frequency content and magnitude of an earthquake can be easily calculated by taking Fast Fourier Transform (FFT) of the recorded motion. Moreover, optimizations are not performed for a specific earthquake and; hence, obtained results can be applied for a wide range of earthquakes by properly selecting the ground acceleration amplitude. The validity of the solution method suggested here is demonstrated by comparing the results obtained from frequency domain and time marching solutions and it is seen that they are in excellent agreement. Moreover, it is observed that damper properties such as slip load and stiffness of the supporting elements have a great effect on inter-story drift and should be optimized for minimum inter-story drift. However, due to challenges in construction, it is not practical to change the stiffness of the damper, i.e. brace stiffness. Therefore, the main important variable in optimization is the slip force of the dampers. Hence, the slip force on each friction damper for a multi story building is optimized by using a hybrid optimization method. It is observed that if the identical slip force on each damper is applied, the maximum inter-story drift is decreased by 83.9% and if the slip loads on the dampers are considered to be independent from each other, then the maximum inter-story drift is decreased by 84.8% for the case study considered in this paper. These results indicate that identical or different slip forces result in similar reductions in the maximum inter-story displacement in the case study under consideration.

References

1. Păuleţ-Crăiniceanu F (1999) A lecture delivered to the 4th year students P100 seismic code. Editura Cermi, Lasi
2. Bhushan B (1999) Principles and applications of tribology, vol 9, 2nd edn. Wiley, New York, pp 89–89
3. Takewaki I, Fujita K, Yamamoto K, Takabatake H (2011) Smart passive damper control for greater building earthquake resilience in sustainable cities. Sustain Cities Soc 1(1):3–15

4. Sanliturk KY, Imregun M, Ewins DJ (1997) Harmonic balance vibration analysis of turbine blades with friction dampers. J Vib Acoust 119(1):96
5. Chen JJ, Menq CH (2001) Periodic response of blades having three-dimensional nonlinear shroud constraints. ASME J Eng Gas Turb Power 123:901–909
6. Cigeroglu E, An N, Menq C-H (2009) Forced response prediction of constrained and unconstrained structures coupled through frictional contacts. J Eng Gas Turb Power 131(2):022505
7. Tabeshpour M, Ebrahimian H (2010) Seismic retrofit of existing structures using friction dampers. Asian J Civil Eng (Building and Housing) 11(4):509–520
8. Lee S (2008) Allocation and slip load of friction dampers for a seismically excited building structure based on storey shear force distribution. Eng Struct 30(4):930–940
9. Kim J (2004) Behavior and design of structures with buckling-restrained braces. Eng Struct 26(6):693–706
10. Lu L, Chung L, Wu L, Lin G (2006) Dynamic analysis of structures with friction devices using discrete-time state-space formulation. Comput Struct 84(15–16):1049–1071

Chapter 13
The *Valle Castellana* Twin-Arch Bridge: Dynamical Tests, Identification, Seismic Performances

R. Alaggio, F. Benedettini, M. Dilena, and A. Morassi

Abstract The assessment of the structural conditions of existing structures and the evaluation of their seismic performances are usually conducted by means of numerical models. Differently than in the case of a new structure when the construction following the design phase should be done trying to reproduce, in the best way, the design assumptions, assessment analysis requires the determination of a numerical model able to accurately reproduce the actual behavior of the existing construction. This latter issue leads to an inverse problem, whose difficulty is always higher than the direct design problem. In this paper, model updating strategies based on dynamic data are applied to a class of six reinforced concrete twin arch bridges located in Provincia di Teramo, Italy, to assess their structural performance under seismic actions. The attention will be mainly focused on the Valle Castellana bridge. The case study has been selected because an apparently strange dynamic behavior emerged in a dynamic campaign carried out on 2002–2003 on this bridge. The peculiar behavior can be linked to a known phenomenon possibly affecting initially curved, symmetric structures, when the initial symmetry is lost for different possible reasons. In addition, on 2009, the Valle Castellana bridge suffered for a sudden settlement of one of the supports, and restoration works were needed to reconstruct the parts subject to failure. Based on the results of dynamic tests carried out on 2011, a calibrated finite element model was determined and used to assess the actual structural behavior of the bridge. A possible structural improvement of its seismic performance based on the validated numerical model is also discussed.

Keywords Output only identification • Seismic analysis

13.1 Introduction

Between 1917 and 1969 six RC twin-arch bridges were built in the territory managed by the *Provincia di Teramo*, in Italy. The paper reports some of the analyses conducted during an assessment campaign promoted by the Local Public Territorial Authority maintaining the bridges. Among all the conducted activities, the paper is concerned with the modal identification in operational conditions of such bridges with the aim of calibrating (in the sense of the model updating) their *FE* models by using the experimental data and to constitute reference modal models for a future damage identification analysis. The last topic is addressed by controlling the evolution of the modal properties as the years goes by. In fact, standard damage detection techniques are usually based on dynamics methods and, in particular on change of natural frequencies [1, 2].

The *FE* models are also the mean to forecast the actual seismic performance and the needed actions to improve it.

The six bridges localized, respectively in Aprati (l = 68.5 m), Frattoli (l = 31.8 m), Morrice-S.Giovanni (l =28.4 m), Montefino (l =47.3 m), Valle Castellana (l =27.2 m) and Villa Passo (l =58.2 m) in provincia di Teramo, have been the object of a preceding work in which peculiarities, similitudes and an accurate report of their dynamical behavior is reported [3].

R. Alaggio • F. Benedettini (✉)
DISAT-University of L'Aquila, L'Aquila, Italy
e-mail: rocco.alaggio@univaq.it; francesco.benedettini@univaq.it

M. Dilena • A. Morassi
DICA-University of Udine, Udine, Italy
e-mail: michele.dilena@email.it; antonino.morassi@uniud.it

J.M. Caicedo et al. (eds.), *Topics on the Dynamics of Civil Structures, Volume 1*,
Conference Proceedings of the Society for Experimental Mechanics Series 26,
DOI 10.1007/978-1-4614-2413-0_13,

In three of the six cases the dynamical analysis, repeated three times between 2002 and 2003 was conducted again on 2011 (Aprati bridge, Frattoli bridge and Valle Castellana bridge).

In particular, the case study of the Valle Castellana bridge has been the object of a work explaining an apparently strange dynamical behavior of the bridge exhibiting *hybrid modes* because of the onset of *veering* conditions and consequent loss of symmetry and, respectively, anti-symmetry, of the couple of modes (one symmetric and one anti-symmetric) involved by the phenomenon of hybridization [4].

The analyses permitted to clearly identify the modal characteristics (natural frequencies, damping factors and modal shapes) useful to perform a tuning procedure on the *FE* models of the tested bridges. On the same time the original technical documentation (structural design) was found and several tests on the constituting materials and soil characteristics were promoted by the Public Territorial Authority maintaining the bridges. All the information have been used to make an assessment of the actual structural conditions mainly oriented to forecasting the maximum ground acceleration the bridges could sustain during an earthquake and to make conjectures on the possible structural improvement.

In fact, after the earthquake reported in Abruzzi on April 6, 2009, great attention is devoted to the analysis and assessment of existing structures, most of which designed without the application of any seismic code.

Among the six different bridges, the case of Valle Castellana bridge will be analyzed in the paper.

For the analyzed bridges a test and identification procedure has been pursued to obtain reliable results by generally using *output only measures* and *ambient excitation* (regular traffic) with the use of the minimum number of sensors able to accurately furnish the first natural frequencies and relevant modal shapes.

The bridges have been tested on 2002–2003 by using between 6 and 10 accelerometers on 6–14 spatial points on the deck measuring only the vertical vibrations.

More recently, during the 2011, a digital array of 35 sensors was used to identify the global 3D dynamic behavior (vertical, longitudinal and transverse modal components) of bridges, needed for the seismic analysis.

The ambient excitation guarantees the *low cost* of the testing procedure conducted without closing the bridges during the measures.

Two different techniques based on output-only measures have been used to identify the modal parameters. The first method is frequency-domain based and makes use of the SVD decomposition of the power spectral density matrix. The second method is a time-domain based method using a stochastic subspace identification technique to fit a parametric model directly from the raw times series returned by the transducers. Both of them were conducted using the commercial software ARTEMIS, controlling the results by using an ad hoc software produced by the research group.

13.2 The Valle Castellana Bridge: Experimental Tests Conducted in 2002 and 2011

The 2002 dynamical tests on the Valle Castellana bridge permitted to put into evidence a seemingly anomalous behaviour interpreted by unfolding the observed phenomenon in the framework of the theory of linear vibrations of mono-dimensional curved structures. The observed behavior was analyzed by means of the FE companion model of the bridge after identifying the relevant parameters; in particular the modification of the two first modal shapes (first anti-symmetric and second symmetric), into a couple of *hybrid flexural modes* has been observed and the phenomenon has been interpreted as a *veering* of subsequent structural modes (see Fig. 13.1). The reported phenomenon is a peculiarity of not symmetric curved structures [5] and it is the evolution of the better known crossover phenomenon affecting, in some cases, perfectly symmetric curved structures [6]; the phenomenon has been reproduced on the identified *FE* model, analyzing the variations of frequencies and modal shapes as the shallowness of the arch is varied around its initial value (geometrical parameter).

Eigensolutions, as well known, depend on system parameters: the mutual approaching, the possible intersection (crossover), the subsequent avoidance (veering) of the root-loci of the frequency of two neighbouring modes when plotted

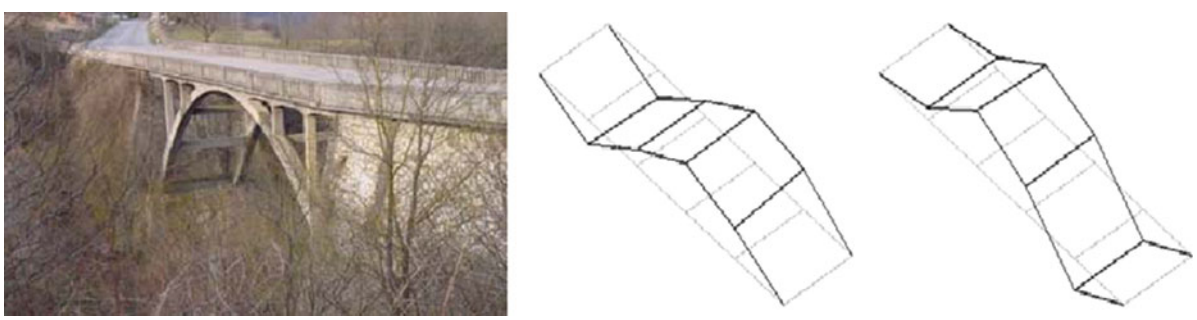

Fig. 13.1 The Valle Castellana bridge and the first and second hybrid modes $\nu_1 = 8.30$ Hz, $\nu_2 = 8.88$ Hz

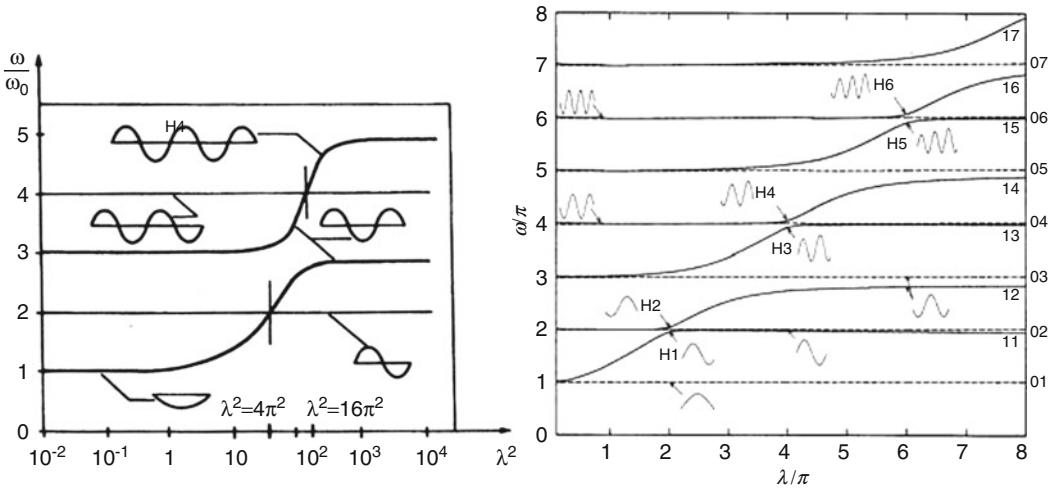

Fig. 13.2 Crossover on a symmetric (*left*) and veering on a asymmetric (*right*) suspended cables

versus the unfolding parameter, is generally of interest in the description of spectral properties of a structure. The reported phenomenon is interesting since affects modal shapes and, consequently, the forced response of the system.

As introduced before, the crossover or veering phenomena in the literature are often related to initially curved structures where some classes of eigenvalues and eigenvectors show a strong dependence on an elastic-geometric parameter. If the loci of the frequencies are plotted versus a significant parameter the relevant curves can cross each other (crossover phenomenon, see Fig. 13.2-left representing the case of a symmetric suspended cable). If the initial configuration is non-symmetric the loci of neighbouring eigenvalues, after approaching, veer instead to cross each other (see Fig. 13.2-right, representing the case of an inclined suspended cable).

Differently from the crossover an important characteristics of the veering of loci is that the modal shapes associated with each locus are interchanged during the veering in a continuous way giving rise to the so called *hybrid modes* strongly evident in the approaching zones (see Fig. 13.2-right). Even if the case of nearly-symmetric curved structures is the most relevant concerning this phenomenon, other situation (e.g. a system sub-matrix with low out diagonal coupling terms) can produce the same behaviour even with symmetric initial configurations. In the case of the Valle Castellana bridge, the identification of two neighbouring *hybrid modes* (see Fig. 13.1), has been unfolded putting into evidence with the help of the companion FE model, the veering parameter and showing the sequence of the *modes-hybridization* of the first two flexural modal shapes (first symmetric and first anti-symmetric, see Fig. 13.3).

Due to high sensitivity of hybrid modal shapes to structural modifications, the occurrence of such phenomenon could be conveniently used to evaluate the possible increasing loss of symmetry due to incremental damages, affecting the bridge [4].

On 2009, the bridge suffered for a sadden settlement of one of the supports and restoration works were needed to reconstruct the parts subjected to failure. A steel cantilever was erected on a new abutment to support the side of the bridge subjected to the settlement. At the end of the restoration works, new dynamical tests were conducted with the aim of understanding how the structural modifications could have affected the dynamical response and, consequently the seismic performance of the bridge. Because of the high sensitivity of the first two modal shapes (*hybrid*, as previously described) to the variation of system parameters a quite remarkable variation in the spectral properties of the bridge was forecasted.

On 2011, as mentioned in the introduction, a more refined instrumentation layout was adopted and the out of plane (deck) components were measured as well (Fig. 13.4):

As expected, the structural modifications affected the spectral properties modifying the symmetry conditions: the first two vertical modes of the deck (second and third in the global order, being the first, a global lateral-cantilever mode of the bridge) evolved and the actual situation appears as follows:

As it is possible to verify (Fig. 13.5), the structural modifications due to restoration works, because of the high sensitivity due to the veering conditions, forced the first two frequency of the deck to further avoiding from each other and to lowering. A (smaller) hybridization is still observable even if the phenomenon is remarkably less evident than during the 2002 tests.

The loss of symmetry further induced by the 2009 restoration works, is also well represented by the first global mode: in Fig. 13.6 it is possible to verify how the side subjected to restoration and now supported by a steel cantilever is more deformable (right side in the figure with higher modal components) in the horizontal direction:

Such a not symmetric behavior will affect, as we will see in the following, the structural response of the bridge.

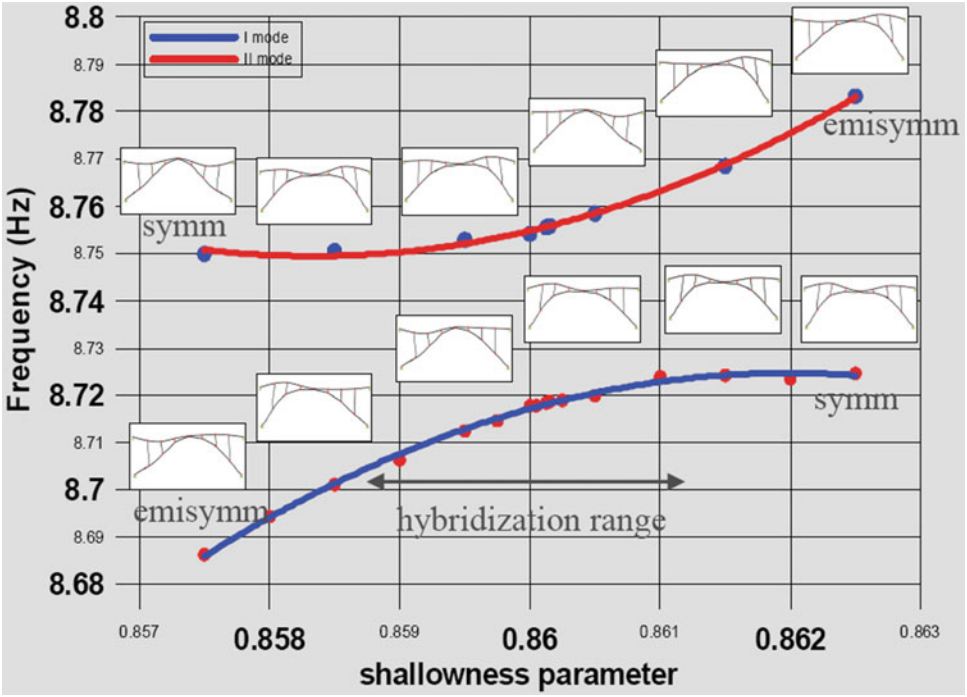

Fig. 13.3 The veering transition in the FE model of the Valle Castellana twin-arch bridge

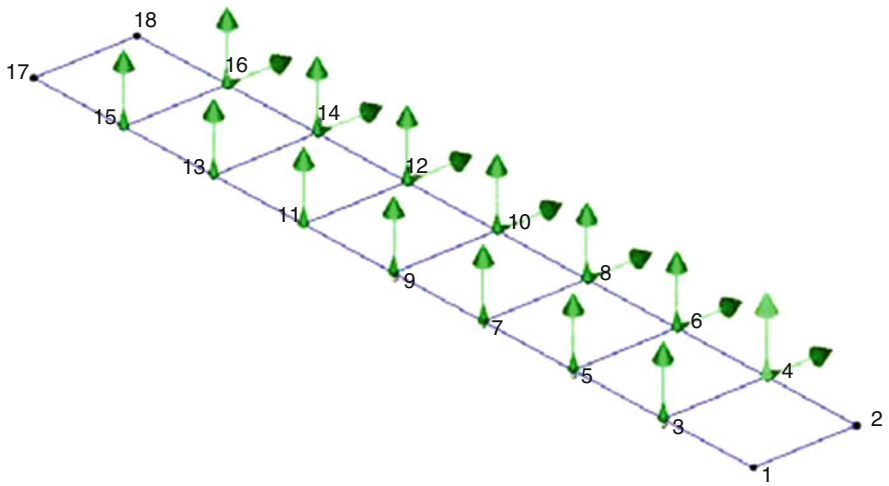

Fig. 13.4 Instrumentation layout, 2011 tests

13.3 The Valle Castellana Bridge: The Assessment of Seismic Performances

Structural assessment of an existing RC bridge is an issue definitely more complex than conventional designing of a new structure. In fact, many construction variables that can be considered as known quantities in the design stage, are unknown for an existing bridge, or they are known with a rather low degree of accuracy. This is the case, for example, of the mechanical properties of materials, which may have suffered accidental or natural processes of degradation during the bridge life. Another example is represented by constructional details that, in many cases, are only partially reported in the available technical documentation. It is mainly for these reasons that assessment of the seismic safety of a bridge must be based on a detailed analysis of the existing structure, in order to determine a numerical model able to accurately reproduce the global dynamical behavior under seismic forces.

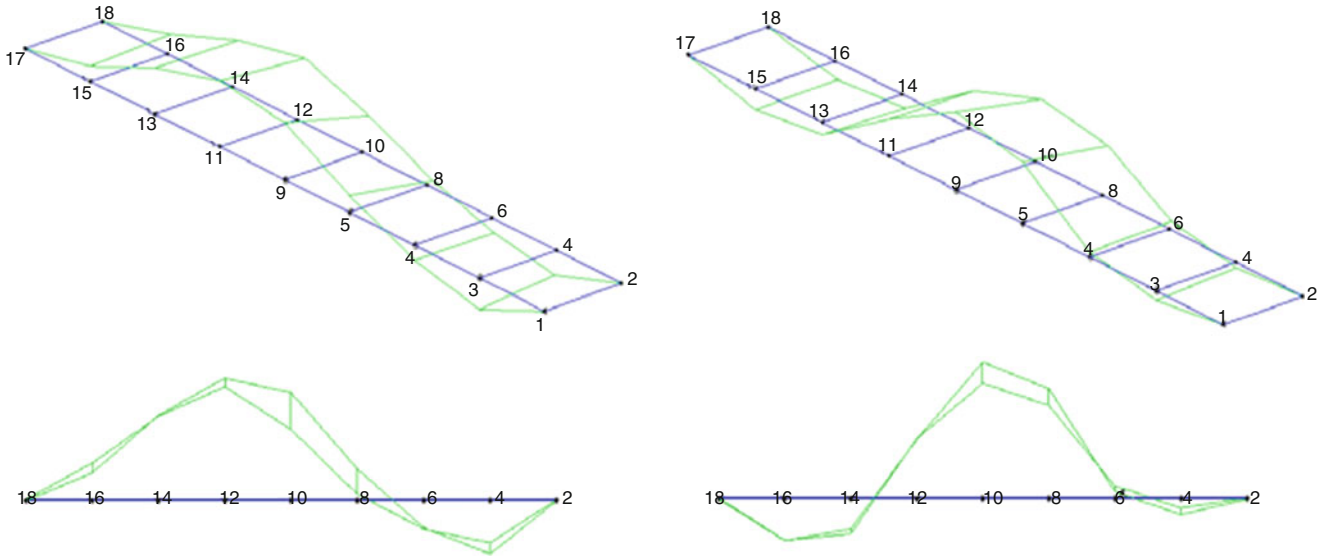

Fig. 13.5 First and second (second and third in the global order) hybrid modes $\nu_1 = 7.32$ Hz, $\nu_2 = 8.34$ Hz

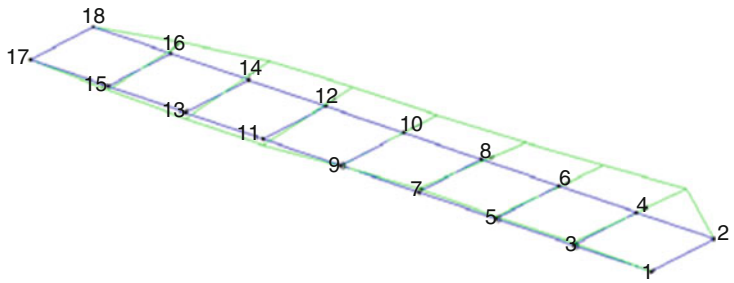

Fig. 13.6 First global mode (horizontal displacement of the deck, $\nu_1 = 3.66$ Hz)

In order to acquire an adequate knowledge of the material characteristics and construction details, the Italian national codes [7] require the execution of a series of experimental investigation and the use of *in-situ* test data to implement the available technical data. These tests can be either partially destructive (drilling of concrete, sampling of reinforced bars and related strength tests, etc.) or non-destructive (magnetometric tests, ultrasounds analysis, etc.). All these investigations are essentially local in nature and, despite the care taken in their execution, they can leave large uncertainties regarding the overall structural behavior of the system. The uncertainties can originate, for example, by the soil-structure interaction phenomena, the inhomogeneity of the materials used, and the difficulty to model real internal constraints and boundary conditions. In fact, despite having experimentally reconstructed local properties of materials and structural details, the global behavior of the bridge may be only partially characterized.

Moreover, taking into account that the entire analysis is aimed at assessing the safety under seismic actions, it is quite natural to assume that a significant role, if not essential, is represented by dynamic properties of the real structure. Basically, these dynamical properties are natural frequencies, vibration modes and associated damping factors. The collection of these *modal parameters* defines a *dynamic signature,* which is typical of every individual bridge and, at least in the range of validity of linear dynamics, allows reconstructing the global bridge response under seismic actions [8].

Experimental Modal Analysis [9] methods can be used to identify the modal parameters of a vibrating system. Many advantages are offered by this class of experimental/analytical methods in comparison with classical static testing. First, it is possible to characterize the structural response to external actions varying on time. As it was remarked above, this is a crucial point in the analysis of the dynamic behavior under seismic loads. Moreover, the use of particularly sensitive sensors, such as accelerometers or seismometers, provides for the possibility of using external forces with limited

amplitude, with the advantage of avoiding extreme loading conditions for situations in which anomalous behavior could be expected.

In the case of bridges, in particular, dynamic tests should occur under *operational conditions*. This choice greatly simplifies the testing procedures and also avoids interference with ordinary traffic. For flexible bridges, the excitation may be provided by the environmental tremor naturally present in every site. Most frequently, ordinary traffic on the bridge can be used as excitation. This solution has the advantage of testing the dynamic response of the bridge under the influence of actions having amplitude comparable with the design service loads. *Operational Modal Analysis* methods operating in the frequency or time domain [10] can be used to extract the modal parameters from the experimental data. The analysis involves the response of dynamic systems to stochastic inputs and the application of advanced identification techniques on spectral autocorrelation and cross-correlation matrices based on output measurements only [11].

Experimental data on natural frequencies and vibration modes can subsequently be used to improve a preliminary numerical model of the bridge and, ultimately, to accurately reproduce the actual dynamical behavior under the influence of seismic forces [12, 13]. As is well known, this issue is part of *Model Updating* strategies, that is, the set of analytical/numerical procedures aimed at improving finite element models based on experimental dynamical data [14, 15].

13.4 The Valle Castellana Bridge: Capacity Analysis

13.4.1 Material Characterization and Mechanical Properties Adopted in the Design

Concerning the material properties, the new Italian code NTC2008 establishes that, after performing in situ tests on the composing materials, instead than the characteristics values, the mean values of the relevant measures should be used to evaluate the elements capacity. Following this rule, the design value for the concrete strenght is obtained as follows:

Characteristic compressive cylinder strength:

$$f_{ck} = \frac{f_{cm}}{FC}; \tag{13.1}$$

Mean value of axial tensile strength:

$$f_{csm} = 0.3 f_{ck}^{2/3}; \tag{13.2}$$

Mean value of flexural tensile strength:

$$f_{cbm} = 1.2 f_{csm}; \tag{13.3}$$

Characteristic 5% value of flexural tensile strength:

$$f_{cbk} = 0.7 f_{cbm}; \tag{13.4}$$

Design values of flexural tensile strength:

$$f_{cbd} = \frac{f_{cbm}}{\gamma_c}; \gamma_c = 1, \quad f_{csd} = \frac{f_{csm}}{\gamma_c}; \gamma_c = 1.5. \tag{13.5}$$

The coefficient γ_c assumes the value 1 in the capacity evaluation of ductile elements and mechanisms (bending), while assumes the value 1.5 in the case of brittle elements and collapses (shear). The *confidence factor FC* is a function of the *level of knowledge LC* and f_{cm} is the mean value of concrete compressive cylinder strength.

Following the same rule, the value of the steel yielding strain is evaluated from the mean yield strength of reinforcement as follows:

Table 13.1 Materials characteristics – main arches

f_{ck} [MPa]	f_{csm} [MPa]	f_{cbm} [MPa]	f_{csd} [MPa]	f_{cbd} [MPa]	E [MPa]
20.8	10.5	12.7	7.0	12.7	29962

Table 13.2 Materials characteristics – pillars and slab

f_{ck} [MPa]	f_{csm} [MPa]	f_{cbm} [MPa]	f_{csd} [MPa]	f_{cbd} [MPa]	E [MPa]
15.0	8.5	10.2	5.6	10.2	23983

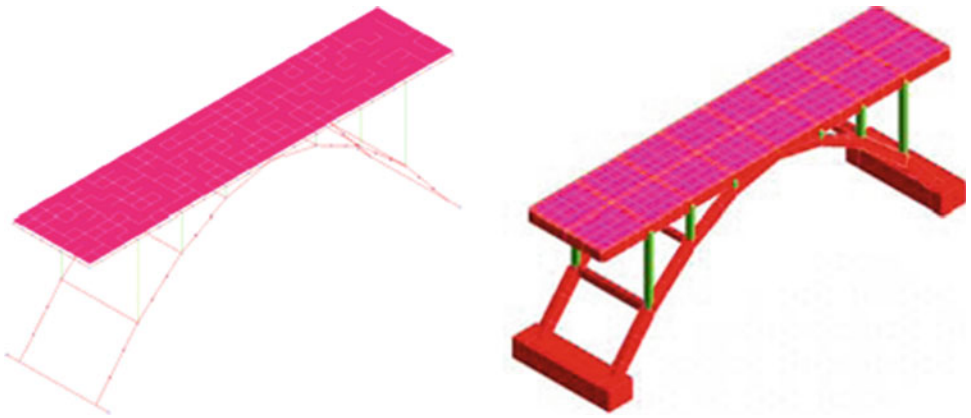

Fig. 13.7 The FE model

Characteristic yield strength:

$$f_{yk} = \frac{f_{ym}}{FC}; \tag{13.6}$$

Design yield strengths:

$$f_{ybd} = \frac{f_{yk}}{\gamma_s}; \gamma_s = 1; \quad f_{ysd} = \frac{f_{yk}}{\gamma_s}; \gamma_s = 1.15. \tag{13.7}$$

The coefficient γ_s assumes the value 1 in the capacity evaluation of ductile elements and mechanisms (bending), while assumes the value 1.15 in the case of brittle elements and collapses (shear). The *confidence factor FC* has been already introduced.

The available data on the constituting materials permits to consider the structure knowledge with a LC2 level *(extensive knowledge)* and, consequently, in the preceding formulas the value FC = 1.2 can be used.

For the elements belonging to the main arches and for surmounting pillars and slab, the following design values of the material characteristics, are obtained respectively (Tables 13.1 and 13.2).

13.4.2 Capacity Analysis

The *FE* model is characterized by about 2,500 d.o.f., 232 beam elements, 256 shell elements. Elastic constraints are considered both at the foundation level and in the conjunction between the bridge deck and the abutments (not visible in Fig. 13.7 representing the *FE* model).

In the seismic analysis the vertical loads due to the passage of vehicles are not considered (infrequent concomitance):

In the following table, according to Italian rules, the seismic parameters characterizing the site hazard are reported (Table 13.3):

Because of the boundary conditions, the transversal direction has been considered as the weakest one and the seismic analysis has been conducted considering a transversal earthquake.

Generally, several structural modes affect the seismic response; in the case of a mode having a participating mass greater than the 80%, it is possible to perform a unimodal nonlinear static analysis (see Fig. 13.8). The method is characterized by

Table 13.3 Seismic hazard parameters of the site

Nominal life [years]	*Class of use*	*Soil category*	*Topografic coeff.*	*SLV* $[A_g/g]$	*SLC* $[A_g/g]$
100	III	E	1	0.377	0.452

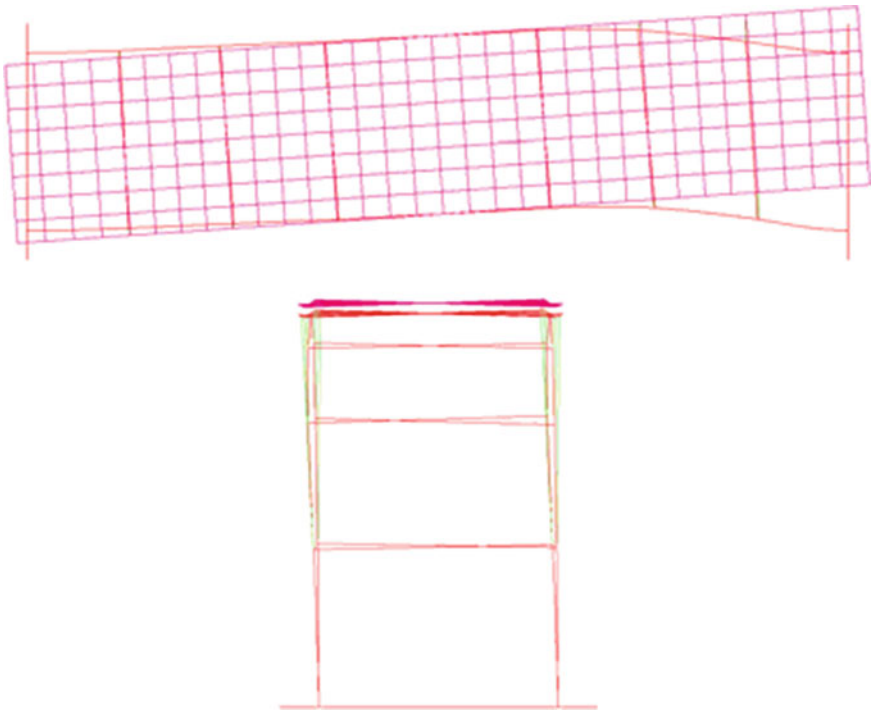

Fig. 13.8 First out of plane (T = 0.28 s) mode used in the capacity analysis

the application of a static scheme of incremental loads (having different spatial distribution) on a nonlinear *FE* model of the structure till reaching the structure capacity in term of stress and strain. Later on, the characteristic curve *(base-shear)/(target displacement)* is produced and the equivalent bilinear system is used to verify the seismic structural response.

The scheme of loads to be applied to the structure is defined as follows:

$f = \lambda M\varphi$, were M is the mass matrix of the considered system, φ is the first modal shape normalized in such a way to have an *unity* value in correspondence of the target d.o.f. The intensity λ is increased till reaching the ultimate structure capacity. The result is furnished plotting the base-shear (total sum of applied loads) as a function of the displacement of the control point.

Given the modal participation factor $\Gamma = (\varphi^T\, M\, 1)\bullet\, (\varphi^T\, M\, \varphi)$, the force V* and the displacement u* of the equivalent 1 d.o.f. system are: $V^* = Vb/\Gamma$ e $u^* = u/\Gamma$. The curve V^*- u^* define the constituting law of the equivalent system having mass $m^* = \varphi^T M1$ (1 column vector having the value of 1 on each row). The bilinear response of the equivalent system is determined by imposing the equivalence condition of equal work with real *V-u* curve.

In the evaluation of the displacement capacity the ultimate value of average rotation (used for the assessment of the collapse limit state SLC) is determined in function of yelding and collapse curvatures obtained by the bilinear approximation of the section bending-curvature law. For the assessment of the life safeguard condition (SLV according to definition in the Italian seismic code) the ultimate value of the rotation is assumed 3/4 times the value corresponding to the collapse.

Assuming the correct values taken by the material characteristics, the elastic constraint at the supports have been estimated by an updating procedure minimizing the difference between the experimental frequencies and modal shapes and the same values forecasted by the *FE* model. The dynamical tests conducted in 2011 put into evidence (as noted above) an higher horizontal flexibility of the deck in the valley support (right in the figures). It is reasonable to imagine that the higher flexibility is linked to the restoration work done on 2009 when a steel cantilever has been erected to repair the collapse of the abutment. Before such works, the horizontal flexibility was assumed equal both for the mount and the valley supports.

Because as we will see later, the capacity analysis showed that the induced asymmetry produces a quite considerable reduction in the seismic performance of the bridge, a restoration work, based on the use of the CAM technology, consisting in wrapping with high-strength steel bands the structural elements, is proposed (see Fig. 13.9)

Fig.13.9 The CAM reinforcement on beams, pillar and joint

The CAM reinforcement, because of the confinement, allows to increase both the concrete strength and the relevant ductility. A corresponding increase in bending and shear capacity of the reinforced elements is obtained as well.

According to Italian seismic code it is possible to evaluate the increased strenght of confined concrete as:

$$f_{cc} = f_c \left[1 + 3.7 \left(\frac{0.5 \cdot \alpha_n \cdot \alpha_s \cdot \rho_s \cdot f_y}{f_c} \right)^{0.86} \right] \tag{13.8}$$

The ultimate strain of confined concrete is:

$$\varepsilon_{cu} = 0.004 + 0.5 \frac{0.5 \cdot \alpha_n \cdot \alpha_s \cdot \rho_s \cdot f_y}{f_{cc}} \leq 0,027 \tag{13.9}$$

where:
$\rho_s = 2A_s(b+h)/(bhs)$ is the volumetric ratio of transversal steel reinforces, α_n and α_s are, respectively, the effectiveness factor of confinement of the section and of the element and can be evaluated as follows:

$$\alpha_n = 1 - \frac{(b-2R)^2 + (h-2R)^2}{3bh} \quad \alpha_s = \left(1 - \frac{s-h_s}{2b}\right)\left(1 - \frac{s-h_s}{2h}\right) \tag{13.10}$$

where R is a linear dimension linked to the steel "L" element usually used to protect the edge of the section, b and h are the section dimensions while h_s is linked to the interval between the transversal steel reinforces.

In particular, the increasing in shear capacity could be evaluated as follows:

$$V_{R-CAM} = 0.9\, d\, \frac{A_{sCAM}}{s} \left(0.5 f_{ywd}\right) \left(ctg\alpha + ctg\vartheta\right) sin\alpha \tag{13.11}$$

Being d the effective height of the section, $A_{s\text{-}CAM}$ is the area of the high strength steel CAM reinforcement, s the interval between the transversal steel reinforces, f_{ywd} the yelding value of the high strength steel CAM reinforcement, α is 90°, θ (variable in the interval 21.8°–45°) the angle of slope of the concrete strut on the respect to the axis of the element.

The seismic performances have been then evaluated by a capacity analysis conducted in the following three cases:

1. Symmetric horizontal elastic constraint at the abutment (condition of the bridge before the collapse of the valley abutment).
2. Asymmetric horizontal constraint corresponding with the actual state.
3. Structure reinforced by applying a system of steel webs confining the beams of the main arches as well as the joint and the first part of each pillar. Such a system denoted as CAM system, when employed on r.c. beams and pillars, allows both the

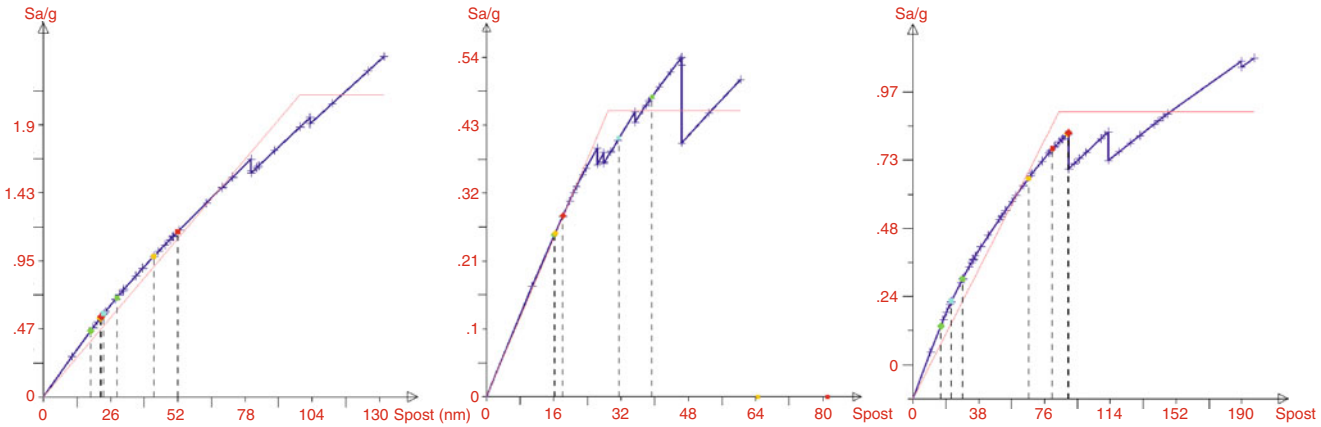

Fig. 13.10 Capacity curves in the three examined cases

Table 13.4 Seismic capacity in the three different conditions

	SLV	*SLC*
Stato	*Pga [ag/g]*	
I	0.12	0.13
II	<0.1	<0.1
III	>0.38[a]	>0.45[a]

[a]Needed capacity on the site according to the Italian seismic code

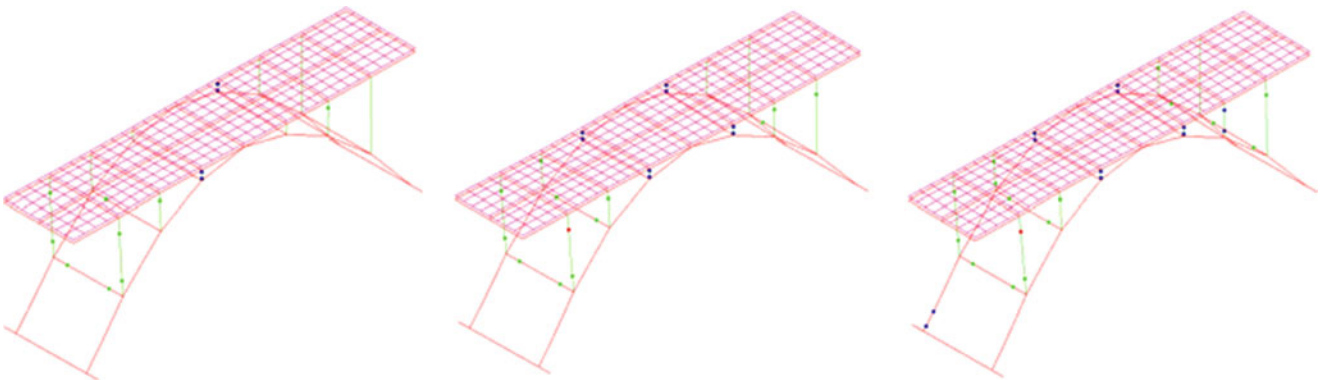

Fig. 13.11 Case n.2: incremental formation of plastic hinges corresponding to brittle failures (*blue points*) (color figure online)

improvement of the strength and strain capability according to the design rule reported above and consequently improves the seismic capacity of the elements and of the whole structure.

It is worth noticing how, when in the past the two abutments were able to furnish a similar value of horizontal constraint to the deck, the seismic performances of the bridge were already quite low, on the respect of what is requested on the site of interest. After the restoration works completed on 2009, the induced asymmetry (steel cantilever on the valley abutment) produces a further considerable lowering of seismic performance that could be completely recovered by the proposed application of the CAM system. The pushover curves pertaining the three mentioned cases are shown in Fig. 13.10 while in Table 13.4 the PGA corresponding to the bridge collapse in the three analyzed cases are reported.

Eventually, in Fig. 13.11, it is possible to observe the incremental formation of plastic hinges in the actual state (corresponding to the second examined case).

13.5 Conclusions

Different experimental dynamic analyses were conducted on 2002 and 2011, on the Valle Castellana bridge with the motivation to help the development of a FE model able to represent the actual dynamic behavior determined by experimental modal analyses. On 2002 the bridge showed an apparently strange behavior that has been unfolded by means of the theory of linear elastic system having initial curvature. The phenomenon of crossover and veering of neighbouring frequencies has been described to explain the anomalous identified behavior. On 2009 the bridge had a failure on the valley abutment and a restoration work consisting in the construction of a new valley support constituted by a steel cantilever, were performed. A dynamic analysis conducted on 2011 showed that the restoration works induced several modification in the spectral properties of the bridge: the main one was a quite considerable asymmetry on the horizontal constraint of the deck due to the different behavior of the two abutments. After calibrating the FE model of the bridge by means of the last dynamical tests, it was possible to verify that such asymmetry has a strong influence on the seismic performances that were considerably lowered by the restoration works. A possible recover of seismic performances has been proposed and it is based on the use of a reinforcing system denoted by CAM and constituted by a series of steel webs surrounding the beam elements of the main arches and partially of the surmounting pillars. With the proposed reinforcement the bridge will be able to have a collapse-PGA greater than the one requested on the site.

References

1. Cerri MN, Ruta GC (2004) Detection of localized damage in plane circular arch by frequency data. J Sound Vib 270:39–59
2. Cerri MN, Vestroni F (2003) Identification of damage due to open cracks by change of measured frequencies. In: Proceedings of 16th conference of Italian association of theoretical and applied mechanics (AIMETA), CD ROM, Ferrara
3. Benedettini F, Alaggio R, Zulli D (2005) Arch bridges in Provincia di Teramo: tests, identification and numerical models. In: Proceedings of the 1st international operational modal analysis conference, Copenhagen, pp 225–236
4. Benedettini F, Zulli D, Alaggio R (2009) Frequency-veering and mode hybridization in arch bridges. In: Proceedings of the 27th international modal analysis conference (IMAC XXVII), Orlando
5. Srinil N, Rega G, Chucheepsakul S (2003) Large amplitude three-dimensional free vibrations of inclined sagged elastic cables. Nonlinear Dyn 33:129–154
6. Benedettini F, Rega G, Vestroni F (1981) Parametric analysis of large amplitude free vibrations of a suspended cable. Int J Solids Struct 20:95–105
7. Norme Tecniche per le Costruzioni, D.M. 14 gennaio 2008 e Circolare 2 febbraio 2009, n. 617, C.S.LL.PP
8. Clough R, Penzien J (1993) Dynamics of structures. McGraw-Hill, New York
9. Ewins DJ (2000) Modal testing: theory, practice and application, 2nd edn. Research Studies Press, Baldock
10. Brincker R, Zhang LM, Andersen P (2000) Modal identification from ambient responses using frequency domain decomposition. In: Proceedings of the 8th international modal analysis conference. San Antonio
11. Bendat JS, Piersol AG (1986) Random data: analysis and measurements procedures, 2nd edn. Wiley, New York
12. Dilena M, Morassi A (2010) Dynamic testing of a damaged bridge. Mech Syst Signal Process 25(5):1485–1507
13. Dilena M, Morassi A, Perin M (2011) Dynamic identification of a reinforced concrete damaged bridge. Mech Syst Signal Process 25:2990–3009
14. Friswell MI, Mottershead JE (1995) Finite element model updating in structural dynamics. Kluwer, Dordrecht
15. Morassi A, Vestroni F (eds) (2008) Dynamic methods for damage detection in structures, vol 499, CISM international centre for mechanical sciences. Springer, Wien

Chapter 14
Directionality in the Transverse Response of Skewed Multi-Span Bridges with Integral Abutments

Seku Catacoli, Carlos E. Ventura, and Steve McDonald

Abstract Skewed bridges tend to rotate due to the pounding between the deck and its abutments or adjacent frames. The rotations increase the transverse displacements leading to transverse unseating of the superstructure. Because skewed bridges have different stiffnesses and strengths depending upon the orientation of the axes along which the properties are determined, an accurate estimation of the transverse demand is connected to determination of the directionality of the transverse response. This in turn is associated to the predominant direction of the transverse mode of vibration. In this research, ambient vibration tests were conducted at two skewed bridges with integral abutments located in British Columbia, Canada. This paper presents the results of the system identification for the transverse direction and how these have been used to illustrate that the predominant direction of transverse response occurs in the azimuth of the skewed bents. For the case of integral abutment bridges, this paper provides experimental support for the recommendations to define the directions of maximum displacement response contained in AASHTO-2009 [1].

14.1 Introduction

Given its deck geometry, skewed bridges are classified as irregular bridges in most seismic specifications (Fig. 14.1a). The tendency for skewed bridges to exhibit more significant damage than straight bridges during earthquakes has been clearly observed. Damage in skewed bridges is mainly caused by superstructure rotations induced by pounding between the deck and its abutments or adjacent frames. The rotation of the deck increases the transverse displacements leading to superstructure unseating or shear damage of columns. For instance, although retrofitted with longitudinal restrainer cables to supplement its short support length (200 mm), the Gavin Canyon Undercrossing fell down during the 1994 Northridge earthquake, which might indicate the importance of the transverse displacement demand in the seismic assessment of skewed bridges (Fig. 14.1b) [2].

Skewed bridges have different stiffnesses and strengths depending upon the orientation of the axes along which these properties are determined. An accurate estimation of the transverse demand is connected to a proper identification of the so called "preferred response direction", the preferred response direction is the direction in which the critical transverse demand occurs (Fig. 14.1c) [3]. This direction is given by the predominant direction of the transverse modes of vibration. A number of authors have conducted experimental and analytical studies to identify the dynamic parameters of skewed bridges mainly in the vertical direction [4–8]. A better understanding of the transverse modes of vibration and their directionality is particularly important in skewed bridges, and this will enable the identification of the direction to evaluate the maximum displacement demand and capacity.

The University of British Columbia (UBC) and the Ministry of Transportation (MoT) have undertaken a study to evaluate the seismic response and the effects of Soil-Structure-Interaction (SSI) on skewed bridges. In this study, the whole soil-foundation-structure and embankment-abutment-structure systems are simulated in one model using 3D finite element analysis. The results are complemented with ambient vibration tests conducted at typical skewed bridges. This paper discusses the results for two multi-span bridges with integral abutments.

S. Catacoli (✉) • C.E. Ventura • S. McDonald
Civil Engineering Department, University of British Columbia, Vancouver, Canada
e-mail: sesamory@interchange.ubc.ca; ventura@civil.ubc.ca; smcivil@interchange.ubc.ca

J.M. Caicedo et al. (eds.), *Topics on the Dynamics of Civil Structures, Volume 1*,
Conference Proceedings of the Society for Experimental Mechanics Series 26,
DOI 10.1007/978-1-4614-2413-0_14,

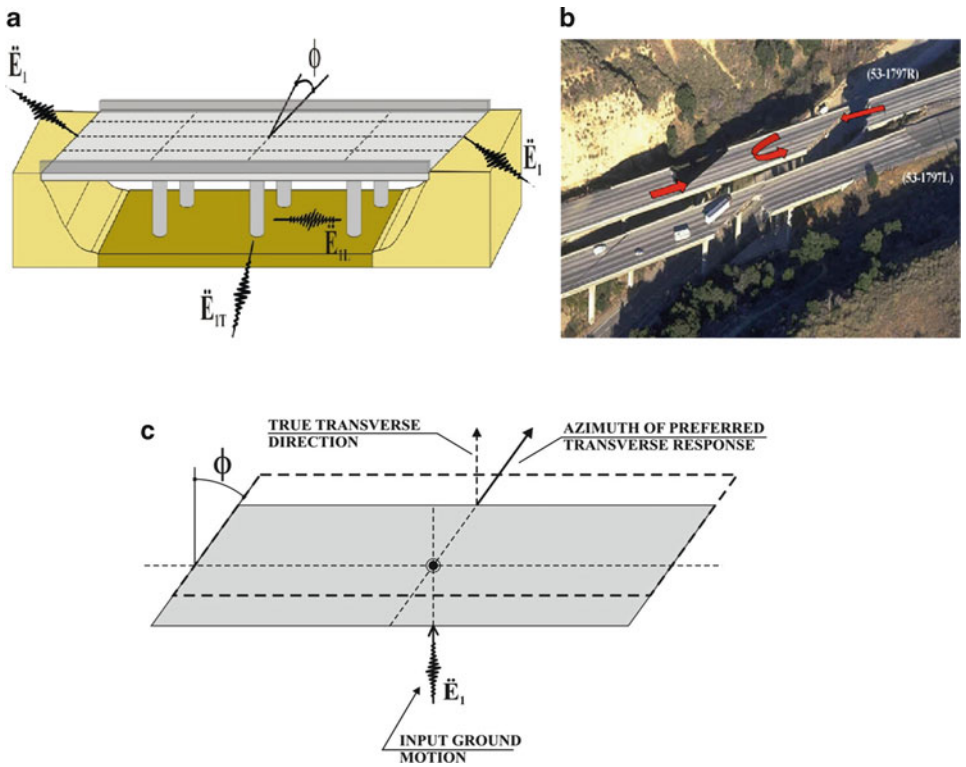

Fig. 14.1 Typical multi-span skewed bridge: (**a**) sketch, (**b**) transverse unseating of superstructure, (**c**) directionality in the transverse response – plan view

14.2 Description of Bridges

Browns River Bridge: The structure was built in 2001 and is located along Highway 19 on Vancouver Island, British Columbia, Canada (Fig. 14.2). The bridge is 90 m long, 23.2 m wide, and has three spans with integral abutments. The superstructure consists of a concrete deck slab supported on six continuous longitudinal steel I-girders which are 2.1 m deep. The substructure consists of 0.9 m diameter, 11.3 m high multi-column frames without cap-beams, connected to the deck by fixed bearings. The abutment foundations consist of steel pipe piles filled with concrete and the pier foundations consist of spread footings.

Black Creek Bridge: The structure was built in 1999 and is also located along Highway 19 on Vancouver Island, British Columbia, Canada (Fig. 14.3). The bridge is 72 m long, 23.2 m wide, and has three spans with integral abutments. The superstructure consists of a concrete deck slab supported on six 1.7 m deep, continuous, longitudinal reinforced concrete I-girders. The substructure consists of multi-column frames which are 0.8 m diameter extended pile shafts. The deck is rigidly connected to the substructure by the cap-beams. The foundations of the abutments consist of steel pipe piles filled with concrete.

The following table summarizes the characteristics of the structures tested (Table 14.1).

14.3 Field Testing

Ambient Vibration Testing involves measuring a structure's response to typical forces that it is subjected to every day. These ambient forces can be wind, traffic, human activities, etc. This method of testing provides a cheap, non-invasive, and non-destructive method for obtaining modal parameters of large structures. With Ambient Vibration Testing you avoid having to physically excite the structure with heavy equipment, which results in the disruption of the structure's typical operation.

Fig. 14.2 Browns River Bridge

Fig. 14.3 Black Creek Bridge

Table 14.1 Bridges tested

Structure	Length (m)	Spans		Width (m)	Clearance (m)	Skew angle (°)	Substructure		Superstructure type	Comments
		No.	Lengths (m)				Type	Abutments		
Browns River	90	3	15-60-15	23.2	11.3	25	Multi-column-frames ($\phi = 0.8$ m)	Integrals	Continuous – steel I-girders	Absence of cap-beams
Black Creek	72	3	20-32-20	23.2	8.2	25	Multi-column-frames ($\phi = 0.8$ m)	Integrals	Continuous – reinforced concrete I-girders	Extended pile shafts

The response that you obtain from these tests is characteristic of the true operating conditions of the structure. To obtain the modal parameters of the structure, Modal Operational Analysis algorithms are used to process the data [4, 5].

Ambient vibration testing is typically carried out by using sensitive accelerometers or other types of sensors, along with a multi-channel data acquisition system. Some inconveniences in using the sensors involve cable handling, sensor balancing, signal clipping, and power supply issues. The Earthquake Engineering Research Facility (EERF) at the University of British Columbia carries out many ambient vibration tests with its three wireless Pinocchio WL380 sensors. These instruments are capable of running up to 12 h and sampling as many as 500 sps. The Pinocchio WL380 sensors are equipped with GPS for time synchronization and two sets of tri-axial geophones for varying amplitude motions. The sensors are equipped with digital cards that can be removed and downloaded to a laptop for extracting data.

In July 2007, two members of the EERF-UBC team carried out ambient vibration tests on the Browns River Bridge and Black Creek Bridge in British Columbia. There were 20 testing locations along the deck of the Browns River Bridge, and 12 along the Black Creek Bridge. The sampling rate was 500 sps. One unit acted as the reference sensor which stayed on the deck, while the other two covered the various testing locations. Each bridge took about 4–6 h to complete testing.

14.4 Data Analysis and Results

The system identification of these bridges for the vertical direction is described in detail by Carvajal et al. [5], the results are summarized in Table 14.2. This paper addresses the system identification for the transverse direction, in particular the predominant direction of the transverse modes are discussed.

The Enhanced Frequency Domain Decomposition (EFDD) technique available in the program ARTEMIS was used to undertake the modal identification analysis [9]. The two first frequencies of vibration of Browns River Bridge in the transverse direction were 5.7 and 7.64 Hz. Figures 14.4 and 14.5 present the corresponding plan and elevation views of the modes of vibration. The elevation views illustrated that the transverse modes of vibration exhibit significant coupling with the vertical components of the torsional and vertical modes. The estimated modal dampings were 1.29% and 0.61% for the first and second modes of transverse vibration.

The predominant direction of the transverse mode is defined as the azimuth in which the mode tends to move. The predominant direction was estimated by comparing, at abutments and at mid-span, the nodal coordinates of the undeformed geometry with respect to the nodal coordinates of the first transverse mode of vibration. The results illustrated that the azimuth varies from 25.26° at abutments to 22.13° at mid-span. These azimuths are similar to the skew angle of the bridge (25°).

Table 14.2 System identification in the vertical direction (Adapted from Carvajal et al. [5])

Browns River Bridge				Black Creek Bridge			
Order	Mode characteristic	Freq. (Hz)	ξ (%)	Order	Mode characteristic	Freq. (Hz)	ξ (%)
1	First vertical	2.2	0.4	1	First vertical	6.1	0.9
2	First torsional	2.3	0.5	2	First torsional	6.6	0.7
3	Torsional	1.9	0.6	3	Torsional	7.1	0.8
4	Torsional	5.1	1.2	4	Torsional	8.5	0.8
5	Second torsional	5.9	0.5	5	Torsional	11.4	0.9
6	Second vertical	6.1	0.6	6	Torsional	14.8	0.8
7	Torsional	7.6	0.6	7	Torsional	15.7	0.5
8	Torsional	9.4	1.1	8	Second vertical	17.4	0.8
9	Torsional	10.9	0.6	9	Second torsional	18.8	0.6
10	Third vertical	11.3	0.2				
11	Torsional	16.3	0.4				

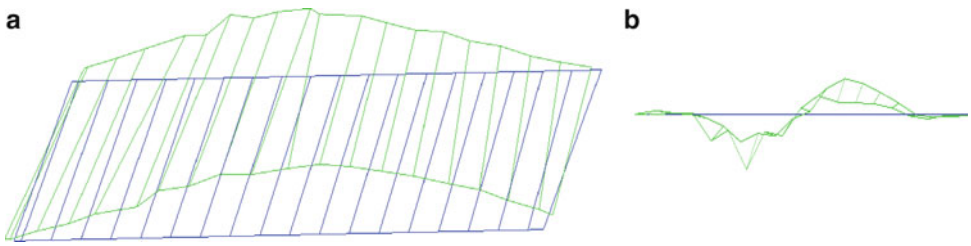

Fig. 14.4 Browns River Bridge – first transverse mode of vibration (ω = 5.7 Hz): (**a**) plan view, (**b**) elevation

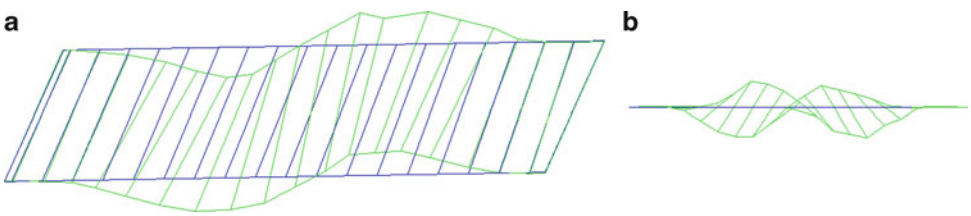

Fig. 14.5 Browns River Bridge – second transverse mode of vibration (ω = 7.64 Hz): (**a**) plan view, (**b**) elevation

Table 14.3 Summary of system identification in transverse direction

	Mode of vibration	Freq. (Hz)	ξ (%)	Predominant direction of transverse mode (°)	Skew angle, ϕ (°)
Browns River Bridge	First transverse	5.7	1.29	25.26–22.13	25
	Second transverse	7.64	0.61	–	25
Black Creek Bridge	First transverse	5.98	1.50	25.05–24.81	25

For the Black Creek Bridge the first frequency of vibration in the transverse direction is 5.98 Hz. The second frequency of vibration was difficult to detect due to the coupling with the vertical components of torsional modes. Similar to the Browns River Bridge, the first mode of transverse vibration was identified and the modal damping was estimated as 1.5%. The evaluation of the predominant direction of the transverse mode of vibration resulted in an azimuth that varies from 25.05° at abutments to 24.81° at mid-span. The azimuths were similar to the skew angle (25°). The following table summarizes the system identification in the transverse direction for the tested bridges (Table 14.3).

14.5 Conclusions

The results of the ambient vibration tests illustrate that the predominant direction of the transverse response in skewed multi-span bridges with integral abutments occurs in the azimuth of the skew bents. These results provide experimental support for the recommendations to define the direction of the maximum displacement demand and capacity contained in AASHTO Specifications for LFRD Seismic Bridge Design [1]. The results also provide an indication to select the direction of the horizontal ground motions to be applied for time history analysis of integral abutment bridges. It is recommended to conduct experimental studies to explore the directionality of the transverse response for bridges with seat type abutments, bridges with rigid decks, and bridges with some level of damage.

Acknowledgements This study was conducted with financial support from the Ministry of Transportation of British Columbia, Canada and the Natural Sciences and Engineering Research Council of Canada. Support provided by Juan Carlos Carvajal and Felix Yao of the EERF at the University of British Columbia is acknowledged with thanks.

References

1. AASHTO – American Association of State Highway and Transportation Officials (2009) Guide specifications for LRFD Seismic Bridge Design
2. Moehle J, Eberhard M (2003) Earthquake damage to bridges. In: Duan L, Chen W-F (eds) Bridge engineering handbook. CRC Press, Boca Raton
3. Stewart JP et al (2011) Representation of bidirectional ground motions for design spectra in building codes. Earthquake Spectra 27(3):927–937
4. Ventura CE et al (1996) Ambient vibration studies of three short-span reinforced concrete bridges. In: Eleventh conference on earthquake engineering, p 921
5. Carvajal JC, Ventura CE, Huffman S (2009) Ambient vibration testing of multi-span bridges with integral deck-abutments. In: Proceedings of the IMAC-XXVII, Orlando, 9–12 Feb 2009
6. Maleki S (2001) Free vibration of skew bridges. J Vib Control 7:935–952
7. Srinivasan RS, Munaswamy K (1978) Dynamic response of skew bridge decks. Earthquake Eng Struct Dyn 6:139–156
8. Ghobarah AA (1974) Seismic analysis of skewed highway bridges with intermediate supports. Earthquake Eng Struct Dyn 2(3):235–240
9. Structural vibrations solutions. Artemis extractor software, vol 5.3, Denmark, 1999–2011

Chapter 15
Analysis of Seismic Records to Evaluate Soil-Structure Interaction Effects on Bridges

Miguel Fraino and Carlos E. Ventura

Abstract Soil-Structure Interaction (SSI) could significantly affect the dynamic behaviour of bridge structures. The most sophisticated approaches used to model the SSI effects deal with kinematic and inertial interaction separately, being unable to consider the combined effect of both phenomena, as it happens in real cases. This supports the need of a better understanding of such effect in order to establish a better SSI modelling technique. This paper presents the results of several analyses conducted with seismic records obtained from instrumented bridges in order to determine how SSI affects their dynamic properties. The data correspond to several selected ground motions, as they were recorded by instruments located on free field, foundation piles, substructure and superstructure, corresponding to Via California bridge (Capistrano Beach, California) and Lake Crowley bridge (Mammoth Lakes, California). The results include fundamental mode properties identified for each bridge, comparison of spectral response quantities, determination of directionality effects and evaluation of signals using frequency domain techniques. The final analysis is done based on the results of the records analysis and the particular overall characteristics of each structural system.

15.1 Introduction

Soil-structure interaction can significantly affect the dynamic properties of certain structures. The characteristics of the structure, foundation soil and earthquake input play a role on this [1]. There are two main physical phenomena that constitute the soil-structure interaction mechanism [2]: (1) the effect of inertia developed in the structure affecting foundation system (called Inertial Interaction), that raises base shear and moment and cause additional displacements of the foundation related to free field, and (2) the difference in stiffness of foundation system and soil, the embedment of the foundation, and the averaging effect of seismic waves passing through the foundation (called Kinematic Interaction). The most sophisticated approaches used to model the effect of SSI include kinematic or inertial interaction separately, but are unable to consider the combined effect of both phenomena, as it happens in real cases. This supports the need of a better understanding of such effect in order to establish a better SSI modelling technique.

In this paper, a method to determine how significant are the SSI effects from the analysis of records obtained from instrumented bridges is presented. The first stage of the proposed method is intended to provide an insight of the dynamic properties of the structure via System Identification methods. Those properties are then used to evaluate the spectral responses, focusing of the difference between free field and column base records, where the displacement spectra are particularly useful considering their sensitivity to the inertial interaction phenomena [3]. Fourier spectra are also analyzed to evaluate the signals characteristics.

M. Fraino (✉) • C.E. Ventura
Department of Civil Engineering, University of British Columbia, Vancouver, Canada
e-mail: mfraino@gmail.com

J.M. Caicedo et al. (eds.), *Topics on the Dynamics of Civil Structures, Volume 1*,
Conference Proceedings of the Society for Experimental Mechanics Series 26,
DOI 10.1007/978-1-4614-2413-0_15,

15.2 Evaluation Method

The main objective of this evaluation method is to highlight some of the effects of soil-structure interaction phenomena in the structural systems, based on the information provided by recorded seismic motions. The method is illustrated by reference to seismic records, geometric characteristics and sensor layouts for all bridges obtained from the California Strong Motion Earthquake Database website (www.strongmotioncenter.org) The following sections describe the steps of the proposed method.

15.2.1 Structural System Identification

The first step is to determine fundamental dynamic properties – i.e. natural period and damping ratio – corresponding to the transverse direction for each bridge. The analysis is based on the seismic records provided by the instruments located on bridge's pier base and deck. The software ArteMis Extractor 4.1 has been used to obtain the required dynamic properties. The Enhanced Frequency Domain Decomposition (EFFD) technique was used for this purpose [4, 5]. The fundamental mode and estimated damping ratio in the transverse direction are obtained based on the Singular Value Decomposition charts, by identifying prominent peaks and evaluating their corresponding modal shapes.

15.2.2 Response Spectra and Directionality

In this step, the response spectra from records obtained from instruments located on the free field, base of bridge piers and deck are computed first. This first stage includes obtaining the response spectra for acceleration, velocity and displacement for each signal, and to conduct a graphical comparison of the computed spectra; this is complemented with a plot of the spectral ratio of column base versus free field. The frequency content of all signals is determined by reference to Fourier spectra plots. The ground motion directionality characteristics are also presented in order to provide a further insight of how the input signal "attacked" the bridge.

15.2.3 Results Analysis

The last step is the evaluation of the results to identify trends that may be used for assess the significance of SSI effects.

15.3 Bridges and Ground Motion Descriptions

In order to illustrate the proposed methodology, the recorded motions from two instrumented bridges in California are considered. The Via California bridge is a six spans reinforced concrete straight bridge, with a total length of 134.4 m. It was constructed in 1960. The superstructure is a six-cell concrete box girder with cantilever abutments, supported by reinforced concrete bents with two columns on spread footing foundations, located on alluvial stratum. The bridge was retrofitted in 1996 and instrumented in 1999. This structure is identified as CESMD 13795 Station and is located at the Interstate five Highway, near Capistrano Beach, California, United States of America.

The Lake Crowley bridge has two spans with straight axis and skewed supporting bent. It was constructed in 1969. The superstructure is a continuous concrete box girder, with diaphragm abutments. The middle bent has two circular reinforced concrete columns with spread footings, founded on alluvial stratum. The bridge was instrumented in 1995. This structure is identified as CESMD Station 54730 and is located at the Highway 395, near Mammoth Lakes, California, United States of America. Figure 15.1 shows general information of the two bridges selected for this study.

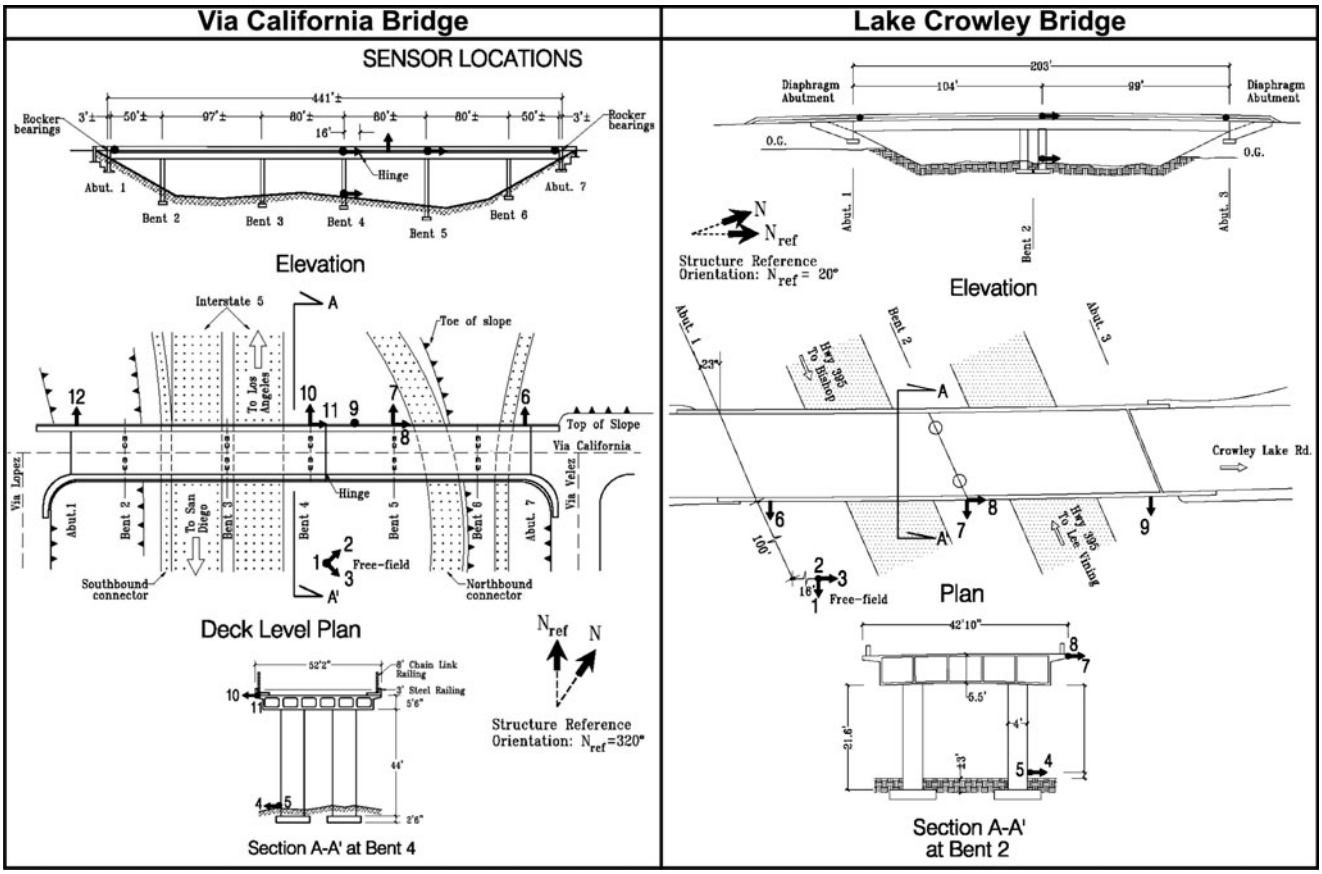

Fig. 15.1 Layouts and sensor location for both bridges (From www.strongmotioncenter.org)

The analysis was done using six low intensity ground motions. The characteristics of those records are provided below, corresponding to the rotated direction perpendicular to the bridge axis.

Bridge	Ground motion no.	Location/date	Epicentral distance (km)	PGA (cm/s^2)	PGV (cm/s)	PGD (cm)
Via California	1	Borrego Springs 07-Jul-2010	110.1	5.9	0.60	0.14
	2	Calexico 04-Apr-2010	337.1	22.8	4.00	2.35
	3	Chino Hills 29-Jul-2008	52.1	30.5	1.14	0.28
Lake Crowley	1	Mammoth Lakes 12-06-2007	12.8	38.1	0.83	0.10
	2	Toms Place 26-11-2006	16.1	12.5	0.25	0.01
	3	Qualeys Camp 18-09-2004	48.7	8.90	0.39	0.07

15.4 System Identification

The experimental model of the Via California bridge was based on the instrumented points that have transverse direction measurements, including channels at the instrumented pier base and on deck. The resulting modal parameters obtained are shown in Table 15.1.

Similarly, the Lake Crowley bridge experimental model was based on the instrumented points that have transverse direction measurement, including channels at pier base and deck. The resulting modal parameters obtained based on each ground motion records are shown in Table 15.2.

The results show consistent values, and the variability for natural frequency in both structures is very similar. The estimated damping ratios show agreement for Lake Crowley bridge, but a variation of about 50% for the Via California

Table 15.1 Transverse fundamental modal parameters for Via California bridge

GM no.	Ground motion	Frequency (Hz)	Damping ratio (%)
1	Borrego Springs 07-Jul-2010	2.688	0.834
2	Calexico 04-Apr-2010	2.518	2.524
3	Chino Hills 29-Jul-2008	2.623	1.753

Table 15.2 Transverse fundamental modal parameters for Lake Crowley bridge

GM no.	Ground motion	Frequency (Hz)	Damping ratio (%)
1	Mammoth Lakes 12-06-2007	5.342	0.356
2	Toms Place 26-11-2006	5.202	0.539
3	Qualeys Camp 18-09-2004	5.379	0.558

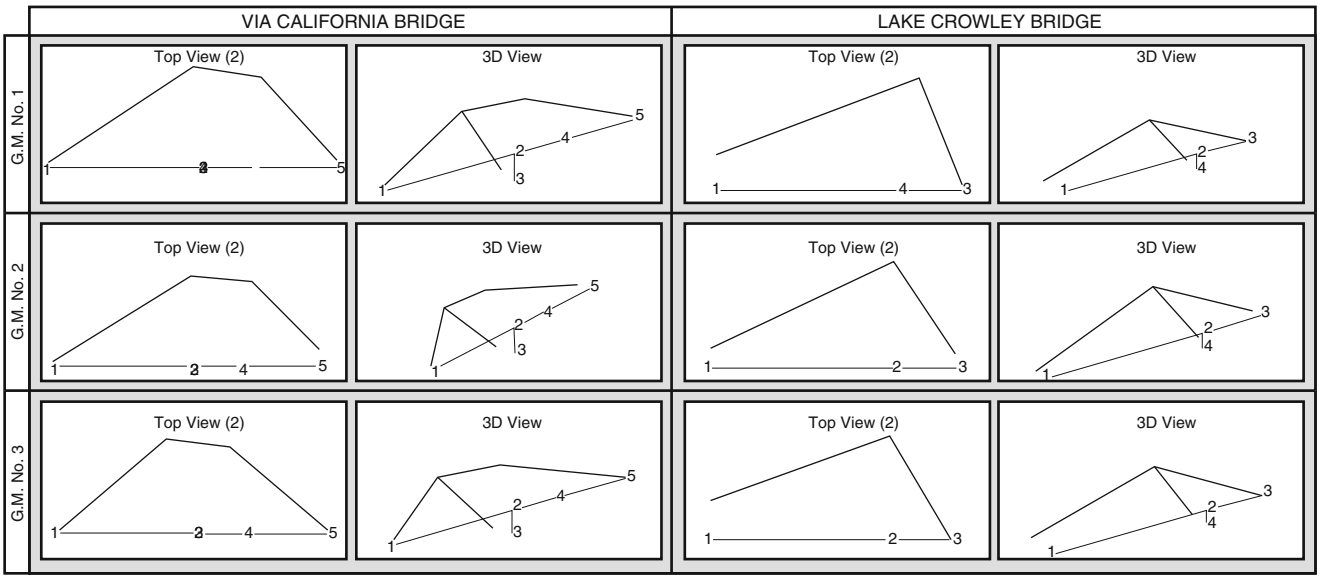

Fig. 15.2 Identified transverse fundamental modal shapes for both Via California and Lake Crowley bridges

bridge is observed. The inferred fundamental modal shapes, based on the limited instrumentation, for each ground motion and bridge are shown in Fig. 15.2.

The modal shapes shown in this plots have an expected behaviour, noticed a rigid axis rotation in the Lake Crowley bridge modal shapes, which may be related to the skewed condition of that structure. The variability in identified damping ratio values for Via California bridge can be originated from several factors, such as soil condition, integrity of the structural elements, and energy-dissipation mechanism acting after the structural retrofitting process carried out in 1999.

15.5 Response Spectra and Directionality

The response spectra for Via California bridge show general agreement in terms of coincidence between peak response and natural period response. The Chino Hills ground motion (No. 3) show a peak acceleration response in free field for periods near 1.5 s. Although the column base spectrum seems to be affected by this, the agreement corresponding to the peak at natural period remains in all cases.

The response spectra corresponding to Lake Crowley bridge case show a consistent peak for Free Field records at periods near 0.1 s, which could be related to dynamic properties of the foundation soil; this condition seems to influence the column

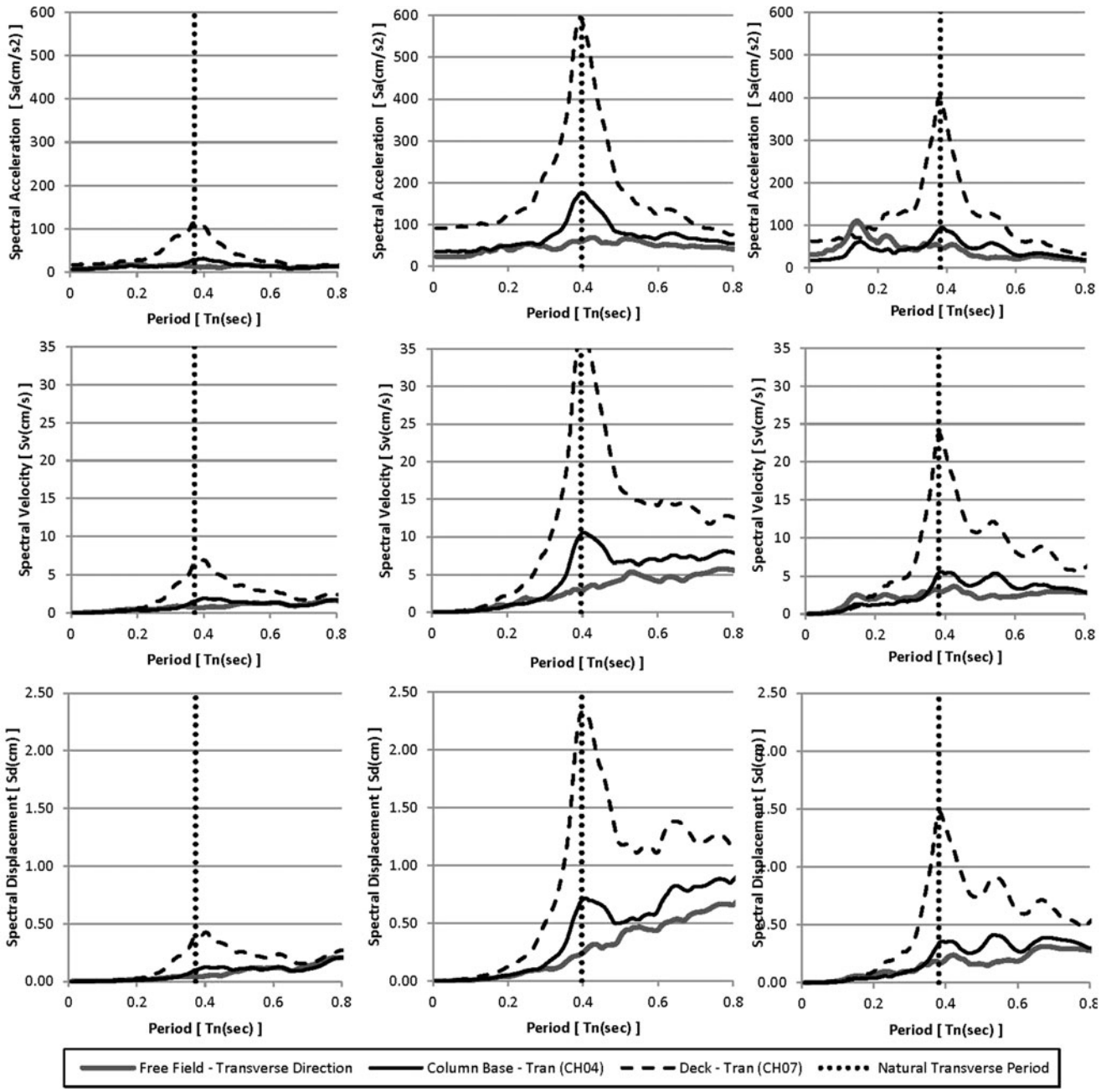

Fig. 15.3 Response spectra for Via California bridge corresponding to ground motions No. 1 (*left*), No. 2 (*center*) and No. 3 (*right*)

base response spectra increasing spectral values near that period. However, there is a fair agreement for having peak spectral values corresponding to the natural period in all cases, only slightly affected in the ground motion No. 3 (Qualeys Camp) case.

For both analyzed structures, the response spectra in all cases shows a point, with period lower and close to the natural period, before which free field spectral response values are higher than column base values. After that point the spectral response based on column base signal is predominantly higher that free field.

Figures 15.3 and 15.4 show the response spectra for both analyzed bridges.

The directionality of the ground motion has to be analyzed considering the incidence to the analyzed structure; the situation is summarized in Fig. 15.5.

In the Via California bridge, the ground shaking seems to be oriented predominantly in the bridge's transverse direction for ground motions 2 and 3. The No. 1 case does not show a clear orientation, which can be defined with similar longitudinal

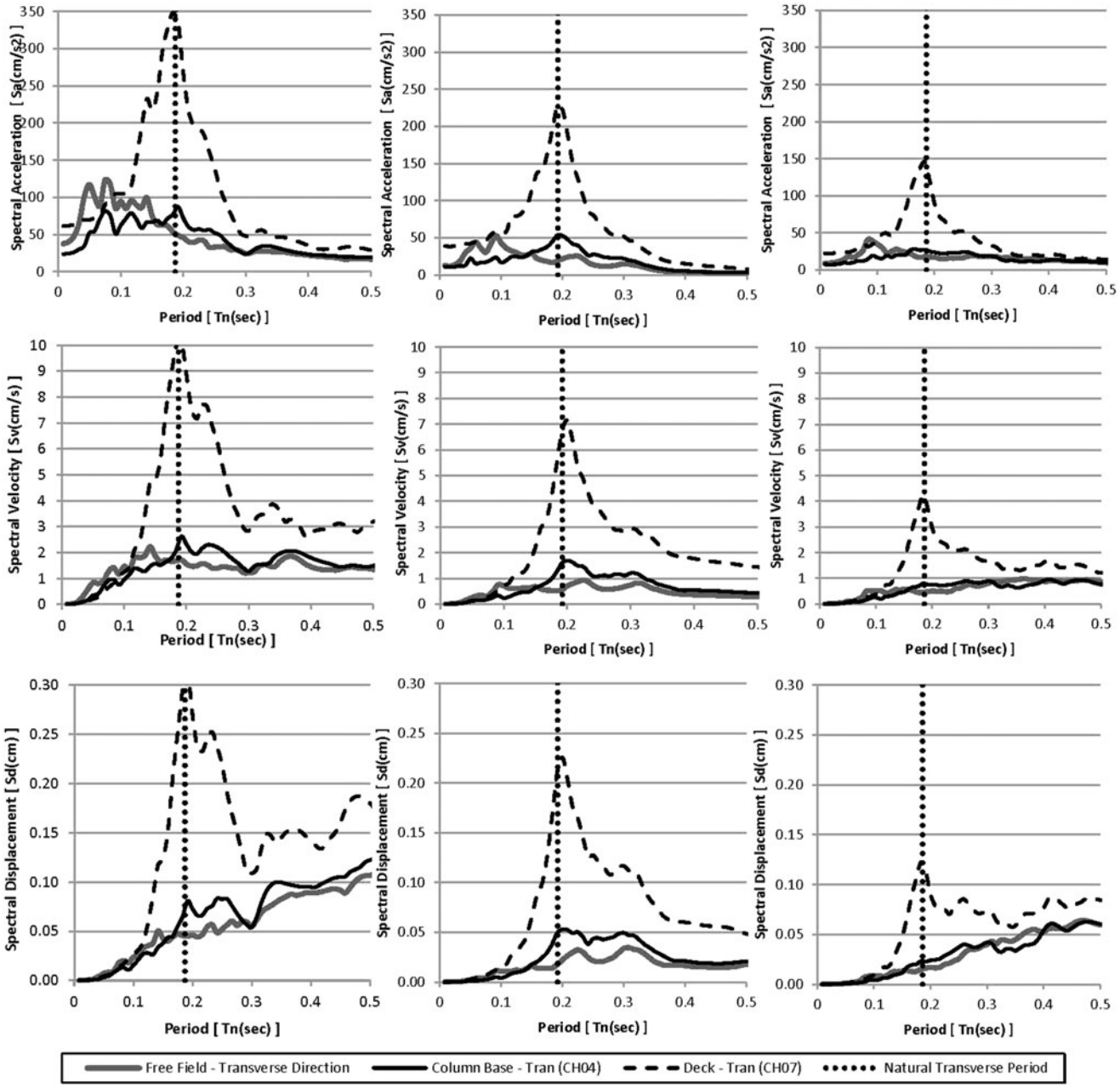

Fig. 15.4 Response spectra for Lake Crowley bridge corresponding to ground motions No. 1 (*left*), No. 2 (*center*) and No. 3 (*right*)

and transverse components related to the bridge axis. Regarding the Lake Crowley bridge case, the second and third ground motions orientations seems to have important components perpendicular to the skewed bent direction, whereas the first analyzed event seems to have more important components parallel to the skewed angle (Fig. 15.6).

The Fourier Amplitude spectra for Via California bridge case show strong agreement between free field, column base and deck for frequencies below 1 Hz in all cases. Frequencies higher that 1 Hz for the column base signal show amplitudes higher than free field, until they pass the amplification range that surrounds the natural frequency and amplitudes become lower in column base compared to free field. The Lake Crowley bridge case shows a similar behaviour, with a threshold frequency of approximately 2.5 Hz for amplitude agreement between signals.

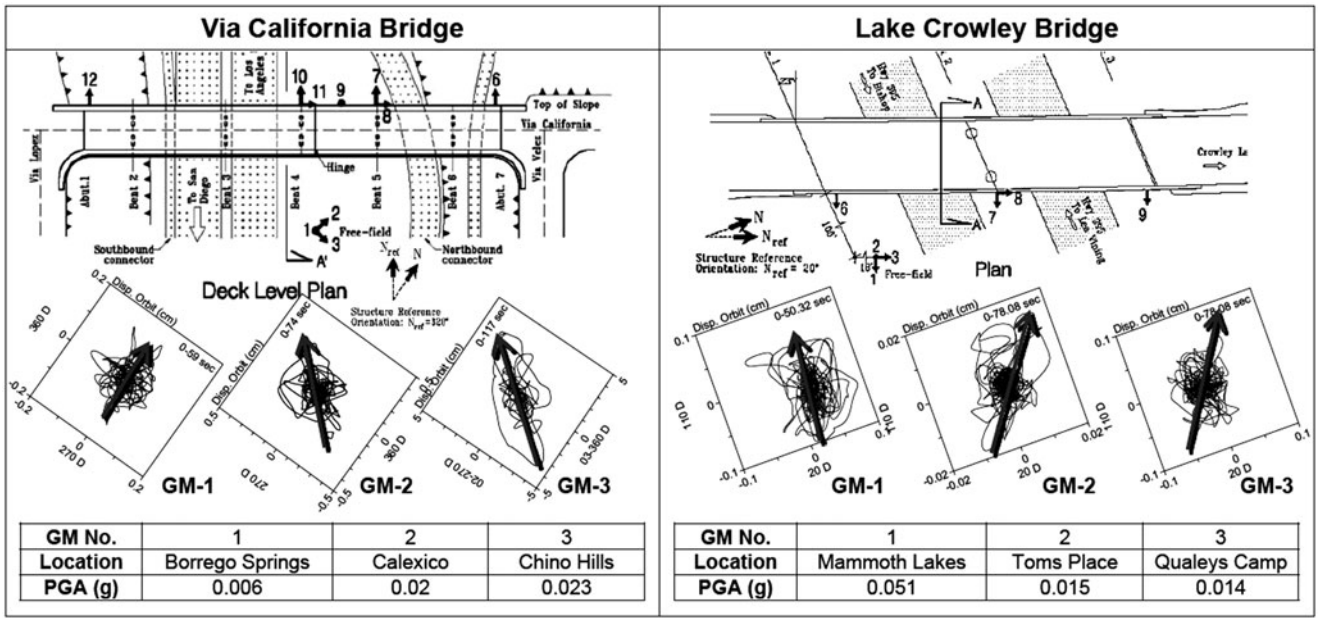

GM No.	1	2	3
Location	Borrego Springs	Calexico	Chino Hills
PGA (g)	0.006	0.02	0.023

GM No.	1	2	3
Location	Mammoth Lakes	Toms Place	Qualeys Camp
PGA (g)	0.051	0.015	0.014

Fig. 15.5 Estimated directionality of ground shakings and incidence to analyzed bridges

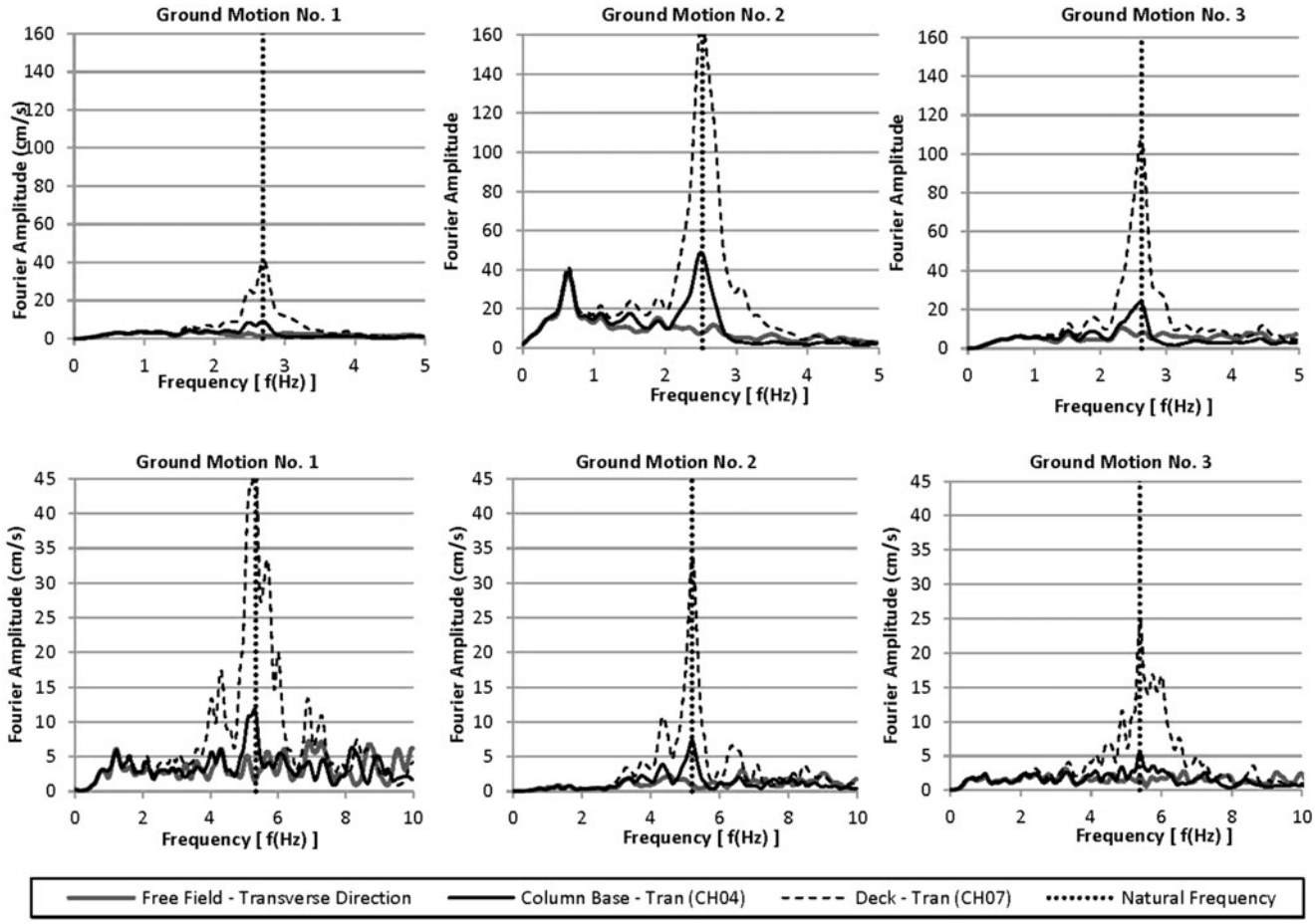

Fig. 15.6 Fourier spectra corresponding to each ground motion for Via California bridge (*top*) and Lake Crowley bridge (*bottom*)

Table 15.3 Spectral response values for Via California bridge

					Free field			Column base			Deck		
No.	Location	PGA (g)	Fn (Hz)	Tn (s)	Sa (cm/s^2)	Sv (cm/s)	Sd (cm)	Sa (cm/s^2)	Sv (cm/s)	Sd (cm)	Sa (cm/s^2)	Sv (cm/s)	Sd (cm)
1	Borrego Springs	0.006	2.688	0.372	11.95	0.71	0.04	28.09	1.52	0.10	110.29	6.28	0.38
2	Calexico	0.02	2.524	0.396	59.69	2.88	0.24	174.77	10.27	0.69	586.39	36.37	2.32
3	Chino Hills	0.023	2.623	0.381	48.07	3.09	0.18	92.26	5.39	0.34	397.87	23.52	1.46

Table 15.4 Spectral response values for Lake Crowley bridge

					Free field			Column base			Deck		
No.	Location	PGA (g)	Fn (Hz)	Tn (s)	Sa (cm/s^2)	Sv (cm/s)	Sd (cm)	Sa (cm/s^2)	Sv (cm/s)	Sd (cm)	Sa (cm/s^2)	Sv (cm/s)	Sd (cm)
1	Mammoth Lakes	0.051	5.342	0.187	51.48	1.70	0.045	81.68	2.33	0.072	342.51	10.05	0.303
2	Toms Place	0.015	5.202	0.192	19.27	0.57	0.018	53.28	1.60	0.050	227.08	6.72	0.212
3	Qualeys Camp	0.014	5.379	0.186	17.58	0.46	0.015	26.49	0.79	0.023	137.76	4.09	0.119

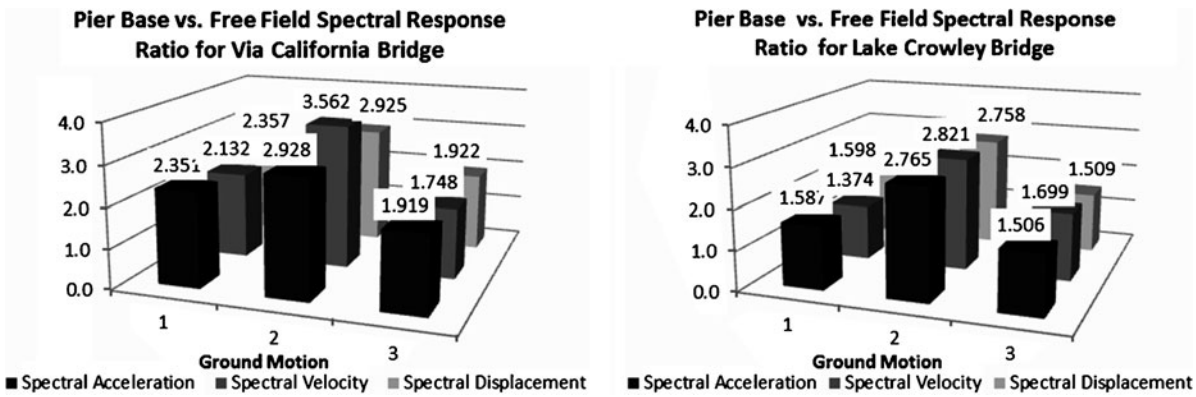

Fig. 15.7 Pier base versus free field spectral response ratios for both bridges corresponding to each ground motion

15.6 Results Analysis

The first parameter to be considered in this study is the spectral response at the corresponding natural period of each bridge, obtained for all ground motions. The resulting values are summarized in Tables 15.3 and 15.4.

Another parameter to be considered is the ratio between free field and pier base spectral responses. The results are shown in Fig. 15.7.

The following remarks can be stated based on the information provided by the previous results reports and information analysis:

- The modal analysis results show consistency in the identified fundamental frequency for both bridges and in damping ratio values for Lake Crowley bridge.
- The spectral response ratios Column Base versus Free Field corresponding to the fundamental period show a general agreement for each ground motion in both analyzed bridges, indicating clear amplification condition in all cases, which is the opposite effect that would be expected due to the soil-structure interaction effect.

- The ground motion No. 2 for Via California bridge has an important increment in that ratio compared to the other motions; considering the previously discussed variability in the identified damping ratios, this could be possibly related to the energy dissipation mechanisms acting in the structure during the event.
- The evaluation of response spectra plots indicate that this amplification effect is noticed in different magnitudes for periods higher than a threshold value, which is always near and below the natural period of the structure. On the other hand, there is a de-amplification of the spectral response for periods smaller than the threshold value.

15.7 Conclusions

The previously developed methodology highlights several aspects that can be related to the soil-structure interaction condition of the bridges, focusing on the information provided by signals at free field, column base and deck, and mainly investigating the difference between parameters obtained from free field and column base records. All the analysis remarks and conclusions in this case are linked to the low level of shaking condition that characterized the ground motions.

This method of analyzing recorded motions from bridges will be implemented by the authors to process the records from a database of recorded motions obtained from instrumented bridges around the world. The results from this investigation will be used to develop guidelines to evaluate the effects of soil-structure interaction on the seismic response of bridges.

Acknowledgements The authors would like to acknowledge the financial support from the Natural Sciences and Engineering Research Council of Canada (NSERC) through a Strategic Grant entitled “Soil-Structure Interaction in Performance Based Design of Bridges”.

References

1. Sextos AG (2009) Few thoughts on the numerical simulation of soil, structure and earthquake input. Earthquake Engineering Workshop (http://www.mendeley.com/profiles/anastasios-sextos/)
2. Stewart J, Seed R, Fenves G (1999) Empirical evaluation of soil-structure interaction effects. Pacific Earthquake Engineering Center, Berkeley, pp 9–13
3. Finn L (2010) Aspects of soil-structure interaction. In: UBC-SEABC soil structure interaction seminar proceedings, Vancouver, Canada
4. Artemis Extractor Software (2010) Structural Vibration Solutions, Inc., 1999–2003. Structural Vibration Solutions, Inc., Denmark
5. Ventura CE, Carvajal JC, Finn L, Traner J (2011) Ambient vibration testing of the Meloland road overpass. In: IOMAC 4th international operational modal analysis conference, Istanbul

Chapter 16
Dynamic Testing of a Truss Bridge Using a Vibroseis Truck

Eric V. Fernstrom, Tim R. Wank, and Kirk A. Grimmelsman

Abstract Dynamic characterization of a bridge structures can often provide a more reliable and quantitative description of its performance and condition than possible from conventional bridge inspection and rating procedures. Such characterizations are typically accomplished at the global level using either controlled or ambient vibration testing methods. Ambient vibration testing is by far the more commonly employed approach for bridges due to numerous practical and logistical advantages it has over controlled dynamic testing methods. However, ambient vibration testing relies on a number of assumptions and can be subject to limitations that may not be readily apparent in the absence of an alternative characterization result. The writers recently conducted a dynamic characterization program on an in-service truss bridge and utilized both controlled and ambient vibration test methods. The structure that was evaluated is a three-span, Parker pony truss bridge that was constructed in 1930. The forced-vibration testing was performed using a vibroseis truck. The controlled vibration tests included both burst random and sine-sweep excitations at several locations in each span. This paper describes the results of the controlled vibration tests. The results are also compared with results from ambient vibration testing of the bridge. The advantages and limitations of each characterization method are discussed.

Keywords Vibroseis truck • Truss bridge • Controlled vibration testing • Ambient vibration testing

16.1 Introduction

Bridges facilitate the efficient transport of people and goods and are vital to the nation's economic well-being. However, the nation's transportation infrastructure and its bridges continue to deteriorate. A 2008 report by AASHTO [1] describes the many significant challenges associated with managing and maintaining the safety and serviceability of bridges. The difficulty of maintaining the bridge population is compounded by limited funding for repair or replacement of structurally deficient bridges, and the significant inflation in construction costs that has occurred over time. The nation's recent concern regarding the budget deficit and the strong push in Washington to cut costs wherever possible will also impact the ability of states to adequately care for their transportation structures. In consideration of the significant number of deteriorated bridges and the limited budgets of the owners, an innovative, quantitative characterization method will be useful for better allocating limited funds for bridge maintenance, repair and replacement activities. A method that utilizes the measured responses of bridge structures would improve the reliability and effectiveness of maintenance decisions by supplementing the conventional qualitative data that is acquired from visual inspection evaluations. Quantitative characterization methods can present a more rational and complete understanding of the health of a structure than visual inspection results, and the methods can thus help focus spending on the most critical repairs.

E.V. Fernstrom, P.E. • T.R. Wank • K.A. Grimmelsman, Ph.D. (✉)
Department of Civil Engineering, University of Arkansas, Fayetteville, AR 72701, USA
e-mail: efernstr@uark.edu; twank@uark.edu; kgrimmel@uark.edu

J.M. Caicedo et al. (eds.), *Topics on the Dynamics of Civil Structures, Volume 1*,
Conference Proceedings of the Society for Experimental Mechanics Series 26,
DOI 10.1007/978-1-4614-2413-0_16,

16.1.1 Quantitative Characterization Methods

Bridges may be characterized at local or global levels by several different methods. Nondestructive evaluation techniques are commonly used for local-level characterizations of a bridge. Static or quasi-static load testing using known truck loads is a common approach for quantitatively characterizing a bridge at its global level. Analytical or numerical modeling may be considered a quantitative local or global level characterization method; however, unless such models are calibrated with measured responses to agree with the actual conditions and performance of a bridge, they represent an idealized characterization of the structure or its components. The other commonly used global characterization approach is dynamic testing.

Dynamic testing is the process of measuring the time-varying response of a structure including the effects of inertia forces. These measured acceleration responses from different locations on the structure are used to identify the modal characteristics of the bridge. The identified dynamic properties can include the natural frequencies, modal vectors, damping ratios, and modal scaling values. Since dynamic properties depend on the mass and stiffness of the structure, they can be considered to be fundamental structural properties. Changes in the structure due to damage, deterioration and environmental effects are reflected by changes in the dynamic properties of the structure. It is often easier and more practical to dynamically characterize a bridge than it is to characterize it using the other methods mentioned previously.

Dynamic testing of large civil infrastructures like bridges is usually performed using the unmeasured and uncontrolled excitation provided by the environment and traffic on the structure. This type of dynamic characterization method is referred to as ambient vibration testing or operational modal analysis (OMA). To enable mathematical analysis of the output data, the unmeasured excitation is assumed to be broadband noise, and the structure is assumed to be lightly damped with well-separated modes. With this assumption, only the measured accelerations of the structure are needed to identify its natural frequencies and mode shapes.

Dynamic testing using a controlled and measureable excitation force is referred to as experimental modal analysis (EMA). With EMA, frequency response functions (FRFs) can be developed from both the excitation and response measurements in the frequency domain. The FRFs can then be used to identify the dynamic properties of the structure using any number of modal parameter identification algorithms. Numerous time domain algorithms are also available for identifying modal parameters from EMA measurements. Controlled dynamic excitation can be provided by drop weights, impact hammers, or by using linear or eccentric mass shakers [2–4]. A primary advantage of EMA when compared to OMA is that the mode shapes can be scaled appropriately to the mass (modal scaling). Mass normalized modal vectors can then be used to generate the flexibility matrix of the structure [5, 6]. The modal flexibility matrix is very useful for globally characterizing bridges and for damage identification. It should be noted that mass normalized modal vectors cannot be developed directly from ambient vibration measurement data.

16.1.2 Objectives

The study reported in this paper focuses on the use of a vibroseis truck as a dynamic excitation device for EMA testing of bridges. Vibroseis trucks are mainly used in the energy production sector to help locate natural gas and oil reserves and are capable of producing significant dynamic forces. The University of Arkansas owns a vibroseis truck that is principally used for geotechnical research.

In this study, a truss bridge with three identical simple spans was dynamically characterized. In one experimental setup, all three spans were outfitted with a sparse array of ten accelerometers each and the vibroseis truck excited the bridge at four identical locations on each span. In the second experimental setup, a dense array of twenty-seven accelerometers was installed on a single span and the vibroseis truck excited the bridge at the same four locations. The use of both a sparse sensor array and a dense sensor array permits the benefits of using more sensors to be evaluated.

This study also examined the effect of the mass and damping characteristics of the vibroseis truck on the dynamic properties of the bridge structure. This issue was considered from two perspectives. First, the characterization developed with the vibroseis truck was compared to a characterization from ambient inputs without any truck weight on the bridge. Second, the mode shapes developed using the truck were compared for the four different truck positions on the bridge. The complete details of the dynamic testing program and the results are described in following sections of this paper.

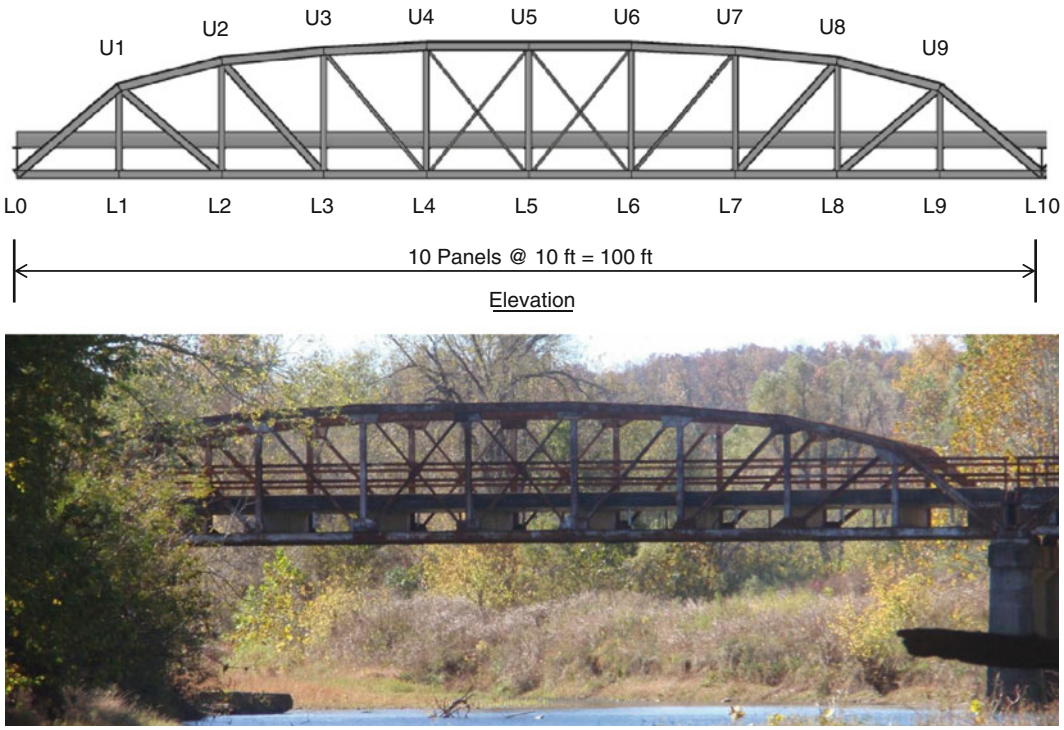

Fig. 16.1 Elevation view and photograph of typical truss span

16.2 Bridge Description

The bridge studied in this project is a Parker pony truss that was built in 1930 and carries two lanes of vehicular traffic across the West Fork of the White River in Fayetteville, Arkansas. The bridge has three identical simply-supported truss spans that are each 100 ft in length and consist of ten panels. The width of the bridge measured from center-to-center of the trusses is 22′-4″ and the vertical height of the truss at midspan is 14 ft. The deck is an 8-in. thick reinforced concrete slab supported by I-shaped rolled steel floorbeams spanning between the lower panel points of the upstream and downstream trusses. The truss members consist of rolled and riveted built-up sections as follows: (1) top chords: two channels, a top cover plate, and lacing bars; (2) bottom chords: two channels with batten plates; (3) verticals: I-beams; and (4) diagonals: I-beams for stress reversal members and two angles with batten plates for tension-only members. Each truss span is simply supported and the adjacent ends of spans share a concrete pier. The outer ends of the two end spans are supported on concrete abutments. Neither construction plans nor shop drawings have been found for the bridge and the foundation details are unknown. Field measurements were used to establish the member geometric and section properties. An elevation view and photograph of a typical span are shown in Fig. 16.1.

16.3 Experiment Design and Execution

16.3.1 Vibroseis Truck

A vibroseis truck imparted controlled vertical dynamic excitation to the truss spans. Figure 16.2 shows a photograph of the vibroseis truck and a schematic of its axle configuration. The truck was weighed at the bridge site and had a total weight of 23,440 lb. According to the manufacturer, the vehicle is capable of producing 6,000 lb of peak dynamic force across a frequency range of 17–225 Hz. As with most dynamic excitation devices, the force generated by the truck diminishes at lower frequencies. The peak force is about 1,000 lb at 5 Hz and about 300 lb at 3 Hz based on the manufacturer's specifications.

The dynamic excitation force is applied to the structure by hydraulically pressing a large steel shoe of approximately 3-foot diameter onto the deck surface, resulting in a portion of the vehicle weight being supported by the shoe. A 311-lb steel weight on the shaker apparatus is moved vertically by hydraulic actuators to produce dynamic forces which are transferred to the structure through the shoe. The hydraulic actuator system is computer controlled and any analog signal can be input.

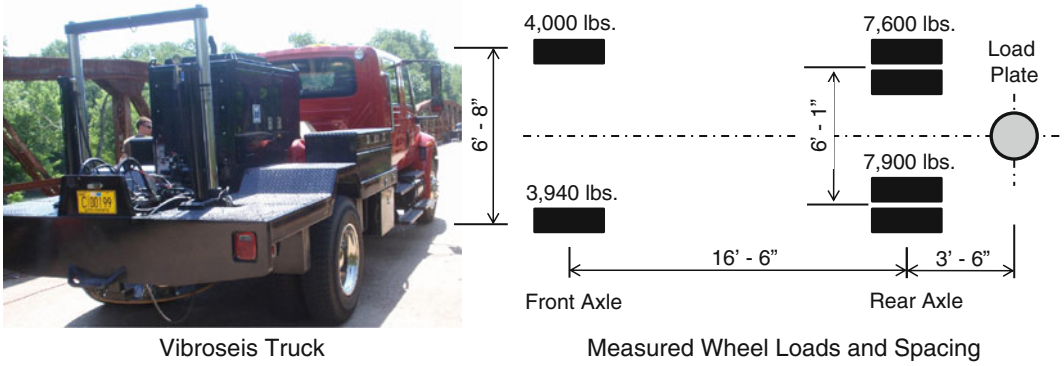

Fig. 16.2 Vibroseis truck and its axle configuration

For this project the truck was positioned at four different locations on each span. A force transducer that was placed between the deck and the loading shoe enabled accurate recording of the dynamic excitation force. Accelerometers installed on both the shoe and on the steel weight were monitored during the testing program; however, only the force transducer data were utilized for this paper.

16.3.2 Instrumentation and Data Acquisition

The instrumentation plan developed for this investigation used two different sensor setups. Setup 1 featured a relatively dense spatial array of vertically oriented accelerometers concentrated in only Span 3. Setup 1 had nine accelerometers with one sensor located at each of the lower interior panel points of the upstream and downstream trusses and nine accelerometers on the deck surface along the longitudinal centerline of the bridge. The floorbeam lines at the supports were excluded from the instrumentation scheme as the vibrations at these locations would have low signal-to-noise ratios. The sensors used were Model 393B05 and Model 393C accelerometers both from PCB Piezotronics, Inc. The 393B05 accelerometer has a nominal amplitude range of ± 0.5 g and a nominal sensitivity of 10 V/g. Twelve of these sensors were used at locations on the truss where the measured vibration amplitudes were expected to be smallest. The 393C accelerometer has a nominal amplitude range of ± 2.5 g and a nominal sensitivity of 1 V/g. Fifteen of these accelerometers were used at locations that were expected to experience larger vibration amplitudes. The instrumentation plan used in Setup 1 is illustrated in Fig. 16.3.

The second instrumentation setup (Setup 2) employed thirty accelerometers with ten in each of the three spans of the bridge crossing. In this setup, the accelerometers were located only at the lower panel points of the upstream and downstream trusses. This relatively sparse sensor layout was planned to evaluate the effect of dynamic excitation being transmitted from one span to another via the piers. Setup 2 used the same types of sensors as Setup 1 and Fig. 16.4 shows their layout on the individual truss spans.

The accelerations were recorded during dynamic testing using a National Instruments PXI mainframe with Model 4472B Dynamic Signal Acquisition Modules. Each eight-channel data acquisition module has 24-bit resolution with 110 dB of dynamic range. The sampling rate used for the testing was 1,000 Hz, which was the minimum recommended sampling rate for these data acquisition modules. This sampling rate provided a usable frequency range of 0–500 Hz for the measurements, which is significantly greater than the frequency band of interest for the dynamic characterization of this bridge.

16.3.3 Dynamic Testing Program

The testing program consisted of placing the vibroseis truck at four different positions in Span 3 for instrumentation Setup 1, and at the same four positions for instrumentation Setup 2 but in each of the three spans. The loading shoe was set at each quarter-point and at midspan along the bridge centerline. The fourth driving point consisted of the shoe being positioned about 5 ft away from the face of the upstream curb at bridge midspan.

Two types of dynamic excitation were used at each driving point location on the bridge using the vibroseis truck. A burst random excitation signal was created in MATLAB from Gaussian white noise and then low pass filtered to produce a forcing signal with a flat power band from about 1 to 120 Hz. The burst random signal starts and ends with approximately zero force to create a periodic signal and minimize the effects of leakage during the fast Fourier transform. The time duration of the burst random signal was 17 s. The second type of excitation was a swept-sine signal that was generated using a built-in function on an arbitrary signal generator and ranged from 3 to 100 Hz. A linear sweep between these frequencies was

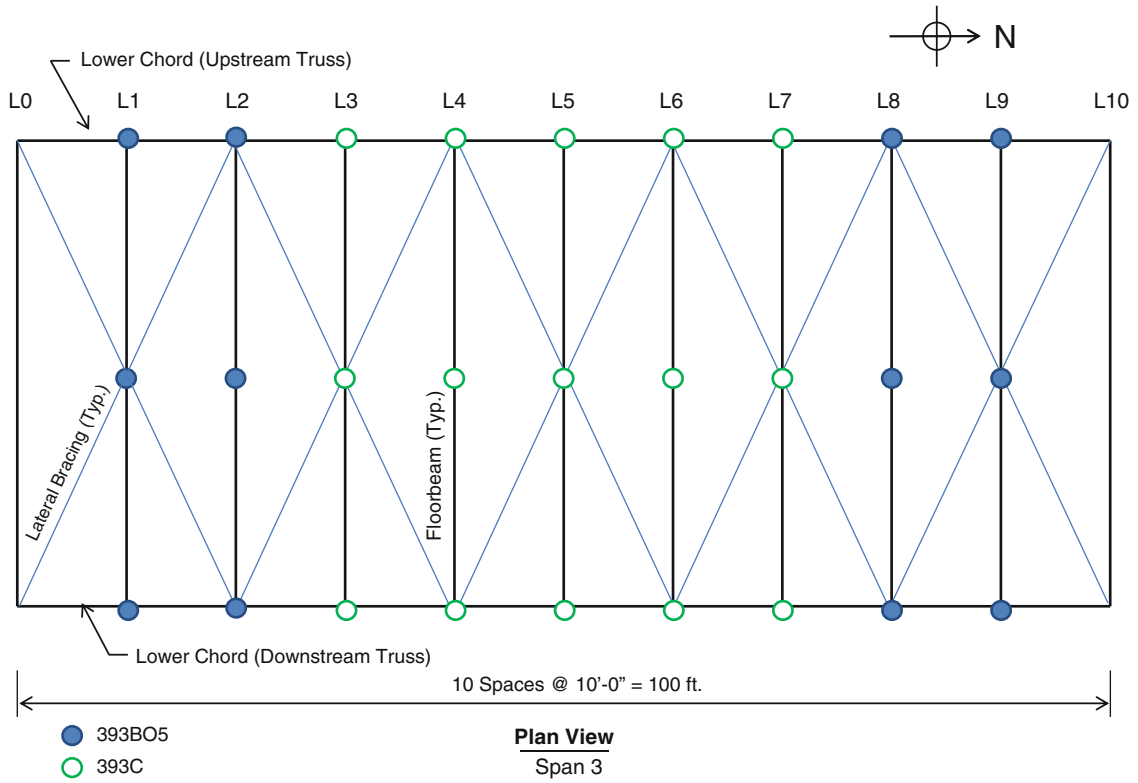

Fig. 16.3 Accelerometer layout for Span 3 – Setup 1

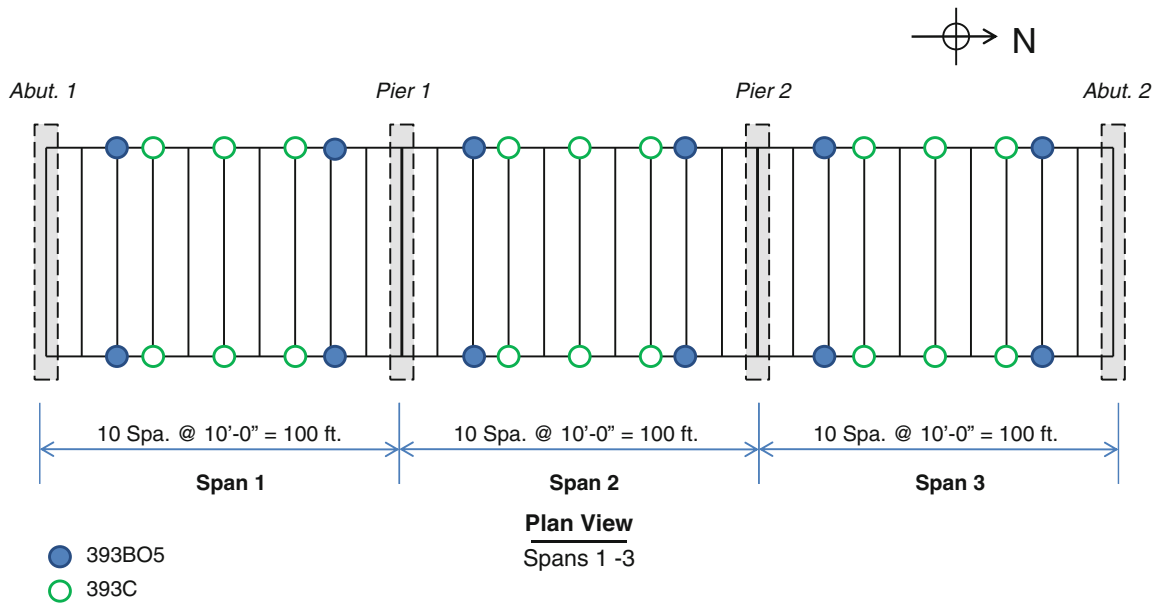

Fig. 16.4 Accelerometer layout for all truss spans – Setup 2

selected and generated over 97 s. The bridge vibrations were recorded for 20 s for each burst random excitation run and for 110 s for each swept-sine excitation run. A total of ten test runs were executed for the burst random signal and five test runs for the swept-sine signal for each truck position to enable averaging of the measurements.

The data used for this paper also included ambient vibration data that were recorded for each of the three spans several months prior to the testing with the vibroseis truck. The ambient vibration data for each span was continuously collected in

5 min blocks at 1,000 Hz for a total duration of 4 h. The bridge is located in a rural area with an estimated ADT of less than 50, and thus the ambient excitation was primarily provided by wind and seismic ground motions.

16.4 Data Processing Procedures

16.4.1 Forced-Vibration Data Processing

The forced-vibration data was processed using code that was written in MATLAB. The raw acceleration (g's) and force (lb-f) measurements were first detrended to remove any DC offset or linear drift from the readings. A fast Fourier transform (FFT) converted the time domain data to the frequency domain, and cross-power and auto-power spectra were calculated. FRFs were constructed from these spectra using the H1 algorithm, which minimizes noise on the output measurements. Each truck position provided one column of the FRF matrix. The complex mode indicator function (CMIF) algorithm was then executed on the H1 FRF matrix. The CMIF algorithm involves singular value decomposition, and peaks in the CMIF plot represent likely natural frequencies of the structure. Enhanced frequency response functions (eFRFs) were then calculated for each selected peak and, finally, the mode shape at each selected natural frequency was plotted. Both the eFRFs and the mode shapes were checked to ensure that selected peaks were vertical natural frequencies of interest of the structure. The specific equations used to implement these algorithms are not shown for brevity, but they are readily available in the literature: H1 algorithm [6], CMIF and eFRF [7–9].

16.4.2 Ambient Data Processing

All data from the ambient vibration cases were processed using the peak-picking (PP) method. The raw data files were first imported into MATLAB and the individual data files were assembled into a single long record. The data were detrended and auto-power spectral density (ASD) and cross-power spectral density (CSD) transforms were computed from the time domain data using Welch's periodogram in MATLAB. The data records were divided into blocks of 4,096 points and a Hanning window was applied to each. The resulting frequency resolution of the spectral data was 0.05 Hz. The ASD spectra computed for the individual sensors were normalized and summed together to create a single mode indicator function for the structure. Peak-picking was performed on this function to identify possible natural frequencies for the bridge span. The operating mode shapes were estimated using the ASD magnitude for each sensor at the identified frequencies to establish the mode shapes. The CSD vectors were used to establish the phase relative to a selected reference channel. A set of operating mode shapes was computed for each peak using all of the accelerometers as reference channels. Each mode shape was reviewed to ensure an actual natural frequency was selected during the peak picking process.

16.5 Analysis 1: Dense Sensor Array Versus Sparse Sensor Array

The subject bridge was designed as three identical statically determinate truss structures. The actual behavior of the bridge is governed by its structural details which lead to uncertainties and redundancies that are not easily quantified from idealized truss assumptions. The in-service bridge is somewhat indeterminate from an analytical perspective since the joints are made with riveted gusset plates, the diagonals include tension-only "counters", and the concrete deck envelops the floorbeam top flanges producing some amount of composite behavior in both the longitudinal and transverse directions. These complexities make the structure an ideal candidate for dynamic characterization since the in-service behavior of the bridge cannot be readily estimated by typically idealized engineering analyses. However, experimental modal analysis of bridge structures is still largely experimental and there is no commonly referenced publication stating how many sensors to use and where to place them for any given structure. Thus, two disparate densities of sensors were used on this bridge to evaluate how much, if any, additional information would be provided by the added sensors.

On this bridge, the additional sensors enabled the identification of far more natural vertical modes of vibration than could be identified otherwise. The 27 accelerometers installed on Span 3 in Setup 1 enabled the easy identification of the first 8 bending modes and the first 4 torsional modes whereas Setup 2 could only confidently identify bending modes 1, 2, 3 and 5

Table 16.1 Natural frequencies found using the dense and the sparse sensor arrays

Mode no.	Description	Dense array freq. (Hz)	Sparse array freq. (Hz)
1	Bending 1	4.65	4.60
2	Torsion 1	6.84	6.71
3	Bending 2	9.43	9.51
4	Bending 3	12.77	12.95
5	Torsion 2	17.02	–
6	Bending 4	17.09	–
7	Bending 5	19.55	19.69
8	Bending 6	22.54	–
9	Torsion 3	23.12	23.27
10	Bending 7	27.50	–
11	Bending 8	29.82	–
12	Torsion 4	30.49	–

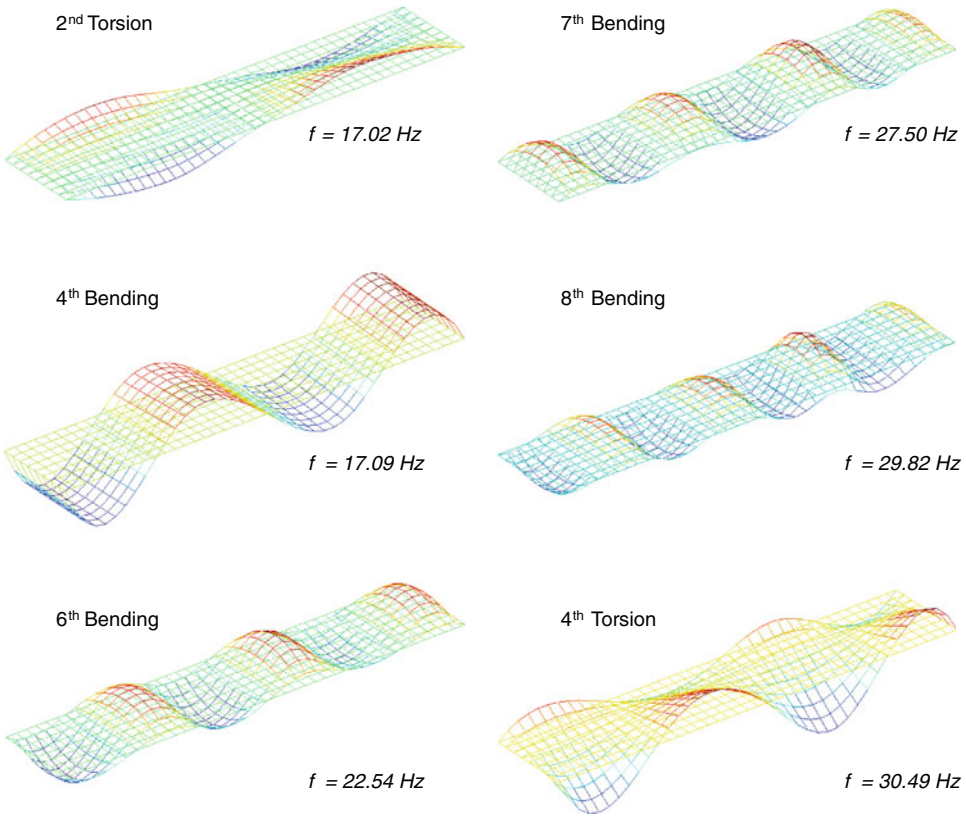

Fig. 16.5 Mode shapes found by dense sensor array but not routinely found by sparse array

and torsional modes 1 and 3. Table 16.1 lists the vertical modes consistently found with each setup and Fig. 16.5 displays the mode shapes identified by Setup 1 that were not identified by Setup 2.

While it is certainly obvious that the exact same modes of vibration existed within the structure independent of the number of sensors employed during the experiment, it is still worth noting that modes can easily be missed without an adequate instrumentation array. Although a truss is typically considered to be the simplest type of structure in terms of engineering analysis, its dynamic behavior is far more complicated than a multi-girder bridge. Overall, this paper does not attempt to present guidance on selecting a minimum instrumentation scheme for simple-span, through-truss structures; however, it is clear that capturing accurate mode shapes requires a significant number and appropriate spatial array of accelerometers.

Table 16.2 MAC values for vibroseis truck in various positions compared to truck at center of span

Mode no.	Description	Driving point 1 (%)	Driving point 2 (%)	Driving point 3 (%)
1	Bending 1	99	99	98
2	Torsion 1	99	99	97
3	Bending 2	100	98	99
4	Bending 3	90	96	98
7	Bending 5	84	93	91
8	Bending 6	83	94	86
9	Torsion 3	78	85	82

16.6 Analysis 2: Vibroseis Truck Mass and Damping Consideration

The vibroseis truck is a useful device for EMA of bridges. First, because the truck is a legal vehicle, it can be easily and rapidly deployed to any bridge location. Second, the truck is purposely built to move between test locations with minimum setup time and the relocation of the truck on a bridge is exceptionally fast. Third, the truck can apply large dynamic forces to the structure in either the vertical or lateral directions so that signal to noise ratio in the measured vibrations is maximized. Finally, the dynamic excitation provided by the truck can be recorded along with the bridge vibration responses. These trucks have drawbacks as well. The first is cost and availability. These vehicles are not extremely common and rental costs can be expensive. Second, using the truck requires a lane closure at the least, and for best results a full bridge closure is recommended so that unmeasured inputs are minimized. The truck is most useful on low ADT roads where traffic excitation may be inadequate for ambient analysis. Third, the weight and damping of the truck may have an impact on the frequencies and mode shapes for some structures.

The weight of the vibroseis truck and the damping provided by its shock absorbers will have some affect on the measured modal characteristics of the structure. To verify this assumption, the mode shapes are compared for different spatial locations of the truck. "Analysis 1" illustrated that the denser sensor array was important in the precision of the mode shapes. Therefore, the mode shape MAC (modal assurance criteria) [10] values are compared utilizing only the mode shapes from Span 3 with experimental Setup 1. Since it is well known that trusses are materially efficient structures that minimize weight, the impact to the fundamental modal properties of the structure are expected to be noticeable given the significant mass of the vibroseis truck.

Table 16.2 shows the variation in MAC values (expressed as a percentage) for Span 3. The mode shape with the vibroseis shoe at span center-point (driving point 4) is used as a baseline, and the mode shapes with the shoe at the other three driving points described previously are compared to this case. The data shows that the position of the heavy truck (23 kips) impacts the mode shapes of the light truss bridge (290 kips per span) for higher modes. The character of the lower mode shapes are not significantly impacted by the truck position.

16.7 Analysis 3: Vibroseis Versus Ambient Characterization

As mentioned previously, the vibroseis truck is a useful tool for dynamic characterization of bridges, but the mass and damping of the truck may alter the output. Therefore, in addition to the discussion immediately preceding, the basic measured natural frequencies of the spans determined with the vibroseis truck are compared with those determined from ambient input alone. To clarify, the previous discussion focused on recognizing that different truck positions altered modal outputs whereas this discussion will focus on the difference in natural frequencies with no truck on the bridge versus those obtained with a (vibroseis) truck on the bridge.

Table 16.3 shows the frequencies of the most basic natural modes of the structure that were captured using the ambient vibration characterization method. Since the average daily traffic (ADT) on this bridge is very low (a few passenger vehicles per hour and no truck traffic), these frequencies are not affected by heavy vehicle crossings. The natural frequencies identified with the vibroseis truck present on the span are also shown and the difference is highlighted. The data shows that the truck has a significant impact on the lower frequencies, but little impact on the higher frequencies. Therefore, EMA using the vibroseis truck must implicitly consider the fact that the truck will alter the results. The vibroseis truck is an able exciter of the structural system, but its mass and damping necessarily modify the results for a light structure.

Table 16.3 Frequencies of selected modes found by vibroseis and by ambient excitation

Mode no.	Description	Vibroseis truck excitation (Hz)	Ambient excitation (Hz)	Percent diff. (%)
1	Bending 1	4.60	4.30	6.5
2	Torsion 1	6.71	6.30	6.1
3	Bending 2	9.51	9.52	0.1
4	Bending 3	12.95	12.99	0.3
7	Bending 5	19.69	19.87	0.9
9	Torsion 3	23.27	23.49	0.9

16.8 Conclusions and Future Work

- The comparison of clear vertical modes found for the dense and sparse sensor arrays greatly favors the dense sensor array on this bridge. It is concluded that the complexity of this "simple" bridge type requires a dense array to capture the mode shapes. However, significant further work is required to establish a minimum spatial array of sensors to capture the necessary modal information.
- It is clear from the data analysis that the vibroseis truck is a capable excitation device for experimental modal analysis of bridges. The truck was able to clearly excite multiple modes of the subject truss bridge.
- The mass and damping of the vibroseis truck alters the higher mode shapes of the relatively light truss structure as shown by MAC comparison with the truck in different positions on a single span. The drive for structural health monitoring requires exceedingly consistent modal data and the changes caused by the added mass of this truck probably exceed those thresholds.
- The mass and damping of the vibroseis truck alters the lower natural frequencies of the truss as shown by ambient characterization methods versus EMA methods. Again, this impacts the usefulness of the truck for structural health monitoring.
- Additional future effort is required to determine why the truck position modifies the higher frequency mode shapes but not the lower frequency mode shapes, and to determine why the presence of the truck alters the lower natural frequencies by not the higher natural frequencies. This may be most readily accomplished through simulations with a finite element model of the bridge.

Overall, the vibroseis truck is a useful platform for EMA. The truck can provide strong dynamic input and is highly transportable. However, the mass and damping of the truck impact modal responses and the import of this must be evaluated on a project by project basis.

Acknowledgements This paper is based upon work supported by the U.S. Department of Homeland Security under Grant Award Number 2008-ST-061-TS00. The views and conclusions in this paper are those of the authors and should not be interpreted as necessarily representing the official policies, either expressed or implied, of the U.S. Department of Homeland Security. The authors would also like to acknowledge Dr. Brady Cox and his Ph.D. student Clint Wood for their expert assistance with the vibroseis truck.

References

1. American Association of State Highway and Transportation Officials (2008) Bridging the gap: restoring and rebuilding the nation's bridges. American Association of State Highway and Transportation Officials (AASHTO), Washington DC, July 2008
2. Farrar CR, Duffey TA, Cornwell PJ, Doebling SW (1999) Excitation methods for bridge structures. In: Proceedings of the 17th international modal analysis conference, Kissimmee, pp 1063–1068
3. Peters B, Meack J, De Roeck G (2000) Excitation sources and dynamic system identification in civil engineering. In: Proceedings of the European COST F3 conference on system identification and structural health monitoring, pp 341–350, June 2000
4. Cunha A, Ceatano E (2006) Experimental modal analysis of civil engineering structures. J Sound Vib 40(6):12–20
5. Zhang Z, Aktan AE (1998) Application of modal flexibility and its derivatives in structural identification. Res Nondestruct Eval 10(1):43–61
6. Allemang RJ (1999) Vibrations: experimental modal analysis. UC-SDRL-CN-20-263-663/664 course notes. UC-Structural Dynamics Research Laboratory, Cincinnati. Retrieved from http://www.sdrl.uc.edu/academic-course-info/vibrations-iii-20-263-663
7. Phillips AW, Allemang RJ (1998) The enhanced frequency response function (eFRF): scaling and other issues. In: Proceedings of the international conference on noise and vibration engineering (ISMA), Katholieke Universiteit Leuven, Belgium, vol 1, pp 385–392
8. Catbas FN, Brown DL, Aktan AE (2006) Use of modal flexibility for damage detection and condition assessment: case studies and demonstrations on large structures. J Struct Eng 132(11):1699–1712
9. Catbas FN, Brown DL, Aktan AE (2004) Parameter estimation for multiple-input multiple-output modal analysis of large structures. J Eng Mech 130(8):921–930
10. Allemang RJ (2003) The modal assurance criterion (MAC) – twenty years of use and abuse. Sound Vib 37(8):14–21

Chapter 17
Modal Identification of a Cable-Stayed Bridge by Means of Truck Induced Vibrations

Tommaso Argentini, Marco Belloli, Lorenzo Rosa, Edoardo Sabbioni, Alberto Zasso, and Marco Villani

Abstract This paper presents the results of a field testing campaign performed on the Adige bridge, a highway cable-stayed bridge located 70 km southeast of Verona, in the north of Italy. The structure has an overall length of 580 m and a main span of 310 m and is currently the longest cable-stayed bridge in Italy. The dynamic tests described were conducted before the bridge opening to the traffic. In order to excite the bridge a 40000 kg truck was run at several constant speeds on a series of rectangular obstacles equally spaced along one of the bridge lanes. The dynamic response of the bridge deck was measured through servo-accelerometers. The position of the accelerometers along the bridge, the distance between the obstacles and the vehicle speeds were selected on the basis of a 3D Finite Element model of the structure. The bridge modal parameters were extracted applying the least square complex exponential method (LSCE) to the free decay time histories obtained through the random decrement technique (RDT) and were compared with the ones of the FE model.

Keywords Cable stayed-bridge • Experimental testing • Modal identification

17.1 Introduction

The increasing span length of recent cable-stayed bridges, allows this configuration to be an alternative to suspension bridges and it implies higher wind and traffic-induced vibrations to be considered at design stage. The complexity of the problem is increased due to the highly nonlinear behaviour of the cables with sag and the coupling between the cables and the bridge deck vibration. Several cases of parametrically excited cable vibrations have been recorded on this type of bridges [1], Variations in cables tension due to girder or tower vibrations, has led to large oscillations in a specific range of frequencies. For this reason it is extremely important to assess the dynamic stability of the structure by the knowledge of the full scale damping. An accurate estimate of this parameter cannot be provided by a finite element model of the structure, since it is affected by the already mentioned geometric non-linearities and by the materials' behaviour, so experimental field tests are generally required.

The present paper deals with the modal identification of the deck of the Adige bridge, a cable-stayed bridge recently erected in locality Piacenza d'Adige (Padova, Italy) in the frame of a new highway link (see Fig. 17.1); the bridge has two towers 100 m high and a main span of 310 m. The excitation of the structure is obtained through an heavy vehicle passage on the bridge deck [2], [3], [4]. In order to properly design the dynamic tests to be performed, a FE model of the bridge was developed and it was used to compute the modal shapes of the structure and predict the force which is required for the excitation system to induce a precise level of vibration on the structure; the model reliability was verified by comparing the numerical frequencies and mode shapes to the one deduced by the accelerometric measurements. The finite element model of the bridge, updated with all the measured modal parameters can also be used as baseline for future health monitoring studies of the structure.

T. Argentini • M. Belloli • L. Rosa • E. Sabbioni (✉) • M. Villani
Dipartimento di Meccanica, Politecnico di Milano, Via La Masa 1, Milan, Italy
e-mail: edoardo.sabbioni@polimi.it

A. Zasso
Department of Mechanical Engineering, Politecnico di Milano, Via La Masa 1, 20156 Milan, Italy
e-mail: alberto.zasso@polimi.it

J.M. Caicedo et al. (eds.), *Topics on the Dynamics of Civil Structures, Volume 1*,
Conference Proceedings of the Society for Experimental Mechanics Series 26,
DOI 10.1007/978-1-4614-2413-0_17,

17.2 Experimental Setup

The bridge excitation required for the modal analysis was obtained through the road-tire interaction of an heavy vehicle moving on the bridge deck; for this purpose, a full load 4-axles truck weighting 40000 kg was run along one lane of the bridge, which was set up with a series of 21 equally spaced obstacles (see Fig. 17.2): the thin steps were planks of wood with rectangular section, 40 cm wide per 3 cm thick. The distance between them was d = 15 m (see Fig. 17.3).

Since the load is asymmetrical with respect to the bridge centre line, both bending and torsional modes are forced. In order to identify at least the first six modes of the structure, a wide band excitation was required; for this reason the tests were carried out for several speed of the moving load, ranging from 5 to 35 km/h.

Fig. 17.1 Overview of the 'Ponte sull'Adige' bridge

Fig. 17.2 Aerial view on the bridge and truck passing on the obstacles on the deck

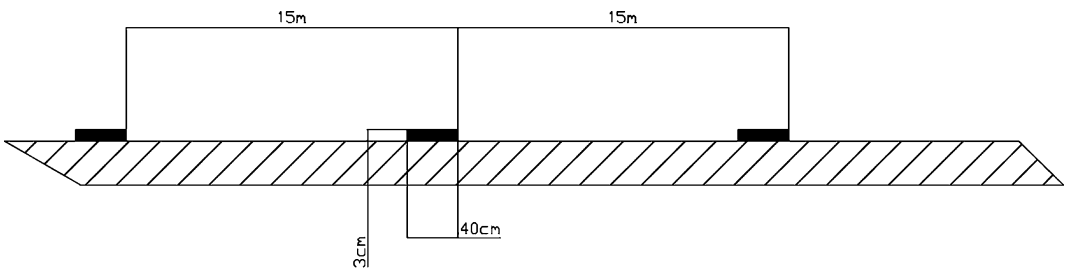

Fig. 17.3 Positions of the obstacles on the bridge lane

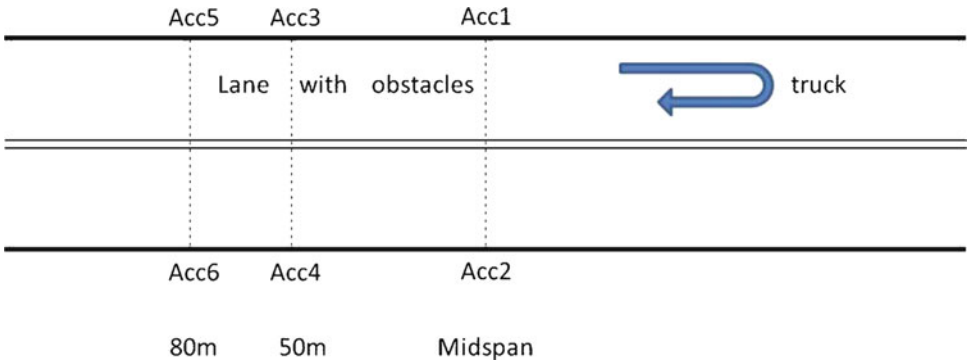

Fig. 17.4 Positions of the servoaccelerometer on the bridge deck

The bridge deck dynamic response was monitored in six measurement points which are considered to be sufficient to identify the modal deflected shapes for the lower natural frequencies. The servoaccelerometers employed for this purpose have a sensibility of 0.1 g/V and their passband starts from zero Hz; as the mode shapes present certain symmetries with respect to the bridge midspan, the sensors were placed on one side only, at the two extremities of the deck, as showed in Fig. 17.4. The distances between the accelerometric sections were chosen on the basis of the expected mode shapes, which were computed in advance for the FE model of the structure. During each acquisition the truck covered back and forth the track, passing on the cleats at constant speed.

17.3 Data Processing

For each run time histories of 240–400 s were recorded, depending on the vehicle speed, using a sampling rate of 100 Hz; the acceleration time histories of the 16 tested speeds were then joined together in order to obtain a single acquisition containing the response of the structure to a wide-band excitation. Since the most relevant modes of the bridge lie in the range below 1.3 Hz, the signal was digitally low-pass filtered in order to preserve the frequency contribution up to 1.4 Hz.

The dynamic tests designed for the bridge rely on a forcing system, which provides a significant amount of energy and allows to properly excite the structure with a series of impulses. The force exerted to the deck remains unknown, but this kind of excitation can be considered very similar to a random process in the investigated frequency range. The identification of the modal parameters was performed using an output-only approach: in the present work the random decrement technique (RDT) was employed together with the least square complex exponential method, LSCE (or Prony method).

The random decrement technique is a time domain signal processing method, which is developed for constructing a characteristic signature from random response signals [5]. Such RD signature represents the free decay vibration of the considered dynamic system under Gaussian white noise assumption and certain initial conditions. In fact, the response of a system to a random input is, composed by three parts: the response to an initial displacement, the response to an initial velocity and the response to the random input loads between the initial state and the current time instant. By averaging a large number of time segments of the response with the same initial condition, the random part of the response will tend to disappear from the average, and what remains is the response to the initial condition, that is, a free vibration decay of the system. The RDT also plays an important role in the reduction of the white noise content of the measured structural response.

The modal identification is performed with the LSCE technique, a time domain method which explores the relations between the impulse response functions (IRF) of a multi-degrees-of-freedom system and its complex poles: the IRFs are approximated by series of complex exponentials, and each of them contains eigenvalues and eigenvectors of a certain mode. The model requires the resolution of a polynomial equation, the so-called Prony equation, whose coefficients are estimated on the basis of the experimental IRF and whose roots are the poles of the system [6]. The IRF can be derived from the inverse Fourier transform of a FRF or from a random decrement process, as in the present case. In this algorithm the number of poles of the mechanical system must be given as an input: if the mathematical model has few degrees of freedom, some of the modes will not be reproduced, while, if the model has too many dofs, some fictitious pole will be detected. In order to overcome this problem the Prony algorithm is iterated many times varying the number of dofs of the model and then poles stabilization diagrams are typically used, in which the computed modal frequencies are plotted as a function of the number of poles. The physical modes of the structure are the ones for which the estimate of the frequency is stable while varying the poles of the model.

17.4 Results

Figure 17.5a shows as an example the concatenated time history measured by acceleration 1, while Fig. 17.5b shows the time history of a single tested speed. The modal identification procedure was performed on specific acceleration signals, choosing the measurement sections located where the mode shapes reach their maximum deflection, or anyway on the time histories with clearer peaks of the structure response.

For instance, in the dynamic response of accelerometer 1, represented in Fig. 17.6a through its Fourier transform, it is possible to appreciate the contribution of the first torsional mode (0.579 Hz) and of the third bending mode (0.978 Hz). The spectrum of the accelerometer 4 (see Fig. 17.6b) shows the peaks of the second torsional mode (1.096 Hz) and of the fourth bending mode (1.28 Hz). As far as the first two bending modes are concerned, their contribution to the measured response is quite small, probably because of a higher modal damping ratio. The random decrement technique was applied on the time histories of this two accelerometers setting as triggering level value the standard deviation of the signal [7] and averaging considering time intervals of 100 s. This time length ensures that the computed free response signals (see Fig. 17.7a, b) contain the whole decaying part of the RD signature.

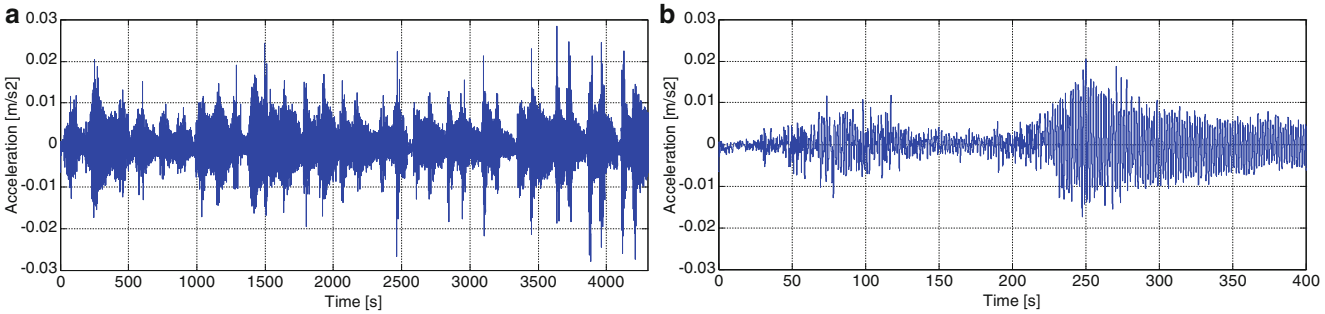

Fig. 17.5 (**a**) Time history at different speeds, accelerometer 1. (**b**) Time history of the first test speed (5 km/h)

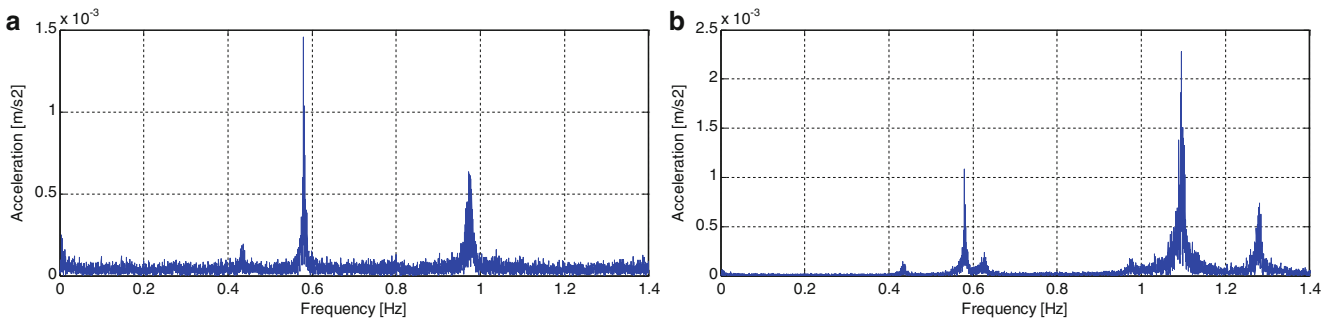

Fig. 17.6 Spectra of the accelerometric overall time history; (**a**) accelerometer 1; (**b**) accelerometer 4

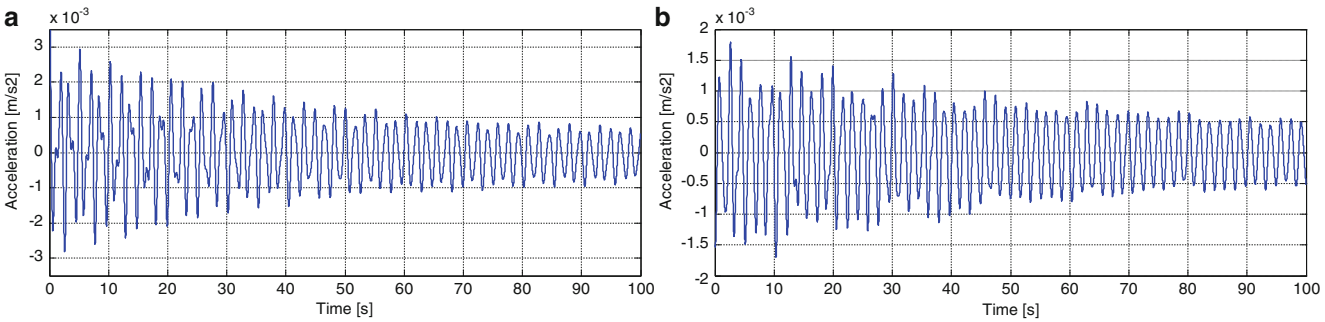

Fig. 17.7 Free decay response obtained with the random decrement technique; (**a**) accelerometer 1; (**b**) accelerometer 4

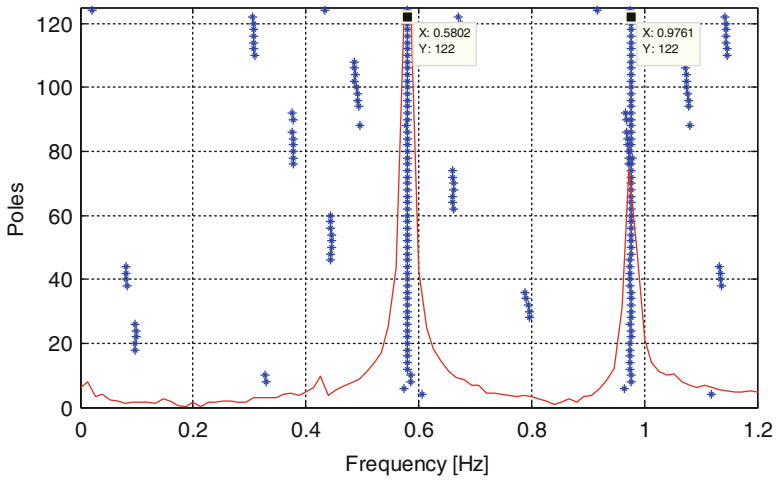

Fig. 17.8 Poles stabilization diagram (accelerometer 1); first torsional mode and third bending mode

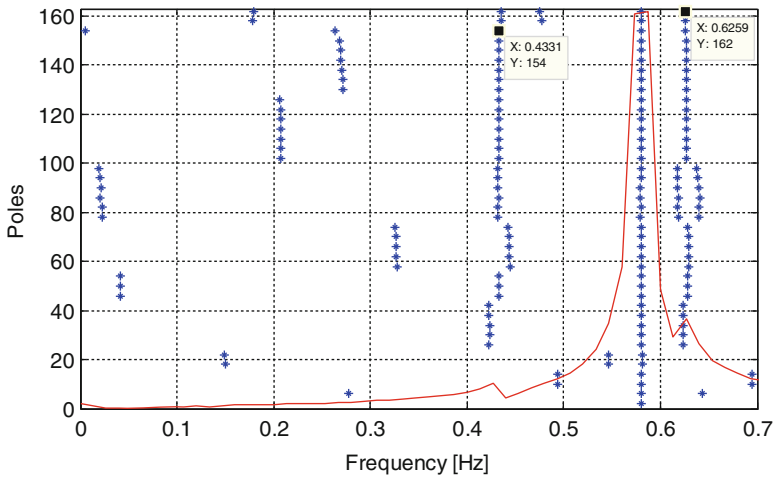

Fig. 17.9 Poles stabilization diagram (accelerometer 4); first and second bending modes

The stabilization diagrams reported in the following part show the modal frequencies (star marker) computed for different values of the number of poles of the mechanical system, obtained applying the LSCE method to the accelerometric time history pre-processed with the RDT. The solid superimposed lines represent the Fourier transform of the RD functions.

The identification of the torsional modes is quite effective, due to the position of the stay-cables in the center line of the deck and the asymmetry of the load, while the identification of the bending modes is more troublesome; as it is possible to notice in Fig. 17.8, the first two bending modes (0.43 and 0.62 Hz, respectively) are hidden by the presence of the first torsional mode, which is placed in the middle (0.58 Hz); a more focused analysis allows to identify this two modes, as showed in Fig. 17.9, where the raw signal was low-pass filtered at 0.7 Hz (instead of 1.4 Hz) before applying the RDT technique and the Prony method. In Fig. 17.10 the stabilization diagram for the second torsional mode and the fourth bending mode is reported; even in this case the structure exhibits a weaker response on the bending mode (1.28 Hz), but its peak is well spaced from the adjacent torsional mode (1.093 Hz) so it can be easily identified.

The modal damping ratios, reported in Table 17.1 together with the modal frequencies, are deduced from the real part of the system poles; for each identified mode the damping ratio is computed at each iteration of the algorithm and the values typically exhibit a certain dispersion, so a mean value has to be considered. In particular the modal damping values do not underline any trend with respect to the natural frequencies. This is confirmed by the studies of Yamaguchi [8]. Unlike suspended bridges, which have modal damping approximately growing with frequency, in cable-stayed bridges there is no particular relation between these parameters.

However, some consideration can be made concerning the great difference between the bending and torsional modes damping ratios: since the stays are anchored in the center-line of the deck they are marginally involved in the torsional motion of the deck, and so are the towers, then these elements contribute less to the energy dissipation with respect to the bending modes, keeping the damping of the torsional modes lower than the one of the bending modes.

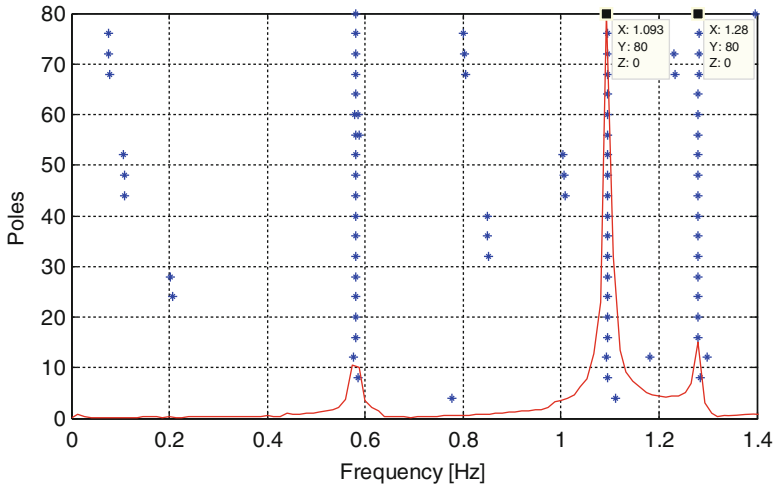

Fig. 17.10 Poles stabilization diagram (accelerometer 4); second torsional mode and fourth bending mode

Table 17.1 Comparison between experimental and numerical modal frequencies; measured damping ratios

Mode	Type	Measured frequency [Hz]	FEM frequency [Hz]	Damping ratio [%]
1	First bending	0.432	0.39	1.23
2	First torsional	0.579	0.616	0.37
3	Second bending	0.624	0.53	1.1
4	Third bending	0.978	0.813	0.59
5	Second torsional	1.096	1.176	0.33
6	Fourth bending	1.28	1.03	0.30

The mode shapes were computed on the basis of the correlations among the six accelerometric time histories; each transfer function of the system was obtained considering each accelerometric signal as an output and considering a reference channel as the input. The FRF was estimated as the ratio of the cross-spectral density of the two signals and the PSD of the input. Each mode shape was reconstructed collecting the values of the six FRFs corresponding to the considered modal frequency and are normalized to one where the mode shape reaches its maximum.

The measured mode shapes are reported in Fig. 17.11 in which for clarity the calculated mode shapes are reconstructed in the six accelerometric points and then mirrored on other four points symmetric with respect to midspan. As it can be seen, the matching between the experimental modes and the ones predicted by the FE model of the bridge is very good (see Fig. 17.12). As far as the modal frequencies are concerned, some discrepancies between the experimental and numerical data can be highlighted: according to the FE model the first torsional mode (0.616 Hz) should be at an higher frequency with respect to the second bending mode (0.53 Hz), and the second torsional mode (1.176 Hz) should come after the fourth bending mode.

17.5 Conclusions

Experimental field tests were performed on the Adige bridge in order to measure the modal parameter of the deck through its dynamic response. A heavy vehicle was employed as an excitation device, and it was run on equally spaced obstacle at different speeds: this system has proved to be effective in providing a proper amount of energy to the structure in the frequency range where the modes of interest lie. The asymmetric position of the moving load and the disposition of the stay-cables allowed to force more efficiently the torsional modes of the deck, but the identification of the bending modes was possible. The identification procedure exploited two time domain techniques, which can be used when output-only measurements are available: the random decrement technique and the Prony method. The measured modal frequencies and mode shapes were compared to the one calculated on the basis of a finite element model of the structure: experimental and numerical results are in a good agreement; the damping ratios for the six modes was estimated. The FE model, updated with the measured parameter can be predictive of the bridge deck behavior and can be thus employed in a future structural health monitoring system.

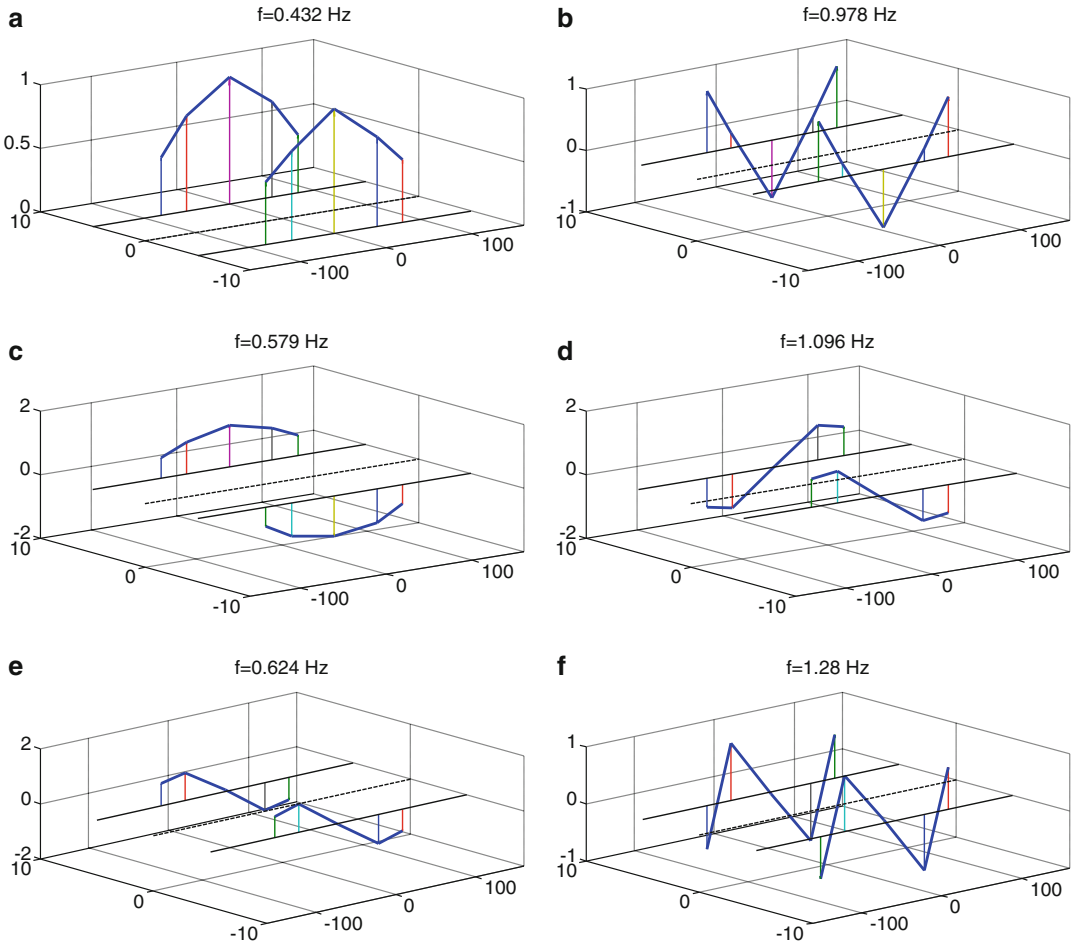

Fig. 17.11 Experimental mode shapes of the bridge. (**a**) First bending - f = 0.432 Hz. (**b**) Third bending -f = 0.978 Hz. (**c**) First torsional - f = 0.579 Hz. (**d**) Second torsional - f = 1.096 Hz. (**e**) Second bending - f = 0.624 Hz. (**f**) Fourth bending - f = 1.280 Hz

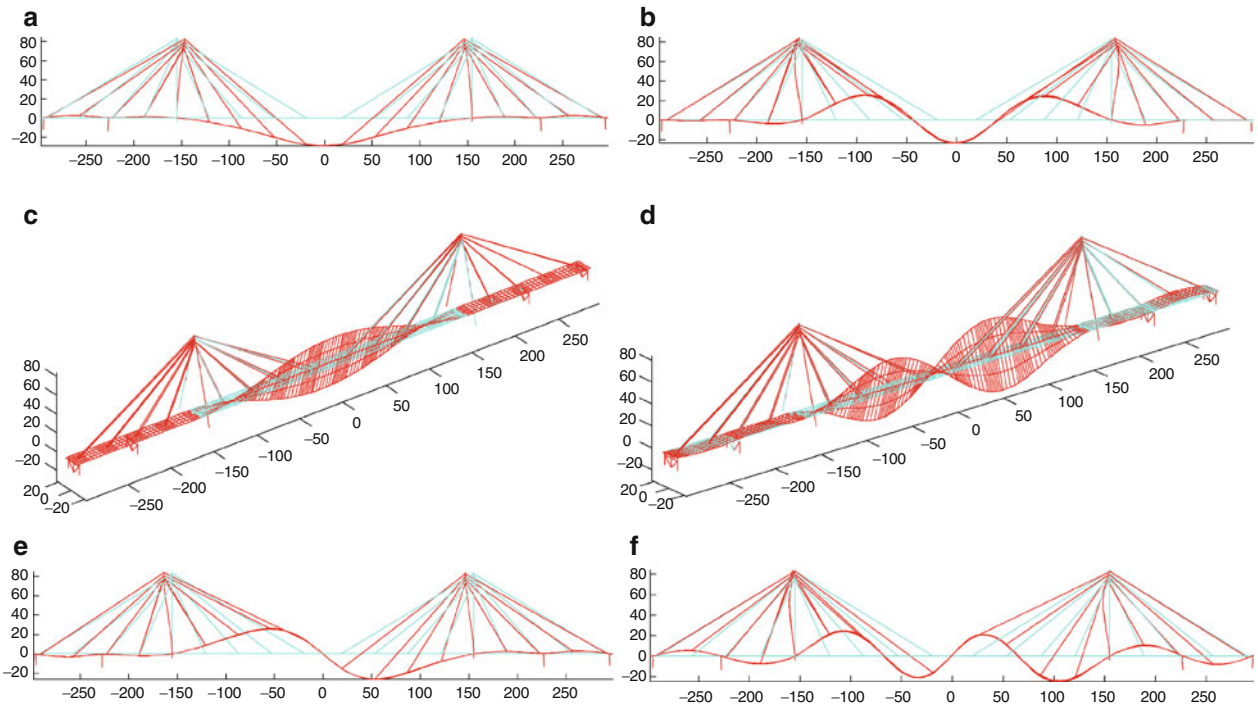

Fig. 17.12 FEM mode shapes of the bridge. (**a**) First bending - f = 0.39 Hz. (**b**) Third bending - f = 0.813 Hz. (**c**) First torsional - f = 0.616 Hz. (**d**) Second torsional - f = 1.176 Hz. (**e**) Second bending - f = 0.53 Hz. (**f**) Fourth bending - f = 1.03 Hz

References

1. Royer-Carfagni GF (2003) Parametric-resonance-induced cable vibrations in network cable-stayed bridges. A continuum approach. J Sound Vib 262(5):1191–1222
2. Conte JP et al (2008) Dynamic testing of Alfred Zampa memorial bridge. J Struct Eng 134(6):1006–1015
3. Xia H, Zhang N (2005) Dynamic analysis of railway bridge under high-speed trains. Comput Struct 83(23–24):1891–1901
4. Lin CW, Yang YB (2005) Use of a passing vehicle to scan the fundamental bridge frequencies: an experimental verification. Eng Struct 27(13):1865–1878
5. He XH et al (2011) EMD-based random decrement technique for modal parameter identification of an existing railway bridge. Eng Struct 33(4):1348–1356
6. Davies P (1983) A recursive approach to Prony parameter estimation. J Sound Vib 89(4):571–583
7. Asmussen JC (1997) Modal analysis based on the random decrement technique - application to civil engineering structures. Ph.D thesis, University of Aalborg, Denmark
8. Yamaguchi H, Ito M (1997) Mode-dependence of structural damping in cable-stayed bridges. J Wind Eng Ind Aerodynamics 72:289–300

Chapter 18
Experimental Modal Test of Civil Concrete Bridges

Alireza Gharighoran, Reza Nematollahi, and Ghader Bagheri

Abstract Concrete bridges are one of the most important civil infrastructures in the new metropolises. Experimental vibration measurement is one of the most widely used approaches for tension and damage analysis of these concrete bridges. The key to success of this technique is the accuracy of identified fundamental frequency of each bridge. In this paper experimental modal analysis of concrete bridges is carried out using output only acceleration records of a concrete bridge. A data analysis approach to determine fundamental frequency is used for case study of Chamran bridge in Isfahan city where the test carried out using ambient vibration measurement showed high identification accuracy and confidence of this method. As the bridge is one of the most important connecting links in the city, and while its building quality was always remained controversial, the output information of this test will be highly valuable for city authority figures to decide for retrofitting or even rebuilding the bridge.

Keywords Experimental modal analysis • Concrete bridge • Isfahan • Damage identification

18.1 Introduction

In past century, the major effort of structural engineers was the development and application of new and numerical approaches to use in the static and dynamic analysis of huge civil engineering structures. The quick development of finite-element techniques accompanied by tremendous technological experience in the computers allowed structural engineers to utilize extreme calculation soft wares for robust simulation of structural elements [1, 2].

Although, the design and construction of complex and huge civil structures, like skyscrapers, large cable stayed and suspension bridges, or other complicated structures have made engineers to evolve new experimental tools to provide the accurate identification of the most usual dynamic properties. These tools should enable trusted data to maintain calibration, updating, and validating of structural analysis numerical models.

The continuous ageing and subsequent structural corrosion of many existing structures have made the development of efficient dynamic-based damage detection techniques provided by structural health monitoring systems.

The tendency of civil engineering researchers was to use user friendly input–output modal identification approaches to robustly identify the main dynamic properties of civil structures.

However, it is challenging to excite huge civil structures in a controlled way. Fortunately, remarkable technological progress in transducers and analog-to-digital converters has helped experimental modal analysis of large structures especially based on measuring the structural response to random excitations and applying suitable stochastic modal identification methods [3].

18.2 Operational Modal Analysis

There are a number of benefits in using the Operational Modal Analysis compared to the more traditional techniques.

A. Gharighoran • R. Nematollahi (✉) • G. Bagheri
Department of Structural engineering, Science and Research Branch, Islamic Azad University, Isfahan, Iran
e-mail: gharighoran@yahoo.com; Reza.nematollahi@gmail.com; Bagheri_gh12@yahoo.com

J.M. Caicedo et al. (eds.), *Topics on the Dynamics of Civil Structures, Volume 1*,
Conference Proceedings of the Society for Experimental Mechanics Series 26,
DOI 10.1007/978-1-4614-2413-0_18,

18.2.1 Multiple Input Multiple Output Modal Technology

The Operational Modal Analysis is Multiple Input Multiple Output, MIMO, techniques. This means that the techniques are capable of estimating closely space modes and even repeated modes with a high degree of accuracy. Traditional modal analysis techniques are typically Single Input Multiple Output, SIMO, or Multiple Input Single Output, MISO, or in the worst case even Single Input Single Output, SISO. Such testing procedures will not be able to find repeated poles due to the lack of mode separation.

18.2.2 Easier Laboratory Modal Testing

There is no need for vibration shaker or impact hammer anymore. If you are in your lab doing modal testing in a test rig on some structural component, just do some random tapping on the structure while you are measuring the vibration response in multiple locations. The tapping must be random in time but also spatially. The excitation produced in this way will be a good approximation of a multivariate white noise stochastic process.

18.2.3 Winning Technology in In-Situ Modal Testing

Vibration shakers and impact hammers are impossible as excitation sources when it comes to in-situ testing of structures, such as buildings or rotating machinery. In cases like this the traditional modal analysis fails, because there are a number of unknown inputs acting on the structures. What is a problem for traditional modal analysis is strength for Operational Modal Analysis. The more random input sources there are the better the modal results gets. Since the real strength of the technology really lies in the in-situ testing it is no wonder why the technology is called Operational Modal Analysis. Other important feature that comes for free is that the estimated modes are based on true boundary conditions, and the actual ambient excitation sources.

Modal identification means the determination of the modal parameters of structures from vibration measurements. The modal parameters are natural frequencies, mode shapes and damping ratios of each mode.

Modal parameters are important because they describe the inherent dynamic properties of structure. They are the Eigen values and eigenvectors of dynamic equations.

These modal parameters can serve as input to Finite Element model updating (such as: the minimum rank perturbation and sensitivity based model update), and proceed to subsequent steps like damage identification and health monitoring.

18.3 Description of the Bridge

Chamran concrete bridge, built more than 10 years ago, has been poorly designed and constructed, while it has been one of the most important connecting links in the city connecting E-W traffic in the city. Whereas its building quality was always remained controversial, the output information of this test would be highly valuable for the city authority figures to decide for retrofitting or even rebuilding the bridge. The location of bridge in the city is shown on a satellite image (Figs. 18.1, 18.2, 18.3, 18.4, 18.5, 18.6, 18.7, 18.8, 18.9).

18.4 Instrumentation

The instruments used for the dynamic measurements of the building were accelerometers (Guralp, force feedback, ModelU5, CMG-DM24 s), cables, a 12-channel data acquisition system, signal conditioner and A\D converter (Kinemetrics, VSS3000), and a laptop computer for the data acquisition and data storage.

Fig. 18.1 Bridge location satellite image

Fig. 18.2 Bridge elevation and vehicle traffic below

Fig. 18.3 Poorly designed columns

Fig. 18.4 Small cracks in concrete slab

Fig. 18.5 Height and geometric specifications

Fig. 18.6 Inappropriate local retrofitting

The data was recorded for a period of 600 s per set-up at 2,000 samples per second (sps) and decimated to 200 sps. Two day was needed to complete the totality of the ambient vibration measurements.

18.5 Sensor Locations

In order to capture the translational modes in the North–South (NS) and East–West (EW) and vertical directions were positioned in the NS direction (Fig. 18.3). Two reference sensors were placed on . . .. . . (one in each direction). The sensors were placed close to concrete slab boarder (Figs. 18.10, 18.11).

Fig. 18.7 Local damage in isolators

Fig. 18.8 Local damage in isolators and inappropriate geometry

18.6 Peak Picking

This method is usually used for its simplicity in analyzing the ambient vibration response, when the input is unknown. The ambient vibration response of a structure cannot be predicted by deterministic models, within reasonable error. Each experiment produces a random time-history that represents only one physical realization of what might occur. In general, the response x(t) of the structure to ambient excitation is recorded for a very long time, even for hours, which enables to cut

Fig. 18.9 Damage in joints

the random process x(t) into a collection of sub registrations $x_k(t)$ which describe the phenomenon. The Fourier Transforms of the *k*th sub registrations of two random processes $x_k(t)$ and $y_k(t)$ are respectively:

$$X_k(f,T) = \int_0^T x_k(t)\exp^{-i2\pi ft}dt \tag{18.1}$$

$$Y_k(f,T) = \int_0^T y_k(t)\exp^{-i2\pi ft}dt \tag{18.2}$$

Fig. 18.10 One of the sensors placed on the bridge

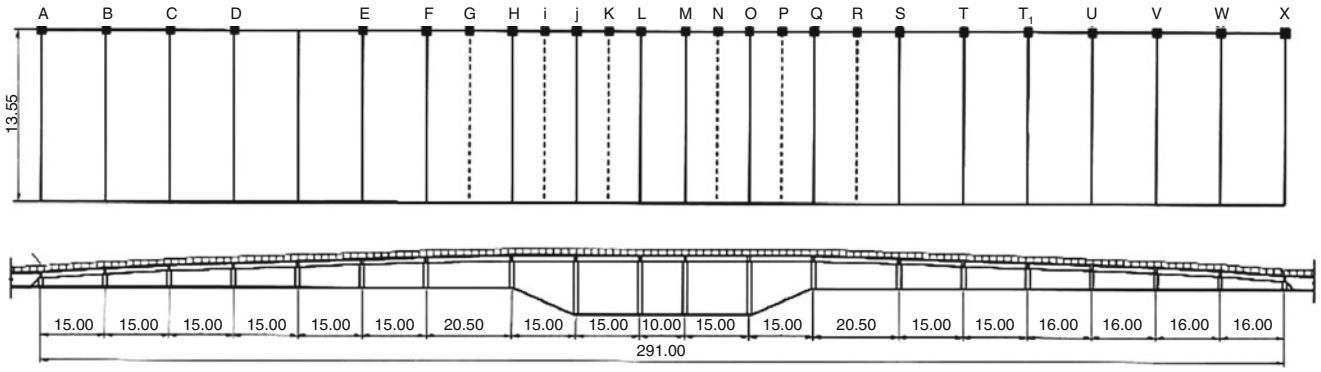

Fig. 18.11 Instrumentation locations and bridge geometry

The auto (or power) spectral density (PSD) and cross-spectral density (CSD) and related coherence function between the two random processes are respectively:

$$S_{xx}(f) = \lim_{T\to\infty} \frac{1}{T} E\left[|X_k(f,T)|^2\right] \tag{18.3}$$

$$S_{xy}(f) = \lim_{T\to\infty} \frac{1}{T} E\left[X_k^*(f,T)Y_k(f,T)\right] \tag{18.4}$$

$$\gamma_{xy}(f) = \frac{|S_{xy}(f)|^2}{S_{xx}(f)S_{yy}(f)} \tag{18.5}$$

where the symbol E[.] indicates an averaging operation over the index k and the asterisk denotes complex conjugate. Let us now assume that x(t) is the input and y(t) is the output. The auto-spectral and cross-spectral density functions satisfy the important formulae:

$$S_{yy}(f) = |H_{xy}(f)|^2 S_{xx}(f) \qquad S_{xy}(f) = H_{xy}(f)S_{xx}(f) \tag{18.6}$$

where $H_{xy}(f)$ is the frequency response function. The simple peak picking method is based on the fact that the auto spectrum (6_1), at any response point, reaches a maximum either when the excitation spectrum peaks or the frequency response

function peaks. To distinguish between peaks that are due to vibration modes as opposed to those in the input spectrum, a couple of criteria can be used. The former concerns the fact that in a lightly damped structure, two points must oscillate in-phase or out-of-phase. Then, the cross spectrum (6_2) between the two responses provides this information, which can be used to distinguish whether the peaks are due to vibration modes or not. The second criterion uses the coherence function (5), which tends to peak at the natural frequencies, as the signal-to-noise ratio is maximized at these frequencies.

18.7 Singular Value Decomposition (Frequency Domain Decomposition)

The second method referred to also relies only on the response to ambient excitations (output only). The method is based on the singular value decomposition of the response spectral matrix, exploiting the relationship:

$$S_{yy}(\omega) = H^*(\omega) S_{xx}(\omega) H^T(\omega) \tag{18.7}$$

Where $S_{xx}(\omega)$ (r × r, r number of inputs) and $S_{yy}(\omega)$ (m × m, m number of measured responses) are the input and output power spectral density matrices, respectively, and $H(\omega)$ is the frequency response function matrix (m × r). Supposing the inputs at the different points are completely uncorrelated and white noise, S_{xx} is a constant diagonal matrix, independent of ω. Thus:

$$S_{yy}(\omega) = S H(\omega) H^T(\omega) \tag{18.8}$$

whose term jk can be written, by omitting the constant S, as:

$$S_{yyjk}(\omega) = \sum_{r=1}^{r} \left(\sum_{p=1}^{n} \frac{\phi_{jp}\phi_{rq}}{\bar{\lambda}_p^2 - \omega^2} \right) \left(\sum_{q=1}^{n} \frac{\phi_{kq}\phi_{rq}}{\lambda_q^2 - \omega^2} \right) \tag{18.9}$$

In the neighborhood of the *i*th resonance, the previous equation can be approximated by:

$$S_{yyjk}(\omega) \cong \sum_{r=1}^{r} \frac{\phi_{ji}\phi_{ri}}{\bar{\lambda}_i^2 - \omega^2} \frac{\phi_{ki}\phi_{ri}}{\lambda_i^2 - \omega^2} = \frac{\phi_{ji}\phi_{ki}}{\left(\bar{\lambda}_i^2 - \omega^2\right)\left(\lambda_i^2 - \omega^2\right)} \sum_{r=1}^{r} \phi_{ri}^2 \tag{18.10}$$

By ignoring the constant r_i, S_{yy} can thus be expressed as the product of the three matrices:

$$S_{yy}(\omega) = \Phi \Lambda_i \Phi^T \tag{18.11}$$

which represents a singular value decomposition of the matrix S_{yy}, where:

$$\Lambda_i = \begin{bmatrix} \frac{1}{\left(\lambda_i^2 - \omega^2\right)\left(\bar{\lambda}_i^2 - \omega^2\right)} & 0\ldots & 0 \\ 0 & 0\ldots & 0 \\ \vdots & \vdots & \vdots \\ 0 & 0\ldots & 0 \end{bmatrix} \tag{18.12}$$

This is valid in the neighborhood of every natural frequency of the system, that hence emerges as a peak of the first singular value. The first column of the matrix Φ contains the first singular vector, which, in the neighborhood of the *i*th resonance, coincides with the *i*th eigenvector. This occurs at each resonance, when the prevailing contribution is given by the related mode. This procedure has recently had great diffusion mainly in in-situ experimental tests and has also been implemented in commercial codes [2, 4, 5].

18.8 Dynamic Characteristics and Structural Responses

The results of spectral analysis of the acceleration responses measured from the sensors located at the indicated places of Chamran bridge are shown in Table 18.1. These spectra were obtained from a direct analysis of the accelerations measured during the daily traffic of bridge. The spectral analysis results show that the acceleration responses of the bridge were primarily in the three natural modes of vibration, but higher modes were also clearly available. Meanwhile, rotational modes of the bridge were not identified owing to the lack of instrumentation due to traffic on the bridge deck. The natural frequencies were also estimated by the FDD method as shown in this table. The first several modes are easily identified in both approaches. The estimates of natural frequencies obtained by the PP method and the FDD method were in good agreement. Output acceleration time history samples for points K and N are shown in Figs. 18.12, 18.13, 18.14, 18.15, 18.16, 18.17, and 18.18. Output acceleration power spectra samples for the mentioned points are shown in Figs. 18.19, 18.20, 18.21, 18.22, and 18.23.

Table 18.1 Natural frequencies of sway modes

	E–W			N–S			Vertical		
Method	1	2	3	1	2	3	1	2	3
PP (Hz)	1.78	1.85	2.04	1.76	3.09	4.05	1.89	2.16	4.51
EFDD (Hz)	1.73	1.80	1.99	1.73	2.99	4.01	1.82	2.09	4.49

Results determined by the PP method are the overall average values of the natural frequencies measured from the several sensors located on the bridge

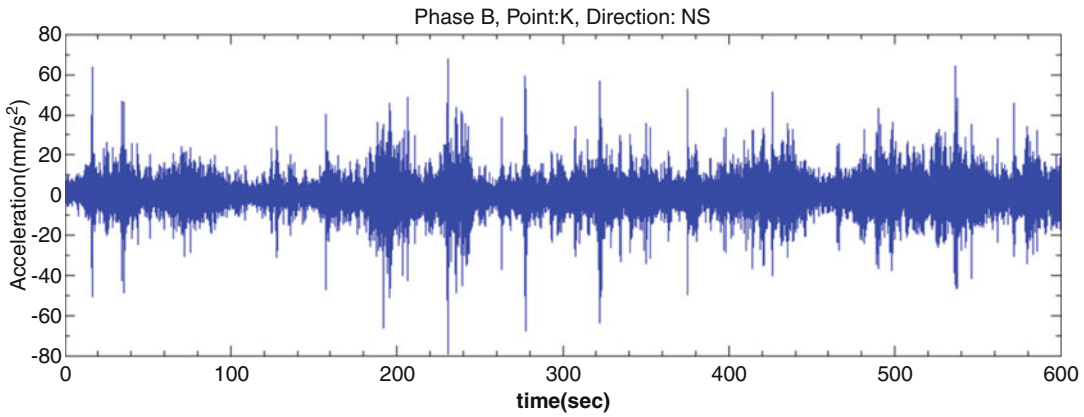

Fig. 18.12 Output acceleration time history sample

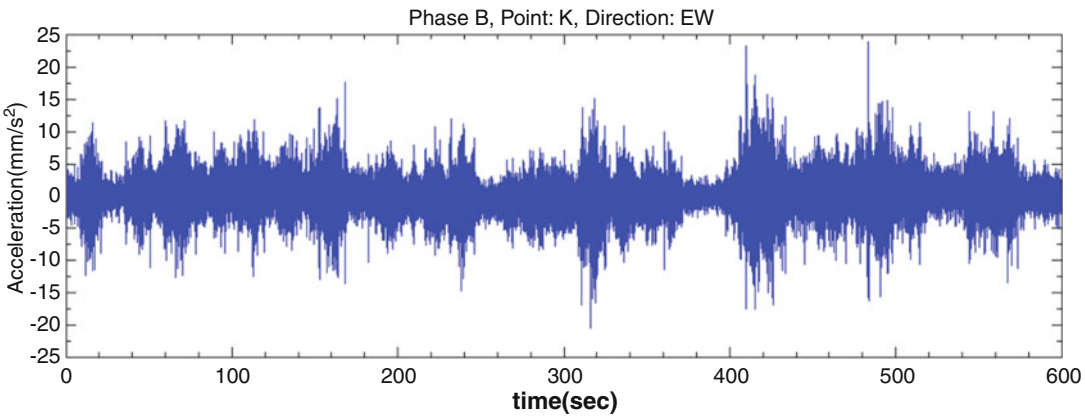

Fig. 18.13 Output acceleration time history sample

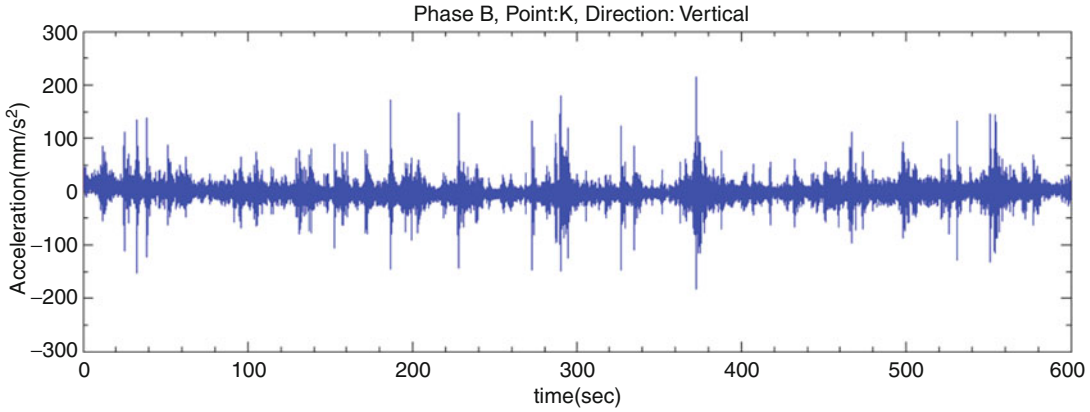

Fig. 18.14 Output acceleration time history sample

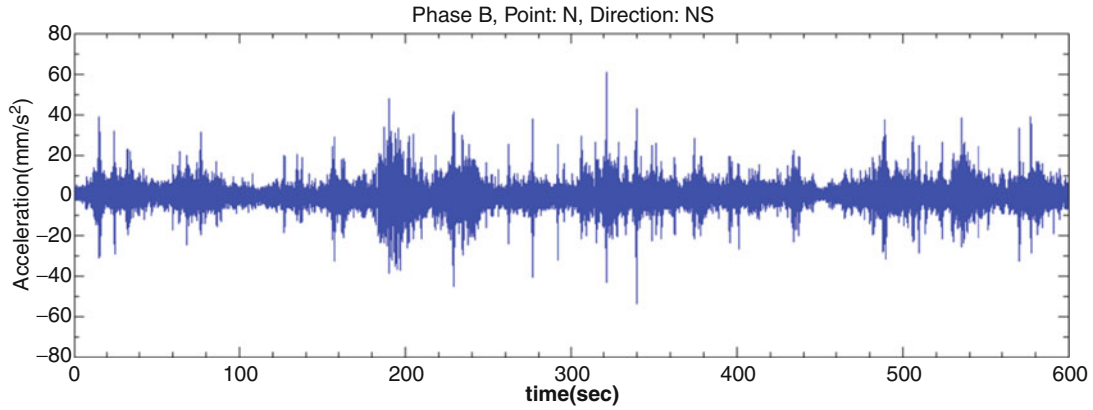

Fig. 18.15 Output acceleration time history sample

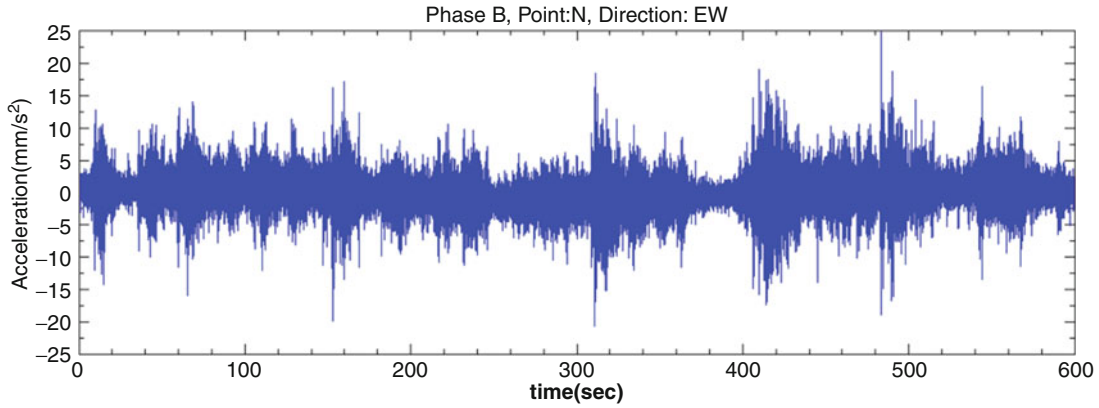

Fig. 18.16 Output acceleration time history sample

Natural frequency is one of the most important parameter for describing the dynamic characteristics of a bridge. Accurate determination of natural frequencies is essential to correctly predict wind and earthquake-induced acceleration for serviceability assessments in the design of bridges.

One of approaches claimed to be successful for the purpose of rapid evaluation of civil concrete bridges, is comparison between analytical models or even simple empirical formulas and experimental modal analysis results.

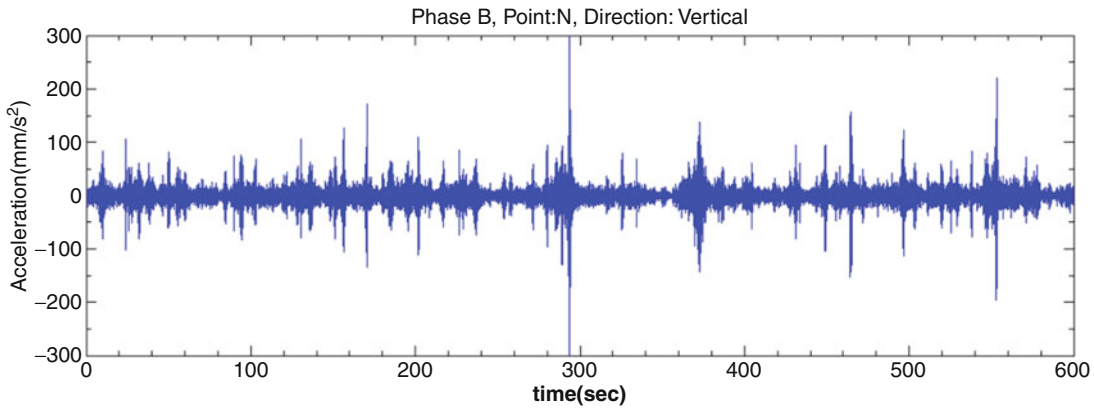

Fig. 18.17 Output acceleration time history sample

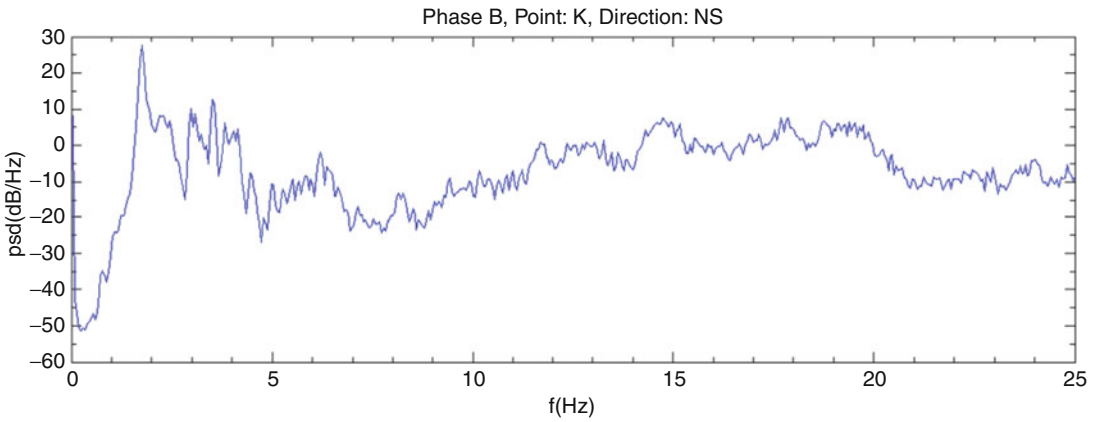

Fig. 18.18 Output acceleration power spectra sample

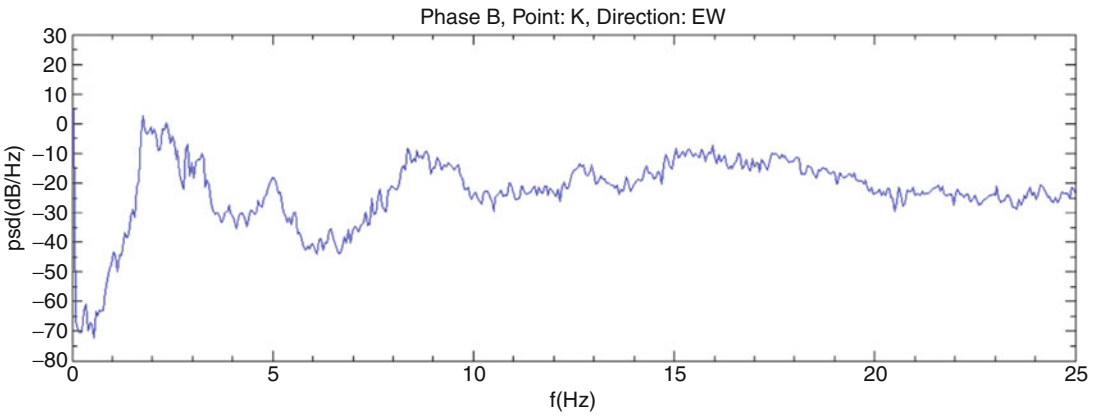

Fig. 18.19 Output acceleration power spectra sample

Several empirical formulas have been developed recently. One of the most widely used empirical equations developed by [6]. The resultant formula is base on dynamic testing of 226 bridges through passage of a single, fully loaded two-axle truck. Maximum span ranges were from 33 to 356.4 ft. The test vehicle was driven at constant speed (18.75–25 mph) whenever possible. Twenty-nine percent of the testing bridges have the natural frequencies of about 3 Hz and the mean natural

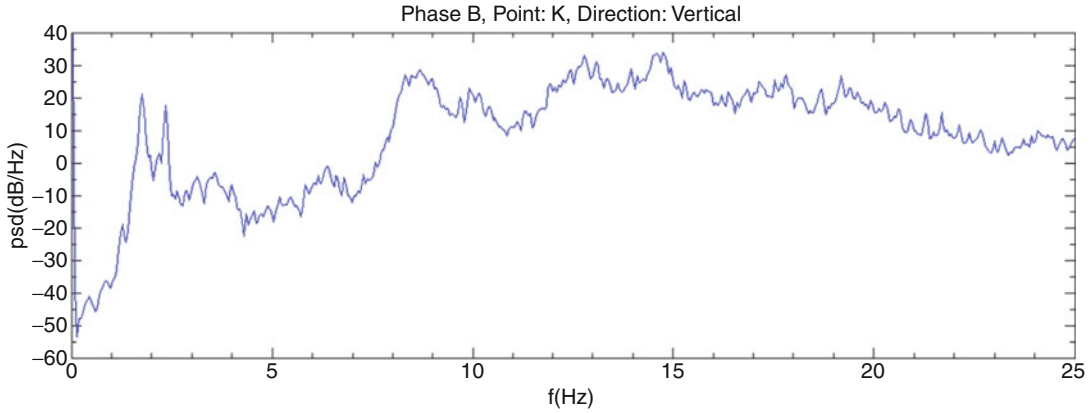

Fig. 18.20 Output acceleration power spectra sample

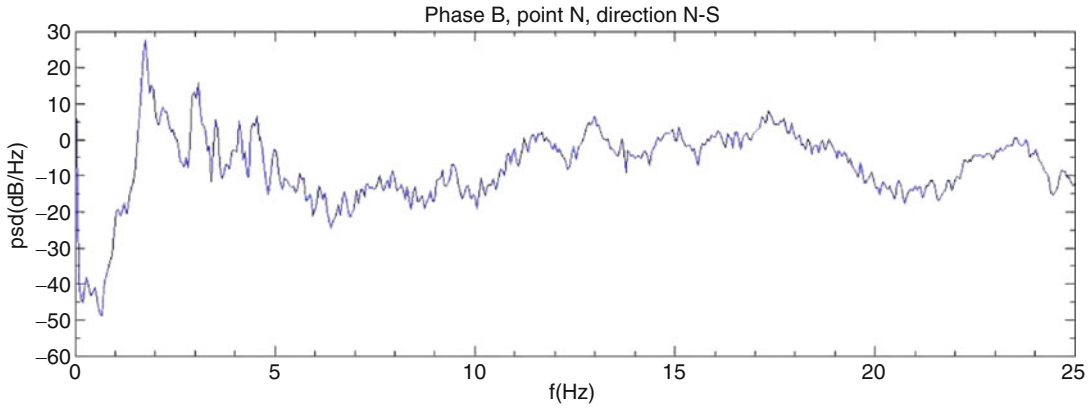

Fig. 18.21 Output acceleration power spectra sample

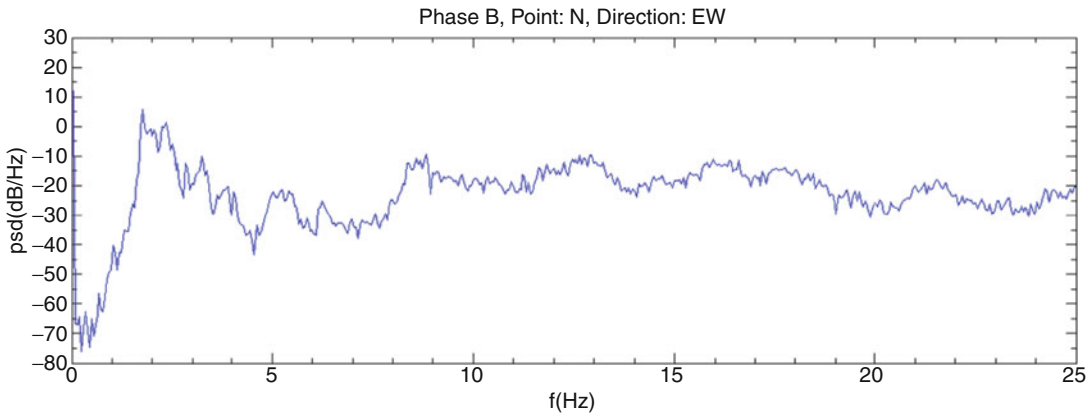

Fig. 18.22 Output acceleration power spectra sample

frequency is 3.6 Hz. From nonlinear regression analyses of the experimental data using the program NLWOOD, Cantieni developed the expression

$$f = 95.4 \times L_{\max}^{-0.933} \tag{18.13}$$

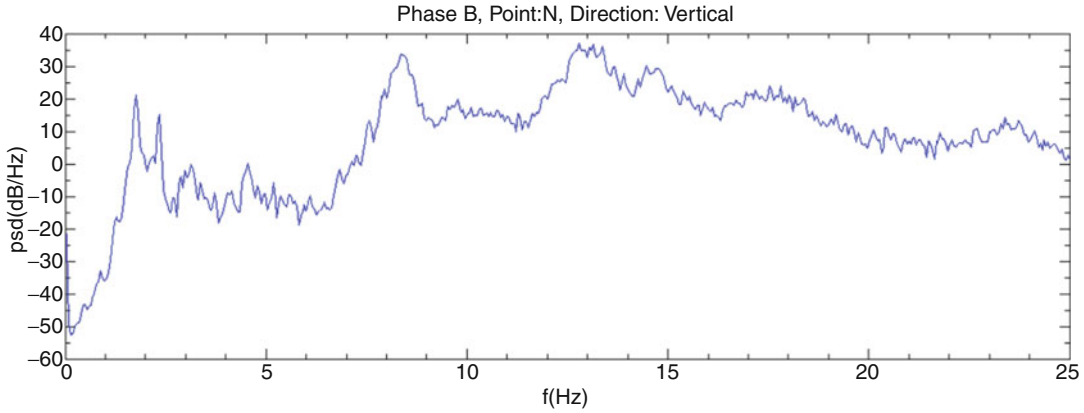

Fig. 18.23 Output acceleration power spectra sample

The scatter of the measurement values around the regression curve (standard deviation = ±0.81 f σ Hz) is considerable because of large variation in geometry and stiffness of the bridges. Alternatively, the following expression was proposed,

$$f = \frac{100}{L[m]} + 0.6 = \frac{328}{L[ft]} + 0.6 \tag{18.14}$$

which also has = ±0.81 f σ Hz. In order to reduce the standard deviation, results from 100 of the above bridges with more similar geometry were considered after eliminating: structures that included cantilever constructions, data not measured from the maximum span, and bridges with horizontal radius of curvature less than 2,953 ft. As a result, the following equation was proposed, which has = ±0.61 f σ Hz

$$f = 90.6 \times L_{\max}^{-0.933} \tag{18.15}$$

For the case study of Chamran bridge with the span length equal to 20.5 m the natural frequency will be 1.868 Hz for the L_{max} = 20.5 m = 64 ft. The difference between experimental and empirical formula results shows from global stand point that there may be some defects in structure that should be evaluated by detail inspection. This method will be a useful easy approach for authority figures to decide about the further inspection, retrofitting or even rebuilding the bridge.

18.9 Conclusion

Today, immense metropolises authority figures have programs for city infrastructures to be inspected visually. These observations and recommendations rely on the experience and skill of the inspector who often uses no equipment or only minimal non-invasive testing to determine the health of the bridge. More often than not, this means that there is no quantitative data collected to support the assessment.

In recent years, civil engineers have pushed government agencies to establish stronger standards for testing bridges that reach beyond visual testing, use experimental modal analysis methodologies that include advanced nondestructive testing, and installation of sensors for the monitoring of bridges.

It is an important aspect of experimental modal analysis that we assure the safety of bridges, collect quantitative data to establish a health record and use and promote methods of monitoring operations that reduce the life-cycle costs associated with the maintenance of bridges. Bridge modal data especially natural frequency has a great effect on loads that should be carried by a bridge and provide a valuable global knowledge of structure health. Should we obtain this quantity for a part of a bridge life span, we will be become able for judgment and evaluating of structure health during that period. There are also several natural empirical formulas that worth to be utilized for judgment about bridge while we always have the chance to use finite element methods as a general solution for the comparison of bridges experimental modal data.

Acknowledgements The authors wish to thank the municipality of Isfahan – civil section for its financial support. Many thanks go to a group of graduate students from the Isfahan University and IIEES for their valuable help during the field tests.

References

1. Cunha A, Caetano E (2006) Experimental modal analysis of civil engineering structures. Sound Vib 40:12–20
2. Brincker R, Zhang L, Andersen P (2000) Modal identification from ambient response using frequency domain decomposition. In: Proceedings of the 18th international modal analysis conference, San Antonio, pp 7–10
3. Daneshjoo F, Gharighoran A (2001) Experimental and theoretical dynamic system identification of damaged RC beams. EJSE Int
4. Lutes LD, Sarkani S (2004) Random vibrations. Elsevier, Amsterdam, pp 170–180
5. Li QS, Asce M, Zhi L-H, Tuan AY, Kao C-S, Su S-C, Wu C-F (2011) Dynamic behavior of Taipei 101 tower: field measurement and numerical analysis. J Struct Eng ASCE 127(1):143–155
6. Haiyong Wu (2003) Influence of live-load deflections on superstructure performance of slab on steel stringer bridges. Ph.D. thesis, Department of Civil and Environmental Engineering Morgantown, West Virginia, chapter 1:40–60

Chapter 19
Dynamic Characterization of Flexible Structures Through Vision-Based Vibration Measurements

G. Busca, A. Cigada, and E. Zappa

Abstract Structural vibration is nowadays a crucial point for both potential safety and comfort problems due to larger structural vibrations. The problem of structural monitoring is therefore increasingly relevant also requiring vibration measurements to both estimate structural dynamic parameters and eventually predict potential damage or even failures. The problem is particularly crucial for very large structures, where the use of classic techniques (such as accelerometer-based measurements and strain estimation using either electric or optical-fiber strain gauges) presents some limitations due for example to access difficulties, for transducers installation. Moreover the load effect due to the transducers mass can become a major concern in the case of extremely slender structure, such as power transmission lines and in all the applications that involving long cables. In these latter cases contactless measuring techniques would be highly preferred, in order to avoid the mentioned load effects and ease of installation and, above all, to measure vibrations in many points at the same time with a single transducer (a camera). An image-based vibration measurement technique is proposed and qualified in this paper and an application to overhead transmission lines is shown as an example.

Keywords Vibration measurement • Vision • Dynamic • Flexible structures

19.1 Introduction

The problem of structural monitoring is increasingly relevant in particular in the case of slender structure, where vibration measurements are required to both estimate structural dynamic parameters and eventually predict potential damage or even failures. The problem is particularly crucial for very large structures, where the use of classic techniques (such as accelerometer-based measurements and strain estimation using either electric or optical-fiber strain gauges) presents some limitations due for example to access difficulties, for transducers installation. Moreover the load effect due to the transducers mass can become a major concern in the case of extremely slender structure, such as power transmission lines and in all the applications that involving long cables. In these latter cases contactless measuring techniques would be highly preferred, in order to avoid the mentioned load effects and ease of installation and, above all, to measure vibrations in many points at the same time with a single camera.

In this paper the problem of vision-based vibration monitoring of slender structures is studied, focusing attention on two aspects of this wide problem: uncertainty for vision based approaches and an application study to the characterization and monitoring of cables on a laboratory span. Cable dynamics ([1]) has direct practical application in different fields, such as: overhead transmission lines (see [2]), cable ways ([3]), train power supply ([4]), marine risers ([5], [6]) and cable stayed bridges ([7]).

It is well known from literature [8] that, to estimate the structural properties of cables, self-damping above all, to properly design additional damping devices, a well established technique requires the measurement of the vibration amplitude in a couple of nodes and in an antinode. If theory is applied, nodes should be absolutely fixed, but the adopted approach, relying on an electric similitude, states that nodes move, although their vibration is at very low levels, with a bad signal/noise ratio and in a situation prone to suffer for load effect, from any environmental small change.

G. Busca • A. Cigada • E. Zappa (✉)
Dipartimento di Meccanica, Politecnico di Milano, via La Masa, 1, 20158 Milan, Italy
e-mail: giorgio.busca@mecc.polimi.it; alfredo.cigada@polimi.it; emanuele.zappa@polimi.it

J.M. Caicedo et al. (eds.), *Topics on the Dynamics of Civil Structures, Volume 1*,
Conference Proceedings of the Society for Experimental Mechanics Series 26,
DOI 10.1007/978-1-4614-2413-0_19,

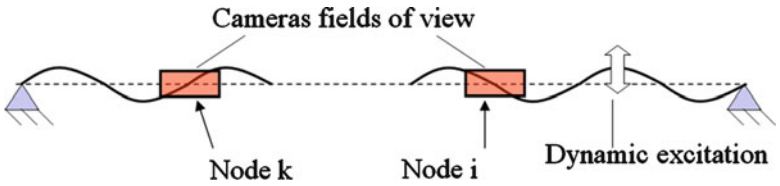

Fig. 19.1 Sketch of the experimental set-up

However it should be underlined that the position of the nodal points changes not only as the vibration frequency changes but also as the cable tension changes (also as a consequence of a temperature drift). Traditional measurement techniques are often used to perform these measurements and in particular the antinode vibration amplitude is usually estimated by means an accelerometer fixed on the cable (but it gives local distortion), while the estimation of the node dynamic displacements is more cumbersome. In [9] it was proposed to measure it using two triangulation laser sensors that measure the displacement of two sections of the cable very close to the node position with the node between the two measuring points. The use of two sensors allows to interpolate the vibration amplitude and to predict it at the node position. Of course some drift occurs and this is compared to very small quantities. This means continuously moving the laser transducer positions to guarantee a proper tracking of the node position, which must fall between the two measuring points.

In order to overcome some limitations of the mentioned method, in this paper a new vision-based measuring technique is proposed and qualified. It is remembered that, although we start from a specific problem, results are to be considered of general value, as the same approach can be applied to all the above mentioned problem categories.

Vision based measuring techniques are 'dense', meaning that they allow for the vibration measurements in a number of points in a large area of the structure being analyzed. For motion in a plane, theoretically every row or every column in the digitized image can be considered to the extent of a displacement sensor. It is therefore possible, for instance, to track the position of minimum (or maximum) vibration sections without any interpolation, as needed in the case of laser-based measurements. This property of vision techniques allows to measure both the node and the antinode vibrations regardless to their position drift (in this case synchronization is an issue to be faced), without modifying the experimental set-up (provided that the points to be measured fall within the camera field of view).

During the tests to estimate the cable damping, this is excited in order to produce vibration in a single plane (see Fig. 19.1); nevertheless it is possible to have transversal vibration too (i.e. vibration in the direction normal to the main vibration plane), for example due to imperfection in the excitation device. Out of plane vibration can lead to misleading results, particularly in the case of cables with small diameter, because small out-of-plane displacements produce a non negligible variation in the laser measurements, due to the cylindrical shape of the cable. Vision based measurement, on the contrary, can be designed in order to be unaffected by out-of-plane displacements (in addition we could think of stereo vision approaches, but this is a more complicated task: in this paper we will focus on other aspects which form the method basis: 3D is an important refinement, to be faced at further stages).

Literature presents a few methods for damping estimation. Two of them are well described in [10]. One of the most used is the Inverse Standing Wave Ratio method [9]. This method was originally derived from an electro-mechanical analogy and later revised in [9] to give a direct mechanical interpretation of it; the technique allows to define the power flowing across a cable section as:

$$P_i = \frac{V^2}{2} S_i \sqrt{Tm} \tag{19.1}$$

where V = ωu is the antinode vibration velocity, u is the antinode vibration amplitude and ω [rad/s] is the vibration circular frequency, while $S_i = (a_i/u)$ is the inverse standing wave ratio and a_i is the vibration amplitude at node i. After some evaluations about the dissipated power along the cable, it can be demonstrated that the self damping of lines conductors is estimated by the following formula:

$$h = \frac{S_k - S_i}{\pi \cdot n_v} \tag{19.2}$$

where k and j denotes two nodes on the cable and n_v the number of antinodes between nodes i and j.

In conclusion this method requires the measurement of the vibration amplitude in two different nodes, and at an antinode, under steady state vibrations at a certain cable natural frequency.

This is a method critical aspect, because the exact node positions should be detected and the displacements to be measured are very small (of the order of 1/1,000 with respect to the antinode ones). Moreover the position of the node may shift during the test, but this has to be kept under control, as too wide changes mean that steady state conditions are not fully achieved.

19.2 Vision-Based Measurement Technique

In this paragraph the vision based measurement technique will be described. Attention will be devoted to a procedure based on edge detection. This is one of the most popular techniques in image processing. In a grey level image, an edge may be defined as a sharp change in intensity and the process detecting the presence and locations of these intensity transitions is the edge detection. Detection of edges in an image is an important task that has been intensively studied for over 50 years. One of the reasons for this interest is that, concentrating attention on edges rather than on the full image, it is possible to dramatically reduce the amount of data to be processed, without any loss of the most important pieces of information about the object shape. Moreover this kind of image description is easy to integrate into a large number of object recognition algorithms, used in computer vision and other image processing applications [11].

As described in the preceding section, the proposed technique will be applied to the monitoring of a slender structure: a cable. However, the method description may be extended to other applications whenever a generic target is considered, for example a marker with an edge. Obviously if the target is one with the object whose motion is being measured, their displacements are the same (this aspect, though seeming odd, is quite important for success).

As shown in Fig. 19.2, the technique requires a camera placed in front of each target (node to be monitored) and the image sensor should be parallel to the target (this can be verified through the same images, provided an object of known shape like a circle is framed). Another important condition is the sampling theorem, i.e. the sampling frequency of the camera must be at least twice the vibration frequency of the object. If this condition is not guaranteed, it is possible to acquire images under controlled aliasing condition (the assumption of stationary harmonic motion is mandatory), but only if the vibration frequency is perfectly known (because it is either measured with other transducers or imposed by the user, as it happens in the case of cable damping estimation). Other solutions may consist in partializing the images, reducing the Field of View, with the risk to miss the real area of interest.

In this work the image acquisition is based on two AVT Marlin F131B digital cameras equipped with a 1280 $\times$ 1024 pixel CMOS sensor and with optics focal length of 25 mm. The two cameras are connected to a common trigger source to obtain a synchronization of the images acquired in the two nodes. A video is acquired for each of the two cable sections close to the selected nodes and the chosen image-processing approach is applied to every frame (Fig. 19.3). The procedure consists in the following steps:

1. The edge is identified by its pixel coordinates for every frame (Fig. 19.3a);
2. A fitting is applied to the pixel coordinates to wipe out the noise affecting data and minimizing the quantization error due to the discrete nature of pixels (Fig. 19.3b);
3. Steps 1 and 2 are iterated for all the acquired frames to define the edge position for every point in the x-direction (see Fig. 19.2) which can be considered an elementary displacement sensor for vertical motion;
4. The vertical displacement of every point in the x-direction is therefore reconstructed in the time domain (Fig. 19.3c).
5. Further analyses can be performed: for instance, in the actual case, the Fourier-transform is calculated for every signal and the displacement amplitude for every point in the x-direction of the sensor is then estimated.

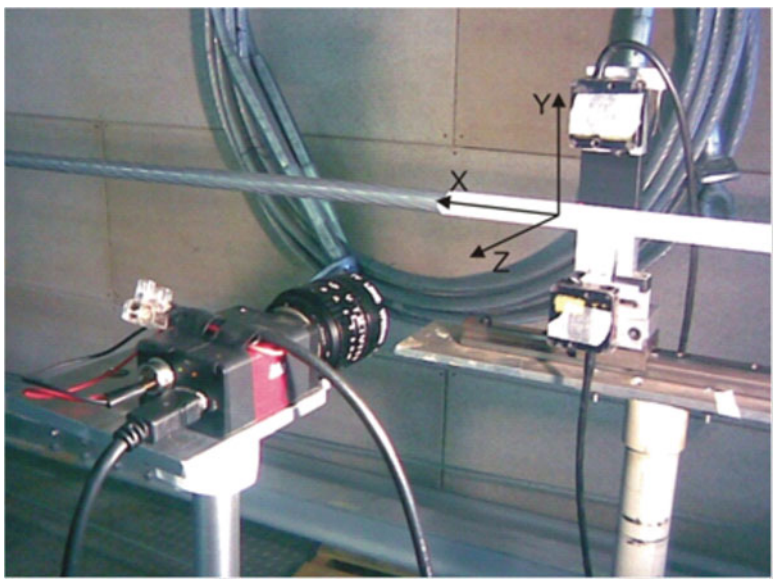

Fig. 19.2 Measurement set-up

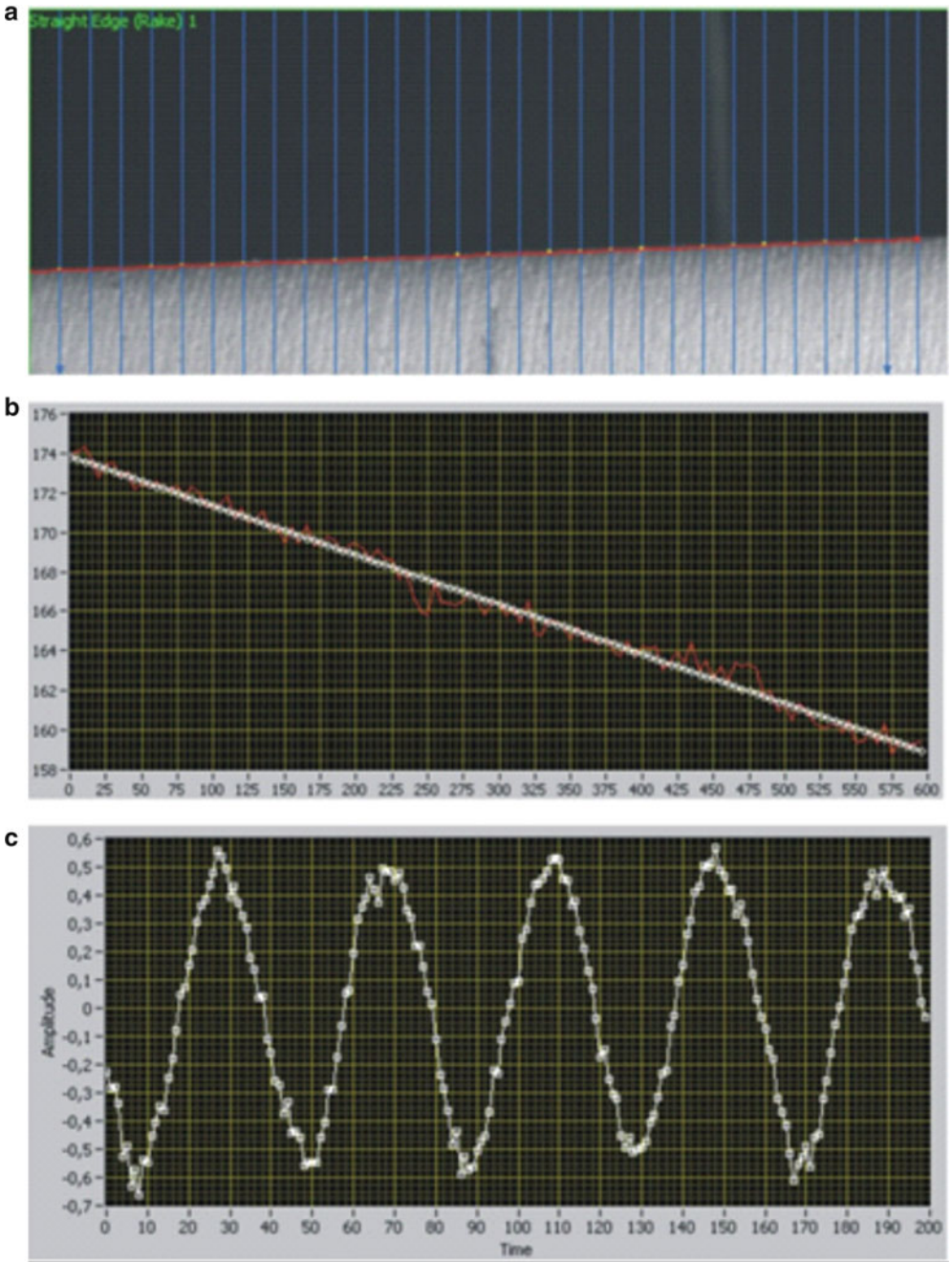

Fig. 19.3 Image elaboration: (**a**) edge detection; (**b**) edge linear fitting; (**c**) reconstructed amplitude vibration for one pixel

Getting the displacement amplitude for every pixel coordinate in the x direction, it is possible to define the envelop of the edge motion. Figure 19.4 shows the final result, giving the envelope of the edge of the vibrating cable.

19.3 Validation of the Measuring Technique

In order to qualify the measuring technique based on image acquisition and processing, a set of experimental tests was designed and carried out. Tests were performed on an electrodynamic shaker; sweep sine tests with frequency ranging from 5 to 40 Hz were imposed to a black and white edge target (constant acceleration levels of 1, 2 and 5 m/s^2 were imposed

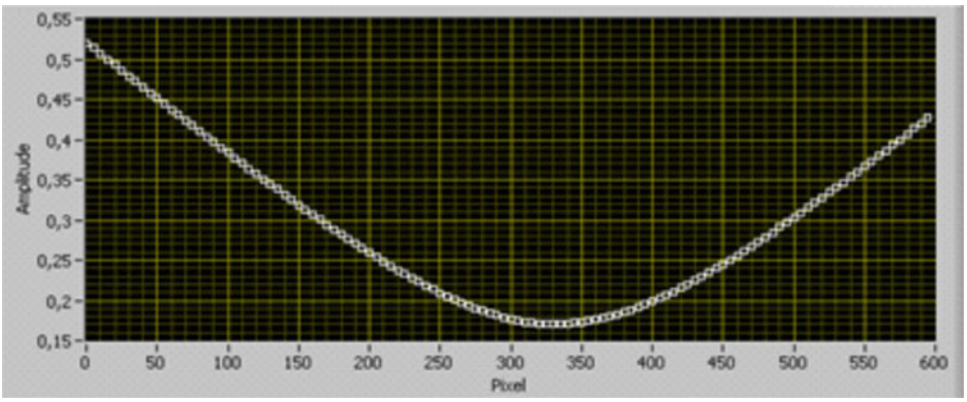

Fig. 19.4 Amplitude vibration envelope

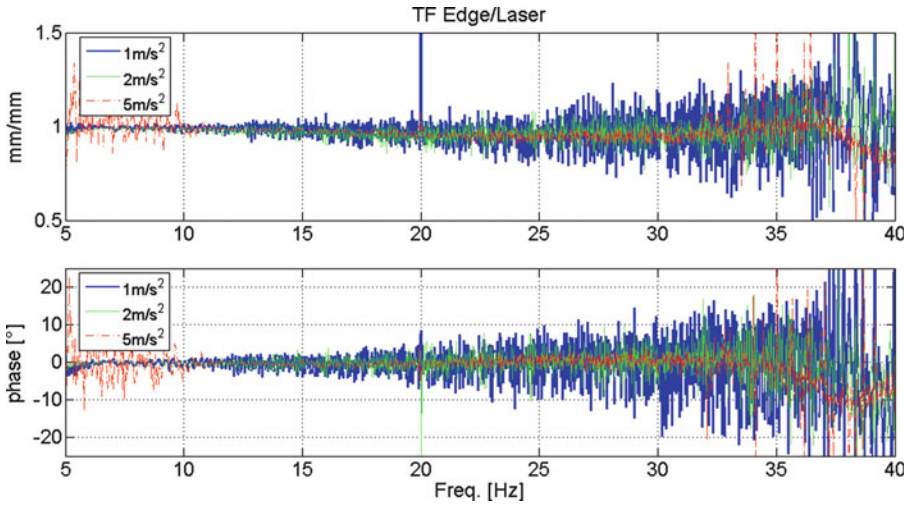

Fig. 19.5 Transfer function between image-based and LDV displacement measurements (input signal: sweep between 5 and 40 Hz for amplitudes of 1 and 2 m/s^2 and between 10 and 40 Hz for amplitude of 5 m/s^2)

according to the chosen design of experiments). A reference for displacement measurement has been provided by a Laser Doppler Vibrometer Polytec OFV 505, hereafter referred to as LDV. The uncertainty of the LDV system is negligible if compared with the image-based measuring techniques; the LDV was therefore used as a reference to estimate the uncertainty of the vision measuring device. The camera was calibrated in order to remove optical aberration and to estimate the pixel to millimetre conversion according to [12].

As mentioned the application of edge detection to the cable, allows to estimate the vertical position of the trend in time of the upper edge of the cable in a number of points. Then a best fitting procedure is applied to the pixel coordinates. The same procedure was used in the tests for uncertainty estimation: the edge detection is applied to 50 columns of the image (typical value in real applications) and the best fitting straight line was searched for. Since that the edge is mounted on a shaker and it vibrates in the vertical direction, the vertical displacement of the target can be estimated as the vertical displacement of the fitting line.

19.4 Uncertainty Qualification of the Vision-Based Displacement Measurement

Figure 19.5 shows the transfer function between the image-based and LDV displacement measurements in the case of input signal with amplitude 1, 2 and 5 m/s^2. The input signal is a sweep between 5 and 40 Hz for amplitudes of 1 and 2 m/s^2 and a sweep between 10 and 40 Hz for amplitude equal to 5 m/s^2 (an acceleration level of 5 m/s^2 al frequencies lower than 10 Hz would have created a displacement exceeding the limits of the experimental set-up).

In the transfer function of Fig. 19.5 both the amplitude and phase show a very good agreement between the reference displacement and the vision based results, for low frequencies and for all the chosen amplitudes, while a worse trend is observed as the frequency increases. This is likely due to the fact that the tests were carried out at constant acceleration amplitude, therefore the displacement amplitude decreases rapidly (according to a square law) as frequency increases. This hypothesis is supported by the comparison of the three different transfer functions at three different acceleration levels: it can be seen that, as the amplitude increases, the spread (which is a random scatter defining uncertainty) in the transfer function estimation decreases.

Of course the uncertainty strongly depends upon optics magnification; in order to get an uncertainty estimation that can be used also in other conditions (i.e. with different zoom levels) it is useful to express results in terms of pixel. In this case the uncertainty related to the dynamic measurement of edge displacement becomes 0.1px.

19.5 Laboratory Estimation of Cables Vibration Amplitude and Damping

In order to qualify the method, some tests were carried out on a 50 m long cable on a laboratory span. Two types of tests were developed, as described below.

19.5.1 First Set of Tests

The first set of tests were focused on the comparison between measurements of the node vertical displacements obtained with triangulation laser sensors and data from the cameras.

Tests have been carried out on an aluminium-based cable with a diameter of 20 mm and a length of 45 m.

Figure 19.6 shows the obtained results. Data refer to a test with a fixed vibration frequency of 32 Hz and five different vibration amplitudes at the antinode.

During the tests each of the two camera was mounted close to one of the selected nodes in order to obtain the maximum magnification, compatibly with the experimental limitations. Thanks to this fact, although uncertainty in the sub-pixel displacement measurement is in the order of 0.1px in the case of vibrating target, the displacement of the nodes could be reliably measured being in the order of 10 μm. It should be noted that, since in this work we are interested in the amplitude of vibration of the edge and since we estimate it thorough a Fourier analysis involving a large number of vibration cycles, the uncertainty linked to the estimated amplitude will be lower than the one linked to a single position measurement. Moreover, in [13] it was demonstrated that edge detection on inclined edges (as in the case of the vibrating cable) allows to estimate displacements with an uncertainty much lower than in the case of perfectly horizontal edges (as in the case of the qualification tests shown above).

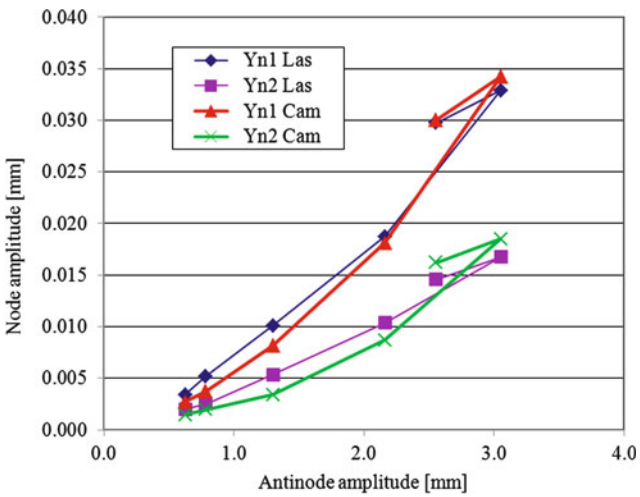

Fig. 19.6 Node amplitude vs antinode amplitude

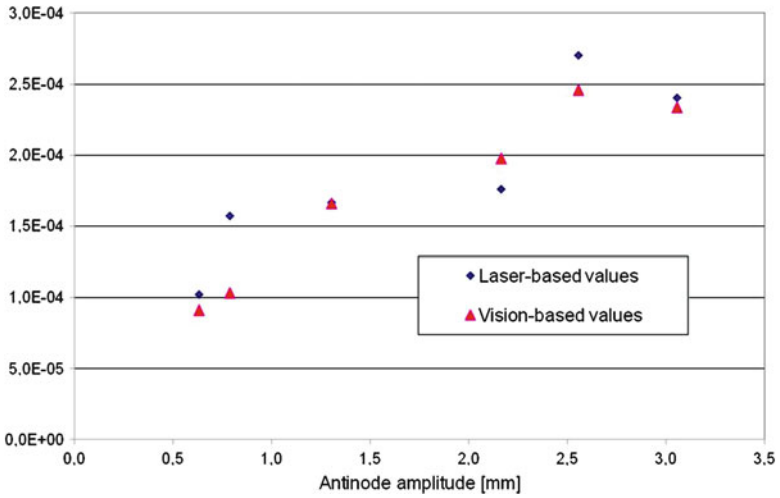

Fig. 19.7 Cable damping estimated with the state-of-the-art and with the proposed technique

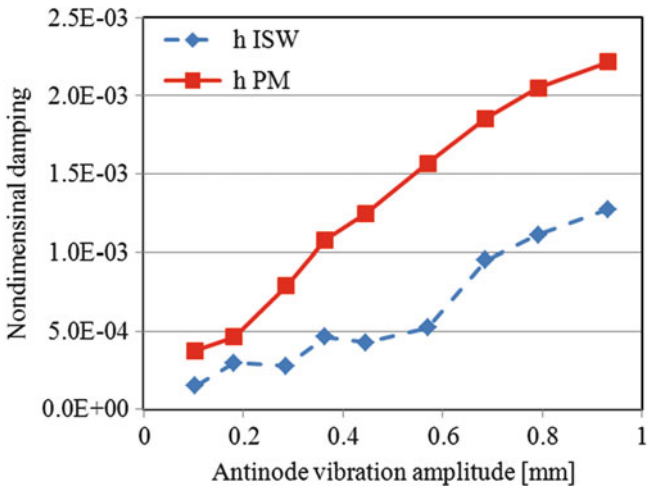

Fig. 19.8 Cable damping estimated at 36 Hz with the power method (h PM) and with the proposed technique (inverse standing wave with camera based node vibration measurement, h ISW)

Figure 19.6 shows similar results in case displacements are obtained from triangulation laser sensors or from the camera. The proposed alternative method is easier to implement, because the measurement setup is very simple to arrange and the requested time is lower. In addition this method is effective even if the node position changes during the tests.

Figure 19.7 shows the cable damping estimated relying on the state-of-the-art technique, based on laser measurements, and the same data measured with the vision-based technique proposed in this work. As can be seen the agreement between the damping values obtained with the two techniques is very good. Therefore the vision-based technique appears to be a valid approach to overcome the drawbacks shown by the traditional approach.

19.5.2 Second Set of Tests

The second set of measurements was devoted to the measurements on a cable, where the power method technique ([14], [9]) was applied to obtain a reference for the cable damping, in order to compare the vision-based data. The cable is for power delivery purposes with a diameter of 44 mm and a mass of 5 kg/m. It should be highlighted that, as stated in literature ([9], [15]), the power method overestimated the obtained damping, mainly because the dead end losses are included in the estimated damping, while in the inverse standing wave method these losses are not considered. The differences in the damping estimations obtained with the power method and with the standing wave one strongly depend on the frequency and amplitude vibration (see [9]), however the inverse standing wave method always gives lower damping values. In Fig. 19.8 an example of the damping data obtained with the power method and the corresponding values estimated with the camera-based technique is shown.

During the tests great care is posed to the experimental set-up in order to induce vibration in the vertical direction only (direction y in Fig. 19.2), nevertheless some small vibration along the z direction are possible; in the traditional laser-based measurements these vibration introduce a non-negligible change of the lasers output. This phenomenon is particularly relevant in the case of small diameter cables because, in these conditions, the effect of the out-of-plane motion strongly increases as the diameter decreases and can lead to inaccurate damping estimation if the inverse standing wave method is applied. On the other hand the power method overestimates the cable damping because of the contribute of the two cable ends. On the contrary the out-of-plane vibrations have an almost negligible effect on the image-based measurements, therefore the proposed measuring technique allows to apply the inverse standing wave technique also with this very low-diameter cables, allowing to estimate the cable damping without including the contribute of the end losses.

19.6 Concluding Remarks

In this paper the problem of vision-based vibration monitoring of slender structures was studied, focusing the attention on two aspects of this wide problem: uncertainty and the application to a practical case to get a cable damping. We proposed a method based on vision measurement techniques. These have the advantage to be 'dense,' meaning that they let to estimate the vibration in a number of points covering a large area of the structure, allowing for example to track the position of minima (or maxima) vibration sections without any interpolation, with an easy approach. In this paper some results about a suspended cable were presented with success, but the technique could be applied efficiently to other slender vibrating structures.

Future work will be needed to qualify the effect of the edge inclination on the uncertainty in measurements in the case of dynamically moving target, or moving towards different image processing techniques, such as blob detections, in a benchmarking approach.

References

1. Fox G (1983) Marine riser fatigue analysis using wave-variance spectra. OCEANS 1984 15:680–683
2. Muddassir N, Faisal K, Paul A (2008) Fatigue reliability analysis of deep water rigid marine risers associated with Morison-type wave loading. Stoch Env Res Risk A 22(3):379–390
3. Cárdenas RA, Viramontes FJC, González AD, Ruiz GH (2008) Analysis for the optimal location of cable damping systems on stayed bridges. Nonlinear Dynam 52(4):347–359. doi:10.1007/s11071-007-9283-5
4. Collina A, Fossati F, Resta F (2001) An innovative OHL diagnosis procedure based on the pantograph dynamics measurements. In: World congress on raylway research, Koln
5. Christenson RE, Spencer BF Jr, Johnson EA (2001) Experimental verification of semiactive damping of stay cables. In: Proceedings of the American control conference, Arlington, 25–27 June 2001
6. Cluni F, Gusella V, Ubertini F (2007) A parametric investigation of wind-induced cable fatigue. Eng Struct 29:3094–3105
7. Weber F, Distl H, Feltrin G, Motavalli M (2009) Cycle energy control of magnetorheological dampers on cables. Smart Mater Struct 18:015005. doi:10.1088/0964-1726/18/1/015005
8. Mul OV, Torres DFM, Kravchenko VP (2008) Dynamics of controlled hybrid systems of aerial cable-ways. Nonlinear Anal Hybrid Sys 2:431–440
9. Diana G, Falco M, Cigada A, Manenti A (2000) On the measurement of overhead transmission lines conductor self-damping. IEEE Trans Power Deliv 15(1):285–292
10. IEEE Std. 563-1978 (1978) Guide on conductor self-damping measurements. Institute of Electrical and Electronics Engineers, New York
11. Cantatore A, Cigda A, Sala R, Zappa E (2009) Hyperbolic tangent algorithm for periodic effect cancellation in sub-pixel resolution edge displacement measurement. Measurement 42:1226–1232. doi:10.1016/j.measurement.2009.06.001
12. Ma Yi, Soatto S, Koseckà J, Sastry S (2004) An invitation to 3-D vision. Springer, New York, ISBN 0-387-00893-4
13. Cigada A, Sala R, Zappa E (2003) On the reduction of sub-pixel error in image based displacement measurement. In: XVII IMEKO world congress metrology in the 3rd millennium, Dubrovnik, 22–27 June 2003
14. Rawlins CB (1988) An efficient method for measuring dissipation by dampers in laboratory spans. IEEE Trans Power Deliv 3(3):1146–1156
15. Schmidt JT, Biedenbach G, Krispin HJ (1997) Laboratory measurement of the power dissipation characteristics of Aeolian vibration dampers. IEEE Trans Power Deliv 12(4):1614–1621

Chapter 20
Rapid Soil Displacements from MEMs Accelerometers

F.M. Levy and D.J. Richards

Abstract The use of measured accelerations to derive ground displacements can result in large signal drift during numerical integration. To overcome this, a digital high pass filter based on Frequency-sampling Design is proposed to attenuate the drift. The filter is benchmarked against other methods in small (< 3 mm) and large displacement (> 5 mm) testing. The proposed algorithm results in calculated displacements that have a very small discrepancy from measured displacements for both the small and large displacements respectively. The performance of the MEMs accelerometers are found to compare favourably with traditional piezoelectric technology. The implementation of a MEMs based ground array to detect the geometry of soil failure mechanism associated with foundation uplift was successful. The peak displacements derived from the measured accelerations corroborate with the laser displacement measurements with an error less than 10%.

Keywords Footings • Foundations • MEMs accelerometers • Soil • High pass filters • Accelerometer integration

20.1 Introduction

The UK high voltage transmission tower network owned by National Grid (Plc) is undergoing extensive modernisation and strengthening in response to future generation patterns associated with European Union carbon targets. A significant component of the modernisation cost originates from the transmission tower footing systems due to an apparent understrength when assessed against current design guidance. However tower footings rarely if ever fail suggesting other components of resistance to uplift exist that are not currently used in design e.g. rate loading effects.

In the past decade there has been significant research employing scaled physical modelling techniques using a geotechnical centrifuge to further understanding on the performance of footings subject to rapid loading. These tests found that there was considerable additional uplift capacity due to the generation of suctions on the base of footings founded on clay [1]. The log rate of model pullout was correlated to the magnitude of suction on the base (Fig. 20.1). These findings are important as peak loads on footings occur at fast loading rates generated by dynamic loading events such as cable breakage [2]. However the design and testing of footings to resist rapid load rates is not currently considered in UK design guidance.

Centrifuge modelling is able to replicate the confining stress state of in situ conditions by creating an artificial gravity to increase the overburden pressure, which maintains the stress/strain behaviour of the soil [3]. However the soil medium in these tests (kaolin) has atypical engineering properties compared to clays encountered in the field suggesting that extrapolation of centrifuge results to full scale may not be fully appropriate. These doubts, coupled with long term climatic effects and construction defects of in situ footing construction have prompted an extended investigation into foundation performance at field scale.

The last reported field test on transmission tower footings subject to rapid uplift was conducted by [4]. This study reported that UK practice considerably underestimated the strength of the footings tested at rapid uplift rates. To update understanding of in situ behaviour a series of tests will be carried out at the BRE London Clay research site in Chattenden, Kent during October 2012. The ground conditions of the site have been well characterised by many studies [5]. The footings will be subject to rapidly applied uplift loads using a 200 t crane connected to a hydraulic loading system.

F.M. Levy (✉) • D.J. Richards
School of Civil Engineering & the Environment, University of Southampton, Highfield, Southampton SO17 1BJ, United Kingdom
e-mail: f.levy@soton.ac.uk

J.M. Caicedo et al. (eds.), *Topics on the Dynamics of Civil Structures, Volume 1*,
Conference Proceedings of the Society for Experimental Mechanics Series 26,
DOI 10.1007/978-1-4614-2413-0_20,

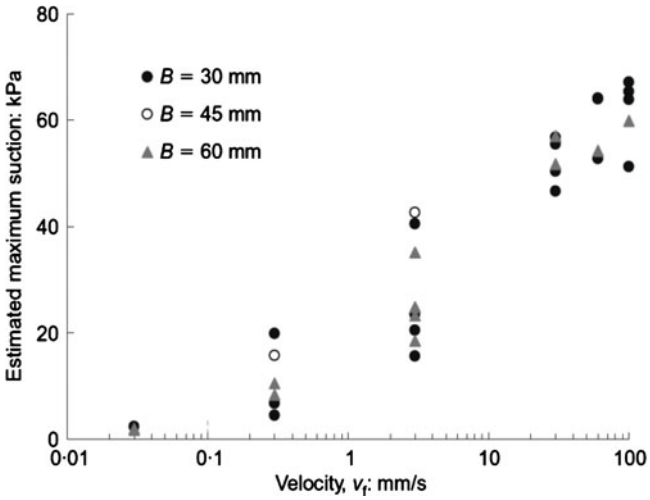

Fig. 20.1 Relationship of peak suction with pullout velocity [1]

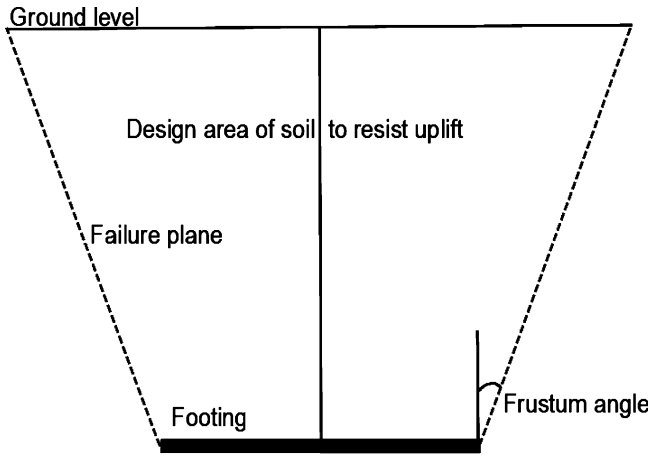

Fig. 20.2 Frustum method

In UK design practice uplift resistance is derived from the weight of the soil above the footing and the weight of the footing. The geometry of soil (constrained by planes of soil failure) assumed to resist loading is an inverted truncated cone (frustum) as depicted in Fig. 20.2. The frustum angles vary from 15° to 25° for low and high strength soils respectively.

Insights into failure plane geometries are commonly gained through excavation of footings post failure coupled with observations of surface cracking. However, both of these practises are extremely subjective. It is possible to view soil deformations directly through half space testing, where a cutaway of the model is viewed as it deforms. However it is well known that in reduced scale testing that stress/strain behaviour and shear bands do not scale requiring careful interpretation.

To overcome these difficulties the direct measurement of sub-surface deformations in soil may be measured using an accelerometer array placed in the region of soil failure where soil displacements are inferred from resultant accelerations. Through the scrutiny of the differential movement of the array the shape and overall volume of soil deforming may be determined.

The use of accelerometers as means to measure soil mass trajectory has not been reported in the geotechnical literature. This has led the authors to carry out a feasibility study into the suitability of MEMs accelerometers to determine ground displacements using signal processing techniques. The ultimate aim is to determine a methodology by which the zone of failure around the footings in Chattenden can be revealed.

Section 20.2 contains a research study into prior usage of accelerometers for displacements. Sections 20.3 and 20.4 detail small (< 3 mm) and large (> 5 mm) displacement tests to compare the efficacy of the methods discussed in Sect. 20.2. Finally Sect. 20.5 contains preliminary results from two footing rapid load tests conducted in the University of Southampton Structures Laboratory.

The data acquisition in Sects. 20.3, 20.4 and 20.5 was carried out using National Instruments (NI) 9234 modules on a NI CompactDAQ-9188 chassis. The chassis was connected via an ethernet cable to a Dell E6400 laptop running LabVIEW. The data was not scaled during acquisition and the TDMS file format was used. All of the accelerometers mentioned herein were sourced from Kistler.

20.2 Displacement Processing

The notion of calculating accelerations from displacements is theoretically sound however in practise this process has been shown to be problematic [6]. It is observed that significant drift can occur dominating the true signal and that the function of this drift is difficult to deduce. The FFT-DDI filter was designed to alleviate this drift after observation of excessive drift during analogue filtering [7]. The first two points of the 2,048 signal FFT are matched to the third and the complex conjugate of the second point is taken to maintain conjugate symmetry (Fig. 20.3). They tested the filter with mixed low frequency sine waves with good performance. However a limitation is that only the first two frequency bins are set so drift may occur at high frequencies.

To test the robustness of the FFT-DDI method two other drift removal filters are used in Sects. 20.3 and 20.4. The FSDR filter is based on the Frequency-sampling Design methodology in [8]. Tabulated values of factors for one to three transition coefficients for bandpass and lowpass filters, but not for highpass filters have been documented [9]. This leads to the assumption that the coefficients ascribed to lowpass filters should work for highpass filters if reversed. The FSDR method uses two transition coefficients, which results in a 24 dB increase in attenuation as well as a narrower stopband.

The coefficients for the first and second transition samples are 0.10323486 and 0.58217779. These coefficients correspond to a FFT with 256 samples and BW of 17 [9]. The penultimate two values before the cut off frequency are weighted by these two coefficients such that the cut off frequency sample is 1. Samples before the first coefficient are made equal to a very small number (1×10^{-8}) to prevent aliasing from occurring due to the removal of spectral leakage [10]. A graphical representation of the filter is show in Fig. 20.4. The second filter was an FIR filter that has a Chebyshev Type II shape. The root mean square (RMS) error of the signal, the mean and maximum peak displacements were used as indicators of performance. For brevity only the mean peak displacements are shown in Sects. 20.3 and 20.4. To quantify the error a 10 s snapshot of the signal was taken after 10 s had elapsed.

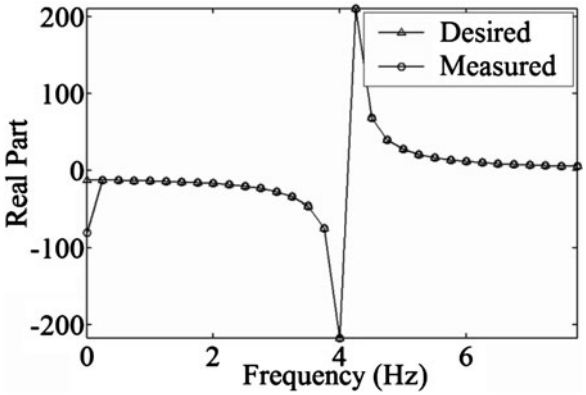

Fig. 20.3 Real part of the FFT-DDI FFT [7]

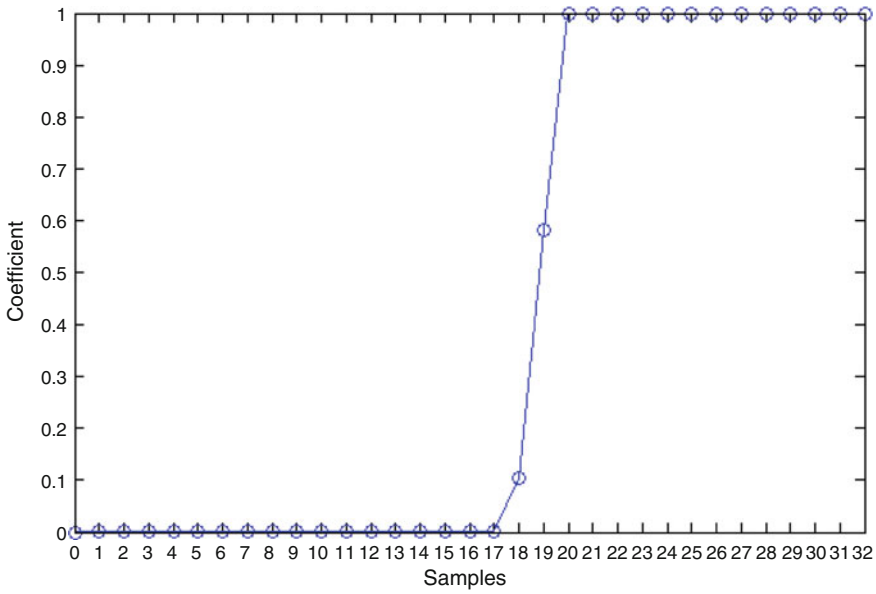

Fig. 20.4 FSDR filter shape

20.3 Small Displacement Tests

The small displacement testing was designed to sample and integrate waveforms that would appear in the expected range of ground response frequencies. The tests were conducted using two MEMs and two piezoelectric accelerometers (Table 20.1). The accelerometers were screwed onto a Devitron shaker with wax placed under the sensors to provide good contact. The arrangement of the sensors and the laser vibrometer is shown in Fig. 20.5 and were excited using sine and sawtooth waveforms, (Table 20.2). The displacement of the shaking table was measured using a Keyence LK G32 laser vibrometer mounted on a clamp that overhung the shaker. The gain on the amplifier was adjusted before sampling to ensure that there was adequate pick up from the laser displacement sensor. This means that the amplitude of displacement for each excitation frequency is not constant across all tests.

Voltage fluctuations from the measurement devices were sampled at 5.12 kHz for 30 s. Each of the sensors' voltages were converted into acceleration, with their offset value removed by deducting the mean value of the signal and then passed through a lowpass FIR Equiripple filter. For the comparison of the filter techniques the cut off frequencies of the FIR and FSDR filters were set to 0.7 Hz. This is because for the FFT-DDI method 0.7 Hz corresponds to the third frequency point in a 2048 FFT used in [7]. The 8315B30 was used as the reference accelerometer to compare the performance of the filters. For the accelerometer comparison the FSDR filter was used across all of the sensors.

In general the FFT-DDI filter under predicts displacements on both waveforms with the FIR and FSDR filters having negligible difference (Fig. 20.6). As the sine wave excitation frequencies increase drift is encountered in the FFT-DDI and FIR methods, however this drift may be remedied in the latter by increasing the cut off frequency. Some drift is also present in the 25 Hz sine wave for the FSDR filter. Nevertheless the FIR and FSDR filters perform better than the FFT-DDI method when compared to the laser vibrometer readings.

The 8315B30 MEMs accelerometer is slightly more accurate than the equivalent but older piezoelectric 8705B25 sensor (Fig. 20.7). The results also emphasise the importance of choosing the correct acceleration range of the sensor. Since the

Table 20.1 Accelerometer details

Name	Type	Range (Hz)	Range (g)
8702B100	Piezoelectric	0.5–10,000	100
8704B25	Piezoelectric	1–8,000	25
8305B100	MEMs	0–500	100
8315B30	MEMs	0–1,000	30

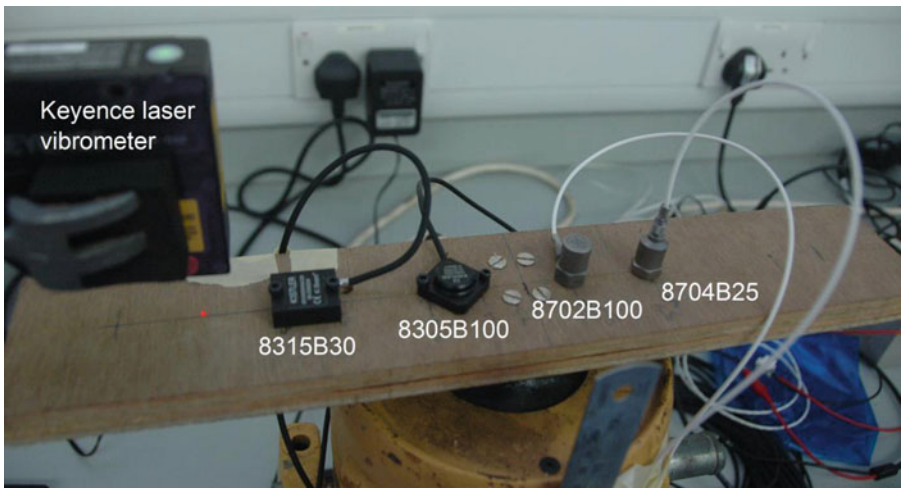

Fig. 20.5 Small displacement setup

Table 20.2 Excitation frequencies

Type	Excitation frequency (Hz)
Sine	1, 5, 10, 15, 20, 25, 40, 75
Sawtooth	1, 5, 10, 15, 20, 25

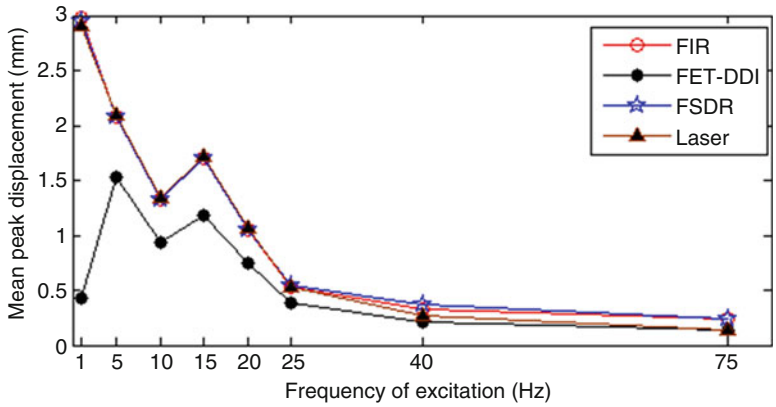

Fig. 20.6 Displacement comparison of different filter methods for sine waveform

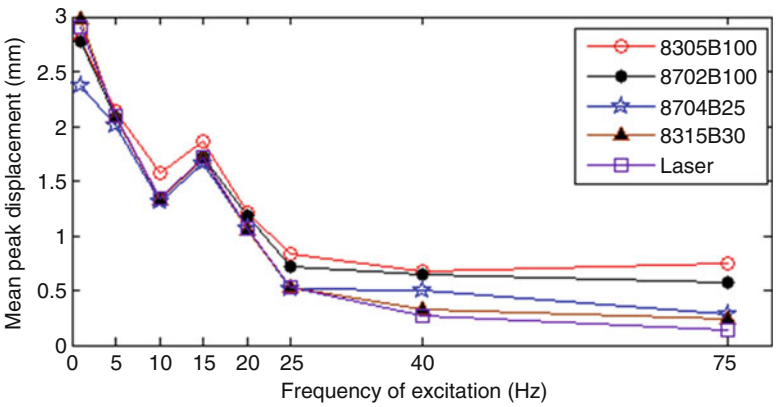

Fig. 20.7 Displacement comparison of different accelerometers for sine waveform

amplitude of the shaker needed to be limited to prevent the laser vibrometer stand from shaking, the sensors of 100 g range only utilised a small fraction of their range (3 g for the 75 Hz sine wave).

This means that the signals would have been close to their respective noise floors and therefore affected the double integration process used to derive displacement. The larger noise floor exhibited by the MEMs sensors is reflected by the relatively large difference in performance of the 8305B100 in comparison to the lower range sensors (Fig. 20.7).

20.4 Large Displacement Tests

The purpose of the large displacement tests was to investigate whether a qualitative prediction of the soil displacement profile as a result of footing uplift could be inferred from accelerometer output. In order to obtain large displacements an Instron structural actuator was configured for positional control executed using an Instron FastTrack 8000 (Fig. 20.8). The output of the displacement transducer (LVDT) within the head of the structural actuator was connected to a spare NI 9234 socket. This allowed the synchronous acquisition of accelerometer outputs and the position of the head of the actuator. The accelerometers were fixed to the head of the actuator using a fabricated mounting block and clamping arrangement. The displacement profiles used were a sawtooth and triangular ramp in Fig. 20.8.

The results of the large displacement tests corroborate from the findings in Sect. 20.4, namely that the FIR and FSDR methods produce similar results and that the FFT-DDI filter consistently under predicts the reference displacement measurement, (Fig. 20.9). The FIR and FSDR filters result in calculated displacements that are within 1.5–2.0 mm of the LVDT measurements. However the 0.5 Hz sawtooth wave displacement calculation using the FIR filter results in a severely distorted profile, this is most likely due to the proximity of the cut-off frequency (0.25 Hz) and the excitation frequency.

With regards to the comparisons of the various accelerometers only the MEMs sensors were measured owing to the failure of the charge coupler used for the piezoelectric accelerometers. At low frequencies of excitation there is a large error (14 mm), in the calculated displacement for the 8305B100 sensor which diminishes to approximately to 1.5 mm (Fig. 20.10).

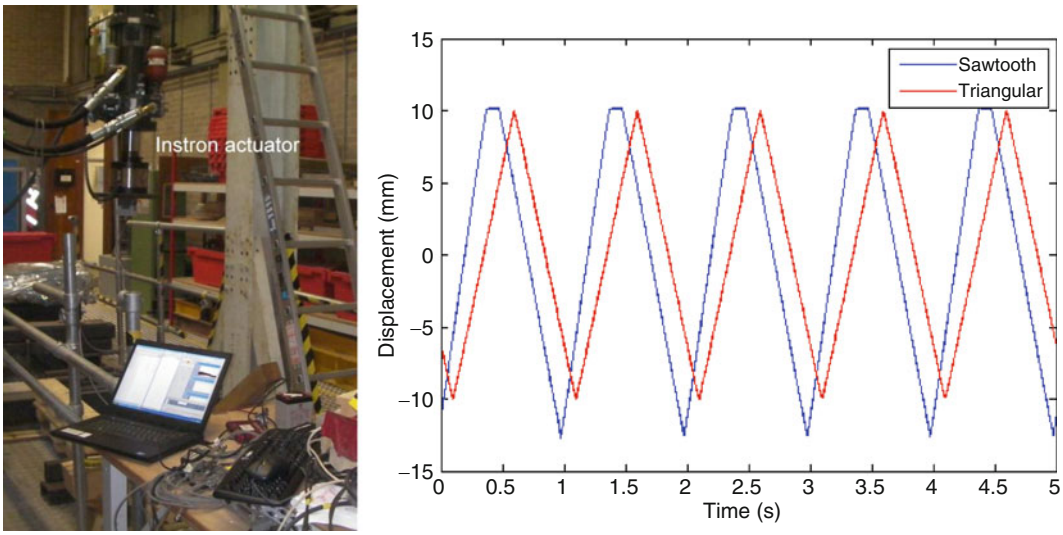

Fig. 20.8 Instron actuator (*left*) and waveforms (*right*)

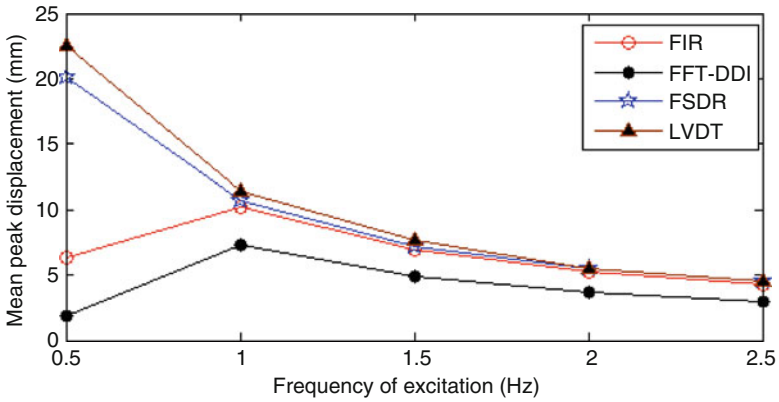

Fig. 20.9 Comparison of different filter methods for sawtooth waveform

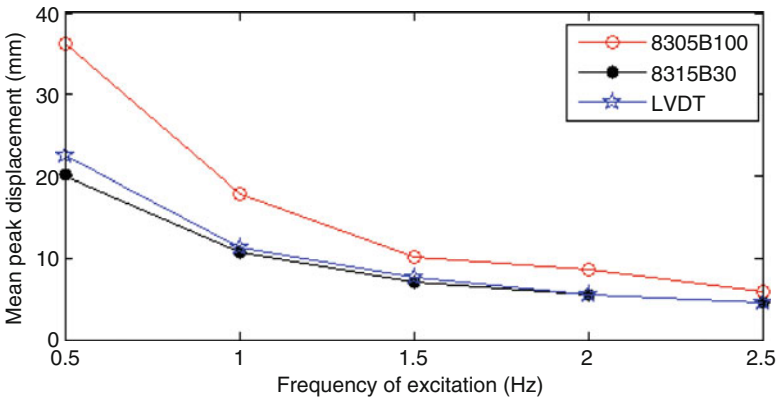

Fig. 20.10 Displacement comparison of MEMs accelerometers for sawtooth waveform

The likely cause is that the signal to noise ratio is very low at low frequencies for the 8305B100, which is not the case for the lower range sensor (Fig. 20.11).

For the triangular waveform the 8305B100 error is much greater (31 mm at 3 Hz) and only decreases slightly with increase in excitation frequency. This is possibly due to the "ringing" that is shown in Fig. 20.11, which may have been from poor accelerometer contact or vibrations in the actuator.

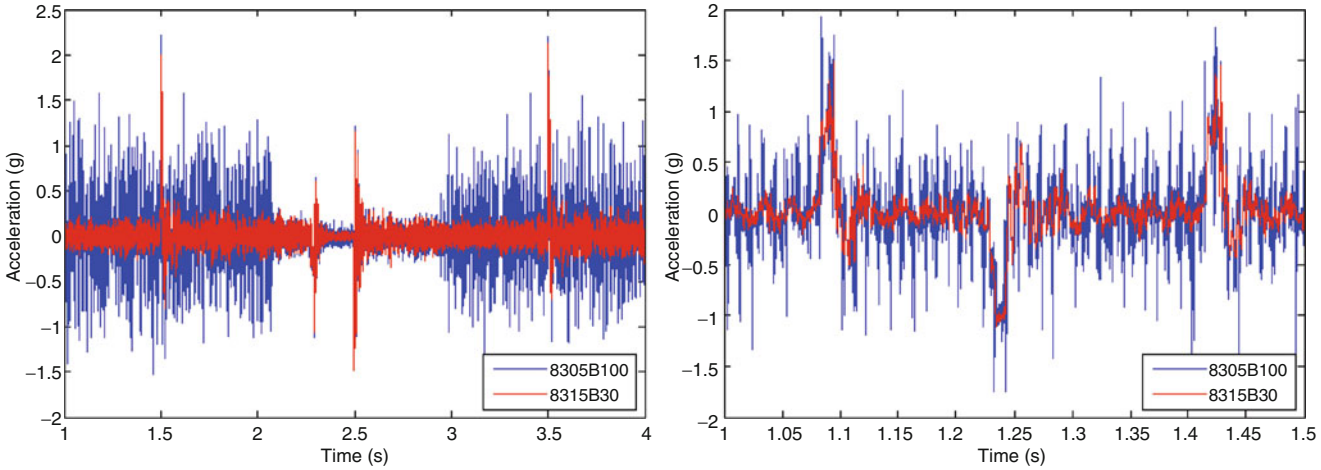

Fig. 20.11 Raw acceleration from MEMs accelerometers 0.5 Hz sawtooth (*left*) and 3Hz triangular (*right*)

20.5 Rapid Load Test

The principle purpose of the scaled laboratory box testing regime was to rigorously test the design of proposed rapid loading system. The secondary objective was to ascertain the resultant magnitude of acceleration of the soil during uplift so that the acceleration range likely to be encountered in the field tests could be specified. The geometry of the footings installed in Chattenden was idealised as a reinforced steel plate (Fig. 20.12).

This section details two preliminary plate uplift tests that were carried out with different peak loads: 1.5 t (Test 1) and 2 t (Test 2). It should be noted that the hydraulic loading system is programmed to apply a peak load within a constrained displacement window meaning that load rate is a function of peak load, available displacement and the resistive force of the soil above the plate. In both tests the constrained displacement was set to 50 mm, equivalent to approximately 11% of the width of the plate (425 mm). The placement of the plate on a granular material meant that no suctions would develop. However it was expected that there would be a rate dependent strengthening of the granular material, which is has not been prior reported in footing uplift testing literature.

A wooden strong box was filled with Type 1 granular fill [11] with the steel plate placed 750 mm below the surface. A total of three layers 350, 300 and 300 mm thick were placed with a further 150 mm loose layer placed on the top of the final compacted layer in order to provide overburden to the sensors placed on the topmost compacted layer (Fig. 20.13).

Three 8315B30 MEMs accelerometers positioned at 0, 225 and 425 mm from the centre of the reinforced plate were laid on top of each compacted layer. It is recommended that the mass of the sensor should be less than 10% of the moving mass so the sensors were screwed onto small wooden plates to maximise the coupling of soil to the sensor [12]. The sensors were placed on and covered with small particles ($d \leq 4.25$ mm) in Test 1 and fine sand in Test 2 to investigate which method better aided the coupling of the sensor to the soil.

The plate displacement and load was measured using a laser displacement gauge and an in-line load cell. The sampling frequency was set to 51.2 kHz, which is the maximum acquisition rate of the NI 9234 module. The data logging in LabVIEW was started manually and there was a gap of approximately 10 s between the start of logging and the application of load. The logging was manually terminated after the hydraulic loading system had reached its constrained displacement and no soil movement was being observed.

The results of the two tests were very encouraging; peak load was reached after 170 ms and 82 ms of load application for Test 1 and Test 2. This resulted in respective loading rates of approximately 86 kN/s and 239 kN/s. The load displacement (normalised as displacement divided by plate width) curves of the plate are shown in Fig. 20.14. In each test peak load was achieved well below the 10 mm criterion set by National Grid for maximum vertical movement. The capacities achieved were at least twice that using the Frustum method (Sect. 20.1). This implies that there is a rate enhancement in addition to suctions which is a scenario not considered thus far in the field of footing uplift, rapid or otherwise.

For brevity only the results from the accelerometers from Test 2 are considered. It was found that the Test 1 and Test 2 accelerometer response were very different (Fig. 20.15). This may have happened for two reasons. The placement of sand in Test 2 as opposed to small particles in Test 1 may have resulted in greater coupling with the Type I fill. Also, the soil was

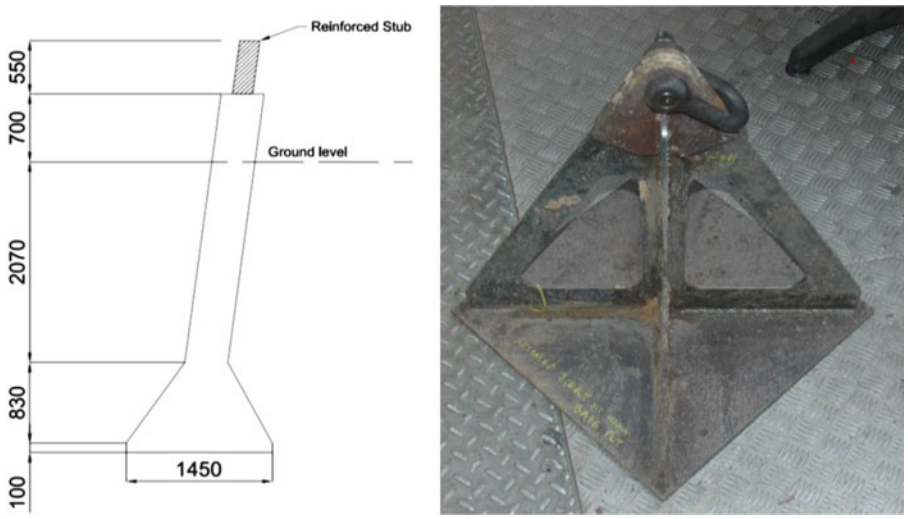

Fig. 20.12 Chattenden footing (*left*) and plate idealisation (*right*)

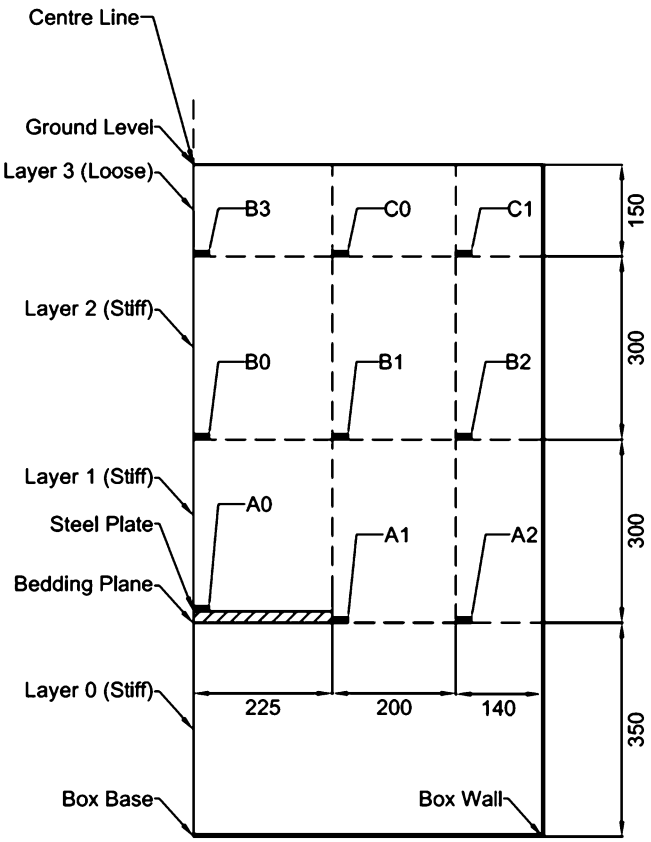

Fig. 20.13 General arrangement of accelerometers and soil layers

seen to be not as compacted in Test 1 as in Test 2, particularly around the central anchor stem. This resulted in a 3% displacement for little load addition indicating compaction was occurring (Fig. 20.14). The resultant movement of individualistic particles around the sensors may have contributed to the noise. Further tests are needed to examine the differences of coupling techniques. Nevertheless, the resultant acceleration impulses were only a single order of magnitude

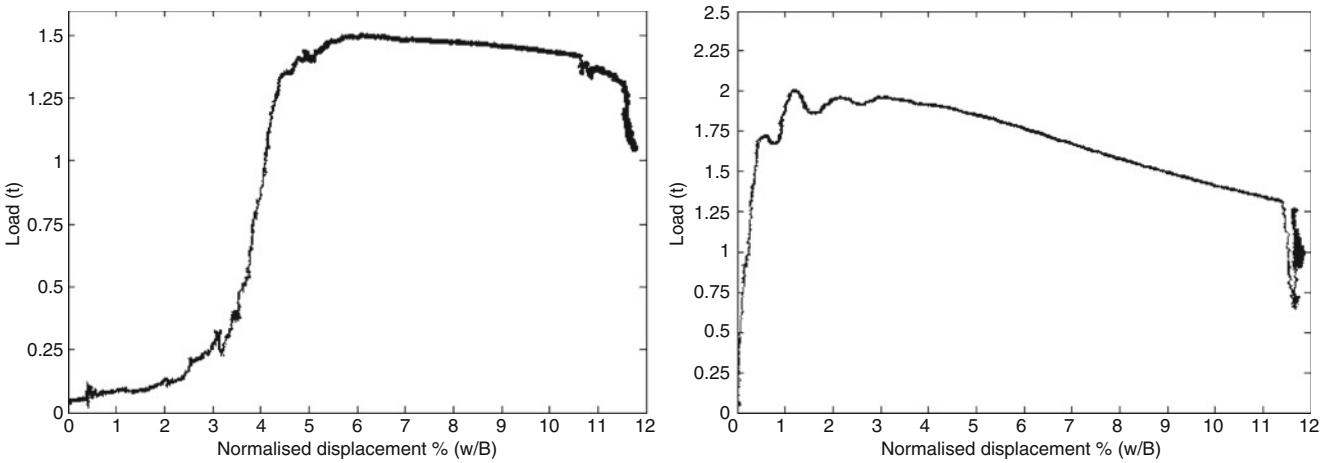

Fig. 20.14 Load displacement response in test 1 (*left*) and test 2 (*right*)

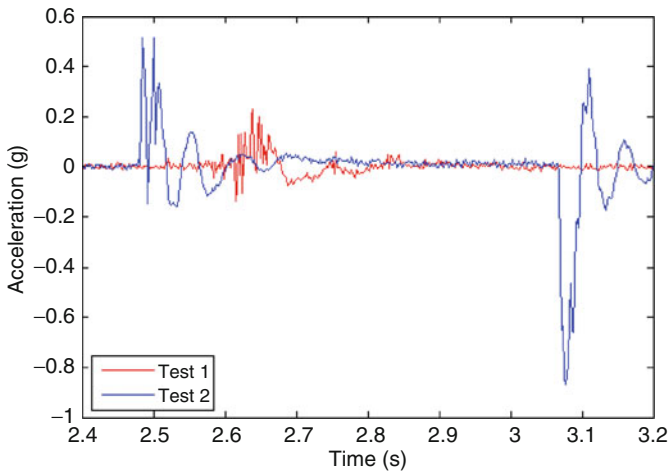

Fig. 20.15 Accelerometer response at B1 (225, 300)

away from the noise floor. By utilising only a fraction of the available range of the accelerometers this complicated displacement processing due to noise contamination.

The accelerometer located on the plate was used to test the feasibility of the filters discussed previously. This is because the laser displacement gauge mounted on the loader provided a reference displacement that the calculated displacements could be compared directly to. However, a preliminary analysis found that successive attempts with the filters in Sect. 20.2 were not successful in inferring the displacement. This implies that the filter techniques invested are more suited to periodic waveforms rather than singular discrete impulses.

In lieu of filtering a manual approach was used to derive displacements. An acceleration signal with its mean removed was numerically integrated then the section of velocity profile between the rapid increases and decreases in velocity was separated. Velocities between the first and last point of this data sequence were set to 0 to ensure that numerical integration could take place with no drift. The offset value of the drift at the first point was then deducted for the segmented velocity sequence. Figure 20.16 shows the adjusted velocity profile for the accelerometer on the plate.

Following this process the velocities were then simply integrated again. The shape of the resulting displacement corroborated with the laser gauge (left in Fig. 20.17). Furthermore, the peak displacements of the accelerometers were with 2 mm of the peak displacement recorded by the laser displacement gauge (right in Fig. 20.17). The peak displacements of the accelerometers shows that granular fill once a failure plane was established moved as a rigid block. This suggests a "locking up" mechanism where further small strain backfill strengthening precedes failure that occurs once the backfill cannot stiffen further. Figure 20.16 shows the stiffening stage occurs in the first 150 ms (2.45–2.60 s) after load followed by failure. The "locked up" energy is released when the granular fill yields resulting in the plate accelerating (2.6–2.85 s) before

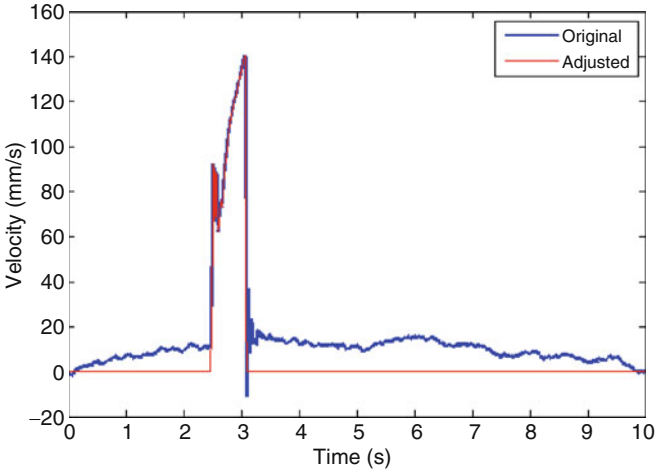

Fig. 20.16 Adjusted velocity profile

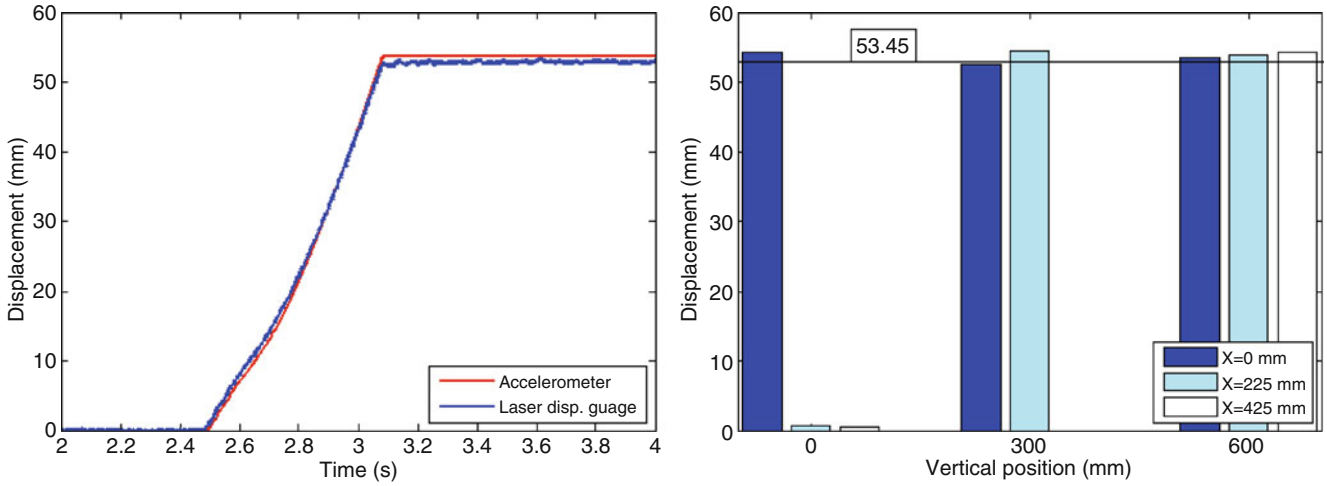

Fig. 20.17 Displacement profile (*left*) and peak displacements (*right*)

the pullout velocity of the loader takes over. Nevertheless, this small strain strength stiffening period adds considerable uplift resistance.

The arrangement of the peak displacements indicates that the failure plane was inclined and also that its extents were between accelerometers B2 (425,300) and C1 (425,600). B2 (425,300) is thought to have rotated during the test due to a change in the mean recorded voltage. This inference suggests that the frustum angle of failure was approximately 25°–33°. The lower value corresponds to a frustum whose sides intercept the side of the box at the surface and the upper value to a failure region in the vicinity of B2 (Fig. 20.18). If the angle of failure is greater than 25° then the full capacity of the frustum was not actually mobilised due to clipping the box walls.

To further validate the shape of the failure zone it was decided that the peak negative accelerations at approximately 3.1 s be used (Fig. 20.15). When the plate had reached its maximum displacement a mass of soil was observed to be moving. It is reasoned that the magnitude of deceleration would indicate the region of failure. This is because it is expected that an accelerometer within the moving mass would decelerate rapidly whereas a sensor outside of this mass would only detect a minor deceleration when displacement ceased.

Using this methodology it was observed that deceleration was constant across the top layer of the accelerometers. This correlated with observations of surface movement. Decelerations were constant (approximately 10 m/s/s) along the centre line of the box but dropped significantly along the bottom layer indicating that the zone of failure was inclined. Using the tilt observation from above the same plane of failure is inferred.

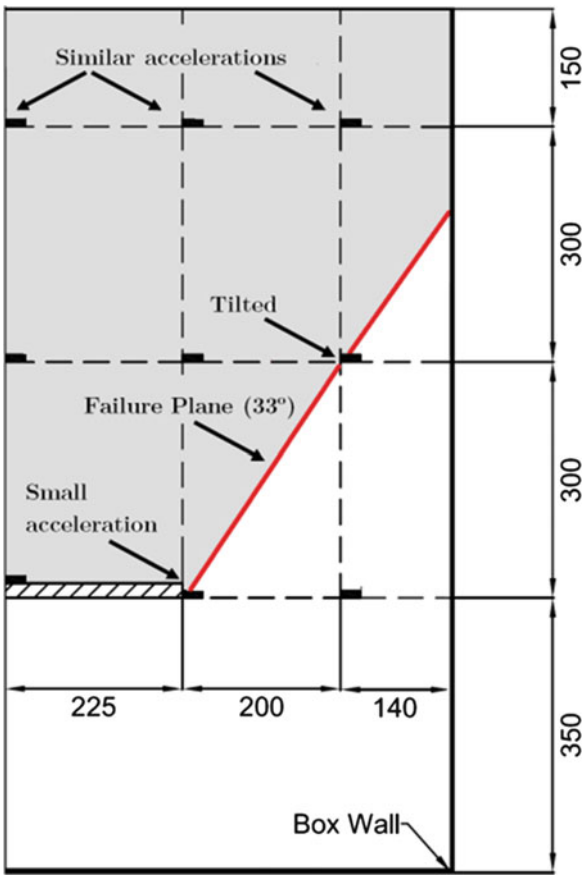

Fig. 20.18 Inferred failure plane

20.6 Conclusions

(a) The small displacement tests found the FIR and FSDR filters performed better than the FFT-DDI filter which is seen to under predict throughout. The MEMS 8315B30 appeared to have better performance to the equivalent 8702B25 piezoelectric accelerometer.
(b) When calculating peak displacements attention needs to be paid to the ratio of peak acceleration to the noise floor. Any extraneous noise will be integrated twice over leading to error in the final displacement calculation.
(c) The large displacement tests showed that it was possible to infer complex displacements from MEMs accelerometers. Again both the FIR and FSDR filters seemed the most applicable to removing the drift encountered.
(d) The attempt using MEMs accelerometers to deduce soil movements during a rapid uplift test was successful. The error encountered was less than 10%.

Acknowledgements The authors would like to thank Dr E. Rustigihi and Prof. P White from the Institute of Sound and Vibration at the University of Southampton for their discussions on accelerometers and postprocessing. We are also grateful to Kistler for loaning the accelerometers for the small and large displacement tests in Sects. 20.3 and 20.4. Finally, the design of the rapid hydraulic loading system is credited to Alan Kenchington of Advanced Structural Monitoring Ltd, UK.

References

1. Lehane BM, Gaudin C, Richards DJ, Rattley MJ (2008) Rate effects on the vertical uplift capacity of footings founded in clay. Géotechnique 58(1):13–21
2. Clayton CRI (1994) The uplift resistance of foundations for electricity transmission towers, CBGE9401/1
3. Schofield AN (1980) Cambridge geotechnical centrifuge operations. Géotechnique 30(3):227–268

4. Yazdanbod A, Sheikh SA, O'Neill MW (1987) Uplift of shallow underreams in jointed clay. In: Foundations for transmission line towers (GSP8), Atlantic city, New Jersey, pp 110–127
5. Crilly MS, Driscoll RMC (2000) The behaviour of lightly loaded piles in swelling ground and implications for their design. Proc Inst Civil Eng Geotech Eng 143:3–16
6. Ribeiro JGT, Freire JLF, de Castro JTP (1999) Some comments on digital integration to measure displacements using accelerometers. In: Proceedings of the society for optical engineering, Boston, Massachusetts, pp 554–559
7. Ribeiro JGT, de Castro JTP, Freire JLF (2003) Using the FFT-DDI method to measure displacements with piezoelectric, resistive and ICP accelerometers. In: Proceedings of the 22nd IMAC conference, Kissimee, Florida
8. Oppenheim AV, Schafer RW (1975) Digital signal processing, 1st edn. Prentice-Hall, Englewood Cliffs
9. Rabiner LR, Schafer RW (1971) Recursive and nonrecursive realization of digital filters designed by frequency sampling techniques. IEEE Trans Audio Electroacoustics 19(3):200–207
10. Smith CC, Dahl JF, Thornhill RJ (1996) The duality of leakage and aliasing and improved digital spectral analysis techniques. J Dynam Syst Meas Control 118(4):741–747
11. Depart of Transport (2009) MCHW volume 1 SHW: roads pavements - unbound cement and other hydraulically bound mixtures. TSO, London, UK
12. Brown MJ (2004) The rapid load testing of piles in fine grained soils. Ph.D Thesis, University of Sheffield

Chapter 21
Blind Source Separation of Convolutive Mixtures towards Modal Identification

Ayan Sadhu and Sriram Narasimhan

Abstract Blind source separation (BSS) based signal processing techniques have shown significant promise for ambient modal identification of structural and mechanical systems. Many of these methods operate on the assumption that the underlying sources are mixed instantaneously, known as the instantaneous mixing model. If the data contains time synchronization (TS) errors, such as offsets and drifts commonly associated with wireless sensor networks, the equations of motion cannot be reduced to the instantaneous form in the time domain, and must be treated as convolutive mixtures. While other avenues such as time-synchronization protocols exist in the literature to address TS issues, an alternate algorithmic solution within the modal identification framework is presented here. In the proposed method, the convolutive mixtures of measurements are first transformed into instantaneous mixtures in the frequency domain, and then the complex BSS method is employed to separate the independent sources in the transformed domain. Finally, inverse Fourier transform is employed to transform the sources back into the time domain. The application of this algorithm is demonstrated using simulation examples.

Keywords Blind source separation • Convolutive mixing • Ambient modal identification • Time synchronization errors • Complex ICA

21.1 Introduction

Output-only modal identification has tremendous potential in the monitoring, retrofit and repair of civil infrastructure. Several time and frequency domain methods have been studied extensively, and the wealth of literature on this topic is vast [1]. More recently, powerful signal processing methods based on blind source separation principles (BSS) [2, 3] have been studied for the same purposes [4, 5, 6, 7, 8]. These methods allow one to easily integrate powerful signal processing methods such as time-frequency decompositions into the basic framework of modal identification.

BSS is a powerful signal processing technique which separates the original source waveforms from their observed mixtures without the knowledge of system information and the sources. For most applications, the sources are related to mixtures by simple linear mixing models as illustrated in Fig. 21.1. In general, there are two ways to represent the mixing of sources: (a) static or instantaneous, and (b) dynamic or convolutive. The instantaneous mixing model [2, 4] is the most basic model where sources $s(k)$ arrive instantly at the sensors $x(k)$ but with differing signal intensities (defined by mixing matrix **A**), and is expressed as:

$$\left.\begin{aligned} \mathbf{x}(k) &= \mathbf{A}\mathbf{s}(k) \\ \hat{\mathbf{s}}(k) = \mathbf{y}(k) &= \mathbf{W}\mathbf{x}(k) \end{aligned}\right\} \tag{21.1}$$

A. Sadhu • S. Narasimhan (✉)
Department of Civil and Environmental Engineering, University of Waterloo, Waterloo, Ontario N2L 3G1, Canada
e-mail: snarasim@uwaterloo.ca

J.M. Caicedo et al. (eds.), *Topics on the Dynamics of Civil Structures, Volume 1*,
Conference Proceedings of the Society for Experimental Mechanics Series 26,
DOI 10.1007/978-1-4614-2413-0_21,

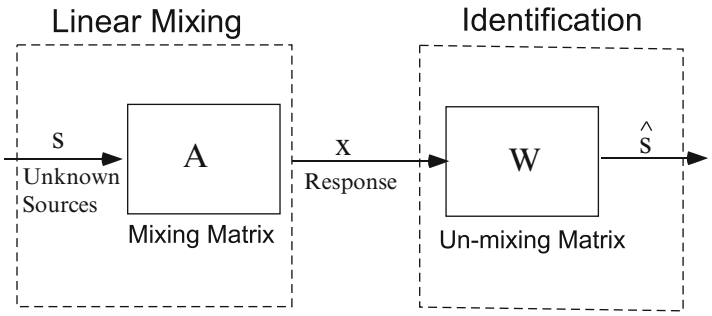

Fig. 21.1 Illustration of blind source separation

where, $\hat{\mathbf{s}}(k)$ is the estimated source and $\mathbf{W}$ is the un-mixing matrix. $\mathbf{W}$ is estimated using the statistics of the sources, which can be either higher order statistics based independent component analysis (ICA) [9], or second-order statistics based blind identification (SOBI) [2]. Different forms of instantaneous mixing models have recently been implemented [10, 6, 7, 8] for improving the efficiency of BSS towards ambient modal identification. In the such models, it is assumed that the equations of motion can be re-cast in the equivalent modal superposition form, and there are no time delays associated with the mixing of independent measurements. While the first assumption does not pose serious issues dealing with the problem of linear modal identification under small amplitude motions, the instantaneous mixing model is not suitable to deal with the issue of time synchronization associated with wireless data acquisition [11, 12]. To separate sources (modes) mixed in this fashion, a convolutive BSS mixing model is necessary to represent the mixing process [12, 13, 14].

Several researchers [15, 16, 17] have evaluated the accuracy of the traditional modal identification methods using data containing unequal time offsets between individual sensors and drifts, collectively known as time synchronization (TS) issues, typically acquired in wireless sensor networks over long periods of time. It was observed that modal frequencies and damping ratios are not influenced by random time delays in the measurements; however, the quality of structural mode shapes obtained using such data suffered significantly. It was concluded that the effect of time delays is comparable, or can even exceed the effect of measurement noise at the sensors [17]. In addition to several TS protocols, there have been several attempts towards developing algorithms to deal with this issue. These include the use of auto-regressive models [15], or using time stamp information [18] and the modified frequency domain decomposition (FDD) technique [19]. In this paper, a new approach combining the advantages of traditional BSS with the new capability of dealing with TS issues in measurements is proposed.

21.2 Mixing Model

A convolutive model can be of two types, *echoic* or *anechoic*. An echoic convolutive mixture can be expressed as [13]:

$$x_i(t) = \sum_{j=1}^{n_s} \left(\int_{-\infty}^{\infty} a_{ij}(\tau) s_j(t-\tau) d\tau \right) \quad i = 1, 2, ..., n_m \tag{21.2}$$

where, n_s and n_m are the number of sources and measurements respectively. Eq. 21.2 represents a dynamic problem where the sources and the outputs have well defined time properties and the coefficients of the un-mixing system are essentially the coefficients of a deconvolution filter (e.g., finite impulse response filter). The instantaneous mixing model is a special case of the convolutive model, where the filter coefficients are constrained to be proportional to delta function $a_{ij}(t) = a_{ij}\delta(t)$. Compared to the echoic (full convolutive) model, anechoic mixture model linearly combines time-shifted and scaled versions of the sources, without permitting multiple occurrences of the same source in the mixture. These models are equivalent to echoic convolutive models for which the filter kernels are constrained to the form $a_{ij}(t) = a_{ij}\delta(t - \tau_{ij})$, resulting in the equation:

$$x_i(t) = \sum_{j=1}^{n_s} a_{ij} s_j(t - \tau_{ij}) \tag{21.3}$$

In the time domain, Eq. 21.3 is similar to the instantaneous mixing model, but the sources are shifted by the delay terms. Thus, the anechoic mixing model describes the superposition of sources with delay and attenuation terms. Fourier transformation on both sides of Eq. 21.3 yields:

$$X_i(\omega) = \sum_{j=1}^{n_s} a_{ij} e^{-i\omega\tau_{ij}} S_j(\omega) \tag{21.4}$$

Considering all the sensor measurements, Eq. 21.4 can be written as:

$$\begin{bmatrix} X_1(\omega) \\ X_2(\omega) \\ X_3(\omega) \\ . \\ . \\ . \\ X_{n_m}(\omega) \end{bmatrix} = \begin{bmatrix} a_{11} & a_{12} & a_{13} & . & . & . & a_{1n_s} \\ a_{21}e^{-i\omega\tau_{21}} & a_{22}e^{-i\omega\tau_{22}} & a_{23}e^{-i\omega\tau_{23}} & . & . & . & a_{2n_s}e^{-i\omega\tau_{2n_s}} \\ a_{31}e^{-i\omega\tau_{31}} & a_{32}e^{-i\omega\tau_{32}} & a_{33}e^{-i\omega\tau_{33}} & . & . & . & a_{3n_s}e^{-i\omega\tau_{3n_s}} \\ . & . & . & . & . & . & . \\ . & . & . & . & . & . & . \\ . & . & . & . & . & . & . \\ a_{n_m1}e^{-i\omega\tau_{n_m1}} & a_{n_m2}e^{-i\omega\tau_{n_m2}} & a_{n_m3}e^{-i\omega\tau_{n_m3}} & . & . & . & a_{n_mn_s}e^{-i\omega\tau_{n_mn_s}} \end{bmatrix} \begin{bmatrix} S_1(\omega) \\ S_2(\omega) \\ S_3(\omega) \\ . \\ . \\ . \\ S_{n_s}(\omega) \end{bmatrix}$$

$$\mathbf{X}(\omega) = A(\omega)S(\omega) \tag{21.5}$$

where $\mathbf{X}(\omega) = \{X_1(\omega), X_2(\omega), \ldots, X_{nm}(\omega)\}$ are n_m frequency domain mixtures, $\mathbf{A}(\omega)$ is the anechoic mixing matrix and $\mathbf{S}(\omega) = \{ S_1(\omega), S_2(\omega), \ldots, S_{ns}(\omega)\}$ are n_s frequency domain transformed sources. It is assumed that the first sensor is a common reference sensor (i.e., $\tau_{1j} = 0$). After transformation, Eq. 21.5 represents instantaneous mixing in the frequency domain. Once the underlying dynamics of the structural system are cast in the form of Eq. 21.5, standard BSS separation methods can then be employed to estimate the sources and the mixing matrix. Please note that the sources contain the dominant frequencies and damping, while the mixing matrix contains the mode shapes.

21.3 Details of the algorithm

The main focus of this paper is to develop a modal identification method to deal with measurements containing TS errors. Specifically, if the measurements are obtained from several independent sensors, the time as measured at the i^{th} sensor (t_i) with respect to a global or reference clock (t) is:

$$t_i = t + \alpha_i t - p_i \tag{21.6}$$

where α_i is the clock drift and p_i is the initial time (clock) offset of the i^{th} sensor with respect to the reference clock. For wireless sensor networks investigated in the literature, clock drifts of 40-50 μs s^{-1} have been measured in Mica2 and Imote2 nodes, respectively [16, 20]. It may be noted that although the term α is typically very small, its effect can be significant for long measurements, such as those undertaken for structural health monitoring. For example, a low cost 8 MHz crystal accumulates TS errors up to 5 ms in a 6 minute of period [21]. The result of TS errors is that the estimated mode shapes correspond poorly to the true ones, and hence the quality of health monitoring strategies may be affected significantly.

Assuming that TS errors exist, the measurement at the i^{th} sensor can be written as a superposition of a finite number of sources (which are the modal responses) as follows:

$$\bar{x}_i(t) = \sum_{j=1}^{n_s} \phi_{ij} q_j(t + \alpha_i t - p_i) \tag{21.7}$$

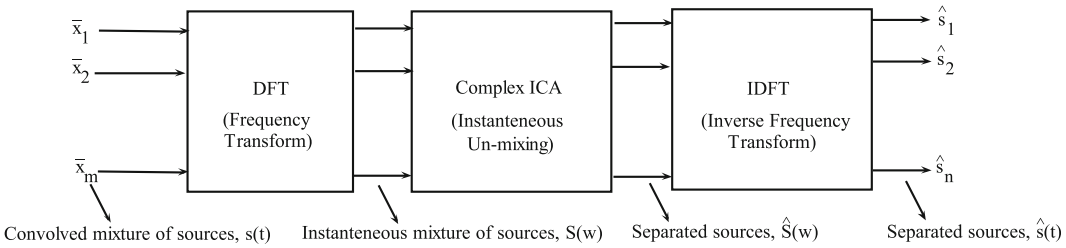

Fig. 21.2 Flowchart of the proposed algorithm

where ϕ_{ij} is the mode shape coordinate of the j^{th} mode for the i^{th} sensor, and $q_j(t)$ is the modal response of the j^{th} mode. Equation 21.7 can be generalized as:

$$\bar{x}_i(t) = \sum_{j=1}^{n_s} \phi_{ij} q_j(t - \tau_{ij}(t)) \quad i = 1, 2, ..., n_m \tag{21.8}$$

where $\tau_{i1}(t) = \tau_{i2}(t) = ... = \tau_{in_s}(t) = p_i - \alpha_i t$, assuming all the underlying sources in the i^{th} mixture are delayed by same amount ($p_i - \alpha_i t$). Comparing Equations 21.8 and 21.3, the problem of modal identification under TS errors can be cast in the form of anechoic mixtures.

Taking the Fourier transform on both sides of Equation 21.8, we get:

$$\bar{X}_i(\omega) = \sum_{j=1}^{n_s} \phi_{ij} \frac{e^{-\frac{i\omega p_i}{1+\alpha_i}}}{1+\alpha_i} Q_j\left(\frac{\omega}{1+\alpha_i}\right) \tag{21.9}$$

Since α is very small (i.e., order of μs), (1 + α) ≈ 1. Therefore Equation 21.9 can be simplified as:

$$\bar{X}_i(\omega) = \sum_{j=1}^{n_s} \phi_{ij} e^{-i\omega p_i} Q_j(\omega) \tag{21.10}$$

Hence, Equation 21.10 can be written in the same form of Equation 21.5:

$$\bar{\mathbf{X}}(\omega) = W(\omega) S(\omega) \tag{21.11}$$

where $\bar{\mathbf{X}}(\omega) = \{\bar{X}_1(\omega), \bar{X}_2(\omega), ..., \bar{X}_{n_m}(\omega)\}$ are n_m frequency domain mixtures, $\mathbf{W}(\omega)$ is the anechoic mixing matrix and $\mathbf{S}(\omega) = \{S_1(\omega), S_2(\omega), ..., S_{n_s}(\omega)\}$ are n_s frequency domain source signals. Equation 21.11 represents instantaneous mixing in the frequency domain, which can be solved by using ICA. For vibration signals, $\bar{\mathbf{X}}(\omega)$ contains the Fourier transform coefficients that are complex numbers, for which a suitable ICA algorithm that can handle complex variables is needed. Like the real-valued ICA, a complex ICA algorithm can exploit either the higher order statistics for separation [22] or use nonlinear functions, such as maximum likelihood [23], information-maximization [24], and maximization of non-Gaussianity [9, 25]. In the present study, higher-order statistics based complex ICA [22] is employed to separate the sources in the complex domain. Once the sources are separated in complex domain, they are transformed into the time domain by using inverse discrete Fourier transform (IDFT). Key steps of the proposed method is illustrated in the flowchart shown in Fig. 21.2. Once the sources are estimated, the mixing matrix **A** can be estimated using the pseudo-inverse of Equation 21.1:

$$\hat{\mathbf{A}} = (\hat{s}^T \hat{s})^{-1} \hat{s}^T \bar{x} \tag{21.12}$$

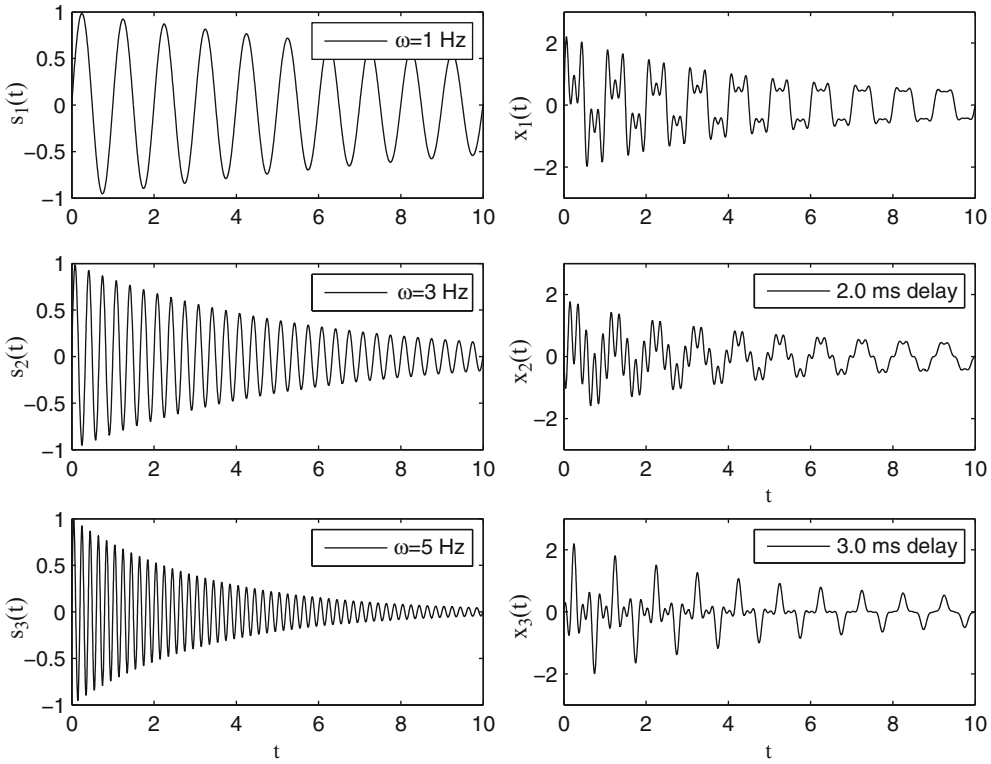

Fig. 21.3 Three sinusoids with $\omega = 1$, 3 and 5 Hz and their mixtures

21.4 Numerical Studies

In order to evaluate the performance of the proposed modal identification approach, numerical simulations are performed on idealized systems. First, the performance of the algorithm is demonstrated for a mixture of sine waves, followed by simulations of a 5-DOF mass-spring-dashpot system. TS errors are introduced into the synthetic measurements and the performance of the algorithm is quantified.

21.4.1 Case Study: Mixture of sinusoids

In this example, three mixtures of sine waves as shown in Fig. 21.3 with frequencies 1, 3 and 5 Hz respectively are considered. Two cases, when only p_i is present and when both p_i and α_i are present, are investigated.

21.4.1.1 Presence of offset only

For this case, $p_2 = 2.0$ and $p_3 = 3.0$ ms is assumed, which corresponds to 2.0 and 3.0 ms offsets, respectively, in the 2^{nd} and 3^{rd} mixtures. The sources estimated using the popular BSS-based SOBI method and the proposed method are shown in Fig. 21.4. From the results, it is clear that the accuracy of source separation using the proposed method is superior to the traditional SOBI method.

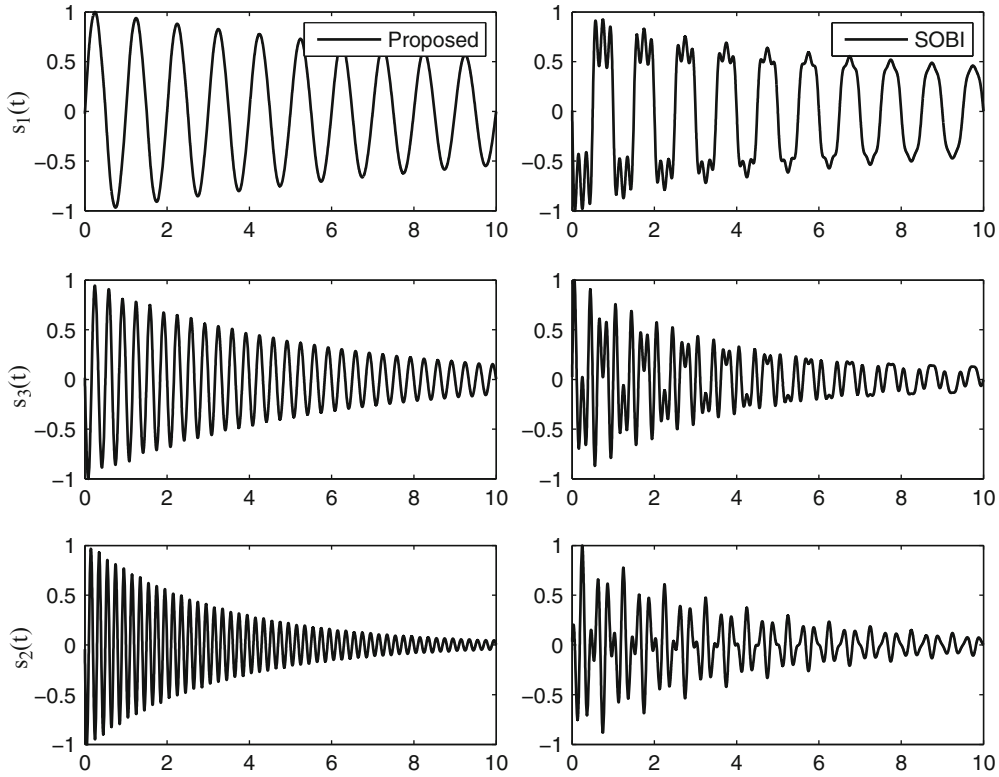

Fig. 21.4 Separated sources using the proposed method and the SOBI method

21.4.1.2 Presence of offsets and drifts

In order to see the effect of α_i in addition to the time offset, a signal of longer duration (10 min) is considered. α_2 and α_3 are assumed to be 40 and 50 μs s^{-1} respectively, while p_i is the same as previously considered. Fourier spectra of the estimated sources are compared in Fig. 21.5, for both SOBI and the proposed algorithm. Results from SOBI indicate that all the harmonics are present in the separated sources, while the proposed algorithm is capable of separating the individual harmonics.

21.4.2 Case Study: Building model

In order to present an application of the proposed method for civil engineering applications, simulations are performed on a 5-storey shear-beam structure model [7]. The state-space model for this system subjected to an external disturbance vector **w** is given by:

$$\begin{aligned} \dot{\mathbf{x}} &= \mathbf{A}\mathbf{x} + \mathbf{E}\mathbf{w} \\ \mathbf{y} &= \widetilde{\mathbf{C}}\mathbf{x} \end{aligned} \tag{21.13}$$

Here, the vector **x** is a vector of states, and the vector **y** represents the output vector, which is governed by $\widetilde{\mathbf{C}}$ matrix. The matrix **E** governs the location of the excitation on the structure. The system matrix **A** is constructed using **M**, **C** and **K** matrices. For the example building, the lumped weight of each floor is assumed to be 19.2 kN, and the damping is assumed to be 2% critical in all modes. The natural frequencies are 0.91, 3.37, 7.11, 10.66 and 12.73 Hz. The mode shape matrix (normalized with respect to top floor) for the building is given by:

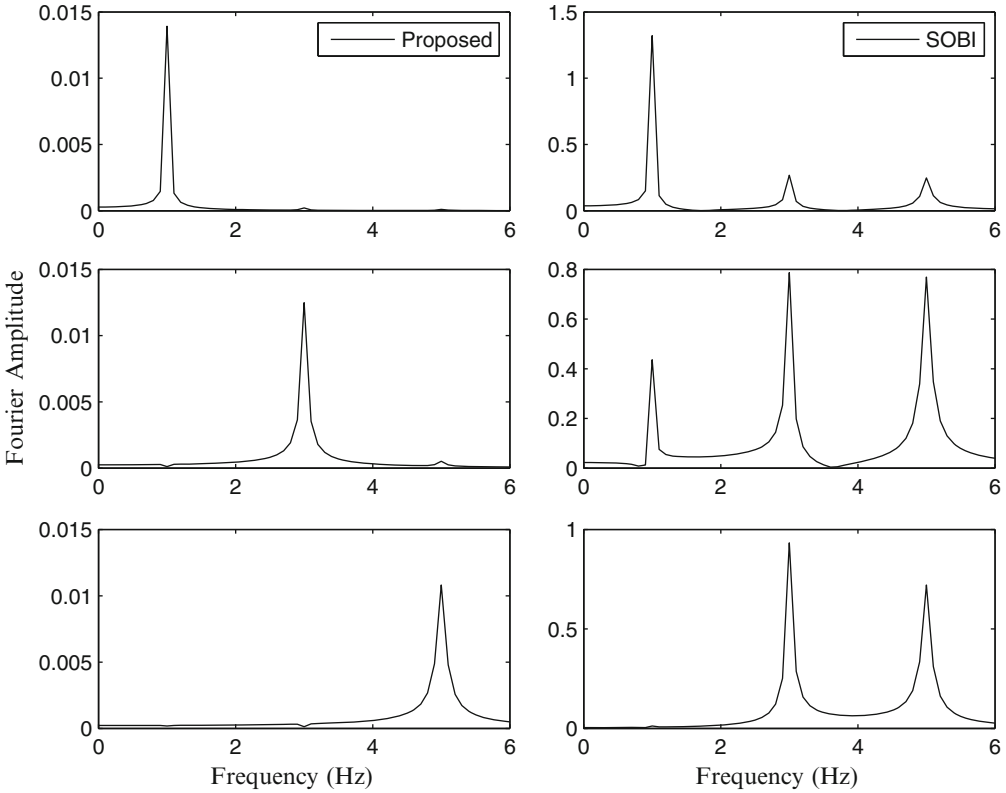

Fig. 21.5 Fourier spectra of the separated sources using the proposed method and the SOBI method

Table 21.1 Case 1: Total time delay = 0.0 ms

Sensor No.	Delay (ms)	$\text{MAC}_{Proposed}$	MAC_{SOBI}
1	0	1.000	1.000
2	0	0.999	0.999
3	0	0.999	0.999
4	0	0.999	0.999
5	0	0.999	0.999

$$\begin{bmatrix} 1.00 & 1.00 & 1.00 & 1.00 & 1.00 \\ 0.82 & -0.087 & -1.29 & -2.52 & -3.39 \\ 0.59 & -0.91 & -0.87 & 1.81 & 5.43 \\ 0.34 & -1.02 & 1.23 & 0.94 & -5.84 \\ 0.11 & -0.48 & 1.35 & -2.86 & 4.84 \end{bmatrix} \tag{21.14}$$

The 5-DOF building ($n_s = 5$) is excited by the zero mean unit variance Gaussian white noise at all floor levels.

21.4.2.1 Presence of offset

The performance of the algorithm is investigated for several values of clock offsets, 0.0, 10.0, 25.0 and 40.0 ms. These offsets are distributed, somewhat arbitrarily, among various sensors as listed in Tables 21.1–21.4. The results of source separation obtained for case 3 (as in Table 21.3) using the proposed algorithm and SOBI along with their Fourier spectra are shown in Fig. 21.6-21.7. It is observed that there is a significant mode mixing in the separated sources estimated using SOBI method, whereas, the sources estimated using the proposed method is nearly mono-component.

Table 21.2 Case 2: Total time delay = 10.0 ms

Sensor No.	Delay (ms)	$MAC_{Proposed}$	MAC_{SOBI}
1	0	1.000	1.000
2	5	0.999	0.992
3	5	0.999	0.942
4	0	0.999	0.949
5	0	0.999	0.989

Table 21.3 Case 3: Total time delay = 25.0 ms

Sensor No.	Delay (ms)	$MAC_{Proposed}$	MAC_{SOBI}
1	0	0.999	0.999
2	10	0.998	0.985
3	5	0.991	0.681
4	10	0.997	0.701
5	0	0.998	0.989

Table 21.4 Case 4: Total time delay = 40.0 ms

Sensor No.	Delay (ms)	$MAC_{Proposed}$	MAC_{SOBI}
1	0	0.999	0.999
2	15	0.997	0.966
3	10	0.987	0.629
4	10	0.994	0.608
5	5	0.981	0.879

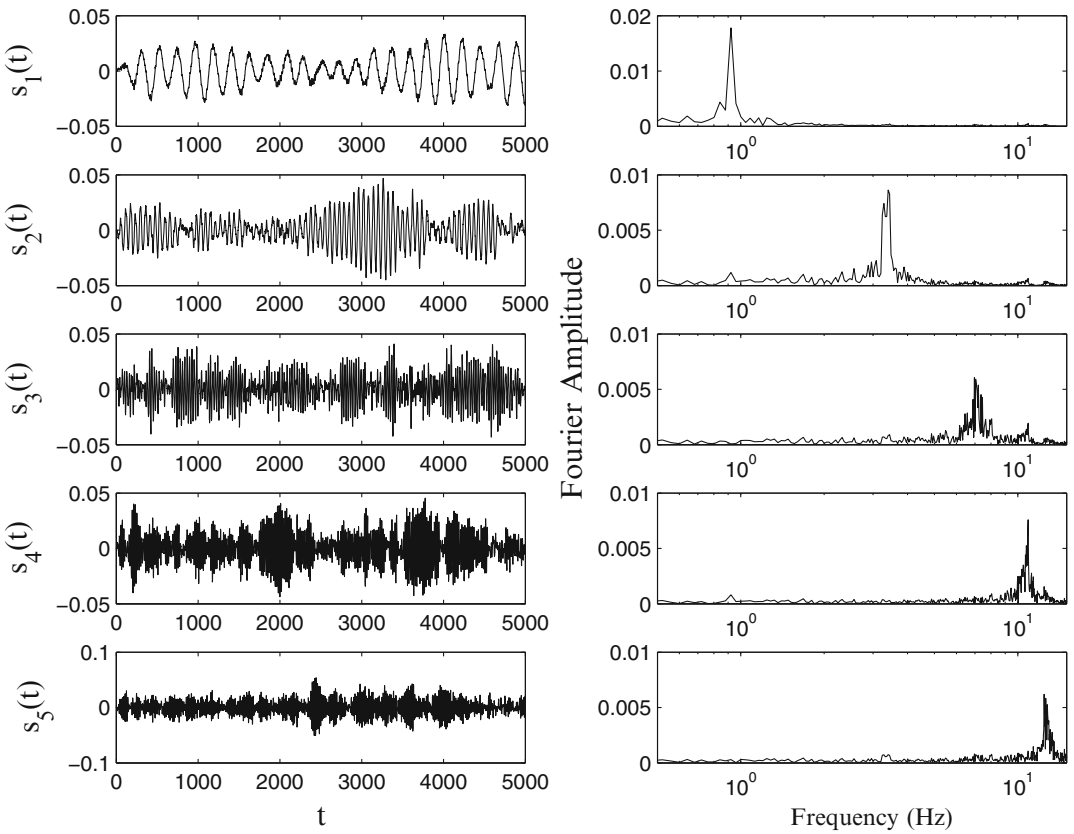

Fig. 21.6 Estimated sources using the proposed method and their Fourier spectra

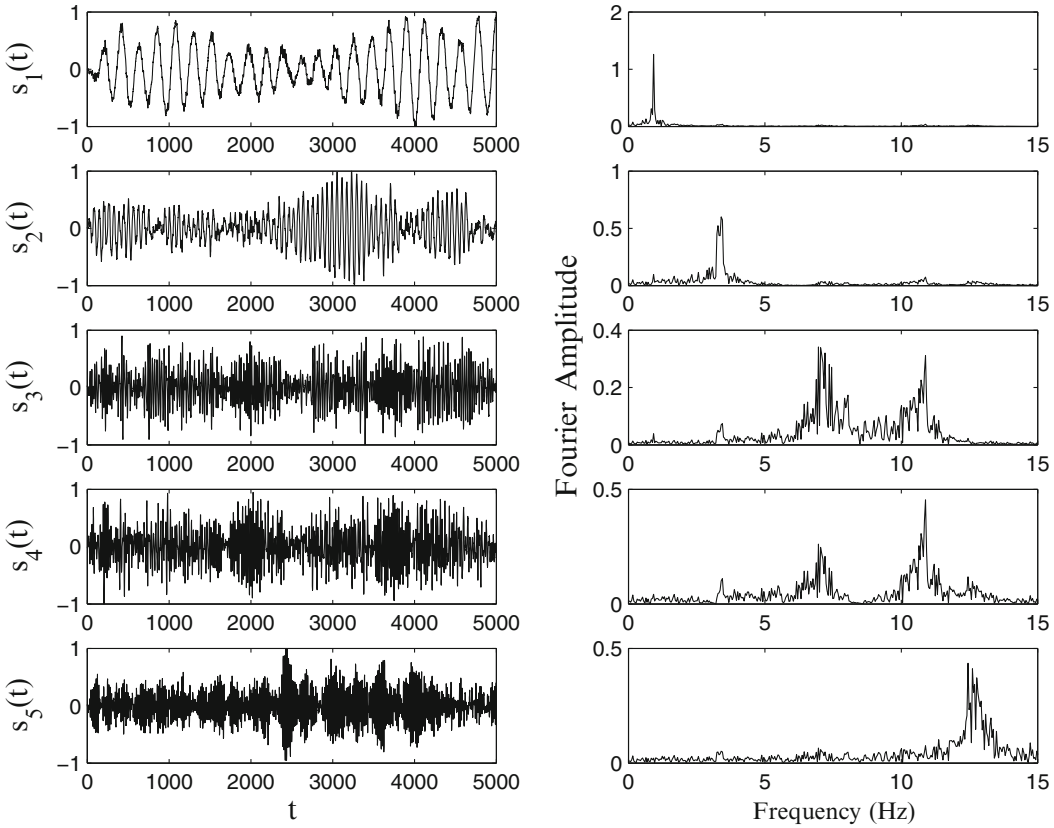

Fig. 21.7 Estimated sources using the SOBI method and their Fourier spectra

Once the sources are estimated as described earlier, the mode shape matrix is estimated using Equation 21.12. The accuracy of the estimated mode shape matrix is evaluated by comparing them with the theoretical modes using the Modal Assurance Criterion (MAC), defined by:

$$MAC_i = \frac{(\psi_{t,i}^T \psi_{e,i})^2}{(\psi_{t,i}^T \psi_{t,i})(\psi_{e,i}^T \psi_{e,i})} \tag{21.15}$$

where $\psi_{t,i}$ and $\psi_{e,i}$ represent the theoretical and the estimated i^{th} mode shape vectors, respectively. A MAC value of 1 implies perfect correlation. In order to evaluate the accuracy in terms of the mode shape estimation, the MAC values are compared for the SOBI method and the proposed method for various clock offsets and summarized in Table 21.1, 21.2, 21.3 and 21.4, respectively. Average MAC values are shown in in Fig. 21.8 as a function of the total delay. It is clear that the SOBI method fails to identify the mode shapes even for small delays (5 ms), whereas the proposed method performs significantly well even under the presence of much larger delays.

21.4.2.2 Presence of offset and drift

For the next case, clock drifts at the rate of 50 μs s^{-1} are considered in sensors 3 and 4, while a drift of 40 μs s^{-1} is considered in sensors 1 and 2. The offsets from Table 21.3 are retained as is. The resulting total time delay in each of the sensors is shown in Fig. 21.9, and the sensor at the 5^{th} DOF is assumed to be the reference sensor. The proposed algorithm is used for modal identification, and resulting mode shapes are shown in Fig. 21.10 along with the true modes. The MAC numbers are within 0.99 for all the modes, indicating that the method is indeed successful in identifying all the modes with a good degree of confidence.

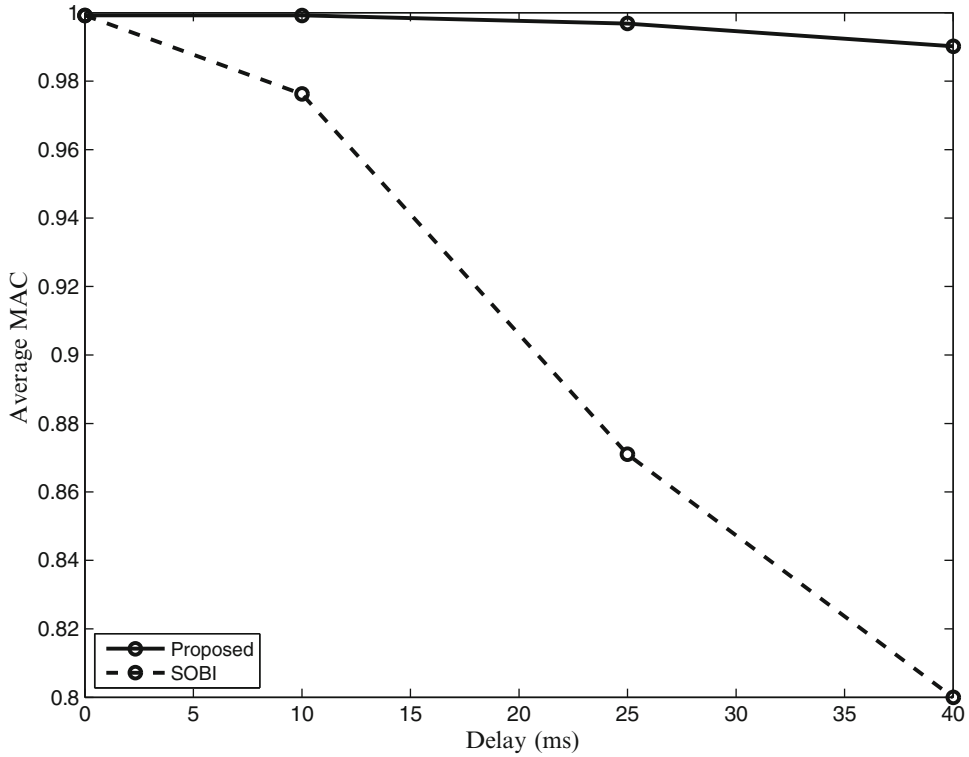

Fig. 21.8 Comparison of the SOBI with the proposed method

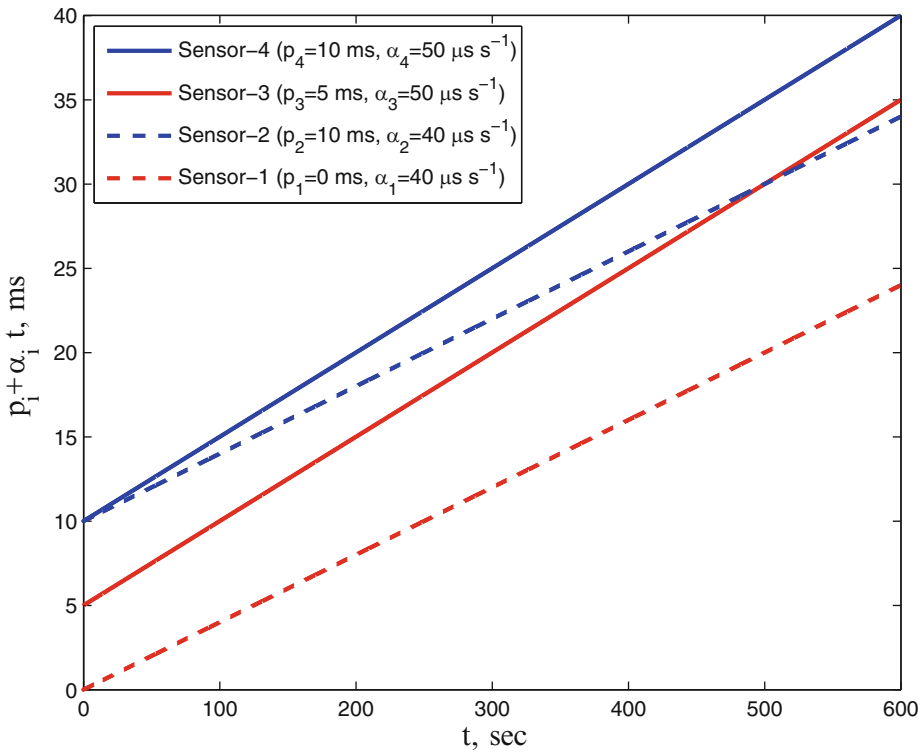

Fig. 21.9 Time varying delays due to clock drift and clock offset in the sensors

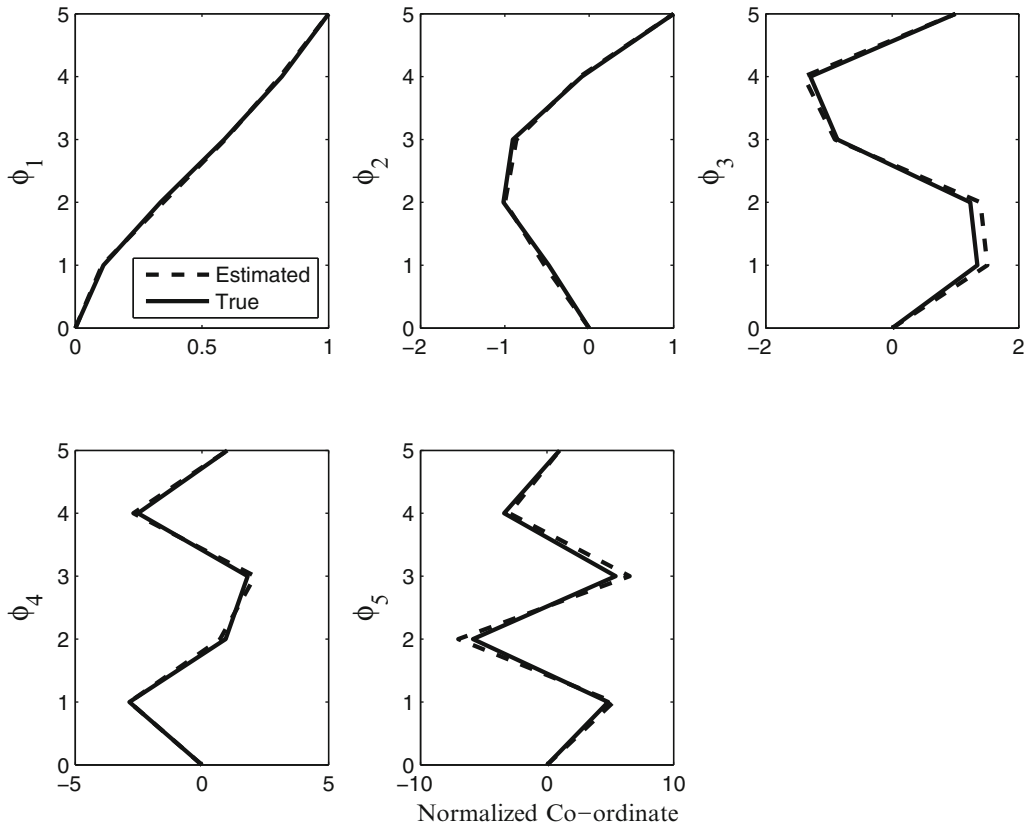

Fig. 21.10 Estimated mode shapes using the proposed method

21.5 Conclusions

In this paper, a novel modal identification method is proposed to address the TS errors in the measured data, commonly encountered in wireless sensor networks. The proposed method is based on BSS principles, where the convolutive anechoic mixing model is utilized to represent the delay associated with TS errors. Numerical studies show significant improvement in the quality of identified modes using the proposed technique, as compared to the popular BSS technique, SOBI.

References

1. Magalhaes F, Caetano E, Cunha A (2007) Challenges in the application of stochastic modal identification methods to a cable-stayed bridge. J Bridge Eng, ASCE 12(6):746–754
2. Belouchrani A, Abed-Meraim K, Cardoso J, Moulines E (1997) A blind source separation technique using second-order statistics. IEEE Trans Signal Process 45(2):434–444
3. Cichocki A, Amari S (2003) Adaptive blind signal and image processing. Wiley, Chichester
4. Antoni J (2005) Blind separation of vibration components: principles and demonstrations. Mech Syst Signal Process 19:1166–1180
5. Kerschen G, Poncelet F, Golinval J (2007) Physical interpretation of independent component analysis in structural dynamics. Mech Syst Signal Process 21:1561–1575
6. Hazra B, Roffel AJ, Narasimhan S, Pandey MD (2010) Modified cross-correlation method for the blind identification of structures. J Eng Mech 136(7):889–897
7. Hazra B, Sadhu A, Lourenco R, Narasimhan S (2010) Retuning tuned mass dampers using ambient vibration response. Smart Mater Struct 19 (11):13pp

8. Hazra B, Sadhu A, Roffel AJ, Narasimhan S (2011) Application of hybrid time-frequency blind source separation towards ambient system identification of structures. Comput Aided Civ Infrastruct Eng (in press)
9. Hyvarinen A, Oja E (1997) A fast fixed-point algorithm for independent component analysis. Neural Comput 9:1483–1492
10. Poncelet F, Kerschen G, Golinval JC, Verhelst D (2007) Output-only modal analysis using blind source separation technique. Mech Syst Signal Process 21:2335–2358
11. Sundararaman B, Buy U, Kshemkalyani AD (2005) Clock synchronization for wireless sensor networks: a survey. Ad Hoc Netw 3:281–323
12. O'Grady PD, Pearlmutter BA, Rickard ST (2005) Survey of sparse and non-sparse methods in source separation. Int J Imaging Syst Technol 15 (1):18–33
13. Smaragdis P (1998) Blind separation of convolved mixtures in the frequency domain. Neurocomputing 22:21–34
14. Omlor L, Giese MA (2011) Anechoic blind source separation using Wigner marginals. J Mach Learn Res 12:1111–1148
15. Lei Y, Kiremidjian AS, Nair KK, Lynch JP, Law KH (2005) Algorithms for time synchronization of wireless structural monitoring sensors. Earthq Eng Struct Dyn 34:555–573
16. Nagayama T, Sim SH, Miyamori Y, Spencer BF Jr (2007) Issues in structural health monitoring employing smart sensors. Smart Struct Syst 3 (3):299–320
17. Krishnamurthy V, Fowler F, Sazonov E (2008) The effect of time synchronization of wireless sensors on the modal analysis of structures. Smart Mater Struct 17:055018
18. Uchimura Y, Nasu T, Takahashi M (2007) Time synchronized wireless sensor network for vibration measurement, SICE annual conference, Kagaya University, Japan: 2940–2946
19. Park JH, Kim JT, Yi JH (2011) Output-only modal identification approach for time-unsynchronized signals from decentralized wireless sensor network for linear structural systems. Smart Struct Syst 7(1):59–82
20. Shamim NP, Gregory LF, Sukun K, David EC (2008) Design and implementation of scalable wireless sensor network for structural monitoring. ASCE J Infrastruct Eng 14:89–101
21. Wang Y, Lynch JP, Law KH (2007) A wireless structural health monitoring system with multithreaded sensing devices: design and validation. Struct Infrastruct Eng 3(2):103–120
22. Cardoso JF, Souloumiac A (1993) Blind beamforming for non-Gaussian signals. Proc Inst Elect Eng – F 140(6):362–370
23. Pham D, Garat P (1997) Blind separation of mixtures of independent sources through a quasi-maximum likelihood approach. IEEE Trans Signal Process 45(7):1712–1725
24. Bell AJ, Sejnowski TJ (1995) An information-maximization approach to blind separation and blind deconvolution. Neural Comput 7 (6):1129–1159
25. Hyvarinen A (1999) Fast and robust fixed-point algorithm for independent component analysis. IEEE Trans Neural Netw 10(3):626–634

Chapter 22
Modal Identification Using SMIT

Minwoo Chang, Shamim N. Pakzad, and Rebecca Leonard

Abstract The objective of this paper is to introduce a Structural Modal Identification Toolsuite (SMIT) for MATLAB that has been recently developed to facilitate system identification of structural systems. SMIT is an integrated toolbox, supporting a user-friendly Graphical User Interface (GUI) for modal identification. In this paper, the results of several system identification methods are compared in terms of accuracy and efficiency. The toolbox is capable of performing several common system identification methods with a standardized process, which is composed of input, eigenvalue estimation, and post processing procedures. The toolbox can present the estimated modal parameters graphically, and conveniently store and recall the identification results. The implemented identification methods consist of several classes of system identification algorithms, including Eigensystem Realization Algorithm (ERA), Auto-Regressive Moving-Average method with eXogenous terms (ARMAX), and Stochastic Subspace Identification (SSI). The performance of SMIT was verified by identifying the modal parameters of Northampton Steel Bridge (NSB), using five identification algorithms. A set of ambient acceleration responses was collected using a Wireless Sensor Network (WSN), and a subset of the sensing nodes was selected to identify vertical and torsional modes of NSB. The comparison of identification results to examine the accuracy and efficiency of each method supports that the SMIT is applicable to identify civil infrastructures effectively.

Keywords Structural Modal Identification Toolbox (SMIT) • Graphical User Interface • Standardized process • System identification

22.1 Introduction

System identification is a widely-used Structural Health Monitoring (SHM) method, capable of estimating modal parameters of a system. The development of computing systems and sensor technology, such as the Wireless Sensor Network (WSN), has extended the applicability of system identification [1]. As a globally-based SHM technique, system identification plays a significant role in connecting the gap between numeric models and physical structures [2]. During the last three decades, numerous methods have been developed to accurately estimate modal parameters of civil infrastructures [3–7]. In order to estimate the performance of identification techniques, several studies have focused on comparing identified modal parameters for a set of input/output sensor data [8–10].

The demand has increased for a compact program that allows users to conveniently access an entire procedure and compare identification results, depending on the methods used. Recently, few research groups have focused on developing a system identification toolsuite as a part of SHM. LANL/UCSD Engineering Institute [11] has been introduced SHMTools, which is a Matlab® package that facilitates the construction of Structural Health Monitoring (SHM) processes. SHMTools provides more than 100 functions, which follow three main steps of SHM processes: (1) Data acquisition, (2) Feature

M. Chang • S.N. Pakzad (✉)
Department of Civil and Environmental Engineering, Lehigh University, 117 ATLSS Drive, Lehigh, PA 18015, USA
e-mail: mic307@Lehigh.edu; snp208@Lehigh.edu; pakzad@lehigh.edu

R. Leonard
Department of Mechanical Engineering, University of Arkansas, 204 Mechanical Engineering Building, Fayetteville, AR 72701, USA
e-mail: rleonard@uark.edu

J.M. Caicedo et al. (eds.), *Topics on the Dynamics of Civil Structures, Volume 1*,
Conference Proceedings of the Society for Experimental Mechanics Series 26,
DOI 10.1007/978-1-4614-2413-0_22,

extraction, and (3) Feature classification. System identification serves as a part of feature extraction, and Auto Regressive with eXogenous input (ARX) or Auto Regressive (AR) methods are utilized in this program. Reynders et al. [12] have developed MACEC ver. 3.2, which is toolbox for modal analysis of structures. The available methods for MACEC consist of a few classes of subspace identification and frequency response methods.

Chang et al. [13] have developed SMIT (Structural Modal Identification Toolsuite for MATLAB®) to provide a more sophisticated and comprehensive program, appropriate for system identification of civil infrastructures. SMIT handles various system identification methods, including Eigensystem Realization Algorithm (ERA), ERA-Observer Kalman filter Identification (OKID), ERA-Natural Excitation Technique (NExT), ERA-NExT-AVG, Structural Realization using Information Matrix (SRIM), ARX/AR, and Numerical algorithms for Subspace State Space System IDentification (N4SID) [14–19]. In order to systematically manage the eigenvalue estimation results from different methods, the program was created with three main procedures: (1) pre-processing, (2) eigenvalue estimation, and (3) post-processing procedures. SMIT has been fitted with a Graphical User Interface (GUI), allowing the user to conveniently select identification options and define variables.

This paper presents the use of newly developed software, SMIT, and the study of its applications. The first section presents the overview of SMIT, followed by the aforementioned main procedures. The second section focuses on the system identification for a set of ambient vibrations of the Northampton Steel Bridge (NSB). The paper ends with few recommendations to improve the functionality of SMIT.

22.2 Overview of SMIT

SMIT is a Matlab®-based system identification toolbox, that is suitable for estimating modal parameters of linear systems. While the program is capable of identifying any type of structure, the mode shape plot is optimized to show shear building structures and bridge systems. SMIT displays a GUI figure for welcome and each main procedure, including pre-processing, eigenvalue estimation, and post-processing. Additionally, there are two optional figures for larger views of the stabilization diagram and mode shapes after plotting those in the post-processing figure.

The welcome window prompts the user to choose either to load a previous identification result (.mat file), which is supposed to be created after eigenvalue estimation procedure, or to start a new session (Fig. 22.1). The pre-processing and eigenvalue estimation procedure is only conducted when the user starts a new session.

22.2.1 Pre-processing Procedure

The pre-processing figure is composed of six panels to assign the structural information and to perform signal processing. The panels are: (1) Data Type, (2) Geometric Information, (3) SI Method, (4) Sampling Frequency, (5) Filtering Options, and (6) Model Order Options.

The Data Type panel is where the user defines whether input/output or only output data is going to be utilized. Accordingly, the user needs to specify the data file (.dat) by clicking the Get Output Data File and the Get Input Data File pushbuttons (if it is activated). The Geometric Information panel has three radio buttons: (1) User-Defined, (2) Simple Shear Structure, and (3) Simple Bridge Structure. The User-Defined option requires specific geometric information, including node ordinate, connectivity between two nodes, sensor locations with a text format (.txt), and additional selection for the Response Direction. The SI Method panel has five options, depending on the data type: (1) ERA, (2) ERA-OKID, (3) ARX, (4) SRIM, and (5) N4SID for input/output system or (1) ERA-OKID, (2) ERA-NExT, (3) ERA-NExT-AVG. (4) AR, and (5) N4SID for the output only system. The Sampling Frequency panel allows the user to specify the sampling frequency and to inspect average of Power Spectral Density (PSD) at each node on the right portion by selecting Inspect PSD pushbutton. The Filtering Option panel shows three available filtering methods: (1) Fast Fourier Transform (FFT), (2) Butterworth, and (3) Chebyshev Type II. Depending on each method, the user needs to specify the filtering parameters as well. The Model Order Option panel is where the user assigns minimum, maximum, and increment of model order.

The user can start the eigenvalue estimation procedure by clicking the Process pushbutton on the bottom-right side of pre-processing figure.

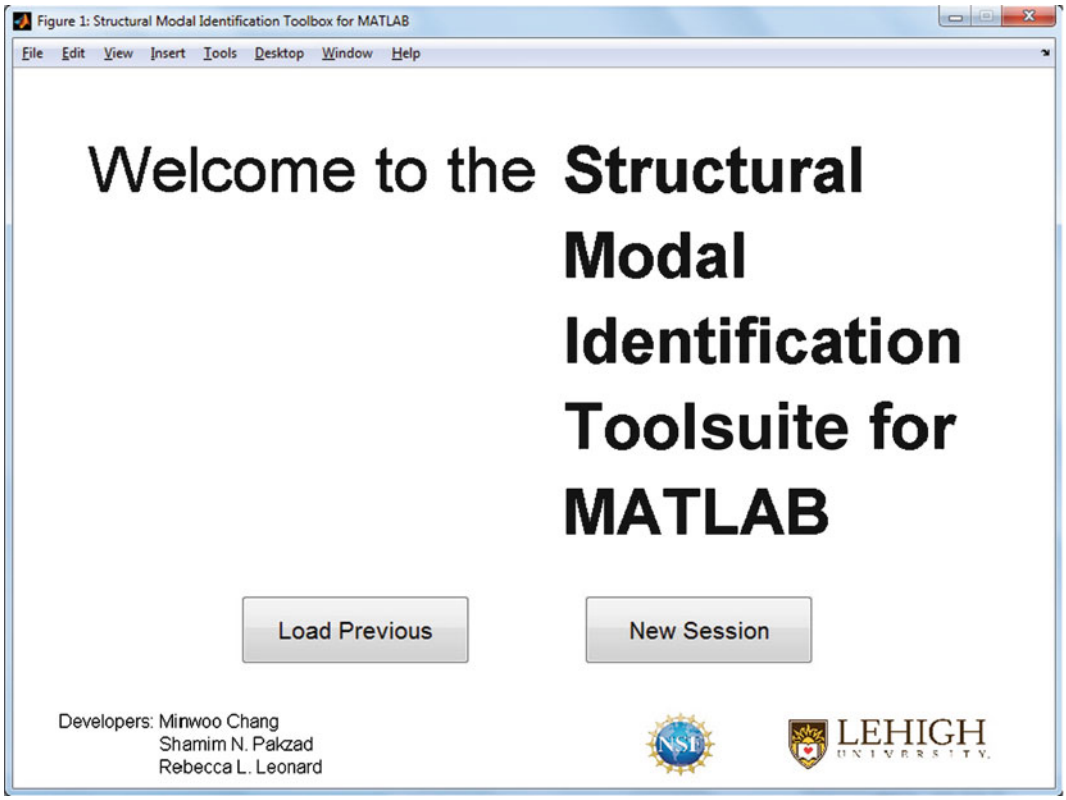

Fig. 22.1 Welcome figure for SMIT

22.2.2 Eigenvalue Estimation Procedure

Based on the information that the user defined in the pre-processing figure, the program starts the eigenvalue estimation procedure. The progress bar displayed on the screen helps the user monitor the model order on which the computing system is working. When the estimation procedure is completed, SMIT saves the identification results and structural information into the [eigen_estim_result.m], which can be used for the post-processing procedure.

See [13] for further information about the system identification methods in SMIT, such as fundamental theory and formulating the equivalent state matrix to the system.

22.2.3 Post-processing Procedure

The post-processing figure is composed of four panels to investigate the results of identification and to determine modal parameters of a system: (1) Stabilization Parameters, (2) Stabilization Diagram, (3) Mode Shape Options, and (4) Mode Shapes.

The Stabilization Parameters panel is where the user defines the convergence bounds for parameters and the ranges of the x-axis. The See plot pushbutton shows the stabilization diagram based on the information defined in the Stabilization Parameters panel. A pushbutton in the upper-left corner, Open a new window pushbutton, shows a larger view of the stabilization diagram immediately, which allows the user to easily observe the result. The Mode Shape Options panel allows the user to decide between three options which modes will be plotted. The user needs to define an approximated frequency or model order in an editable box. If the user wants to plot specific modes, they should select a set of points from the stabilization diagram and export it to the workspace. The selected mode shapes appear after the user clicks one of pushbuttons on the Mode Shape Options panel. The user can observe mode shapes in larger window by selecting the Open a new window pushbutton and they may save modal parameters and computational time corresponding to that model order in a mat file [SIModal_Para.mat].

22.3 System Identification for Northampton Steel Bridge

The ambient vibration response was measured from the Northampton Steel Bridge (NSB) across the Delaware River, connecting Easton, Pennsylvania to Phillipsburg, New Jersey. The NSB is a cantilever truss bridge with a total span length of 550 ft, supported by two piers. The WSN was formulated with 22 wireless sensors to measure ambient vibration response in vertical and transverse directions of the bridge [20]. In this study, ten sensors were chosen to identify five vertical and two torsional modes. The deployment of sensors is shown in Fig. 22.2, where seven sensors, supposed to track mode shapes of the bridge, are mounted on the north side, and the other three sensors, supposed to distinguish the type of mode whether it is vertical or torsional, are mounted on the south side.

The Imote2, developed by Intel Co., is a processing board used to formulate the WSN by communicating with sensor board. The SHM-A sensor board, developed at University of Illinois Urbana-Champaign, is attached to the Imote2 and utilizes 3-axis Micro-Electro-Mechanical Systems (MEMS) to collect accelerations with the measuring range ± 2 g. A TinyOS-based software package from the Illinois Structural Health Monitoring Project (ISHMP) was used to operate wireless sensors and to collect data efficiently [21].

The geometric information used in this identification is saved in three text files [node_info.txt, connectivity.txt, sen_lo.txt] as shown in Fig. 22.3. [node_info.txt] contains three dimensional geometric coordinates for all sensing nodes and supports. The node number is automatically recognized by counting the number of lines. [connectivity.txt] generates structural members by connecting two nodes, and [sen_lo.txt] indicates the node number where the sensors have been attached.

After launching the SMIT in the Matlab® command window, the user needs to select New session pushbutton to start a new system identification. Figure 22.4 shows the pre-processing figure to identify an output-only system, using ambient vibration data with specific geometric information. The response of the NSB is sampled down to 40 Hz by using Chebyshev Type II. Then, all five methods, including ERA-OKID, ERA-NExT, ERA-NExT-AVG, AR, and N4SID, are applied for even model orders between 2 and 100.

Figure 22.5 is a post-processing figure, where the stabilization diagram and mode shapes are plotted based on the eigenvalue estimation result of N4SID. The convergence bounds for [natural frequency, damping ratio, MAC value] to plot a stabilization diagram are set to [0.1, 0.9, 0.2], respectively, and the frequency range up to 10 Hz is considered. The cohesion of identified modal parameters helps to determine the structural modes from computational noise.

There are eight distinguishable modes which are continuously converged when the model order increases. The mode shapes in Fig. 22.5 are plotted by selecting points one by one from the stabilization diagram. For each set of consistently identified parameters, a point from highest model order is chosen. The separate view of mode shapes can be plotted by selecting the Open in new window pushbutton, as shown in Fig. 22.6, where five vertical and two torsional modes are plotted. The eighth mode is difficult to distinguish due to the limited number of sensing nodes, which can be overcome by adding more sensing nodes.

Table 22.1 shows the modal natural frequencies, damping ratios, and computational time to complete eigenvalue estimation for the corresponding model order from each identified mode. The modal damping ratios have shown differences up to nearly 50%, depending on the methods. However, the errors in modal natural frequencies are almost

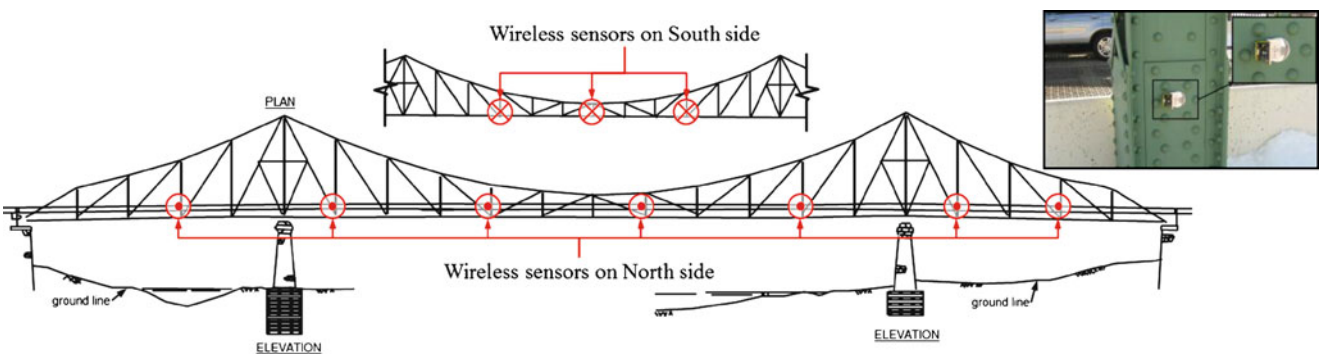

Fig. 22.2 Deployment of wireless sensors on NSB

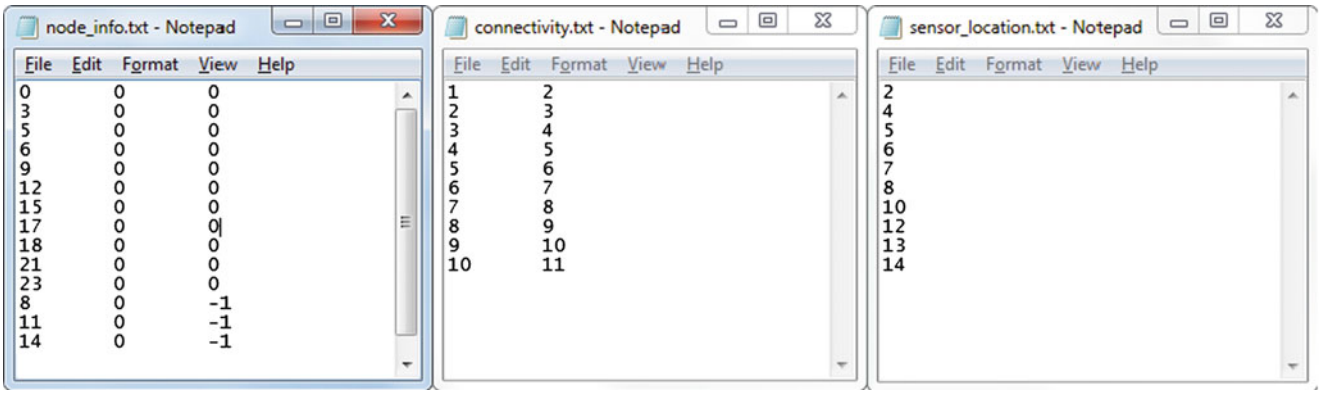

Fig. 22.3 Three text files [node_info.txt, connectivity.txt, sen_lo.txt] for geometric information of NSB

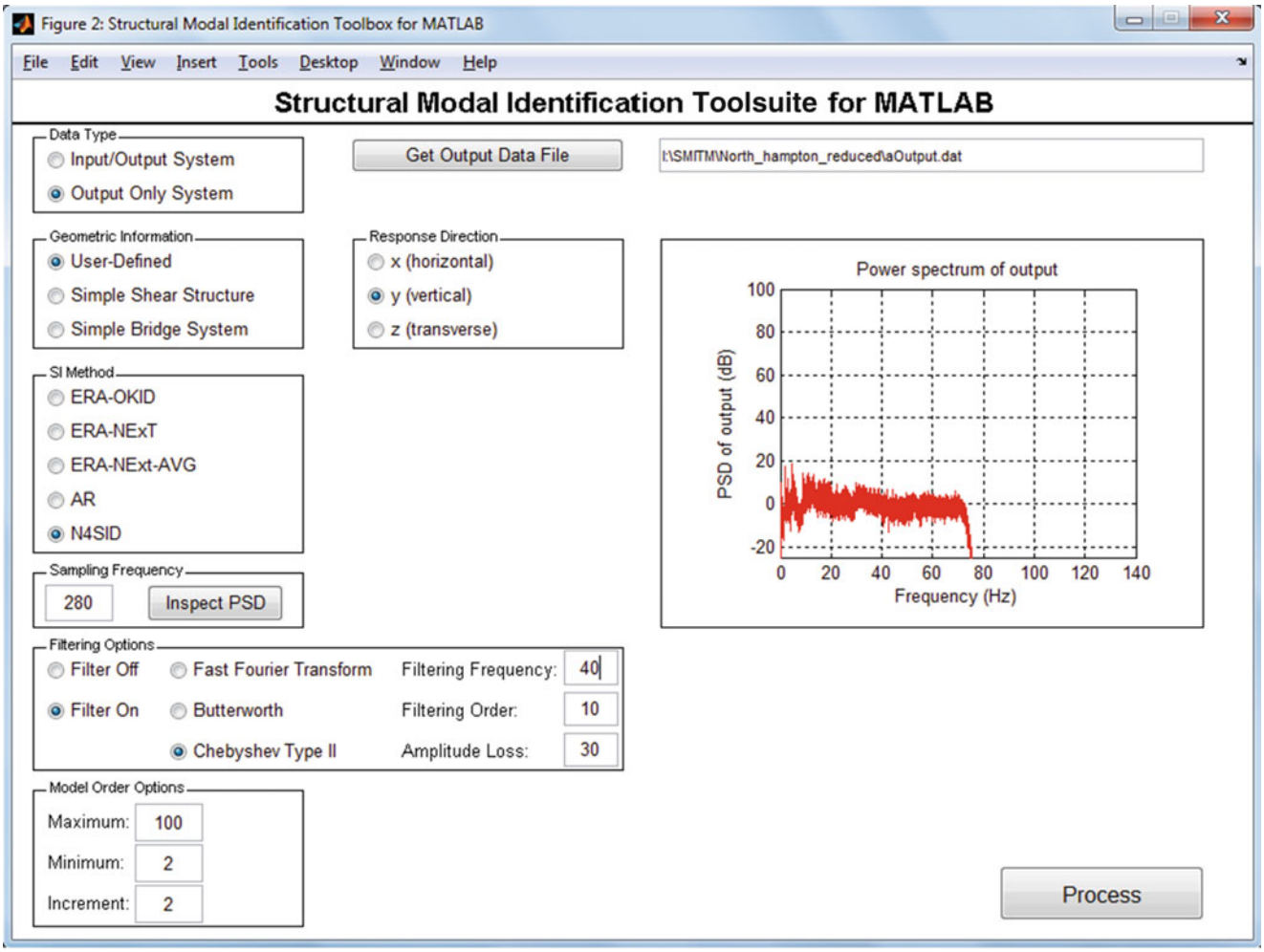

Fig. 22.4 Pre-processing figure of SMIT composed of six panels

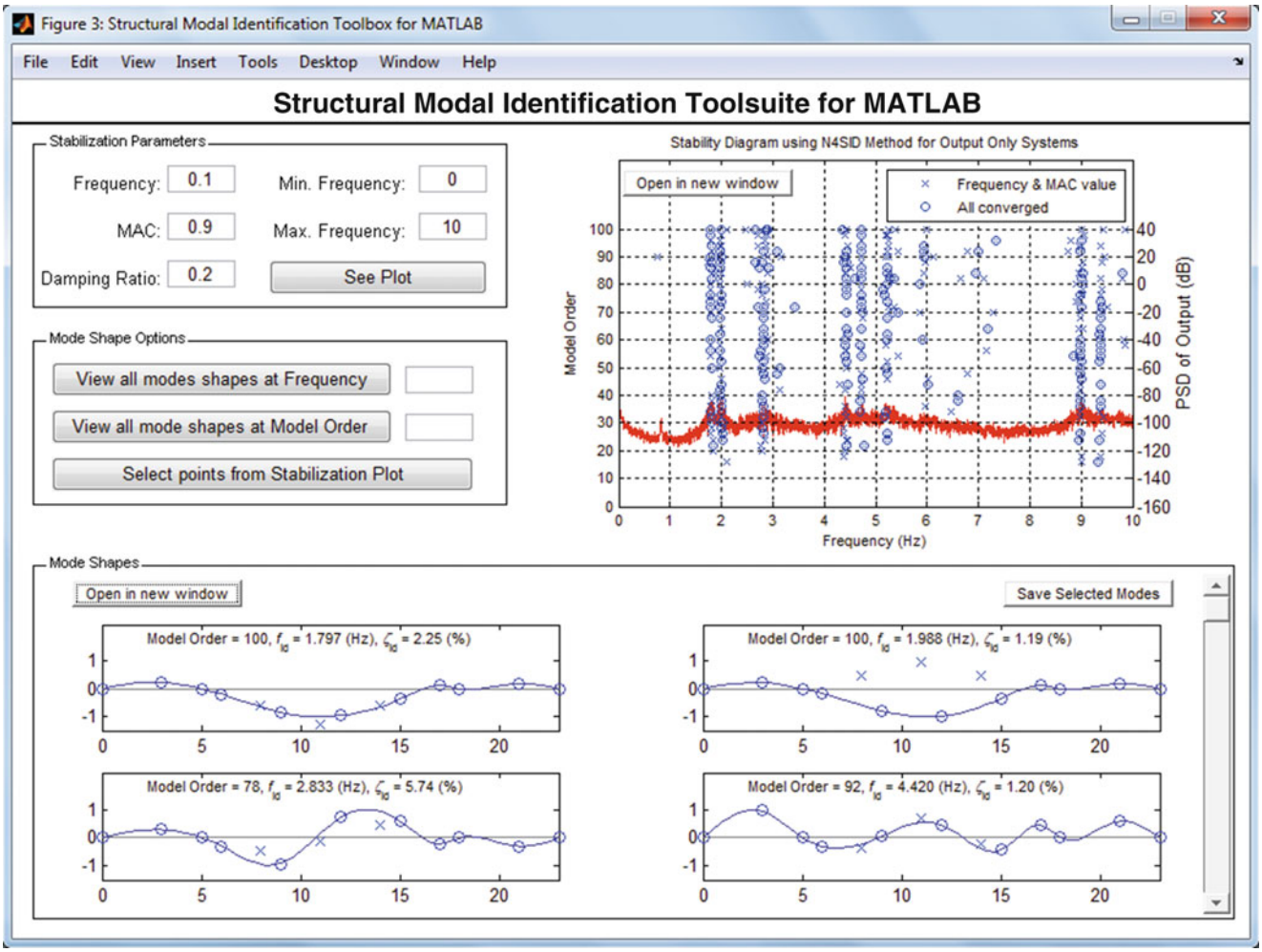

Fig. 22.5 Post-processing figure of SMIT composed of four panels

negligible. In order to investigate the efficiency of each method, the computational time to estimate modal parameters for a corresponding model order are recorded. Normally, ERA-NExT-AVG method takes least time while N4SID consumes an extremely large amount of time to complete eigenvalue estimation procedure, compared to other stochastic identification methods.

22.4 Conclusion

The application study of SMIT is presented in this paper. Extensive testing of various system identification methods has shown that each method is capable of estimating modal parameters of a system. However, it requires considerable effort to obtain modal representation from structural responses. The toolbox software, SMIT, provides a convenient way to connect a gap between numeric models and experimental data. The GUI makes it easy to input required data and offers visual support to investigate the identification results. The result of the eigenvalue estimation procedure allows the user to plot a stabilization diagram and mode shapes without repeating the main computational tasks.

The example of the ambient vibration of NSB identified seven structural modes using ERA-OKID, ERA-NExT, ERA-NExT-AVG, AR, and N4SID methods. Based on this application study, SMIT is expected to provide useful results in estimating modal parameters for structural systems and health monitoring. In addition to the modal parameters, the program

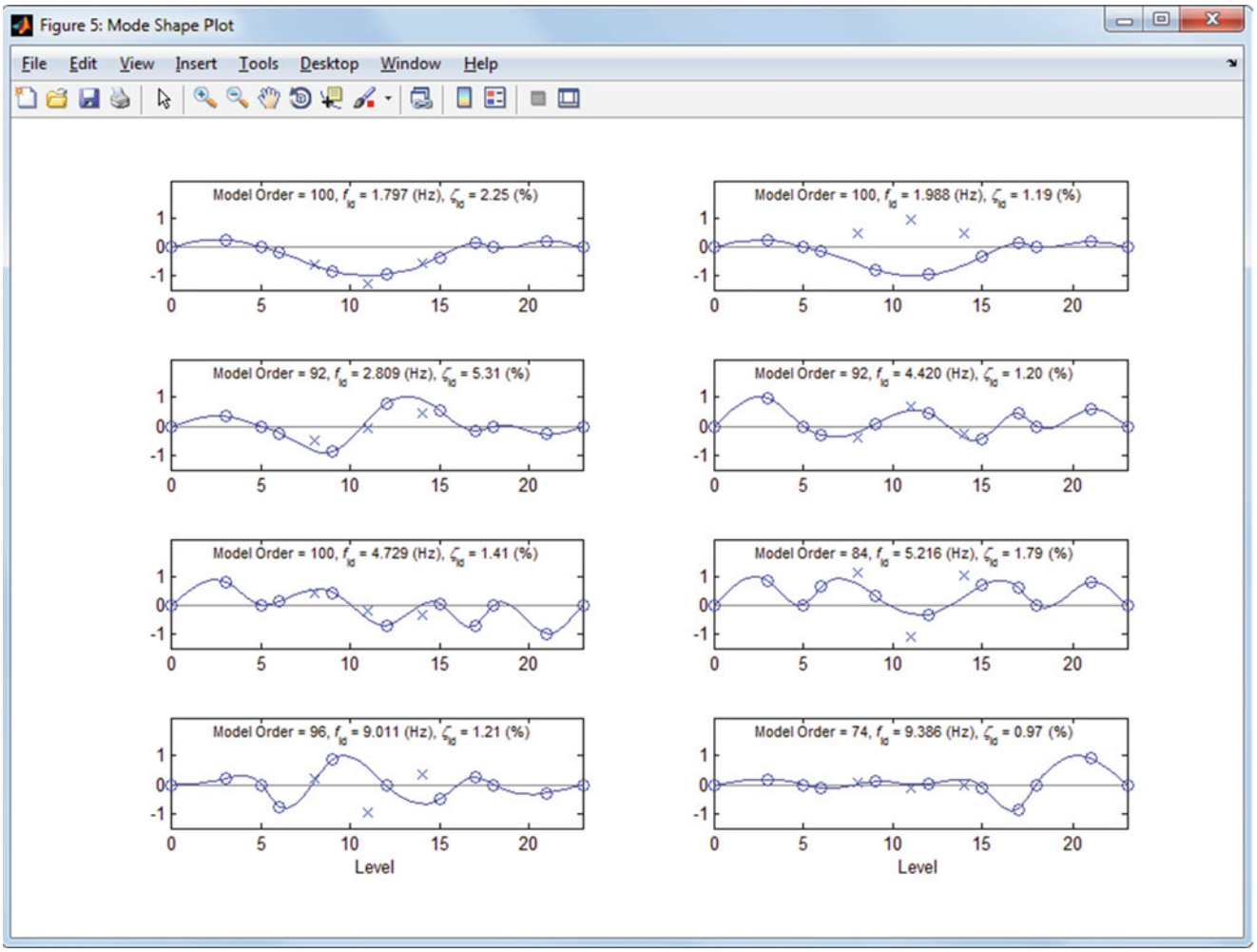

Fig. 22.6 Mode shape figures

Table 22.1 Identified modal parameters and computational time using ten sensing nodes on NSB

		ERA-OKID	ERA-NExT	ERA-NExT-AVG	AR	N4SID
1V	ω_{id} (Hz)	1.79	1.80	1.79	1.79	1.80
	ζ_{id} (%)	1.64	2.03	1.69	1.69	2.25
	t_{comp} (s)	15.54	13.00	2.14	6.87	587.22
2V	ω_{id} (Hz)	2.82	2.83	2.86	2.83	2.81
	ζ_{id} (%)	5.74	5.13	6.61	5.37	5.31
	t_{comp} (s)	13.08	10.85	0.68	5.24	497.79
3V	ω_{id} (Hz)	4.42	4.42	4.40	4.40	4.42
	ζ_{id} (%)	0.82	1.54	0.64	1.02	1.20
	t_{comp} (s)	13.08	7.77	2.07	6.87	497.79
4V	ω_{id} (Hz)	4.74	4.74	4.73	4.72	4.73
	ζ_{id} (%)	1.59	1.14	1.32	1.34	1.41
	t_{comp} (s)	15.54	13.00	2.14	6.13	587.22
5V	ω_{id} (Hz)	5.20	5.23	5.22	5.20	5.22
	ζ_{id} (%)	2.16	1.76	1.04	1.46	1.66
	t_{comp} (s)	10.53	3.75	1.06	6.87	376.65
1T	ω_{id} (Hz)	1.98	1.98	1.99	1.98	1.99
	ζ_{id} (%)	0.87	1.20	1.09	0.87	1.19
	t_{comp} (s)	15.54	11.79	2.14	6.87	587.22
2T	ω_{id} (Hz)	9.00	8.98	8.96	9.00	9.01
	ζ_{id} (%)	0.78	0.93	0.78	0.78	0.97
	t_{comp} (s)	15.54	10.58	1.39	6.87	508.51

V vertical mode, *T* torsional mode, ω_{id} identified modal natural frequency, ζ_{id} identified modal damping ratio, t_{comp} computational time

records the computational time to investigate efficiency of algorithm. SMIT, however, is currently in the development stage and is still being tested to uncover any programming bugs. SMIT developers are always open to improving the program's functionality and insert novel identification algorithms; users are encouraged to contact the developers with any suggestions.

Acknowledgements This research was partially supported by the National Science Foundation under grant CMMI-0926898 by Sensors and Sensing Systems program, and by a grant from the Commonwealth of Pennsylvania, Department of Community and Economic Development, through the Pennsylvania Infrastructure Technology Alliance (PITA).

References

1. ASCE SEI Committee on Structural Identification of Constructed Systems (2010) Structural identification of constructed facilities: approaches, methods and technologies for effective practice of St-Id (unpublished manuscript)
2. Chang PC, Flatau A, Liu SC (2003) Review paper: health monitoring of civil infrastructure. Struct Health Monit 2:257–267
3. Juang JN, Pappa RS (1985) An eigensystem realization algorithm for modal parameter identification and model reduction. J Guid Control Dynam 8:620–627
4. Pandit SM (1991) Modal and spectrum analysis. Wiley, New York
5. Van Overschee P, De Moor B (1994) N4SID: subspace algorithms for the identification of combined deterministic-stochastic systems. Automatica 30(1):75–93
6. Juang JN (1997) System realization using information matrix. J Guid Control Dynam 20(3):492–500
7. Arici Y, Mosalam KM (2005) Modal identification of bridge systems using state-space methods. J Struct Control Health Monit 12:381–404
8. Lew JS, Juang JN, Longman RW (1993) Comparison of several system identification methods for flexible structures. J Sound Vib 167 (3):461–480
9. Peeters B, De Roeck G, Hermans L, Wauters T, Krämer C, De Smet CAM (1998) Comparison of system identification methods using operational data of a bridge test. In: Proceedings of ISMA 23. Leuven, Belgium, pp 923–930
10. Chang M, Pakzad SN, Schanck C (2011) Framework for comparison study of stochastic modal identification considering accuracy and efficiency. In: Proceedings of the 8th iWSHM, Stanford, USA
11. LANL/UCSD Engineering Institute (2010) Structural health monitoring tools (SHMTooks). Getting started. Los Alamos National Security, LLC, Los Alamos
12. Reynders E, Schevenels M, De Roeck G (2011) MACEC 3.2: a Matlab toobox for experimental and operational modal analysis. Leuven University, Belgium
13. Chang M, Pakzad SN, Leonard RL (2012) Interactive Structural Modal Identification Toolsuite (SMIT) for MATALAB (in writing)
14. Juang JN, Pappa RS (1985) An eigensystem realization algorithm for modal parameter identification and model reduction. J Guid Control Dynam 8:620–627
15. Juang JN (1994) Applied system identification. Prentice Hall, Englewood Cliffs
16. James GHI, Carne TG, Lauffer JP (1993) The natural excitation technique (NExT) for modal parameter extraction from operating wind turbines. SAND92-1666, UC-261
17. Chang M, Pakzad SN (2012) Modified natural excitation technique for stochastic modal identification. J Struct Eng, doi:10.1061/(ASCE) ST.1943-541X.0000559
18. Juang J (1997) State-space system realization with input- and output-data correlation. NASA TP 3622
19. Van Overschee P, De Moor B (1994) N4SID: subspace algorithms for the identification of combined deterministic-stochastic systems. Automatica 30(1):75–93
20. Dorvash S, Pakzad SN, Knorr RC, Horwath LM (2011) Modal identification of steel truss bridges using wireless sensor network. In: Proceedings of the 8th iWSHM, Stanford, USA
21. ISHMP (2009) http://shm.cs.uiuc.edu/software.html

Chapter 23
Iterative Modal Identification Algorithm; Implementation and Evaluation

Saivash Dorvash and Shamim N. Pakzad

Abstract Applying Wireless sensor networks (WSNs) in structural health monitoring (SHM) systems has received significant interest from research communities in recent years. While incorporating wireless technology in monitoring systems has provided considerable improvements, new approaches are still needed to address existing challenges in their application. A major challenge in application of WSNs in SHM is the limited power resources of wireless sensors and the latency in the data processing due to the low communication bandwidth. The performance of the networks on both of these factors can be improved through the use of an iterative modal identification algorithm, called IMID. This algorithm uses the local processing capability of wireless sensors and provides a substantial reduction in required communication for identification of system's modal properties. The iterative approach is such that, starting from an initial estimate of the system's parameter, all of the nodes of the network use their local measurement and update the estimated modal parameters one-by-one until the convergence of results happens. In this manner, the system's parameters are the only data that need to be transmitted through the network for updating. This approach results in the significant reduction in the total volume of communication. This paper presents the application of the IMID in modal identification of a 3-D steel truss structure. The results are discussed and the performance of the algorithm is evaluated.

Keywords Wireless sensor networks • Structural health monitoring • Iterative modal identification

23.1 Introduction

Identification of dynamic parameters of structural systems through vibration monitoring is important for the assessment of structural performance and calibration of finite element models. Over the past few years, vibration monitoring systems have significantly improved by incorporating the advancements in sensing and communication technology. One of the distinct improvements in the vibration monitoring is application of wireless technology for communication in the sensing networks. Using Wireless Sensor Networks (WSNs), the prohibitive costs associated with wiring is eliminated and the instrumentation of the network becomes considerably more affordable. At the same time, each sensor in a WSN is integrated with a low-power microcontroller which enables local data processing task in the sensing network. As the advantages of WSN became evident, researchers developed different WSN platforms and deployed in Structural Health Monitoring (SHM) systems [1–3].

Utilizing WSNs in health monitoring of infrastructure raised the demand of having scalable sensing networks, functional in long term scenarios. The major challenges in scalability of WSNs are limited communication bandwidth and the finite power resource at remote nodes. One of the most power consuming tasks among all the tasks, performed at the sensor nodes, is data communication. Realizing the fact that the on-board computation consumes significantly less energy compared to communication, researchers focused on strategies in which the computational core of the sensors contributes in data processing tasks, aiming to minimize the communication. These approaches assist with both preserving the limited available power at remote nodes and the communication bandwidth. The basic idea in distributing computational task within the sensing network is to perform a portion of data interrogation locally and communicating the more informative data to the base station.

S. Dorvash (✉) • S.N. Pakzad
Department of Civil and Environmental Engineering, Lehigh University, Bethlehem, PA, USA
e-mail: sid208@lehigh.edu; pakzad@lehigh.edu

J.M. Caicedo et al. (eds.), *Topics on the Dynamics of Civil Structures, Volume 1*,
Conference Proceedings of the Society for Experimental Mechanics Series 26,
DOI 10.1007/978-1-4614-2413-0_23,

Use of embedded algorithms on remote sensors started with basic approaches such as filtering, data compression [4] and conversion of the data from time to frequency domain [5]. Numerous researchers also developed distributed algorithms for detecting and quantifying damage in the instrumented structure [6–8]. While distributed algorithms have been successful in data interrogation and, to some extent, in damage detection, they are still lacking in the implementation of modal identification techniques. The challenge in distributing modal identification process among remote sensors is the need for having spatial information at central computational core. A number of researchers studied this problem and proposed methodologies to address this challenge. One of the early proposed approaches was implementation of peak picking algorithm and transmission of imaginary components of Fourier spectra at modal peaks, thus capturing system's poles with their phase information [9]. A family of techniques involving hierarchical network topology has been also presented in the literature [10–12] in which the network is divided into a number of overlapped sub-networks with cluster heads. The basic idea in these approaches is to transmit data from cluster heads to the rest of the cluster nodes (called leaf nodes), local calculation of correlation functions, and at the end, transmission of the correlation functions from sub-networks to the base station for estimation of global modal properties. Another proposed approach for distribution of modal identification algorithms is the use of Regularized Auto Regressive (AR) Models [13]. In this method a restriction is applied on AR parameters of the Multivariate AR models which eliminates the computation of correlation between signals measured at nodes that are far apart, thus reducing the volume of data passed through the network, particularly when multi-hop data transmission is applied.

While proposed approaches reduce the amount of communicated data in specified architectures, they are restricted by the underlying identification algorithms. Recently, a new approach proposed on this topic in which the modal properties of a system are identified in an iterative method [14]. This method, called Iterative modal Identification (IMID) relies on an iterative estimation method which estimates unknown parameters in the absence of complete information about the system. IMID assigns the computational task of modal identification to each remote node and limits the data communication to transmission of only modal analysis results. A basic assumption in implementation of the algorithm was availability of system's input function at remote nodes of the network. Evidently, such an assumption would be challenging in deployment of the algorithm on large scale, real structures. In this paper, IMID algorithm is adapted to work with the output data while the input is impulse. The algorithm is deployed on a set of data collected from a truss structure to identify the modal properties iteratively. The obtained results validate the performance of the algorithm and the convergence of the iteration. The modal properties of the truss are also estimated by traditional centralized modal identification algorithm and are used as a reference for validation of results from IMID. The obtained results are discussed and the significance of the approach is evaluated in the paper.

23.2 Iterative Modal Identification, Methodology

Implementation of most of the existing modal identification algorithms requires the access to the entire measured data. This requirement is the main restriction in developing distributed algorithm for WSNs. The advantage of IMID is that it estimates the modal parameters of the system without requiring simultaneous access to the entire data. The technique which is used in this algorithm relies on a class of estimation algorithm, called Expectation-Maximization (EM). EM estimates unknown parameter (θ), given the measurement data (Y) in the presence of some hidden data ($\hat{Y}$), or in other words, in the presence of incomplete data [15].

Considering the log-likelihood function of unknown parameters θ as:

$$L(\theta) = \log(p(Y/\theta)) \tag{23.1}$$

the estimation of unknowns (θ) is given by maximizing the function, L(θ), over θ:

$$\theta = Arg.\max(L(\theta)) \tag{23.2}$$

where Y is the available data (complete measured data).

Now considering the case that the entire data for estimation is not available, the EM becomes applicable. EM first estimates the complete data using assumed parameters, θ_p, (expectation phase), then maximizes the likelihood function over system's parameter to find θ_{p+1} (maximization step) and continues until the convergence for the parameters is achieved. The concept of EM is also illustrated in Fig. 23.1.

The presence of incomplete data in EM is similar to situation when each remote node has access to its own collected data, and the data from the rest of the sensors are not available. IMID offers that each node separately estimates the system's

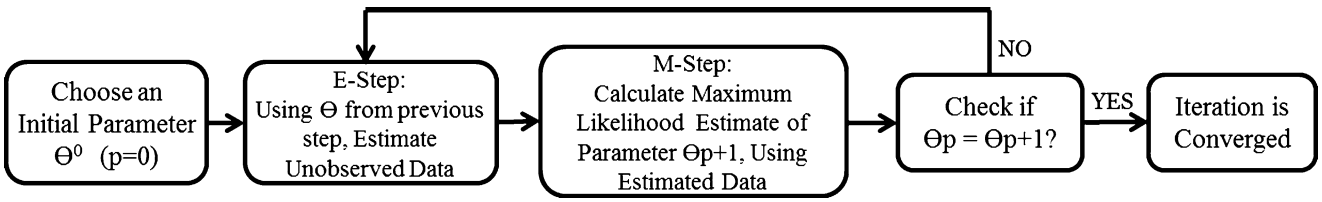

Fig. 23.1 The block chart presenting the Expectation-Maximization algorithm

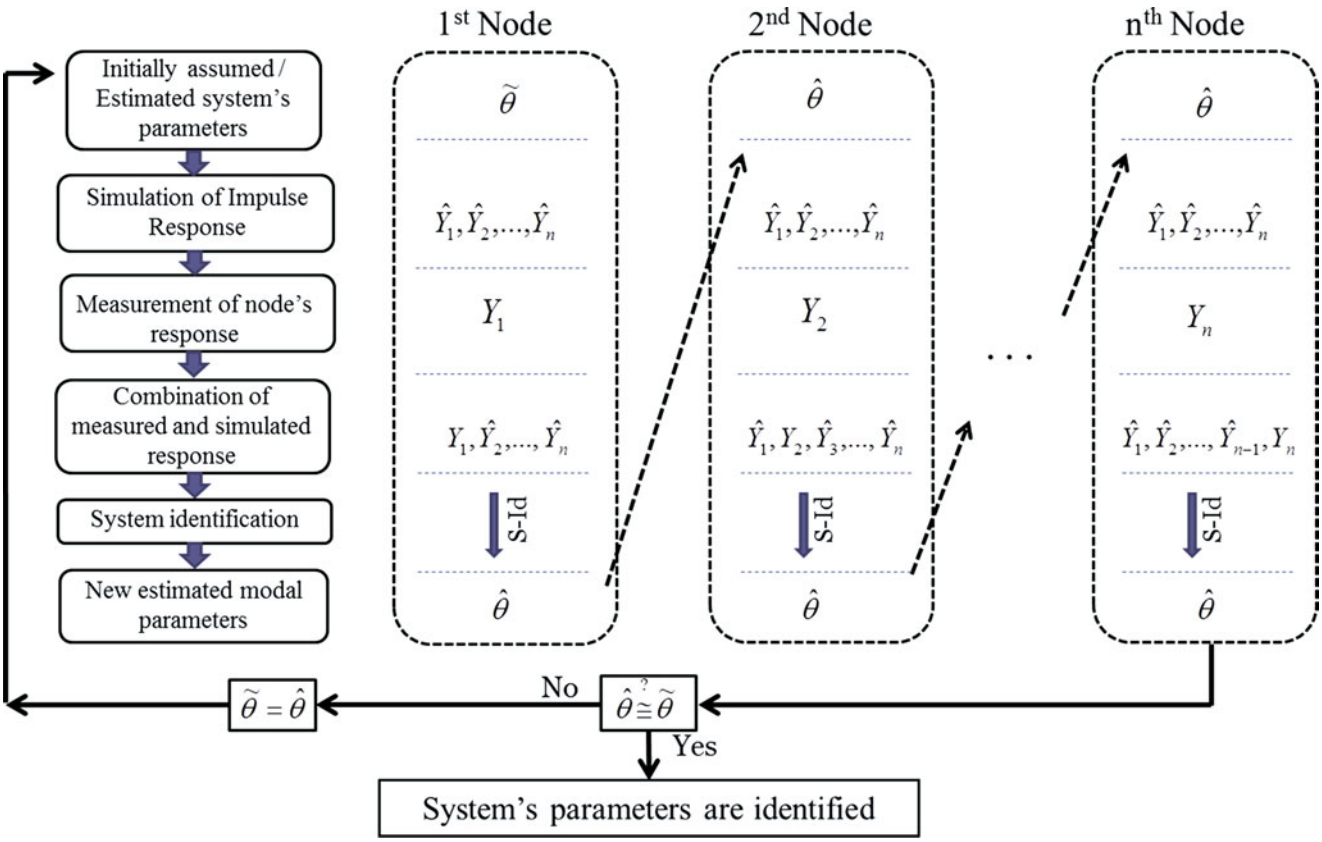

Fig. 23.2 The block chart presenting the iterative modal identification algorithm

parameter (θ) based on its observation (measured data), Y, and the assumed responses in the other nodes, $\hat{Y}$. An initial estimate of system's parameters is used for making assumption on the response at other nodes.

Considering the implementation of IMID on a structure instrumented by N sensor nodes, the first node uses the initial value of the parameters and makes a numerical simulation to estimate the response on other nodes (expectation step in EM algorithm). The simulated response and the measured data at this node are used to make an estimate on system's modal parameters (maximization step in EM algorithm). Then this node sends the system's parameters to the next node in the network for a similar local processing. The same steps are taken in all of the nodes of the network one-by-one. However, for simulation of the response, each node uses the system's parameter estimated at its previous node. Therefore, each node influences on the estimation by its measured data. This procedure is continued inside the network until the estimated parameters are converged. Note that as a requirement for implementation of the algorithm, an initial estimation of system's parameters should be available.

Considering the fact that the size of estimated parameters is very small, compared to that of the time history data, depending on the number of iteration cycles, IMID can significantly reduce the communication burden of the network. Figure 23.2, shows a step-by-step block chart, illustrating IMID.

The two steps in IMID are (1): simulation of the response using the estimated parameters, and (2): modal identification using the collected data and simulated response. A variety of algorithms is available for both simulation and modal

identification (e.g. Newmark and Central Difference numerical methods for simulation and Eigensystem Realization Algorithm (ERA), Stochastic Subspace Identification (SSI), and ARX algorithm for modal identification).

One of the valid models for characterizing linear systems is Auto Regressive with Exogenous (ARX) model. ARX can be used for both simulation and identification steps. The ARX model can be written as:

$$\sum_{i=0}^{p} \alpha_i y(n-i) = \sum_{i=1}^{q} \beta_i u(n-i) + e(n) \tag{23.3}$$

where $y = [y_1(n)\ y_2(n)\ \ldots\ y_m(n)]$ and $u(n) = [u_1(n)\ u_2(n)\ \ldots\ u_r(n)]$ are matrices including output and input vectors respectively. α_i's and β_i's are ARX coefficients, $e(n)$ represents the noise and measurement error, and p and q are orders of the autoregressive and exogenous parts of the ARX model. For IMID based on ARX model, ARX parameters are considered to represent the structural system and therefore, these parameters are communicated throughout the network.

Having the ARX parameters of the system, response at any time step can be estimated based on the past inputs and outputs and the current input. Considering the noise has zero mean, (23.3) can be rewritten to estimate for the response at time step n:

$$\bar{y}(n) = -\sum_{i=1}^{p} \alpha_i y(n-i) + \sum_{i=0}^{q} \beta_i x(n-i) \tag{23.4}$$

Now considering the input is impulse function, for $n > p + 1$, (23.4) will be simplified to:

$$\bar{y}(n) = -\sum_{i=1}^{p} \alpha_i y(n-i) \tag{23.5}$$

This equation can be used for one-step output prediction. For multi-step output prediction, the vector of s steps responses can be obtained directly from following relationship [16]:

$$\begin{bmatrix} y(n) \\ y(n+1) \\ \vdots \\ y(n+s-1) \end{bmatrix} = - \begin{bmatrix} \alpha_p & \alpha_{p-1} & \cdots & \alpha_1 \\ \alpha_p^{(1)} & \alpha_{p-1}^{(1)} & \cdots & \alpha_1^{(1)} \\ \vdots & \vdots & \ddots & \vdots \\ \alpha_p^{(s-1)} & \alpha_{p-1}^{(s-1)} & \cdots & \alpha_1^{(s-1)} \end{bmatrix} \cdot \begin{bmatrix} y(n-p) \\ y(n-p+1) \\ \vdots \\ y(n-1) \end{bmatrix} \tag{23.6}$$

where:

$$\alpha_1^{(0)} = \alpha_1$$

$$\alpha_1^{(k)} = \alpha_{k+1} - \sum_{i=1}^{k} \alpha_i \alpha_1^{(k-i)} \quad for \quad k < p$$

$$\alpha_1^{(k)} = -\sum_{i=1}^{p} \alpha_i \alpha_1^{(k-i)} \quad for \quad k \geq p$$

Therefore, having the AR parameters of the system, and knowing that the system is excited by impulse, the response can be easily simulated.

The second major step in IMID is identification step. The main goal in the identification step is to estimate the system's AR parameters. However, to check the convergence, it is required to also extract the modal properties of the system. To this end, the AR model can be rearranged to the state space representation for modal identification purpose. Consider the state space model as:

$$x(n+1) = A_d x(n) + B_d u(n) \tag{23.7}$$

$$y(n) = Cx(n) + Du(n) \tag{23.8}$$

where $x(n)$ is the state vector, $y(n)$ is the observation vector, and $u(n)$ is the input vector at time step n; A_d is the state and B_d is input matrices in discrete format, C is the observation matrix and D is transmission matrix. Choosing the state vector as:

$$x(n) = [y(n) \quad y(n+1) \quad \cdots \quad y(n+k-1)]'$$

the state matrix can be expressed in the controller form as:

$$A_d = \begin{bmatrix} 0 & I & \cdots & 0 \\ \vdots & \vdots & \ddots & \vdots \\ 0 & 0 & \cdots & I \\ -\alpha_p & -\alpha_{p-1} & \cdots & -\alpha_1 \end{bmatrix} \tag{23.9}$$

and the observation matrix as:

$$C = [I \quad 0 \quad . \quad . \quad 0 \quad 0] \tag{23.10}$$

where $[I]$ and $[0]$ are identity and zero matrices with appropriate dimensions, respectively. Eigenvalue decomposition of the state matrix (A_d) results in the matrices of eigenvalues (λ_i's) and eigenvectors (ψ_i's) from which the natural frequencies, damping ratios and mode shapes of the system can be obtained using following relationships:

$$\lambda_{c_i}, \lambda_{c_i}^* = -\zeta_i \omega_i \pm j\omega_i \sqrt{1-\zeta_i^2} \tag{23.11}$$

$$\phi_i = C\Psi_i \tag{23.12}$$

where ω_i and ζ_i are natural frequencies and damping ratios and λ_c is the eigenvalue of the continuous state matrix. λ_c can be obtained from this equation:

$$\lambda_{c_i} = \frac{\ln(\lambda_i)}{\Delta t} \tag{23.13}$$

where Δt is the sampling time.

Estimating these modal properties at each node, the convergence of the IMID is assessed and when these parameters are stabilized, the iteration can be stopped and the final results will be sent to the base station. This way, no further process is required at the base station since the modal properties are already estimated.

23.3 Implementation on a Truss Structure

To validate the IMID when the input is impulse, the algorithm is applied in modal identification of a three dimensional steel truss structure. The truss has 27.5 ft length and six panels as shown in Fig. 23.3. A network of 10 wireless sensors is installed on lower chord of the truss to collect the acceleration data in lateral and vertical directions. Figure 23.3b shows the configuration of sensor network on the truss. The accelerometers are LIS3L02AS4 [17] with 50 μg/√Hz noise density in X and Y direction and resolution of 0.66 V/g, capturing acceleration in ±2 g range.

Having a relatively stiff structure with natural frequencies all above 10 Hz, a relatively long response measurement with a high sampling rate is required for obtaining fundamental natural modes. For the experiments, the impacts were applied on location 2 (Fig. 23.3b) in both vertical and lateral directions. It takes about 30–40 s to have the impulse response with a peak of 0.6 g fully attenuated. The sampling rate was 280 Hz and the length of the data used for the algorithm was 10,000 points. Figure 23.4 shows the collected response from sensor number 3 at the mid-span and its power spectrum. Using AR algorithm, the modal frequencies, damping ratios and mode shapes of the truss are identified to be used as a reference for validation of the results, obtained from IMID implementation. Figure 23.5 shows the identified modal properties.

To begin the iteration process, an initial estimation of the structural model is required as the starting point of the iterative process. For this purpose, random masses are added to different nodes such that the additional masses make about 10% changes into the natural frequencies of the system. An AR model is fitted to the response of the altered truss to represent the initial estimate of the structure.

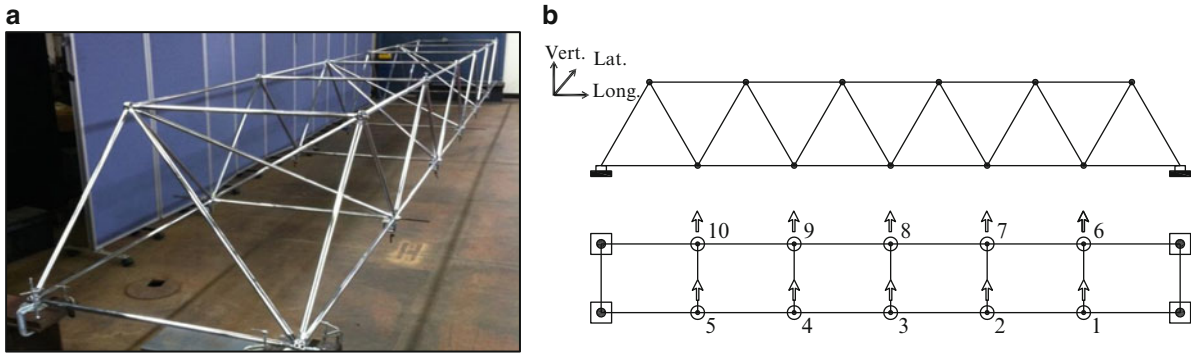

Fig. 23.3 (**a**) The truss structure, (**b**) the location of sensors on the truss

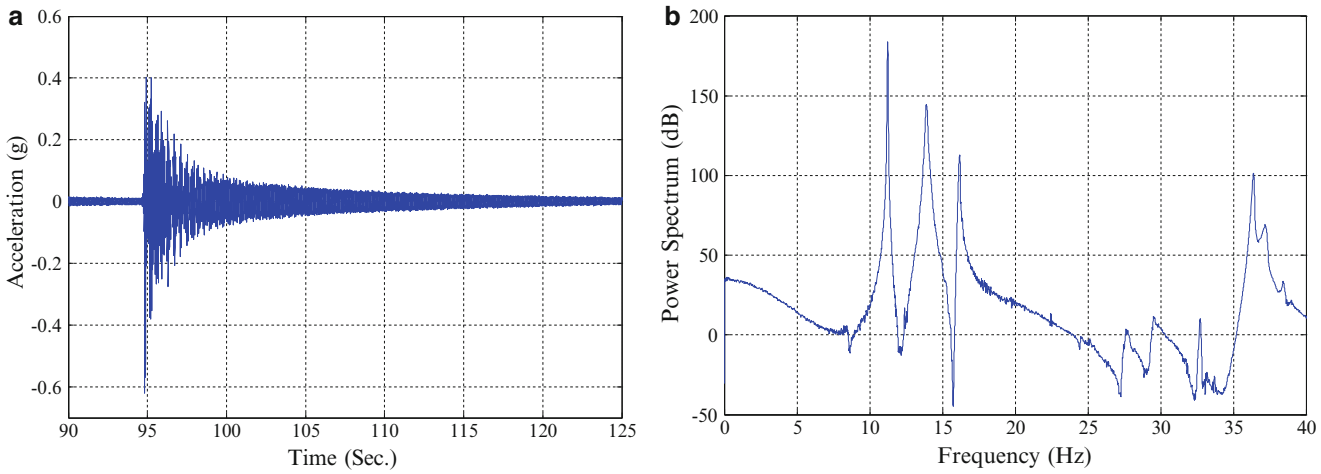

Fig. 23.4 (**a**) The impulse response at mid-span, (**b**) the power spectrum of the response

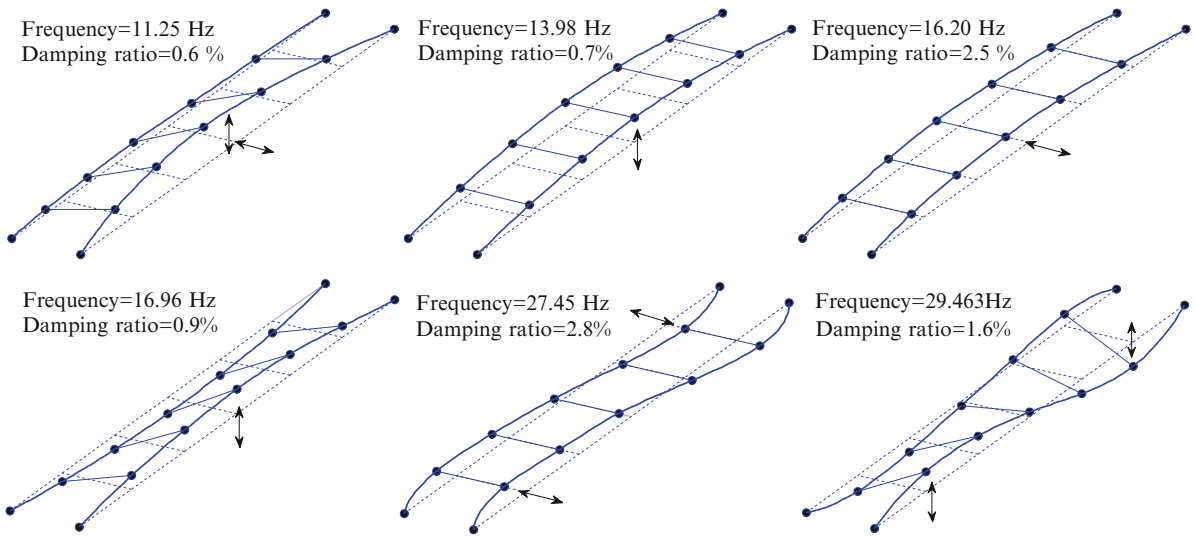

Fig. 23.5 Fundamental identified modes of the truss structure

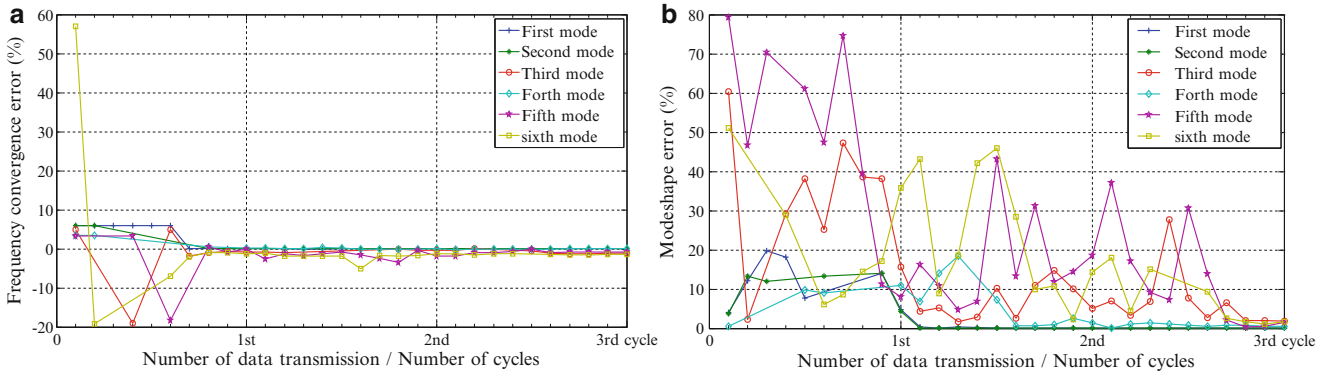

Fig. 23.6 (**a**) Frequency convergence error, (**b**) the mode shapes convergence error

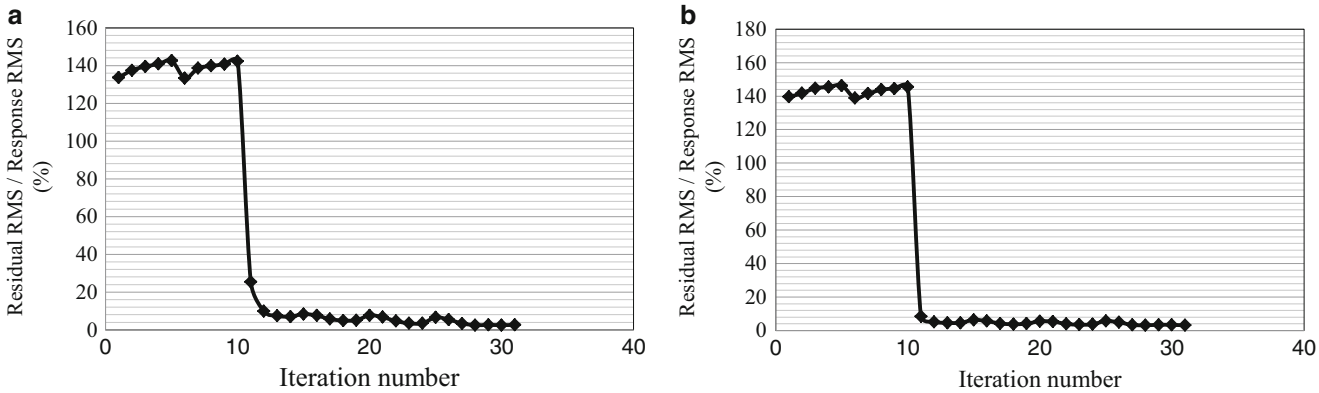

Fig. 23.7 Residual to response ratio during iteration at different nodes, (**a**) lateral direction (**b**) vertical direction

An important parameter in IMID is the order of the AR model. Usually, higher model order result in better representation of the fitted model which particularly enhance the accuracy in simulation step. However since the AR parameters should be transmitted through the network, increasing the model order increases the size of communication burden in the network. The selected model order for this implementation is 10 which results in 10 matrices of AR parameters, communicated among the nodes of the network.

To check the convergence of the results, identified frequencies and mode shapes are estimated at each node, having the estimated AR parameters received from previous node. Then these modal properties are compared to those estimated from the parameters updated at the node. The criterion for convergence of modal properties can be defined by a predetermined threshold for the changes in the parameters. Modal Accuracy Criterion (MAC) value is used for comparison of mode shapes in consecutive cycles. This criterion is defined as:

$$MAC = \frac{(\phi_p^T \times \phi_{p+1})^2}{(\phi_p^T \times \phi_p) \times (\phi_{p+1}^T \times \phi_{p+1})} \tag{23.14}$$

where $\phi_p$and $\phi_{p+1}$are the estimated mode shapes at iteration cycles p and $p + 1$.

Figure 23.6a, b shows the error percentage in estimated natural frequencies and mode shapes, versus the iteration cycles. Another parameter which shows the convergence of the procedure is the residual to response ratio. Available at each node are the measured response and the simulated response at the node location. The difference of these two signals defines the residual signal. The ratio of the residual-to-response RMS can be also considered as a parameter for assessing the convergence status. Figure 23.7a, b present this ratio for lateral and vertical directions over the iteration cycles. It can be seen that this ratio drops after one full cycle (passed through all 10 nodes) and becomes relatively small before the third full cycle.

From both Figs. 23.6 and 23.7, it is realized that before three full cycles the natural frequencies and mode shapes variation is less than 2% and the iteration is almost converged. Considering the three cycles of iteration, the total data points need to be communicated through the network are:

$$N_{\text{total}} = 3 \times 10(10 \times 100) = 30000$$

which is significantly less than the required communication in centralized network (less than 30%, considering collection of 10,000 samples from each sensor). Comparing to the previous implementation of the IMID algorithm, this experiment resulted in higher communication burden. However, this implementation does not need availability of input function at remote nodes, thus more applicable in structural monitoring scenarios.

23.4 Conclusion

This paper presents deployment of a distributed modal identification algorithm, called IMID, for estimation of modal properties of a 3-D truss structure. In this algorithm the modal properties are expected to be estimated iteratively and locally in the sensing nodes of a network. However in this work, the algorithm is applied on a set of collected data, from a laboratory test on the truss structure. A network of 10 wireless sensors is deployed on the lower chord of the truss to capture the acceleration in vertical and lateral directions.

One of the requirements of the IMID is to have access to the input function for simulating the response of the estimated model. However in this implementation the input is impulse, thus no information about the input is required for simulation of the response. The obtained results showed the convergence of estimated fundamental modes of the structure before three full cycles of iteration. AR algorithm is used for simulation and identification steps and AR parameters are passed through the iteration cycles to represent the updated structural model. However, to check the convergence, modal properties are extracted at each cycle. As an additional parameter for checking the convergence, residual-to-response RMS ratio is defined and plotted over the iterations. A relatively sharp drop after one cycle of iteration and attenuation of the ratio is observed which shows the convergence trend of the iterative algorithm.

Acknowledgment The research described in this paper is supported by the National Science Foundation through Grant No. CMMI-0926898 by Sensors and Sensing Systems Program and by a grant from the Commonwealth of Pennsylvania, Department of Community and Economic Development, through the Pennsylvania Infrastructure Technology Alliance (PITA).

References

1. Pakzad SN, Fenves GL, Kim S, Culler DE (2008) Design and implementation of scalable wireless sensor network for structural monitoring. ASCE J Infrastruct Eng 14(1):89–101
2. Whelan MJ, Janoyan KD (2009) Design of a robust, high-rate wireless sensor network for static and dynamic structural monitoring. J Intell Mat Syst Struct 20(7):849–863
3. Jang S, Jo H, Cho S, Mechitov K, Rice JA, Sim SH, Jung HJ, Yun CB, Spencer BF Jr, Agha G (2010) Structural health monitoring of a cable stayed bridge using smart sensor technology: deployment and evaluation. Smart Struct Syst 6(5–6):439–459
4. Lynch JP, Sundararajan A, Law KH, Kiremidjian AS, Carryer E (2003) Power-efficient data management for a wireless structural monitoring system. In: Proceedings of the 4th international workshop on structural health monitoring, Stanford, pp 1177–1184, 15–17 Sep 2003
5. Caffrey J, Govindan R, Johnson E, Krishnamachari B, Masri S, Sukhatme G, Chintalapudi K, Dantu K, Rangwala S, Sridharan A, Xu N, Zuniga M (2004) Networked sensing for structural health monitoring. In: Proceedings of the 4th international workshop on structural control, New York, pp 57–66, 10–11 Jun 2004
6. Lynch JP, Sundararajan A, Law KH, Kiremidjian AS, Carryer E (2004) Embedding damage detection algorithms in a wireless sensing unit for operational power efficiency. Smart Mat Struct 13(4):800–810
7. Gao Y, Spencer BF Jr, Ruiz-Sandoval M (2006) Distributed computing strategy for structural health monitoring. J Struct Control Health Monit 13(1):488–507
8. Hackmann G, Sun F, Castaneda N, Lu C, Dyke S (2008) A holistic approach to decentralized structural damage localization using wireless sensor networks in *IEEE RTSS*, 2008
9. Lynch JP, Wang Y, Loh K, Yi JH, Yun CB (2006) Performance monitoring of the Geumdang Bridge using a dense network of high-resolution wireless sensors. Smart Mat Struct 15(6):1561–1575
10. Nagayama T, Spencer BF Jr (2007) Structural health monitoring using smart sensors. Newmark Structural Engineering Laboratory (NSEL) Report Series, No. 1, University of Illinois at Urbana-Champaign, Urbana. http://hdl.handle.net/2142/3521

11. Sim SH, Spencer BF (2009) Decentralized strategies for monitoring structures using wireless smart sensor networks. NSEL Report Series, ISSN: 1940–9826
12. Sim SH, Carbonell-Marquez J, Spencer BF Jr, Jo H (2010) Decentralized random decrement technique for efficient data aggregation and system identification in wireless smart sensor networks DOI:dx.doi.org. Probabilistic Eng Mech 26(1):81–91
13. Pakzad SN, Rocha GV, Yu B (2011) Distributed modal identification using restricted auto regressive models. Int J Syst Sci, First published on 24 May 2011. doi: 10.1080/00207721.2011.563875
14. Dorvash S, Pakzad SN, Cheng L. An iterative modal identification algorithm for structural health monitoring using wireless sensor networks. Earthq Spectra (in review)
15. Dempster AP, Laird NM, Rubin DB (1997) Maximum likelihood from incomplete data via the EM algorithm. J Roy Stat Soc R 39(1):1–38
16. Juang JN, Phan MQ (2001) Identification and control of mechanical systems. Cambridge University Press, Cambridge, UK
17. STMicroelectronics (2005) LIS3L02AS4 MEMS inertial sensor, Geneva

Chapter 24
Modal Testing of Non-structural Components for Seismic Risk Assessment

Manuel Archila, Carlos Ventura, Alicia Figueira, and Yan Yang

Abstract The continuing operation of non-structural components after an earthquake is of utmost importance for essential facilities such as hospitals, power generation plants, emergency operations centers and nuclear power plants. Failure of non-structural components becomes a hazard to the facility occupants and could disrupt the required operations of the facility after an earthquake event. Modal testing was implemented at a hospital to determine the modal parameters of non-structural components in hospitals located in Vancouver, British Columbia. A database with the modal parameters of these components was created which also included details pertaining to the type of restraint or isolation system. The testing program focused on operational components that perform essential services in these critical buildings such as plumbing, mechanical, and electrical system components. The tests were performed using excitations from ambient vibration and impact test. The tests were done using tri-axial accelerometers, their application was validated by comparing a modal model from accelerometer measurements to a model from laser vibrometer measurements. The information contained in the database will be used to develop methods for assessing seismic risk of non-structural components in essential facilities, assessment which can be used to mitigate risks and improve seismic performance.

Keywords Non-structural components • Critical facilities • Floor response spectrum method • Seismic risk

24.1 Introduction

The continuing operation of essential facilities after an earthquake depends on an adequate seismic performance of the structural and non-structural components. Failure of non-structural components becomes a hazard to the facility occupants and could disrupt the required operations of the facility after an earthquake event; this performance is not acceptable for essential facilities. Non-structural components are provided for the normal operation of buildings and they are not usually intended to carry loads. The non-structural components include building contents, architectural finishes, and building service systems.

In the past decades building codes prescribed seismic design provisions to protect the integrity of the building structure only, leaving non-structural components with little protection against earthquake damage. Based on lessons learned from earthquake damage to non-structural components, nowadays building codes are being complemented towards seismic design of non-structural components. For instance in Canada the Standard for *Seismic Risk Reduction of Operational and Functional Components of Buildings* CSA S832–06 [1] is available.

This Standard allows the use of alternative analytical methods for assessment of seismic risk of non-structural components, among them is the floor response spectra (FRS) method. This method stems from the fact that even though non-structural components are subject to earthquake excitations altogether with the building structure that supports them; it is likely the dynamic response of these components to the excitation will be different from the structure's dynamic response.

M. Archila (✉) • C. Ventura • A. Figueira • Y. Yang
Department of Civil Engineering, The University of British Columbia, 6250 Applied Science Lane, Vancouver, BC V6T-1Z4, Canada
e-mail: marchila@interchange.ubc.ca

J.M. Caicedo et al. (eds.), *Topics on the Dynamics of Civil Structures, Volume 1*,
Conference Proceedings of the Society for Experimental Mechanics Series 26,
DOI 10.1007/978-1-4614-2413-0_24,

Therefore determination of modal parameters of non-structural components is fundamental to estimate seismic demands with FRS. Using experimental modal analysis, a database which compiles modal parameters of non-structural components was developed and is presented in this paper. Such databases are useful for application of FRS method.

24.2 Description of the Test

24.2.1 Testing Technique

The experimental modal analysis method of output-only modal analysis (OMA) was used in this study [2]. The modal parameters of interest were natural frequencies, mode shapes and damping ratios. Therefore input excitations were not recorded. The Enhanced Frequency Domain Decomposition method available in the program ARTeMIS v. 4.31 [3] was implemented for processing the data.

The non-structural components with large dimensions were tested using a reference sensor and a set of roving sensors. For other smaller non-structural components a single setup of sensors was used. Operational and forced vibrations were the source of excitations for the tests. Mechanical and electrical components were tested under normal operation conditions with a sampling rate of 512 Hz. Pipes of the fire suppression system were tested using a roving impact and a sampling rate of 1,024 Hz.

24.2.2 Test Setup

An illustration of a test setup for a pipe is shown in Fig. 24.1. The location of the roving impact is indicated along with the accelerometers mounted on the pipe. The measuring equipment was mounted using mounting tape (double-sided tape). All the measuring equipment was synchronized to measure the response of the pipe to the excitation.

24.2.3 Measuring Equipment

Among several devices available for modal testing the equipment selected was a set of eight wireless MEMS tri-axial accelerometers. These accelerometers were convenient for the following reasons:

1. Accelerometers were light and would not significantly affect the modal properties of the component being tested.
2. The long distance range of the wireless was suitable for testing large components where conventional wired accelerometers would have been impractical.
3. Tri-axial accelerometers were convenient to easily determine modal parameters in 3D.

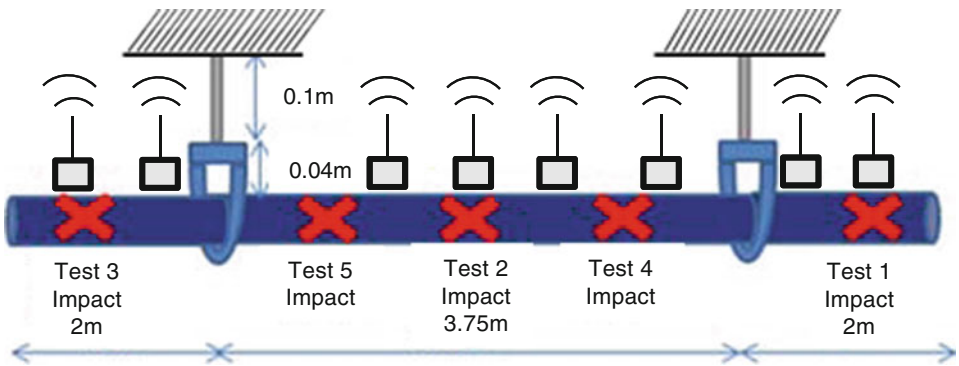

Fig. 24.1 Side view of setup of wireless sensors on pipe and roving impact

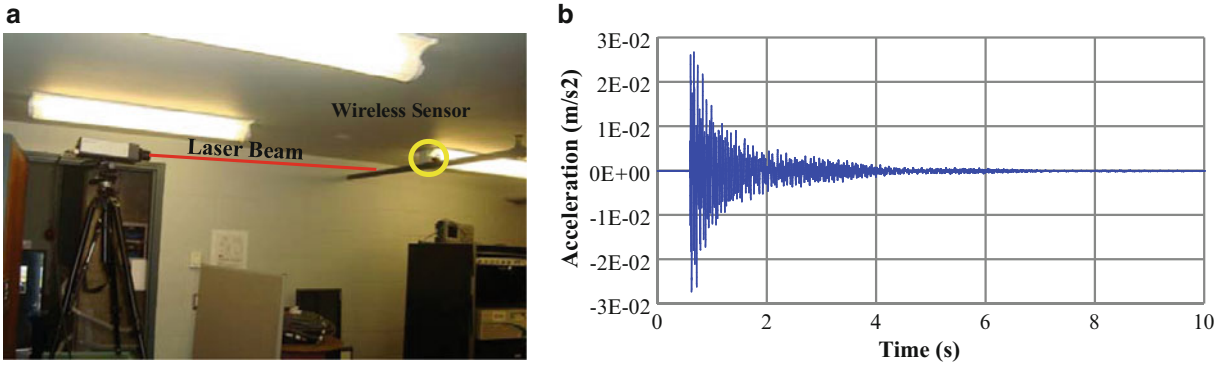

Fig. 24.2 Testing equipment, pipe tested and recording from impact test. (**a**) Laser vibrometer, wireless sensor and pipe. (**b**) Pipe vibration recorded with laser for impact test

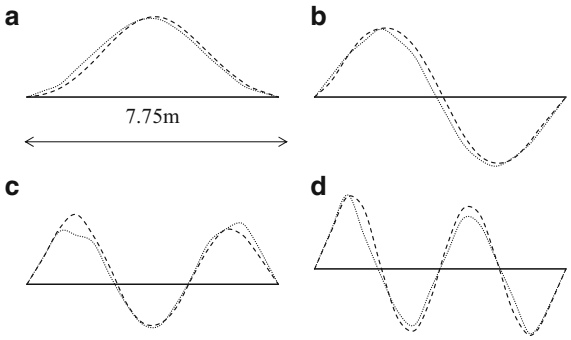

Fig. 24.3 Mode shapes in horizontal and transverse direction of pipe. (**a**) First mode. (**b**) Second mode. (**c**) Third mode. (**d**) Fourth Mode. *Dot line*: using MEMS wireless, *Hidden line*: using laser vibrometer, *Continuos line*: undeformed shape

Prior to performing all the tests a modal model obtained from measurements with these MEMS accelerometers was validated against a modal model from measurements taken with a laser vibrometer. The modal model corresponded to a suspended steel pipe with a run of 7.75 m long, which was part of a fire suppression system. The laser vibrometer, a wireless sensor and the tested pipe are shown in Fig. 24.2a. A record of pipe vibration under the impact test obtained with the laser vibrometer is shown in Fig. 24.2b, the motion decays in less than 8 s. The pipe restraint conditions and location of intermediate hangers are given in Fig. 24.1 and Table 24.1.

Figure 24.3 shows the mode shapes in the transverse horizontal direction of the pipe obtained with the laser vibrometer and the MEMS wireless accelerometers. It can be observed that the mode shapes for this pipe run are well defined and resemble the mode shapes of a uniform beam with fixed boundary conditions.

The mode shapes from the laser vibrometer test were smoother than the mode shapes obtained with MEMS accelerometers. This is due to a higher resolution of measurements that was used during the laser vibrometer test. In spite of the different resolutions used for both tests, the differences were not significant for the first and second modes but for the third and fourth modes.

The Modal Assurance Criterion (MAC) was implemented to assess the correlation of the mode shapes from both tests. Figure 24.4 presents the 3D MAC between mode shapes obtained with the MEMS wireless accelerometer and the laser vibrometer. The coefficients were 0.99, 0.96, 0.93, and 0.76 for modes 1, 2, 3 and 4 respectively. A coefficient equal to one indicates that mode shapes are fully correlated whereas a value of zero indicates they are uncorrelated. The difference in the resolution of measurements used during both tests was evidenced by a low correlation in the fourth mode which inherently had a more complex pattern of deformation.

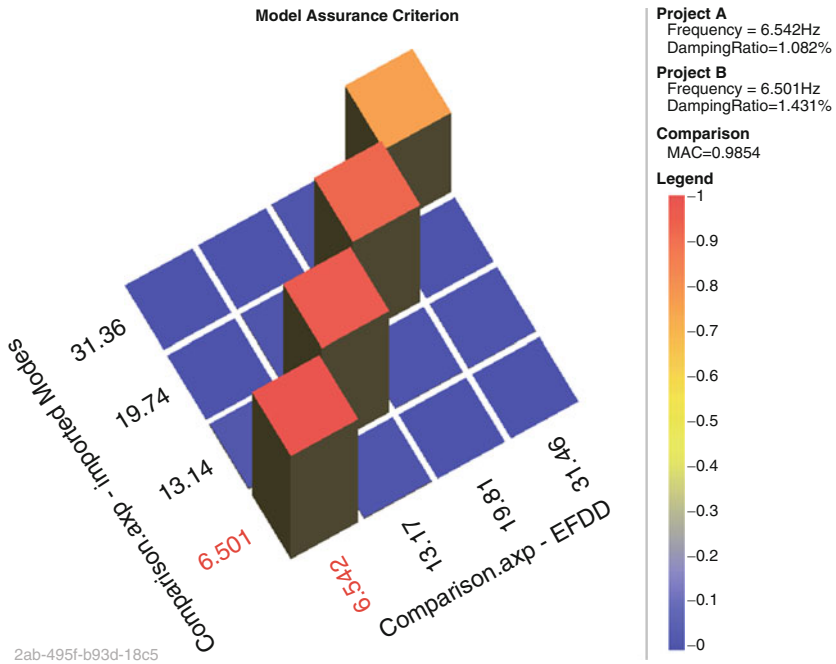

Fig. 24.4 3D MAC for validation test of MEMS accelerometers

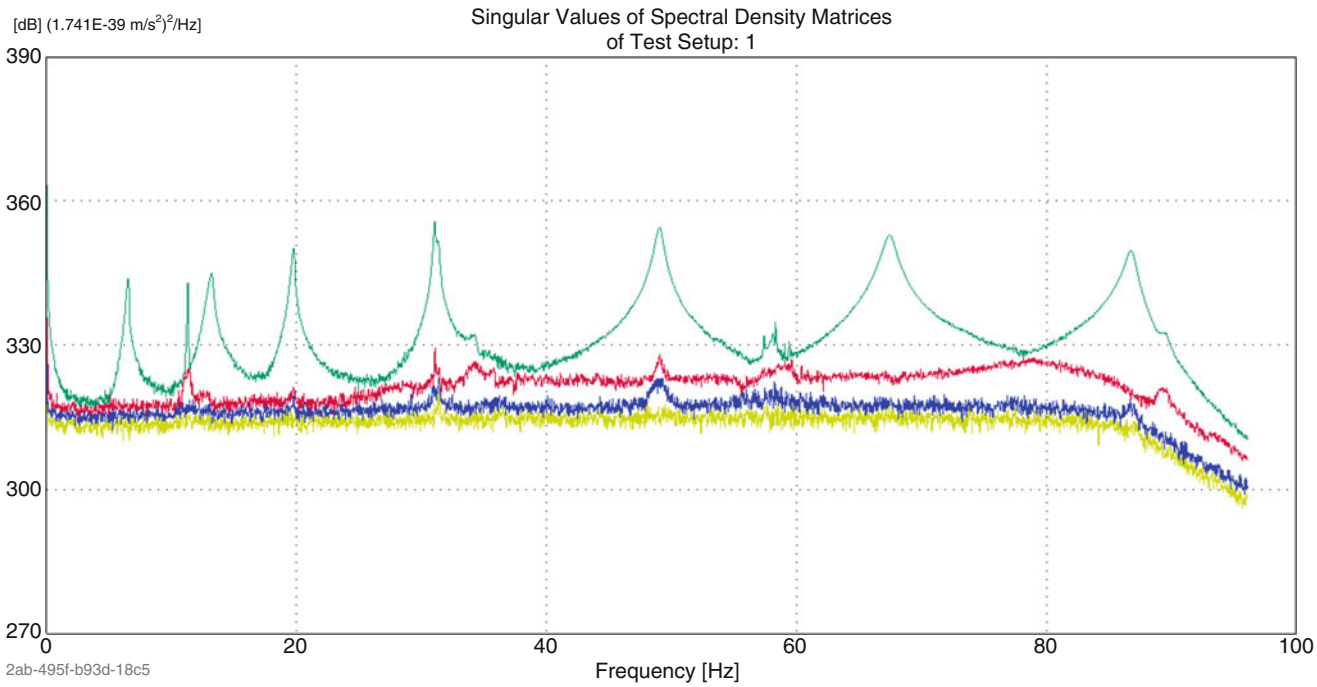

Fig. 24.5 Single-value-decomposition plot from impact test

The fundamental frequency for vibration in the transverse direction of the pipe was obtained as 6.50 and 6.54 Hz, for the test done with MEMS accelerometers and the laser vibrometer respectively. For practical purposes it was concluded that the results of both tests were well correlated for the fundamental mode and higher modes.

Analytical formulation was used to verify the fundamental frequency estimated for this pipe. The pipe was idealized as a uniform beam of 7.75 m long and with a diameter of 51 mm (black steel schedule 40). The fundamental frequency for an

undamped uniform beam of fixed ends was calculated using the formulation given by Humar [4]; the calculation gave a fundamental frequency of 5.50 Hz. This value was considered an adequate approximation to the fundamental frequency found from the tests above.

24.3 Modal Testing Results

In Fig. 24.5 the singular value decomposition for the impact test on a pipe is shown. Clear distinct peaks were obtained at each one of the natural frequencies. The database of modal parameters of non-structural components tested in this study is displayed in Tables 24.1 and 24.2. A complementary database with modal parameters of other non-structural components can be found in the Report EERF 07–08 [5] and [6].

In Figs. 24.6, 24.7, 24.8 and 24.9 the elevation of the each pipe hung from the ceiling is shown. The figures show the location of the roving impact and the intermediate rod hangers.

Table 24.1 Modal parameters for mechanical and electrical components

Component	Mode	Natural frequency (Hz)	Damping ratio (%)	Restraint conditions
Air handler	1 transverse	16.09	0.18	Seating on six isolators with lateral and vertical restraints
	1 torsional	29.54	0.09	
	1 transverse	16.09	0.18	
Electrical panel	1 transverse	13.58	–[a]	Unknown
	1 out of plane	57.42	0.15	
Electrical panel	1 out of plane	43.69	0.26	Unknown
				
Transformer #1	1 rocking	26.89	0.39	Seating over two C-channels with lateral and vertical restraints
				

[a]Value could not be determined with confidence

Table 24.2 Modal parameters for fire suppression system pipes

Component	Length (m)	Mode	Natural frequency (Hz)	Damping ratio (%)	Restraint conditions
Pipe No 1 ∅ 45 mm 	4.87	1 trans. 2 trans. 3 trans.	19.35 21.55 46.29	2.61 1.96 1.09	One end fixed, one end partially restrained. Three intermediate hangers
Pipe No 2 ∅ 51 mm 	7.75	1 trans. 2 trans. 3 trans. 4 trans. 1 vert.	6.50 13.14 19.74 31.36 11.27	1.42 1.60 0.60 0.04 1.31	Two ends fixed. Two intermediate hangers
Pipe No 3 ∅ 45 mm 	8.55	1 trans. 2 trans. 3 trans.	6.34 15.49 23.79	1.58 1.52 0.75	One end partially restrained, one end free. Three intermediate hangers
Pipe No 4 ∅ 36 mm 	6.55	1 trans. 2 trans. 3 trans. 1 vert.	9.76 18.45 24.24 12.50	1.86 2.25 2.07 1.09	Two ends partially restrained. Two intermediate hangers
Pipe No 5 ∅ 227 mm 	7.20	1 coup.	25.75	0.39	Supported at each end on a steel saddle. Free to rotate, slide longitudinally and displace vertically. Pipe was insulated
Pipe No 6 ∅ 60 mm 	7.20	1 trans. 1 vert.	9.60 10.36	0.93 0.40	Hung from a metal frame at each end with rod hangers

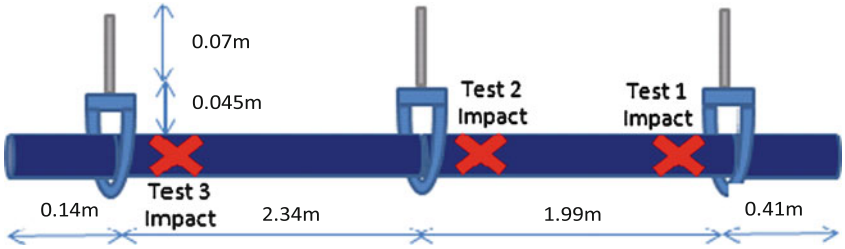

Fig. 24.6 Fire suppression system Pipe No 1

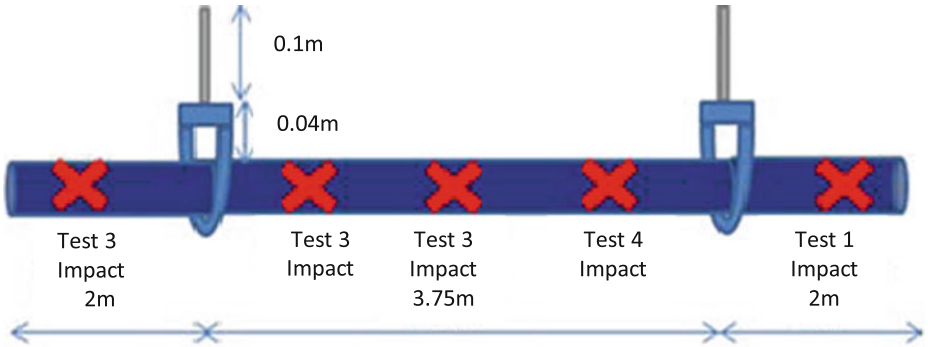

Fig. 24.7 Fire suppression system Pipe No 2

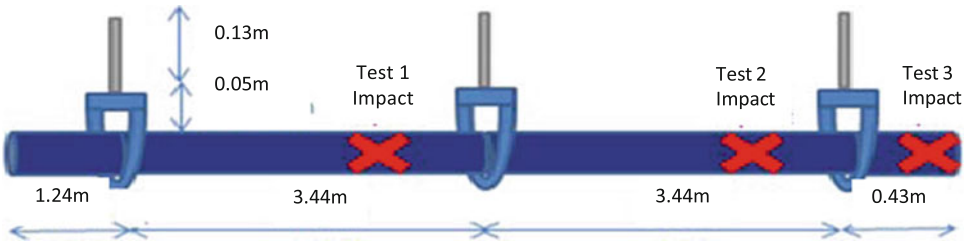

Fig. 24.8 Fire suppression system Pipe No 3

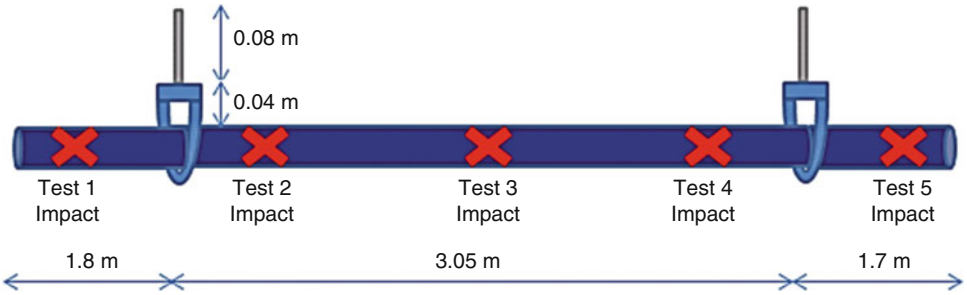

Fig. 24.9 Fire suppression system Pipe No 4

24.4 Conclusions and Recommendations

The results obtained from modal test done with the MEMS wireless accelerometers were validated against the results from the laser vibrometer test. This provided confidence on the capabilities of the wireless sensors which were exclusively used for the tests presented.

The results obtained from the tests done provide the modal parameters of some non-structural components that perform essential building services. These results can be used to verify or improve assumptions in the current approach of seismic risk assessment.

Most of the fundamental frequencies of the pipes tested were below 16 Hz ($T \geq 0.06$ s). The pipes hung from the ceiling with intermediate rod hanger lengths less than 0.15 m exhibited lower frequencies in the transverse direction of motion when compared to the vertical direction. This suggested that rod hangers were more engaged as partial restraints in the vertical direction than in the transverse direction. According to the Canadian Standard Association S832-06, these non-structural components are categorized as flexible and do not have a lateral restraint (clause G.1 and Fig. G.3).

The damping ratios corresponding to the fundamental mode of the pipes tested ranged between 0.4% and 2.6% and were below 0.4% for the remaining components. The appropriate damping ratio should be considered when spectral demands are determined, either through the Floor Response Spectra method or from prescriptive seismic design code provisions. The seismic provisions for lateral force in non-structural components given in clause 4.1.8.18 of the National Building Code of Canada [7] consider spectral demands for a damping ratio of 5%. A similar approach is followed by building code provisions in the United States. This could lead to significant underestimates of the spectral demands, given that the measured damping ratios are significantly less than 5%.

In future studies by the authors the sensitivity of the modal parameters to the amplitude of the excitation will be evaluated. The results presented in this paper were obtained for low levels of excitation and it is uncertain how they would be affected by stronger excitations such as earthquake shaking. The authors will also study this topic in the future.

Acknowledgements The financial support from Natural Sciences and Engineering Research Council of Canada (NSERC) through the Canadian Seismic Research Network (CSRN) and an strategic project grant to study "Post-Earthquake Functionality of Schools and Hospitals in Eastern Canada" to conduct the studies discussed in this paper is acknowledged with thanks.

References

1. Canadian Standards Association (2006) CAN/CSA-S832-06 – seismic risk reduction of operational and functional components (OFCs) of buildings
2. Brincker R, Zhang L, Andersen P (2000) Modal identification from ambient responses using frequency domain decomposition. In: Proceedings of the 18th international modal analysis conference – IMAC, San Antonio, pp 625–630
3. Artemis Extractor Pro 2008 (2006) Vers. 4.1. Structural Vibration Solutions A/S, Denmark
4. Humar JL (1990) Dynamics of structures. Prentice Hall, Englewood Cliffs
5. Ventura CE, Juarez H, Heydari G (2008) Dynamic characteristics of nonstructural components in critical infrastructure in UBC. Report EERF 07–08
6. Juarez H, Ventura CE (2008) Seismic performance of operational and functional components (OFCS): field observations and shake table testing
7. National Research Council Canada (2010) National building code of Canada 2010 (NBC). NRC Institute for Research in Construction, Ottawa

Chapter 25
Dynamic Characterization of Multiple Arch Dams: A Finite Element Approach

Ethan Ritz and Ziyad Duron

Abstract In this study, a typical large multiple arch dam located in the Sierra Nevada of California was evaluated for possible retrofit options to enhance its seismic performance. Field data was collected and used to validate the behavior of a detailed finite element model of this specific dam. By examining this computational model in the time and frequency domains, structural features influencing performance were identified, with particular attention paid to strut elements. A lumped element approximation of an n-dimensional multiple arch dam was created and analyzed; from this model, novel retrofit options were conceptualized and tested using the original finite element model. This process, although executed on a single specific dam, was designed to be general enough to be used as a valid approach to analyze and retrofit other dams of this type.

Keywords Seismic response • Finite element modeling • Aperiodic design • Arch dam

25.1 Introduction

Health monitoring of large civil infrastructure poses a unique engineering problem, one which must confront both age-related deterioration and potentially sub-optimal construction strategies of generations past. The extent of upkeep of these structures is ultimately a question of available resources—a balance must be achieved between repair and operational costs, which include money, time, and safety. The structure of focus in this study is the large multiple-arch dam, an example of which is included in Fig. 25.1.

The main advantage of this design is that it uses comparatively little concrete, making it useful for construction in wilderness areas where transport of material is difficult. However, the hollow structure of each arch decreases the performance of the system in an earthquake scenario, of critical concern due to the fact that the mountainous areas in which these dams are constructed may also exhibit heightened seismic activity. This study confronts the question of how to retro-fit dams of this type, some over 100 years old, to improve seismic performance in a cost effective manner. Note that the purpose of this study is not to evaluate a specific dam site under specific loading conditions. It focuses on gaining general insights and understanding of what governs the dynamics of large, redundant civil structures. The particular dam chosen to study as an example is typical in construction and size for this purpose.

25.2 Description of Critical Dam Components

A diagram of components associated with a typical large multiple arch dam is given in Fig. 25.2.

In 2009, data concerning modal response characteristics from a typical multiple arch dam was collected, which facilitated the creation and validation of a finite element model of this structure. The finite element model used is shown in Fig. 25.3.

The material properties of each of the elements were chosen to be consistent with conditions present at the site, and properties are given in Table 25.1. The mesh type and size for these elements are given in Table 25.2. A Lanczos Eigensolver was used to find the first 50 resonant frequencies and mode shapes of the structure, and a dynamic explicit load case used to apply earthquake time histories.

E. Ritz (✉) • Z. Duron
Harvey Mudd College, 301 Platt Blvd, Claremont, CA 91711, USA
e-mail: eritz@hmc.edu

J.M. Caicedo et al. (eds.), *Topics on the Dynamics of Civil Structures, Volume 1*,
Conference Proceedings of the Society for Experimental Mechanics Series 26,
DOI 10.1007/978-1-4614-2413-0_25,

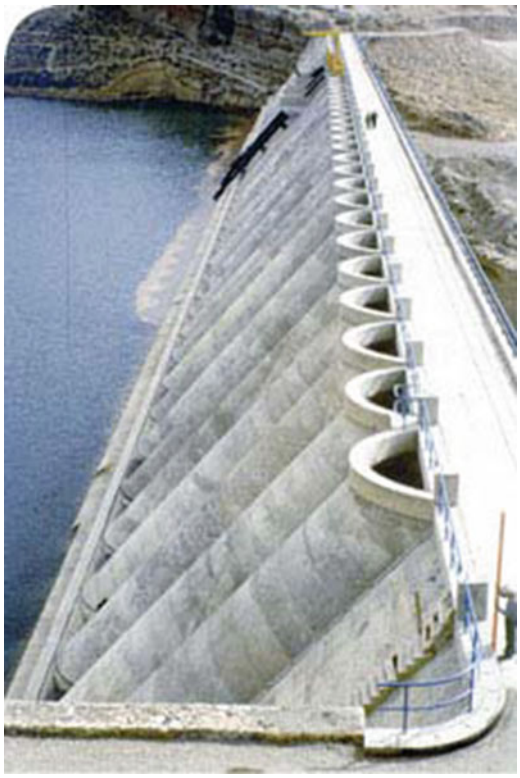

Fig. 25.1 Beni-Bahdel multiple arch dam, Algeria (not dam used in this study) http://www.lyc-lavoisier-porcheville.ac-versailles.fr/btstp/Cours/4-Ouvrages%20hydrauliques/Les%20barrages.pdf

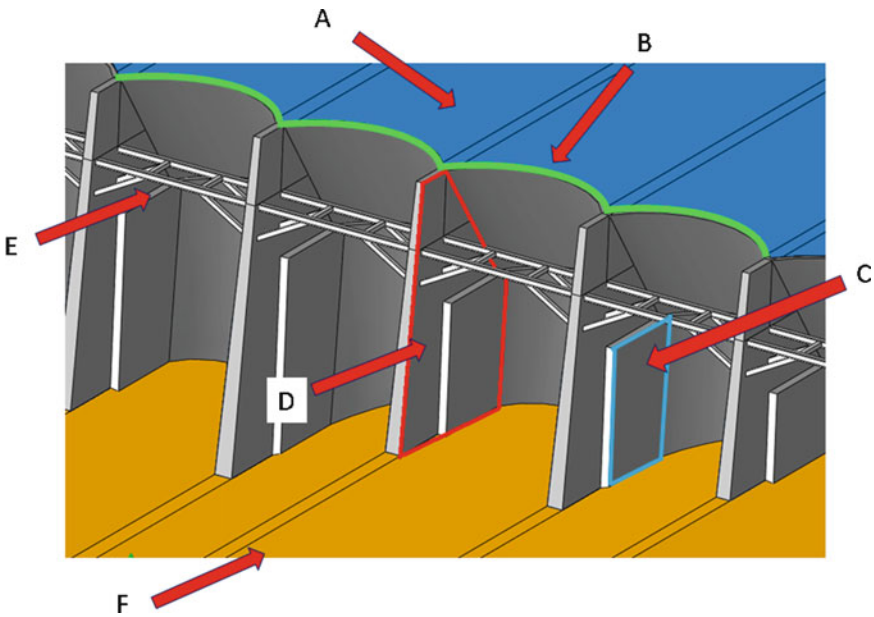

Fig. 25.2 Components of large multiple arch dam; water (**a**), arches (**b**), gravity (**c**), buttress (**d**), strut (**e**), foundation (**f**)

25.3 Evaluation Metrics

Although multiple arch dams are constructed from many discrete components, each of which affects the structure's global response to seismic activity, the focus of this study was narrowed to the impact of changing strut configuration on the stability of the system. Recognizing that material costs are at a premium, concentrating on only strut elements was justified with their ease of replacement and small physical size.

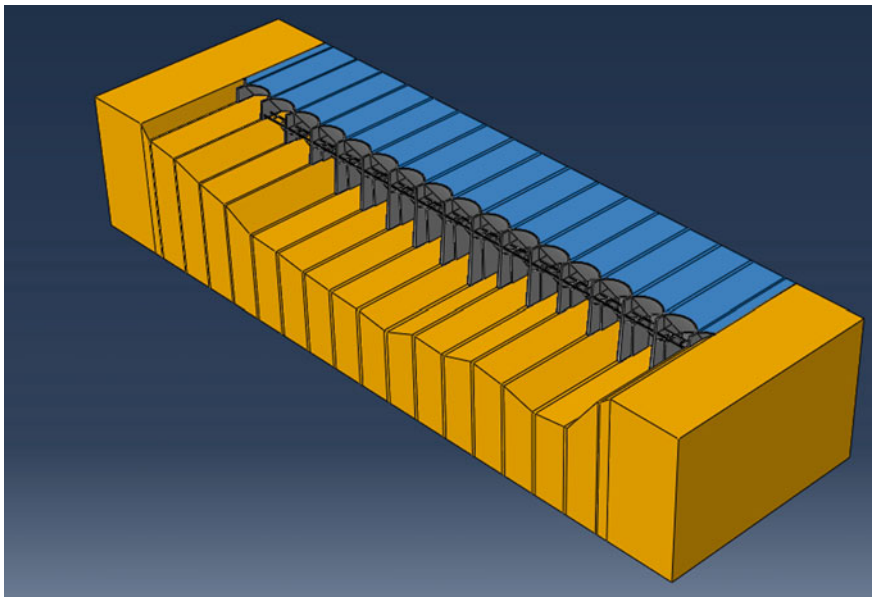

Fig. 25.3 Global view of FEM model

Table 25.1 Material properties

Property	Measured	Model
Concrete (arches, gravity, struts)		
Density (kg/m^3)	2.24E + 03	2.40E + 03
Young's modulus (Gpa)	15186	15186
Poisson's ratio	0.2	0.2
Concrete (buttress)		
Density (kg/m^3)	2.24E + 03	1.22E + 04
Young's modulus (Gpa)	10342	10342
Poisson's ratio	0.2	0.2
Foundation (rock)		
Density (kg/m^3)	N/A	2.4
Young's modulus (Gpa)	20684	20684
Poisson's ratio	0.25	0.2
Water (reservoir)		
Density (kg/m^3)	1	1
Bulk modulus (Gpa)	2150	2150

Table 25.2 Mesh parameters

Part	Mesh type (hexahedral)	Approx. mesh size	Number of elements
Arches	C3D8	1500	7478
Foundation	C3D8	10000	1248
Gravity	C3D8/C3D8R	800	9563
Struts	C3D8	570	166
Water	AC3D8	5000	1918

In order to develop effective adjustments to the dam, probable failure modes were determined and maximum principal stress (MPS) in the arches at crest elevation was used to indicate performance. Following this methodology, a time series of MPS measurements at 15 distinct locations was extracted at intervals of 1/400s over the entire 20s earthquake record. The data was expressed as the maximum MPS at each critical point over the given earthquake record, and a tensile stress limit of 400 psi was used. A plot of these measurements for the original, unmodified model can be seen in Fig. 25.4.

Though quantitative analysis provides critical insight to the problem, it also was acknowledged that the response of such a complex structure cannot be predicted easily. The simple method above, though effective in capturing general earthquake

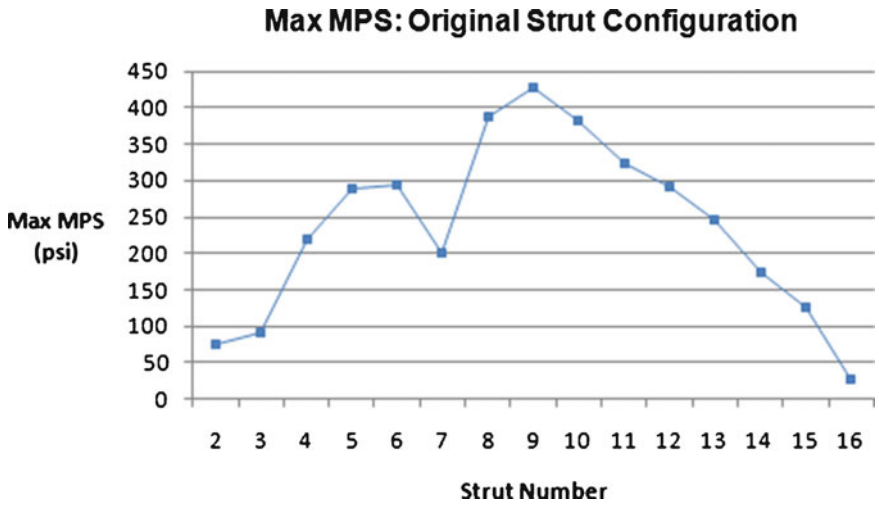

Fig. 25.4 'Base Case' for earthquake response, original model with no strut alteration

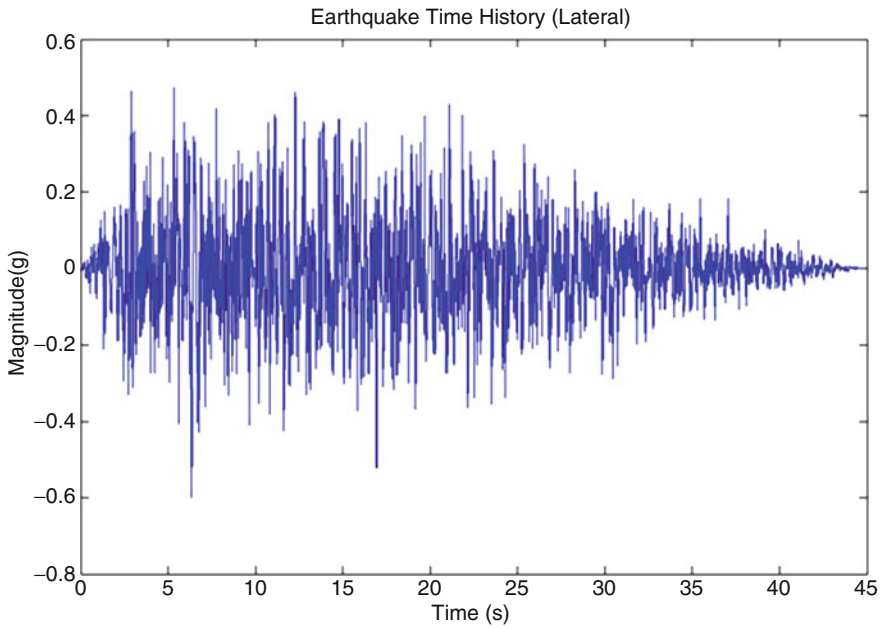

Fig. 25.5 MCE record used in this study

response information, provides little guidance for reducing stress levels, and modal analysis can be employed as an additional guide for improved performance. The inherent structure of large multiple arch dams implies vulnerability to cross-gorge excitation. Therefore, the qualitative presence of modes exhibiting this type of action, henceforth referred to as a 'domino mode' because of the global in-phase motion of all buttress elements, was considered in the study as an additional descriptor of the dam's vulnerability across different strut configurations.

It should also be noted that the frequency content of earthquakes is typically low, with the highest energy content below 20 Hz. This is true in the case of the dam studied; based on Maximum Credible Earthquake (MCE) records formulated for the surrounding geology shown in Fig. 25.5, significant energy rolloff is predicted to occur before 25 Hz. This can be seen in Fig. 25.6.

One strategy for avoiding the absorption of earthquake energy is to shift the resonant frequencies of the structure up and out of the range of maximum excitation as much as possible, making the natural frequencies $\omega_{n1}, \omega_{n2}, \ldots, \omega_{nk}$, where k is the number of mode shapes solved for, another relevant criteria by which to judge each design.

This study was performed as a two stage process. In the first stage, the impact of strut configuration on mode shape and ω_n was analyzed, with focus paid on trends which could control $\omega_n$and domino modes of the system. In the second stage, the models with the best modal analysis performance were tested via an MCE base excitation using the time history in Fig. 25.5. The MPS stress criterion described in Fig. 25.4 is used for determining which configurations perform best under seismic loading.

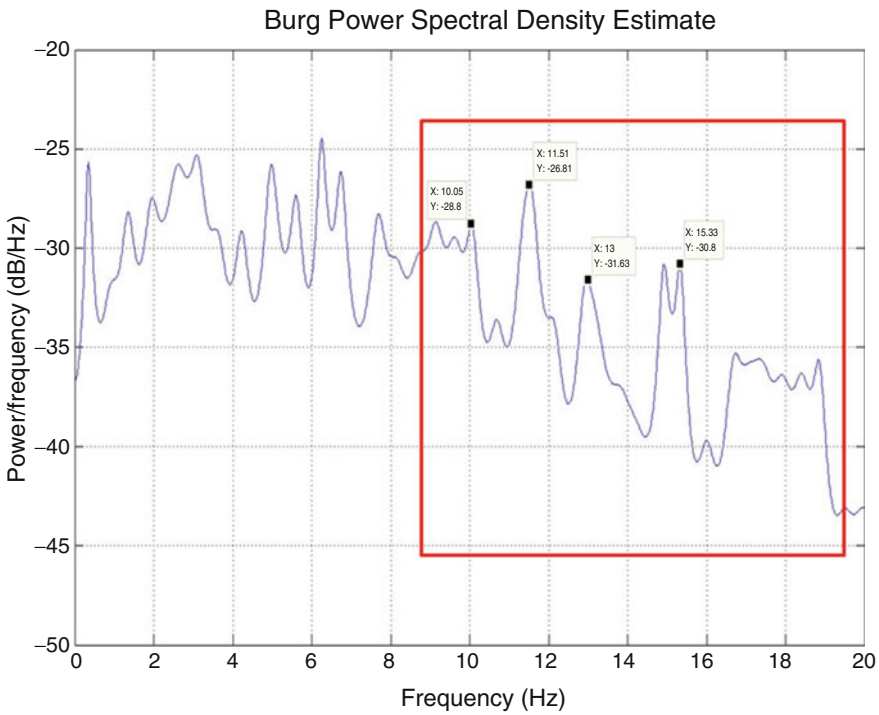

Fig. 25.6 PSD of MCE record in Fig. 25.5

25.4 Mode Shape Optimization

In the first stage of testing, many possible strut shapes and configurations were tested to discover trends in terms of domino mode behavior and ω_n. The struts of the original model were removed from the assembly, and each new strut design was incorporated into the model, upon which an eigenanalysis was employed to determine solutions up to 30 Hz. The designs were periodic in nature, meaning each strut was identical to every other strut in its respective design. The irregular end arches, which were too small to support many strut patterns, were filled with concrete (between buttresses 1–4 and between buttresses 13–16). It was found that this addition did not greatly affect the modal behavior of the structure (see Table 25.3) and was therefore used in the first stage (qualitative, non-stress-based) of analysis.

Increasing stiffness in the strut elements led to an increasing set ofω_n as expected since stiffer structures are traditionally associated with higher ω_n. It was also found that a lower (i.e. below crest elevation) strut position resulted in higher natural frequencies. Since the ability to test the effect of each of these parameters on earthquake response independently was considered ideal, an effort was made to decouple these parameters.

25.5 Aperiodic Strut Approach

To discern the impact of domino mode alone on seismic response, an effort was made to develop a strut configuration that would attenuate domino modes. Since such a wide range of struts had been explored previously, a fundamentally different approach was used to generate struts that would result in a non-domino model. It was observed that all configurations explored thus far had been periodic in nature; therefore, an aperiodic approach involving many different struts could possible exhibit deviations from the previously found trends.

Support for an aperiodic design was the hypothesis that the domino modes were a result of global, in-phase motion caused by each subsection of the structure being tuned to a similar resonant frequency. It was thought that if the resonant behavior of the structure could be made locally unique for each buttress or small group of buttresses, than the domino behavior of the system as a whole might be reduced.

This design was realized by randomly generating a series of ten spline functions, which were used to generate extruded three-dimensional beam elements (see Fig. 25.7). These elements were placed at various heights between the remaining

Table 25.3 Comparison of filled versus unfilled end arches

Model	First natural frequency (Hz)	Frequency of first domino mode (Hz)
No struts	9.69	11.00
Filled, no struts	9.71	11.10

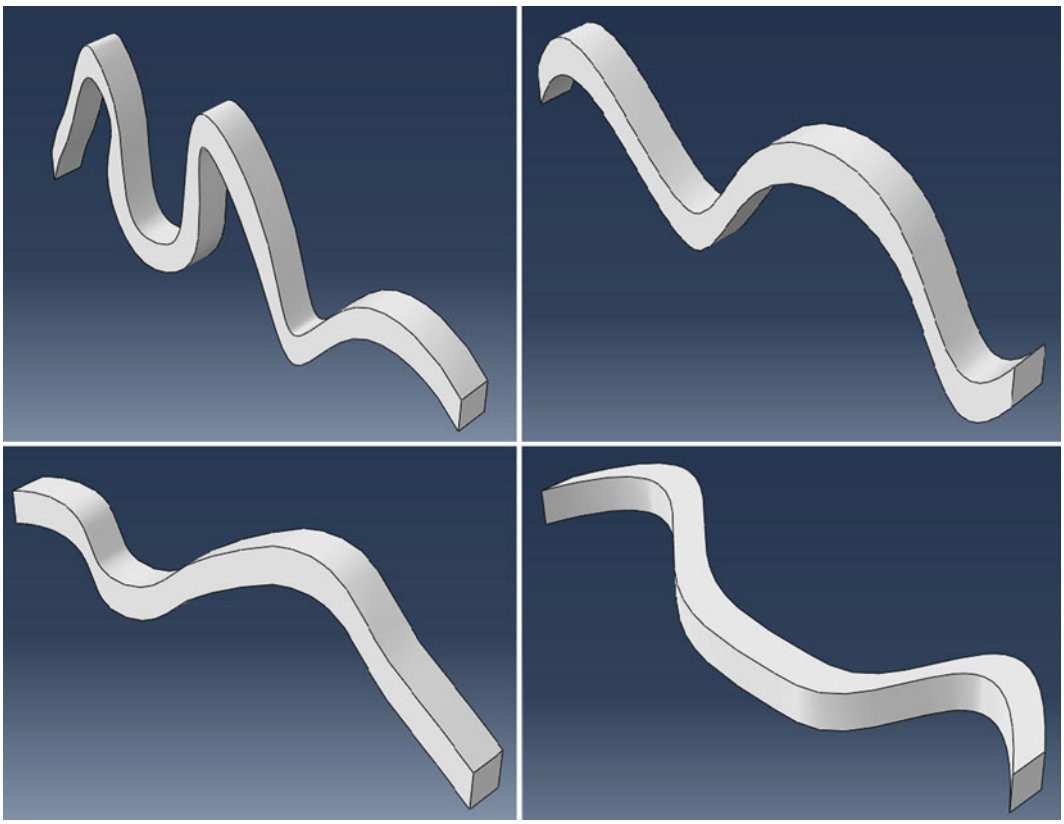

Fig. 25.7 Four of ten 'spline' struts

non-filled arches, with material properties chosen to mimic those of the original strut elements. Although these elements would be unrealistic to implement physically, they were chosen as a theoretical extreme useful in determining the effect of non-uniformity on global behavior.

25.6 Earthquake Simulation

It was found that an aperiodic approach did indeed deviate from the previous tradeoff between high ω_n and reduced domino motion; both significantly higher natural frequencies and few domino mode shapes were achieved. Since it was possible to generate a structure where both relatively high ω_n could be paired with an attenuated domino mode, earthquake stress analysis was performed on this configuration.

As can be seen in Fig. 25.8, a uniform stiffening of the arches by an order of magnitude results in significant attenuation of the MPS. Figure 25.9 indicates a surprising result, namely that the aperiodic design, which exhibits highly attenuated domino modes, performs relatively worse than the original or stiffened cases.

These findings support the case for an increase in stiffness enhancing seismic performance. Therefore, it can be said that a reduction of domino behavior using this method results in elevated stress levels throughout the entire structure, and an extreme case of aperiodicity produces the opposite of the desired effect on stress levels. These surprising computational results can be interpreted in two ways. One possibility is that domino mode is not as great a vulnerability as originally thought. The other explanation is that new system characteristics are introduced that degrade performance.

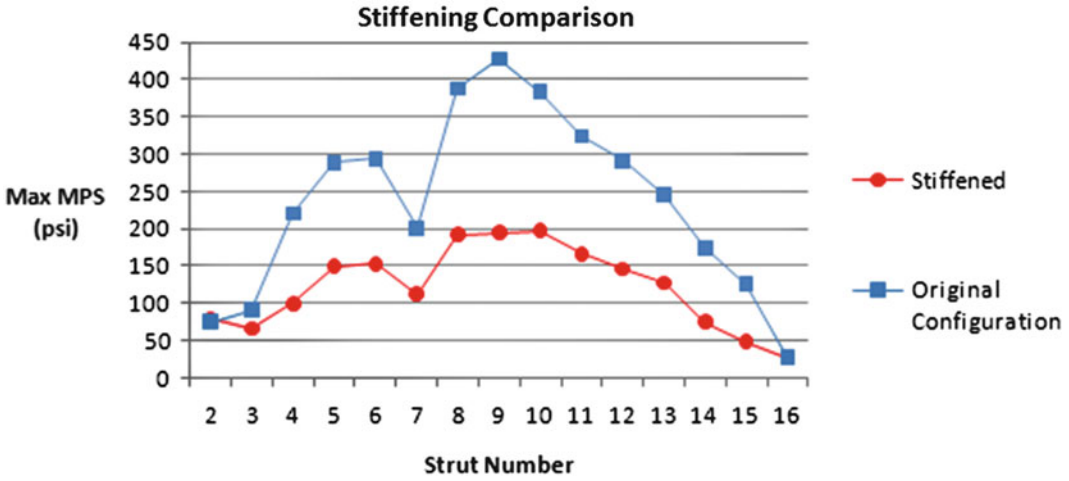

Fig. 25.8 Stiffened arch elements exhibit reduced stress levels when compared to original model

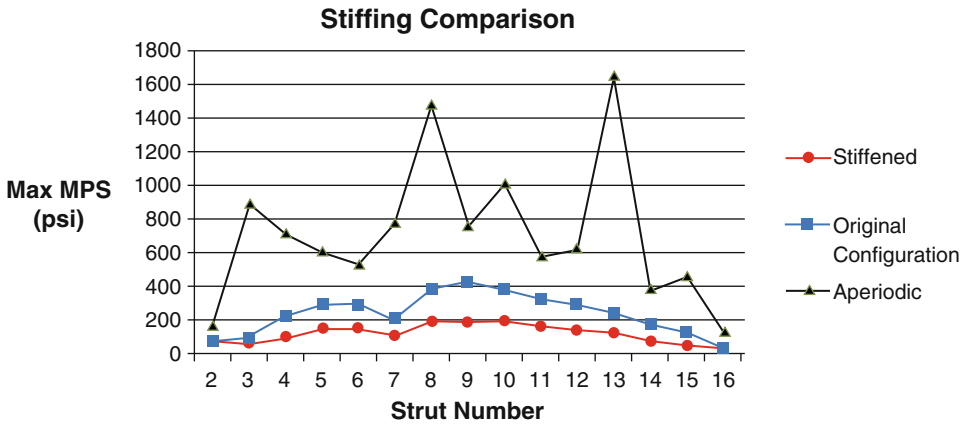

Fig. 25.9 Aperiodic spline struts increase stress levels across the entire structure

25.7 Non-strut Based Optimization

With the information gained from the aperiodic design, it was determined that minimizing the domino mode was not an effective strategy to reduce stress levels in the arches. This motivated a new approach, under the hypothesis that by removing the elements linking each arch to the next (struts), less energy would be able to propagate through the system. By also making the stiffness of each buttress high, the arches could act like many decoupled subsystems operating at different natural frequencies. A design that increased stiffness with a low material cost was implemented in the form of a fixed-fixed 'flying buttress' element, extending from the approximate middle of the buttress to the foundation, as seen in Fig. 25.10.

The Max MPS plot as used in the earthquake analysis of previous models is shown for the flying buttress configuration in Fig. 25.11.

Significant attenuation is seen for this stress criterion used in this study, especially for the right half side of the dam, when compared to the original and strutless models. However, it was noted that less attenuation was experienced in the left half side; in fact, for buttress 7, the stress was increased from that of the base cases. In an effort to discover if this behavior was intrinsic to a linked structure similar to a base case, the hybrid model in Fig. 25.12 was used, preserving the original configuration for a portion of the system surrounding buttress 7. As can be seen in Fig. 25.13, this results in significant attenuation across the entire structure, suggesting that a retrofit of this type could be an effective way to improve response to seismic loading. Additionally, keeping elements of the original structure intact for use in the final design is a cost efficient strategy.

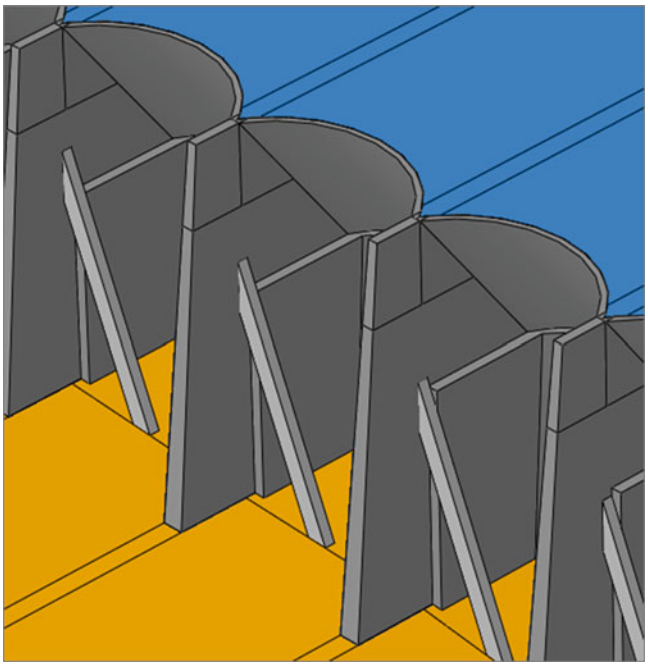

Fig. 25.10 Flying buttress concept applied to FEM (subset shown, buttresses applied to all arches)

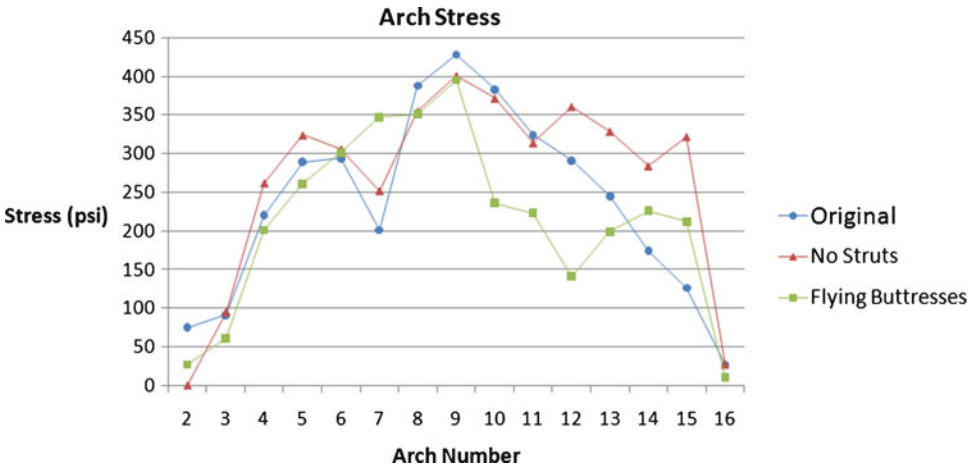

Fig. 25.11 Max MPS criterion for flying buttress model shown in Fig. 25.19

25.8 Critical Strut Analysis

Lastly, the same problem of seismic instability was approached with an entirely different method; namely, to find the areas for which reinforcing existing struts would have maximum impact. These results could be useful in the case where alternative approaches, such as the flying buttress design, are too expensive or otherwise unfeasible.

Initially, the base case in Fig. 25.13 for original design and strutless case were re-examined, and from the max MPS criterion it was concluded that strut inclusion may not benefit all buttresses. In buttresses 2–11, the stress in each configuration is roughly comparable; in fact, for arches 8–11, the stress is greater for the original strut case. Since the strut located between buttresses 15 and 16 seemed to influence stress levels most significantly, this strut was examined for features separating it from the others. As can be seen in Fig. 25.14, this strut is unique in that it does not attach directly to another arch; the elevated stress levels could be due to reflection of energy back from the foundation, or other factors influenced by the much greater stiffness of the solid rock gorge face.

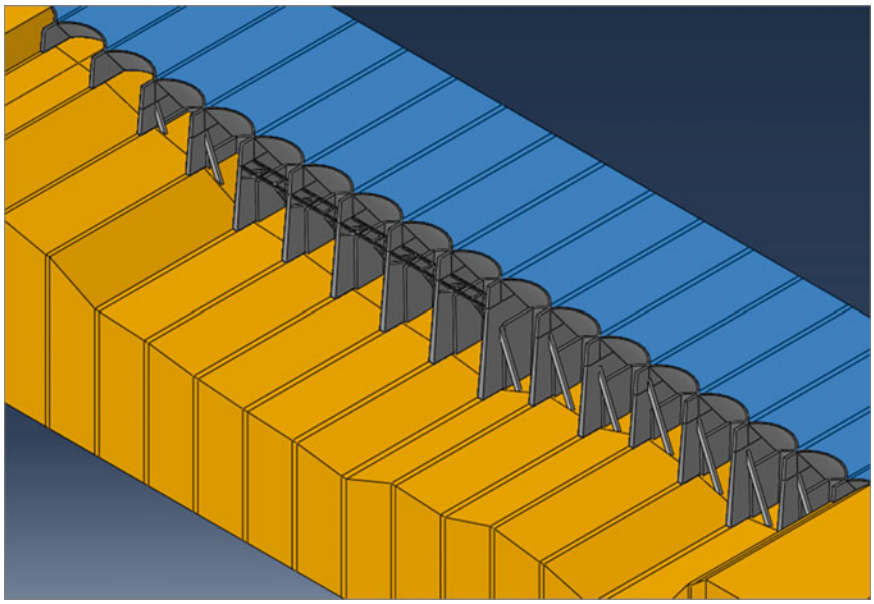

Fig. 25.12 Hybrid model, using both original struts and flying buttress elements

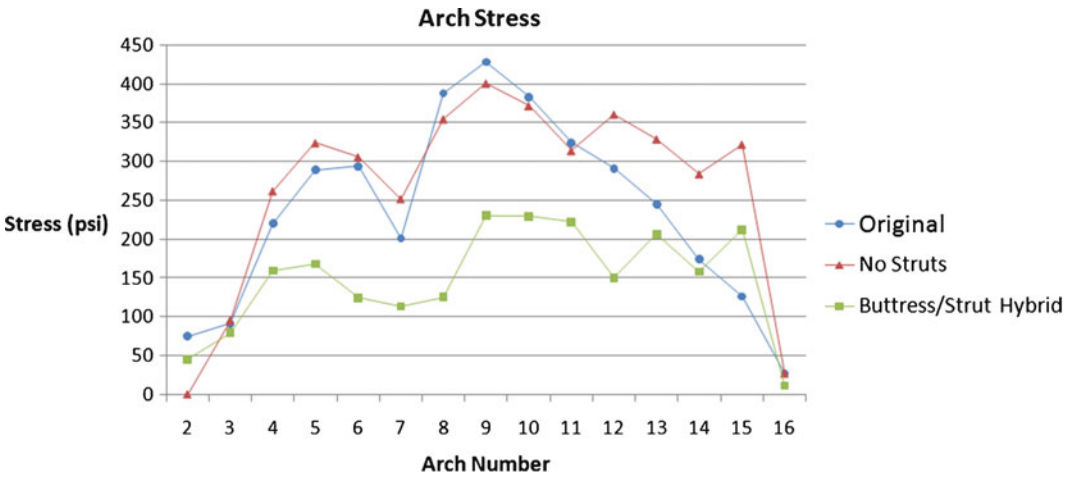

Fig. 25.13 MPS result of model in Fig. 25.12 shown in *green* against the base cases; attenuation is seen at almost every arch

To replicate a situation for which all strut elements failed except #15, the earthquake analysis was run with the model shown in Fig. 25.15, the results of which can be seen in Fig. 25.16.

It is clear that struts greatly affect the stress levels of buttresses they are nearest to, with little long-range impact. This means that a valid strategy for determining maximum impact struts is to find the ratio of max MPS for the no strut case to the original full strut case. As this ratio was greatest for arches 10–15, a second analysis was run with struts only in arches 10–15, as shown in Fig. 25.17, with results shown in Fig. 25.18.

The resulting stress levels are very similar to those of the full strut case, indicating that some struts add more lateral stability than others. In the case studied here, the struts in the right half of the dam are much more effective in reducing arch stress than the rest of the struts. If only enough resources were available to retrofit a single strut, a case could be made for concentrating those resources on strut #15 in this particular model. This analysis process allows cost effective and informed retrofit solutions to be considered.

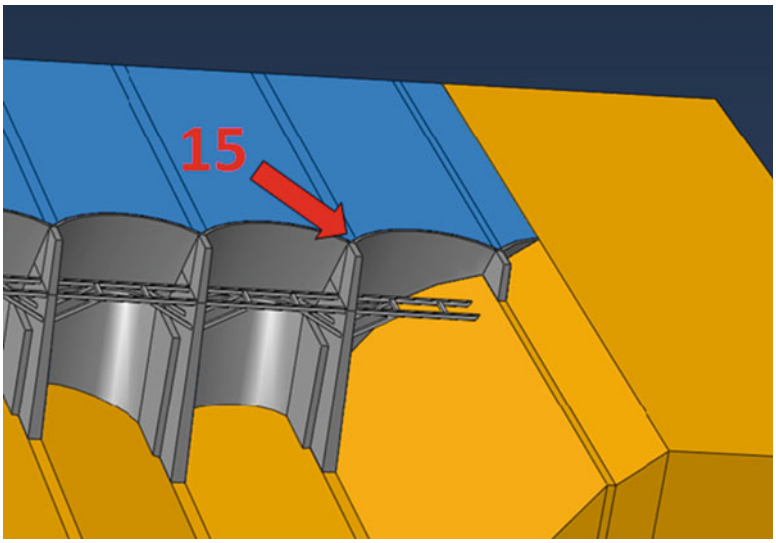

Fig. 25.14 Strut 15 is significantly different than the other struts, and experiences much higher stress levels

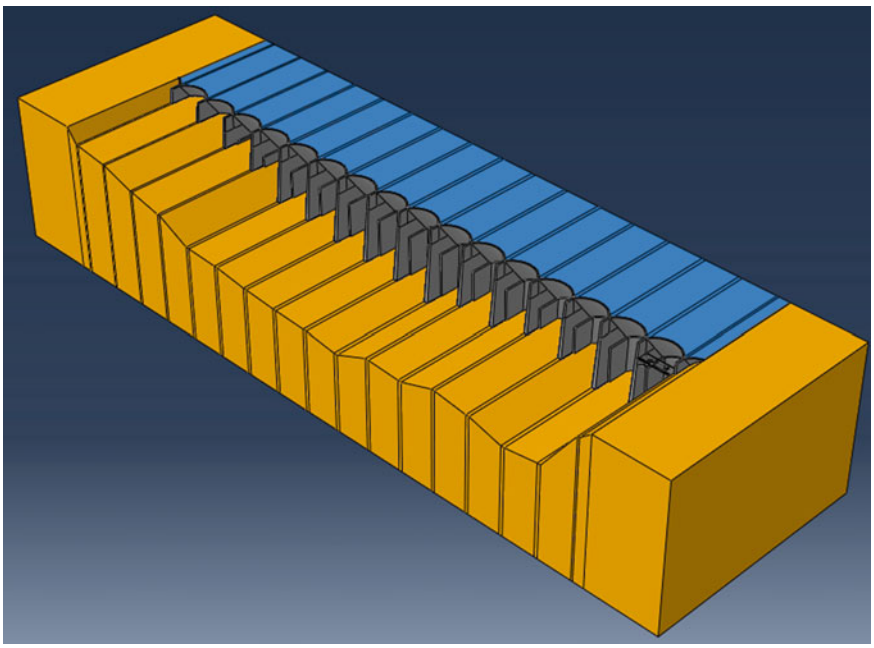

Fig. 25.15 All struts removed except strut 15 to determine this arch's effect alone on dam behavior

25.9 Modal Analysis Verification of Methods

Although the system with flying buttresses did reduce stress levels throughout the dam, the results do not clearly indicate exactly how these elements improved performance. Additional exploration was needed to show that reducing the linkage between each arch and an increase in buttress stiffness were the actual sources of improvement, and not because of some other characteristic of the flying buttress design.

To gain theoretical insight into the system, a mathematical representation of an n-dimensional multiple-arch dam was constructed using lumped spring-mass elements, and its theoretical behavior determined using modal analysis to construct its frequency response. The lumped element model used in this study can be seen in Fig. 25.19.

In this two-dimensional cross-gorge representation of an n-buttress dam, n masses are used, $M_1 \ldots M_n$ representing the dynamic mass of each buttress. 'Dynamic mass' refers to the mass mobilized in each buttress by earthquake motion, and includes some of the mass of the buttress itself, some arch mass, and also moving water. Fixed springs $K_{F1} \ldots K_{Fn}$ refer to the bending stiffness associated with each buttress represented as an upstream fixed-free cantilever beam (Fig. 25.20).

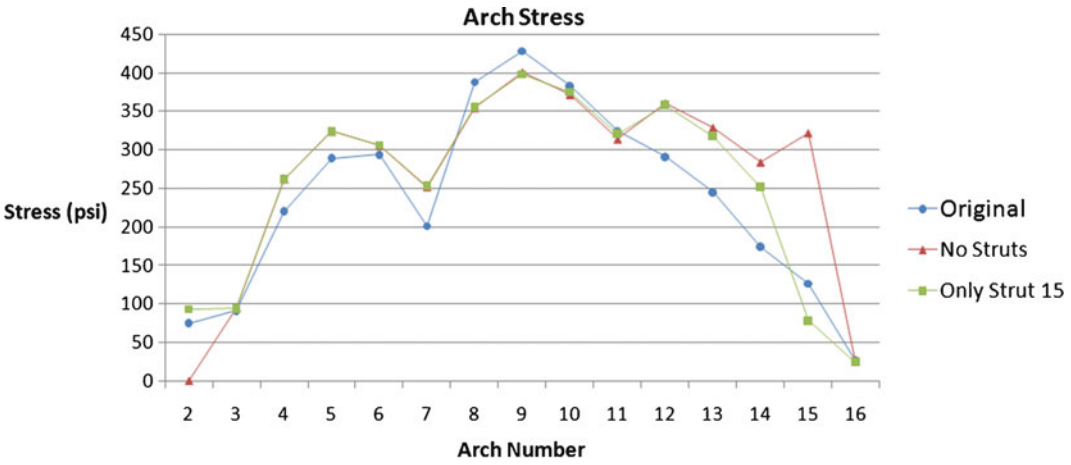

Fig. 25.16 Stress results of model shown in Fig. 25.15 in *green* compared to base case

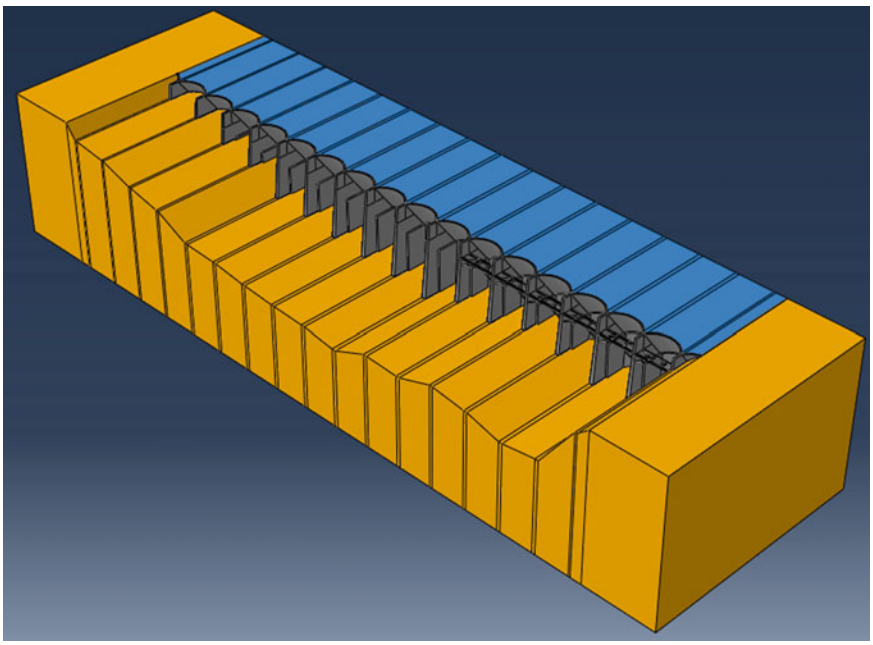

Fig. 25.17 Struts in right half of dam only

The values of $K_{F1}...K_{Fn}$ were generated using the function $K_{Fn} = F_0 Shape[n]$, where Fo is an experimentally derived scaling factor representing the stiffness of the shortest arch. Function *Shape[n]* is the 'shape function' of the foundation's profile from a direction perpendicular to the dam; it returns a problem-specific scaling of the height of the lowest arch $Shape[n] = \frac{H_{Low}}{H_n}$ and acknowledges that each arch is not of uniform height. The arches, if roughly simplified to an Euler-Bernoulli element, will have a tip deflection proportional to L^3; thus taller arches will have lower bending stiffness. Each specific dam will have a different shape function. For this study, a fairly simple shape function g[n] was chosen, and is given in Fig. 25.21.

For visualization purposes, this shape function corresponds to a dam with a foundation that decreases from the sides of the gorge to a low point in the center.

Linking springs between each mass $K_{L1}...K_{Ln}$ correspond to the stiffness between each buttress contributed by arch and strut elements. The values of K_L were chosen such that $K_L[n] = RK_0$, where R is a 'linking ratio' which allows the user to define the stiffness of the arch and strut relative to the buttress stiffness, as inspired by [1, 2].

The values of the mass elements were generated with the function $M[n] = \frac{M_0}{Shape[n]}$. From this model, the equations of motion for each of the elements $i = 1,2,...,n$ can be formed using methods outlined in Ref. [3].

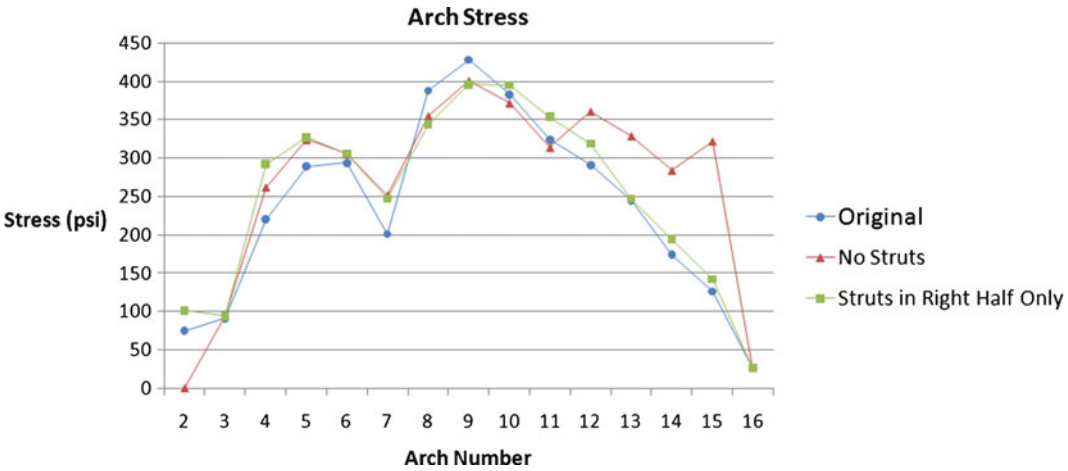

Fig. 25.18 Stress results for model in Fig. 25.17

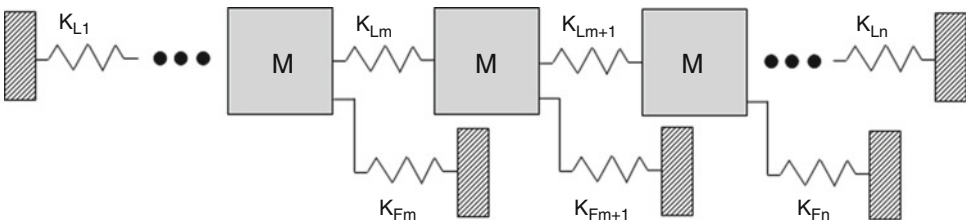

Fig. 25.19 Proposed lumped element approximation

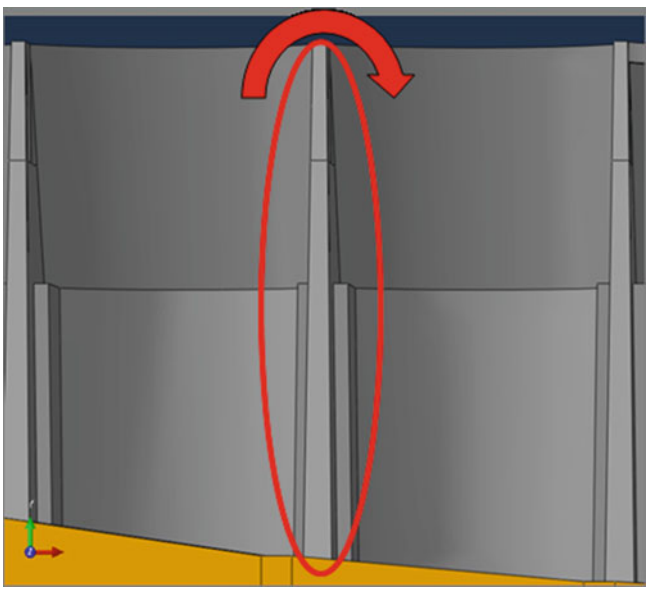

Fig. 25.20 Cantilever stiffness justification

The equations of motion are expressed below where x_n represents the displacement of each mass, and y the earthquake excitation.

$$M_n\ddot{x} + K_{Ln}(x_n - x_{n-1}) + K_{Ln+1}(x_n - x_{n+1}) + K_O x_n = K_O y \tag{25.1}$$

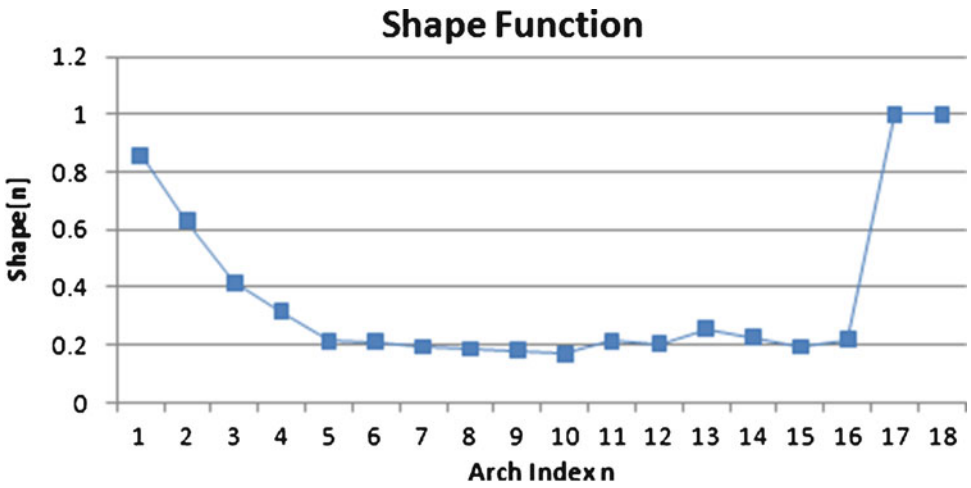

Fig. 25.21 Shape function used in this study

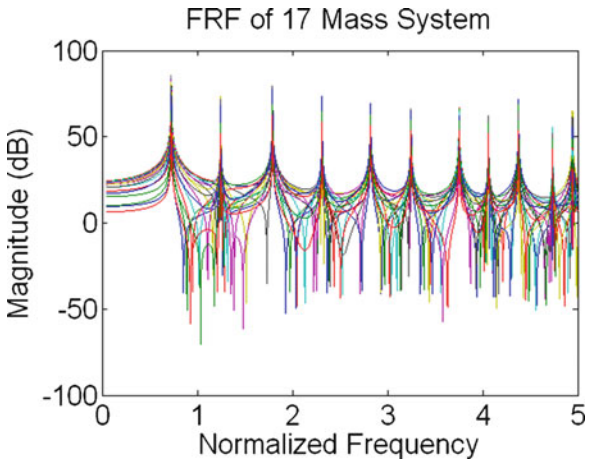

Fig. 25.22 FRF of all 17 mass elements

The eigensystem formed by the modal analysis of (25.1) was solved using a MATLAB script. The natural frequencies were normalized by

$$\overline{\omega}_{ri} = \frac{\omega_{ri}}{\sqrt{k_O/M}} \tag{25.2}$$

for ease of manipulation, and to entirely nondimensionalize the problem. In this context, the natural frequencies of the system can be seen as multiples of the first natural frequency of the system, and relative conclusions can be made about adjustments to the system without direct determination of Mo and Ko. The solution to this eigensystem was used to find the response of the system by the use of the impedance method. A structural damping value of 0.001 was added to the system in order to ensure an finite response at resonant frequencies.

Modes of vibration and frequency response functions (FRF) of the system described in (25.1) with n = 17 were found, and is shown in Fig. 25.22.

Although a separate FRF is associated with each mass, it was determined that a better representation of this data would be with a plot of the envelope of the maximum of the set of all response levels from every arch at each frequency, as shown in Fig. 25.23

White noise generated with a Gaussian distribution of specified amplitude was added to all spring and mass element parameters to represent variations in the actual dam. This acknowledges the fact that a perfectly symmetric system, which

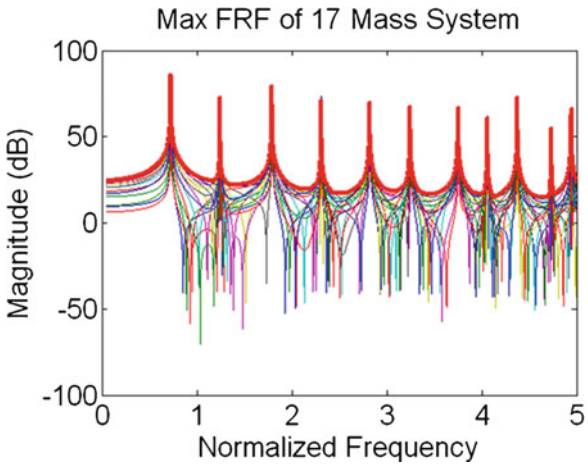

Fig. 25.23 Envelope of Max FRF at each frequency

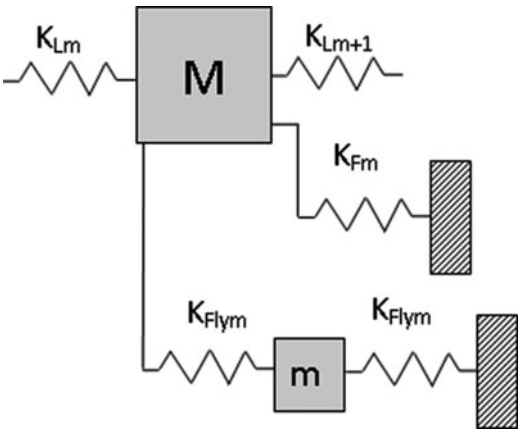

Fig. 25.24 Auxiliary system added for each mass

could display anomalous modal behavior, would likely not exist in the physical world. The noise was added to the linking spring using (25.3).

$$L_n = \frac{R(\in_L N[n] + Shape[n])}{mean(eG[n])} \tag{25.3}$$

Noise was added to fixed springs using the same equation without the shape function, and to masses with the same equation. In this equation, $\in_L$ (or, $\in_F$, $\in_M$ for fixed springs and mass), represents the 'disorder factor', and afford control over the level of 'noise' in the system. The mass and stiffness of the system were scaled to ensure that the average magnitude of the parameters would not be affected by changing the disorder factors.

To replicate the flying buttress elements used in the FEM stage, an auxiliary spring-mass system (termed 'flying buttress') was joined to each buttress, with mass m and stiffness $\frac{K_{fly}}{2}$ as seen in Fig. 25.24. Noise was added in the same method as for the other elements, although the shape function was not employed in this case.

25.10 Results of Modal Analysis

A plot of the envelope FRF for the original system is show in Fig. 25.24.

A linking constant of R = 50 was chosen based on data from the finite element model. A constant load was applied to the buttress element and to the arch element separately, and it was found that the deflection of the arch was approximately 1/50 that of the buttress.

We can determine the effect of changing linking stiffness by comparing Fig. 25.25 to a model where R = 1, very low linking stiffness, in Fig. 25.26.

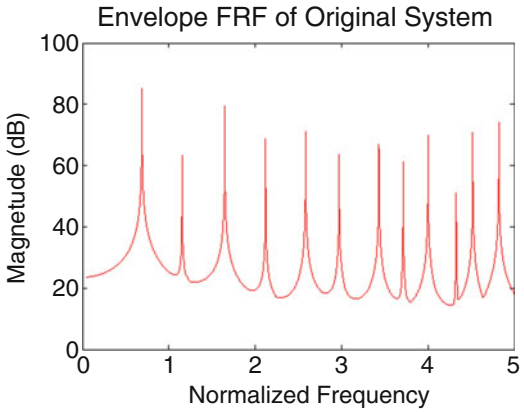

Fig. 25.25 Original system FRF, R = 50

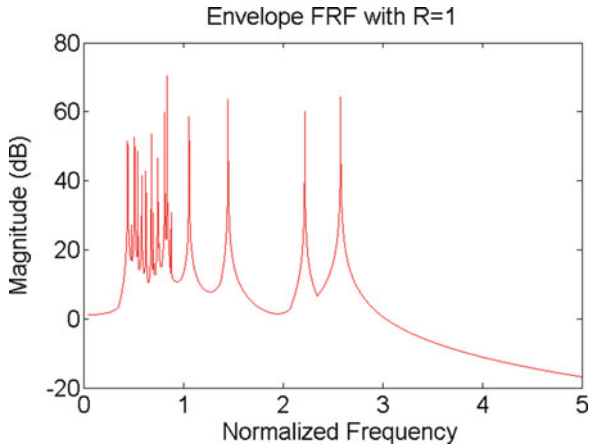

Fig. 25.26 Original system FRF, R = 1

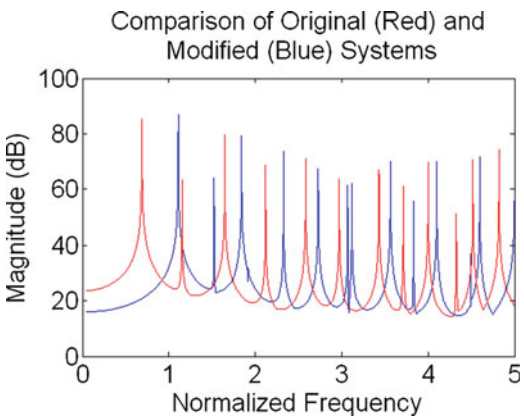

Fig. 25.27 Comparison of flying buttress model (*blue*) to original model with R = 50 (*red*)

It can be seen that an increase in arch stiffness results in a general shift of peaks to higher frequencies and a small increase in response magnitude. However, the first and most critical peak remains relatively stationary, making this a suboptimal result.

The effect of the addition of a "flying buttress" element with mass equal to 0.05 that of the main dynamic mass and K_{fly} equal to 10 (with linking spring still at R = 50) is shown in blue in Fig. 25.27, overlaid with the same plot as Fig. 25.25 (in red).

It can be seen that changes in this element do not drastically affect the shape of the excitation band in the same manner as the linking springs, but instead push this band to a higher frequency range. In Fig. 25.27, the lowest resonant frequency is moved more significantly in response to an increase in flying buttress spring stiffness, and the level of the response across the band of excitation does not increase as much as in the linking spring case. In addition, significant reduction of the response

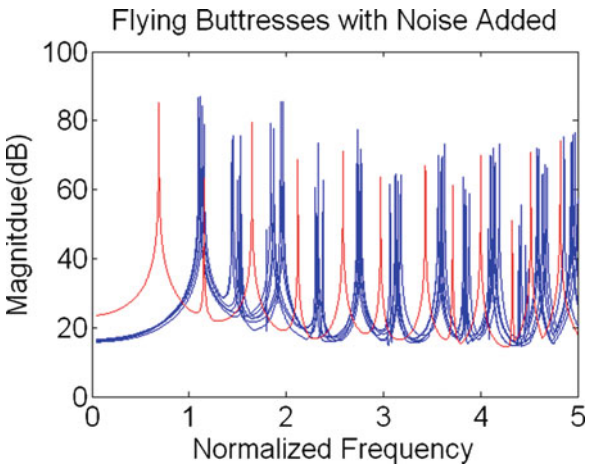

Fig. 25.28 Flying buttress system is robust against noise

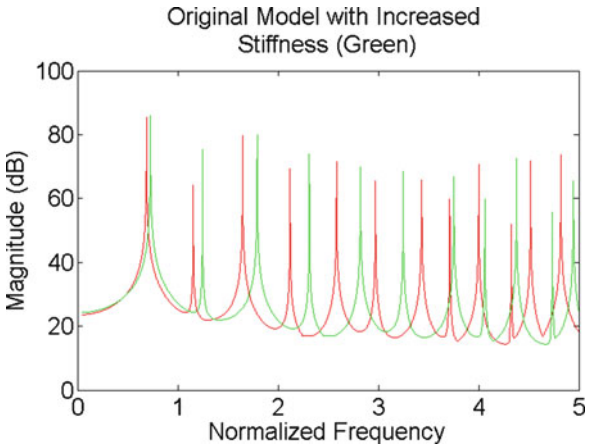

Fig. 25.29 Original system (*red*) and original system with stiffness increased (*green*)

for frequencies below the first resonance is observed. In fact, it was observed that for simulations for which no linking springs were used (such as in Fig. 25.14), the response approaches 0 dB as normalized frequency approaches zero, regardless of the magnitude of the fixed springs.

The system is also robust against noise, indicating that damage or natural variance of flying buttress elements will not have a large effect on the design. A system with six different flying buttress sets generated with noise value of $\in = 90$ is shown in Fig. 25.28.

This is an important finding, since during construction it would difficult to manufacture identical flying buttress elements. Also, during an earthquake situation, drastic failure would not occur if some elements began to crack or buckle.

Additionally, the observed increase in performance with the auxiliary system cannot be attributed to a direct stiffness increase; this model run with linking $R = 60$ and no flying buttresses almost precisely replicated Fig. 25.25, as seen in Fig. 25.29. This indicates that adding an equal amount of material to the flying buttresses is more effective than adding it to the arches.

With these results, we can be confident that decreasing the linking stiffness while increasing the buttress stiffness with an auxiliary system is indeed a good strategy for improving frequency response. The lowest peaks are shifted further out, and low frequency energy absorption is attenuated, which supports what is seen in the FEM earthquake simulations. It is also shown is that simplified modeling techniques can capture complex behavior in any periodic structure, not just dams, and that the modeling techniques used here could have applications to other structural considerations.

25.11 Conclusions

In this study, a typical multiple arch dam was modeled using finite element methods, and the stress response in key elements of the structure evaluated. The shape and configuration of the struts were analyzed for their effect on seismic response, and it was found that reduction of 'domino modes', though intuitively the mode that most matches the failure pattern of these structures, significantly worsens earthquake behavior, a surprising result. A simple lumped element model of the dam was created, which indicated that changing strut elements was not likely to reduce resonance bands in lower frequencies, even for very high stiffness. An additional element was integrated into the lumped element model, and it was found that modest stiffness values were very effective in both shifting resonant peaks up, as well as dropping the magnitude of low frequency bands. An implementation of this additional lumped element was made in the FEM model, and it was shown that this new flying buttress structure could be used effectively to reduce stress across the entire structure. Additionally, an auxiliary study was taken to determine which struts were most critical to the survival of the structure. It was concluded that each strut does not contribute equally to seismic performance, indicating that running counter to traditional retrofit methods, the same repairs need not be performed uniformly across the dam. This allows for a more cost effective design.

25.12 Future Work

One possible avenue of exploration involves examining exactly what influences the stress levels in end arches, and if there exist definable poor and optimal configurations of the arches as they join the canyon. Another area of study is to explore the design space of flying buttresses; in this study, only a simple beam was used, and there may exist better options for this dam component.

Acknowledgements I would like to thank Mike Knarr, P.E., S.E., John Yen, P.E., Mr. Nick von Gersdorff, and Dr. Matthew Muto for their technical review of the ideas presented in this study. I would also like to thank the De Pietro fellowship for supplying the resources required for the project, without which this work would not have been possible.

References

1. Cha PD, Pierre C (1991) Vibration localization by disorder in assemblies of mono-coupled, multi-mode component systems. ASME J Appl Mech 58(4):1072–1081
2. Pierre C, Cha PD (1989) Strong mode localization in nearly periodic disordered structures. Am Inst Aeronaut Astronaut J 27(2):227–241
3. Meirovitch L (1996) Principles and techniques of vibrations. Prentice Hall, Upper Saddle River

Chapter 26
Estimation of Unmeasured DOF's Using the Local Correspondence Principle

Anders Skafte and Rune Brincker

Abstract This paper will present a new method to estimate unmeasured Degrees of Freedom (DOF's) in a structure using only a limited amount of sensors. The method applies the Locale Correspondence Principle (LCP) to estimate a linear transformation between experimentally determined mode shapes, and mode shapes from a Finite Element (FE) Model. Mode shapes from the FE model are then altered to fit the real mode shapes of the structure, creating a set of estimated mode shapes covering all nodes.

The method is easy to perform and has a wide variety of application within civil- and mechanical engineering.

26.1 Introduction

The main idea of this paper is to combine the knowledge from the *true* but *limited* information found when performing an Operational Modal Analysis (OMA) [1], with the *fictive* but *expanded* information given by an FE model.

The method relies on the Local Correspondence Principle (LCP) which states that any set of mode shapes can be described as linear transformation of another set of mode shapes, as long as the variation between the two set of mode shapes is small. If a limited number of coinciding coordinates from each of the two mode shape matrices is known, an estimate of the linear transformation can be achieved. This transformation can be used to modify the set of mode shapes which contains more coordinates. The transformation is done mode by mode with the result being a new set of estimated mode shapes.

In this paper the LCP is used to analyze the mode shapes of a rectangular steel plate. A modified version of the plate – with changes in mass and stiffness – is used to represent the *true* structure which physics has changed over time. A perfect version of the plate is used to represent a *fictive* structure as it was at its virgin state.

An estimate of the *true* mode shapes of a structure can be found by performing an OMA on the measured response. The disadvantage with the OMA is that it only provides information at the DOF's where the sensors are placed, leaving information in all other DOF's unknown. However using a FE model of the structure provides a set of *fictive* mode shapes and with information in as many DOF's as wanted. When using the LCP the FE modes are altered to fit the real structure and creates an estimated set of mode shapes which holds as many DOF's as present in the FE model.

Application of this new method has a wide range of possibilities. When the mode shape coordinates are known in a large number of DOF's it is possible to estimate the response all over the structure. This will provide a more detailed Operational Deflection Shape (ODS) [2] analysis given the enhanced information of the response. Furthermore it enables a possibility to predict the response in places where it is not possible to place a sensor. The estimated response can furthermore be transformed to stresses and strains, which could benefit when investigating fatigue.

A. Skafte (✉)
Engineering College of Aarhus, Dalgas Avenue 2, Aarhus C 8000, Denmark
e-mail: ask@iha.dk

R. Brincker
Aarhus School of Engineering, Aarhus University, Ny Munkegade 120, Building 1521, Aarhus C 8000, Denmark

J.M. Caicedo et al. (eds.), *Topics on the Dynamics of Civil Structures, Volume 1*,
Conference Proceedings of the Society for Experimental Mechanics Series 26,
DOI 10.1007/978-1-4614-2413-0_26,

26.2 Theory

The main reason why it is necessary to estimate the mode shapes is that it is almost impossible to make an FE model where the modal parameters corresponds closely with the real structure. Often one will be satisfied if the MAC-value [3] between the modes of importance is above 0.85. This is due to the fact that the modal parameters of a structure will change according to a wide variety of factors such as temperature, humidity, wind and changes in mass and stiffness. These factors can be hard to implement in a FE model.

26.2.1 Understanding the LCP

This paragraph will give a short introduction to the LCP. The reader is referred to [4] for a more detailed description.

The fundamental basis for understanding LCP is found by investigating the sensitivity of mode shapes. Nelson [5] was one of the first to deduct an expression for the derivative of a mode shape. This was later modified by Heylen et al. [6] to describe the influence from changes in mass or stiffness:

$$\frac{\partial \varphi_i}{\partial u} = -\frac{1}{2m_i}\varphi_i^T \frac{\partial M}{\partial u}\varphi_i\varphi_i + \sum_{r=1, r\neq i}^{N_m} \frac{1}{\lambda_i - \lambda_r}\frac{1}{m_i}\varphi_r^T(-\lambda_i \frac{\partial M}{\partial u} + \frac{\partial M}{\partial u})\varphi_i\varphi_r \tag{26.1}$$

Where φ is the mode shape, M is the mass matrix, K is the stiffness matrix and λ is the eigenvalue. N_m refers to the number of modes and m_i is the modal mass of the corresponding mode.

By considering a finite small change in mass or stiffness, it can be shown that

$$\psi_{True} = \psi_{Fic,ex} T \tag{26.2}$$

is a reasonable approximation. T is aâ matrix describing the linear transformation between the two sets of mode shapes, in this equation denoted *True* and *Fic* (fictive). The subscript *ex* refers to selected DOF's.

An estimate of the transfer matrix can then be found by:

$$\hat{T} = \psi_{Fic,ex}{}^{\dagger}\, \psi_{True} \tag{26.3}$$

Where $\hat{T}$ indicates an estimate and † refers to the pseudo inverse.

And the estimate of the full mode shape matrix is found by:

$$\psi_{Est} = \psi_{Fic}\hat{T} \tag{26.4}$$

However in praxis the estimation of the mode shape matrix is done mode by mode. Equation 26.1 is only exact when all the modes in the system are known. This will never be the case with a real structure. By examining the second part of (26.1) it clearly shows that only the modes shapes close to the regarded mode have influence of importance when estimating a given mode. So when creating the estimated mode shape matrix mode by mode, (26.3) and (26.4) is transformed into:

$$\hat{t} = \psi_{Fic,ex}{}^{\dagger}\, \varphi_{True} \tag{26.5}$$

$$\varphi_{Est} = \psi_{Fic}\hat{t} \tag{26.6}$$

The trick is to find the number of FE modes that gives the best fit for the given mode. The number of FE modes can't be larger than the number of DOF's due to (26.3). The optimization is done by leaving some of the known DOF's out of the equation using these as a parameter for the optimization. In this way the number of FE modes in (26.5) and (26.6) can be increased to the optimal estimation is found. Due to (26.1) only modes nearby the mode observed is used in the estimation.

26.3 Example with Rectangular Steel Plate

To validate the method two different cases are presented. An FE model of a rectangular steel plate with changes in mass and stiffness is used to generate two sets of *true* mode shapes. These mode shapes should represent the result of measurements on a structure which physics has changes from its virgin state.

Furthermore the mode shapes from a perfect version of the steel plate are extracted, creating a set of *fictive* mode shapes. These will be modified to fit the two different cases where the changes have been made.

26.3.1 FE Model

The FE model measures 530×320×3 mm and holds 81 DOF's. The Young modulus is, E = 210,000 MPa and the Poisson ratio is, ν = 0.3. The plate is modeled with "free-free" supports.

Figure 26.1 gives an overview of the DOF's used in the FE model. The DOF's marked with "o" are used in the estimation and the DOF's marked with "x" are used as reference.

26.3.2 Cases

Two different cases will be presented. In the first case three point loads of each 1.92 N are added in node 22, 37 and 54 increasing the total mass with approximately 15%. In the second case both mass and stiffness change have been made to the plate. A point load of 1.92 N has been added to node 16 and the stiffness of the material has been reduced to ¼ in two rectangular areas of the plate – see Fig. 26.2.

Before using the LCP algorithm each mode shapes from the two cases are subjected to 2% noise by:

$$\varphi_n = \varphi + \sigma_\varphi \, \varepsilon \, \bar{x} \tag{26.7}$$

Where:

σ_φ is the standard deviation of the given mode shape.
ε is the noise ratio (2%).
$\bar{x}$ is a stochastic process generating Gaussian white noise$(\mu = 0,\ \sigma = 1)$.

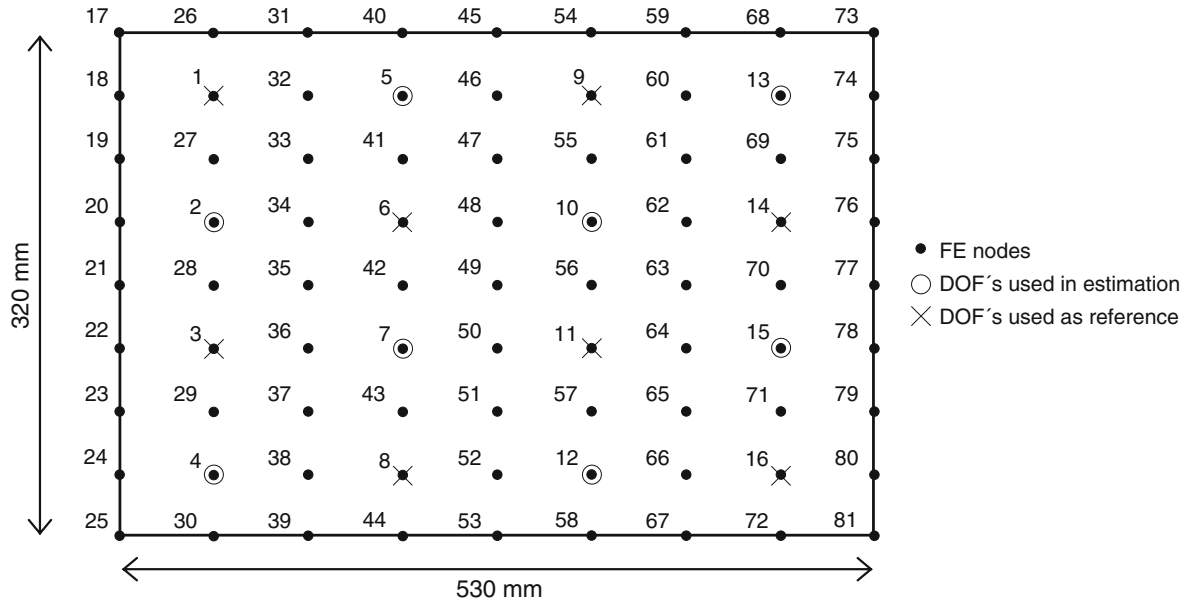

Fig. 26.1 Overview of DOF's in FE model

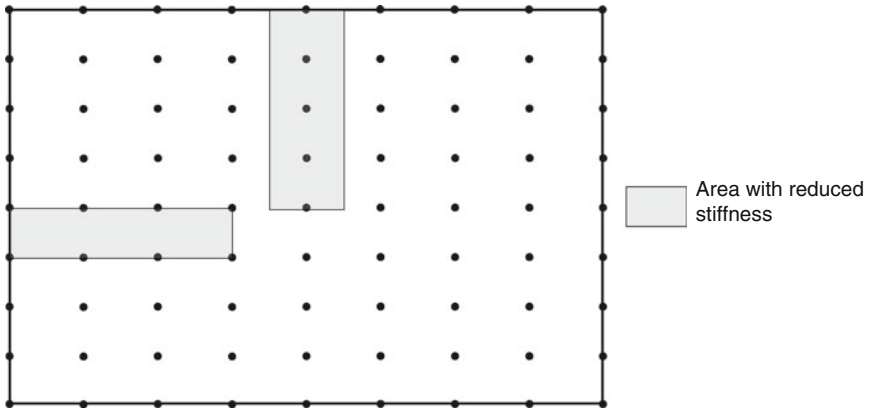

Fig. 26.2 *Grey areas* indicate where the stiffness has been reduced in the second case

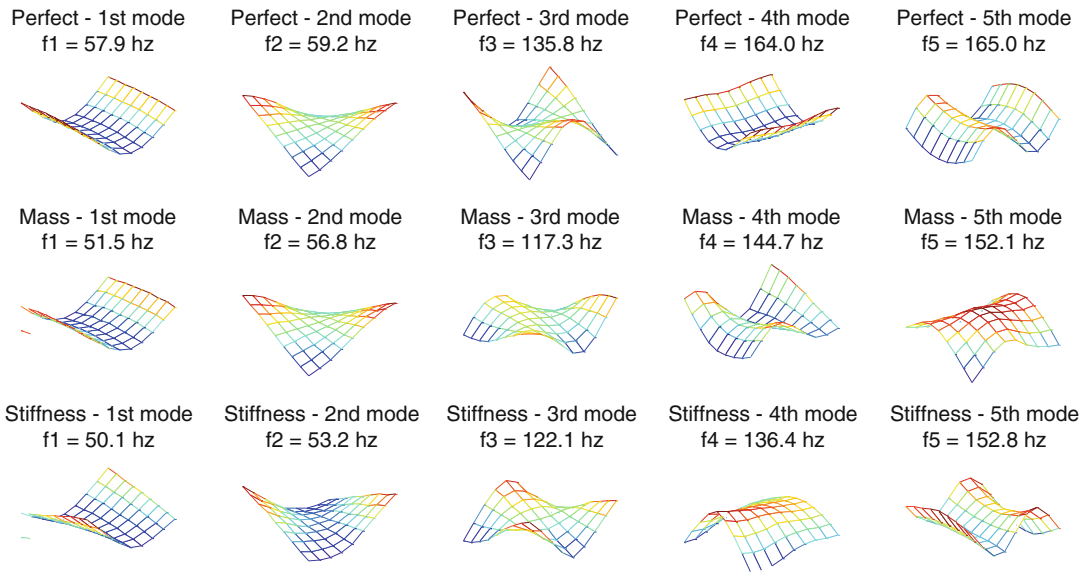

Fig. 26.3 *First row*: mode shapes from the "perfect" plate. *Second row*: mode shapes from the plate with added masses + noise. *Third row*: mode shapes from the plate with change in stiffness + noise

This is done to simulate that the mode shapes are found by using an identification algorithm.

The first row in Fig. 26.3 shows the first five mode shapes from the *fictive* structure, where no changes have been made. The second row shows the mode shapes where the three point loads have been added. In this case the first two mode shapes do not change significantly, whereas large changes are found in the third, fourth and fifth mode shapes. The third row shows the mode shapes from the model with both changes in mass and stiffness. Here the first two modes display large changes. The MAC-value [3] is used as a measure for the correlation between two mode shapes.

$$MAC(\varphi_i, \varphi_j) = \frac{\left(\varphi_i^H \varphi_j\right)^2}{\left(\varphi_i^H \varphi_i\right)\left(\varphi_j^H \varphi_j\right)} \tag{26.8}$$

The MAC-values between the set of *fictive* mode shapes and the two cases are listed in Table 26.1 (using the same eight DOF's as in the estimation).

The MAC-values listed in Table 26.1 reveals the effect of closely spaced modes especially in the first case where mode 4 and 5 have switched place.

Table 26.1 MAC-values between the two cases and the mode shapes from the "perfect" plate

	First mode	Second mode	Third mode	Fourth mode/ (fifth mode)	Fifth mode/ (fourth mode)
MAC – mass:	0.956	0.985	0.590	0.072/(0.857)	0.011/(0.472)
MAC – stiffness	0.770	0.755	0.982	0.835	0.936

Table 26.2 MAC-values and optimal number of FE modes

	MAC-value	Number of FE modes
First mode	0.956	1
Second mode	0.985	1
Third mode	0.826	8
Fourth mode	0.924	3
Fifth mode	0.909	5

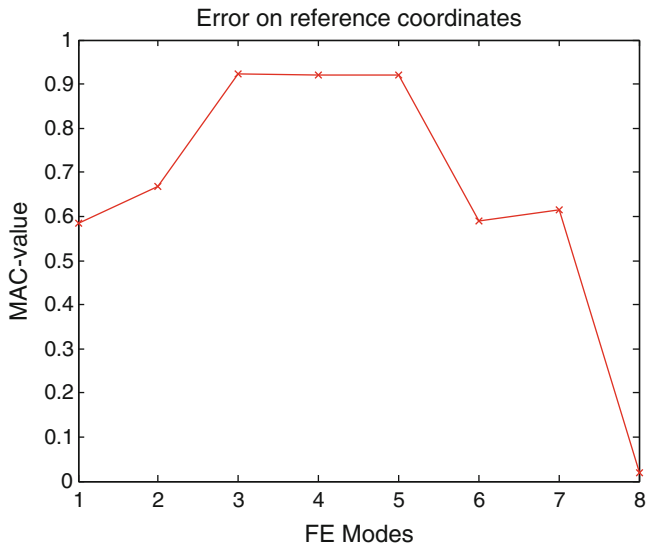

Fig. 26.4 MAC-value as a function of numbers of FE modes used in the estimation

26.3.3 Case with Added Masses

The modified plate represents the *true* structure and in this case 16 mode shape coordinates are pretended to be known. The mode shapes from the "perfect" plate represents the *fictive* structure where all 81 mode shape coordinates are known.

By using (26.5) and (26.6) the FE mode shapes are now altered to fit the real structure. This is done mode by mode using eight mode shape coordinates in the estimation and eight as reference. The number of FE modes used in (26.5) and (26.6) are increased one by one, and the estimate which gives the highest MAC-value defines the given mode shape (Table 26.2).

The MAC-value for the first two modes has not changed which is explained by their initially high value. There is only used one FE mode in the estimation meaning the result of (26.5) is a scalar. The estimate is then only a scaled version of the FE mode.

The third mode is optimized from 0.590 to 0.826 using the maximal number of FE modes. This optimization is not as good as expected which could be explained by different reasons: Either there is not enough information (eight mode shape coordinates) to make a reasonable estimate, or the known mode shape coordinates are placed in a way the gives poor estimate for this particular mode.

The fourth and fifth mode shows considerably increasing in their MAC-value using 3 and 5 FE modes respectively. Figure 26.4 shows how an optimum is found when estimating the fourth mode.

Figure 26.5 shows a plot of the estimated, *true* and *fictive* version of the fourth mode.

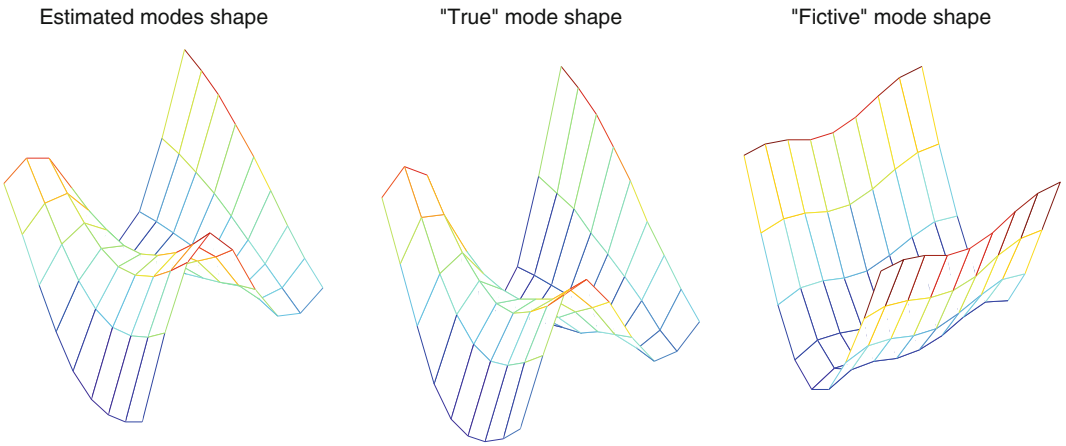

Fig. 26.5 The estimated, "true" and "fictive" mode shape of the fourth mode

Table 26.3 MAC-values and optimal number of FE modes

	MAC-value	Number of FE modes
First mode	0.985	2
Second mode	0.993	3
Third mode	0.982	1 (8)
Fourth mode	0.982	4
Fifth mode	0.987	5

Fig. 26.6 MAC-value as a function of the number of FE modes used in the estimation

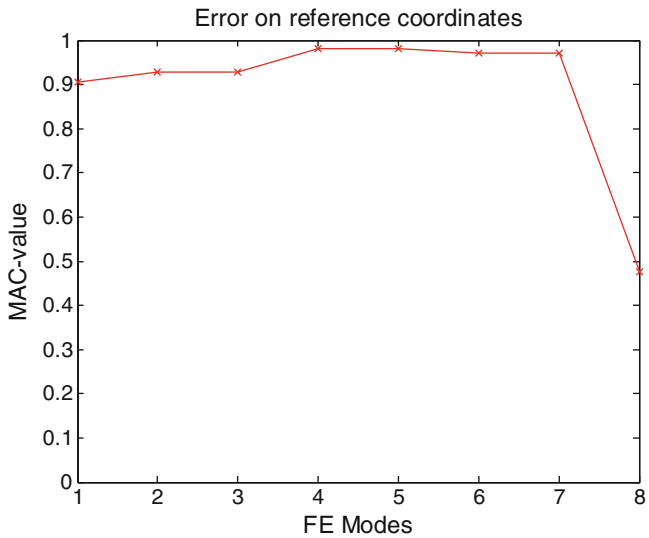

26.3.4 Case with Reduced Stiffness and Added Mass

In this case two parts of the plate has been replaced with a material where the E-modulus is reduced to ¼ of the initial value. Furthermore a point load has been applied in node 16. The estimation is made using the exact same method as the case above (Table 26.3).

The first two modes shows considerably changes in the MAC-value due to a combination of only two and three FE modes. The initially MAC-value of the third mode is so high that any further improvement can't be made. The calculation actually shows that using eight FE modes would give a slight improvement of the MAC-value, but this result is disregarded. The fourth and fifth mode also show improvement of the MAC-value.

In general this case reveals good results with all five estimated modes having a MAC-value above 0.97.

Once again the estimation of the fourth mode is specified (Fig. 26.6).

Figure 26.7 shows a plot of the estimated, *true* and *fictive* version of the fourth mode.

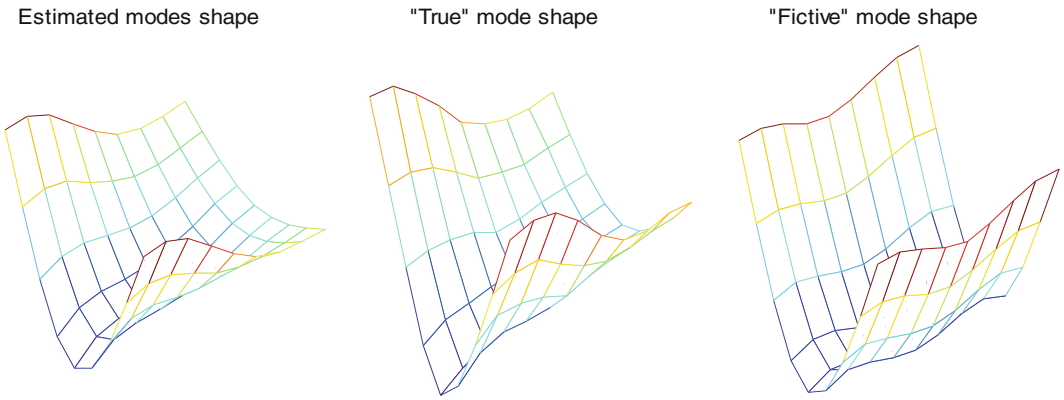

Fig. 26.7 The estimated, "true" and "fictive" mode shape of the fourth mode

26.4 Conclusion

This paper has presented a new method for estimating unmeasured DOF's. The method relies on the Local Correspondence Principle which uses a linear transformation between two sets of mode shapes. The method has been tested on two different cases using a rectangular steel plate as reference. The first case was modified with changes in the mass, whereas the second case was modified with changes in both mass and stiffness. Mode shapes from a perfect version of the plate was used to create a set of estimated mode shapes which covers unknown DOF's. Both cases show that mode shapes in unknown DOF's are estimated with high precision.

References

1. Brincker R (2000) Modal identification from ambient responses using frequency domain decomposition. In: Proceedings of the IMAC XVIII, A conference on structural dynamics, San Antonio
2. Døssing O (1997) Structural stroboscopy – measurements of operational deflection shape. Sound Vib Mag
3. Allemang RJ, Brown D (1982) A correlation coefficient for modal vector analysis. In: Proceedings of the IMAC I, SEM, pp 110–116
4. Brincker R A local correspondence principle for mode shapes in structural dynamics (not yet published)
5. Nelson RB (1976) Simplified calculations of eigenvector derivatives. AIAA J 14(9):1201–1205
6. Heylen W, Lammens S, Sas P (1997) Modal analysis theory and testing, Faculty of Engineering, Department of Mechanical Engineering, Katholieke Universiteit Leuven, Belgium

Chapter 27
Use of FBG Sensors to Detect Damage from Large Amount of Dynamic Measurements

Masoud Malekzadeh, Mustafa Gul, and F. Necati Catbas

Abstract Fiber Optic Sensors (FOS) offer several promising features for long term Structural Health Monitoring such as distributed sensing capability, durability, stability and immunity to electrical noise. There are different FOS technologies with a wide range of performance metrics that define their suitability for different applications. One of the most widely used fiber optic sensing technologies are point sensors (Fiber Bragg Gratings-FBG). If the data collected with the FBG sensors are analyzed and handled effectively, important information about the behaviour of the structure can be obtained. In this study, a recently developed damage detection method based on strain correlation analysis is employed using strain data collected with FBG sensors. In pursuing these objectives, different damage scenarios have been designed and tested on a 4-span bridge model in the laboratory environment. The efficiency of both FBG sensors and correlation analysis method for detection and localizing damage is explored. It is shown that damage can be clearly identified and localized for most of the cases under investigation.

Keywords FBG sensor • Cross correlation analysis • Structural health monitoring • Damage detection

27.1 Introduction

27.1.1 Structural Health Monitoring

Structural Health Monitoring (SHM) offers a proactive approach to continuously monitor the condition of different structures such as bridges, buildings, airplanes [1]. A key inspiration for SHM was the sensing and data processing capabilities of humans. These capabilities basically depend on two individual key components, sensing (including transmission of the signals via neural network) and processing of the data for extracting information. Therefore the most preliminary step towards simulating the human sensing and reacting procedure, in the terms of feeling and processing data, is to develop a well-designed sensing network over the structure. There are various types of sensors available, which can provide different types of data. Comparing several aspects, such as spatial resolution, durability, stability and immunity to electrical noise, Fiber Optic Sensors (FOS) are among the most desirable types of sensors [2]. Subsequently, the next step is to explore and develop powerful algorithms that can process and interpret the data from the sensing network to extract useful information. For SHM, damage detection algorithms are among the most critical processing algorithms. Numerous damage detection methods have been developed and implemented in the context of SHM. In this study, a damage detection algorithm, which can be referred as a strain correlation analysis, developed by the authors recently has been investigated using FOS. In the following sections, first a brief discussion about the basic principles of FOS will be presented. Afterwards, the strain correlation based damage detection technique will be discussed. Finally, experiments conducted on a 4-span bridge structure, where four different damage scenarios were considered, will be presented. The strain correlation analysis based method, for the purpose of investigating the efficiency of the algorithm, will be applied to the data acquired with the FBG sensors installed on the 4-span bridge model.

M. Malekzadeh • F.N. Catbas (✉)
Department of Civil, Environmental and Construction Engineering, University of Central Florida, Orlando, FL 32816, USA
e-mail: m.malekzadeh@knights.ucf.edu; catbas@ucf.edu

M. Gul
Department of Civil and Environmental Engineering, University of Alberta, Edmonton, AB T6G 2W2, Canada
e-mail: mustafa.gul@ualberta.ca

J.M. Caicedo et al. (eds.), *Topics on the Dynamics of Civil Structures, Volume 1*,
Conference Proceedings of the Society for Experimental Mechanics Series 26,
DOI 10.1007/978-1-4614-2413-0_27,

27.2 Fiber Optic Sensors

27.2.1 FOS and Fiber Bragg Grating (FBG) Sensors

There has been a dramatic increase in the FOS implementations in the context of SHM due to aforementioned advantages brought by these types of sensors. FBG sensor, which are point types of sensors, are among the widely used FOS. The basic working principles of FOS and FBG sensors are reflection and filtration of different wavelengths of light [3]. Beside the FBG sensors, Brillouin Optical Time Domain Analysis (BOTDA) and Brillouin Optical Time Domain Reflectometry (BOTDR) two of the widely used distributed types of FOS [4]. For FBG sensors, grating property enables the optical fiber to transmit the entire wavelength except the particular reflected wavelength entitled as grating process. A brief introduction to theory of the optical fiber is presented in the following section.

27.2.2 Theory Behind the FBG Sensors

As it is briefly discussed above, the FBG function is fundamentally based upon reflection and filtration of the wavelength which travels throughout the grated segment. The reflection of pre-defined wavelength occurs, as soon as the launched broadband light reaches the grated segment of fiber optic line. This reflected wavelength is referred as Bragg wavelength and it is expressed by the following equation:

$$\lambda_B = 2n_e\Lambda \tag{27.1}$$

where λ_B represents of the Bragg wavelength, while n_e and Λ are the effective refractive index and the grating period respectively (illustrated in Fig. 27.1). When strain is induced, the Bragg wavelength is expected to have a proportional shift. The strain can be determined by analyzing the change in the wavelength. According to this principle, FBG can sense any possible changes, shift forward or backward, in the period of scattered wavelength and based on that it can measure strain in grating segment. The wavelength shift is proportional to strain, and absolute strain can be measured by using this shift [5].

27.3 Damage Detection Algorithm

27.3.1 Strain Correlation Analysis

One of the main goals pursued through SHM is timely detection and localization of damage so that appropriate decisions can be made in order to mitigate any potential detrimental effect on the structure. Therefore, powerful damage detection algorithms

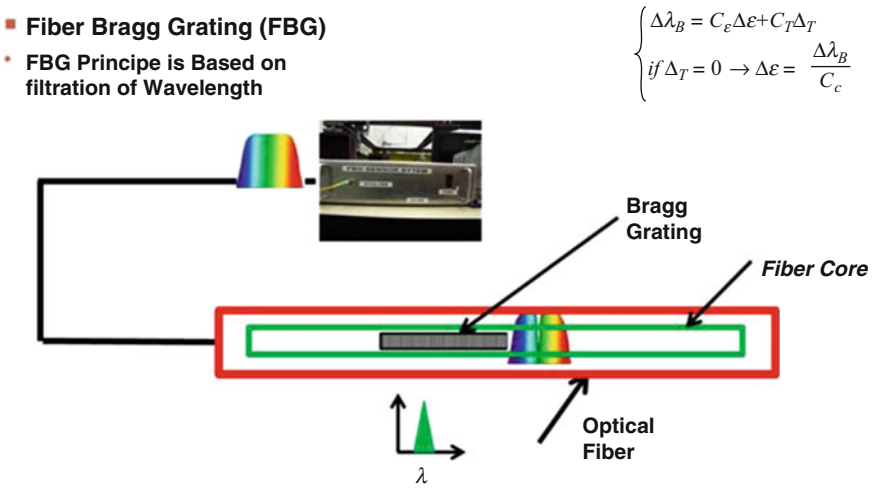

Fig. 27.1 FBG Fundamental Concept of FBG sensors

should be developed and implemented with different sensor networks. Herein, strain correlation analysis based method which was recently developed by the authors is implemented to FBG data for the purpose of verifying the algorithm [6].

Correlation is a measure of the similarity between two data sets; having similar behavior gives higher correlation, whereas having dissimilar behavior gives lower correlation. The methodology is based on comparing the correlation matrices for the baseline and damaged cases. The cross correlation coefficients of the strain data at one location and all other locations are calculated to create the first row of the cross-correlation matrix. Then, the same procedure is repeated for all of the sensors and a full cross-correlation coefficient matrix is created. After obtaining these matrices for baseline and damaged conditions, they are compared to detect and locate the damage. When comparing two signal pairs, the correlation can be obtained using the following formula:

$$\rho_{ij}(t) = \frac{\sum_{k=1}^{n} (S_i(t_k) - \mu_i)(S_j(t_k) - \mu_j)}{\sqrt{\sum_{k=1}^{n} (S_i(t_k) - \mu_i)^2} \sqrt{\sum_{k}^{n} (S_j(t_k) - \mu_j)^2}} \tag{27.2}$$

where ρ_{ij} is the correlation between the sensors i and j, n is the total number of time observations during the monitoring duration, $S_i(t_k)$ and $S_j(t_k)$ are the values of the sensors i and j at time t_k, and, μ_i, μ_j are the mean values of the sensors i and j.

27.3.2 Generating the Cross-Correlation Matrices

Baseline correlation matrices are generated based on the data captured from undamaged structure. For each baseline data set, a baseline correlation matrix, which consists of the correlation of individual pairs of sensors, is generated. Baseline correlation matrix is an $n \times n$ matrix where n refers to number of sensors existing on monitored structure. Each row (or column) in the matrix is presenting the correlation of a sensor with the rest of sensors. Creating the baseline matrix, the state of structure prior to damage occurrence is characterized. The same steps should be taken for data sets measured from damaged (or unknown state) structure to obtain the new matrices. Afterwards, these two sets of matrices are compared in order to obtain damage location matrices. Finally, these damage location matrices are compared to the threshold matrices to identify if there is any significant deviation. The determination of the threshold is explained below.

27.3.3 Setting the Threshold

Setting the threshold, defining a criteria between damage and undamaged condition, is one of the most critical components in damage identification algorithms. Herein, in the purpose of setting the threshold, baseline matrices were divided into three main groups, and then based on comparing the first two groups the value for threshold was defined. Subsequently, the third group was employed to verify the accuracy of threshold the value. Again, the threshold is used to determine if the changes in the damage location matrix is significant to imply a structural change as shown in (27.3). Figure 27.2 illustrates different processes which should be undertaken in order to detect the damage location through strain correlation analysis.

$$Damage\ Location\ Matrix = (Damaged\ Matrix) - (Baseline\ Matrix) - (Threshold) \tag{27.3}$$

27.3.4 Filtering Out the High Frequency Data

Prior to applying strain correlation analysis based algorithm to the raw data captured from FBG sensors, which were distributed over the bridge; a critical issue is pre-processing of the data. The data consists of both low and high frequency strain responses. However high frequency part is not desired in this study since the correlation values are inversely affected by this high frequency data. As a result, high frequency data should be filtered out by using a low pass filter. It is shown in Fig. 27.3 that the first two vibration modes of the bridge are around 5 and 7.5 Hz. The cut-off the frequency of the low pass filter was determined in a way that these modes would be eliminated from the data. After this pre-processing, damage detection algorithm can be applied for evaluation of the structure.

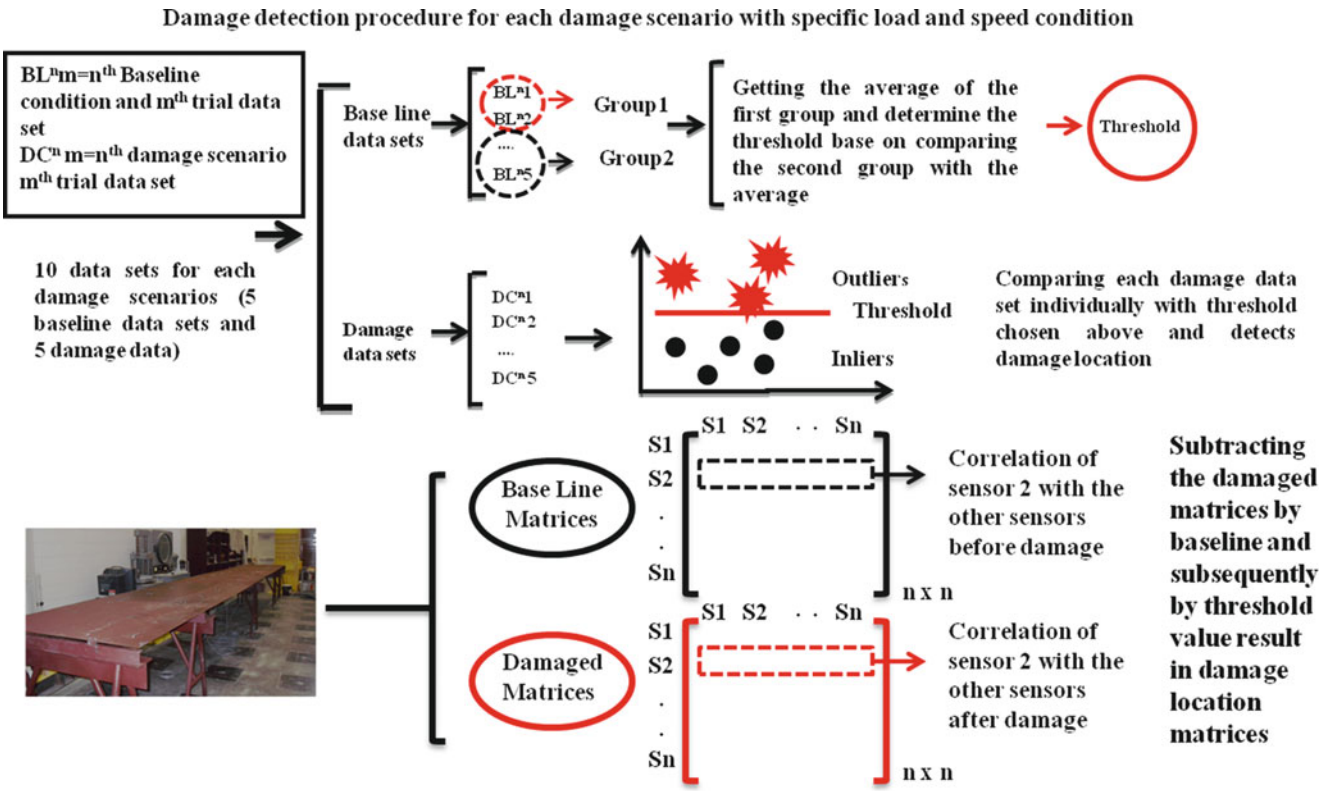

Fig. 27.2 Damage detection procedure for correlation analysis method

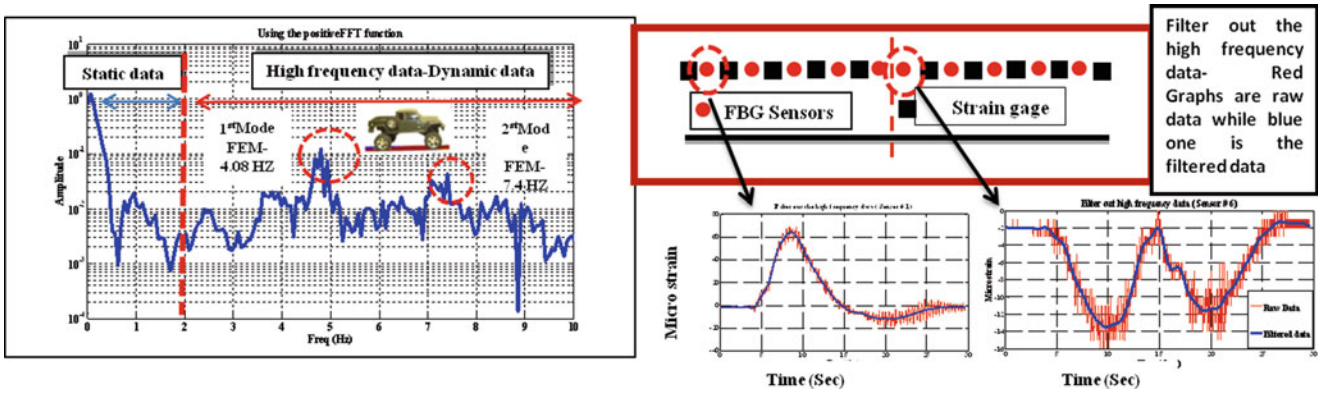

Fig. 27.3 Conversion of responses to frequency domain and filtering out the high frequency response

27.4 Experimental Studies

27.4.1 Structure Description and Instrumentation (UCF 4-Span Bridge)

For the sake of evaluating the strain correlation analysis based algorithm using FBG sensors, several experiments with a laboratory bridge model were designed and conducted taking four common damage scenarios into consideration. The structure consists of two 120 cm approach (end) spans and two 304.8 cm main spans with a 3.18 mm thick, 120 cm wide steel deck supported by two HSS 25×25×3 girders separated 60.96 cm from each other. Using the 4-span bridge model in the UCF structural laboratory (Fig. 27.4), it is feasible to simulate and test a variety of damage scenarios that are commonly observed in bridge type structures [7–9]. It is possible to simulate most of the common boundary conditions, including rollers, pin, and fixed support. In addition to these, the bolts connecting the girders and deck can be loosened or

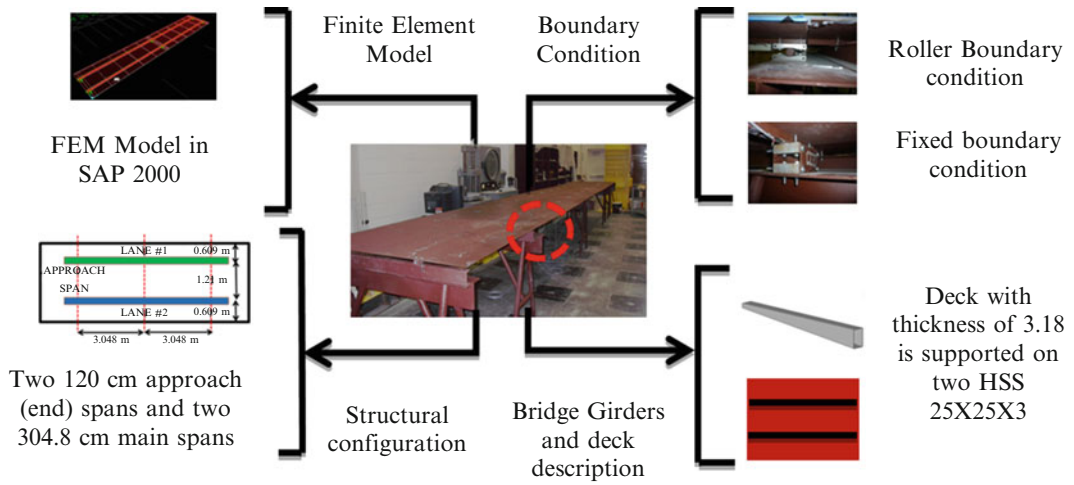

Fig. 27.4 Structure description and instrumentation (UCF 4-span Bridge)

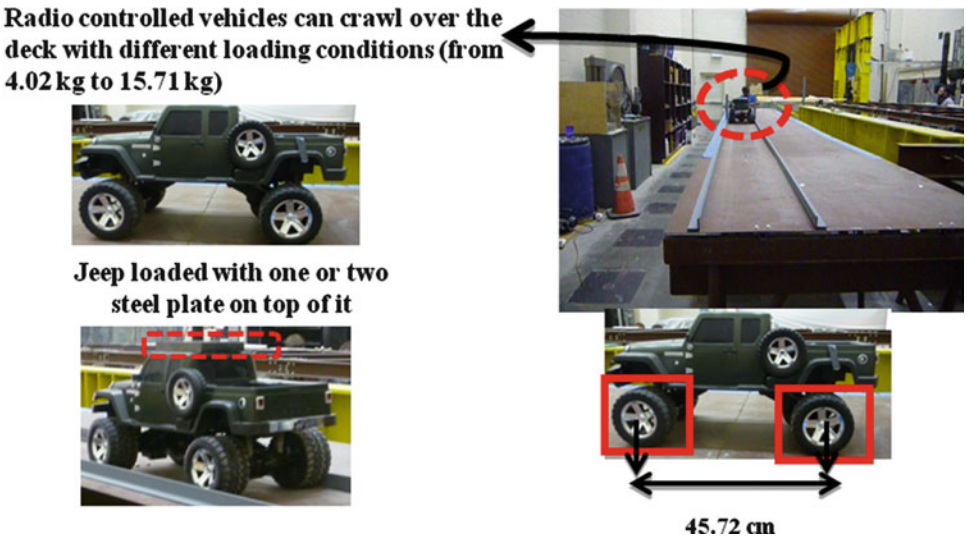

Fig. 27.5 Vehicle (Jeep): Axle dimension, weight and characteristics

removed at different locations to modify the stiffness of the system and to simulate damage. In other words, the first feature provides the opportunity to simulate the global damage scenarios while; the second one is desirable for local damage simulations. It should be pointed out that even though the structure is not a scaled down model of a specific bridge, its responses are representative of typical values for medium-span bridges. Radio controlled vehicles were crawled over the deck with different loadings (from 4.02 to 15.71 kg) and with different speeds to excite the structure (Fig. 27.5).

27.4.2 Damage Scenarios

Inspired by discussions with the Department of Transportation (DOT) engineers, several critical and common damage scenarios were identified and simulated on the 4-span bridge model. A crucial type of damage which was observed in bridges is alterations in boundary conditions. These types of alterations may cause stress redistributions and in most cases it may result in additional load in different elements. Therefore, three cases were devoted to this type of damage using the advantage of the ability to shift from pinned to fix or roller condition or vice versa. Missing bolts and section stiffness reductions are also cases observed in existing bridges. Fourth damage case simulates the loss of connectivity between the girder and the deck generating localized stiffness reduction. The damage scenarios implemented in this study are illustrated in Fig. 27.6.

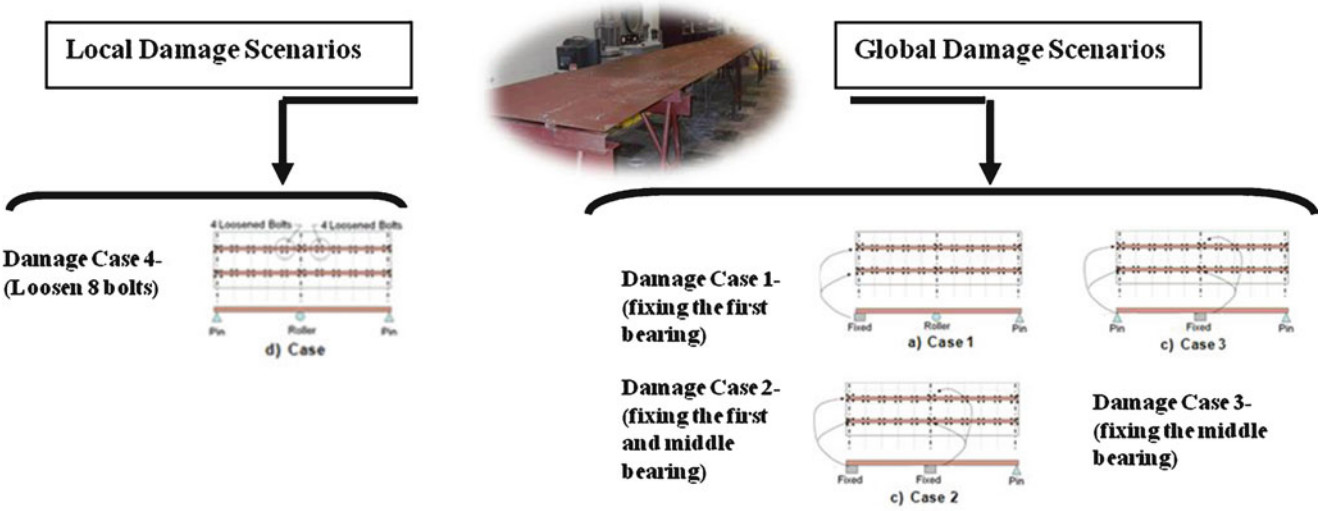

Fig. 27.6 Damage scenarios

27.5 Damage Assessment

27.5.1 Global Damage Scenarios

Damage location matrices, corresponding to individual damage scenarios, are presented in Figs. 27.7, 27.8, 27.9 and 27.10. It is noted from the figures that damage location matrices have values mostly close to zero, shown with dark blue color, except that values for sensors that are close to the damage locations. In other words, all arrays in each individual column of damage location matrix are close to zero except for the columns corresponding to the sensors with abnormal behavior due to damage. As mentioned previously, each individual column in the damage location matrix corresponds to one particular sensor on the structure .Consequently, in pursuance of detecting damage location on the bridge model, each column should be investigated to determine if the sensor shows any abnormal behavior due to damage. It should be also pointed out that the color bar range changes from one figure to another one.

Figure 27.7 shows results corresponding to five different trials captured from damage case 1, which is simulated by fixing the first bearing on both girders. These figures represent the case in which the toy truck was loaded with one plate and pulled along the first girder over 4-span bridge. Based on observations from Fig. 27.7, sensor 1 expresses the most abnormal behavior among all other sensors. In other words, correlation of this sensor, which is located next to damage location, with the other sensors has experienced dramatic change due to the applied damage. Furthermore, sensors 2, 3 and 4, all of which are located on the first span, did not show changes as much as observed by the sensor 1 still expressing alterations to some extent. Sensors 6, 7, 8, 9 and 10 did not show any significant changes due to fixing the first bearing. This implies that fixing the first bearing at the beginning of the first span does not affect the second span significantly. The consistency of the results for different trials should also be noted. Figure 27.8 presents the damage location matrix for the second damage case, which is fixity of the middle support in addition to the end supports that was fixed for damage case 1. The most prominent difference between Figs. 27.7 and 27.8 (first and second damage scenario) is distribution of abnormal behavior over the first span and also sensor 6 which was located on the second span and next to middle bearing. In other words, fixing the middle bearing in addition to the first one caused the damage effect not only on sensors 1 and 2 but also on sensors 3, 4, 5 and 6. Sensors 5 and 6 are next to the middle bearing and it was expected that any change on the middle bearing would have an effect on the behavior of those sensors. One important point to note here is that the fixity of the middle support did not change the correlation values significantly compared to the fixity of the end support. This is due to the fact that the girder is continuous over the roller support and this causes a limited resistance to rotation (like a semi-fixed support) even for the healthy case. Therefore, fixing this support does not affect the behaviour of the structure as much as fixing the end supports, which are allowing rotation freely for the healthy case.

Subsequently, Fig. 27.9 displays the damage case 3, which is fixing only the middle bearing. First thing that should be noted here is that the values of the damage location matrix are significantly smaller than the previous cases due to the reason explained above (semi-fixity of the middle support). In addition, Sensors 5 and 6 experienced maximum changes for this

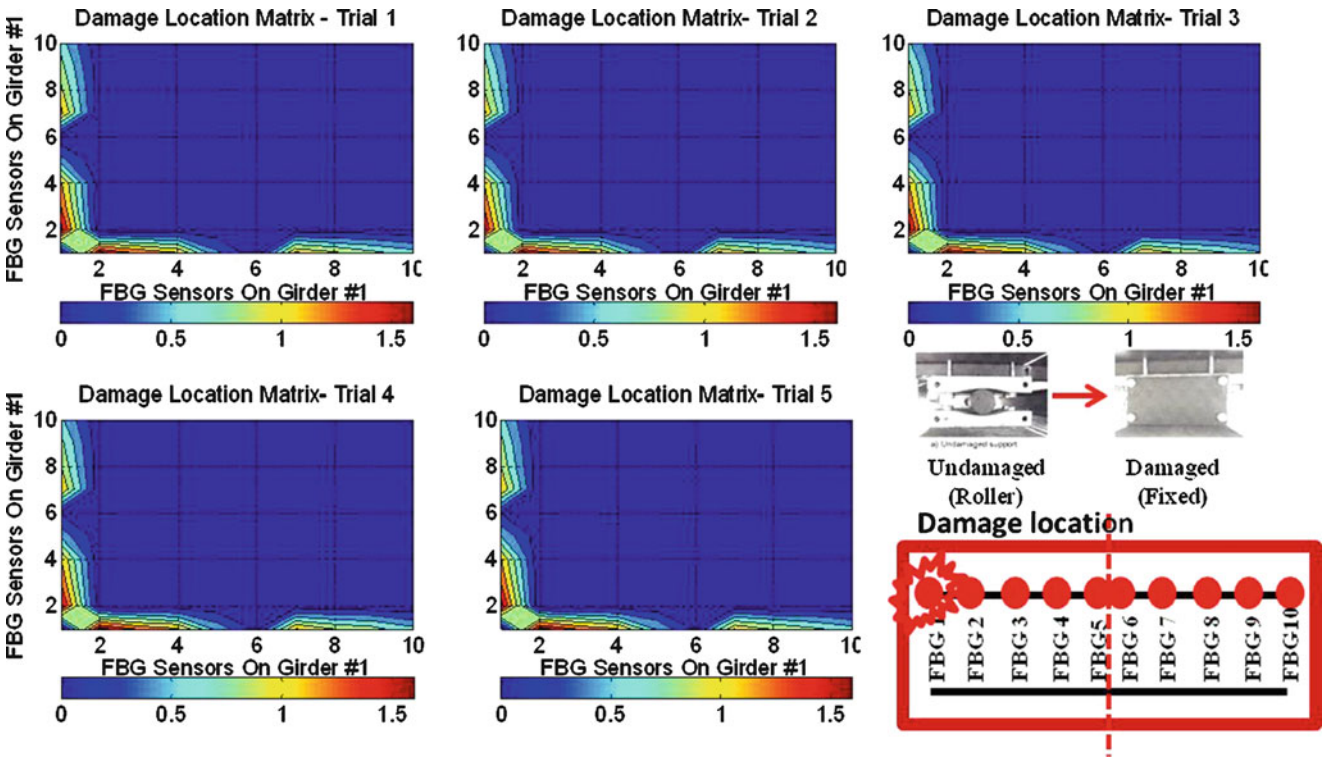

Fig. 27.7 Damage matrices for damage case 1

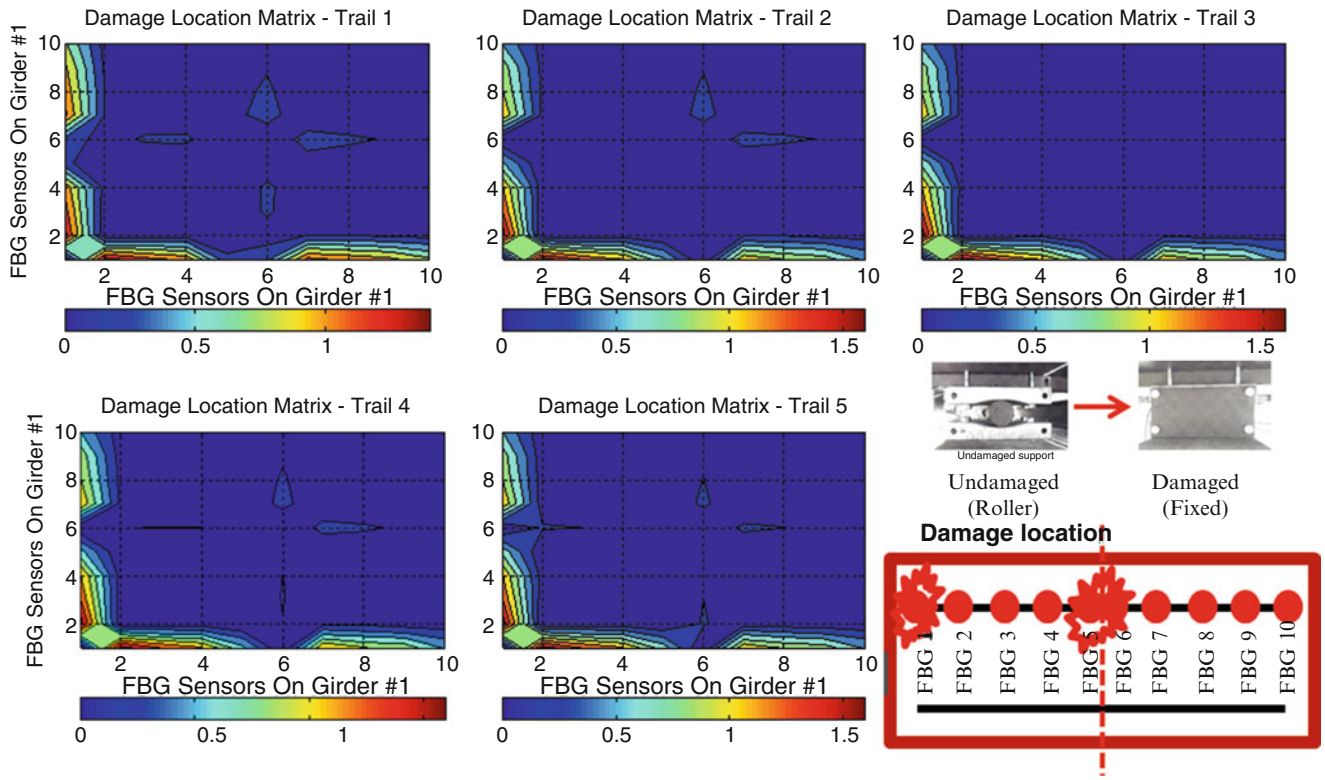

Fig. 27.8 Damage matrices for damage case 2

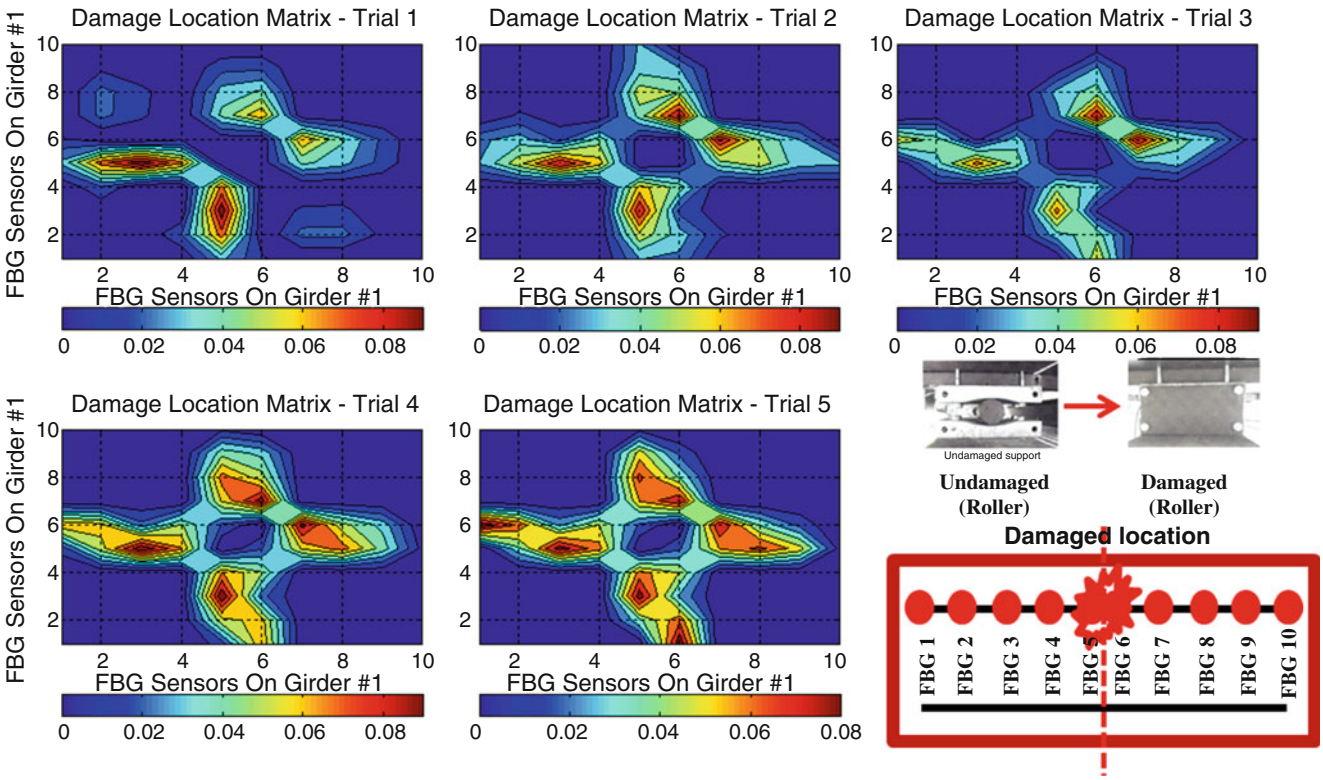

Fig. 27.9 Damage matrices for damage case 3

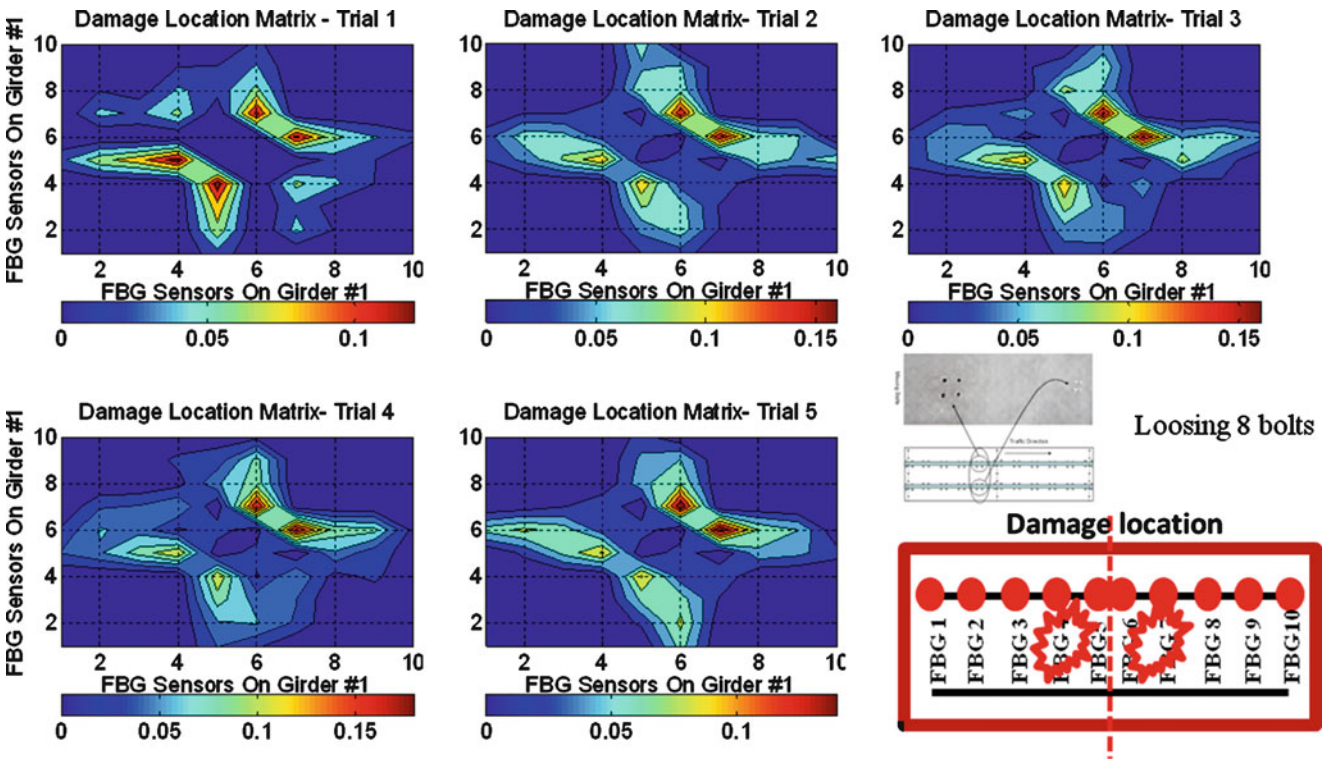

Fig. 27.10 Damage matrices for damage case 4

scenario. As it was noted above, these sensors are located at left and right side of middle bearing. Sensors 1, 9 and 10 which are located far away from damage location, express no significant alteration during the test performed under damage case 3. Sensor 4 and 7 are experienced slight alteration in their behaviour before and after damage occurrence as well. Investigating the first three damage scenarios throws light upon the performance of bridge after applying individual global damage.

The last damage scenario is a local stiffness reduction, which was simulated by removing a total of eight bolts at two locations. In order to simulate this local damage scenario, four bolts on the first span and close to middle bearing and four bolts, symmetrically, from the second span are removed; see Fig. 27.4 for more details. The results are presented in Fig. 27.10 for five individual trials. Comparing the forth damage scenario with the third one, it is observed that unfastening eight bolts next to middle bearing has more detrimental effect on the bridge than fixing the just middle the bearing. The most critical change is observed at sensor 4, 5, 6 and 7 and a small portion from sensor 8 for this case.

27.6 Conclusions

The efficiency of FBG sensors when coupled with a strain correlation based damage detection method is investigated for damage assessment of a 4 span bridge model. The FBG sensors were installed under the bridge girders and simulated damage, four individual damage scenarios including three global and one local damage scenario, were applied to the bridge. Time domain signal correlation analysis method is implemented for detecting the changes in the structure. The results help exploring the effectiveness of both FBG sensors and correlation analysis method in detecting and locating the damage. Based on the findings presented through this paper, the strain correlation analysis can be deemed as a promising method to observe and detect both local and global damage scenarios. Fixing the first and middle bearing caused the most detrimental effect on the bridge from severity point of view while fastening eight bolts from the first and second span, the forth damage scenario, explore the most critical response from distribution point of view. In other words, taking all four damage scenarios into account, the second damage scenario is the most critical scenario since it is the most severe one (highest changes in the damage location matrices). On the other hand, the last damage scenarios is the most detrimental one considering the number of locations affected by this damage although the severity is smaller.

Acknowledgment The authors would like to acknowledge Dr. Il-Bum Kwon from KRISS Korea for his expertise and support for the fiber optic sensing development and work at the University of Central Florida. For this, the authors are grateful to Dr. Kwon for his guidance and know-how. The research project described in this paper is supported by the Federal Highway Administration (FHWA) Cooperative Agreement Award DTFH61-07-H-00040. The authors would like to express their profound gratitude to Dr. Hamid Ghasemi of FHWA for his support of this research. The authors would also like to acknowledge the contributions of their research collaborators and their research team. The opinions, findings, and conclusions expressed in this publication are those of the authors and do not necessarily reflect the views of the sponsoring organization.

References

1. Aktan AE, Catbas FN, Grimmelsman KA, Tsikos CJ (2000) Issues in infrastructure health monitoring for management. J Eng Mech ASCE 126(7):711–724
2. Ferdinand P, Magne S, Marty-Dewynter V, Martinez C, Rougeault S, Bugaud M (1997) Applications of Bragg grating sensors in Europe. In: Proceedings of the 12th international conference on optical fiber sensors, Williamsburg, 28 Oct 1997
3. Hill KO, Fuji Y, Johnson DC, Kawasaki BS (1978) Photosensitivity in optical fiber waveguides: application to reflection fiber fabrication. Appl Phys Lett 3(2):647
4. Kwon IB, Baik SJ, Im K, Yu JW (2002) Development of fiber optic BOTDA sensor for intrusion detection. Sensor Actuator A 101:77–84
5. Majumder M, Gangopadhyay TK, Chakraborty AK, Dasgupta K, Bhattacharya DK (2008) Review: Fibre Bragg gratings in structural health monitoring—Present status and applications. Sensor Actuator A 147:150–164
6. Catbas FN, Gokce HB, Gul M (2011) Non-parametric analysis of structural health monitoring data for identification and localization of changes: concept, lab and real life studies. Struct Health Monit (under review)
7. Gul M, Catbas FN (2008) Ambient vibration data analysis for structural identification and global condition assessment. J Eng Mech ASCE 134(8):650–662
8. Zaurin R, Catbas FN (2011) Structural health monitoring using computer vision and influence lines. Struct Health Monit J 10(3):309–332, SAGE
9. Zaurin R, Catbas FN (2010) Integration of computer imaging and sensor data for structural health monitoring of bridges. J Smart Mater Struct 19(1):015019, 15

Chapter 28
Bayesian FE Model Updating of the Dowling Hall Footbridge

Iman Behmanesh, Babak Moaveni, and Geert Lombaert

Abstract The Dowling Hall Footbridge is located on the Medford campus of Tufts University. The bridge consists of two 22 m spans and it is 3.9 m wide. The footbridge is composed of a steel frame with a reinforced concrete deck. Figure 28.1 shows the south view of the footbridge.

Keywords Bridge monitoring • Finite element • Model updating

A continuous monitoring system was designed and deployed on the Dowling Hall Footbridge in the fall of 2009 and has been providing continuous data since January 2010. The monitoring system consists of eight accelerometers and ten thermocouples, which are connected to a data acquisition device and a communication system that transfers the measured data wirelessly to a host computer in the Department of Civil and Environmental Engineering at Tufts University. A 5-min data sample is recorded once each hour, beginning at the top of the hour or when the 1-s root-mean square (RMS) value of each acceleration channel exceeds 0.03 g (Fig. 28.1).

The data-driven stochastic subspace identification (SSI-Data) method is applied to the cleaned ambient vibration data for modal identification of the footbridge. The first six most excited modes are selected to update the unknown model parameters in this study [1]. In Fig. 28.2, the variation of identified natural frequencies during 17 weeks of collecting data from January 2010 to May 2010 is shown. The identified modal parameters show significant variability during the monitoring period due to changing environmental conditions (mainly temperature) as well as estimation error. The uncertainty in the modal parameters propagates to the finite element (FE) model calibration process resulting in large variability in the obtained calibration parameters. This uncertainty/variability of the identified modal parameters is taken into account via application of a Bayesian FE model updating, and the model calibration parameters are computed in probabilistic terms.

A FE model of the footbridge is created based on the design drawings and visual inspection of the footbridge, using the MATLAB-based structural analysis software FEDEASLab [2]. Five substructures are defined based on the location of accelerometers. The model parameters ($\boldsymbol{\theta}$) are defined as effective elastic modulus of each substructure, and their marginal kernel probability distribution is estimated through Bayesian inference. In Bayesian inference approach, an assumed prior probability density functions (PDFs) of the model parameters are updated based on the identified modal parameters to obtain their posterior PDFs.

Posterior probability of model parameters (θ) that accounts for the experimental data $\mathbf{d}$, is obtained from the prior distribution $\mathrm{p}(\theta)$ by Bayes theorem as follows:

$$\mathrm{p}(\theta|\mathbf{d}) = \frac{\mathrm{p}(\mathbf{d}|\theta)\mathrm{p}(\theta)}{\mathrm{p}(\mathbf{d})} \tag{28.1}$$

I. Behmanesh • B. Moaveni (✉)
Department of Civil and Environmental Engineering, Tufts University, Medford, MA, USA
e-mail: babak.moaveni@tufts.edu

G. Lombaert
Department of Civil Engineering, K.U. Leuven, Leuven, Belgium

J.M. Caicedo et al. (eds.), *Topics on the Dynamics of Civil Structures, Volume 1*,
Conference Proceedings of the Society for Experimental Mechanics Series 26,
DOI 10.1007/978-1-4614-2413-0_28,

Fig. 28.1 South view of Dowling Hall Footbridge

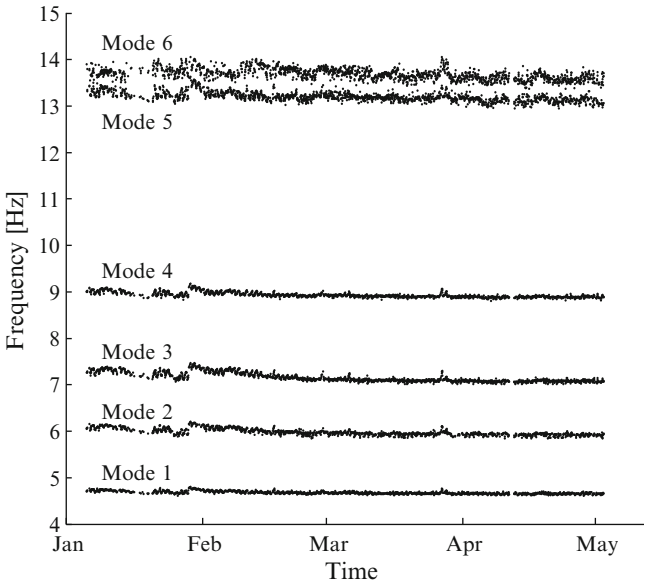

Fig. 28.2 Variation of identified natural frequencies versus time during the 17-week monitoring period

where $p(\mathbf{d}|\theta)$ is the probability of observing measured data, $\mathbf{d}$, given the parameter θ. Once the observations $\mathbf{d}$ are made, the corresponding numerical values $\tilde{\mathbf{d}}$ are inserted in the probability distribution $p(\tilde{\mathbf{d}}|\theta)$, which only depends on θ, and is defined as likelihood function $L(\theta|\tilde{\mathbf{d}})$. The vector $\tilde{\mathbf{d}}$ contains identified circular frequencies $\tilde{\boldsymbol{\omega}}$ and mode shapes $\tilde{\phi}$ of the first six most excited modes of the footbridge. The errors between identified modal parameters and modal parameters of the FE model originate from measurement noise and modeling error. They are defined as the difference between the identified and FE frequencies or mode shapes. Assuming the errors in both natural frequencies and mode shapes have Gaussian distribution, the likelihood function can be written as:

$$L(\theta|\tilde{\mathbf{d}}) \propto \left[\Pi_{i=1}^{N} \sigma_{\omega_i}^{-N_s} \sigma_{\phi_i}^{-N_s N_0} \right] \exp\left[-\frac{1}{2} \sum_{j=1}^{N_s} \left(\sum_{i=1}^{N} \frac{\left(\omega_i(\theta) - \tilde{\omega}_i^j\right)^2}{\sigma_{\omega_i}^2 \left(\tilde{\omega}_i^j\right)^2} + \sum_{i=1}^{N} \frac{\left\| \phi_i(\theta) - \gamma_i \tilde{\phi}_i^j \right\|^2}{\sigma_{\phi_i}^2 \left\| \gamma_i \tilde{\phi}_i^j \right\|^2} \right) \right] \tag{28.2}$$

where γ_i is mode shape scaling factor, N is number of identified modes, N_s is number of identified data set, N_0 is number of mode shape components.σ_{ω_i} and $\sigma_{f\ i}$ are standard deviation of measured natural frequencies and mode shapes of mode i, which are computed from the measured data. The posterior density is calculated as the product of prior distribution $p(\theta)$ and the likelihood function $L(\theta|\mathbf{d})$. A Markov Chain Monte Carlo algorithm is used to sample the posterior density. Based on

these samples, marginal kernel PDFs of the model parameters are estimated. The marginal posterior densities are then used to calculate the Maximum a Posterior Estimate $\hat{\boldsymbol{\theta}}^{\mathrm{MAP}}$ of model parameters [3, 4]. Finally, the marginal PDFs of model parameters are compared with the corresponding histograms computed using a frequentist approach [5].

References

1. Moser P, Moaveni B (2011) Design and deployment of a continuous monitoring system for the Dowling Hall Footbridge. Exp Tech, doi: 10.1111/j.1747-1567.2011.00751.x
2. Filippou FC, Constantinides M (2004) FEDEASLab getting started guide and simulation examples. Technical Report NEESgrid-2004-22. Available from http://fedeaslab.berkeley.edu. Accessed Nov 2004
3. Lombaert G, Conte JP (2009) Uncertainty quantification in model updating based on experimental modal analysis. Report BWM-2008, K.U. Leuven
4. Yuen KV (2010) Bayesian methods for structural dynamics and civil engineering. Wiley, Hoboken
5. Moaveni B, Behmanesh I (2011) Effects of changing environmental temperature on finite element model updating of the Dowling Hall Footbridge. In: Proceedings of EURODYN 2011, Leuven

Chapter 29
Design of Experiments Study to Obtain a Robust 3D Computational Bridge Model

Yahia M. Al-Smadi, Ashish Bhargava, Onur Avci, and Mostafa Elmorsi

Abstract Ambient traffic vibration tests for the three continuous span bridge were conducted to investigate the dynamic response of the bridge in order to identify the natural frequencies and the mode shapes. Understanding the dynamic response of the bridge in its existing, unretrofitted condition is the starting point for developing confidence in the computer model because the same model will evolve from the existing bridge to the retrofitted bridge. A robust 3D computational model is developed using design of experiments (DOE) techniques. Extensive full factorial experiments are carried out to determine simultaneously the individual and interactive effects of many factors such as concrete density, concrete modulus of elasticity and steel modulus of elasticity that could affect the natural frequencies of the bridge. Data is processed to derive natural frequencies and modes shapes, which are remarkably consistent over the range of experiment conditions. ANSYS is used to complete the finite element model and analysis. In the DOE each factor is given two values. The set of allowable model factors which causes the model to match the tested natural frequencies and mode shapes are presented in this paper.

Keywords 3D bridge model • Robust bridge modeling • Design of experiment • Orthogonal arrays • Bridge vibration modeling • Computer aided experimental design • Bridge dynamic analysis

29.1 Problem Description

The bridge structure consists of three levels arranged from bottom to top as follows: vehicular traffic level, pedestrian level, and canopy roof (Fig. 29.1). Each one of these levels contributes to the complexity of the analysis. An in-depth analysis was performed for the existing bridge to study the dynamic behavior using ANSYS software. Understanding the dynamic response of the bridge in its existing, unretrofitted condition is the starting point for developing confidence in computer models.

The goal of the dynamic analysis was to analyze the properties of the bridge in terms of natural frequencies. A field natural frequency test was conducted for the bridge as an initial step to assist in understanding the dynamic behavior and develop confidence in the computer model. Many challenges were exposed in planning for accurate bridge modeling. The complex bridge structure was carefully studied. The depth of the girders plays a very important role in the analysis, instead of using a stick model for deep girders, shell elements were used instead and a proper thickness was assigned for structural members (Fig. 29.2).

Another important factor in this analysis is understanding the composite action between the bridge framing structure and concrete slabs that would change the stiffness and the mass load of the model. Model staging technique would also play an important role in approaching robust, reliable and sound results.

Other factors like in-situ concrete strength properties, actual depth of deck slab, and deck slab to structural steel connection details affect the model and the simulation results. Hence, a direct way to determine cause and effect is to run experiments on the model. An imperative DOE technique considering orthogonal arrays principle will be used. Experiments of all sizes can then be designed easily as long as all factors involved are tested at two levels.

Y.M. Al-Smadi (✉) • A. Bhargava • O. Avci • M. Elmorsi
Special Practices Group, AECOM, 20 Exchange Place, New York, NY 10005, USA
e-mail: yahia.al-smadi@aecom.com

J.M. Caicedo et al. (eds.), *Topics on the Dynamics of Civil Structures, Volume 1*,
Conference Proceedings of the Society for Experimental Mechanics Series 26,
DOI 10.1007/978-1-4614-2413-0_29,

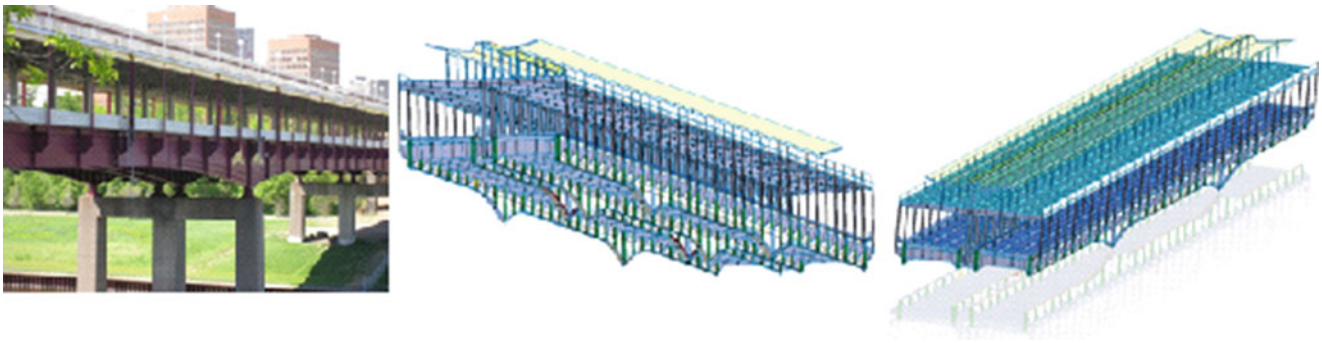

Fig. 29.1 Bridge photo with CAD model views

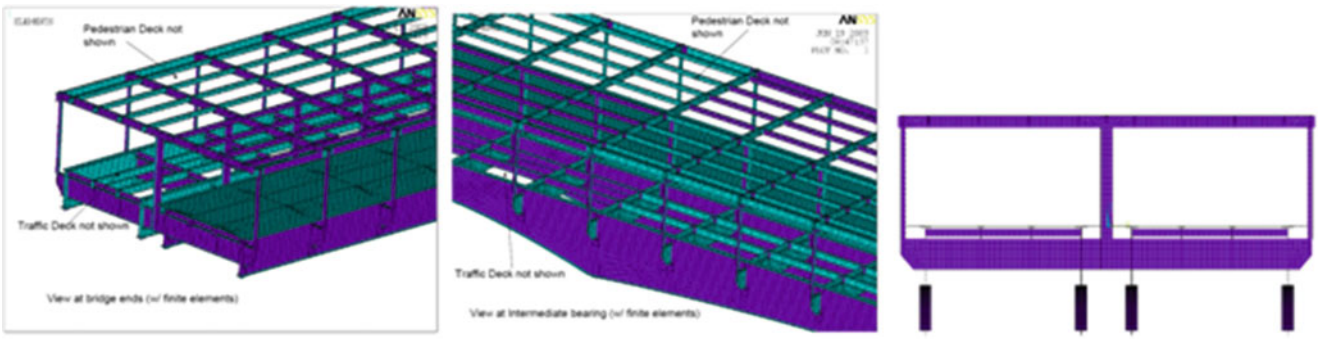

Fig. 29.2 Shell element used in the analysis

29.2 Measured Frequencies and Mode Shapes

Natural frequencies and mode shapes were derived from field measurements as described below. These properties were exposed by dynamic excitation of the bridge generated by the transit of special vehicles and by ordinary diffuse traffic. Table 29.1 summarizes two of the selected measured natural frequencies and suggests a description of the accompanying mode shape. Mode shapes may be visualized in the accompanying computer-generated diagrams (Fig. 29.3); these are obtained by imposing the measured modal displacements on a computational model of the bridge. The pedestrian enclosure is included in the computational model but is omitted from the diagrams for visual clarity. Interpretation of the mode shapes should be guided by the fact that the sensors were placed where peak modal displacements were expected.

29.3 Design of Experiments (DOE)

The DOE is a statistical technique developed by Fisher in the 1920s [1–5] and was used to study the effect of multiple variables simultaneously. Fisher's mathematical modeling was based on a theory given by information matrix as depicted in (29.1). The DOE technique helps studying many factors (variables) that affect or may affect the dynamic simulation simultaneously and most economically. By studying the effects of individual factors on the results, the best factor combination can be determined. When applied to simulation modeling, the technique helps to seek out the best simulation factors (variables) among the many alternatives. The technique can also be used to solve scientific problems whose solution lies in the proper combination of factors rather than innovations or single identifiable causes as discussed in [1–5]

$$M = E_{Y|\theta}\left\{\left(\frac{\partial \log p(Y|\theta)}{\partial \theta}\right)^{T}\left(\frac{\partial \log p(Y|\theta)}{\partial \theta}\right)\right\} \tag{29.1}$$

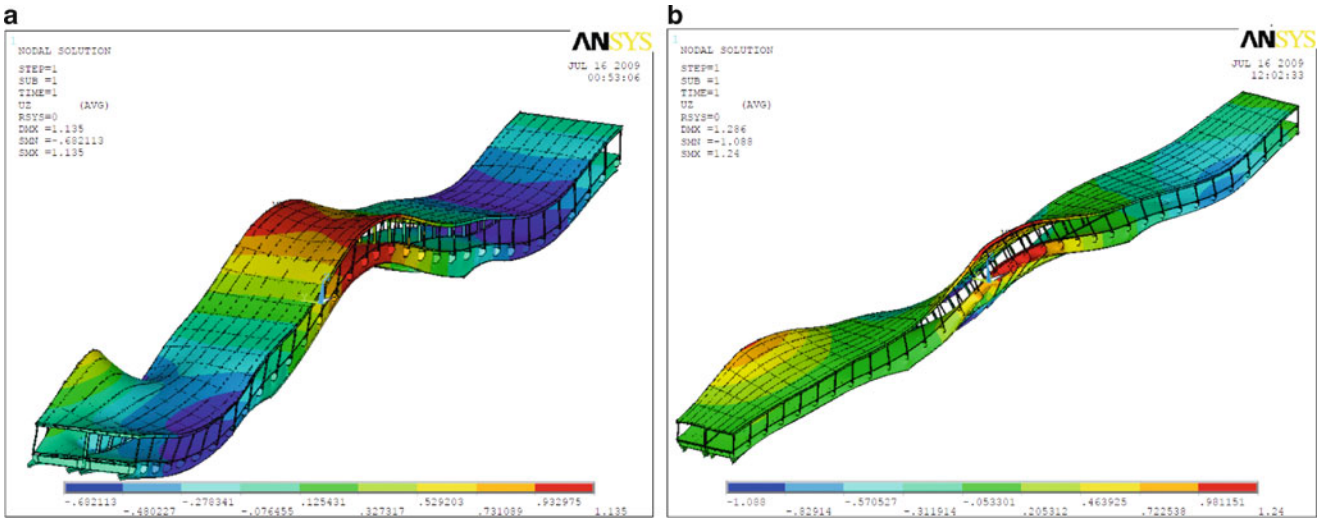

Fig. 29.3 Experimental results. (**a**) Mode 1 0.95 Hz. (**b**) Mode 2 1.40–1.45 Hz

Table 29.1 Measured natural frequencies

No.	Frequency [Hz]	Comments/description
1	0.95	First symmetrical longitudinal flexural mode
2	1.40–1.45	First symmetrical torsional mode

Table 29.2 Factors and their levels

Factor	Level 1	Level 2
γ_{conc} (A)	1,800 kg/m^3 (a_1)	2,400 kg/m^3 (a_2)
E_{conc} (B)	2×10^4 MPa (b_1)	2×10^4 MPa (b_2)
γ_{steel} (C)	7,145 kg/m^3 (c_1)	7,850 kg/m^3 (c_2)

where

$p(Y|\theta)$: Marginal density function
$E_{Y|\theta}$: Expectations for random variable θ

For general reference, a model in its functional state can be viewed as a process. So it is a process whose performance is to be improved. Obviously, questions such as what performance is, what factors are in the process, and what the input and output are, occupy one's thoughts. Measurement of performance depends on the process under consideration.

Three factors were selected, in this paper, to study their impact on the performance of the simulated natural frequencies of the bridge model. The investigated factors are concrete density (γ_{conc}), concrete modulus of elasticity (E_{conc}) and steel density (γ_{steel}), they can all be fine-tuned by appropriately designed experiments. The range of values for these factors can be found in [6]. Two tests for each factor are the minimum number of tests to compare the results and determine the desirable level for the best (optimum) performance. Two levels were assigned for each factor. Therefore, these three factors are called out as two-level factors which are illustrated in Table 29.2.

Here, the factor level selected is changed while all other factors known to affect performance are held fixed. At least two experiments at two different levels of the factor are necessary to draw any conclusions about its influence. Additional experiments with more than two levels of the factor, as well as multiple tests at the same level, produce better information but cost more to conduct.

29.4 Trend Plots of Influencing Factors

DOE uses trend plots (Fig. 29.4a, b) to describe the interaction of each factor on the simulation target. In this paper, liner trend plots (Fig. 29.4a) will be used, the straight line representing the average effect can be sloping up or sloping down, then the data would fall in a normal distribution bell shape. If the line happens to be horizontal (slope = 0), this indicates that the

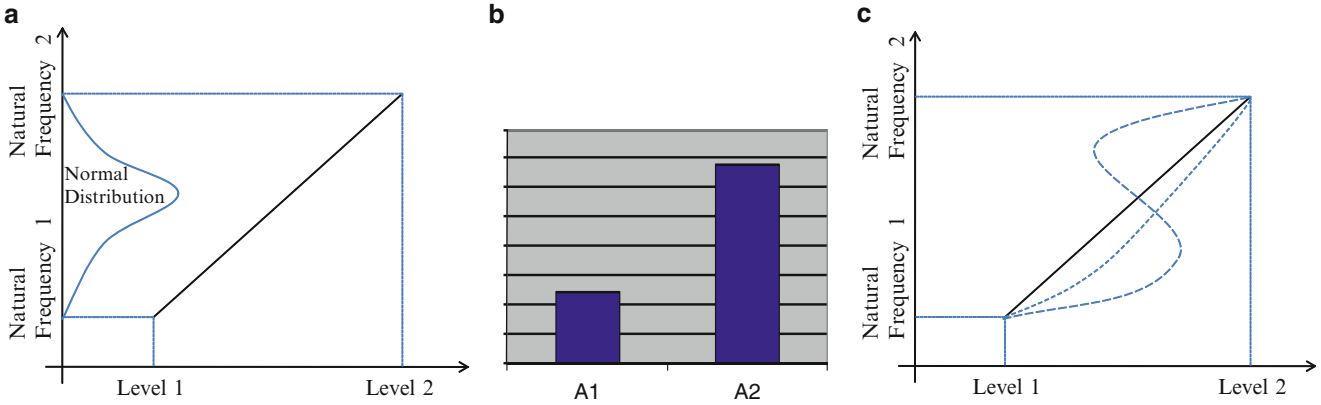

Fig. 29.4 Trends of influencing factor (**a**) linear trend, (**b**) histogram trend (**c**) nonlinear trend

result is unaffected by the change of the factor within the range bounded by the levels. Such a flat response would also indicate that this particular factor is not responsible for any variation of the result, and may be not be the focus of future investigations. Use of the trend of influence lines to predict the results of an arbitrary level by means of extrapolation and interpolation may be possible when the factor is of the continuous type.

Although it is only logical to show the influence between two levels by a straight line joining two points, the actual influence is unlikely to follow straight lines. The behavior of a continuous factor is more likely to be a smooth line (continuous). Thus, an approximation, represented by a curve (quadratic or at least-squares fit), as shown by the dotted lines in Fig. 29.4c, is more likely. The exact shape of the influence is known only by conducting a large number of tests on many levels of the factor. If the actual behavior of the factor influence is sinusoidal (highly nonlinear; Fig. 29.4c), four levels of the factor will have a better chance of identifying the trend of influence.

29.5 Investigating Several Factors One at a Time

The goal is to examine for each factor the desirable level and its trend of influence. Under certain conditions it is possible to study N factors by doing $N + 1$ experiments instead of $2 \times N$ experiments. Using the notations for factors and their levels as shown in Table 29.2, This kind of notation makes description of larger experiments easier, the four experiments layout for three factors (A, B and C) should be described and carried out as shown in Table 29.3.

Observe that in the description of experiment 1, where all factors are held at level 1 (a_1, b_1, c_1), may be considered as a reference level (say, current condition). In the second experiment, only the level of factor A is changed; all other factors are held at level 1. In the next experiment, factor A is brought back to level 1 and factor B is changed to level 2. This process is repeated for all other factors. Note that the results (R_1, R_2, etc.) shown for each experiment are performance evaluations.

The experiments are described as follows:

$$\text{Experiment 1} : \gamma_{\text{conc}} = 1800\,\text{kg/m}^3,\ \text{E}_{\text{conc}} = 2 \times 10^4\,\text{MPa},\ \gamma_{\text{steel}} = 7145\,\text{kg/m}^3$$

$$\text{Experiment 2} : \gamma_{\text{conc}} = 2400\,\text{kg/m}^3,\ \text{E}_{\text{conc}} = 2.4 \times 10^4\,\text{MPa},\ \gamma_{\text{steel}} = 7850\,\text{kg/m}^3$$

and so on.

The effect of individual factors can be extracted by comparing the four test results shown in Table 29.3. Comparison of experiments 1 ($a_1\ b_1\ c_1$) and 2 ($a_2\ b_1\ c_1$) shows the effects of factor A, while others are kept the same. The effects of factors B and C are obtained similarly, by comparing experiment 3 with experiment 1 and experiment 4 with experiment 1, respectively.

Notice that even though all factors are studied together here as part of the research, it is still looked at one factor at a time since only one factor is changed between the comparing experiments. Figures 29.5 and 29.6 shows the trend of factor influence. The trend is a straight line, as there are only two points (at levels 1 and 2 for each factor).

One cannot be sure that the factor influence is truly linear unless additional tests are run. Prediction about an unexpected result at any other level of the factor can only be done based on the linear behavior.

Table 29.3 Experimental description

	Factor			Result	
Experiment	A	B	C	First natural bending frequency (Hz)	First natural torsional frequency(Hz)
1	a_1	b_1	c_1	0.888 (R_1)	1.205 (R_5)
2	a_2	b_1	c_1	0.795 (R_2)	1.059 (R_6)
3	a_1	b_2	c_1	0.949 (R_3)	1.415 (R_7)
4	a_1	b_1	c_2	0.879 (R_4)	1.198 (R_8)

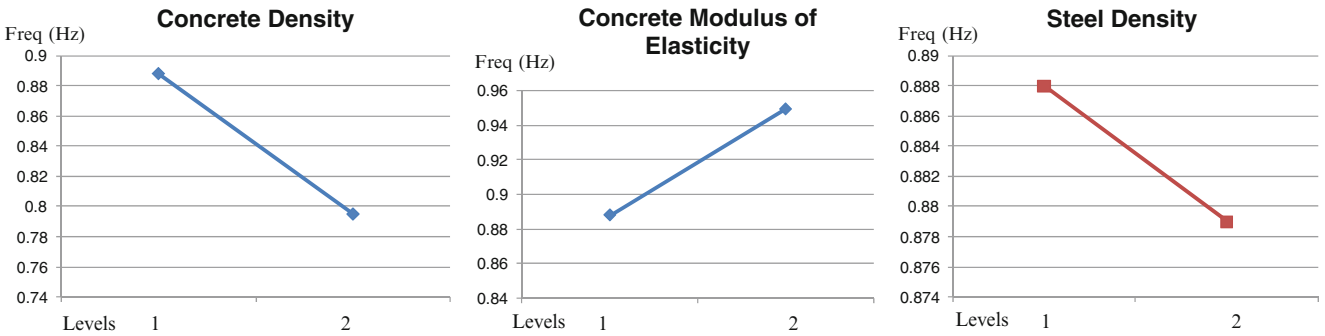

Fig. 29.5 Natural frequency (Hz) – first bending mode shape; trend plots of 3 two-level influencing factors

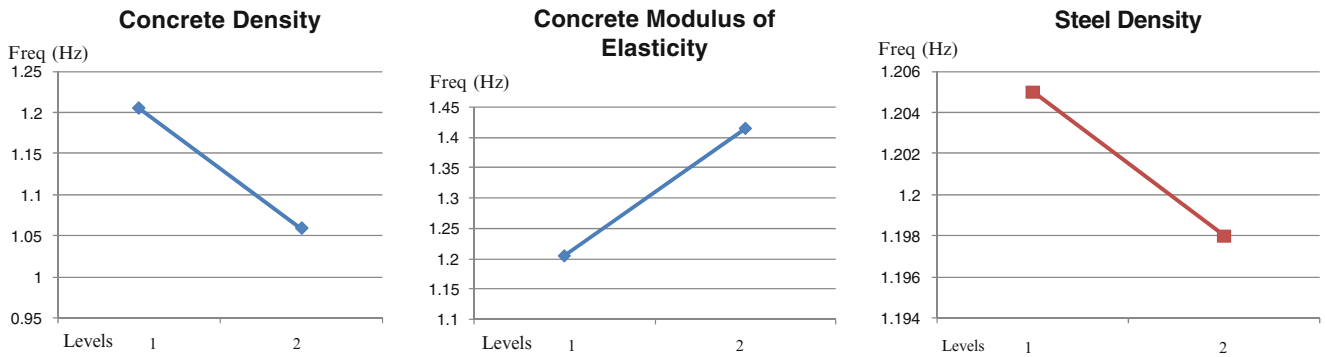

Fig. 29.6 Natural frequency (Hz) – first torsional mode shape; trend plots of 3 two-level influencing factors

The influence of factor *A* was determined by comparing the effect of the factor at level 2 with that at level 1. In both experiments 1 and 2, the levels of factors *B* and *C* were held at level 1. But there is no assurance that factors *B* and *C* would always be at level 1, nor how different factor *A* behaves when one or both factors *B* and *C* are held at their second levels. Interaction among factors occurs and cannot be disregarded. Otherwise, results will be totally unreliable. Multiple experiments were conducted either to verify the performance of finalized natural frequency compared to the field tested natural frequency or to ascertain the variability present in the performance of the results.

29.6 Experimental Design Using Orthogonal Arrays

In the language of DOE, the possible combinations of factor levels are called *full factorial* combinations [7]. If all such possible combinations were to carry out, a full factorial experiment would be performed, as a result determined behavior would be more reliable. But conducting full factorial experiments is often costly and prohibitive. Given a number of factors and their levels, the total number of possible combinations is easily determined by using the combination formula:

$$\text{Total number of combinations} = (\text{number of levels})^{\text{number of factors}} \tag{29.2}$$

Table 29.4 Experiment description using level notations

	Factor			Result	
Experiment	A	B	C	First natural bending frequency (Hz)	First natural torsional frequency (Hz)
1	1	1	1	0.888 (R_1)	1.205 (R_9)
2	1	1	2	0.879 (R_2)	1.198 (R_{10})
3	1	2	1	0.949 (R_3)	1.415 (R_{11})
4	1	2	2	0.938 (R_4)	1.398 (R_{12})
5	2	1	1	0.795 (R_5)	1.059 (R_{13})
6	2	1	2	0.788 (R_6)	1.055 (R_{14})
7	2	2	1	0.848 (R_7)	1.259 (R_{15})
8	2	2	2	0.859 (R_8)	1.305 (R_{16})

$$2^2 = 4 \qquad \text{for 2 two} - \text{level factors}$$

$$2^3 = 8 \qquad \text{for 3 two level factors}$$

and so on.

The interaction between 3 two-level factors A (levels a_1 and a_2), B (levels b_1 and b_2) and C (levels c_1 and c_2) can be studied. Eight experiments would occur which are obtained by combining the two factor levels.

$$\text{Factors} : A(a_1, a_2), B(b_1, b_2) \text{and } C(c_1, c_2)$$

$$\text{Experiments} : a_1b_1c_1 \quad a_1b_1c_2 \quad a_1b_2c_1 \quad a_1b_2c_2$$
$$a_2b_1c_1 \quad a_2b_1c_2 \quad a_2b_2c_1 \quad a_2b_2c_2$$

Three factors at two levels each can also be written using notation 1 for level 1 and 2 for level 2 of the factor assigned to the column, as shown in Table 29.4. Reading a row at a time, the eight experiments are described as follows:

$$\textit{Experiment } 1 : 1 \quad 1 \quad 1 \quad \text{as} \quad a_1b_1c_1$$

$$\textit{Experiment } 2 : 1 \quad 1 \quad 2 \quad \text{as} \quad a_1b_1c_2$$

and so on.

The mode shapes obtained for these eight experiments are shown in Appendix Figs. A.1, A.2, A.3, A.4, A.5, A.6, A.7 and A.8.

29.7 Analyzing the Results

The purpose is to determine the best model simulation condition and influence of factors as described comprehensively in [1–5]. The results collected from experiments contain information that delineates the primary reason of the experiment and can be analyzed to develop key information using statistical techniques.

Method of calculating average effects of factor levels [7] will be considered. In other words, the average of all results of factor A at level 1 is called the average effect. Calculations of the average effects of the first bending natural frequency of all three factors follow (29.3a).

$$\begin{aligned}
\overline{A_1} &= \frac{R_1 + R_2 + R_3 + R_4}{4} = \frac{0.888 + 0.879 + 0.949 + 0.938}{4} = 0.914 \\
\overline{A_2} &= \frac{R_5 + R_6 + R_7 + R_8}{4} = \frac{0.795 + 0.788 + 0.848 + 0.859}{4} = 0.823 \\
\overline{B_1} &= \frac{R_1 + R_2 + R_5 + R_6}{4} = \frac{0.888 + 0.879 + 0.795 + 0.788}{4} = 0.838 \\
\overline{B_2} &= \frac{R_3 + R_4 + R_7 + R_8}{4} = \frac{0.949 + 0.938 + 0.848 + 0.859}{4} = 0.899 \\
\overline{C_1} &= \frac{R_1 + R_3 + R_5 + R_7}{4} = \frac{0.888 + 0.949 + 0.795 + 0.848}{4} = 0.870 \\
\overline{C_2} &= \frac{R_2 + R_4 + R_6 + R_8}{4} = \frac{0.879 + 0.938 + 0.788 + 0.859}{4} = 0.866
\end{aligned} \tag{29.3a}$$

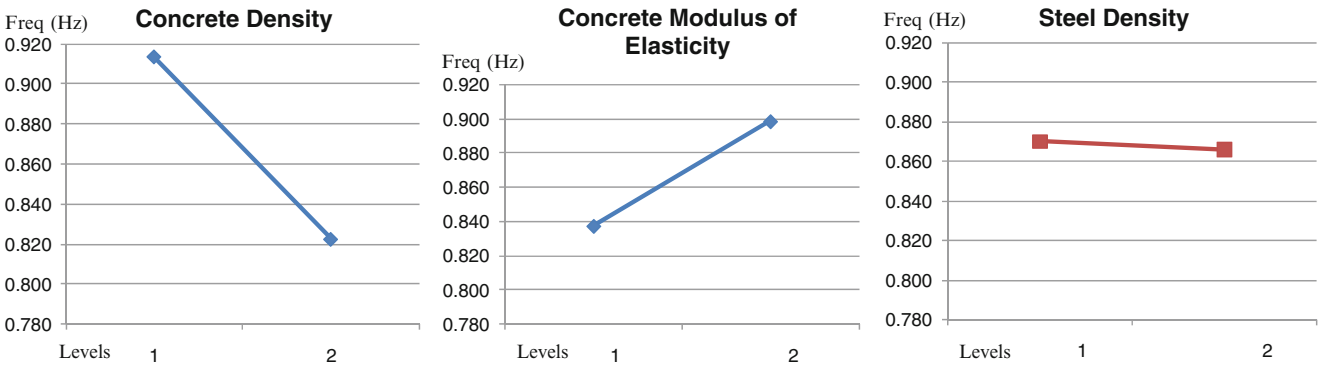

Fig. 29.7 Natural frequency – first bending mode shape; plots of average effects of three factors

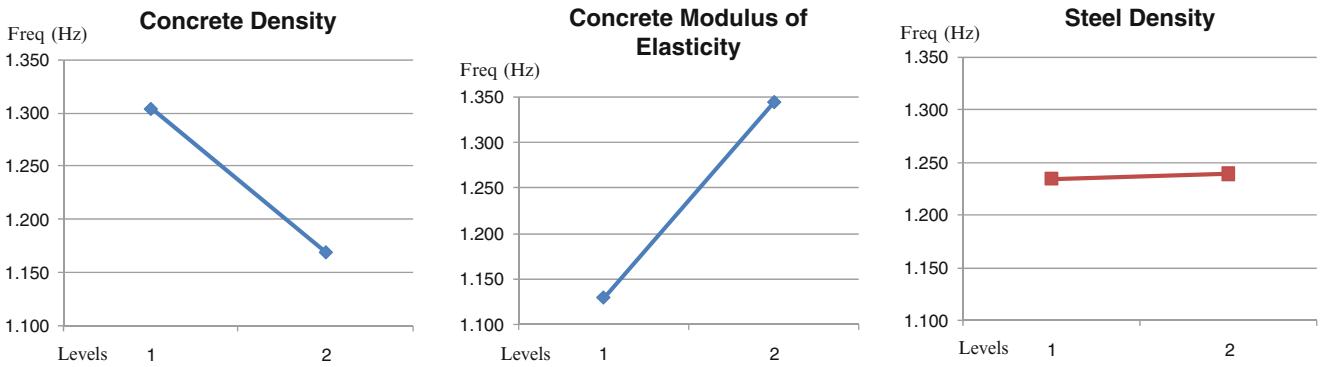

Fig. 29.8 Natural frequency – first torsional mode shape; plots of average effects of three factors

Calculations of the average effects of the first Torsional natural frequency of all three factors follow (29.3b).

$$
\begin{aligned}
\overline{A_1} &= \frac{R_9 + R_{10} + R_{11} + R_{12}}{4} = \frac{1.205 + 1.198 + 1.415 + 1.398}{4} = 1.304 \\
\overline{A_2} &= \frac{R_{13} + R_{14} + R_{15} + R_{16}}{4} = \frac{1.059 + 1.055 + 1.259 + 1.305}{4} = 1.170 \\
\overline{B_1} &= \frac{R_9 + R_{10} + R_{13} + R_{14}}{4} = \frac{1.205 + 1.198 + 1.059 + 1.055}{4} = 1.129 \\
\overline{B_2} &= \frac{R_{11} + R_{12} + R_{15} + R_{16}}{4} = \frac{1.415 + 1.398 + 1.259 + 1.305}{4} = 1.344 \\
\overline{C_1} &= \frac{R_9 + R_{11} + R_{13} + R_{15}}{4} = \frac{1.205 + 1.415 + 1.059 + 1.259}{4} = 1.235 \\
\overline{C_2} &= \frac{R_{10} + R_{12} + R_{14} + R_{16}}{4} = \frac{1.198 + 1.398 + 1.055 + 1.305}{4} = 1.240
\end{aligned}
\tag{29.3b}
$$

where $\bar{A}_1$is the average effect of factor A at level 1(i.e. average effect of $\gamma_{conc} = 1{,}800$ kg/m^3) and R_1 is the result of experiment 1. Plots of average effects are obtained by plotting the average factor-level effect against the corresponding factor level. They are shown in Figs. 29.7 and 29.8.

Plots of average effects are used primarily for the selection of a level of best performance. They show the nature of the trend of influence of the factor to the result as it changes from level 1 to level 2, and indicates the sensitivity of the factor's performance (results). By inspecting the slope alone, it is evident that the concrete density, which has the steeper slope, is the most influential factor for the first bending shape. And concrete modulus is the most influential factor for the first torsional shape. Steel density has an almost flat slope, therefore it has no influence on the natural frequency mode shapes.

Performance expected at optimum condition (R_{opt}) is calculated by (29.4),

$$R_{out} = \overline{T} + (\overline{A_1} - \overline{T}) + (\overline{B_2} - \overline{T}) + (\overline{C_1} - \overline{T}) \tag{29.4}$$

where $\overline{T}$ is the grand average performance of all trial results. $\overline{T}$= 0.860 Hz, adding all contributions from all factors to the grand average of performance.

$$R_{out} = 0.860 + (0.914 - 0.860) + (0.899 - 0.860) + (0.899 - 0.860) = 0.990 \text{ Hz}$$

The result calculated R_{out} can only be expected to be close to the actual natural frequency of the first bending mode shape. Same analysis can be done for natural frequency of the first torsional mode shape which has R_{out} = 1.401 Hz.

29.8 Conclusion

Design of Experiments (DOE) techniques are widely used in industry to help designers produce robust and higher yield designs prior to going into production. DOE is used in computer aided experimental design (CAED) to determine simultaneously the dynamic behavior of the bridge through individual and interactive effects of many factors. Due to lack of drawing details, DOE was used to provide a full insight of interaction between many factors. Three two-level factors were investigated specifically for their influence on the dynamic simulation results. Interpolation for a level within the range of levels tested is quite often done satisfactorily. The work shown in this paper is just an introduction of how DOE can be used in the structural analysis field and helps to pin point the sensitive parts and sensitive areas in the model in order to fix them before a retrofitted bridge model is actually built. The CAED model using ANSYS proved to be reliable and robust for expecting dynamic results as close as the field results. Future work will include more factors with more levels such as sensitivity of mesh size, slab thickness, staging technique, support conditions, and connection conditions between structural members.

Acknowledgement The authors wish to thank all colleagues at AECOM including Mr. Dennis Miller and Dr. Jeremy Isenberg for their valuable comments on the paper and Mr. Bernie Hertlien and Mr. Dominik Duschlbauer whose expertise in data acquisition and processing was essential to the project.

Appendix

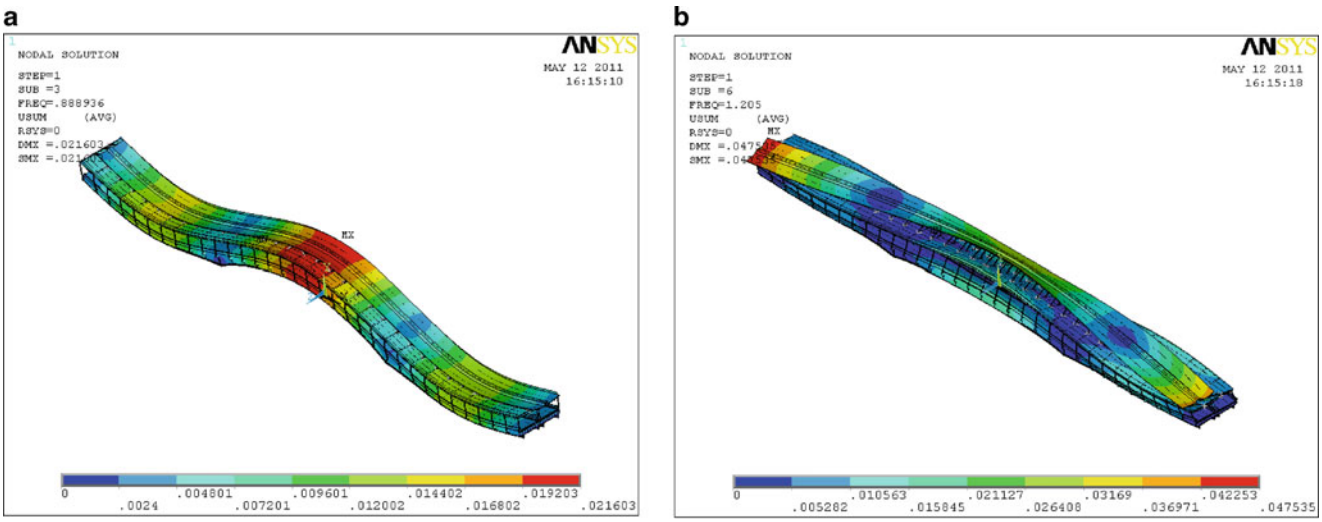

Fig. A.1 Experiment 1 results. (**a**) First bending mode. (**b**) First torsional mode

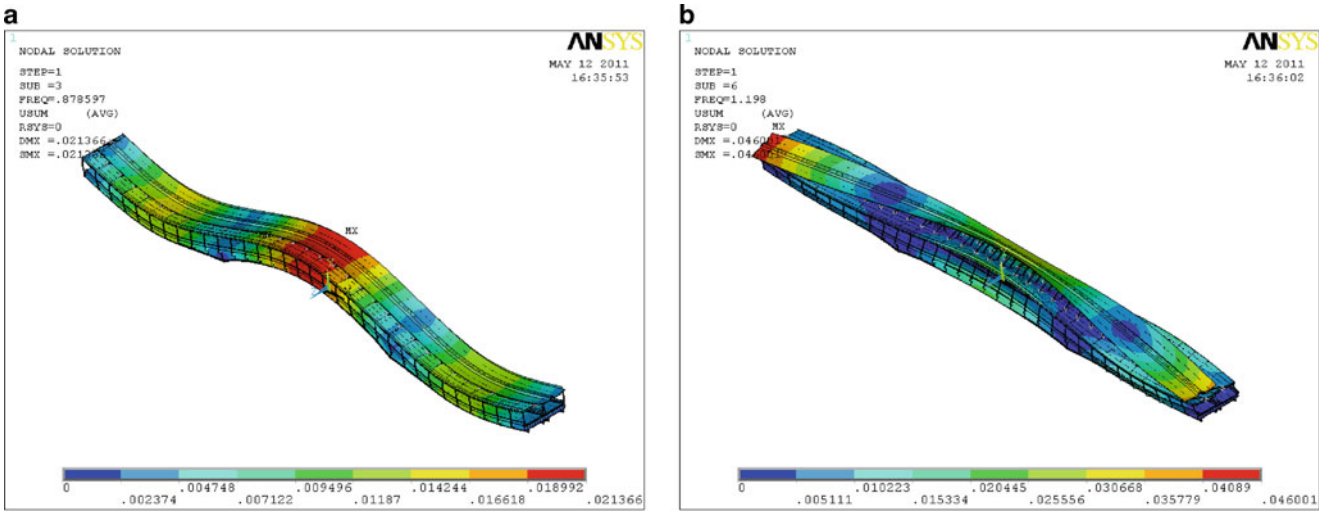

Fig. A.2 Experiment 2 results. (**a**) First bending mode. (**b**) First torsional mode

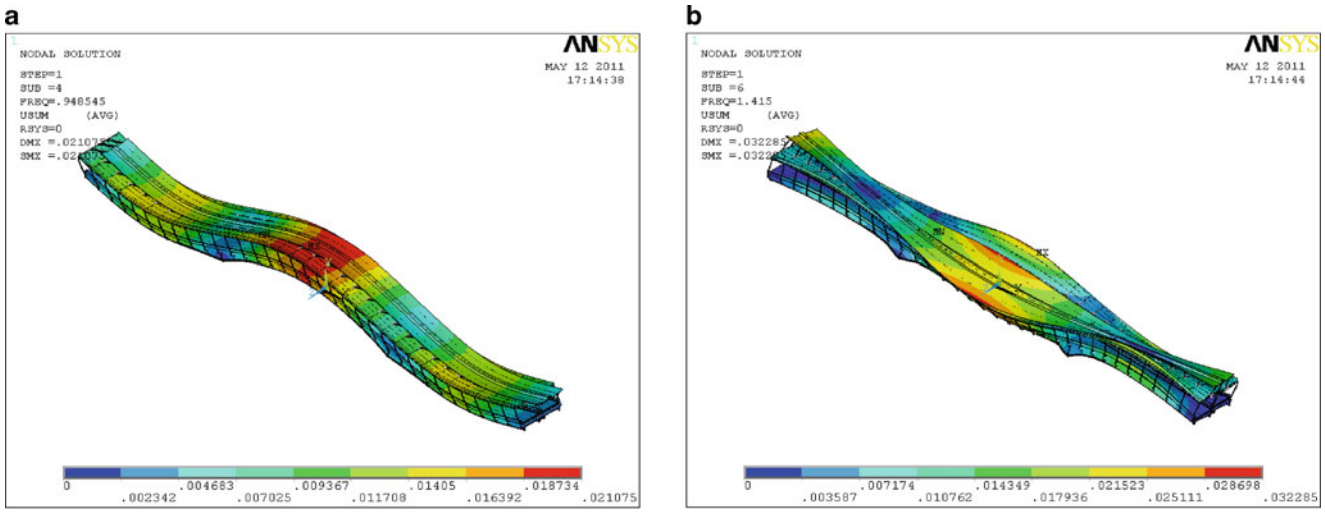

Fig. A.3 Experiment 3 results. (**a**) First bending mode. (**b**) First torsional mode

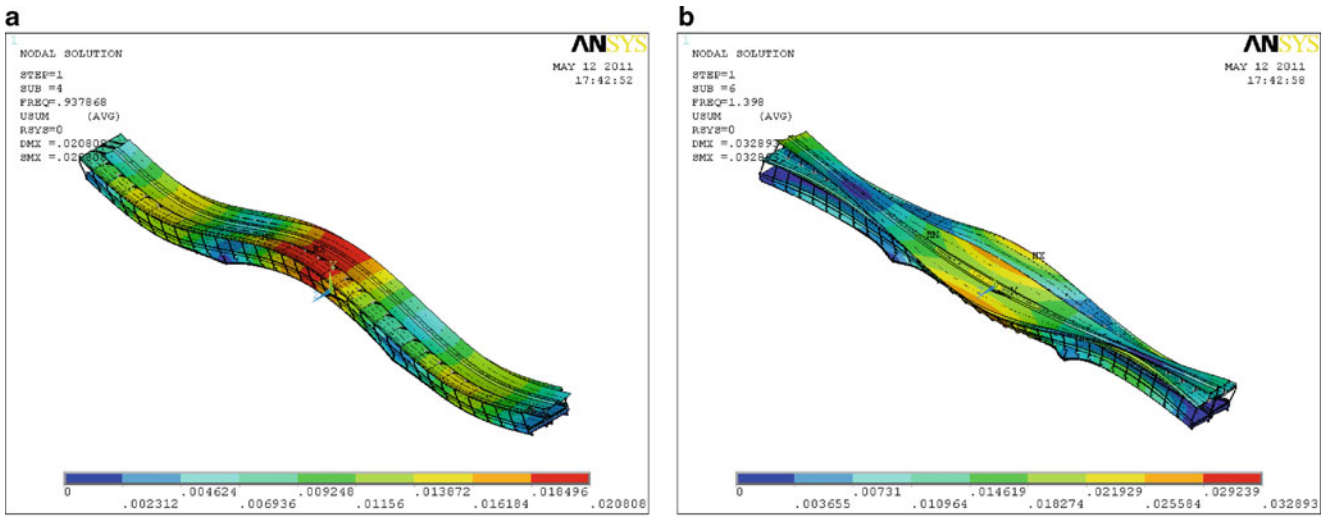

Fig. A.4 Experiment 4 results. (**a**) First bending mode. (**b**) First torsional mode

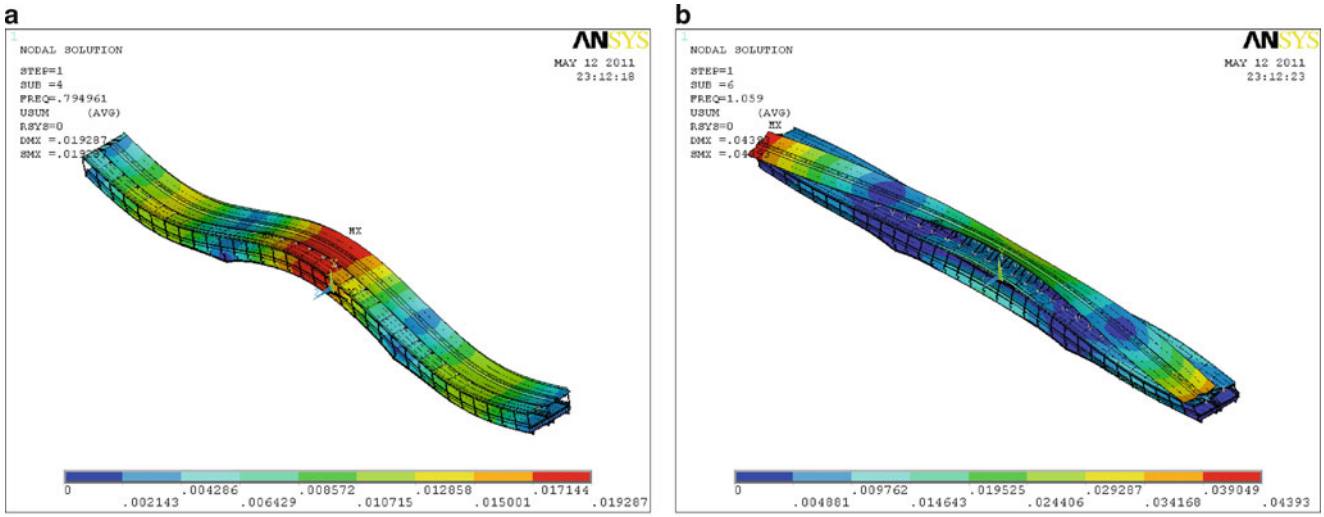

Fig. A.5 Experiment 5 results. (**a**) First bending mode. (**b**) First torsional mode

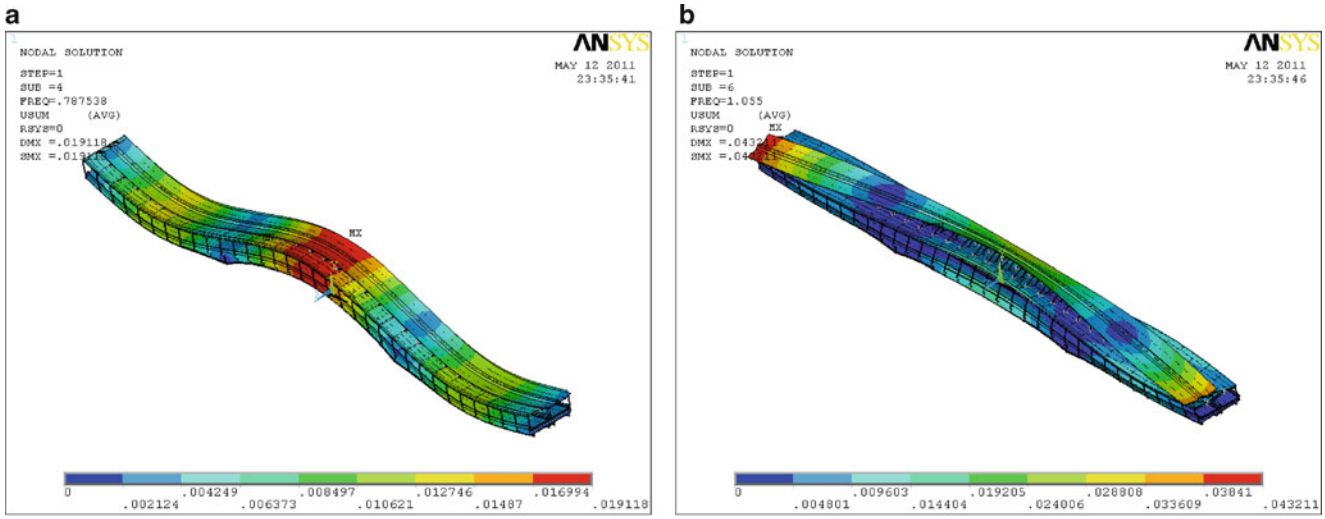

Fig. A.6 Experiment 6 results. (**a**) First bending mode. (b) First torsional mode

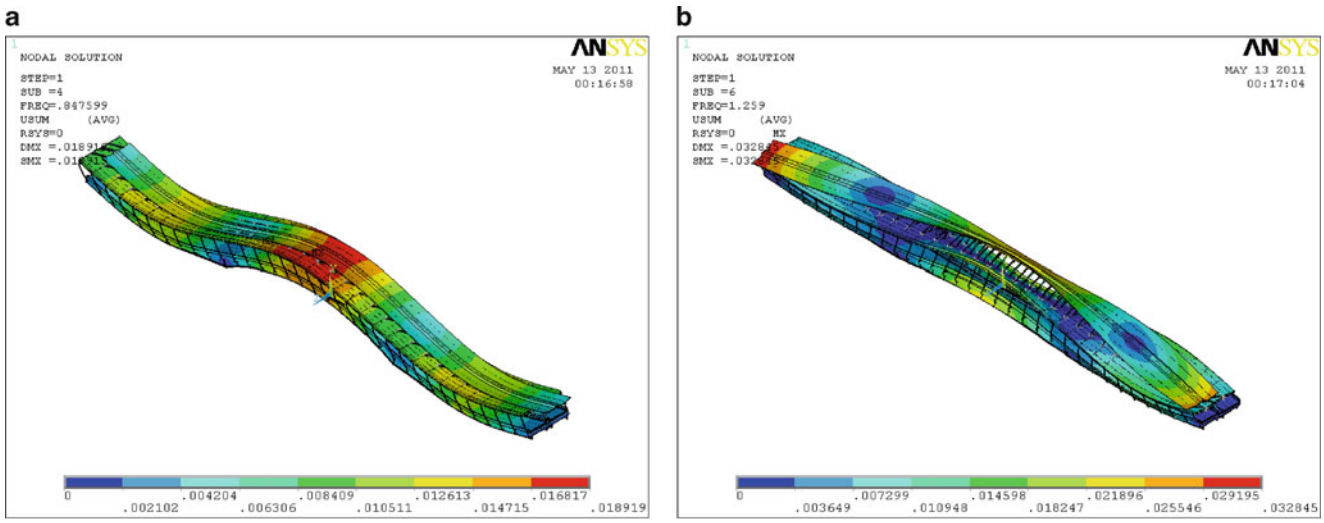

Fig. A.7 Experiment 7 results. (**a**) First bending mode. (**b**) First torsional mode

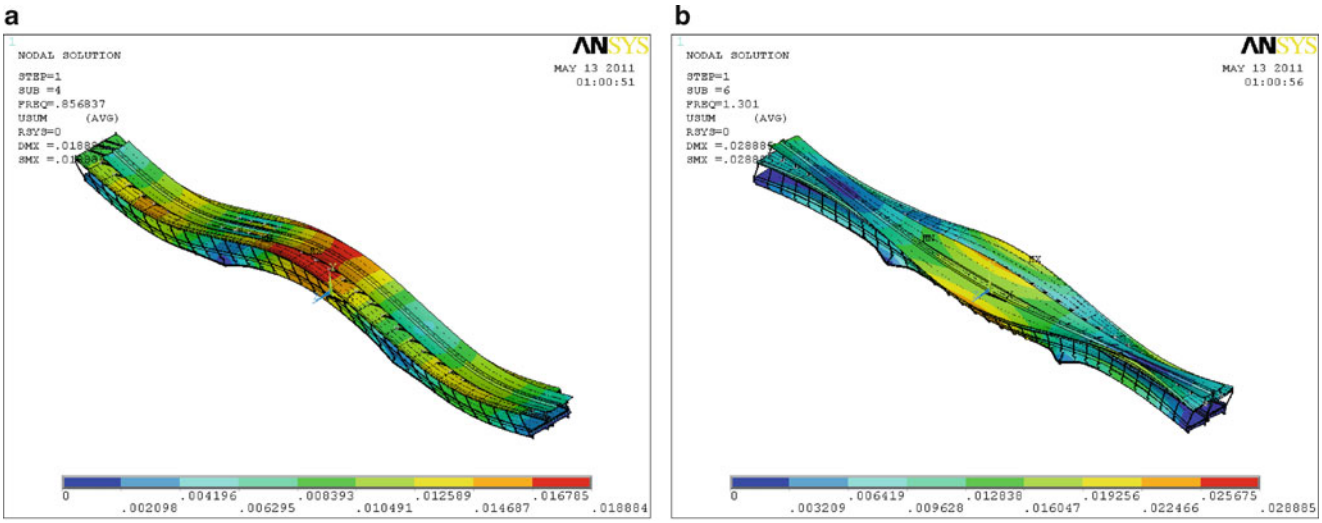

Fig. A.8 Experiment 8 results. (**a**) First bending mode. (b) First torsional mode

References

1. Hedayat AS, Sloane NJA, Stufken J (1999) Orthogonal arrays: theory and applications. Springer, New York
2. Goodwin GC, Payne RL (1977) Dynamic system identification: experiment design and data analysis. Academic, New York
3. Rains EM, Sloane NJA, Stufken J (2000) The lattice of N-run orthogonal arrays. Journal of Statistical Planning and Inference, 102 (2002): 477–500
4. Boddy R, Smith G (2010) Effective experimentation for scientists and technologists. Wiley, New York
5. Lorenzen TJ, Anderson VL (1993) Design of experiments: a no-name approach. CRC Press, New York
6. Dorf R (1996) Engineering handbook. CRC Press, New York
7. Montgomery DC (2001) Design and analysis of experiments. Wiley, New York

Chapter 30
Structural Damage Detection Using Multivariate Time Series Analysis

Ruigen Yao and Shamim N. Pakzad

Abstract Much research has been focused in the past few decades on data-driven structural health monitoring based on sensor measurements. Modal parameters from system identification are the most widely studied structural state indicators adopted for this purpose; however, recent research has showed that they are not sensitive enough to local damage. In an effort to seek more effective alternatives, univariate autoregressive (AR) modeling on structural response has been investigated in several publications, where model characteristics are used as damage indices. Although these methods are generally successful, they tend to generate false alarms when the environmental conditions are varying because responses from only one location/sensor are considered. To strike a balance between sensitivity and stability, in this paper autoregressive with exogenous input modeling on measurements from several adjacent sensing channels is presented and applied to detect damage in a space truss structure. The damage feature is extracted from the residuals obtained via fitting the baseline model to data from the current structure. Also, damage localization is attempted by examining the estimated mutual information statistic between data from adjacent sensing channels. The damage identification/localization results thus obtained are then compared to those from univariate AR modeling to evaluate their relative pros and cons.

Keywords Structural health monitoring • Damage detection • Time series analysis • Autoregressive modeling • Information statistics

30.1 Introduction

Damage detection using structural vibration measurements is a field that has been actively investigated by the civil engineering research community in the past few decades [1, 2]. It is hoped that through these investigations automatic structural condition assessment can be realized 1 day, thereby reducing the cost on infrastructure maintenance as the involvement of human experts becomes less necessary. One of the earliest damage indicators studied is the estimated modal property from system identification [3, 4], as it is directly related to structural physics according to classical dynamics theory. However, system identification algorithms, especially those that operate in time domain, are sometimes computationally intensive to implement. Also, the effectiveness of modal property as damage indicator varies depending on the structural layout and damage type. Studies have shown that it can be insensitive to local/minor damage [1]. Its performance could often be improved by feeding the modal property to a finite model updating scheme [5], but that is at the cost of increased algorithm complexity. To circumvent these problems, more efficient alternatives are needed.

Univariate time series analysis on vibration measurements have been successfully adopted in several recent research papers [6–9] for damage identification purposes. This method bears certain similarities to traditional system identification as both are concerned with numerical modeling, yet the former is more flexible because it uses various damage features that do not necessarily have an explicit physical meaning. Damage features can be functions of either model parameters or model coefficients, and well-known statistical concepts are applied to set the critical damage threshold for the features extracted.

R. Yao (✉) • S.N. Pakzad
Department of Civil and Environmental Engineering, Lehigh University, Bethlehem, PA18015, USA
e-mail: ruy209@Lehigh.edu; pakzad@Lehigh.edu

J.M. Caicedo et al. (eds.), *Topics on the Dynamics of Civil Structures, Volume 1*,
Conference Proceedings of the Society for Experimental Mechanics Series 26,
DOI 10.1007/978-1-4614-2413-0_30,

Since the method only utilizes responses from a single sensor node at each time, it is relatively sensitive to local damage. But for the same reason, the results produced become less reliable when the environmental condition is not stationary. Moreover, the damage location in general cannot be inferred from the value of the damage indices, confining the application of this method to preliminary damage detection (detecting only the damage existence).

In this paper, multivariate autoregressive (AR) time series analysis [10] will be applied for damage detection. Basically, this method seeks to reach a balance between damage sensitivity and output stability by constructing the model on responses from several adjacent nodes. The damage feature used here is based on the autocorrelation function (ACF) of model residuals, and through examining the amount of change occurred in the feature value obtained for different node combinations damage localization will be attempted. In addition, an index that represents the mutual information [11] between two sensing channels is also used for damage detection here. While being easier to compute than the one based on multivariate AR modeling, this index nonetheless served the purpose for damage detection/localization in the application presented in Sect. 30.4.

The organization of the paper is as follows; Sect. 30.2 is a brief review of the univariate AR modeling method for damage identification, and Sect. 30.3 presents the multivariate AR modeling method and the mutual information method. Section 30.4 contains the application of the established and new methods to acceleration measurements collected from a space truss structure under ambient loading, and the performances of different algorithms are compared and contrasted.

30.2 Univariate AR Time Series Analysis for Damage Identification

Autoregressive models have long been successfully applied to model, validate and predict signals from various types of sources. The definition of a univariate AR model is shown below:

$$x(t) = \sum_{j=1}^{p} \phi_{xj} x(\mathrm{t\ -\ j}) + \varepsilon_x(t). \tag{30.1}$$

where ϕ_{xj} are the AR model coefficients, $\varepsilon_x(t)$ is the model residual, and $x(t)$ is the time series to be analyzed. It is easy to see that this model basically attempts to predict the future output using a linear combination of previous outputs.

Univariate AR model parameters can be very efficiently estimated from a signal using one of the standard algorithms. According to the specific feature extraction process, the damage features from AR model can be classified into two categories: model coefficients based and model residual based. In the remainder of this section, examples from both categories will be presented.

30.2.1 AR Coefficients Based Damage Indicators

It has been proved that if the signal is really an AR process, then any regular coefficients estimator $\{\phi_{xj}\}$ from the signal is asymptotically unbiased and normally distributed with covariance matrix $\sigma_e^2 \Gamma_p^{-1}$ [10]. Therefore, Mahalanobis distance, a metric that represents the deviation in the probability space of normal distribution, seems to be a good choice of damage feature.

The estimator of the Mahalanobis distance between a potential outlier vector x_ξ and a baseline sample set can be obtained as

$$D_\xi = (x_\xi - \bar{x})^T \hat{\Sigma}^{-1} (x_\xi - \bar{x}). \tag{30.2}$$

where $\bar{x}$ is the average of the baseline sample feature vectors, and $\widehat{\Sigma}$ the estimated covariance matrix. When applied for damage identification, an assessment of the current structural state is made by comparing the Mahalanobis distances obtained within the baseline/healthy state and those obtained from unknown/current state.

Cosh spectral distance [12] of AR model spectra, another model coefficients based feature, has a formulation similar to that of Mahalanobis distance feature. Corresponding spectrum plot (Fig. 30.1) can be constructed given an AR model:

$$S_{AR}^{(p)}(\omega) = \frac{\sigma_e^2}{|\phi(e^{j\omega})|^2} = \frac{\sigma_e^2}{|\sum_{k=0}^{p} \phi_k e^{-j\omega k}|^2}. \tag{30.3}$$

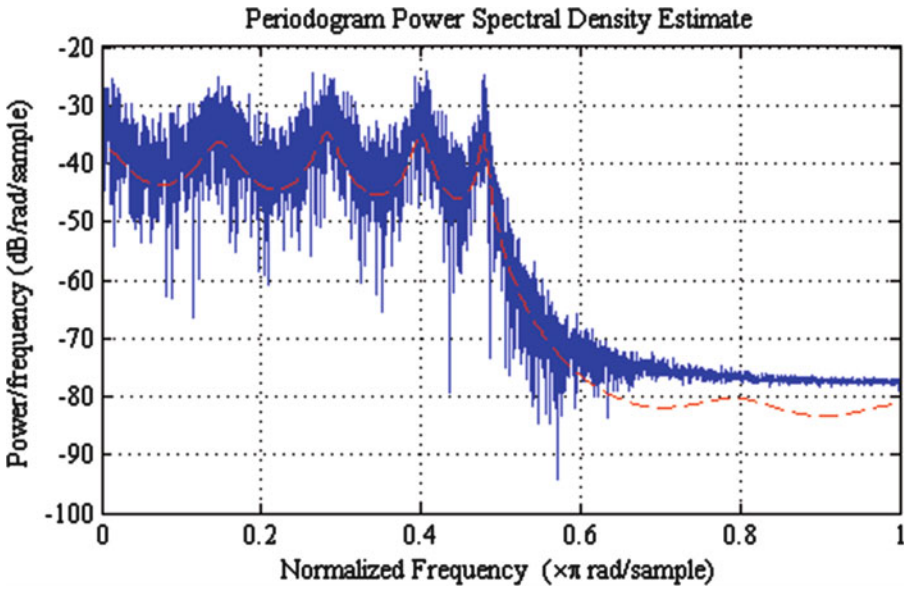

Fig. 30.1 Comparison between an AR signal power spectrum density and the estimated AR model spectrum (*dashed line*)

In application σ_e^2 is not calculated and set to 1, since its value is determined by excitation level. And Cosh spectral distance between the mean of baseline spectra $\bar{S}(\omega_j)$ and an unknown state spectrum $S(\omega_j)$can be computed from (30.4):

$$(S, \bar{S}) = \frac{1}{2N} \sum_{j=1}^{N} \left[\frac{S(\omega_j)}{\bar{S}(\omega_j)} - \log \frac{S(\omega_j)}{\bar{S}(\omega_j)} + \frac{\bar{S}(\omega_j)}{S(\omega_j)} - \log \frac{\bar{S}(\omega_j)}{S(\omega_j)} - 2 \right]. \tag{30.4}$$

When the system is damaged, the Cosh distance value would increase.

30.2.2 AR Residual Based Damage Indicators

When applying the AR coefficients based algorithms, the modeling process generally has to be repeated for a large number of times to get enough coefficient vectors for structural diagnosis. In the residual based algorithms, however, the model is constructed only once from the baseline signal. Residuals can then be generated by fitting the model to the signals collected.

If the system is damaged, the baseline model will no longer produce a good fit of the new data. In other words, the difference between predicted response from baseline model and real signal will increase. The model residual variance in most cases provides a valid measure of this difference, and has been used to detect damage in several literatures [6, 8]. More sensitive damage features could be obtained by taking into consideration the entire autocorrelation function (ACF) of the residuals, i.e. employing the Ljung-Box statistic [13]:

$$Q = n(n+2) \sum_{j=1}^{h} \frac{\rho_j^2}{n-j}. \tag{30.5}$$

where n is the sample size, h is the number of lags, and ρ_j is the autocorrelation at the j^{th} lag. This Q – statistic follows a χ^2 distribution under the normality assumption of the signal.

30.3 Damage Identification/Localization Using Multi-channel Responses

Time series analysis on measurements from a single sensor node provides an efficient way for damage detection. However, applications have shown that their effectiveness as damage location indicator depends on the specific structural type. Also, due to the information limitation, this family of methods tends to suffer from false alarms when the environmental

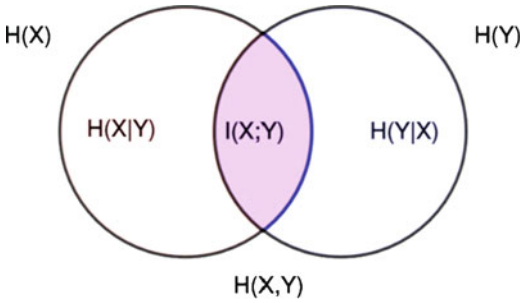

Fig. 30.2 An illustration of the definition of mutual information as the sum of the separate entropies of two random variables X and Y subtracted by their joint entropy H(X,Y) [11]. Entropy is essentially a measure of uncertainty for random variables

conditions are varying. Here in this section, damage features constructed from measurements from several adjacent sensors will be introduced in hope of improving algorithm stability and damage localization capability.

30.3.1 ARX Analysis Using Several Adjacent Nodal Responses

(SISO) ARX model [4] is defined as follows:

$$x(t) = \sum_{i=1}^{a} \alpha_i x(t-i) + \sum_{j=1}^{b} \beta_j u(t-j) + e_x(t). \tag{30.6}$$

where $x(t)$and $u(t)$are the output and input signal, respectively. Notice that this is also a linear regression model that associates the current response of a signal with its previous values and an exogenous input. If there are several exogenous inputs (multi-input-single-output case), each input will have its corresponding coefficient vector $\{\beta_j\}$.

Here when this model is applied for damage identification, the output signal will be from a certain sensor node (possibly at a potential damage location) and the input signals will be from its neighboring nodes. Here the damage indicators will be computed from residuals analysis, with the general procedure almost the same as that for univariate AR modeling. Model parameter based analysis will not be attempted here because it will require estimation of the multivariate model for many times, thereby resulting in high computational cost.

30.3.2 Mutual Information Between Signals Collected from Adjacent Nodes

Mutual information [11] is a statistic defined to measure the mutual dependence/similarity between random variables (Fig. 30.2). It is first proposed in communication theory to quantify the capacity of data transmission channels. Given the probability distributions of two random variables X and Y, their mutual information can be computed as;

$$I(X;Y) = \int_X \int_Y p(x,y) \log \frac{p(x,y)}{p(x)p(y)} dxdy. \tag{30.7}$$

$p(\cdot,\cdot)$and $p(\cdot)$here denote the joint and marginal probability distribution. It is clear that the value of this metric is always non-negative, and equal to zero only when X and Y are statistically independent. The definition can also be easily extended to the case where X and Y are random vectors.

If both X and Y are assumed to follow a Gaussian distribution, then the mutual information statistic can be obtained directly from their second-order statistical moments:

$$I(X;Y) = \frac{1}{2} \log \frac{|K\{X\}||K\{Y\}|}{|K\{X,Y\}|}. \tag{30.8}$$

where $K\{X\}$stands for the variable covariance matrix and $|\cdot|$ is the matrix determinant. Mutual information can be more efficiently estimated from this formula than from the previous one, as it requires only the variance of the variables, instead of the complete distribution.

In the next section, mutual information between responses from two adjacent sensors will be employed as damage index. If damage (stiffness reduction) occurs between these two nodes, then it is expected that their mutual information value will decrease significantly. Since structural responses at any measured location are always correlated over time, they cannot be treated as single random variable. Rather, a time window of length L will be applied to each response signal and the estimated mutual information $\hat{I}(x_1(t);x_2(t))$between two signals $x_1(t)$ and $x_2(t)$ becomes:

$$\hat{I}(x_1(t);x_2(t)) = I(x_1(t),x_1(t+1),...,x_1(t+L-1);x_2(t),x_2(t+1),...,x_2(t+L-1)) \tag{30.9}$$

Here the parameter L needs to be chosen with care so that the autocorrelation of signals after *Lth* lag will be close to zero.

30.4 Experimental Validation of the Statistical Algorithms

The statistical algorithms described in the above two sections are applied to acceleration measurements collected from a space truss in the lab. The truss has its four supports fixed to sturdy I-beam sections, and 10 wireless sensors are mounted on the truss nodes in the midspan (Fig. 30.3). Artificial damage is introduced by removing one interior diagonal member between sensor node 1 and 8. For each structural state (undamaged/damaged), two sets of data are collected at a sampling frequency of 280 Hz. As an effort to reduce the noise content, a low-pass filter is applied to all the data, which are subsequently downsampled to 70 Hz. The compressed data is then used as input to the damage detection algorithms, and dataset 1 is the selected baseline signal for all the implementations.

30.4.1 Damage Identification Results from Univariate AR Coefficients Based Method

Figure 30.4 shows the model coefficient based Mahalanobis distance features and model spectrum based Cosh spectral distance features extracted from different datasets. The first two datasets are from the healthy state of the structure, and the last two datasets are from the damaged state. In application of both methods, the signals are divided into many short

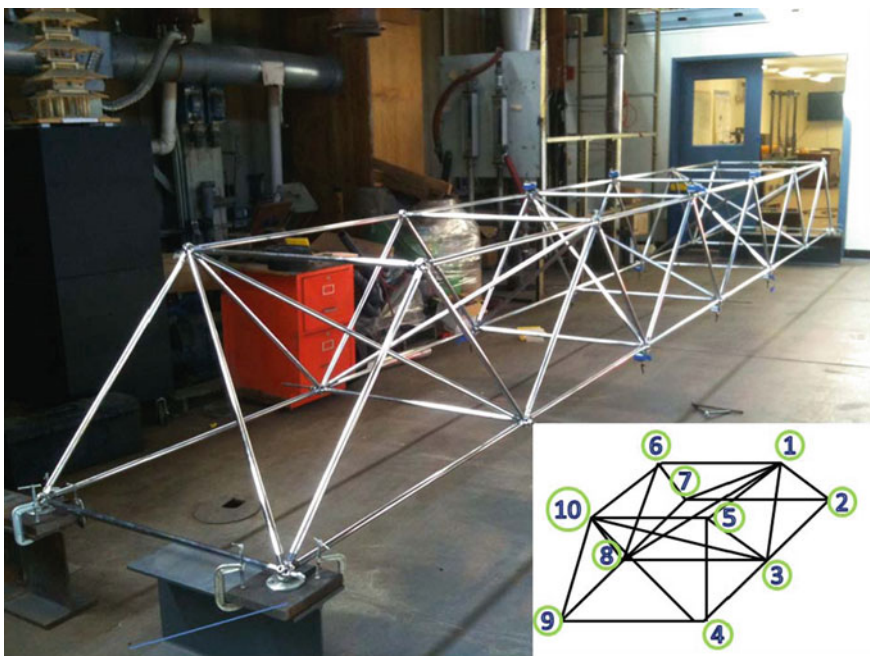

Fig. 30.3 The space truss model with the sensor node numbers shown in the lower right corner

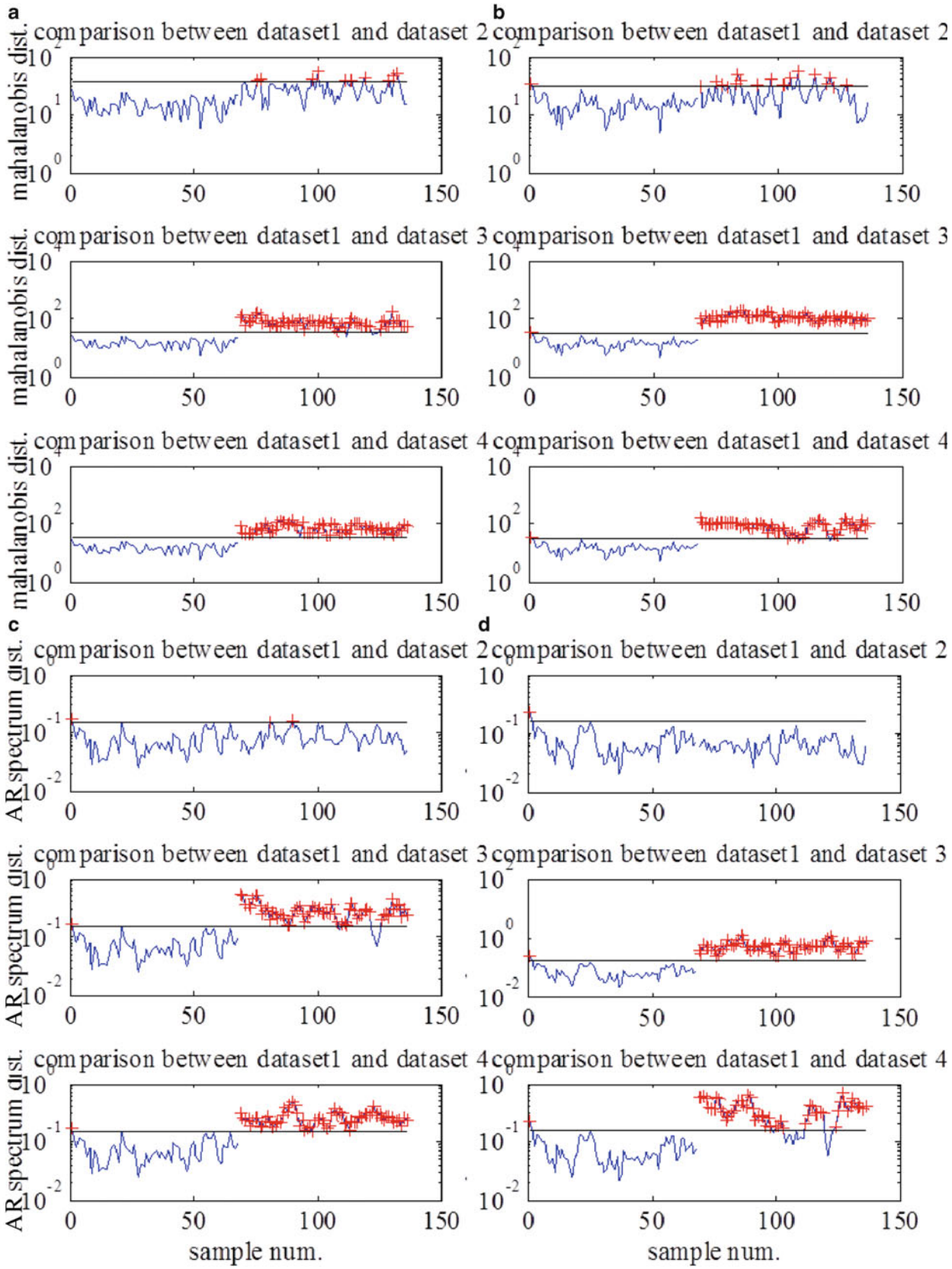

Fig. 30.4 Damage identification results using AR coefficients based method. (**a**) and (**c**) are the Mahalanobis distance and Cosh spectral distance features obtained from measurements at sensor 4, while (**b**) and (**d**) are those from sensor 8

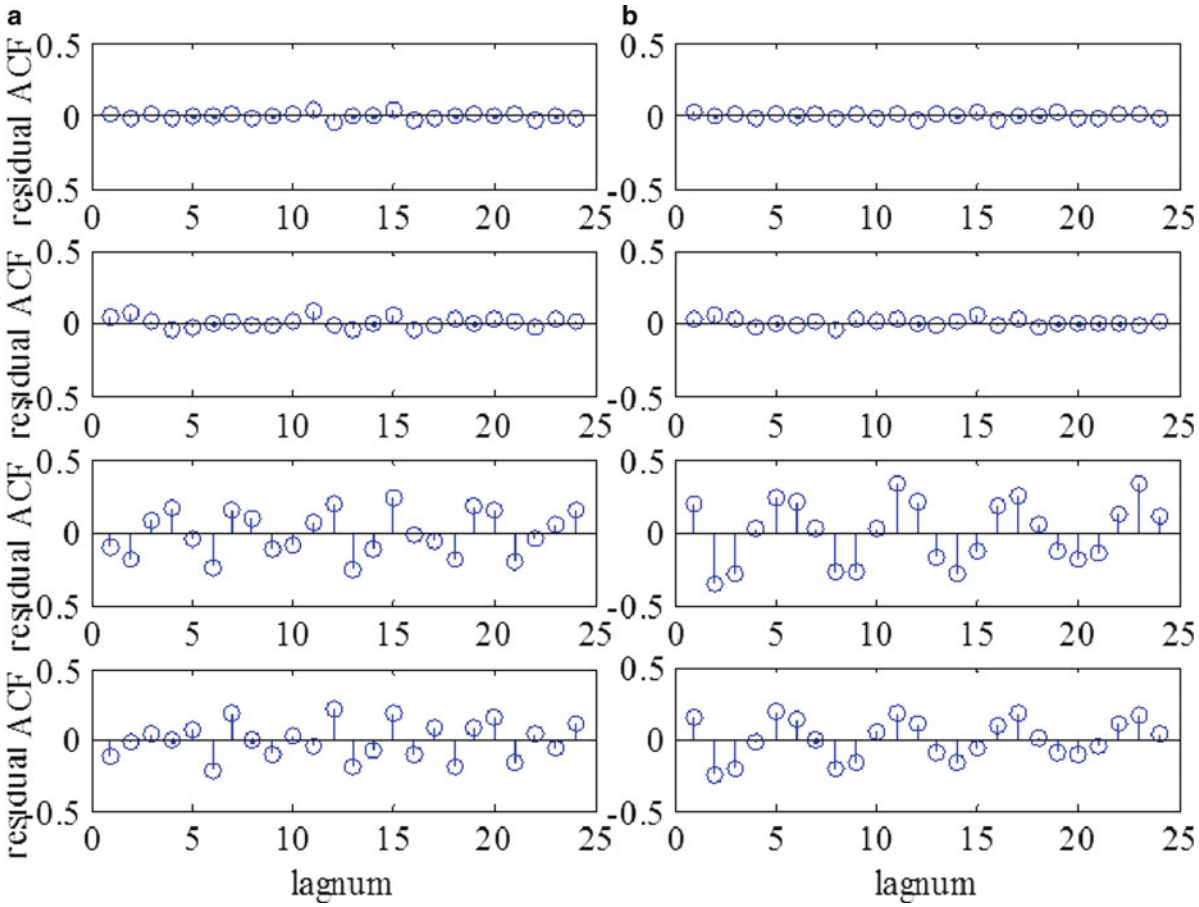

Fig. 30.5 Damage identification results using AR residual based method. (**a**) Contains the residual autocorrelation function plots obtained from measurements at sensor 4, with subplot 1–4 corresponding to dataset 1–4. (**b**) Contains plots obtained from sensor 8 using the same procedure. Dataset 1 is used as the baseline here

segments with large overlap among them so as to produce enough AR coefficient vectors from them for structural state evaluation. It can be seen from the plots that after the damage, a lot of outliers will appear. Also, the Mahalanobis distance method is not as stable as the Cosh spectral distance, i.e. more false alarms are observed in plots of the former. This is because spectral distance generally assigns more weight to the position of system poles than that of system zeros, and thus is less susceptible to noise disruptions. Both damage indices are ineffective damage location indicators in this case, as the magnitude of change in feature values as a result of damage is more or less the same for the two sensing locations, despite one is much closer to the damage than the other.

30.4.2 Damage Identification Results from Univariate AR Residuals Based Method

As stated in Sect. 30.2, damage detection can also be based on the autocovariance/autocorrelation function of the residuals. Figure 30.5 contains the ACF plots of the residuals obtained from applying the AR modeling to measurements at sensor 4 and 8. After the structure is damaged, the absolute values of the ACF at non-zero time lags increase significantly. Accordingly, an increase in Ljung-Box statistic of the residual series will also be observed. Due to space limitations, however, its results are not presented here.

Table 30.1 Results from the MISI ARX method. The standard deviations are all normalized with respect to the baseline

		Dataset 1	Dataset 2	Dataset 3	Dataset 4
$3_x/1_x,2_x,4_x,5_x,10_{x,y}$	Normalized σ_e	1.000	0.962	1.576	1.460
	Log Ljung-Box statistic	5.504	6.070	8.706	7.999
$8_x/1_x,6_x,7_x,9_x,10_{x,y}$	Normalized σ_e	1.000	0.990	2.127	1.905
	Log Ljung-Box statistic	5.107	5.873	9.596	9.696
$3_x/1_x,2_x,4_x,5_x$	Normalized σ_e	1.000	0.937	1.257	1.254
	Log Ljung-Box statistic	5.618	6.155	8.153	7.665
$8_x/6_x,7_x,9_x,10_{x,y}$	Normalized σ_e	1.000	0.993	1.479	1.264
	Log Ljung-Box statistic	5.210	6.148	9.563	8.602

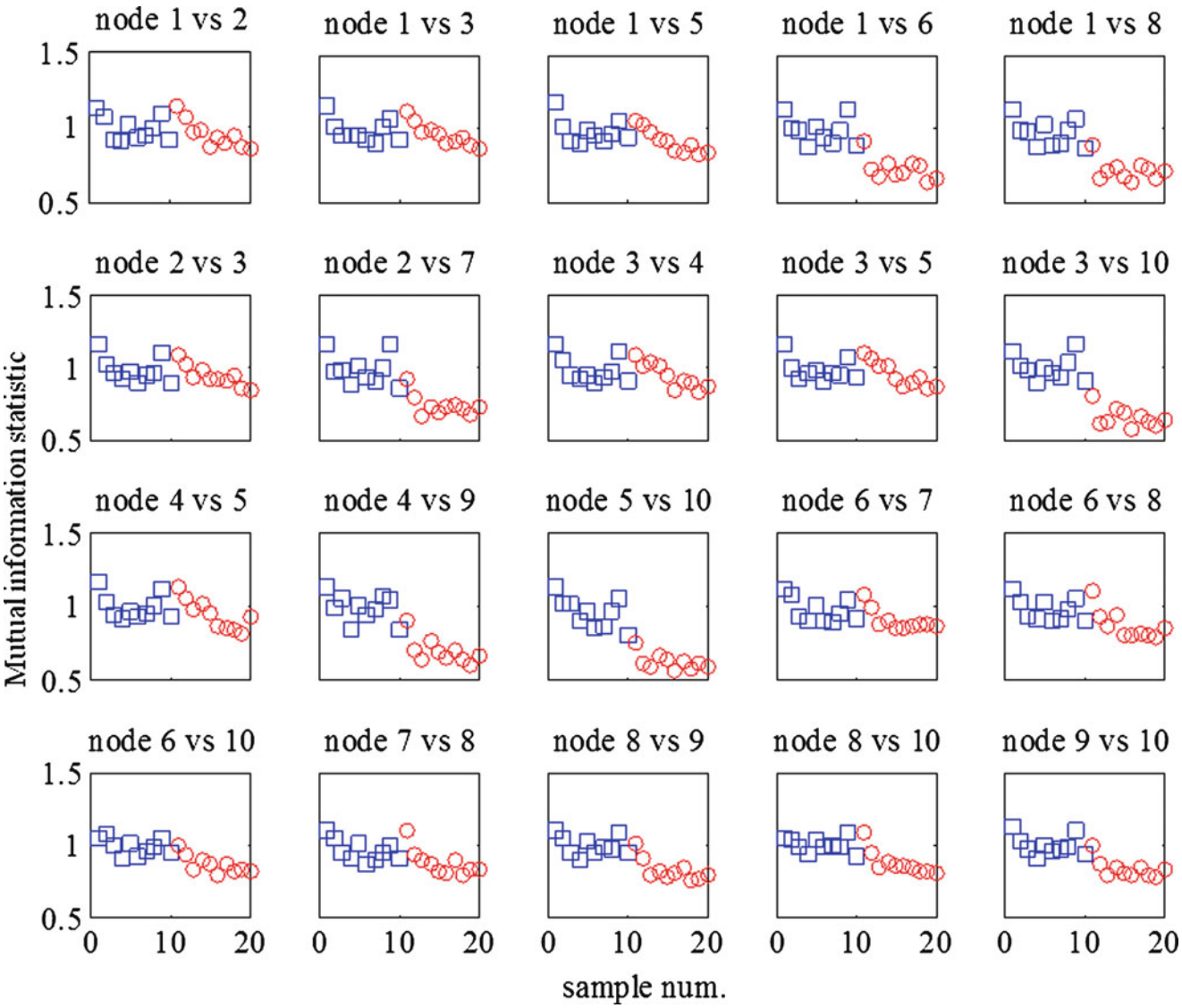

Fig. 30.6 Damage identification results from mutual information method. The *blue squares* are features from the undamaged state, and the *red circles* are from damaged state

30.4.3 Damage Identification Results from MISO ARX Modeling Method

Here the acceleration measurements in the vertical direction from sensor node 3 and 8 are used as output in the ARX model, and measurements from their respective neighboring nodes will be used as the model input. Table 30.1 summarizes the normalized residual standard deviations and the log Ljung-Box statistics computed from signals 1–4. In the first column of

the table, the number before the slash represents the output sensor node, where those after the slash are the input nodes. And for the subscripts of these numbers, *x*stands for measurements in the vertical direction, and *y*the horizontal direction. Damage localization can be achieved by comparing results from models constructed with different output nodes (e.g. node 3 versus 8), and/or models with different combinations of exogenous inputs; a more significant increase in feature values can be observed for models using the sensor 8 as the output node, and for the models that include all neighboring node responses as inputs. Note that the artificial damage occurs between sensor 1 and 8. Because here only 10 truss nodes are instrumented with accelerometers, results from other nodes cannot be presented as the responses of several of their neighbor nodes are unknown.

30.4.4 Damage Identification Results from Mutual Information Method

The damage index based on mutual information also succeeds to identify the damage existence and location. Figure 30.6 is a series of plots containing the estimated mutual information obtained from vertical acceleration measurements from pairs of adjacent nodes. Five estimates are computed from each dataset. In each of these plots, the features are normalized with the mean from the baseline sample group to facilitate cross-comparison. It can be observed that the damage features based on the node pairs located in the vicinity of damage exhibited the most significant change in their values. In addition, the estimates based on nodes that do not lie in the same vertical pane are more sensitive to damage than the rest, indicating that the damage occurs at the interior connections.

30.5 Conclusion

Two damage detection methods using time series analysis on responses from several adjacent nodes are described and applied to acceleration measurements on a space truss model here. The first method employs MISO ARX modeling, while the other method utilizes the mutual information concept for feature construction. Their performances are then compared with those of the established damage identification techniques based on AR modeling of responses from a single sensing channel. It is observed that the multivariate time series analysis produces viable damage indices and in the meanwhile is able to predict damage location with greater accuracy.

Univariate AR modeling algorithms has certain advantages when applied for damage identification; they are computationally efficient, suitable for on-sensor-board data processing, and sensitive to small scale damages. As seen in Sect. 30.4, their application to detect damage existence in the truss model is altogether successful. However, they are not effective at damage localization. Moreover, since this family of algorithms monitors only the statistical properties of the measurements at a single sensor node, it is susceptible to changes in operation conditions that do not concern the structure itself. Such innate false-positive characteristic of these algorithms will make them unreliable for practice.

The MISO ARX modeling algorithm is slightly more sophisticated than the univariate AR method, as more parameters need to be estimated in the former case. But then, the damage localization capability of the algorithm is visibly improved by adding the neighbor nodes responses as external outputs in the model. Recognizing the increased computational cost, the mutual information damage index is introduced and applied to the specimen. This method is of a simpler formulation than the ARX algorithm, yet nonetheless achieves the aim of damage detection/localization as shown in Sect. 30.3.

In summation, the multivariate time series analysis approach is proposed here as an intermediate approach that seeks to combine the merits of traditional system identification and univariate time series modeling. By including several responses from adjacent nodes, model parameter estimation becomes less affected by excitation variation; yet the model is still constructed on measurements from only a part of the structure, thus retaining the sensitivity to local damage and algorithm computation efficiency. The experimental application used here has confirmed the effectiveness of proposed algorithms, and they will be further examined through implementation on different types of structures in the future.

References

1. Doebling SW, Farrar CR, Prime MB, Shevitz DW (1996) Damage identification and health monitoring of structural and mechanical systems from changes in their vibration characteristics: a literature review. Report No. LA-13070-MS, Los Alamos
2. Farrar CR, Duffey TA, Doebling SW, Nix DA (1999) A statistical pattern recognition paradigm for vibration-based structural health monitoring. In: 2nd international workshop on structural health monitoring, Standford National Laboratory, Los Alamos, NM

3. Alvin KF, Robertson AN, Reich GW, Park KC (2003) Structural system identification: from reality to models. Comput Struct 81 (12):1149–1176
4. Ljung L (1987) System identification: theory for the user. Prentice Hall, New Jersey
5. Messina A, Williams EJ, Contursi T (1998) Structural damage detection by a sensitivity and statistical-based method. J Sound Vib 216(5):791–808
6. Fugate ML, Sohn H, Farrar CR (2001) Vibration-based damage detection using statistical process control. Mech Syst Signal Process 15(4):707–721
7. Gul M, Catbas FN (2009) Statistical pattern recognition for structural health monitoring using time series modeling: theory and experimental verifications. Mech Syst Signal Process 23(7):2192–2204
8. Sohn H, Farrar CR, Hunter NF, Worden K (2001) Structural health monitoring using statistical pattern recognition techniques. J Dynam Syst Meas Control 123(4):706–711
9. Yao R, Pakzad SN (2011) Data-driven methods for threshold determination in time-series based damage detection. In: Proceedings of the 20th annual structures congress, Las Vegas
10. Brockwell PJ, Davis RA (1991) Time series: theory and methods, 2nd ed. Springer, New York
11. Cover TM, Thomas JA (2006) Elements of information theory. In: Wiley series in telecommunications and signal processing, 2nd edn. Wiley-Interscience, Hoboken
12. Wei B, Gibson JD (2000) Comparison of distance measures in discrete spectral modeling. In: Proceedings of IEEE digital signal processing workshop, Hunt, TX, pp 1–4
13. Ljung GM, Box GEP (1978) On a measure of lack of fit in time series models. Biometrika 65(2):297–303

Chapter 31
Changes in the Statistics of Ambient Excitations in the Performance of Two Damage Detection Schemes

J. Strout, M. Döhler, D. Bernal, and L. Mevel

Abstract Data driven damage detection is often carried out by computing a metric that can be extracted from measurements and whose statistics depend on the structural state. A well known difficulty arises because changes in environmental conditions also lead to changes in the metric and these fluctuations need to be minimized for the methods to have adequate resolution. Two techniques that have been investigated for some time in damage detection are: (1) the Kalman Filter innovations whiteness test and (2) a subspace approach based on the left kernel of the output covariance. Recent work by the authors showed that both techniques lost significant resolution when the statistics of the ambient excitation changed from the time the filters were formulated to the interrogation time. Work to formulate modified versions that can operate more robustly under a changing loading environment was undertaken and this paper reports on the modifications developed as well as on the effectiveness of the new procedures compared to the original strategies.

Keywords Damage detection • Kalman Filter • Statistical subspace

31.1 Damage Detection Methods

31.1.1 Statistical Subspace Based Damage Detection

31.1.1.1 Models and Parameters

The behaviour of a mechanical system is assumed to be described by a stationary linear dynamical system

$$M\ddot{Z}(t) + C\dot{Z}(t) + KZ(t) = v(t) \tag{31.1a}$$

$$Y(t) = LZ(t) \tag{31.1b}$$

where t denotes continuous time, M, C and K are the mass, damping and stiffness matrices, high-dimensional vector Z collects the displacements of the degrees of freedom of the structure, the non-measured external force v modelled as non-stationary Gaussian white noise, the measurements are collected in the vector Y and matrix L indicates the sensor locations.

The eigenstructure of (31.1a, 31.1b) with the modes μ and mode shapes φ_μ is a solution of

$$\det(\mu^2 M + \mu C + K) = 0 \tag{31.2a}$$

$$(\mu^2 M + \mu C + K)\phi_\mu = 0 \tag{31.2b}$$

J. Strout (✉) • D. Bernal
Northeastern University, 360 Huntington Ave, Boston, MA 02115, USA
e-mail: james.a.strout@gmail.com

M. Döhler • L. Mevel
Campus de Beaulieu, Rennes Cedex 35042, France

J.M. Caicedo et al. (eds.), *Topics on the Dynamics of Civil Structures, Volume 1*,
Conference Proceedings of the Society for Experimental Mechanics Series 26,
DOI 10.1007/978-1-4614-2413-0_31,

$$\varphi_\mu = L\phi_\mu \tag{31.2c}$$

Sampling model (31.1a, 31.1b) at some rate $1/\tau$ yields the discrete model in state-space form

$$X_{k+1} = FX_k + V_{k+1} \tag{31.3a}$$

$$Y_k = HX_k \tag{31.3b}$$

whose eigenstructure is given by

$$\det(F - \lambda I) = 0 \tag{31.4a}$$

$$(F - \lambda I)\phi_\lambda = 0 \tag{31.4b}$$

$$\phi_\lambda = H\varphi_\lambda \tag{31.4c}$$

Then, the eigenstructure of the continuous system (31.1a, 31.1b) is related to the eigenstructure of the discrete system (31.3a, 31.3b) by

$$e^{\tau\mu} = \lambda \tag{31.5a}$$

$$\varphi_\mu = \varphi_\lambda \tag{31.5b}$$

The collection of modes and mode shapes (λ,φ_λ) is a canonical parameterization of system (31.3a, 31.3b) and considered as the system parameter θ

$$\theta = \begin{pmatrix} \Lambda \\ vec\Phi \end{pmatrix} \tag{31.6}$$

where Λ is the vector whose elements are the eigenvalues λ and Φ is the matrix whose columns are the mode shapes φ_λ.

31.1.1.2 Statistical Subspace-Based Covariance-Driven Damage Detection

To obtain the system parameter θ from measurements $(Y_k)_{k=1,\ldots,N}$, the covariance-driven output-only subspace identification algorithm [1, 2] can be used. From the data, a block Hankel matrix $\mathbf{H}$ is filled with the correlation lags $R_i = \mathbf{E}(Y_k Y_{k-i}{}^T)$ of the output data

$$H = \begin{pmatrix} R_0 & R_1 & \cdots & R_{q-1} \\ R_1 & R_2 & \cdots & R_q \\ \vdots & \vdots & \ddots & \\ R_p & R_{p+1} & & R_{p+q} \end{pmatrix} \tag{31.7a}$$

$$R_i = \sum_{k=i+1}^{N} Y_k Y_{k-1}^T \tag{31.7b}$$

It possesses the factorization property

$$H = OC \tag{31.8}$$

into observability matrix

$$O = \begin{pmatrix} H \\ HF \\ \vdots \\ HF^p \end{pmatrix} \tag{31.9}$$

and controllability matrix **C**, where **O** is obtained from **H** by an SVD and truncation at the desired model order

$$H = \begin{pmatrix} U_1 & U_2 \end{pmatrix} \begin{pmatrix} \Delta_1 & \\ & \Delta_0 \end{pmatrix} V^T \tag{31.10a}$$

$$O = U_1 \Delta_1^{1/2} \tag{31.10b}$$

The matrices H and F can be recovered from the observability matrix **O** to finally obtain the eigenstructure $(\lambda,\varphi_\lambda)$ of the system (31.3a, 31.3b) and system parameter θ in (31.4a, 31.4b, 31.4c)–(31.6).

In order to detect changes in the system parameterθ, the statistical subspace-based damaged detection from [3–5] is recalled, where a residual function for damage detection is associated with the subspace identification from above. This function compares the system parameter θ_0 of a reference state with a block Hankel matrix $\hat{H}$ as in (31.7a, 31.7b) computed on new data corresponding to an unknown, possibly damaged state, without computing the system parameter θ in the unknown state.

Let S be the left null space of the block Hankel matrix (31.7a, 31.7b), which can be obtained from $\mathrm{S} = \mathrm{U}_0$. Then, the characteristic property of the system in the reference state writes

$$S^T \hat{H} = 0 \;\; if \;\; \theta = \theta_0 \tag{31.11}$$

For checking whether new data agree with the reference state corresponding to θ_0, the residual function

$$\zeta_N = \sqrt{N} vec(S^T \hat{H}) \tag{31.12}$$

is introduced in [3, 4] where N is the number of samples on which **H** is computed. It was shown that this residual function is asymptotically Gaussian for large N with zero mean in the reference state and non-zero mean in the damaged state. Let Σ_ζ be the residual covariance matrix. Then, a change in the system parameter θ corresponds to a change in the mean value of the residual function and manifests itself in the χ^2 test statistics

$$\chi_N^2 = \zeta_N^T \hat{\Sigma}_\zeta^{-1} \zeta_N \tag{31.13}$$

where $\hat{\Sigma}_\zeta$ is a consistent estimate of Σ_ζ. To assess the occurrence of damage, ${\chi_N}^2$ should be compared with a threshold. Note that χ^2 test (31.13) is the empirical version of the damage detection test, where the Jacobian of the residual ζ_N is not taken into account.

31.1.1.3 The Kalman Filter Innovations Covariance (KFIC) Detector

The Kalman Filter is a state observer whose gain depends on the statistics of the unmeasured disturbances and the measurement noise. For linear systems with Gaussian disturbances, the Kalman filter is the optimal observer, and for disturbances with arbitrary statistics, it is the optimal linear observer. Use of the Kalman Filter as a damage detector was introduced by [6] and is based on the fact that the innovations are white when the filter is consistent. In the original version, the system is described by a model based on physics, and the Kalman gain is obtained from assumed knowledge of the covariance matrices of the noise. These assumptions, however, are unrealistic for the conditions that prevail in the envisioned applications of this project, so we utilize, instead, a Kalman Filter formulated from measurements [7, 8]. The fact that this can be done with no loss of useful information when the objective is detection derives from the fact that: (1) the basis of the

state is not needed for the computation of innovations, (2) the optimal filter gain is entirely determined by the output covariance [9] and (3) off-line computations are feasible.

A finite dimensional linear time invariant system of order n with m sensors subjected to uncorrelated stationary unmeasured disturbances and measurement noise can be described by

$$x^-(k+1) = Ax^-(k) + Le(k) \tag{31.14}$$

with

$$y(k) = Cx^-(k) + e(k) \tag{31.15}$$

where, $x \in R^{nx1}$is the state vector, $y \in R^{mx1}$is the measurement vector, $A \in R^{nxn}$ is the discrete time state transition matrix, C is the state to output matrix and e are the innovations. In (31.14) L is

$$L = AK \tag{31.16}$$

where K is the Kalman filter gain. In (31.14) and (31.15) the minus superscript indicates a prediction prior to the arrival of the measurement. The state estimate after the measurement arrives is

$$x^+(k) = x^-(k) + Ke(k) \tag{31.17}$$

and it follows from (31.15) that the innovations are

$$e(k) = y(k) - Cx^-(k) \tag{31.18}$$

Substitutions show that the state estimation needed in (31.18) is given by the recurrence

$$x^-(k+1) = (A - KC)x^-(k) + Ly(k) \tag{31.19}$$

Given a triplet {A,C,K} and a time history of measured output it is a simple matter, therefore, to compute the innovation sequence using (31.18) and (31.19). We note that extraction of the triplet {A,C,K} from the data is equivalent to the formulation of an ARMAX model.

31.1.1.4 Whiteness Test

Once the innovations sequence at each output sensor has been obtained, one proceeds by evaluating

$$H = \frac{1}{M}\sum_{j=1}^{M}(e_j - \bar{e})(e_j - \bar{e})^T \tag{31.20}$$

$$\tilde{e} = H^{-1/2}(e_j - \bar{e}) \tag{31.21}$$

$$C_k = \frac{1}{M-k}\sum_{j=1}^{M}\tilde{e}_j\tilde{e}_{j-k}^T \tag{31.22}$$

$$q = M \cdot \sum_{j=1}^{M} C_k^2 \tag{31.23}$$

where M is the length of the sequences and $k = 1,2,\ldots p$, where p is the lag number. It can be shown that q has a χ^2 distribution with p degrees of freedom. The threshold for announcing damage is obtained by looking at the CDF of the χ^2 distribution and deciding on a level of confidence.

31.2 Influence of Variable Ambient Excitation

31.2.1 Statistical Subspace-Based Damage Detection

If the unknown covariance $Q = \mathbf{E}(V_k V_k^T)$ of the ambient excitation does not change between the reference state and the possibly damaged state, the covariance Σ_ζ of the residual can be estimated only once in the reference state [3]. However, a change in Q also influences matrix $\mathbf{H}$ and thus changes the residual covariance Σ_ζ. In this case, a possibility would be to re-estimate Σ_ζ in each possibly damaged state. However, this is computationally expensive. Moreover, often longer data sets are available in the reference state than in possibly damaged states, which allows better estimates in the reference state.

A residual function that is robust to changes in the ambient excitation and a statistical χ^2 test on this residual were proposed in [10].

31.2.2 KFIC Detector

Changes in the noise due to variation in Q and R have a significant effect in the whiteness test of the KFIC [11]. The threshold for evaluating damage increases due to the effect of variation in Q and R on the chi-squared values. The increased threshold makes it very difficult to distinguish changes in statistics due noise from changes due to damage. Work by [11] showed that when Q and R varied Kalman Filter's detection capability decreased dramatically. A modified whiteness test that is capable of dealing with changes in ambient excitation was proposed in [12].

31.3 Improved Methods

31.3.1 Robust Subspace-Based Damage Detection

In [10] a damage detection test robust to changes in the ambient excitation was proposed. It is based on the fact that matrix U_1 in (10) defines the observability matrix of the considered system (and U_0 defines the left null space), while U_1 has orthonormal columns and is thus normed and independent of the excitation.

The resulting residual function

$$\xi_N = \sqrt{N} vec(S^T \hat{U}_1) \tag{31.24}$$

is – similarly to ζ_N in (31.12) – asymptotically Gaussian with zero mean in the reference state and non-zero mean in the damaged state. An estimate of its covariance Σ_ξ is computed only once in the reference state. It is based on the computation of the empirical covariance of $\mathbf{H}$ by cutting the available sensor data into blocks and on a sensitivity analysis of the left singular vectors in U_1. It is explained in detail in [10]. Then, the χ^2 test on the robust residual (31.24) writes as

$$\gamma_N^2 = \xi_N^T \hat{\Sigma}_\xi^{-1} \xi_N \tag{31.25}$$

and is compared to a threshold to assess the occurrence of damage.

31.3.2 Modified Whiteness Test

When Q and R vary the KFIC formed for the reference state becomes an arbitrary observer [12] for which one can has

$$C_0 = CPC^T + R \tag{31.26}$$

$$C_j = C\bar{A}^j PC^T - \bar{C}A^{(j-1)}AKR \tag{31.27}$$

where P is the solution of

$$P = \bar{A}P\bar{A}^T = GQG^T + AKRK^TA^T \tag{31.28}$$

(31.27) and (31.28) can be combined to form

$$vec(C_j) = E_{QQ}vec(Q) + E_{RR}vec(R) \tag{31.29}$$

where

$$E_{QQ} = (C \otimes C\bar{A}^j)N^{-1}E_Q \tag{31.30}$$

$$E_{RR} = [(C \otimes C\bar{A}^j)N^{-1}E_R - (I \otimes C\bar{A}^{(j-1)}AK)] \tag{31.31}$$

Due to the fact that the filter is stable, the matrix $\bar{A}$ has values that are less than one. As the lag number, j, increases the norm of $\bar{A}$ decreases. It follows that by shifting the first lag used to create the metric one can minimize the effects of the variation in Q and R. A modified whiteness test can be written as

$$q_p = M\sum_{m_p}^{m_{p+j}} \tilde{C}_k^2 \tag{31.32}$$

where m_p corresponds to the first lag taken and j is the total number of lags. In addition to the concept of a lag shift in order to improve observations of disturbances in covariance function due to damage the issue of optimal number of lags has been investigated. Numerical results suggest that there is an optimal "window" of lags that maintains sensitivity to the damage metric. Results of the Modified KFIC detector reflect optimal lag shift and number.

31.4 Numerical Results

A five-mass, seven spring structure is utilized for this research. Figure 31.1 shows a detailed diagram of the structure.

31.4.1 Statistical Subspace Based Damage Detection Versus Robust Subspace Based Detection

The overall damage detection rate for the statistical subspace based detection is 15%. Use of the robust subspace based detector improves the overall damage detection rate to 68%. Tables 31.1 and 31.2 illustrate a detailed breakdown of the effectiveness of the standard subspace based detector and the robust version. Tables are organized by detection rate based on

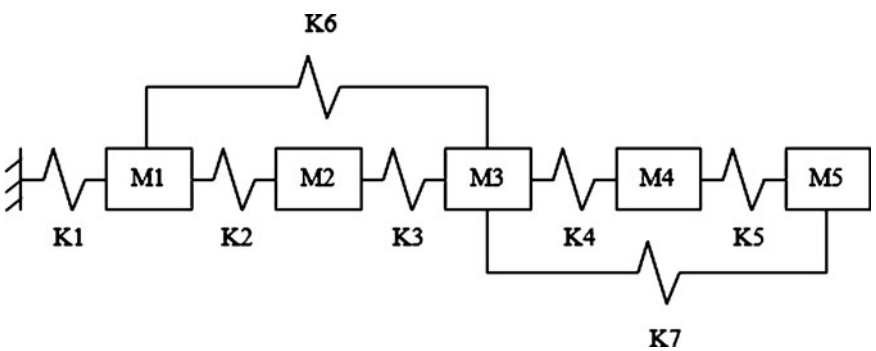

Fig. 31.1 Mass-spring testing structure: the structure consists of five masses and seven springs. Masses are denoted by M and the mass number 1–5. Springs are denoted by K and the number 1–7. Note the mass and spring number for use when referring to Tables 31.1, 31.2, 31.3 and 31.4

Table 31.1 Damage detection rate: conventional statistical subspace based damage detection

		Damaged spring #						
		K1	K2	K3	K4	K5	K6	K7
Sensor placement	M1	20	6	10	11	26	15	14
	M2	15	15	27	11	21	9	13
	M3	11	6	18	10	17	12	9
	M4	16	10	11	9	21	15	10
	M5	19	12	12	15	29	17	14

Table 31.2 Damage detection rate: robust subspace based damage detection

		Damaged spring #						
		K1	K2	K3	K4	K5	K6	K7
Sensor placement	M1	100	99	13	100	100	100	100
	M2	100	43	100	5	100	3	49
	M3	73	97	100	88	100	82	52
	M4	41	6	1	20	98	84	11
	M5	81	56	6	54	100	98	69

Table 31.3 Damage detection rate: KFIC detector

		Damaged spring #						
		K1	K2	K3	K4	K5	K6	K7
Sensor placement	M1	11	4	9	10	19	10	12
	M2	2	11	30	3	22	5	10
	M3	10	7	20	6	39	13	7
	M4	9	21	1	17	33	29	9
	M5	6	10	2	10	65	17	9

Table 31.4 Damage detection rate: modified KFIC detector

		Damaged spring #						
		K1	K2	K3	K4	K5	K6	K7
Sensor placement	M1	100	38	1	100	100	99	99
	M2	87	76	100	90	100	83	51
	M3	98	73	100	43	100	98	78
	M4	87	86	2	89	100	100	61
	M5	98	59	4	74	100	96	62

sensor placement and damaged spring number. The values shown in the table represent the percentage of correctly identified damage when the reduction in stiffness is 10%. It is clear that the variation of the Q and R leads to a poor damage detection capability and that the robust detector improves performance. However, overall detection rate of 68% is less than ideal.

31.4.2 KFIC Detector Versus Modified KFIC Detector

The overall damage detection rate for the KFIC Detector is 14%. Use of the Modified KFIC Detector improves the overall damage detection rate to 78%. Tables 31.3 and 31.4 illustrate a detailed breakdown of the effectiveness of the KFIC detector and the Modified KFIC detector respectively. The values in the table represent the percentage of correctly identified damage cases due to a 10% reduction in stiffness.

31.5 Conclusions

Variation of the Q and R rendered the two detectors deficient. Modification of the algorithms allowed the detectors to distinguish between changes in the system due to noise variation versus damage more efficiently, although overall detection performance at 10% damage remains less than ideal. Namely, with the threshold set at 5% of false positives the subspace had 68% detection rate and the Kalman Whiteness test 78%

Acknowledgements Part of this research was supported by NSF under grant # 10000391, this support is gratefully acknowledged. The first author was additionally supported by NSF under the Integrative Graduate Education and Research Traineeship (IGERT) Intelligent Diagnostics Fellowship (Award Number NSF DGE-0654176). The authors from INRIA were supported by the European projects FP7-PEOPLE-2009-IAPP 251515 ISMS and FP7-NMP CP-IP 213968-2 IRIS.

References

1. Benveniste A, Fuchs JJ (1985) Single sample modal identification of a non-stationary stochastic process. IEEE Trans Aut Control 30(1):66–74
2. Peeters B, De Roeck G (1999) Reference-based stochastic subspace identification for output-only modal analysis. Mech Syst Signal Process 13(6):855–878
3. Basseville M, Abdelghani M, Benveniste A (2000) Subspace-based fault detection algorithms for vibration monitoring. Automatica 36(1):101–109
4. Basseville M, Mevel L, Goursat M (2004) Statistical model-based damage detection and localization: subspace-based residuals and damage-to-noise sensitivity ratios. J Sound Vib 275(3):769–794
5. Balmès É, Basseville M, Mevel L, Nasser H, Zhou W (2008) Statistical model-based damage localization: a combined subspace-based and substructuring approach. Struct Contr Health Monit 15(6):857–875
6. Mehra RK, Peschon J (1971) An innovations approach to fault detection and diagnosis in dynamic systems. Automatica 7(5):637–640
7. Di Ruscio DD (1997) Model based predictive control: an extended state space approach. In: Proceedings of the 36th IEEE conference on decision and control, San Diego, pp 3210–3217
8. Van Overschee P, De Moor B (1996) Subspace identification for linear systems: theory, implementation and applications. Kluwer, Dordrecht
9. Anderson B, Moore A (2005) Active learning for hidden Markov models: objective functions and algorithms. In: Proceeding of the 22nd international conference on machine learning (ICML'05), Bonn, Germany, pp 9–16
10. Döhler M, Mevel L (2011) Robust subspace based fault detection. In: Proceedings of the 18th IFAC world congress, Milan
11. Wright C, Bernal D (2011) Residual analysis for damage detection: effects of variation on the noise model. In: Conference proceedings of the society for experimental mechanics series, vol 12. Jacksonville, pp 357–365
12. Bernal D, Bulut Y (2011) A modified test for damage detection using Kalman filter innovations. In: Conference proceedings of the society for experimental mechanics series, vol 8. Jacksonville, FL, pp 399–404

Chapter 32
Damage Identification from Flexibility Matrix Using Wavelet Transform

M. Masoumi and M.R. Ashory

Abstract In this paper, a new approach is proposed to localize the damages in structures using continuous wavelet transform (CWT) based on uniform load surface (ULS) and without implementing baseline model parameters. Uniform load surface is derived from the flexibility matrix technique which is highly sensitive to the cracks of structures. In the last decades, CWT has introduced itself as a powerful tool in the field of damage detection due to its inherent merits of finding abnormalities in the time and spatial signals. This work develops a new method to investigate the location of crack in the beam-type structures by uniform load surface method. ULS is derived from the mode shapes of the damaged structure and CWT is utilized to find its irregularities. A numerical simulation is conducted to demonstrate the effectiveness of the procedure. In order to investigate the sensitivity of method to noisy data, different noise levels are considered in the numerical model. Finally, in order to show the practicability of this technique, an experimental test has been performed.

Keywords Damage detection • Wavelet transform • Flexibility matrix

32.1 Introduction

Defects and flaws in some structures such as railway and road bridges or aircraft's bodies caused by environmental effects or accidental loads may result in disastrous consequences. Due to its crucial importance, several investigations with the purpose of introducing new effective approaches to localize damages in structures have been performed over the past century.

The idea of using vibration based methods is to identify damage in any system due to the fact that it causes changes in dynamic behavior of structure. Changed by damages, modal parameters (mode shape, damping ratio, natural frequency) can be used as valuable factors to localize defects.

Wavelet transform has achieved a considerable reputation as an effective method for localizing damages in structures due to its intrinsic properties to diagnose small irregularities of signals. Recently, significant efforts have been devoted to use wavelet transform as a practical tool for analyzing the signals which are obtained from vibration measurements. Taha et al. [1] provided a useful and intensive review of using wavelet transform in structural health monitoring. Wang and Deng [2] suggested an approach based on spatial Haar discrete wavelet transform with the purpose of directly studying structural response signals such as displacement, strain or acceleration measurements. Continuous wavelet transform was applied on mode shapes by Hong et al. [3]. Gentile and Messina [4] provided a useful study on applying continuous wavelet transform (Gaussian family) on mode shapes of a beam with open crack.

Damage detection technique based on changes in flexibility of structures developed due to the fact that although stiffness matrix is changed by cracks, this matrix is dominated by higher mode shapes which are difficult to measure in practice. In conflict with stiffness, flexibility matrix is dominated by lower mode shapes and then it is easier to construct. Zhang and Aktan [5] suggested utilizing Uniform Load Surface (ULS) instead of flexibility matrix. Wu and Law [6] developed ULS curvature for 2-D plate and they used Chebyshev polynomial approximation as an alternative way to localize damage.

M. Masoumi (✉) • M.R. Ashory
School of Mechanical Engineering, Semnan University, P.O. Box 35195–363, Semnan, Iran
e-mail: masoumi.masoud@gmail.com; mashoori@semnan.ac.ir

J.M. Caicedo et al. (eds.), *Topics on the Dynamics of Civil Structures, Volume 1*,
Conference Proceedings of the Society for Experimental Mechanics Series 26,
DOI 10.1007/978-1-4614-2413-0_32,

Bernal and Gunes [7] put forward a technique on the basis of out-put only data. Realizing that it is impossible to construct flexibility matrix form out-put only data, they used alternative matrix which did not cause any problem to implement damage locating vector (DLV) procedure.

Generalized Fractal Dimension, Simplified Gapped-smoothing, central difference and Chebyshev polynomial in association with ULS have been used as damage identification methodologies [6, 8]. The objective of this paper is to propose a new approach based on CWT in conjunction with ULS obtained from only damaged structure. A brief review of two concepts is introduced, and then a numerical simulation is conducted with the aim of demonstrating procedure. In order to probe the sensitivity of method to noisy data, different noise levels are studied. Finally, for the purpose of showing the practicability of this technique, an experimental test is performed.

32.2 Theory

32.2.1 Theory of Wavelet

Slight damages do not yield drastic changes in dynamic behavior of structures. Signal processing can be used as an effective instrument to diagnose small abnormalities in response signals of vibration test. One of the State-of-the-art signal processing methods which recently has been come into focus in damage detection area is wavelet transform (WT) owing to its advantages over traditional methods to analyze signals based upon windowing and variable -sized regions process. Continuous wavelet transform of a time signal *f(t)* is presented as:

$$W(\tau, s) = \frac{1}{\sqrt{s}} \int_{-\infty}^{\infty} f(t)\psi\left(\frac{t-\tau}{s}\right) dt \tag{32.1}$$

where $s > 0$ and τ are scaling (dilation) and position (shift) parameters of the wavelet function $\psi(t)$, respectively. Position parameter denotes moving window site and dilation points to size of this window. Selecting different complex functions $\psi(t)$ called *mother wavelet* leads to create various families of wavelets. Although, mother wavelet can be any arbitrary function, it should satisfy specific conditions:

$$\int_{-\infty}^{\infty} \psi(t)dt = 0, \tag{32.2}$$

$$\int_{-\infty}^{\infty} |\psi(t)|^2 dt < \infty \tag{32.3}$$

where second term is refer to energy of mother wavelet and therefore it should be limited. Number of vanishing moments is important when it comes to find abnormalities of signals. For any wavelet with n vanishing moments there is function $\theta(x)$ and it is defined as [9].

$$\psi(x) = (-1)^n \frac{d^n\theta(x)}{dx^n}, \int_{-\infty}^{+\infty} \theta(x)dx \neq 0 \tag{32.4}$$

Gentile and Messina [4] showed that a CWT with n vanishing moment and small scale s is equivalent to nth derivative except for the intervals near the boundary conditions where there are discrepancies in two approaches. As the number of discrete points increases, accuracy of CWT in boundaries upsurges. Although wavelets holding greater number of vanishing moments lead to better performance, we should yearn for reconciliation between number of vanishing moments and number of data points because higher vanishing moments needs longer support.

Granted, number of vanishing moments plays a prominent role in damage detection, but there is another important parameter and it is mother wavelet. Up to now, several kinds of mother wavelet have been implemented to analyze mode shapes [3, 10, 11–16]. In this study three kinds of CWTs are considered including; Gaussian with four vanishing moments, symmetrical 4 and bior 6.8, in order to find abnormalities of ULS.

32.2.2 Theory of ULS Method

Definition of modal flexibility matrix for a system with m lower measured modes is given by [5]:

$$f_{i,j} = \sum_{k=1}^{m} \frac{\phi_k^i \phi_k^j}{\omega_k^2} \tag{32.5}$$

where ϕ_k^i and ϕ_k^j are i^{th} and j^{th} elements of k^{th} mass normalized mode shape, respectively. ω_k denotes k^{th} natural frequency and $f_{i,j}$ is the modal flexibility at point i due to the unit load at the point j. For a linear system, deflection at point i due to the uniform load all over the structure is obtained as

$$u(i) = \sum_{j=1}^{n} f_{i,j} = \sum_{j=1}^{n} \left(\sum_{k=1}^{m} \frac{\phi_k^i \phi_k^j}{\omega_k^2} \right) = \sum_{k=1}^{m} \frac{\phi_k^i \sum_{j=1}^{n} \phi_k^j}{\omega_k^2} \tag{32.6}$$

where n indicates the number of degree-of-freedom. Having its advantages over modal flexibility, ULS is privileged in terms of lower contribution of higher order modes which it leads to more convergence with the lower modes and makes it as a valuable and stable damage indicator. Moreover, it is less vulnerable to noise due to the fact that summation of all the modal coefficients of a specific mode averages out the random error at every measurement point [5].

32.3 Damage Identification Procedure

In order to interrogate of damages by suggested technique, mode shapes obtained from damaged beam is utilized to construct ULS based on (32.6) and then CWT uses to investigate abnormality as damage location. Objective of this section is met in two steps; first, a numerical investigation of proposed damage detection methodology on a cantilever beam will carry out and its sensitivity to noisy data is analyzed. Then a laboratory test is performed with the aim of verifying the method.

32.3.1 Numerical Analysis Studies

To explain how wavelet transforms in conjunction with ULS method can be used as a damage detection indicator, a cantilever beam is considered. Geometry of the beam and its material properties are as follows: Young's modulus $E = 200\,Gpa$, density $\rho = 7,850\ \text{kg/m}^3$, length $l = 750\,mm$, Cross sectional area is $A = w \times h = 50 \times 10\,mm$. Total number of elements of FE model is 50. Damage is considered as a reduction in stiffness matrix while mass matrix is unchanged and it is simulated by the method proposed by Gentile and Messina [17] (Fig. 32.1).

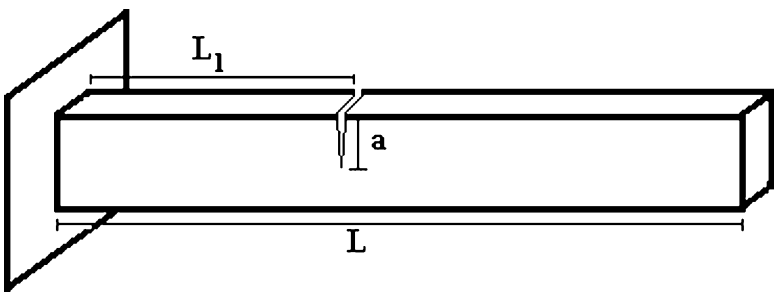

Fig. 32.1 Schematic damaged beam

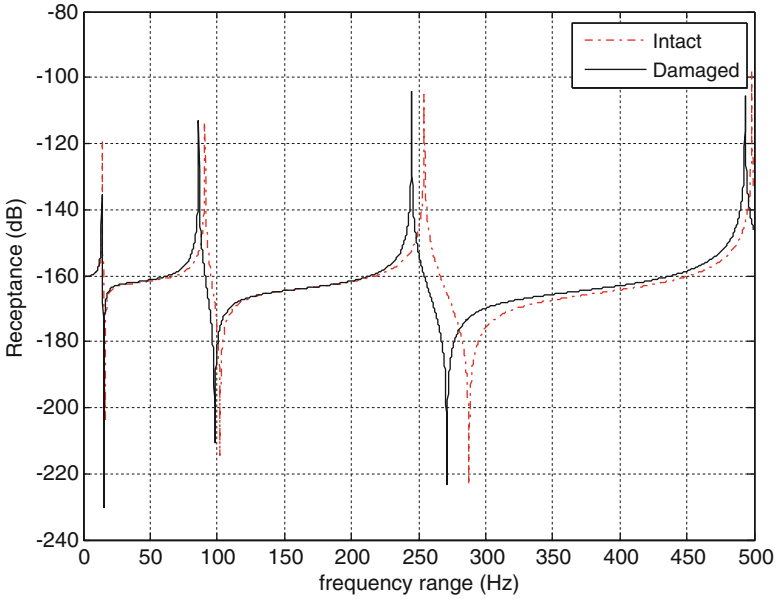

Fig. 32.2 FRF of intact and damaged beam at a typical measurement point for 20% damage

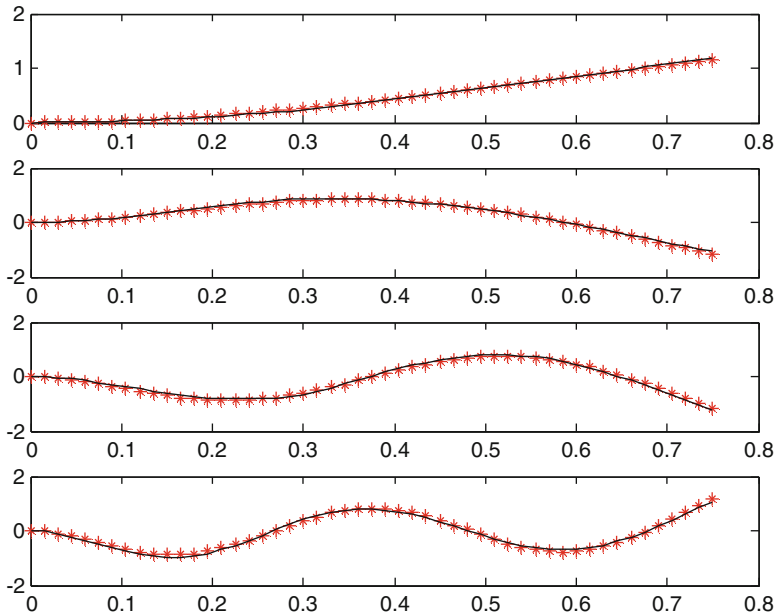

Fig. 32.3 The first three mode shapes of intact (*) and damaged (−) beam for 20% damage

32.3.1.1 Noise Free Mode Shapes

Twenty percent damage is considered and it's induced at $l_1 = 300$ mm. In Fig. 32.2 frequency response functions (FRFs) of intact and damaged beam at a typical measurement point is presented. As expected, damage results in shifts in natural frequencies. Also Fig. 32.3 shows that the first three mode shapes of beam before and after inducing 20% damage are not noticeably different.

In order to perform the method, ULS for the damaged case calculated by (32.6) and then sp-line interpolation and extrapolation was utilized to obtain refined grid points between measurement points and at boundary condition points, respectively. Refined ULS analyzed by three CWTs which have been mentioned in Sect. 32.2. Figure 32.4 shows the results.

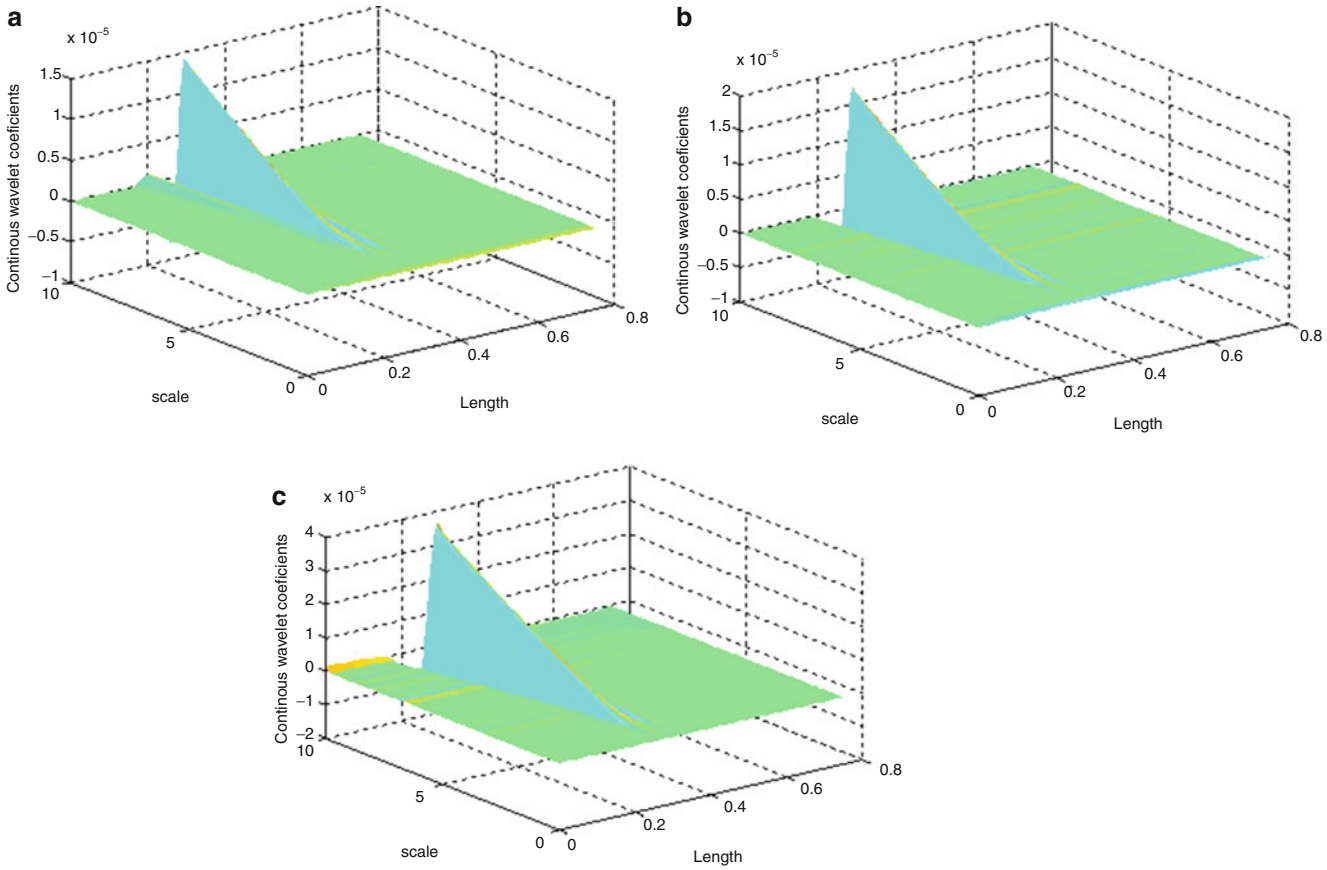

Fig. 32.4 Twenty percent damage (**a**) bior 6.8 (**b**) sym4 (**c**) gaus4

Coefficients for three kinds of wavelets are nearly zero at the locations far from crack sites and they considerably surge when they meet the crack. Although, *symmetrical 4* and *Gaussian* wavelets like *bior 6.8* are useful instrument for localizing damage, there are irregularities in some scales. In compare with *bior 6.8,* maximum values of coefficients are greater at crack site.

32.3.1.2 Contaminated Mode Shapes

In order to cope with noises which are inexorable in experimental tests, effects of noise in damage detection methods should be probed. In this section with the aim of investigating the ability of proposed method to deal with noises, contaminated mode shapes are utilized to construct ULS and outcome has used to draw a comparison between earlier ULS method which employs central difference and introduced approach which implements wavelet transforms to magnify irregularities. Simulated mode shapes of damaged case are contaminated with different level noises. Function that is used to aim to this goal is as follow [18]:

$$\varphi'_{ij} = \phi_{ij} + r_{ij}\rho\phi_{rms,j}$$

where ρ is the level of random noise, ϕ_{ij} and φ'_{ij} are noise free mode shapes and contaminated mode shapes, respectively; r stands for normally distributed random variables with a zero mean and variance equal to 1 and $\phi_{rms,j}$ is the root of mean square of j^{th} mode shape. Contaminated mode shapes have been considered and three wavelets appointed have been used to interrogate crack location. Results pertaining to 20% induced damage tainted with $\rho = 0.0003$ noise level is showed in Fig. 32.5.

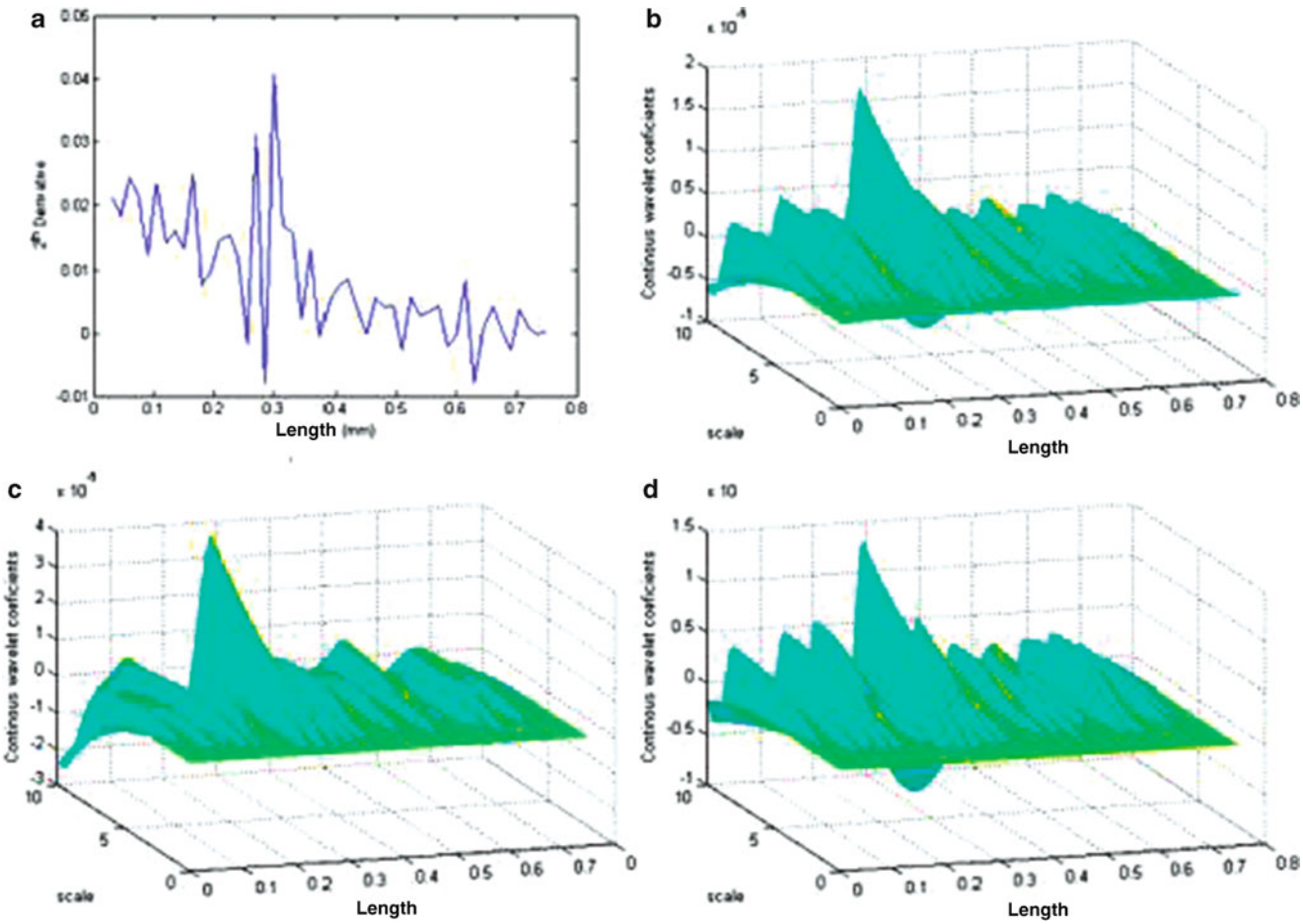

Fig. 32.5 Comparison between three wavelet methods and central difference in presence of noise ($\rho = 0.0003$), (**a**) central difference, (**b**) symmetrical 4, (**c**) Gaussian 4 (**d**) bior 6.8

As results show, with this level of noise both of central difference method and three kinds of wavelets are able to identify crack location. By increasing noises to $\rho = 0.0005$ wavelet methods manifest their abilities to discern damage (Fig. 32.6)

32.3.2 Experimental Studies

A cantilever beam has been used as an experimental case to investigate the practicality of proposed method. The dimensions of the damaged beam are 750×50×10 mm and a 20% damage was located at $l_1 = 300mm$. The displacement data is sampled at 36 data points and a sp-line interpolation and extrapolation has been utilized to refine the ULS. An accelerometer was located at 270 mm from clamped end (Fig. 32.7).

Figure 32.8 shows frequency response function (FRF) for point 12 where three first natural frequencies of beam are 11.6968, 79.2722, 222.9036 (Hz) respectively.

Results of applying three wavelets to ULS demonstrate that using bior 6.8 is an effective way to find crack location where sym4 has been less helpful and Gaussian has been feeble to detect damage in this test (Fig. 32.9).

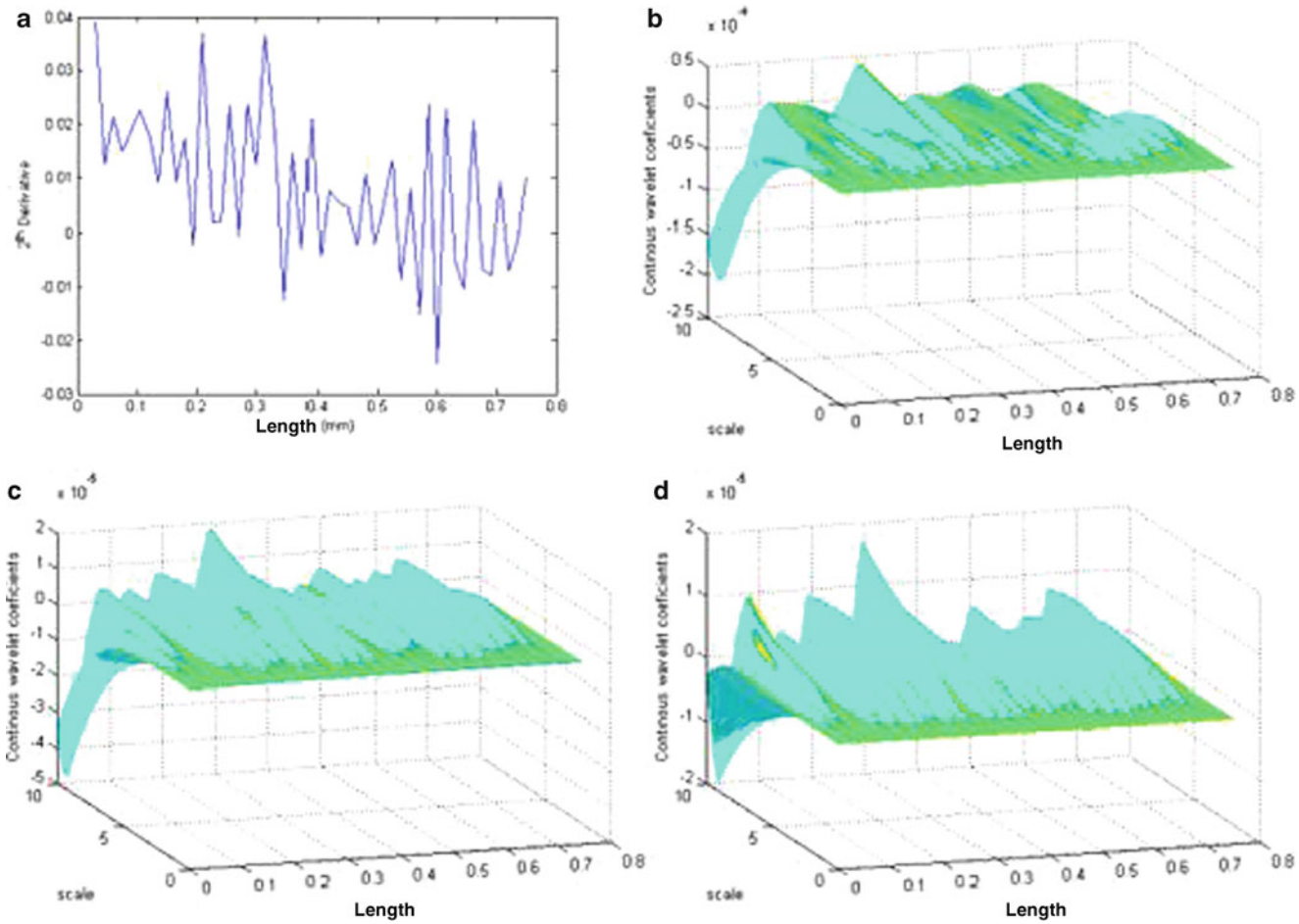

Fig. 32.6 Comparison between three wavelet methods and central difference method in presence of noise ($\rho = 0.0005$), (**a**) central difference, (**b**) Gaussian 4, (**c**) symmetrical 4 (**d**) bior 6.8

Fig. 32.7 Experimental case study

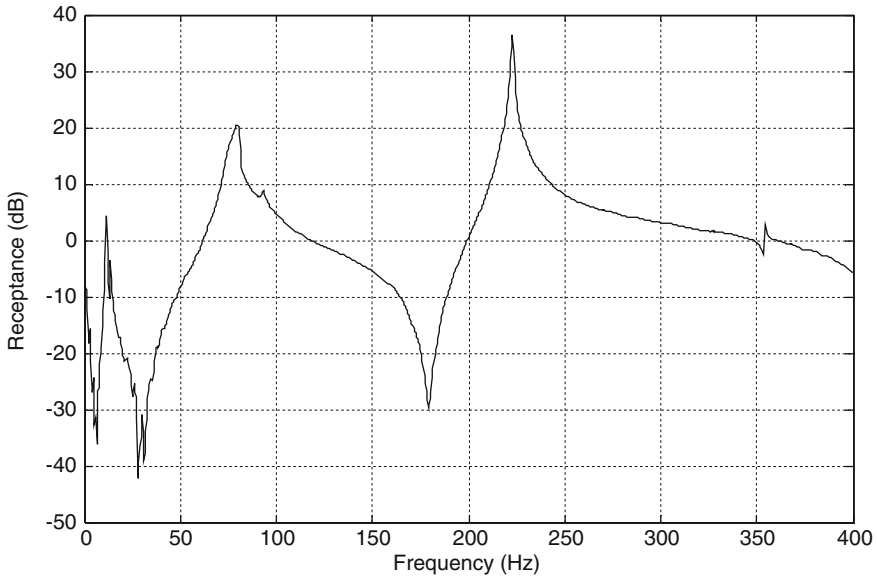

Fig. 32.8 Frequency response function for point 12

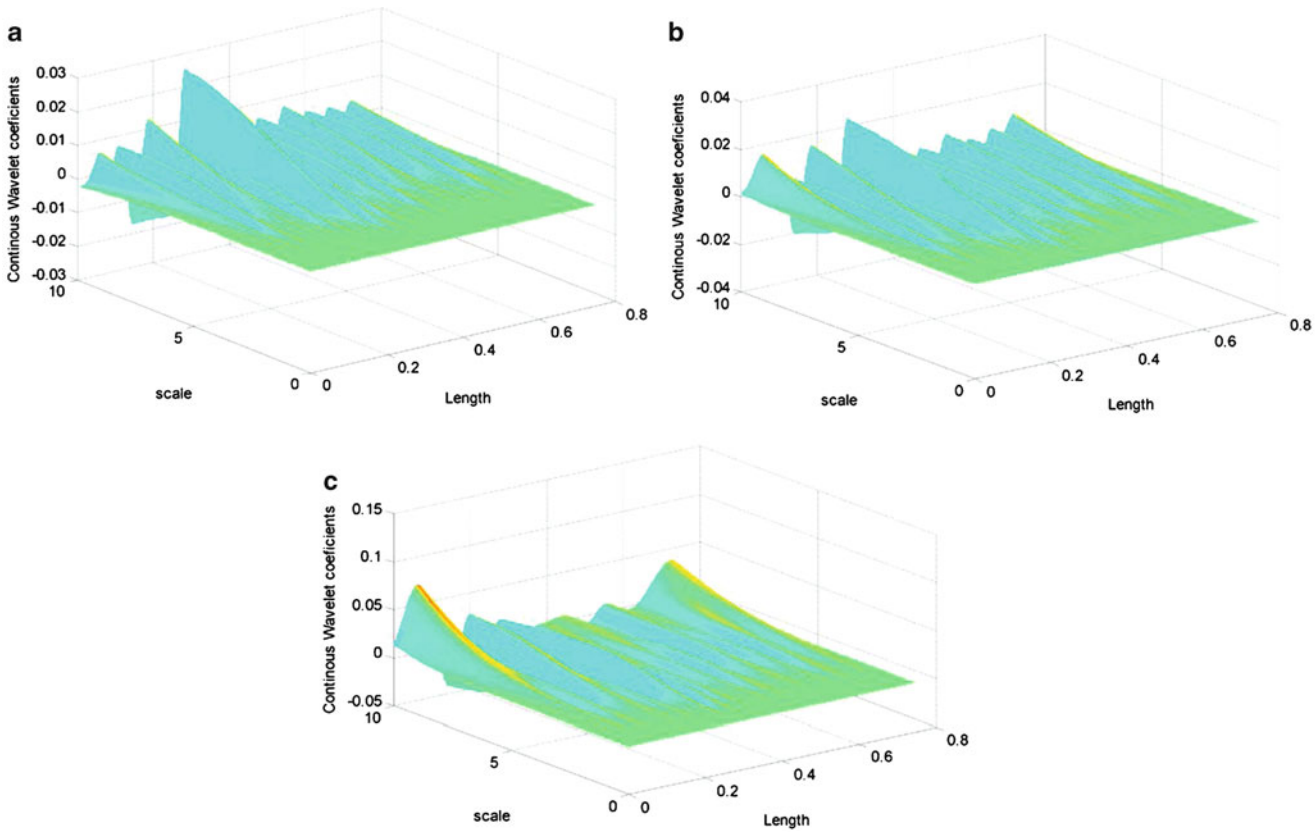

Fig. 32.9 Experimental results for (**a**) bior 6.8 (**b**) sym4 (**c**) Gaussian

32.4 Conclusions

This paper has adopted a new approach to damage identification of structures where wavelets have been employed to investigate abnormality in ULS as sign of crack instead of using finite difference. Although when noise free mode shapes used to compare proposed method with former ULS technique both of them were able to find crack sites, new approach manifests its capabilities in presence of noise. A cantilever beam as an experimental case used to verify the procedure and results showed that bior 6.8 is an effective mother wavelet in this approach. Symmetrical 4 was less useful and Gaussian 4 was unable to discern damage. Some of these incapacities stem from this fact that wavelet methods like finite difference methods cause irregularities at boundary condition points and changing the extrapolation functions at these points may result in better outcomes.

References

1. Taha MMR, Noureldin A, Lucero JL, Baca TJ (2006) Wavelet transform for structural health monitoring: a compendium of uses and features. Struct Health Monit 5:267–295
2. Wang Q, Deng X (1999) Damage detection with spatial wavelets. Int J Solids Struct 36:3443–3468
3. Hong JC, Kim YY, Lee HC, Lee YW (2002) Damage detection using the Lipschitz exponent estimated by the wavelet transform: applications to vibration modes of a beam. Int J Solids Struct 39:1803–1816
4. Gentile A, Messina A (2003) On the continuous wavelet transforms applied to discrete vibrational data for detecting open cracks in damaged beams. Int J Solids Struct 40:295–315
5. Zhang Z, Aktan AE (1998) Application of modal flexibility and its derivatives in structural identification. Res Nondestruct Eval 10:43–61
6. Wu D, Law SS (2004) Damage localization in plate structures from uniform load surface curvature. J Sound Vib 276:227–244
7. Bernal D, Gunes B (2004) Flexibility based approach for damage characterization: benchmark application. J Eng Mech 130:61–70
8. Wang J, Qiao P (2007) Improved damage detection for beam-type structures using a uniform load surface. Struct Health Monit 6:99–110
9. Mallat S, Zhong S (1992) Characterization of signals from multi-scale edges. IEEE Trans Pattern Anal Mach Intell 14:710–732
10. Quek ST, Wang Q, Zhang L, Ang KK (2001) Sensitivity analysis of crack detection in beams by wavelet technique. Int J Mech Sci 43:2899–2910
11. Rucka M, Wilde K (2006) Application of continuous wavelet transform in vibration based damage detection method for beams and plates. J Sound Vib 297:536–50
12. Douka E, Loutridis S, Trochidis A (2003) Crack identification in beams using wavelet analysis. Int J Solids Struct 40:3557–69
13. Okafor AC, Dutta A (2000) A structural damage detection in beams by wavelet transforms. Smart Mater Struct 9:906–17
14. Rucka M, Wilde K (2006) Crack identification using wavelets on experimental static deflection profiles. Eng Struct 28:279–88
15. Ovanesov AV, Su'arez LE (2004) Applications of wavelet transforms to damage detection in frame structures. Eng Struct 26:39–49
16. Carri'on FJ, Lozano A, Castão VM (2006) Condition monitoring of vibrating steel reinforced concrete beams through wavelet transforms. Struct Surv 24:154–62
17. Gentile A, Messina A (2002) Detection of cracks by only measured mode shapes in damaged conditions. In: Proceedings of the 3rd international conference on identification in engineering systems, Swansea
18. Fan W, Qiao P (2011) Vibration-based damage identification methods: a review and comparative study. Struct Health Monit 10:83–111

Chapter 33
Optimum Column Layout Design of Reinforced Concrete Frames Under Wind Loading

P. Sharafi, Muhammad N.S. Hadi, and Lip H. Teh

Abstract The geometric layout optimization of a structure is a significant stage in a design process, and selecting an appropriate geometric layout can impact all the subsequent stages of the design procedure and the relevant costs. This study presents a heuristic approach for the optimum layout design of two-dimensional reinforced concrete frames in order to optimize the total cost and controls the application under wind loadings. The aim is to find the optimum column layout design for 2D frames under wind loadings considering the involved cost elements. A heuristic methodology is developed in order to achieve a new design space and an objective function for the cost and layout optimization problem. The proposed method has the capability to make use of action effects of the structure as alternative design variables in place of the commonly used cross-sectional ones. Such a feature provides the method the ability to be easily employed in large and realistic structural optimization problems, and helps the optimization algorithms to take less time, in an iterative optimization process. Then, an Ant System based algorithm is proposed to solve the presented optimization problem. Examples are included to illustrate the robustness of the methodology.

Keywords Cost optimization • Layout optimization • Reinforced concrete • 2D frame • ACO

33.1 Introduction

Layout optimization is a relatively new but extremely rapidly expanding research field, which has interesting theoretical implications in applied mathematics but also important practical applications by the manufacturing and structural industries. The main motivation of the present paper comes from the study of the impacts of the column layout optimization of frames on the total cost under wind loading. In fact, due to the sensitivity of the structural layout to the lading system, the effects of wind loads on optimum column layout design is studied.

Primary layout design of a frame impacts the entire design process and consequently, the total costs of the building. In order to select the most economical plan among various layouts, which satisfy architectural requirements, one needs a full awareness of the reciprocal effects of cost factors and layout variables. That is, achieving an economical layout plan, particularly in reinforced concrete structures, requires to consider both cost and layout elements simultaneously.

Cost optimization of RC structures has, over the past decades, been developed using a variety of methods. However, one limiting feature of such methods which have been developed is that the representation is limited to either single structures or structures with predefined shapes. A review of past work done in the field of optimal design of RC structures shows that a large fraction of the early works are mostly confined to cost optimization of individual members [1]. A number of studies have been published on either cost optimization or layout optimization of RC structures.

Balling and Yao [2] and Zou et al. [3] considered the optimization of the RC frames. Shaw et al. [4] developed a method for columns layout for orthogonal buildings. Nimtawat and Nanakron [5, 6] proposed a genetic algorithm based method for beam–slab layout design of rectilinear floors without considering the cost elements. Zhu and Zhang [7] presented a new

P. Sharafi • M.N.S. Hadi (✉) • L.H. Teh
School of Civil, Mining and Environmental Engineering, University of Wollongong, Northfields Avenue, Wollongong, NSW 2522, Australia
e-mail: mhadi@uow.edu.au

J.M. Caicedo et al. (eds.), *Topics on the Dynamics of Civil Structures, Volume 1*,
Conference Proceedings of the Society for Experimental Mechanics Series 26,
DOI 10.1007/978-1-4614-2413-0_33,

method for designing the structures layout. Sahab et al. [8, 9] considered the cost and topological optimization of flat slab buildings. There are also a large number of published studies on the cost optimization of RC beams and columns [1]. This small number of papers in this field is mainly due to the complexity of such a formulation for large reinforced concrete structures. Even so, the reciprocal effects of cost and topology of large RC structures have not been adequately considered.

In this study, a methodology is proposed to deal with the cost optimization problem of reinforced concrete beams and columns, which can be used in layout optimization of 2D RC frame buildings. Then, using this new function and employing the Ant System method, a new algorithm is proposed in order to find the optimum locations of columns under wind loads to minimize the cost of 2D frame as a multi-variable optimization problem, which considers geometric layout and cross-sectional variables simultaneously. The first ACO algorithm was Ant System (AS), developed by Dorigo et al. [10] which has successfully been applied to many combinatorial optimization problems. Kaveh et al. [11] presented an ACO algorithm for structural topology optimization. Camp et al. [12] proposed an Ant based algorithm for design of steel frames.

33.2 The Problem Definition and Mathematical Formulation

One of the most important phases in the optimal design process is the selection of the cost function which is generally a function of design variables. Depending on the nature of the optimization problem, the process of achieving an optimum feasible solution might be much quicker, shifting from one design space to another by changing design variables as the space dimensions. That is, one may shift from one set of design variables to another that causes a new definition for the objective function and may lead to changes in constraints and even vary their nature from design variables to behavior ones and vice versa. A cost function generally includes the cost of materials, transportation, fabrication and even maintenance costs, in addition to repair and insurance costs, which can be presented by a weighted sum of a number of properties. The effect of these factors in optimal cost can be imposed on the weighted coefficients of the cost function. In concrete structures, at least three different cost items should be considered in optimization: costs of concrete, steel, and the formwork. So, the general cost function for a 2D reinforced concrete frame consisting of beams and columns can be expressed in the following form:

$$\begin{cases} C^{(b)} = c_c A_c^{(b)} + c_{sl} A_{sl}^{(b)} + c_{sv} A_{sv}^{(b)} + c_f \ P_f^{(b)} \\ C^{(c)} = c_c A_c^{(c)} + c_{sl} A_{sl}^{(c)} + c_{sv} A_{sv}^{(c)} + c_f \ P_f^{(c)} \\ C = \sum_1^{N_b} C^{(b)} + \sum_1^{N_c} C^{(c)} \end{cases} \tag{33.1}$$

where c_c, c_{sl}, c_{sv} and c_f are the unit costs of concrete, longitudinal steel, shear steel and formwork respectively and A_c, A_{sl}, A_{sv} and P_f are their corresponding quantities. The superscript (c) stands for the columns parameters and the superscript (b) for beams and N_c and N_b are the number of columns and beams in the frame respectively.

In most published studies, the cost optimization functions deal only with cross-sectional variables which mainly suits structures with a small number of members and a predefined geometric layout. In fact, in layout design of structures, the cross-sectional variables are functions of design action effects which are not determinate and vary as the shape changes. Therefore, in an iterative procedure to solve an optimization problem, each step includes dealing with both the structural analysis and structural design variables. In such cases, unless alternative design variables are selected for the cost function, the optimization procedure might be too unwieldy.

That is while parameters like cross-sectional variables are mainly obtained from implicit functions of structural analysis outputs based on the suggested relations and constraints in the design standards. On the other hand design standards do not uniquely provide the exact values for these cross-sectional parameters and they are not obtained from an explicit mathematical procedure.

In a layout optimization problem considering the cost elements, besides the classic cross-sectional variables, the layout of a structure and consequently the outputs of structural analysis would be the variables of the problem. If the reciprocal relationships between the cross-sectional design factors and the design action effects are determined the cost function can be presented by a function of design action effects. In the design process, design action effects are determined for the critical sections of members and then cross-sectional variables are calculated for each section. Cross-sectional parameters along the structural members are obtained from their value in critical sections and based on the relations in the design standards. In fact, having the design action effects in critical sections, all the cross-sectional parameters and consequently, the total cost based on (33.1) can be calculated. To put it simply, using structural analysis outputs, say internal actions of a member, as design variables has some advantages over using structural design outcomes such as cross-sectional characteristics of a

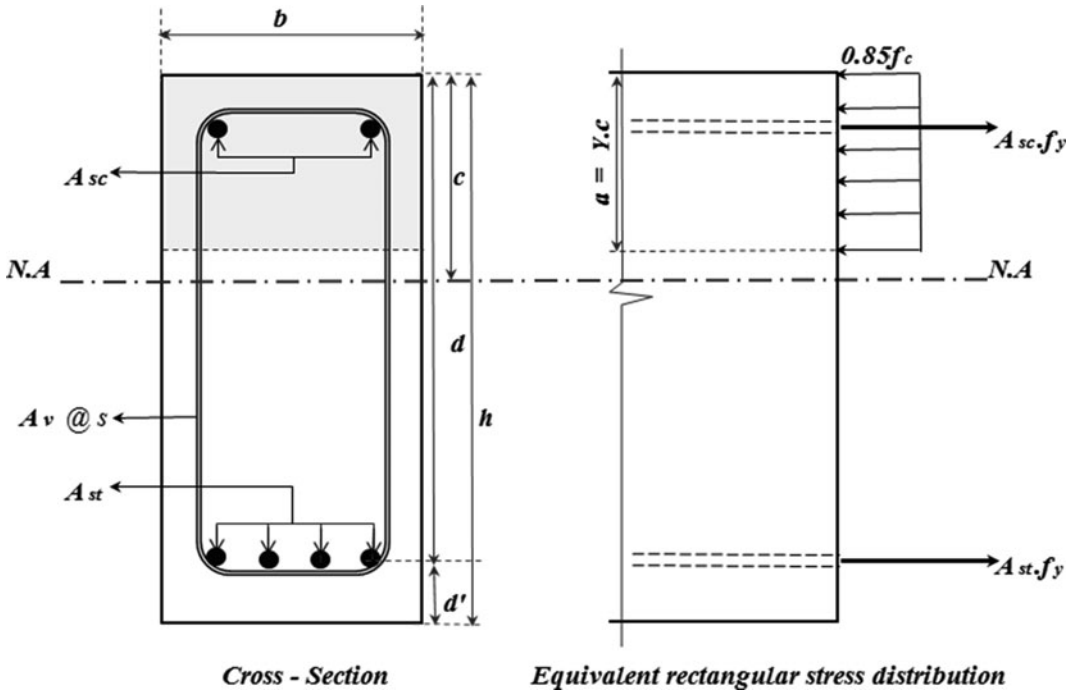

Fig. 33.1 Cross-sectional parameters for a beam

beam. Firstly, design action effects of each section can be easily obtained from structural analysis, and in an iterative mathematical procedure, re-analyzing a structure is considerably less time-consuming and more precise than re-designing the structure. Moreover, using action effects, the cost function will be considered in a section rather than a member. It enables the designer to select a number of sections for each member and in the whole structure to control the cost, and there is no necessity to conduct the optimization process over the entire member.

Therefore the aim is to explore the relation between the variations of action effects of RC members with the variations of the cross-sectional parameters and find out how these two types of variables affect each other. Then, based on such relations, a new cost function is obtained which is a function of action effects rather than cross-sectional parameters.

In order to formulate the structural optimization problem this study makes use of the relations in the Australian standards for concrete structures (AS3600-2009) [13] and Structural design actions for wind (AS/NZS1170.2-2011) [14], which is based on the limit state design method of concrete structures. Frames consist of two groups of structural elements: beams and columns; which have key roles in the total cost of a frame.

33.2.1 Formulation for Beams

For a beam to be designed, three action effects are taken into consideration: positive bending moment, negative bending moment and shear forces. Consider an arbitrary section of a rectangular reinforced concrete beam as shown in Fig. 33.1. The dimensions of the section are b and $h^{(b)}$, the areas of tension and compression reinforcement steel are $A_{st}^{(b)}$, $A_{sc}^{(b)}$ and the area of shear reinforcement steel in a unit length of beam is $A_{sv}^{(b)}/s$.

Now, consider (33.2) as a potential alternative cost functions to (33.1) in an arbitrary RC beam section.

$$C_i^{(b)} = c_1 M_{u_i}^{+(b)} + c_2 M_{u_i}^{-(b)} + c_3 V_{u_i}^{(b)} \tag{33.2}$$

The capacity or the ultimate strength of the section in negative and positive flexure and shear for Section i are $M_{u_i}^{-(b)}$, $M_{u_i}^{+(b)}$ and $V_{u_i}^{(b)}$ respectively,

In order to shift from (33.1) to (33.2) and come up with the set of $\{c_1, c_2, c_3\}$, the first step is to determine how variations of $A_c^{(b)}$, $A_{sl}^{(b)}$, $A_{sv}^{(b)}$ and $P_f^{(b)}$ affect $M_u^{+(b)}$, $M_u^{-(b)}$ and $V_u^{(b)}$, and vice versa. That is, the reciprocal relationships between these two

sets of variables need to be identified to find out how increasing or decreasing the amount of each cross-sectional feature influences the section strength capacities and how one should change the cross-sectional parameters to vary section capacities. Given the unit costs c_c, c_{sl}, c_{sv} and c_f, the cost function can be defined using (33.1) for each section of a beam. The parameters $A_c^{(b)}, A_{sl}^{(b)}, A_{sv}^{(b)}$ and $P_f^{(b)}$ are obtained from the sum of the cross-sectional variables for all beams. If any of cross-sectional parameters changes, the cost function varies as follows

$$\Delta C^{(b)} = c_c \Delta A_c^{(b)} + c_{sl} \Delta A_{sl}^{(b)} + c_{sv} \Delta A_{sv}^{(b)} + c_f \Delta P_f^{(b)} \tag{33.3}$$

On the other hand, using (33.2) variations in section capacities would change the cost function as follows

$$\Delta C^{(b)} = c_1 \Delta M_{u_i}^{+(b)} + c_2 \Delta M_{u_i}^{-(b)} + c_3 \Delta V_{u_i}^{(b)} \tag{33.4}$$

Equations 33.3 and 33.4 show the contribution of each factor to cost changes and sensitivity of the cost to each term. For example, changing a unit of $A_c^{(b)}$ causes a change of c_c units in cost. Therefore, if the effect of variations of $A_c^{(b)}, A_{sl}^{(b)}, A_{sv}^{(b)}$ and $P_f^{(b)}$ on the variations of $M_u^{+(b)}$, $M_u^{-(b)}$ and $V_u^{(b)}$ are determined, the contribution of each section capacity to cost changes, that is the set of $\{c_1, c_2, c_3\}$, can be found out.

According to the calculations presented in the Appendix, and the relevant relations and clauses in AS3600-2009 [13], the set of $\{c_1, c_2, c_3\}$ in (33.4) can be presented with regard to the set of predefined cost coefficients $\{c_c, c_{sl}, c_{sv}, c_f\}$ in (33.1).

$$\begin{cases} c_1 = \frac{1}{3} c_c K_4 + \frac{1}{2} c_{sl} K_1 + \frac{2}{3} c_f K_7 \\ c_2 = \frac{1}{3} c_c K_3 + \frac{1}{2} c_{sl} K_1 + \frac{2}{3} c_f K_6 \\ c_3 = \frac{1}{3} c_c K_5 + c_{sv} K_2 + \frac{2}{3} c_f K_8 \\ \quad - - - - - - - - - - - - - - - \\ K_1 = \left(f_{yl}\, d^{(b)} (1 - 0.5\gamma\, k_u)\right)^{-1} \\ K_2 = \left(f_{yv}\, d\right)^{-1} \Delta V_u^{(b)} \\ K_3 = \left[f_{yl} \frac{A_{sc}^{(b)}}{b} (1 - 0.5\gamma\, k_u) \right]^{-1} \\ K_4 = \left[f_{yl} \frac{A_{st}^{(b)}}{b} (1 - 0.5\gamma\, k_u) \right]^{-1} \\ K_5 = \left[f_{yl} \frac{A_{st}^{(b)}}{b} (1 - 0.5\gamma\, k_u) \right]^{-1} \\ K_6 = 2\left[f_{yl} A_{sc}^{(b)} (1 - 0.5\gamma\, k_u) \right]^{-1} \\ K_7 = 2\left[f_{yl} A_{st}^{(b)} (1 - 0.5\gamma\, k_u) \right]^{-1} \\ K_8 = \left[\frac{2}{\frac{f_{yu} A_{sv}^{(b)}}{s} + \beta b (f'_c)^{\frac{1}{2}}} + \frac{1}{\beta d (f'_c)^{\frac{1}{2}}} \right] \end{cases} \tag{33.5}$$

where f_{yl} is the yield strength of the longitudinal reinforcement, f_{yv} is the yield strength of the shear reinforcement, f'_c is the characteristic compressive cylinder strength of concrete at 28 days, The coefficients γ and k_u are calculated based on the characteristic strength of the concrete and reinforcing steel, β is a coefficient based on the standard, and s is the centre-to-center spacing of shear reinforcement. Other parameters are shown in Fig. 33.1. The obtained coefficients c_1, c_2 and c_3 determine how the variations of bearing capacities $M_{u_i}^{+(b)}$, $M_{u_i}^{-(b)}$ and $V_{u_i}^{(b)}$ contribute to the variation of cost function. K_1 trough K_8 are calculated based on the equations presented in the Appendix.

33.2.2 Formulation for Columns

Consider an arbitrary section of a square reinforced concrete column as shown in Fig. 33.2. The dimensions of the section are $h^{(c)}$, the areas of longitudinal reinforcement steel is $A_{sl}^{(c)}$ and the area of shear reinforcement steel in a unit length of beam is $A_{sv}^{(c)}/S$.

Now, consider (33.6) as a potential alternative cost functions to (33.2) in an arbitrary RC column section.

$$C_i^{(c)} = c_4 N_{u_i}^{(c)} + c_5 M_{u_i}^{(c)} + c_6 V_{u_i}^{(c)} \tag{33.6}$$

where $N_{u_i}^{(c)}$, $M_{u_i}^{(c)}$ and $V_{u_i}^{(c)}$ are the axial load-carrying capacity, bending moment capacities and the shear capacity of the ith column section respectively. If an appropriate set of $\{c_4, c_5, c_6\}$ could be found, in such a way that (33.6) represents the cost of the section, the design variables would shift from $A_c^{(c)}$, $A_{sl}^{(c)}$, $A_{sv}^{(c)}$ and $P_f^{(c)}$ to $N_u^{(c)}$, $M_u^{(c)}$ and $V_u^{(c)}$.

If any of cross-sectional parameters changes, the cost function varies as follows

$$\Delta C^{(c)} = c_c \Delta A_c^{(c)} + c_{sl} \Delta A_{sl}^{(c)} + c_{sv} \Delta A_{sv}^{(c)} + c_f \Delta P_f^{(c)} \tag{33.7}$$

On the other hand, using (33.6) variations in section capacities would change the cost function as follows

$$\Delta C^{(c)} = c_4 \Delta N_u^{(c)} + c_5 \Delta M_u^{(c)} + c_6 \Delta V_u^{(c)} \tag{33.8}$$

Equations 33.7 and 33.8 show the contribution of each factor to cost changes and sensitivity of the cost to each term. Therefore, if the effect of variations of $A_c^{(c)}$, $A_{sl}^{(c)}$, $A_{sv}^{(c)}$ and $P_f^{(c)}$ on the variations of $M_u^{+(c)}$, $M_u^{-(c)}$ and $V_u^{(c)}$ are determined, the contribution of each section capacity to cost changes, that is the set of $\{c_1, c_2, c_3\}$, can be found out.

According to the calculations presented in the Appendix, and the relevant relations and clauses in AS3600-2009 [13], the set of $\{c_4, c_5, c_6\}$ in (33.7) can be presented with regard to the set of predefined cost coefficients $\{c_c, c_{sl}, c_{sv}, c_f\}$ in (33.1).

$$\begin{cases}
c_4 = \dfrac{1}{3}c_c K_{12} + \dfrac{1}{2}c_{sl} K_9 + \dfrac{1}{3}c_f K_{15} \\
c_5 = \dfrac{1}{3}c_c K_{13} + \dfrac{1}{2}c_{sl} K_{10} + \dfrac{2}{3}c_f K_{16} \\
c_6 = \dfrac{1}{3}c_c K_{14} + c_{sv} K_{11} + \dfrac{2}{3}c_f K_{17} \\
\quad - - - - - - - - - - - - - - \\
K_9 = \left(E_s \sum_i^n \varepsilon_i\right)^{-1} \\
K_{10} = \left(E_s \sum_i^n \varepsilon_i e_i\right)^{-1} \\
K_{11} = \left(f_{yv}\, d^{(c)}\right)^{-1} \\
K_{12} = (0.85\gamma k_u f'_c)^{-1} \\
K_{13} = (0.85\gamma k_u f'_c e_c)^{-1} \\
K_{14} = \left(\dfrac{f_{yv} A_{sv}^{(c)}}{2hs} + \beta (f'_c)^{0.5}\right)^{-1} \\
K_{15} = \left(0.85\gamma k_u f'_c \dfrac{h^{(c)}}{2}\right)^{-1} \\
K_{16} = \left(0.85\gamma k_u f'_c \dfrac{h^{(c)}}{2} e_c\right)^{-1} \\
K_{17} = \left(\dfrac{f_{yv} A_{sv}^{(c)}}{4s} + \dfrac{1}{2}\beta h^{(c)} (f'_c)^{0.5}\right)^{-1}
\end{cases} \tag{33.9}$$

in which E_s is the modulus of elasticity of reinforcement, $A_{sl_i}^{(c)}$ and e_i are respectively the cross-sectional area of reinforcement and the distance from the extreme compression fiber for each bar, n is the number of bars in a column, ε_i is the strain in

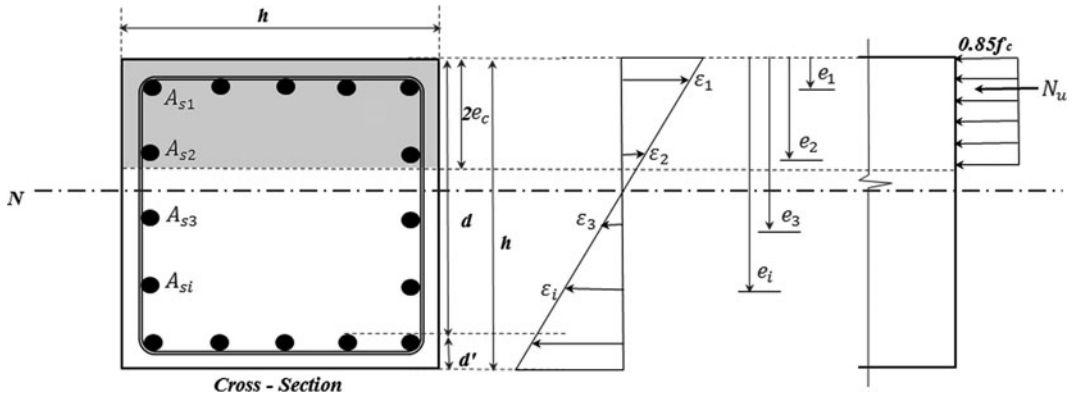

Fig. 33.2 Cross-sectional parameters for a column

reinforcement. The parameters e and e_c are the eccentricity of the axial force from the centroidal axis and the distance from the extreme compression fiber for compressive force in the concrete of the cross-section, respectively. Other parameters are shown in Fig. 33.2. Obviously, if the column section is subject to a biaxial bending moment or shearing forces bending moment and shear force are considered for both axes.

The coefficients c_4, c_5 and c_6 determine how the parameter $N_{u_i}^{(c)}$, $M_{u_i}^{(c)}$ and $V_{u_i}^{(c)}$ contribute to the cost function.

33.2.3 Optimization Formulation for Frames

Having the described coefficients in order to re-analyze a frame and to achieve the optimum criteria, one can use (33.2) and (33.6) in lieu of (33.1). For this purpose, the cost will be the sum of cost functions of all selected sections in the structure based on (33.2) and (33.6).

Using the summation of (33.2) and (33.6) as an alternative cost function to (33.1), the design variables can be shifted from cross-sectional variables to action effect ones.

For a 2D RC frame under an arbitrary loading system $f(x)$ to be optimally designed in order to optimize the cost and layout, the general formulation for the structural optimization problem can be written as follows:

$$\begin{cases} \min\limits_{l_1,l_2,\ldots,l_{NSP}} Cost(l_1,l_2,\ldots,l_{NSP}) = \sum_1^{NBS} C_i{}^{(b)} + \sum_1^{NCS} C_i{}^{(c)} \\ \quad - - - - - - - - - - - - - - - - - - \\ s.t \begin{cases} \phi\left\{M_u^{+(b)}\right\} \geq \left\{M^{*^{+(b)}}\right\} \\ \phi\left\{M_u^{-(b)}\right\} \geq \left\{M^{*^{-(b)}}\right\} \\ \phi\left\{V_u^{(b)}\right\} \geq \left|V^{*(b)}\right| \\ \phi\left\{N_u^{(c)}\right\} \geq \left\{N^{*(c)}\right\} \\ \phi\left\{M_u^{+(c)}\right\} \geq \left\{M^{*(c)}\right\} \\ \phi\left\{V_u^{(c)}\right\} \geq \left\{V^{*(c)}\right\} \\ \{u_{max}\} \leq \{\Delta_{max}\} : for\ all\ members \\ \{l_{min}\} \leq \{l_i\} \leq \{l_{max}\} : for\ all\ spans \\ other\ constraints\ based\ on\ standards \end{cases} \end{cases} \tag{33.10}$$

where *NBS* and *NCS* are the total number of control beams and columns sections in the structure respectively, $C_i^{(b)}$ and$C_i^{(c)}$ are obtained from (33.2) and (33.6) and l_{min} and l_{max} are the maximum and minimum length of each span, which might be applied in order to satisfy architectural considerations, and *NSP* is the total number of spans in x and y directions. N_i^*, M_i^* and $|V_i^*|$ are axial force, flexure and shear action effects of Section i, either in columns or beams and ϕ is strength reduction factors. The serviceability requirements limit the maximum deflection u_{max} on the entire member to Δ_{max} under the serviceability load case. Other constraints for durability, fire resistance, minimum cover and minimum flexural strength, can be easily added to the problem as well, based on relevant design codes.

There are several ways to deal with the above cost optimization problem. Although the problem of finding the layout of a frame is a continuous optimization problem, it can be dealt with as a discreet problem by discretizing the domain. In fact, in the design process, we usually deal with the dimensions as discrete sizes, and in practical problems, it is often the case that design variables must be chosen within a discrete manufacturer's inventory. The dimensions of concrete sections are usually varied by a certain size, e.g. 25 or 50 mm a step, which makes the section dimensions discrete. Therefore, one can define the optimization problem of RC sections as a discrete optimization problem rather than a continuous one. In the next section, an Ant Colony Algorithm, as a discrete optimization tool, is proposed to solve the problem.

33.3 The Developed Ant Colony Algorithm

33.3.1 Principles of Ant Colony Optimization Algorithms

Many of the present Ant Colony Optimization (ACO) algorithms are the extension of the Ant System (AS) algorithm. Two main phases of the AS algorithm are the Ants' solution construction and the pheromone update. In AS a good heuristic to initialize the pheromone trails is to set them to a value slightly higher than the expected amount of pheromone deposited by the ants in each iteration. The reason for this choice is that if the initial pheromone values are too low, then the search is quickly biased by the first tour generated by the ants, which in general leads to the exploration of inferior zones of search space. On the other hand, if the initial pheromone values are too high, then many iterations will be lost waiting until pheromone evaporation reduces enough pheromone values to allow the pheromone added by ants to bias the search.

After defining the construction graph and the necessary constraints, and specifying the magnitudes of the pheromone trails and heuristic information for the problem, the ants start making the trails. Initially, ants are put on chosen nodes of the graph. At each construction step, Ant k applies a probabilistic action choice rule, known as *random proportional rule*, to decide which node to visit next. In particular, the probability with which the Ant k currently at Node i, chooses to go to Node j is:

$$p_{ij}^k = \begin{cases} \dfrac{\left[\tau_{ij}\right]^{\alpha}\left[\eta_{ij}\right]^{\beta}}{\sum\limits_{l \in N_i^k} [\tau_{il}]^{\alpha}[\eta_{il}]^{\beta}} & \text{if } j \in N_i^k \\ 0 & \text{if } j \notin N_i^k \end{cases} \tag{33.11}$$

This relationship forms the basis of the AS algorithm and shows that if Ant k is positioned on Node i, it will move to the next Node j with the probability of ${\rho_{ij}}^k$. In this relationship, τ_{ij} is the magnitude of pheromone on the trails and η_{ij} is the heuristic value. α and β are two parameters which determine the relative influence of the pheromone trail and the heuristic information. ${N_i}^k$ is the feasible neighborhood of Ant k when being at Node i, that is, the set of nodes that Ant k is allowed to choose as its next destination, and is decided depending on the problem in hand. The probabilistic choice of the next node then works analogous to the roulette-wheel selection procedure of evolutionary computation. The quantity of pheromone trail and heuristic value on the edges determine the size of the slice on a circular roulette wheel. Obviously, the higher pheromone or higher heuristic value on the edges will increase the possibility of selecting the corresponding node.

After all the ants have constructed their tours, the pheromone trails are updated. This act is done by first lowering the pheromone value on all arcs by a constant factor ρ (pheromone evaporation), and then adding pheromone on the edges the ants have crossed (pheromone depositing). If m ants are used for constructing the solution, then pheromone updating is implemented by

$$\tau_{ij} \leftarrow (1-\rho)\tau_{ij} \; \forall (i,j) \in A \tag{33.12}$$

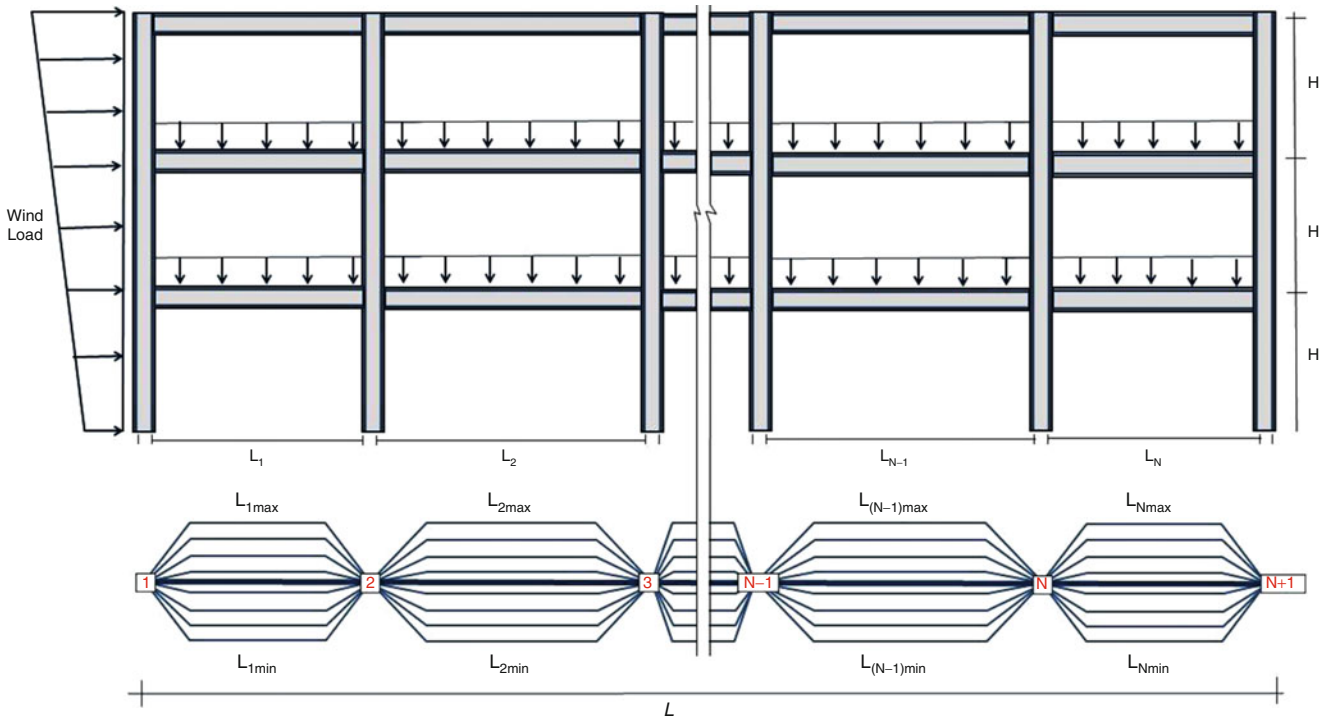

Fig. 33.3 The construction graph for a 2D frame

$$\tau_{ij} \leftarrow \tau_{ij} + \sum_{k=1}^{m} \Delta \tau_{ij}^{k},\ \forall (i,j) \in A \tag{33.13}$$

where $\Delta\tau_{ij}{}^{k}$ is the pheromone added to τ_{ij} by Ant k, and defined as follows:

$$\Delta \tau_{ij}^{k} = \begin{cases} 1/C^{k} & \text{if edge } (i,j) \text{ belongs to } T^{k} \\ 0 & \text{otherwise} \end{cases} \tag{33.14}$$

The value of C^k can be taken as the cost of the best trail or the best iteration and T^k is the set of suitable solutions, depending on the conditions of the problem.

33.3.2 The Developed Ant Colony Optimization Algorithm

Two main phases of the Ant System algorithm are the ants' solution construction and the pheromone update [10]. After defining the construction graph and the necessary constraints, and specifying the magnitudes of the pheromone trails and heuristic information for the problem, the ants start making the trails. Initially, the ants are put on chosen nodes of the graph. At each construction step, Ant k applies a probabilistic action choice rule, known as random-proportional rule, to decide which node to visit next. If an ant is positioned on a node it will move to the next node with a probability proportion to the amount of the pheromone in the trails. That is, the probabilistic choice of the next node then works analogous to the roulette-wheel selection procedure of evolutionary computation. The quantity of pheromone trail and heuristic value on the edges determine the size of the slice on a circular roulette wheel. Obviously, the higher pheromone or higher heuristic value on the edges will increase the probability of selecting the corresponding node. After all the ants have constructed their tours, the pheromone trails are updated. This act is done by first lowering the pheromone value on all arcs by a constant factor (pheromone evaporation), and then adding pheromone on the edges the ants have crossed (pheromone depositing).

The aim of the developed ACO algorithm in this study is to find the optimum layout or columns locations of a 2D RC frame which leads to finding the optimum spans lengths the frame, as shown in Fig. 33.3, in a way that optimize the relevant costs. The heights of stories (columns heights) are considered to be determinate and unchanging.

As the first step, the domain needs to be discretized. As such the construction graph is defined assuming that span lengths are bounded in $[L_{min}\ L_{max}]$, with intervals (accuracy) equal to ε. That is, each L_i rests in the set of $\{L_{min}, L_{min} + \varepsilon, L_{min} + 2\varepsilon, \ldots, L_{max} - \varepsilon, L_{max}\}$. Obviously, the smaller ε is chosen, the more accurate results will be obtained and the more running time the algorithm needs. As shown in Fig. 33.3, a construction graph is defined to demonstrate the possible spans lengths of the 2D frame. In order for the construction graph to stand for the structure layout, the total number of spans and the number of nodes need to be N and $N + 1$ respectively, in which N is the total number of spans. Hence, the construction graph is defined as a graph with $N+1$ nodes and $((L_{max} - L_{min})/\varepsilon * N)$ edges. Each pair of nodes are connected with $(L_{max} - L_{min})/\varepsilon$ edges, i.e. there are $(L_{max} - L_{min})/\varepsilon$ choices for each ant on each node to select another one, for making its trail (solution). It should be pointed out that, as stated in the definition of constraints and shown in Fig. 33.3, L_{max} and L_{min} might be specified differently for each span. In this case, the number of choices for ants on each node might differ from the other ones. Now that the construction graph is prepared, ants can start their solution process in the following phases [15].

In the first phase, two groups of artificial ants are located on the first and last nodes of the construction graph, i.e. Nodes 1 and $N + 1$, to construct their solution. Since there are as many as $(L_{max} - L_{min})/\varepsilon$ edges that connect every two successive nodes, the dimension of these two matrices will be $N*(L_{max} - L_{min})/\varepsilon$.

For organizing the heuristic matrix and initial pheromone matrix, one can make use of structural analysis experience. As boundary conditions and constraints, plus any loads can affect the length of spans, the entries of heuristic matrix and initial pheromone matrix might be organized based on such parameters. Moreover, in order to save time, some criteria like the symmetry of the plan are considered when the heuristic matrix is defined. In this case, the entries of heuristic matrix relating to preferred choices might receive higher numbers relative to the entries of the other ones. Using such a heuristic matrix or defining the initial pheromone matrix using the above-mentioned structural rules helps the algorithm converge sooner. Thus, each value (i,j) of choice information matrix, which is obtained by multiplying the corresponding arrays of heuristic matrix by those of pheromone matrix, shows the tendency or desirability of the ant located on Node i of the construction graph to choose Edge j to move towards Node $i + 1$.

The next phase consists of two segments that form the basis of the heuristic. In the first segment of this phase, using the random proportional rule ants located on the starting nodes of the construction graph, whether Node 1 or Node $N + 1$, start to construct their solutions. That is, two groups of ants are located on the graph, one at Node 1 and one at Node $N + 1$. In this method, the feasible neighborhood is defined as the edges between Nodes i and $i + 1$, when the ant is located at Node i in either route, that is, from Node $N + 1$ to Node 1. The ant leaves its source Node $i \in \{1,2,\ldots,N + 1\}$ on the construction graph to destination node on the connecting Edges $j \in \{1, 2, \ldots, (L_{max} - L_{min})/\varepsilon\}$, using the random proportional rule, similar to the random roulette wheel rule and quite randomly. The probability of Edge j to be chosen by an ant on Node i is proportional to the entry (i, j) of the choice information matrix. The bigger the entry (i,j) of the choice matrix is, the more probable Node j is to be chosen by Ant i. The ants continue constructing their solution and move from a node to the next one, until getting to Node $N + 1$ as the end of their trail. The constraint for ants is that the sum of all spans must be equal to L. Therefore, two groups of ants are located on both ends of the graph, so that every edge has the same overall probability of being chosen by the ants. Now the values of N lengths and thereby the new geometrical layout for the column layout is obtained. Through the structural analysis method for frames, and using the behavior constraints, design actions effects in the identified sections are determined and using other constraints, the required strength capacities for each section are calculated. Based on the strength capacity of sections, the cost function or the cost of this solution is obtained.

The last phase consists of updating information and statistics, and then updating pheromone trails. Using the information obtained in the phase of constructing the solution, the trail presenting the best cost, up to this stage, is selected as the best so-far iteration. Then pheromone trails of construction graph are updated. For this purpose, ants are allowed to deposit pheromone on the edges associated with the best so-far iteration and the quality of the solutions in each step. The process of pheromone updating consists of two segments. The first segment corresponds to pheromone evaporation. In this segment the evaporation parameter depends on the number of steps defined for termination criteria, and initial pheromone and heuristic values. The second segment is depositing pheromone. For depositing pheromone, the pheromone values on the edges associated with the best iteration up to now increase and the ant deposits an amount of pheromone equal to $1/cost$ on the edges of construction graph associated with the best so-far iteration and the cost of each solution.

The above procedure continues until the termination criterion is satisfied; then the optimum layout will be the best-so-far solution for spans. In each step, a basic structural analysis is required to calculate the section actions. Making use of a structural analysis approach, say finite element method or simplified methods based on the design standards, such a calculation takes a small amount of time for each section. Using (33.1) as the objective function would be significantly more time-consuming than using (33.2) and (33.6). Due to the variation of lengths in each step, the estimation of design variables in each step would be considerably encumbered; apart from the fact that, in each step, the algorithm would iteratively need to deal with the design formulas. Equations 33.2 and 33.6 make the optimization process much tangible and greatly usable in the layout optimization of large structures.

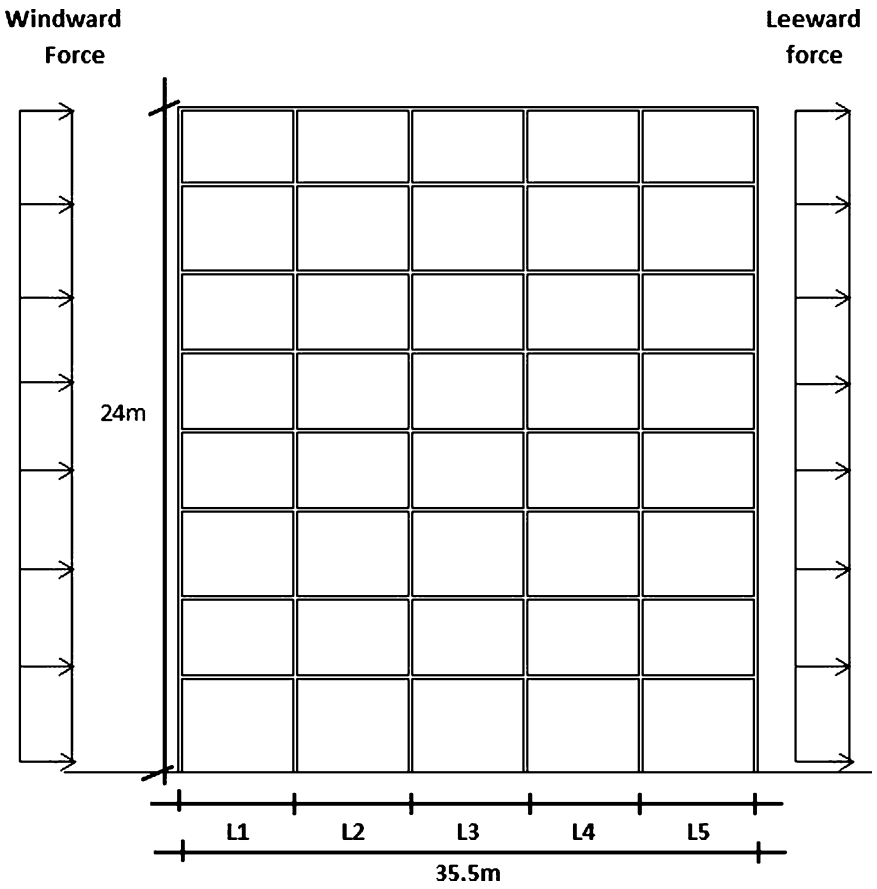

Fig. 33.4 Numerical example: an eight story building

33.4 Numerical Example

To demonstrate the robustness of the proposed approach, a realistic example is presented. All computations were performed on P9700 @2.80 GHz computer running MATLAB R2009b. In order to ensure that the obtained solution from ACO is global or near global optimum, many runs were made in parallel. Since each run is fully independent of the others, the program can be run in parallel so that the total execution time will be practically the same as required for a single run.

Example: The column layout of a five-span eight-storey East–west oriented reinforced concrete frame of a building located in Wollongong on a 20 m hill, as shown in Fig. 33.4, is optimized. Height of the building is 24.0 m (each story 3.0 m height). The live load and the total dead load are 5.0 and 4.0 kN/m^2 respectively. The live load is 5.0 kN/m^2 and the dead load, excluding the self-weight of concrete, is 2.5 kN/m^2. The dynamic effect of the wind loading is modeled by two distributed windward and leeward impulse loads as shown in Fig. 33.4.

The average unit price for concrete is assumed to be 55 units/m^3, and 3,900 units/m^3 for steel. The average unit price for formwork is 20 units/m^2. Other design parameters used in this example are the characteristic tensile strength of reinforcement $f_y = 460$ N/mm^2, the characteristic strength of concrete $f'_c = 35$ N/mm^2, and the cover of steel bars $c = 25$ mm.

The permissible spans lengths are defined within the bounds of $L_{max} = 9.0$ m and $L_{min} = 5.0$ m. As a primary design for the proposed ACO algorithm, spans lengths are considered $L_1 = L_2 = L_3 = L_4 = L_5 = 7.5$ m. It should be added that every initial design based on preliminary judgment of the designer and/or using approximate charts or formulas, which meet the design standard requirements, can be used as the initial design and as the starting point of the optimization process. Based on the above-mentioned primary design, the primary cost of the structure based on (33.1) is equal to 55,971 units.

For this example, three control sections are selected for every member. Using the above-obtained equations the values of K_1 to K_{18}, and consequently the values of c_1 to c_6 for all selected columns and beams sections are obtained. Having the necessary coefficients, the optimization problem can be formulated, based on (33.10). The Ant algorithm attempts to find the optimum spans based on the objective function and observing other relevant constraints. After 130 iterations, which was defined as a termination criterion, and at CPU time of 41.27 s, the optimum lengths of $L_1 = 5{,}600$ mm, $L_2 = 7{,}100$ mm, $L_3 = 7{,}900$, $L_4 = 8{,}400$ mm and $L_5 = 8{,}500$ mm are obtained. Having determined the optimum lengths, sections are

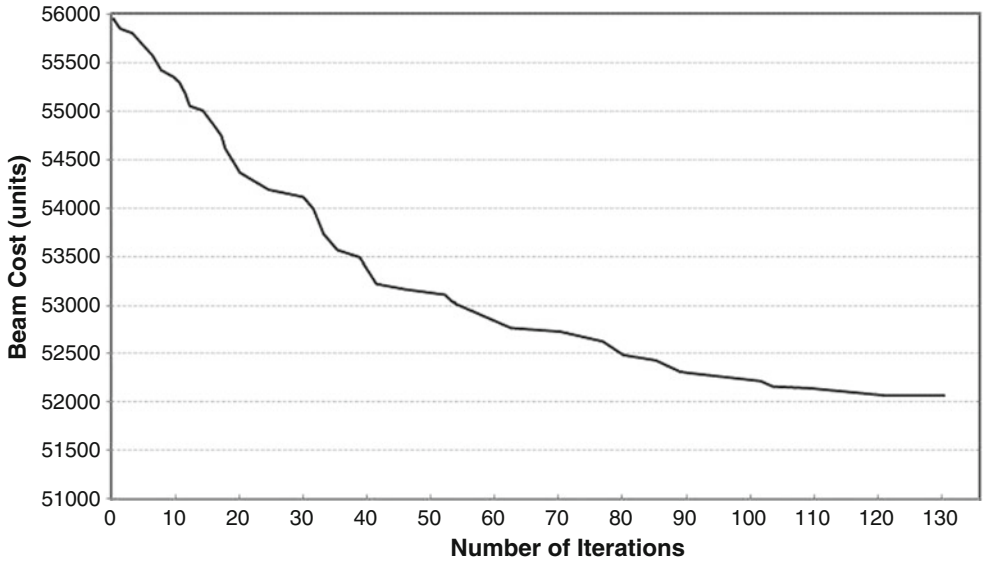

Fig. 33.5 Typical convergence history for the presented ACO algorithm

designed based on AS3600 [13] resulting in a total cost of 52,058 units (6.99% cost saving). It should be noted that if one employed an optimization method of design, say replacing the first line of (33.10) with (33.1) as an objective function and some modifications in constraints, instead of using the conventional method in the last step, further cost saving might be achieved. Figure 33.5 shows a typical convergence history of the proposed ACO algorithm for the example. If the impulse load, caused by wind, is removed, the optimum spans lengths of 7,100, 7,800, 7,700, 7,800, 7,100 at the cost of 50,113 would be obtained due to static vertical loading system. It shows that the wind loads results in a further 3.5% cost. Figure 33.5 shows a typical convergence history for the ACO algorithm for this example.

33.5 Conclusion

This study aims to propose a new layout optimization model, used for the cost optimization of 2D reinforced concrete frames under wind loading. The cost function proposed in this study simplifies the process of cost optimization of 2D reinforced concrete frames and is applicable to multi-variable optimization of RC structures; say the cost and layout optimization problem. The proposed algorithm for solving the cost optimization problem is an Ant System based algorithm, which can be easily employed for optimizing the span lengths and column locations and also is capable of working with different cost functions and loading systems. The presented examples show that the proposed algorithm using the new cost optimization function provides satisfactory results.

Appendix

Mathematical Calculations for (33.5) and (33.9)

A.1. Beams: Calculations for (33.5)

Any changes in the longitudinal steel $A_{sl}^{(b)}$ results in changes in the capacities of a beam section as follows:

$$\begin{cases} \dfrac{\Delta M_u^{-(b)}}{\Delta A_{sl}^{(b)}} \cong f_{yl}(d^{(b)} - d_c^{(b)}) \rightarrow \Delta A_{sl}^{(b)} = (f_{yl}\, d^{(b)}(1 - 0.5\gamma\, k_u))^{-1} \Delta M_u^{-(b)} = K_1\, \Delta M_u^{-(b)} \\ \dfrac{\Delta M_u^{+(b)}}{\Delta A_{sl}^{(b)}} \cong f_{yl}(d^{(b)} - d_c^{(b)}) \rightarrow \Delta A_{sl}^{(b)} = (f_{yl}\, d^{(b)}(1 - 0.5\gamma\, k_u))^{-1} \Delta M_u^{+(b)} = K_1\, \Delta M_u^{+(b)} \\ \dfrac{\Delta V_u^{(b)}}{\Delta A_{sl}^{(b)}} \cong 0 \rightarrow \Delta V_u^{(b)} \textit{ and } \Delta \mathrm{A}_{sl} \textit{ are independent of each other} \end{cases} \tag{A.1}$$

If $A_{sv}^{(b)}/s$ changes the variation of the beams bearing capacities are

$$\begin{cases} \Delta M_u^{-(b)} \textit{and } \dfrac{\Delta A_{sv}^{(b)}}{s} \textit{are independent of each other} \\ \Delta M_u^{+(b)} \textit{ and } \dfrac{\Delta A_{sv}^{(b)}}{s} \textit{are independent of each other} \\ \dfrac{\Delta V_u^{(b)}}{\frac{\Delta A_{sv}^{(b)}}{s}} \cong f_{yv} d \rightarrow \dfrac{\Delta A_{sv}^{(b)}}{s} \cong (f_{yv}\, d)^{-1}\, \Delta V_u^{(b)} = K_2\, \Delta V_u^{(b)} \end{cases} \tag{A.2}$$

If the effective area of the beam section $\Delta A_c^{(b)}$, i.e. bd varies:

$$\Delta A_c^{(b)} = \Delta\,(bd) = b\,\Delta d + d\,\Delta b + \Delta b\,\Delta d = b\,\Delta d \tag{A.3}$$

$\Delta M_u^{-(b)}$ is not a function of b, and based on the second assumption, the dependence of $\Delta M_u^{+(b)}$ on the changes of b is neglected. Moreover, the first term of $V_u^{(b)}$ is not dependent on b as well. So, the variations of the section capacities due to variation of cross-section area are

$$\frac{\Delta M_u^{(b)}}{\Delta A_c^{(b)}} = \frac{\Delta M_u^{(b)}}{\Delta\,(bd)} \cong \frac{\Delta M_u^{(b)}}{b(\Delta\, d)} \tag{A.4}$$

$$\begin{cases} \dfrac{\Delta M_u^{-(b)}}{\Delta\,(bd^{(b)})} \cong \dfrac{f_{yl} A_{sc}^{(b)}}{b}(1 - 0.5\gamma k_u) \rightarrow \Delta A_c^{(b)} = \Delta\,(bd^{(b)}) \cong \left[f_{yl} \dfrac{A_{sc}^{(b)}}{b}(1 - 0.5\gamma k_u) \right]^{-1} \Delta M_u^{-(b)} = K_3\, \Delta M_u^{-(b)} \\ \dfrac{\Delta M_u^{+(b)}}{\Delta\,(bd^{(b)})} \cong \dfrac{f_{yl} A_{st}^{(b)}}{b}(1 - 0.5\gamma k_u) \rightarrow \Delta A_c^{(b)} = \Delta\,(bd^{(b)}) \cong \left[f_{yl} \dfrac{A_{st}^{(b)}}{b}(1 - 0.5\gamma k_u) \right]^{-1} \Delta M_u^{+(b)} = K_4\, \Delta M_u^{+(b)} \\ \dfrac{\Delta V_u^{(b)}}{\Delta\,(bd^{(b)})} \cong \dfrac{f_{yv} A_{sv}^{(b)}}{bs} + \beta (f'_c)^{1/2} \rightarrow \Delta A_c^{(b)} = \Delta\,(bd^{(b)}) \cong \left[\dfrac{f_{yv} A_{sv}^{(b)}}{bs} + \beta (f'_c)^{0.5} \right]^{-1} \Delta V_u^{(b)} = K_5\, \Delta V_u^{(b)} \end{cases} \tag{A.5}$$

The variation of the perimeter of a rectangular beam section, which determines the variation of the beam formwork, affects the section capacity as follows:

$$\Delta P_f^{(b)} = \Delta b + 2\Delta d^{(b)} \tag{A.6}$$

$$\begin{cases} \dfrac{\Delta M_u^{-(b)}}{\Delta b + 2\Delta d^{(b)}} \cong f_{yl} A_{sc}^{(b)} \rightarrow \Delta P_f^{(b)} = \Delta b + 2\Delta d^{(b)} \cong 2\left[f_{yl} A_{sc}^{(b)}(1 - 0.5\gamma k_u) \right]^{-1} \Delta M_u^{-} = K_6 \Delta M_u^{-} \\ \dfrac{\Delta M_u^{+(b)}}{\Delta b + 2\Delta d^{(b)}} \cong f_{yl} A_{st}^{(b)} \rightarrow \Delta P_f^{(b)} = \Delta b + 2\Delta d^{(b)} \cong 2\left[f_{yl} A_{st}^{(b)}(1 - 0.5\gamma k_u) \right]^{-1} \Delta M_u^{+} = K_7 \Delta M_u^{+} \\ \dfrac{\Delta V_u^{(b)}}{\Delta b + 2\Delta d^{(b)}} \cong \dfrac{1}{\frac{f_{yl} A_{sv}^{(b)}}{s} + \beta b (f'_c)^{1/2}} + \dfrac{1}{\beta d (f'_c)^{1/2}} \rightarrow \Delta P_f^{(b)} = \Delta b + 2\Delta d^{(b)} \cong \left[\dfrac{2}{\frac{f_{yv} A_{sv}^{(b)}}{s} + \beta b (f'_c)^{1/2}} + \dfrac{1}{\beta d (f'_c)^{1/2}} \right] \Delta V_u = K_8\, \Delta V_u \end{cases} \tag{A.7}$$

Now, that the reciprocal relationships between the variations of cross-sectional variables and strength capacity parameters of a beam section are obtained, multiplying both sides of (A.1) by csl/2, (A.2) by csv, (A.5) by cc/3 and (A.7) by cf/3 and then adding them up result in:

$$\begin{aligned} c_c\Delta A_c^{(b)} + c_{sl}\,\Delta A_{sl}^{(b)} + c_{sv}A_{sv}^{(b)} + c_f\Delta P_f^{(b)} = &\left(\frac{1}{3}c_cK_4 + \frac{1}{2}c_{sl}K_1 + \frac{2}{3}c_fK_7\right)\Delta M_u^{+(b)} \\ &+ \left(\frac{1}{3}c_cK_3 + \frac{1}{2}c_{sl}K_1 + \frac{2}{3}c_fK_6\right)\Delta M_u^{-(b)} \\ &+ \left(\frac{1}{3}c_cK_5 + c_{sv}K_2 + \frac{2}{3}c_fK_8\right)\Delta V_u^{(b)} \end{aligned} \tag{A.8}$$

A.2. Columns: Calculations for (33.9)

Any changes in the longitudinal steel $A_{sl}^{(c)}$ results in changes in the capacities of a column section as follows:

$$\begin{cases} \dfrac{\Delta N_u^{(c)}}{\Delta A_{sl}^{(c)}} \cong E_s \sum_i^n \varepsilon_i \rightarrow \Delta A_{sl}^{(c)} = \left(E_s \sum_i^n \varepsilon_i\right)^{-1} \Delta N_u^{(c)} = K_9\ \Delta N_u^{(c)} \\ \dfrac{\Delta M_u^{(c)}}{\Delta A_{sl}^{(c)}} \cong E_s \sum_i^n \varepsilon_i\, e_i \rightarrow \Delta A_{sl}^{(c)} = \left(E_s \sum_i^n \varepsilon_i\, e_i\right)^{-1} \Delta \mathrm{M}_u^{(c)} = K_{10}\ \Delta M_u^{(c)} \\ \dfrac{\Delta V_u^{(c)}}{\Delta A_{sl}^{(c)}} \cong 0 \rightarrow \Delta V_u^{(c)} \text{ and } \Delta A_{sl}^{(c)} \text{ are independent of each other} \end{cases} \tag{A.9}$$

With respect to $A_{sv}^{(c)}/s$, the variations of the column capacities are

$$\begin{cases} \Delta N_u^{(c)} \text{ and } \dfrac{\Delta A_{sv}^{(c)}}{s} \text{ are independent of each other} \\ \Delta M_u^{(c)} \text{ and } \dfrac{\Delta A_{sv}^{(c)}}{s} \text{ are independent of each other} \\ \dfrac{\Delta V_u^{(c)}}{\frac{\Delta A_{sv}^{(c)}}{s}} \cong f_{yv}\, d^{(c)} \rightarrow \dfrac{\Delta A_{sv}^{(c)}}{s} \cong \left(f_{yv}\, d^{(c)}\right)^{-1} \Delta V_u^{(b)} = K_{11}\ \Delta V_u^{(b)} \end{cases} \tag{A.10}$$

If the cross-section area of the column varies:

$$\begin{cases} \dfrac{\Delta N_u^{(c)}}{\Delta A_c^{(c)}} \cong 0.85\gamma k_u f'_c \rightarrow \Delta A_c^{(c)} \cong (0.85\gamma k_u f'_c)^{-1} \Delta N_u^{(c)} = K_{12}\ \Delta N_u^{(c)} \\ \dfrac{\Delta M_u^{(c)}}{\Delta A_c^{(c)}} \cong 0.85\gamma k_u f'_c e_c \rightarrow \Delta A_c^{(c)} \cong (0.85\gamma k_u f'_c e_c)^{-1} \Delta M_u^{(c)} = K_{13}\ \Delta M_u^{(c)} \\ \dfrac{\Delta V_u^{(c)}}{\Delta A_c^{(c)}} \cong \dfrac{f_{yv}A_{sv}^{(c)}}{2hs} + \beta(f_c')^{0.5} \rightarrow \Delta A_c^{(b)} = \Delta\left(h^{(c)}d^{(c)}\right) \cong \left(\dfrac{f_{yv}A_{sv}^{(c)}}{2hs} + \beta(f_c')^{0.5}\right)^{-1} \Delta V_u^{(c)} = K_{14}\ \Delta V_u^{(c)} \end{cases} \tag{A.11}$$

The variation of the perimeter of a square column section, which determines the variation of the column formwork, affects the section capacity as follows:

$$\begin{cases} \dfrac{\Delta N_u^{(c)}}{\Delta P_f^{(c)}} \cong 0.85\gamma k_u f'_c \dfrac{h^{(c)}}{2} \rightarrow \Delta P_f^{(c)} \cong \left(0.85\gamma k_u f'_c \dfrac{h^{(c)}}{2}\right)^{-1} \Delta N_u^{(c)} = K_{15}\ \Delta N_u^{(c)} \\ \dfrac{\Delta M_u^{(c)}}{\Delta P_f^{(c)}} \cong 0.85\gamma k_u f'_c \dfrac{h^{(c)}}{2} e_c \rightarrow \Delta P_f^{(b)} \cong \left(0.85\gamma k_u f'_c \dfrac{h^{(c)}}{2} e_c\right)^{-1} \Delta M_u^{(c)} = K_{16}\ \Delta M_u^{(c)} \\ \dfrac{\Delta V_u^{(c)}}{\Delta P_f^{(c)}} \cong \dfrac{f_{yv} A_{sv}^{(c)}}{4s} + \dfrac{1}{2}\beta h^{(c)} \left(f_c^{'}\right)^{0.5} \rightarrow \Delta P_f^{(c)} \cong \left(\dfrac{f_{yv} A_{sv}^{(c)}}{4s} + \dfrac{1}{2}\beta h^{(c)} \left(f_c^{'}\right)^{0.5}\right)^{-1} \Delta V_u^{(c)} = K_{17}\ \Delta V_u^{(c)} \end{cases} \tag{A.12}$$

The reciprocal relationships between the variations of cross-sectional variables and those of strength capacity variables of a column section are obtained by multiplying both sides of (A.9) by csl/2, (A.10) by csv, (A.11) by cc/3 and (A.12) by cf/3 then adding them up :

$$\begin{aligned} c_c\ \Delta A_c^{(c)} + c_{sl}\ \Delta A_{sl}^{(c)} + c_{sv}\ A_{sv}^{(c)} + c_f\ \Delta P_f^{(c)} = & \left(\frac{1}{3}c_c K_{12} + \frac{1}{2}c_{sl} K_9 + \frac{1}{3}c_f K_{15}\right) \Delta N_u^{(c)} \\ & + \left(\frac{1}{3}c_c K_{13} + \frac{1}{2}c_{sl} K_{10} + \frac{2}{3}c_f K_{16}\right) \Delta M_u^{(c)} \\ & + \left(\frac{1}{3}c_c K_{14} + c_{sv} K_{11} + \frac{2}{3}c_f K_{17}\right) \Delta V_u^{(c)} \end{aligned} \tag{A.13}$$

References

1. Adeli H, Sarama KC (1998) Cost optimization of concrete structures. J Struct Eng 124(5):570–578
2. Balling RJ, Yao X (1997) Optimization of reinforced concrete frames. J Struct Eng 123(2):193–202
3. Zou XK, Chan CM, Wang G, Li Q (2007) Multiobjective optimization for performance-based design of reinforced concrete frames. J Struct Eng 133(10):1462–1474
4. Shaw D, Miles J, Gray A (2008) Determining the structural layout of orthogonal framed buildings. Comput Struct 86(19–20):1856–1864
5. Nimtawat A, Nanakorn P (2010) A genetic algorithm for beam–slab layout design of rectilinear floors. Eng Struct 32(11):3488–3500
6. Nimtawat A, Nanakorn P (2009) Automated layout design of beam-slab floors using a genetic algorithm. Comput Struct 87(21–22):1308–1330
7. Zhu JH, Zhang WH (2010) Integrated layout design of supports and structures. Comput Methods Appl Mech Eng 199(9–12):557–569
8. Sahab MG, Ashour AF, Toropov VV (2005) Cost optimisation of reinforced concrete flat slab buildings. Eng Struct 27(3):313–322
9. Sahab MG, Ashour AF, Toropov VV (2005) A hybrid genetic algorithm for reinforced concrete flat slab buildings. Comput Struct 83 (8–9):551–559
10. Dorigo M, Stüzle T (2004) Ant colony optimization. MIT Press, Cambridge, MA
11. Kaveh A, Hassani B, Shojaee S, Tavakkoli SM (2008) Structural topology optimization using Ant colony methodology. Eng Struct 30 (9):2559–2565
12. Camp CV, Barron JB, Scott PS (2005) Design of steel frames using Ant colony optimization. J Struct Eng 131(3):369–379
13. AS3600: Standards Australia, Concrete structures. Sydney, 2009
14. AS/NZS1170.2: Structural design actions Part 2: Wind actions. Sydney, 2011
15. Kaveh A, Sharafi P (2008) Optimal priority functions for profile reduction using Ant colony optimization. Finite Elem Anal Des 44(3):131–138

Chapter 34
Robust Design Optimization to Account for Uncertainty in the Structural Design Process

Sarah K. Dalton, Ismail Farajpour, C. Hsein Juang, and Sez Atamturktur

Abstract Structural systems are subject to inherent uncertainties due to the variability in many hard-to-control '*noise factors*' including but not limited to external loads, material properties, and construction workmanship. Two design methodologies were developed to quantify the variability associated with the design process: Allowable Stress Design (ASD) and Load and Resistance Factor Design (LRFD). These traditional approaches explicitly recognize the presence of uncertainty, however they do not take robustness against this uncertainty into consideration. Overlooking robustness against uncertainty in the structural design process has two main problems. First, the design may not satisfy the safety requirements if the actual uncertainties in the noise factors are underestimated. Thus, the safety requirements can easily be violated because of the high variation of the system response due to noise factors. Second, to guarantee safety in the presence of this high variability of the system response, the structural designer may be forced to choose an overly conservative, inefficient and thus costly design. When the robustness against uncertainty is not treated as one of the design objectives, this trade-off between the over-design for safety and the under-design for cost-savings is exacerbated. This paper demonstrates that safe and cost-effective designs are achievable by implementing *Robust Design* concepts originally developed in manufacturing engineering to proactively consider the robustness against uncertainty as one of the design objectives. Robust Design concepts can be used to formulate structural designs which are insensitive to inherent variability in the design process, thus save cost, and exceed the main objectives of user safety and serviceability. This paper presents two methodologies for the application of Robust Design principles to structural design utilizing two optimization schemes: *one-at-a-time* optimization method and *Particle Swarm Optimization (PSO)* method.

Keywords Robust design • Optimization • Structural modeling and design • Uncertainty quantification in structural design

34.1 Introduction

The root of the structural engineer's job is to systematically make decisions regarding design parameters. There are infinite possible design configurations to choose from with the goal of achieving a constructible, serviceable, safe, and cost-effective design. These goals are in and of themselves, competing objectives, in that the safest design is most likely not the most cost efficient. These conflicting objectives force designers to make trade-offs to meet as many design goals as possible. To further complicate the process, these decisions are all made under uncertainty.

The life-cycle of a structural system is plagued by uncertainty, from design through operation. Uncertainty manifests itself in many forms such as; time (trying to predict the future or be confident in the past), statistical limits (designers use discrete samples to predict the behavior of a whole system), model limits (the structural model developed in design and analysis simplifies reality obviating higher level physics in the system), randomness (structural properties are not a single value as designers assume, rather they vary spatially) and human error (mistakes can be made during the design, fabrication, and construction processes which alter the *true* design or analysis) [1]. The inherent variability in these factors must be accounted for during the design process to ensure the proposed design objectives are met under all circumstances. Design codes and approaches have been formulated to incorporate the aforementioned variability in the design process.

S.K. Dalton • I. Farajpour • C.H. Juang • S. Atamturktur (✉)
Clemson University, Clemson, SC 29634, USA
e-mail: sez@clemson.edu

J.M. Caicedo et al. (eds.), *Topics on the Dynamics of Civil Structures, Volume 1*,
Conference Proceedings of the Society for Experimental Mechanics Series 26,
DOI 10.1007/978-1-4614-2413-0_34,

Two prominent design approaches have evolved in the structural engineering field to account for the variability in design parameters. The first, allowable stress design (ASD), is based on a deterministic design approach. This method does not try to quantify the different sources of uncertainty, rather, applies a single subjective 'factor of safety' to capture *all* the variability in loads and resistance. The result is a conservative and safe design, but one which may be inefficient and *over-designed* [2]. The second approach, load and resistance factor design (LRFD), is reliability-based. In this design approach, uncertainties in the design process are quantified into two categories, nominal capacities and resistance factors. This separation allows for predictability of material properties and construction tolerances through nominal capacities, and predictability of variable loads through resistance factors. While this method accounts for variability and incorporates risk assessment, the success of the LRFD approach hinges on the availability and accuracy of statistical data [3]. In reliability-based designs, uncertainty is modeled as random variables or processes. If there is an abundant amount of accurate statistical data, and the distributions of each random variable is well established, then uncertainties can be accurately accounted for in the design. However, if there is a lack of statistical data and the distributions of parameters are estimated, then the random variables themselves induce uncertainties into the design process [3]. Therefore, the safety requirements might be violated due to the potentially underestimated variability in the structural behavior.

An alternative approach, Robust Design processes, originated in Manufacturing Engineering and employed in this paper, target the robustness of the product output against "hard-to-control" input parameters (called "noise factors"), by adjusting "easy-to-control" input parameters (called "design parameters") [4, 5]. In the design of a concrete frame building (used as an example throughout this paper), the column dimensions and the stiffness of the bracing elements may be treated as design parameters; the uncertain material properties or the forcing functions may be treated as noise factors; and the structural response such as, stresses, strains and displacements may be treated as the product of the design process. Since these noise factors represent hard-to-control parameters, one cannot reduce or eliminate them in any feasible way. The aim should then be to reduce the effects of the noise factors on the structural response. This is precisely what Robust Design principles aim to achieve. By exploiting the non-linear interactions between the design parameters and the noise factors, Robust Design aims to find design parameters that yield a structural design which is robust to the hard-to-control noise parameters, thereby reducing the variability of the structural response and yielding not only safe but also cost-effective designs.

Focusing on a concrete-frame model, this paper demonstrates the validity and applicability of robust design principles in structural engineering. Herein, the principles of robust design are implemented through two distinct optimization methodologies: *Coordinate Descent* optimization method and *Particle Swarm Optimization (PSO)* method. Section 34.2 of this paper overviews the genesis of Robust Design principles as well as work completed to improve upon it. Section 34.3 follows with the methodologies used in this paper to apply the Robust Design principles to our problem and finally, in Sects. 34.4 and 34.5, results and discussion for each of the optimization cases, respectively, will be presented.

34.2 Background

To reiterate, the goal of robust design is to manipulate easy-to-control parameters (design parameters), those parameters that the designer has the ability to manipulate, such as material type or dimensions, to minimize the effects of hard-to-control control parameters (noise factors), making the process more robust against noise and improving quality, and reliability at low costs [4, 6]. This process utilizes interactions between design parameters and noise factors to identify the design parameter settings, which reduce the effects of noise on the desired outcome the most *by reducing variability and adjusting the mean to a target value* [7, 8]. This goal can be reached in several ways through utilizing the traditional two-step methodology as outlined by Taguchi [7], Bayesian Inference techniques [9], the multi-objective optimization techniques [10, 11], or through a single-objective robust optimization scheme [10, 11].

Taguchi [7] developed a two-step process for Robust Design (Fig. 34.1). The first step focuses on minimizing the variation. This step seeks the optimum settings of the design variables by maximizing what Taguchi coins the *signal-to-noise (S/N)* ratio, which is a ratio of response to the variation of the response caused by the noise factors. Three different classes of S/N ratios are defined. The first is *nominal-the-best,* where a certain target value is desired. Second is *smaller-the-better,* where the most robust option is a zero value response, and likewise, the third class of S/N ratios, called *larger-the-better,* which ideally aims to achieve a target value of infinity. Equations 34.1, 34.2 and 34.3 summarize the different classifications of S/N ratios, respectively, where μ is the mean of the system response, σ is the standard deviation of the response due to noise, and y_i are observed responses [12].

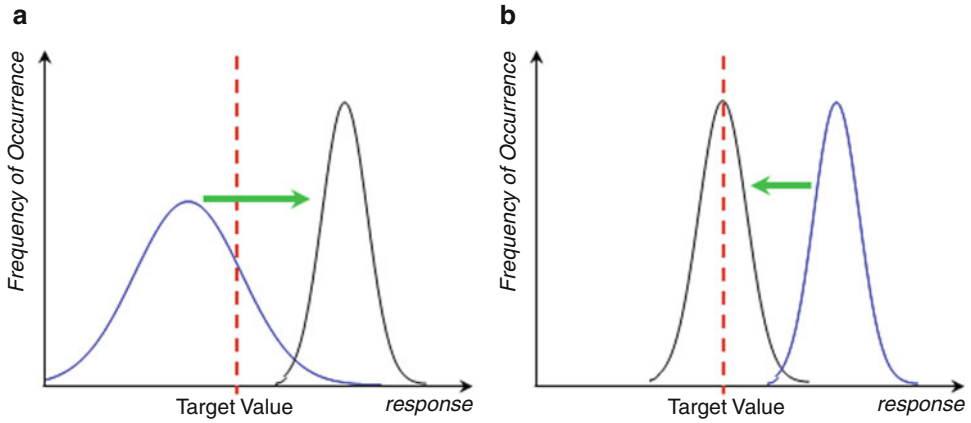

Fig. 34.1 Two-step robust design methodology; (**a**) minimize variability by altering design parameters – *left* (**b**) move mean of distribution on target through the application of a scale factor – *right*

$$\eta = 10\log_{10}\left(\frac{\mu^2}{\sigma^2}\right) \tag{34.1}$$

$$\eta = -10\log_{10}\left[\frac{1}{n}\sum_{i=1}^{n} y_i{}^2\right] \tag{34.2}$$

$$\eta = -10\log_{10}\left[\frac{1}{n}\sum_{i=1}^{n}\frac{1}{y_i{}^2}\right] \tag{34.3}$$

It is important to note that many design parameters may influence both the mean and variation of the result, thus a coincident shifting of the mean, although unintentional, can be expected in this step [7, 13]. Moving the mean to the desired target is then accounted for in step 2 of Taguchi's method. This can be accomplished through the careful selection of a design parameter(s) which affects *only* the mean of the distribution, while preserving the maximized signal-to-noise ratio achieved in step 1. This design parameter is considered a scale factor used to *scale* the mean to a desired value and can be calculated according to (34.4) where s is the scale factor, m is the target value, and μ is the mean of the current distribution.

$$s = \frac{m}{\mu}. \tag{34.4}$$

Taguchi first developed this methodology for process design, i.e. design of experiments, and not for product design. Due to its simplicity and proven advantages, the Taguchi method has been applied to various aspects of engineering [14–20]. In the adaptation of the principles of Taguchi's method to a feasible methodology for other applications, several problems were encountered which led to subsequent research and updated methods [21]. Some of these problems include the inability to locate a scale factor [22–24], high computational effort needed to gain insight into all factor interactions [25–27], and the inability of the method to include design constraints [12, 28–30]. Of these, the most widely studied is the lack of a scale factor.

There are design situations where all parameters significantly affect both the mean and standard deviation, proving the isolation of a single parameter which affects only the mean impossible. In such situations, Taguchi's two-step method is no longer applicable because the maximized signal-to-noise ratio is not upheld. In these instances, optimization methods [21, 31–38] or Bayesian inference [39–41] techniques can be employed to obtain design parameters while simultaneously considering the mean and standard deviation of the response.

34.3 Robust Structural Design Methodology

This manuscript presents a simulation based proof-of-concept case-study, which seeks to find a structural design that is robust against noise parameters given certain performance and cost constraints.

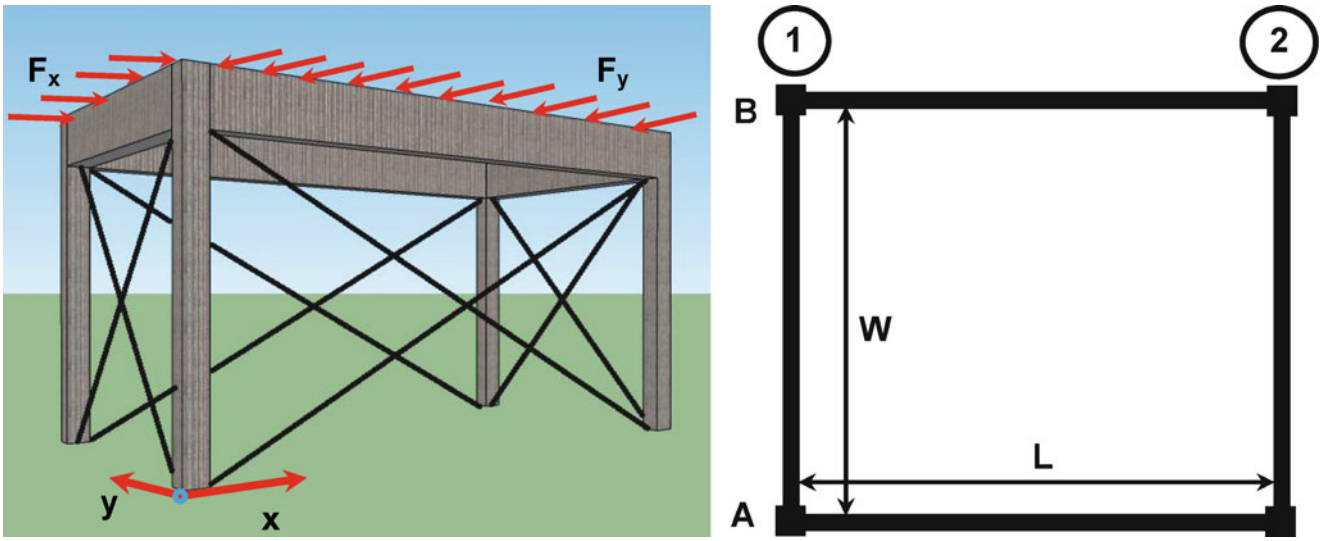

Fig. 34.2 Basic prototype geometry and boundary conditions – *left* elevation, *right* plan view

34.3.1 Prototype Structure and Robust Methodology

For this proof-of-concept study, a one-story, one-bay, reinforced concrete frame structure with steel cross-bracing was chosen as the prototype. The geometry of the structure can be seen in Fig. 34.2. A nominal structural design for the frame was completed in accordance to ACI 318-08: Building Code Requirements for Structural Concrete and Commentary Standard, 2008 version.

In the first step of Robust Design methodology, the control and noise parameters, as well as the ranges in which they may vary, must be defined. In the structural design context, easy-to-control design parameters include member dimensions and material strengths. For the purposes of this research, eight design parameters are employed for both optimization cases: (1) width of columns, X, (2) depth of columns, Y, (3) dimensions of the floor plan, L and W, (4) cross-sectional area of the bracing in the x plane, A_x, (5) cross-sectional area of the bracing in the y plane, A_y, (6) height of the beams, h_b, (7) strength of concrete, f_c' and (8) column reinforcement ratio, ρ. To observe design trade-offs between safety and cost-efficiency, as a practicing structural engineer would, a sufficiently complex structure with many design parameters was necessary. In an effort to ensure that a sufficient number of parameters are influential on the performance, the force is applied in both x and y directions. The applied force in the x-direction is assumed to be twice that in the y-direction. A single noise parameter, varying force, is considered; however the procedure can easily be extended to consider multiple noise factors as outlined in the introduction. In the context of robust design aiming to develop a design which is insensitive to noise factors, one might expect the bounds of the force to begin essentially at zero; however in doing so, a sensitive design would be developed due to the fact that the drift value at zero force is always zero. The noise factor, which is the applied force at the top of the frame, is therefore evaluated within an interval and represented within two bounding levels. In this study these bounds are defined based on engineering judgment; whereas in real life, probabilistic analysis of the forces would be necessary to define such plausible bounds.

Much consideration went into ensuring the resulting optimal designs were both feasible to construct and allowable by the building codes. Thus, design constraints, seen in Table 34.1, were imposed on the candidate designs. The design objective for this study is to achieve robustness for the drift of column B2 when exposed to uncertainty in the loading at roof level along members A1-A2 (in the y-direction) and A1-B1 (in the x-direction) (See Fig. 34.2). To achieve the stated objective function, a defined threshold for drift values was also specified to be no more than 0.048 ft (0.575 in.). It should be noted that this threshold is not the value at failure, rather has a factor of safety applied in order

As robustness, in the most theoretical sense, also promotes efficiency, a secondary goal is to optimize for cost. To achieve cost-efficiency, a second threshold representing cost was specified to be 500 unit price. Such constrain reduced the member dimensions of selected, plausible designs to only cost effective designs. For the purposes of this research cost is defined as in (34.5) where V_c is the total volume of concrete, V_s is the total volume of steel bracing, and ϕ is the unit price of each material. The unit price for steel is assumed to be five times that of concrete [42]. It should be noted that steel rebar and structural steel connections are included in their respective unit prices.

Table 34.1 Design parameters and their constraints

Parameter	Range of acceptable values
Width of columns (X)	6–24 in.
Depth of columns (Y)	6–24 in.
Floor plan dimensions (L and W)	Square footage ~400 ft^2 (L*W = 400)
Area of bracing in x plane (A_x)	0–8 in.^{2}
Area of bracing in y plane (A_y)	0–8 in.^{2}
Height of beams (h_b)	12–36 in.
Strength of concrete (f_c')	2,500–5,500 psi
Column reinforcement ratio (ρ)	0.01–0.08

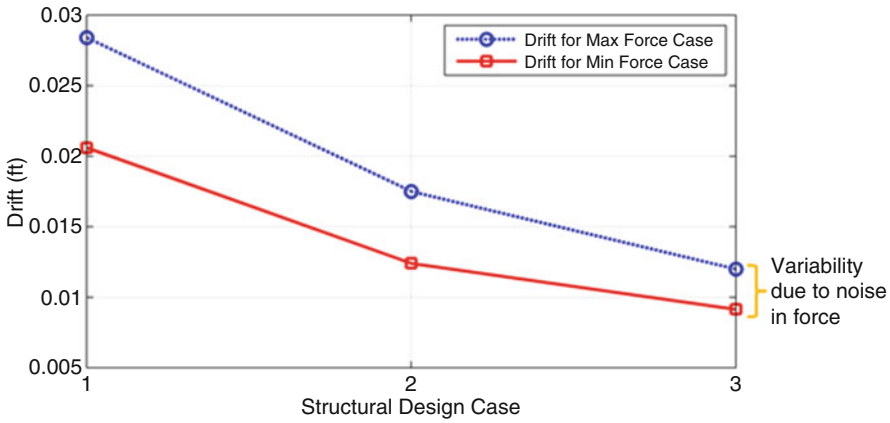

Fig. 34.3 Effect of altering the width of columns on the objective

$$Cost = \sum V_c * \phi_c + \sum V_s * \phi_s \tag{34.5}$$

As mentioned earlier, one approach to Robust Design is to utilize a two-step robust design process with the goal of altering design parameters in order to first minimize the variability in drift values due to changing loads, followed by a shift in the mean of the distribution so it approaches the threshold value without actually exceeding it [20]. However, this approach works only when the parameters that affect the variability can be separated from those that solely affect the mean of the response. In this particular example, such classification was proven difficult due to the strong influence of all design parameters on both the mean and standard deviation.

Figure 34.3 shows the effect of changing the width of columns (parameter X) on the drift value. Along the x-axis in this figure, three different design cases are represented with differing column widths, while all other design parameters remain constant. In the first design, the width of columns (X) is the minimum value of 6 in. The second design case changes the value for X to a mean value of 12 in., while the third design case adjusts the value for X to its maximum allowed value of 24 in. The two lines represent bounded varying force levels; the dashed line is the response due to the maximum expected force value while the *solid* line is the response for the minimum expected force values. As expected, higher force values result in higher drift values; however, what is interesting to note is the effect of this parameter on both the mean and standard deviation. Solely by changing the width of the columns, while keeping all other parameters constant, the mean of the distribution is dropped from 0.0246 ft for Design Case 1–0.0105 ft for Design Case 3. This is a 57% decrease in the mean value. Concurrently, the range, which is representative of the sensitivity of this particular noise factor (i.e. force level), drops from 0.00787 to 0.00295 ft, a 63% change. From these values it is clear that through the alteration of the column width, *both* the mean and standard deviation of the drift value distribution are significantly affected. When the parameters cannot be classified into groups that solely affect the mean or solely affect the standard deviation, the alternative approach is to seek for a design in a single step where both the mean and standard deviation must be evaluated simultaneously.

If we can conceptualize a graph with the noise levels (force values) on the x-axis, and system response (maximum drift) on the y-axis, as seen in Fig. 34.4, designs exposed to uncertainty can be represented by a single line connecting the drift values at each noise level. The ideal robust design, in this sense, is a line with a slope of zero (i.e., infinite robustness) precisely at the desired threshold level, meaning there is no change in the constraint over all noise levels. With the establishment of a constraint threshold, the objective of the robust optimization method presented in this paper can then

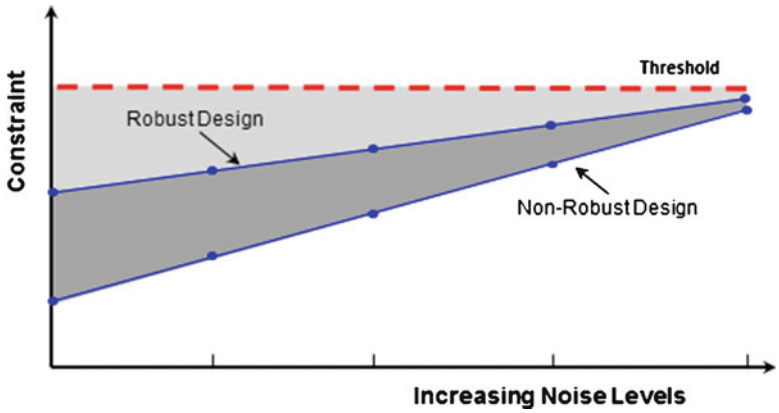

Fig. 34.4 Robust optimization methodology

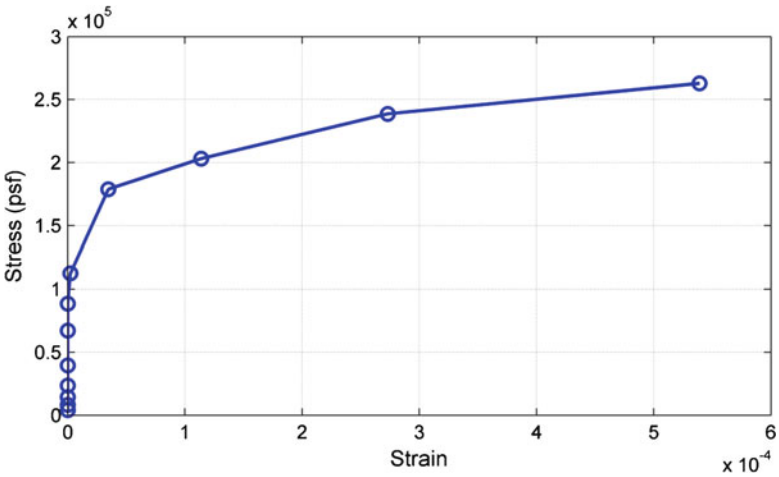

Fig. 34.5 Concrete material model

be outlined as follows: minimize the area between the constraint vs. noise curve by altering design parameters within their allowable domain, while ensuring the constraint values approach, without exceeding, the specified threshold value. For the remainder of this paper, the area between the threshold and constraint vs. noise curve is defined as the insensitivity index.

Through this approach, both the mean and standard deviation of the drift distribution for a given design are simultaneously optimized, and in this case no differentiation between parameters which affect only the mean or standard deviation is necessary. This will produce a design which is robust in that the *slope* of the constraint vs. noise curve is minimized, thereby resulting in an insensitive design, while the mean drift value is as close to the threshold as possible, resulting in an inexpensive design.

34.3.2 Prototype Structure Finite Element (FE) Formulation

Toward the goal of presenting a proof-of-concept study on the application of robust design techniques to structural design procedures, a numerical model of the prototype structure, described in Sect. 34.3.1 of this paper, was developed using the commercial FE modeling package, ANSYS version 13.0. To simulate the complex nonlinear behavior of concrete, Solid65, a dedicated solid isoparametric element, is utilized in this research. Solid65 is a three-dimensional brick element with eight nodes, each allowing three translational degrees of freedom in the global x, y, and z directions [43]. As seen in Fig. 34.5, a multilinear constitutive material model based on the triaxial behavior of concrete developed by William and Warnke was used to simulate failure [44]. The concrete is capable of cracking in three orthogonal directions, plastic deformation, and creep; however, in order to achieve convergence, crushing capabilities were turned off. This element was of particular interest due to its ability of incorporating reinforcement bars directly into the element through a smeared cross-section, thereby increasing the computational efficiency of the simulation. The rebar modeled in Solid65 is capable of tension, compression, plastic deformation, and creep.

34.4 Robust Optimization Case Study: Coordinate Descent Method

34.4.1 Coordinate Descent Optimization Method

Coordinate Descent Method, also known as the *one-at-a-time* optimization algorithm [45, 46], minimizes the objective function by solving a series of scalar minimization sub-problems. Each sub-problem minimizes along a certain coordinate, while all other coordinates remain constant [47]. The objective function can be defined as ω, which is a function of *n* variables defined as:

$$\omega = f(x_1, x_2, x_3, \cdots, x_n) \tag{34.6}$$

The optimization is achieved by the sequential variation of one variable at a time while all others are fixed. At the first iteration of the algorithm, all variables are held constant with the exception of the first parameter (x_1). A new value is found for this variable which reduces the objective function. Upon the completion of this step, the first variable becomes fixed and the algorithm moves onto the second variable (x_2). This parameter is then varied to reduce the objective function. This process is followed for *n* iterations, where afterwards, the process returns to the first variable and the cycle is repeated until the solution converges to a local optimal value [46]. In the context of this research, the objective function, ω, which is a function of the eight design parameters outlined in Table 34.1 (X, Y, L and W, A_x, A_y, h_b, f_c', ρ), is to control the drift through the minimization of the insensitivity index. The design parameter values are fixed at a nominal case and subsequently varied following the optimization scheme outlined here. In order to retain computational efficiency, interval analysis [48] was used to reduce the number of runs necessary to achieve the optimum solution. The results from this optimization methodology are presented herein.

34.4.2 Optimization Results and Discussion

To begin the optimization process a nominal design is defined. The values for each of the eight nominal parameters are outlined in Table 34.2. The nominal design was one of the many possible designs that satisfy the code requirements. The design methodology for this particular design utilized the *trade-off* of slender frame members for strong concrete and more bulky cross-bracings. After 500 Coordinate Descent Method iterations at four noise levels each, two designs (See Table 34.2) were found; one which minimizes the insensitivity index and is sufficiently close to the threshold, and one which also concurrently optimizes the cost. Through the robust design optimization scheme presented in this paper, the insensitivity index is decreased by 31% for the most insensitive design, and 21% for the most insensitive design which also optimizes cost; this can be seen graphically in Figs. 34.6 and 34.7. The unit price of each of the three designs was computed in an effort to assess the efficiency of each design. The most insensitive design was priced most costly while, interestingly, the optimized design which also accounted for cost was priced essentially the same as the nominal design, proving that increased robustness can be achieved at reasonable cost; thus proving the practical applicability of the Robust Design methodology to structural engineering. The fact that the design which accounts for cost effectiveness does not result in the most insensitive design, demonstrates the trade-offs engineers are fraught with on a daily basis.

Table 34.2 Comparison of nominal and robust design parameters

	Nominal design values	Robust design values (cost not considered)	Robust design values (cost considered)
Width of columns (X)	9 in.	12 in.	15 in.
Depth of columns (Y)	15 in.	18 in.	18 in.
Floor plan dimensions (L and W)	24 ft by 17 ft	22 ft by 18 ft	24 ft by 17 ft
Area of bracing in x plane (A_x)	5.25 $in.^2$	1.25 $in.^2$	2.60 $in.^2$
Area of bracing in y plane (A_y)	9.0 $in.^2$	7.75 $in.^2$	7.75 $in.^2$
Height of beams (h_b)	27 in.	45 in.	18 in.
Strength of concrete (f_c')	4,750	3,750	4,250
Column reinforcement ratio (ρ)	0.015	0.08	0.025
Insensitivity index	775	532	610
Cost of design	445 units	596 units	446 units

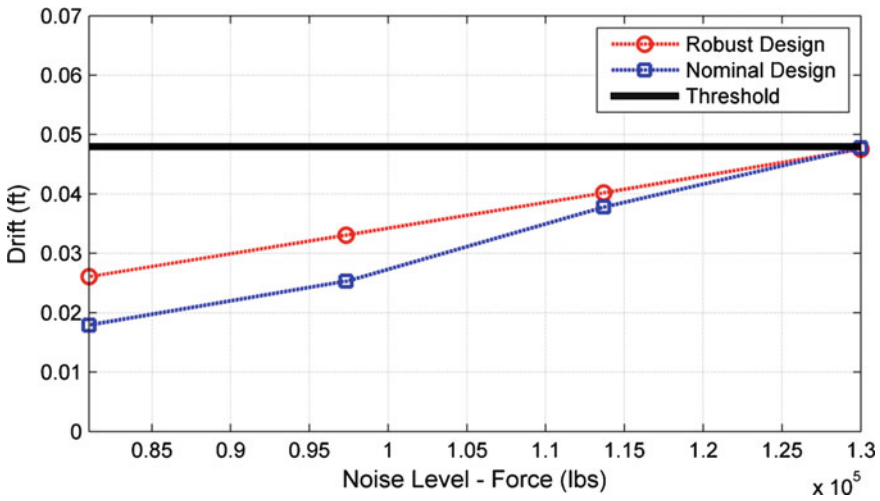

Fig. 34.6 Graphical depiction of objective function for nominal and robust design cases cost not considered

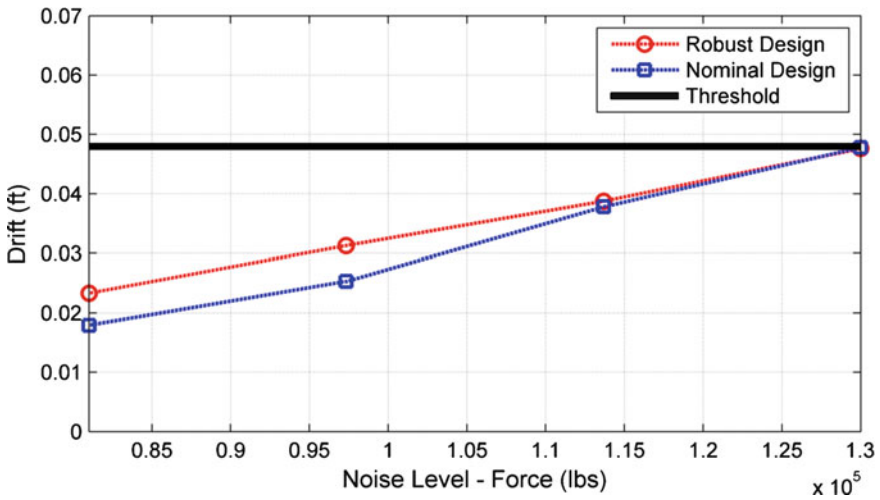

Fig. 34.7 Graphical depiction of objective function for nominal and robust design cases when cost considered

34.5 Robust Optimization Utilizing Particle Swarm Optimization

34.5.1 Particle Swarm Optimization Method

To achieve the desired objective of maximizing robustness while maintaining safety and minimizing cost, a more detailed study is conducted utilizing the particle swarm optimization (PSO) method. This method is a probability-based search algorithm initially developed by Eberhart and Kennedy [49], which falls under the swarm intelligence category of optimization algorithms [50]. The observed behavior of animal's instinctive movement to find food sources motivated the development of this method [51]. Using biological nomenclature as inspiration, the population is defined as a swarm and each individual within the swarm is called a particle. In order to control the distance a particle will travel in a single iteration of the process, PSO uses three parameters, swarm size, social acceleration coefficient, and cognitive acceleration coefficient to reach a local minima [49]. The utilization of PSO is advantageous in this research due to its well-suited nature for the nonlinear and discontinuous domain which is observed in the research problem presented in this manuscript [52].

A sufficient number of FE simulated designs are needed to start the optimization process. Five-hundred designs, each with four noise levels were simulated. Latin-hypercube design, a sampling method developed at Los Alamos National Laboratory, is used to ensure an adequate coverage and exploration of the eight parameters' design domain (See Table 34.1). Similar to the case-study, interval analysis was used to keep computational costs due to simulations at a tractable level. The input–output relationship between the response of the structure and the input parameters is represented by a fast running 'response surface function', also known as an emulator or surrogate model. A matrix function is used to train the response

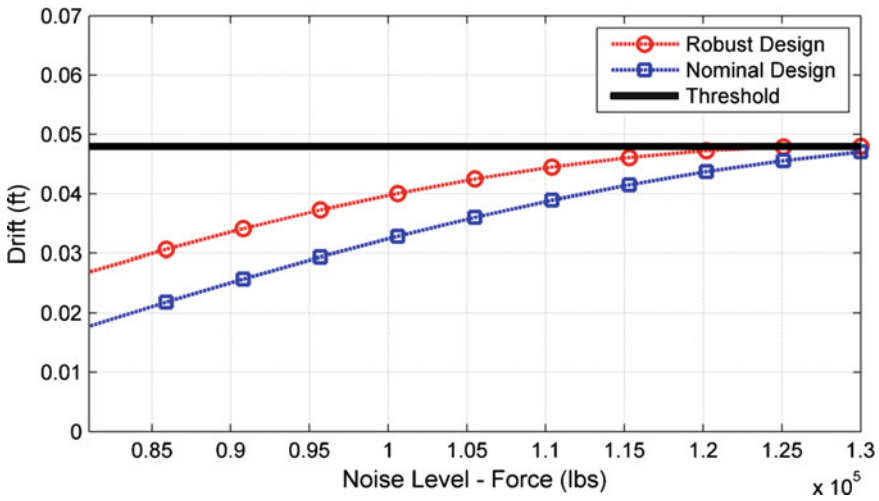

Fig. 34.8 Graphical depiction of objective function utilizing particle swarm optimization

Table 34.3 Comparison of robust and nominal designs using PSO

	Nominal design values	Robust design values cost considered
Width of columns (X)	16 in.	19 in.
Depth of columns (Y)	15 in.	24 in.
Floor plan dimensions (L and W)	30 ft by 13 ft	30 ft by 13 ft
Area of bracing in x plane (A_x)	5.2 $in.^2$	2.60 $in.^2$
Area of bracing in y plane (A_y)	1 $in.^2$	1.30 $in.^2$
Height of beams (h_b)	48 in.	12 in.
Strength of concrete (f_c‘)	3,550	5,500
Column reinforcement ratio (ρ)	0.01	0.08
Insensitivity index	648	354
Cost of design	652 units	500 units

surface to the FE simulated data and is used in place of the computationally expensive FE model. This response surface can, within reason, accurately predict the outcomes of all possible design configurations (within the defined ranges for the design parameters), at a computationally efficient level. The response surface is a function of the eight design parameters; column width, column depth, floor plan dimensions, cross-sectional area of bracing in the x plane, cross-sectional area of bracing in the y plane, height of beams, strength of concrete, and reinforcement ratio.

Using this response surface, the objective is then to minimize the area between the specified drift threshold (that is constant for all noise levels presenting infinite robustness, in the most ideal case) and the performance of alternative designs for varying noise levels, as depicted in Fig. 34.8. Therefore, the PSO algorithm operates on minimizing this area.

$$\omega = Area\left(f\left(X, Y, L \text{ and } W,\ A_x, A_y, h_b, f_c', \rho\right)\right) \tag{34.7}$$

34.5.2 Optimization Results and Discussion

As discussed in Sect. 34.4.2, in order to achieve the stated robust design definition, cost must be optimized in addition to the design's insensitivity to noise. In accordance, PSO methodologies are utilized, incorporating the optimization for cost, using a swarm size of 25, social acceleration coefficient of 1.3, and a cognitive acceleration coefficient of 2.8 to complete the optimization process and quantify the robustness, or the insensitivity of a number of designs. To initialize the optimization algorithm, parameter values for the first iteration of the algorithm are obtained by selecting a design from the available simulated data that minimizes the insensitivity index. The resulting robust design outlined is in Table 34.3. The nominal design for this case was randomly chosen from the set of 500 designs simulated using FE software. Through the optimization process, a design was developed which minimizes the insensitivity index by 43% and cost by 23%, a significant decrease in

both insensitivity and cost. The reduction in the insensitivity index can be seen in Fig. 34.8. Not only is the insensitivity index minimized for the robust design case, pictured as the dashed line with circular markers, but it is also very robust at high noise levels, exploiting the highly nonlinear design parameter and noise relationship.

The results presented here, reinforce the applicability of this methodology to structural design problems. Through the use of PSO methods, a more continuous design domain is established at a computationally tractable manner, allowing the most robust design to be established within the definitions presented in this paper. The resulting design maximizes its insensitivity to noise parameters, while simultaneously ensuring the design's cost stays within an efficient region.

34.6 Conclusion

The results provided in this paper prove the validity of robust design principles as applied to the structural engineering process. This paper presents two methodologies which successfully demonstrate the application of robust design principles as both a design and a decision making tool for design engineers. With the robust optimization methodologies presented here, a single structural design can be found which is more insensitive to noise parameters than the nominal design, while maintaining, or reducing, the cost for design, thus, proving a more efficient structure. This process also creates a design which is more resilient to unforeseen forces in the event of an earthquake or hurricane, by considering possibility of high variability in forces (noise levels) and not relying on the statistics used in the traditional reliability-based design methods.

Future work to improve the methods presented in this paper includes the exploration of more design constraints, maximum allowable stresses and strains, first natural frequency, buckling, etc., as well as noise types, material and structural properties and fabrication errors. Moreover, to improve upon the accuracy of the PSO method, more FE simulation runs may be completed to provide more *experimental data* to train the surrogate model. In addition, a study that considers multiple design constraints and noise factors is essential to validating this methodology for full scale operational structures. Lastly, a more detailed cost analysis for each design case will be advantageous in assessing the efficiency of designs.

Acknowledgements This material is based upon work supported by the National Science Foundation under Grant No. 1011478.

References

1. Bulleit WM (2008) Uncertainty in structural engineering. Pract Period Struct Des Construct 13(1):24–30
2. Mohsine A, Kharmanda G, El-Hami A (2006) Improved hybrid method as a robust tool for reliability-based design optimization. Struct Multidiscip Optim 32(3):203–213
3. WangW,Wu J (Y-T), Lust RV. Deterministic design, reliability based design and robust design. Project Report, Southwest Research Institute and General Motors Research and Development Center. This paper was presented at the MSC 1997 Aerospace Users Conference, printed in their proceedings.
4. Chen W, Wiecek M, Zhang J (1999) Quality utility: a compromise programming approach to robust design. ASME J Mech Des 121(2):179–187
5. Chen W, Allen JK, Tsui K-L, Mistree F (1996) A procedure for robust design. ASME J Mech Des 118(4):478–485
6. Shoemaker AC, Tsui K-L, Wu CFJ (1991) Economical experimentation methods for robust design. Technometrics 33(4):415–427
7. Taguchi G (1986) Introduction to quality engineering: designing quality into products and processes. Qual Resour, White Plains
8. Nair VN, Abraham B, MacKay J, Nelder JA, Box G, Phadke MS et al (1992) Taguchi's parameter design: a panel discussion. Technometrics 34(2):127–161
9. Vanik MW, Beck JL, Au SK (2000) Bayesian probabilistic approach to structural health monitoring. J Eng Mech 126(7):738–745
10. Beyer H, Sendhoff B (2007) Robust optimization – a comprehensive survey. Comput Method Appl Mech Eng 196:3190–3218
11. Park G-J, Lee T-H, Lee KH, Hwang K-H (2006) Robust design: an overview. AIAA J 44(1):181–191
12. Phadke MS (1989) Quality engineering using robust design. Prentice Hall, Englewood Cliffs
13. Taguchi G (1987) Systems of experimental design. vols 1 and 2. Krauss International, New York
14. Cunha MDC, Sousa JJDO (2010) Robust design of water distribution networks for a proactive risk management. J Water Res Plan Manag March/April:227–236
15. Marano GC, Sgobba S, Greco R, Mezzina M (2008) Robust optimum design of tuned mass dampers devices in random vibrations mitigation. J Sound Vib 313(3–5):472–492
16. Unal R, Wu KC, Stanley DO (1997) Structural design optimization for a space truss platform using response surface methods. Qual Eng 9(3):441–447
17. Lee MCW, Mikulik Z, Kelly DW, Thomson RS, Degenhardt R (2010) Robust design – a concept for imperfection insensitive composite structures. Compos Struct 92:1469–1477

18. Schoen MP, Hoover RC, Chinvorarat S, Schoen GM (2009) System identification and robust controller design using genetic algorithms for flexible space structures. J Dynam Syst Measure Control 131:31003
19. Kim JH, Lee JE, Chang SH (2008) Robust design of microfactory elements with high stiffness and high damping characteristics using foam-composite sandwich structures. Compos Struct 86:220–226
20. Ku KJ, Rao SS, Chen L (1998) Taguchi-aided search method for design optimization of engineering systems. Eng Optim 30(1):1–23
21. Park G-J, Lee T-H, Lee KH, Hwang K-H (2006) Robust design: an overview. AIAA J 44(1):181–191
22. Box GEP, Bisgaard S, Fung CA (1988) An explanation and critique of Taguchi's contributions to quality engineering. Qual Reliab Eng Int 4(2):123–131
23. Montgomery DC (1991) Design and analysis of experiments. Wiley, Singapore, pp 417–433
24. Lee KH, Park GJ (1996) Robust design for unconstrained optimization problems using the Taguchi method. AIAA J 34(5):1059–1063
25. Welch WJ, Yu TK, Kang SM, Sacks J (1990) Computer experiments for quality control by parameter design. J Qual Tech 22(1):15–22
26. Vining GG, Myers RH (1990) Combining Taguchi and response surface philosophies: a dual response approach. J Qual Tech 22(1):38–45
27. Shoemaker AC, Tsui KL (1993) Response model analysis for robust design experiments. Commun Stat B 22(4):1037–1064
28. Shiau GH (1990) A study on the sintering properties of iron ores using the Taguchi's parameter design. J Chinese Stat Assoc 28:253–275
29. Tai CY, Chen TS, Wu MC (1992) An enhanced Taguchi method for optimizing SMT processes. J Electron Manuf 2(3):91–100
30. Tsui K-L (1999) Robust design optimization for multiple characteristic problems. Int J Prod Res 37(2):433–445
31. Beyer H-G, Sendhoff B (2007) Robust optimization – a comprehensive survey. Comput Method Appl Mech Eng 196:3190–3218
32. Rackwitz R, Christensen PT (1992) Reliability and optimization of structural systems. Springer, Berlin
33. Rao SS (1996) Engineering optimization. Wiley, New York
34. Siddall JH (1984) A new approach to probability in engineering design and optimization. J Mech Transm Automat Des 106(1):5–10
35. Chen X, Sim M, Sun P (2007) A robust optimization perspective on stochastic programming. Oper Res 55(66):1058–1071
36. Eggert RJ, Mayne RW (1993) Probabilistic optimal design using successive surrogate probability function. J Mech Des 115(3):385–391
37. Oishi Y (2007) Robust control and robust optimization: a method for problems with nonlinear uncertainty. J Jpn Soc Sim Tech 26(2):95–100
38. Deb K, Pratap A, Agarwal S (2002) A fast and elitist multiobjective genetic algorithm: NSGA-II. IEEE Trans Evol Comput 6(2):182–197
39. Kumar A, Nair PB, Keane AJ, Shahpar S (2008) Robust design using Bayesian Monte Carlo. Int J Numer Method Eng 73:1497–1517
40. Neal RM (1996) Bayesian learning for neural networks. Springer, Berlin
41. O'Hagan A, Kennedy M, Oakley J (1999) Uncertainty analysis and other inference tools for complex compute codes (with discussion). Bayesian Stat 6:503–524
42. Construction Publishers and Consultants (2005) RS means and Masonry cost data, 23rd edn. Reed Construction Data, Kingston
43. ANSYS (2004) Theory reference for ANSYS and ANSYS workbench
44. William KJ, Warnke ED (1975) Constitutive model for the triaxial behaviour of concrete. In: Proceedings of the international association for bridge and structural engineering, vol 19. ISMES, Bergamo, p 174
45. Luo ZQ, Tseng P (1992) On the convergence of the coordinate descent method for convex differentiable minimization. J Optim Theor Appl 72(1):7–35, View record in Scopus | | Full text via CrossRef | Cited by in Scopus (63)
46. Nocedal J, Wright Stephen J (2006) Numerical optimization, 2nd edn. Springer Science/Business Media, New York
47. Li Y, Osher S (2009) Coordinate descent optimization for l1 minimization with application to compressed sensing: a greedy algorithm. Inverse Probl Imag 3(3):487–503
48. Moore R, Weldon L (2003) Interval analysis and fuzzy set theory. Fuzzy Set Syst 135(1):5–9
49. Eberhart RC, Kennedy J (1995) A new optimizer using particle swarm theory. In: Proceedings of the sixth international symposium on micro machine and human science. IEEE, Nagoya, pp 39–43
50. Parsopoulos KE, Vrahatis MN (2007) Parameter selection and adaptation in unified particle swarm optimization. Math Comput Model 46(1–2):198–213
51. Tsoulos IG, Stavrakoudis A (2010) Enhancing PSO methods for global optimization. Appl Math Comput 216(10):2988–3001
52. Plervis V, Papadrakakis M (2011) A hybrid particle swarm–gradient algorithm for global structural optimization. Comput Aided Civ Infrastruct Eng 26(1):48–68

Chapter 35
Optimum Spans' Lengths of Multi-span Reinforced Concrete Beams Under Dynamic Loading

P. Sharafi, Muhammad N.S. Hadi, and Lip H. Teh

Abstract In the design of continuous beams, say bridges, achieving an economical layout is one of the primary objectives, and requires simultaneous consideration of cost and layout variables. This study aims to figure out an explicit methodology for the optimum layout design of multi-span reinforced concrete beams under dynamic loadings in order to optimize the total cost. The aim is to determine the optimum spans lengths for continuous beams under dynamic loadings considering the involved cost elements. For this purpose a new methodology is developed in order to shift from the traditional design space to a new one. Then, an objective function for the cost and layout optimization problem is formulated in the new space. The proposed method employs action effects of the beams as alternative design variables in lieu of the cross-sectional ones. This ability enables the method to be easily used in realistic structural optimization problems rather than simple models, and helps the layout design procedure to take less time, in an iterative optimization process. In order to solve the formulated optimization problem, an Ant Colony Optimization algorithm is proposed. The robustness of the methodology is illustrated through a number of examples.

Keywords Cost optimization • Layout optimization • Reinforced concrete beam • Multi-span beam • Ant colony optimization

35.1 Introduction

Layout optimization is nowadays an appreciated instrument at all scales of structural design. Layout optimization of structures offers more material savings and high performance optimal designs, and can also provide innovative structures. The optimal design of the structure involves the topology optimization of the structural system and the cross-sectional design of structural members.

In contrast to steel structures, where the cost optimization can, more or less, be formulated as a weight minimization problem; for concrete structures, the optimization problem needs to be formulated as a cost minimization problem; because different materials are involved. In practice, a minimum weight design may not lead to a minimum cost design in concrete structures. Ideally, the optimization problem should be considered in terms of costs of materials, fabrication, erection, maintenance, and disassembling the structure at the end of its life cycle, which is referred to as life cycle cost [1].

The significant research on optimum design of RC beams based on cost minimization goes back to the early 1970s. In recent years, some optimization heuristics such as Evolutionary Algorithms have been utilized in order to deal with the discrete form of cost optimization of concrete beams. Although in theory the size of RC members and their dimensions in building structures are continuous, in the design process, we usually deal with the dimensions as discrete sizes. The dimensions of concrete sections are usually varied by a certain size, e.g. 25 or 50 mm a step, which makes the section dimensions discrete. The amount of reinforcement is also determined by the number of bars in a RC section. Therefore, one can define the optimization problem of RC sections as a discrete optimization problem rather than a continuous one. A number of methods have been developed as general methods for the discrete optimization of structures. Hadi [2] employed

P. Sharafi • M.N.S. Hadi (✉) • L.H. Teh
School of Civil, Mining and Environmental Engineering, University of Wollongong,
Northfields Avenue, Wollongong, NSW 2522, Australia
e-mail: mhadi@uow.edu.au

J.M. Caicedo et al. (eds.), *Topics on the Dynamics of Civil Structures, Volume 1*,
Conference Proceedings of the Society for Experimental Mechanics Series 26,
DOI 10.1007/978-1-4614-2413-0_35,

a Neural Network method to deal with the cost optimization of RC beams. Leps and Sejnoha [3], Govindaraj and Ramasamy [4] and others have attempted to make use of evolutionary methods like Genetic Algorithm (GA), to deal with the problem in discretized form. Recently, using new heuristics, some different methods have been employed for the layout optimization of structures by Nimtawat and Nanakron [5, 6], Zhu and Zhang [7] and Shaw et al. [8].

Nevertheless, the applications of these methods are limited to either cost optimization of structures with predefined shapes or layout optimization of structures without considering the relevant costs, say weight minimization.

In this study, first, a new cost function is proposed to deal with the cost optimization problem of rectangular RC beams, which can be used in layout optimization of multi-span RC beams as well as considering the cross-sectional action effects under various loading systems. Then, using this new function and employing Ant Colony Optimization method a new algorithm is proposed in order to find the optimum length of spans to minimize the cost of multi-span beams under dynamic loading systems. Ant colony, as a metaheuristic, has been used as a combinatorial optimization tool in the past decade. Ant colony algorithms study models derived from the observation of real ants' behavior. As an evolutionary approach, this method is one of the random methods for combinatorial optimization problems that moves toward the final solution of the problem by adding the modified solution in each step. The first Ant Colony Optimization (ACO) algorithm used in 1992 by Dorigo et al. [9] was known as Ant Systems (AS). Some modifications on this metaheuristic in recent years made it an appropriate method for solving combinatorial optimization problems.

35.2 Problem Definition

The design variables can be classified into four types: material design variables such as type of concrete to be used; topological design variables such as number of spans in a frame; geometric layout variables such as length of spans in a continuous beam; and finally, cross section design variables such as dimensions of a concrete section. In most occasions, the designer is not free to set the pre-assigned parameters and design variables, and the existing circumstances may dictate to the designer what to do. Exploiting experience, nevertheless, one may shift from one set of variables to another that causes a new definition for the objective function (cost function in this case). Moreover, any changes in choosing design variables may lead to changes in constraints and even vary their nature from design variables to behavior ones and vice versa. In other words, depending on the nature of the optimization problem, the process of achieving an optimum feasible solution may be much quicker, shifting from one design space to another by changing design variables as the space dimensions.

The selection of the cost function can be considered the most important decision in the entire optimal design process. Therefore, it is essential to introduce a cost function that represents the most influential cost components and more importantly, is applicable for a variety of similar optimization problems. Furthermore, it must be capable of matching the explicit constraints of structures, which are often given by formulas in design codes.

In concrete structures, at least three different cost items should be considered in optimization: costs of concrete, steel, and formwork. So, the general cost function for a reinforced concrete beam can be expressed in the following form:

$$C = c_c A_c + c_{sl} A_{sl} + c_{sv} A_{sv} + c_f P_f \tag{35.1}$$

where c_c, c_{sl}, c_{sv} and c_f are the unit costs of concrete, longitudinal steel, shear steel and formwork respectively and A_c, A_{sl}, A_{sv} and P_f are their corresponding quantities. In most published optimization studies, the costs are calculated for a member such as a beam, and coefficients and quantities are presented based on members or the unit length of each member in (35.1). If such a classic cost function for a beam optimization problem is used, some or all of the parameters A_c, A_{sl}, A_{sv} and P_f are considered the design variables. Then, based on explicit constraints, which are presented in codes and/or implicit behavior constraints of the problem, the optimum values of the design variables will be found using optimization techniques. In other words, most current cost optimization functions deal only with cross-sectional variables.

In case of the multi-objective optimization of large structures including a combination of material, geometrical layout, topological and cross-sectional design variables, using currently available formulation leads to a significant number of design variables and constraints. This is because each of the stated conditions might require a complicated trial and error procedure. In fact, the design variables of this kind, even in the traditional methods of design, require sound engineering judgment to be chosen, and it can be extremely time-consuming to determine their solution for each section of each member. Therefore, unless alternative design variables are selected for the cost function, the optimization procedure might be too unwieldy.

The reason why parameters like cross-sectional area, perimeter of concrete section or area of reinforcement steel are not truly suitable as design variables in a multi-objective optimization problem is that, such variables are not obtained from an explicit mathematical procedure. These parameters are mainly calculated using suggested relations in design codes, which

do not uniquely provide the exact values for these parameters. Furthermore, in order to determine such parameters, the first step is to complete the structural analysis procedure. Then, using the structural analysis outputs such as forces and moments together with design code requirements, the cross-sectional characteristics of the concrete beam are primarily determined. To put it simply, if the problem is a multi-objective optimization one and/or comprises a combination of different types of optimization, using such an optimization formulation, each step of the multi-variable optimization of a structure includes both analysis and design processes. In this case, besides the classic cross-sectional variables, the layout of a structure and consequently the outputs of structural analysis would be variables of the problem and designer has to repeat the design procedure to achieve the optimal cross-sectional variables that are usually functions of other analysis outputs.

Consider (35.2) as a potential alternative cost function to (35.1) in an arbitrary beam cross-section.

$$C = c_1 M_u^+ + c_2 M_u^- + c_3 V_u \tag{35.2}$$

where M_u^+ and M_u^- are the positive and negative bending moment capacities and V_u is the shear capacity of the section. If an appropriate set of $\{c_1, c_2, c_3\}$ could be found, in such a way that (35.2) represents the cost of the section, the design variables would shift from A_c, A_{sl}, A_{sv} and P_f to M_u^+, M_u^- and V_u. In fact, due to the relationship between the capacity factors of the section and structural analysis outputs in design codes, the aim of using cost functions such as (35.2) is to use structural analysis outputs instead of structural design factors.

In (35.2), the cost function is considered in a section rather than a member. It enables the designer to select a number of sections for each member and in the whole structure to control the cost, and there is no necessity to conduct the optimization process over the entire member. Since the cross-sectional characteristics of a member, say a RC beam, such as A_c, A_{sl}, A_{sv} and P_f varies along the memb, in order to come up with an accurate cost function for a member, one needs to have a clear idea about the probable distribution of bending moments and shear forces. Such a requirement makes the formulation extremely complited and sometimes impractical for some multi-objective or multi-variable problems.

35.3 Mathematical Formulation

In formulating the cost optimization of a beam and the relevant constraints, the Australian design standard for reinforced concrete structures, AS-3600 [10] is used, which is based on limit states design method of concrete structures. The evaluation of the area of steel reinforcement and the area of concrete section are based on the strength limit states of the section that can occur in either concrete or steel.

Consider an arbitrary section of a rectangular reinforced concrete beam as shown in Fig. 35.1. The dimensions of the section are b and h, the areas of tension and compression reinforcement steel are A_{st}, A_{sc} and the area of shear reinforcement

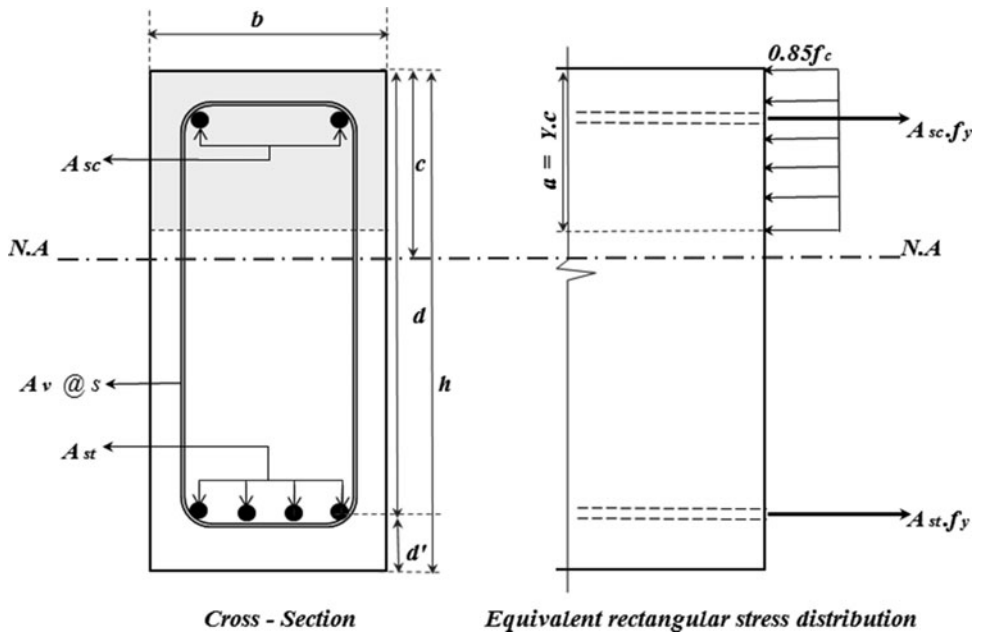

Fig. 35.1 An arbitrary section of a rectangular RC beam

steel in a unit length of beam is A_{sv}/s. The set of $\{c_1, c_2, c_3\}$ in (35.2) can be presented with regard to the set of predefined cost coefficients $\{c_c, c_{sl}, c_{sv}, c_f\}$ in (35.1) as follows [11]:

$$\begin{cases} c_1 = \frac{1}{3}c_c K_4 + \frac{1}{2}c_{sl}K_1 + \frac{2}{3}c_f K_7 \\ c_2 = \frac{1}{3}c_c K_3 + \frac{1}{2}c_{sl}K_1 + \frac{2}{3}c_f K_6 \\ c_3 = \frac{1}{3}c_c K_5 + c_{sv}K_2 + \frac{2}{3}c_f K_8 \\ ---------- \\ K_1 = (f_{yl}\, d^{(b)}(1 - 0.5\gamma k_u))^{-1} \\ K_2 = (f_{yv}\, d)^{-1}\ \Delta V_u^{(b)} \\ K_3 = \left[f_{yl}\frac{A_{sc}^{(b)}}{b}(1 - 0.5\gamma k_u)\right]^{-1} \\ K_4 = \left[f_{yl}\frac{A_{st}^{(b)}}{b}(1 - 0.5\gamma k_u)\right]^{-1} \\ K_5 = \left[f_{yl}\frac{A_{st}^{(b)}}{b}(1 - 0.5\gamma k_u)\right]^{-1} \\ K_6 = 2\left[f_{yl}A_{sc}^{(b)}(1 - 0.5\gamma k_u)\right]^{-1} \\ K_7 = 2\left[f_{yl}A_{st}^{(b)}(1 - 0.5\gamma k_u)\right]^{-1} \\ K_8 = \left[\frac{2}{\frac{f_{yv}A_{sv}^{(b)}}{s} + \beta b(f'c)^{\frac{1}{2}}} + \frac{1}{\beta d(f'_c)^{\frac{1}{2}}}\right] \end{cases} \tag{35.3}$$

where f_{yl} is the yield strength of the longitudinal reinforcement steel, f_{yv} is the yield strength of the shear reinforcement steel, f_c' is the characteristic compressive cylinder strength of concrete at 28 days, and β is a coefficient based on the standard. Other parameters are shown in Fig. 35.1. The coefficients c_1, c_2 and c_3 determine how the parameters M_u^-,M_u^+ and V_u contribute to the cost function. Now, in order to re-analyze a rectangular beam to achieve the optimum criteria, one can use (35.3) in lieu of (35.2). For this purpose, the cost will be the sum of cost functions of all selected sections in the structure.

$$C_t = \sum_{i=1}^{NS} C_i = \sum_{i=1}^{NS} (c_{1i} M_{ui}^+ + c_{2i} M_{ui}^- + c_{3i} V_{ui}) \tag{35.4}$$

where C_t is the total cost of the structure and NS is the number of selected sections to control the cost.

Now, consider a multi-spans Euler-Bernoulli beam under an arbitrary loading system $F(x,t)$, N sets of attached springs, lumped masses, and dampers (SMD), as shown in Fig. 35.2. The transverse displacement $w(x,t)$ is governed by (35.6) [12].

$$\rho \frac{\partial^2}{\partial t^2} w(x,t) + \mu \frac{\partial}{\partial t} w(x,t) + EI \frac{\partial^4}{\partial t^4} w(x,t) = F(x,t) - f(x,t) \qquad 0 \le x \le L \tag{35.5}$$

where ρ, EI, and L are the linear density, bending stiffness, and length of the beam, respectively; μ is either the viscous damping coefficient or the coefficient of the elastic foundation; and $F(x, t)$ is the external force. The $f(x, t)$ represents constraint forces exerted to the beam by the attached SMD's, and is given by (35.6).

$$f(x,t) = \sum_{i=1}^{N} \partial(x - x_i)(m_i \frac{\partial^2}{\partial t^2} + c_i \frac{\partial}{\partial t} + k_i) w(x,t) \tag{35.6}$$

Equation 35.5 can be solved by eigenfunction expansion or modal expansion. To this end, the transverse displacement $w\{x, t\}$ of the beam is approximated by a modal series of n terms which leads to the matrix differential equation for the beam.

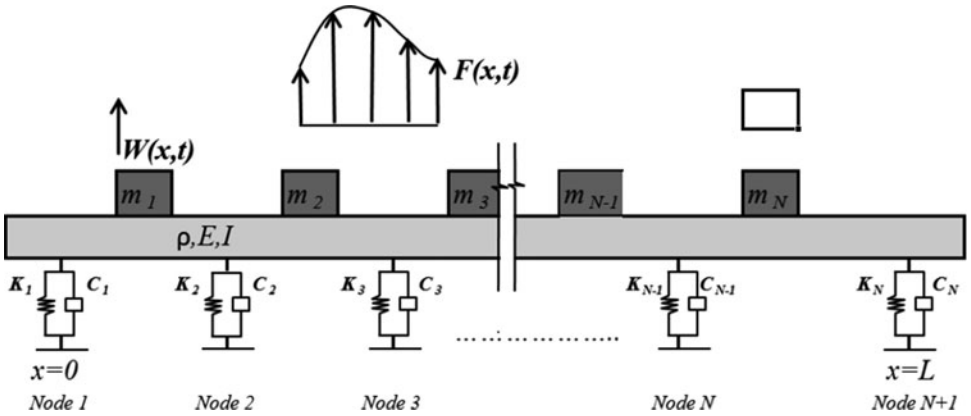

Fig. 35.2 A model for multi-span beams under a dynamic loading system

$$w(x,t) \approx \sum_{i=1}^{N} \Phi_k(x) q_k(t) = [\Phi]^T \{q(t)\} \tag{35.7}$$

$$[M]\{\ddot{q}(t)\} + [D]\{\dot{q}(t)\} + [K]\{q(t)\} = \{B_f\} f(t) \tag{35.8}$$

The $q_k(t)$ are unknown generalized coordinates, and $\Phi_k(x)$ are the eigenfunctions of the beam, and $\{B_f\}$ is a force distribution vector. The aim is to re-design the beam to determine the optimum span lengths in order to minimize the cost. This multi-variable optimization problem includes two structural optimization problems. Optimizing the span lengths as a geometric layout problem and optimizing the cross-section parameters as a cross-sectional optimization problem. Therefore, to come up with a solution for such a problem, one needs to deal with two sets of the above-mentioned variables; that is, the final cost will be a function of two sets of variables. Based on (35.4), the total cost is a function of the beams' action effects under the dynamic loading systems, which in turn are functions of the span lengths. The general formulation of the optimization problem is:

$$\begin{cases} \min\limits_{l_1, l_2, \cdots, I_N} Cost(l_1,\ l_2,\ ...,\ l_N) = \sum_{i=1}^{NS} (c_{1i} M_{ui}^{+} + c_{2i} M_{ui}^{-} + c_{3i} V_{ui}) \qquad for \quad i = \{1, 2, ..., NS\} \\ \quad - \\ \quad s.t \begin{cases} [\mathrm{M}]\{\ddot{q}(\mathrm{t})\} + [\mathrm{D}]\{\dot{q}(\mathrm{t})\} + [\mathrm{K}]\{\mathrm{q(t)}\} = \{\mathrm{B_f}\}\mathrm{f(t)} \\ \emptyset_f \{\ M_u^{+}\} \ \geq \{\ \mathrm{M}^{*^{+}}\} \\ \emptyset_f \{\ M_u^{-}\} \ \geq \{\ \mathrm{M}^{*^{-}}\} \\ \emptyset_s \{V_u\} \geq |V^*| \\ \{u_{max}\} \leq \{\Delta_{max}\} \\ \{l_{min}\} \leq \{l_i\} \leq \{l_{max}\} \\ other\ constraints\ based\ on\ standards \end{cases} \end{cases} \tag{35.9}$$

in which, $M_i^{*^{+}}$, $M_i^{*^{-}}$. and $|V_i^*|$ are positive and negative flexure and shear action effects of Section i. $\emptyset_f$ and $\emptyset_s$ are strength reduction factors in flexure and shear respectively. The serviceability requirements limit the maximum deflection u_{max} on the entire member to Δ_{max} under the serviceability load case. Other constraints for durability, fire resistance, minimum cover and minimum flexural strength, can be easily added to the problem as well, based on relevant design codes. The first constraint is the behavior constraint of the structural optimization problem determining the relation between design bending moments $\{M^{*^{+}}\}$ and $\{M^{*^{-}}\}$ based on general formulation of the displacement method. The dimension of variable constraint vectors, say $\{M_{ui}^{+}\}$, $\{M_{ui}^{-}\}$, is NS; because these constraints and cost function will be evaluated in NS critical sections. Furthermore, the length of each span can be constrained between l_{min} and l_{max} in order to satisfy architectural considerations.

35.4 Ant Colony Algorithm for Optimization of Multi-span Beams

The developed algorithm in this study attempts to find optimal lengths of spans, for a multi-span beam to minimize the cost function employing an ACO approach. The aim is to find a set of integers as the lengths of spans to minimize the cost function. In other words, the algorithm deals with the discrete form of the problem and the first step will be discretizing the domain. For this purpose, a graph named *construction graph* is defined.

In order to discretize the domain of answers, assume that span lengths are bounded in $[l_{min}, l_{max}]$ with intervals (accuracy) equal to ε, then each l_i rests in the s.t of $\{l_{min}, l_{min} + \varepsilon, l_{min} + 2\varepsilon, \ldots, l_{max} - \varepsilon, l_{max}\}$. Obviously, the smaller ε is chosen, the more accurate results will be obtained and the more running time the algorithm needs. The number of spans (beam elements) and the number of nodes in the continuous beam is N and $N + 1$respectively; hence the construction graph is defined as a graph with $N + 1$ nodes and $(l_{max} - l_{min})/\varepsilon * N$ edges as shown in Fig. 35.3. Each pair of nodes are connected with $(l_{max} - l_{min})/\varepsilon$ edges, i.e. there are $(l_{max} - l_{min})/\varepsilon$ choices for each ant on each node to select another one, for making its trail (solution). It should be pointed out that, as stated in the definition of constraints and shown in Fig. 35.3, l_{max} and l_{min} might be specified differently for each span, say $l_{i\ max}$ and $l_{i\ min}$. In this case, the number of choices for ants on each node might differ from the other ones. Now that the construction graph is prepared, ants can start their solution process in three phases [13].

1. *The phase of initial data processing and preliminary calculation*: In this phase, the primary values are given and the calculations start and data are entered. Artificial ants are located on the first and last nodes of the construction graph, i.e. Nodes 1 and $N + 1$, to construct their solution. The lengths of paths are introduced and parameters α, β, ρ and the termination criteria are defined and initial pheromone and heuristic matrix are organized. Each value (i,j) of pheromone matrix and heuristic matrix shows the tendency of the ant located on Node i of the construction graph to choose Edge j to move towards the next node. Since there are as many as $(l_{max} - l_{min})/\varepsilon$ edges that connect every two successive nodes, the dimension of these two matrices will be $N*(l_{max} - l_{min})/\varepsilon$.

For organizing the *heuristic matrix* and *initial pheromone matrix*, we can make use of structural analysis experience. As the type of supports and other boundary conditions and constraints, plus any loads can affect the length of spans, the entries of heuristic matrix and initial pheromone matrix might be organized based on such parameters. For example, one might define the length of spans adjacent to an elastic or free ends shorter than the others might. In this case, the entries of heuristic matrix relating to shorter choices might receive higher numbers relative to the entries relating to longer ones. Using such a heuristic matrix or defining the initial pheromone matrix using the above-mentioned structural rules helps the algorithm converge sooner. Thus, each value (i,j) of *choice information matrix*, which is obtained by multiplying the corresponding arrays of heuristic matrix by those of pheromone matrix, shows the tendency or desirability of the ant located on Node i of construction graph to choose Edge j to move toward Node $i + 1$.

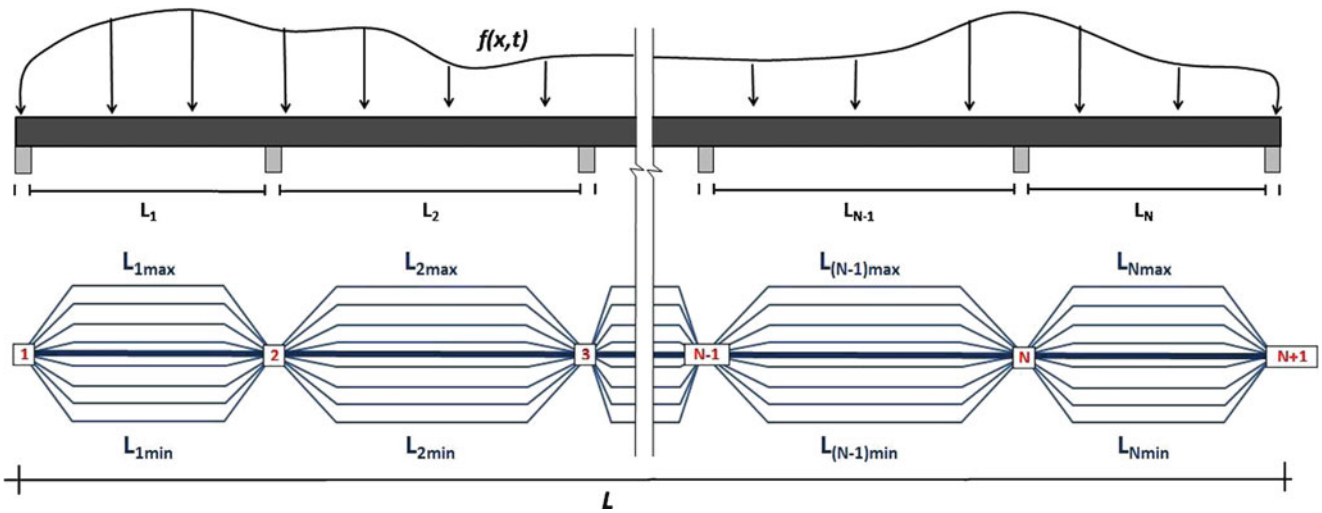

Fig. 35.3 A multi-span rectangular RC beam and the relevant construction graph for the Ant algorithm

2. *The phase of the construction of solution*: This phase consists of two segments that form the basis of the heuristic. In the first segment of this phase, ants located on the starting nodes of construction graph, whether Node *1* or Node $N + 1$, start to construct their solutions, using the random proportional rule [9]. In this method, the feasible neighborhood N_i^k is defined as the edges between Nodes i and $i + 1$, when the ant is located at Node i in either rout.

The ant leaves its source Node $i \in \{1,2,\ldots,N + 1\}$ on the construction graph to destination node on the connecting Edges $j \in \{1, 2, \ldots, (l_{max} - l_{min})/\varepsilon\}$, using the random proportional rule, similar to the random roulette wheel rule and quite randomly. The probability of Edge j to be chosen by Ant on Node i is proportional to the entry (i, j) of the choice information matrix. The bigger the entry (i, j) of the choice matrix is, the more probable Node j is to be chosen by Ant i. The ants continue constructing their solution and move from a node to the next one, until getting to Node $N + 1$ as the end of their trail. The constraint for ants is that the sum of all spans must be equal to L. Therefore, two groups of ants are located on both ends of the graph, so that every edge has the same overall probability of being chosen by the ants.

After the segment of random choice, the values of N lengths and thereby the new geometrical layout for the beam is obtained. Through structural analysis method and using the behavior constraints, design actions effects in the identified sections are determined and using other constraints, the required strength capacities for each section are calculated. Based on the strength capacity of sections, the cost function or the cost of this solution is obtained.

3. *The phase of updating*: This phase consists of updating information and statistics, and then updating pheromone trails. Using the information obtained in the phase of constructing the solution, the trail presenting the best cost, up to this stage, is selected as the best so-far iteration. Then pheromone trails of construction graph are updated. For this purpose, Ants are allowed to deposit pheromone on the edges associated with the best so-far iteration. The process of pheromone updating consists of two segments. The first segment corresponds to pheromone evaporation. In this segment the parameter ρ depends on the number of steps defined for termination criteria, and initial pheromone and heuristic values. The second segment is depositing pheromone. For depositing pheromone, the pheromone values on the edges associated with the best iteration up to now increase and the ant deposits an amount of pheromone equal to $1/cost$ on the edges of construction graph associated with the best so-far iteration; where *cost* is the value of cost function obtained from best iteration.

The above procedure continues until the termination criterion is satisfied; then the optimum spans will be the best-so-far solution. As seen, in each step a simple structural analysis is required to calculate the beam actions. Making use of various finite element methods, such a calculation takes a small fraction of a second for each beam. Using (35.1) as the objective function would be significantly time-consuming than using (35.2). Due to the variation of lengths in each step, the estimation of design variables in each step would be considerably encumbered; apart from the fact that, in each step, algorithm would iteratively need to deal with the design formulas. Equation 35.2 makes the optimization process much tangible and greatly usable in cost optimization of large structures.

35.5 Numerical Example

To demonstrate the efficiency of the proposed methodology a numerical example is solved employing the abovementioned methodology. All computations were performed on P9700 @2.80 GHz computer running MATLAB R2009b. In order to ensure that the obtained solution from ACO is global or near global optimum, many runs were made in parallel. Since each run is fully independent of the others, the program can be run in parallel so that the total execution time will be practically the same as required for a single run.

Example: A five-span continuous beam with a total length of 25,000 mm is considered as shown in Fig. 35.4. The material properties and relative cost factors are: f′c = 25 MPa, fyl = 500 MPa, fyv = 250 MPa, cc = 1, csl = 75, csv = 64, cf = 0.45. The beam is under a uniformly distributed impulse load of 20 kN/m. The aim is to find the optimum l1, through l5, so that the cost is minimized. The 11 sections A through K, are taken as the control sections. The number of selected sections completely depends on the number of critical or control ones, and one may choose more sections to achieve much accurate results.

The preliminary design of the beam comprised five equal spans, which results in a total cost of 6,967 units. It should be added that every initial design based on preliminary judgment of the designer and/or using approximate charts or formulas, which meet the design code requirements, can be used as the initial design and as the starting point of optimization process. Using (35.3) the values of K_1 to K_8, and then, the values of c_1, c_2 and c_3 for sections A to K are obtained. Having the necessary coefficients, the cost function can be defined, based on (35.9).

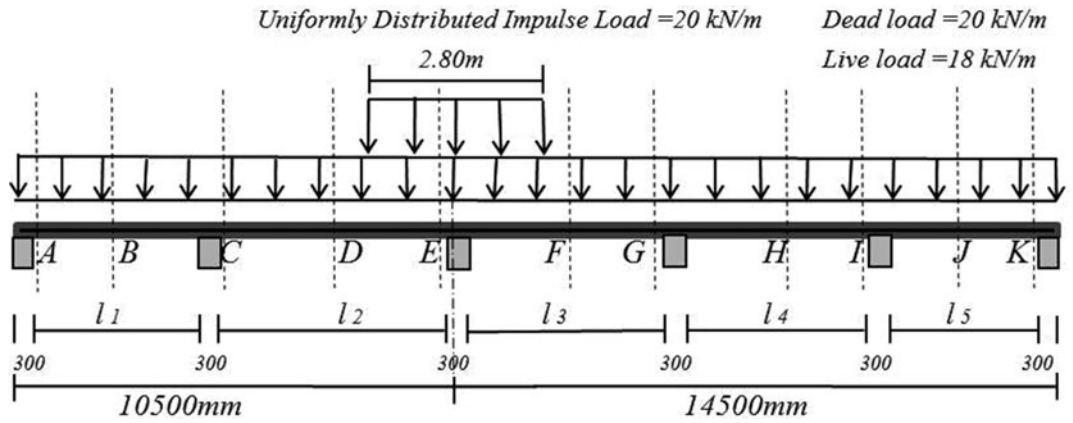

Fig. 35.4 Example: a five span beam and selected sections to control the cost

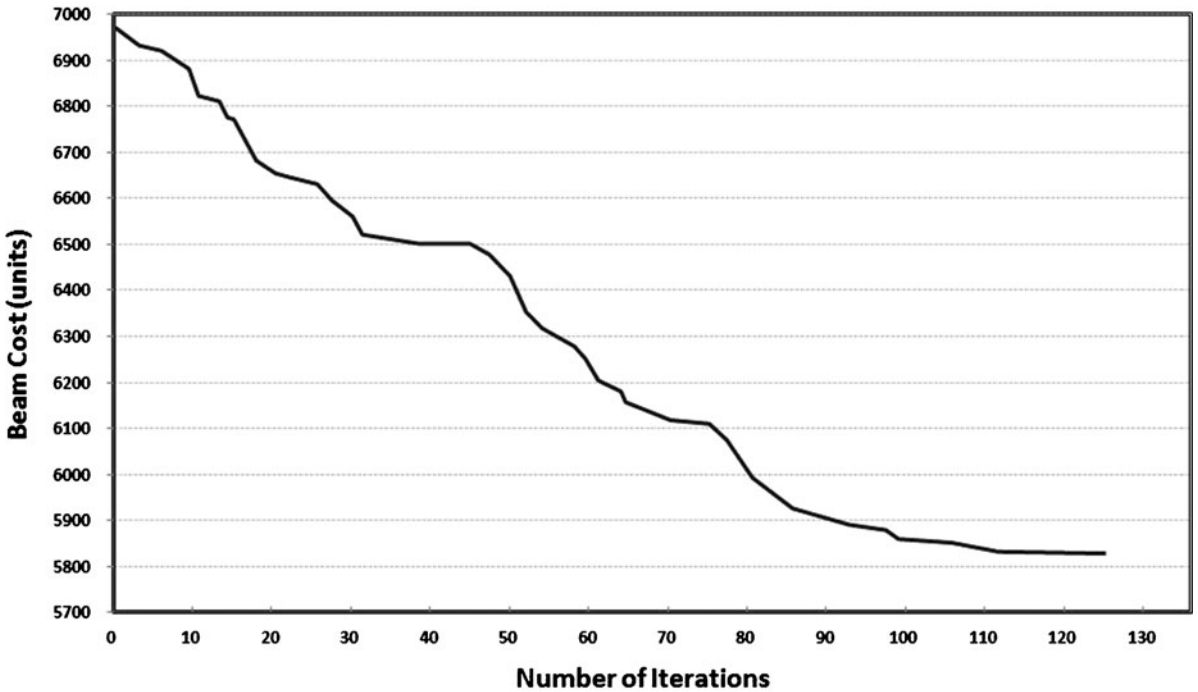

Fig. 35.5 Typical convergence history for the presented ACO algorithm

The Ant algorithm attempts to find the optimum spans using (35.9) as its objective function and observing other relevant constraints. Using the proposed Ant algorithm, after 125 iterations, and at CPU time of 31.59 s, the optimum lengths of $l1 = 4{,}800$ mm, $l2 = 4{,}100$ mm, $l3 = 6{,}900$ mm, $l4 = 4{,}200$ mm and $l5 = 5{,}000$ mm resulting in a total cost of 5,833 units, based on (35.1), are obtained (equals to 16.2% cost saving). The interesting point is if an equivalent static load is employed in lieu of the impulse load, the optimum spans lengths of 4,000, 5,900, 5,200, 5,900, 4,000 at the cost of 5,648 would be obtained. It shows that the dynamic analysis results in a further 3.2% cost. Figure 35.5 shows a typical convergence history for the ACO algorithm for this example.

35.6 Conclusion

The main objective of this study is to propose a new model for cost and layout optimization of multi-span RC beams, which can be easily used under dynamic loading systems. The cost function proposed in this study simplifies the process of cost optimization of multi-span beams and is applicable to multi-variable optimization of RC beams for various loading systems. In order to illustrate the capability of the proposed cost function, it was used in the problem of finding the optimum span lengths of RC multiple-span beams. The proposed algorithm for solving the cost optimization problem is an Ant System based algorithm, which can be easily used for optimizing the span lengths and also is capable of working with different cost functions. The presented example shows that the proposed algorithm using the new cost optimization function provides acceptable results.

References

1. Adeli H, Sarama KC (2006) Cost optimization of structures: fuzzy logic, genetic algorithms, and parallel computing. Wiley, England
2. Hadi MNS (2003) Neural networks applications in concrete structures. Comput Struct 81(6):373–381
3. Leps M, Sejnoha M (2003) New approach to optimization of reinforced concrete beams. Comput Struct 81:1957–1966
4. Govindaraj V, Ramasamy JV (2007) Optimum detailed design of reinforced concrete frames using genetic algorithms. Eng Optim 39(4):471–494
5. Nimtawat A, Nanakorn P (2010) A genetic algorithm for beam–slab layout design of rectilinear floors. Eng Struct 32(11):3488–3500
6. Nimtawat A, Nanakorn P (2009) Automated layout design of beam-slab floors using a genetic algorithm. Comput Struct 87(21–22):1308–1330
7. Zhu JH, Zhang WH (2010) Integrated layout design of supports and structures. Comput Methods Appl Mech Eng 199(9–12):557–569
8. Shaw D, Miles J, Gray A (2008) Determining the structural layout of orthogonal framed buildings. Comput Struct 86(19–20):1856–1864
9. Dorigo M, Stüzle T (2004) Ant colony optimization. MIT Press, USA
10. Standards Australia (2009) AS3600: concrete structures. Sydney
11. Sharafi P, Hadi MNS, Teh L (2012) Optimum column layout design of reinforced concrete frames under wind loading. In: IMAC-XXX conference and exposition on structural dynamics, Jacksonville
12. Weaver W, Timoshenko S, Young DH (1990) Vibration problems in engineering, 5th edn. Wiley, USA
13. Kaveh A, Sharafi P (2008) Optimal priority functions for profile reduction using Ant colony optimization. Finite Elem Anal Des 44(3):131–138

Chapter 36
Imposing Node on Linear Structures During Multi-harmonic Excitations

E. Jamshidi, S. Arshi, M.R. Ashory, and N. Nematipoor

Abstract Vibration absorbers are usually designed using the Finite Element (FE) model of structures. However, the FE models of structures are not always precise due to inaccurate estimation of the physical properties of structure, discretization errors of distributed parameters, poor approximation of boundary conditions, inadequate modeling of joints and computational errors. In contrast, modal testing is an experimental approach to build the mathematical model of structures. As the test structure is modeled by direct measurement on the structure, the modal models are more accurate than FE models. In this paper, a method is proposed to impose node on an arbitrary point of a linear structure subjected to a multi-harmonic excitation by attaching two spring mass absorbers. The method is based on the structural modification Using experimental frequency Response Functions (SMURF) technique and estimates the mass values of the absorbers for the suggested stiffness values. The advantage of this approach is that there is no need to have the theoretical or FE models of the structure and it is not restricted to a particular geometry. A cantilever beam subjected to multi-harmonic excitations is considered as a numerical case study in a simulated test and the sprung masses are designed to suppress the vibration amplitude of the beam at a selected arbitrary point.

Keywords Dynamic vibration absorber • Multiharmonic excitation • FRF • SMURF

Nomenclature

$\alpha_{lk}^{(i,j)}$	Receptance of the second system with two absorbers
α_{lk}	Receptance of a primary system
α_{mm}	Receptance of absorber
α_{nn}	Receptance of absorber
K	Absorber stiffness
m	Absorber mass
ω	Excitation frequency receptance of second system with two absorbers

36.1 Introduction

In recent years, controlling of the vibration amplitude of flexible structures using the tuned vibration absorbers has attracted much attention and has been studied by many authors. Jacquot [1] proposed a method that eliminates the vibration of a harmonically excited Euler-Bernoulli beam. The method gives the vibration absorber parameters based on a single mode of beam. Therefore, it is limited in application. Ozgüven and Candir [2] extended the previous method to suppress any two resonances. They performed an optimization procedure for the response in any desired mode using assumed-modes approach. Mani Kanahally and Crocker [3] gave the optimized stiffness and damping parameters for a certain chosen

E. Jamshidi (✉) • S. Arshi • M.R. Ashory • N. Nematipoor
Department of Engineering, Semnan Branch, Islamic Azad University, P.O. Box: 35145–179, Semnan, Iran
e-mail: ehsan.jamshidi@gmail.com; ehsan.jamshidi@semnaniau.ac.ir

J.M. Caicedo et al. (eds.), *Topics on the Dynamics of Civil Structures, Volume 1*,
Conference Proceedings of the Society for Experimental Mechanics Series 26,
DOI 10.1007/978-1-4614-2413-0_36,

mass to suppress the significant modes in which the absorbers are tuned to operate. Keltie and Cheng [4] used point masses to absorb the vibration amplitude of any arbitrary point of structure. The method finds the optimized location of certain point mass to reduce the vibration level at the desired location of the structure. Alsaif and Foda [5] proposed a method to optimize the mass or stiffness amount and the absorber location on beam in order to decrease the vibration of arbitrary point via Green function. Ozer and Royston [6] proposed a method which gives the vibration absorber parameters mounted to a damped multi-degree-of-freedom structure based on Sherman-Morrison matrix inversion formula. The method is capable to minimize the overall vibration amplitude of a multi-degrees-of-freedom system. Cha and Pierre [7] proposed a method to impose a single node using the normal modes of a supported linear structure bymounting a chain of absorbers. Cha and Zhou [8] used a set of sprung masses and rotational absorbers to enforce one or more fixed nodes for any supported linear structure subjected to harmonic excitations.

Nematipoor et al. [9] proposed a method based on SMURF technique to suppress vibration amplitude of an arbitrary point on a linear structure subjected to harmonic excitation. Nematipoor et al. [10, 11] extended the method to impose two arbitrary points on the structure. The method is beneficial because there is no need to have the theoretical or FE model of structure and it is not related to a particular geometry. Sun et al. [12] applied dynamic vibration absorbers to control the vibration of structures under multi-frequency harmonic excitation. In this paper, a method is proposed to impose node on an arbitrary point of a linear structure subjected to a multi-harmonic excitation by attaching two sprung mass absorbers based on SMURF technique. The proposed method estimates the mass values of the absorbers for suggested stiffness values. The advantage of this approach is that there is no need to have the theoretical or FE models of the structure and it is not restricted to particular geometry.

36.2 Theory

Figure 36.1 shows a structure with two absorbers at points i and j. The relation between a receptance of the beam with two absorbers at point i and j, and the receptances of beam only with absorber at point j can be given by [13]:

$$\alpha_{lk}^{(i,j)} = \alpha_{lk}^{(j)} - \frac{\alpha_{ik}^{(j)}\alpha_{li}^{(j)}}{\alpha_{nn} + \alpha_{ii}^{(j)}} \tag{36.1}$$

where

$$\alpha_{nn} = \left(\frac{1}{k_i} - \frac{1}{m_i\omega^2}\right) \tag{36.2}$$

In which m_i and k_i are the mass and stiffness values of the attached absorber at point i.

On the other hand, the receptances of beam and absorber at point j can be written with respect to the receptances of the original structure. For instance for $\alpha_{lk}^{(j)}$:

$$\alpha_{lk}^{(j)} = \alpha_{lk} - \frac{\alpha_{jk}\alpha_{lj}}{\alpha_{mm} + \alpha_{jj}} \tag{36.3}$$

where

$$\alpha_{mm} = \left(\frac{1}{k_j} - \frac{1}{m_j\omega^2}\right) \tag{36.4}$$

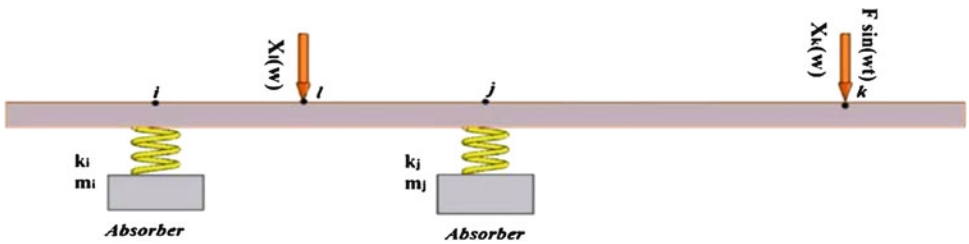

Fig. 36.1 A beam with two absorbers

In which m_j and k_j are the mass and stiffness values of the attached absorber at point j.

Inserting (36.3) and other receptances into (36.1), we have:

$$\alpha_{lk}^{(i,j)} = \alpha_{lk} - \frac{\left[\alpha_{jk}(\alpha_{ii}+\alpha_{nn}) - \alpha_{ji}\alpha_{ik}\right]\alpha_{lj}}{(\alpha_{jj}+\alpha_{mm})(\alpha_{ii}+\alpha_{nn}) - \alpha_{ij}\alpha_{ji}} + \frac{\left[\alpha_{jk}\alpha_{ij} - \alpha_{ik}(\alpha_{jj}+\alpha_{mm})\right]\alpha_{li}}{(\alpha_{jj}+\alpha_{mm})(\alpha_{ii}+\alpha_{nn}) - \alpha_{ij}\alpha_{ji}} \tag{36.5}$$

Equation 36.5 is a general equation. It can be used for designing the suitable absorbers at points i and j to impose node at point l on the structure. The receptances $\alpha_{lk}^{(i,j)}(\omega_1)$ and $\alpha_{lk}^{(i,j)}(\omega_2)$ of the structure with two absorbers can be written with respect to the original receptances as:

$$\begin{aligned}\alpha_{lk}^{(i,j)}(\omega_1) = \alpha_{lk}(\omega_1) &- \frac{\left[\alpha_{jk}(\omega_1)(\alpha_{ii}(\omega_1)+\alpha_{nn}(\omega_1)) - \alpha_{ji}(\omega_1)\alpha_{ik}(\omega_1)\right]\alpha_{lj}(\omega_1)}{(\alpha_{jj}(\omega_1)+\alpha_{mm}(\omega_1))(\alpha_{ii}(\omega_1)+\alpha_{nn}(\omega_1)) - \alpha_{ij}(\omega_1)\alpha_{ji}(\omega_1)} \\ &+ \frac{\left[\alpha_{jk}(\omega_1)\alpha_{ij}(\omega_1) - \alpha_{ik}(\omega_1)(\alpha_{jj}(\omega_1)+\alpha_{mm}(\omega_1))\right]\alpha_{li}(\omega_1)}{(\alpha_{jj}(\omega_1)+\alpha_{mm}(\omega_1))(\alpha_{ii}(\omega_1)+\alpha_{nn}(\omega_1)) - \alpha_{ij}(\omega_1)\alpha_{ji}(\omega_1)}\end{aligned} \tag{36.6}$$

and

$$\begin{aligned}\alpha_{lk}^{(i,j)}(\omega_2) = \alpha_{lk}(\omega_2) &- \frac{\left[\alpha_{jk}(\omega_2)(\alpha_{ii}(\omega_2)+\alpha_{nn}(\omega_2)) - \alpha_{ji}(\omega_2)\alpha_{ik}(\omega_2)\right]\alpha_{lj}(\omega_2)}{(\alpha_{jj}(\omega_2)+\alpha_{mm}(\omega_2))(\alpha_{ii}(\omega_2)+\alpha_{nn}(\omega_2)) - \alpha_{ij}(\omega_2)\alpha_{ji}(\omega_2)} \\ &+ \frac{\left[\alpha_{jk}(\omega_2)\alpha_{ij}(\omega_2) - \alpha_{ik}(\omega_2)(\alpha_{jj}(\omega_2)+\alpha_{mm}(\omega_2))\right]\alpha_{li}(\omega_2)}{(\alpha_{jj}(\omega_2)+\alpha_{mm}(\omega_2))(\alpha_{ii}(\omega_2)+\alpha_{nn}(\omega_2)) - \alpha_{ij}(\omega_2)\alpha_{ji}(\omega_2)}\end{aligned} \tag{36.7}$$

The necessary conditions to impose node on the beam at point l when it is excited at point k with a multi-harmonic excitations, are:

$$\begin{aligned}\alpha_{lk}^{(i,j)}(\omega_1) = \alpha_{lk}(\omega_1) &- \frac{\left[\alpha_{jk}(\omega_1)(\alpha_{ii}(\omega_1)+\alpha_{nn}(\omega_1)) - \alpha_{ji}(\omega_1)\alpha_{ik}(\omega_1)\right]\alpha_{lj}(\omega_1)}{(\alpha_{jj}(\omega_1)+\alpha_{mm}(\omega_1))(\alpha_{ii}(\omega_1)+\alpha_{nn}(\omega_1)) - \alpha_{ij}(\omega_1)\alpha_{ji}(\omega_1)} \\ &+ \frac{\left[\alpha_{jk}(\omega_1)\alpha_{ij}(\omega_1) - \alpha_{ik}(\omega_1)(\alpha_{jj}(\omega_1)+\alpha_{mm}(\omega_1))\right]\alpha_{li}(\omega_1)}{(\alpha_{jj}(\omega_1)+\alpha_{mm}(\omega_1))(\alpha_{ii}(\omega_1)+\alpha_{nn}(\omega_1)) - \alpha_{ij}(\omega_1)\alpha_{ji}(\omega_1)} = 0\end{aligned} \tag{36.8}$$

and

$$\begin{aligned}\alpha_{lk}^{(i,j)}(\omega_2) = \alpha_{lk}(\omega_2) &- \frac{\left[\alpha_{jk}(\omega_2)(\alpha_{ii}(\omega_2)+\alpha_{nn}(\omega_2)) - \alpha_{ji}(\omega_2)\alpha_{ik}(\omega_2)\right]\alpha_{lj}(\omega_2)}{(\alpha_{jj}(\omega_2)+\alpha_{mm}(\omega_2))(\alpha_{ii}(\omega_2)+\alpha_{nn}(\omega_2)) - \alpha_{ij}(\omega_2)\alpha_{ji}(\omega_2)} \\ &+ \frac{\left[\alpha_{jk}(\omega_2)\alpha_{ij}(\omega_2) - \alpha_{ik}(\omega_2)(\alpha_{jj}(\omega_2)+\alpha_{mm}(\omega_2))\right]\alpha_{li}(\omega_2)}{(\alpha_{jj}(\omega_2)+\alpha_{mm}(\omega_2))(\alpha_{ii}(\omega_2)+\alpha_{nn}(\omega_2)) - \alpha_{ij}(\omega_2)\alpha_{ji}(\omega_2)} = 0\end{aligned} \tag{36.9}$$

Equations 36.8 and 36.9 are required to be solved simultaneity to find the mass values of the absorbers (m_i and m_j) for suggested stiffness values.

36.3 Numerical Case Study

A cantilever beam was considered to evaluate the performance of method. The specifications of beam are given in Table 36.1.

The beam is excited by a harmonic force with the frequency of ω_1 =314 rad/s (50 Hz) at points i, j and k (Fig. 36.2). The receptances α_{lk}, α_{jk},α_{ii},α_{ji}, α_{ik},α_{lj},α_{jj} and α_{li} are measuring the responses at points l, i and j. this procedure was repeated by exciting the beam using a harmonic force with the frequency of ω_2= 471 rad/s (75 Hz). Considering $k1$ = 10,000 N/m, $k2$ = 10,000 N/m, m_i= 0.132 kg and m_j = 0.023 kg are obtained (Fig. 36.2).

Figure 36.3 shows the receptance $\alpha_{lk}$of the beam with and without the designed absorbers. As can be seen the amplitude of vibration has decreased considerably after attaching the absorbers at the frequencies of 50 and 75 Hz.

Table 36.1 Beam specifications

Length (mm)	Width (mm)	Thickness (mm)	Density $\left(\frac{Kg}{m^3}\right)$	Modulus of elasticity $\left(\frac{GN}{m^2}\right)$
1,000	48	6	7,870	206

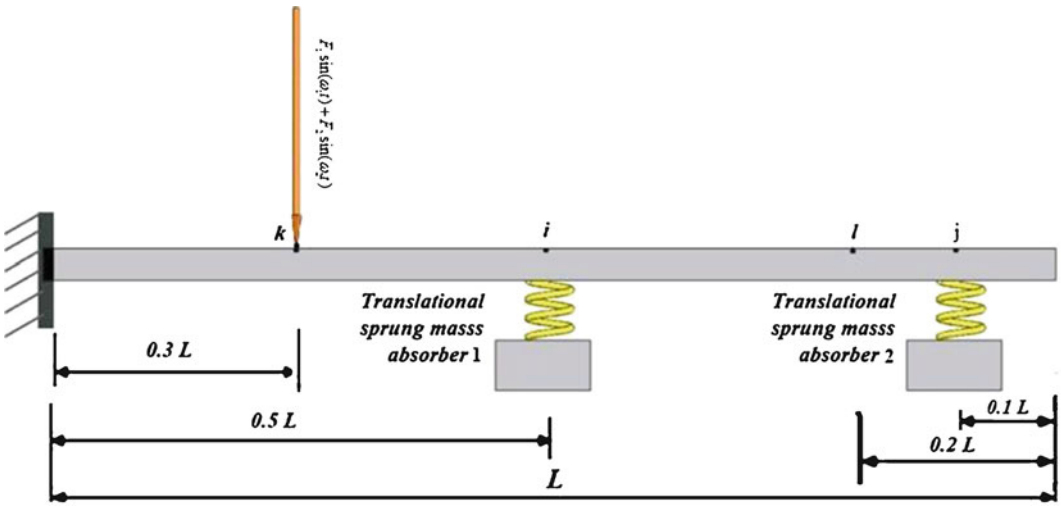

Fig. 36.2 Numerical case study of a beam

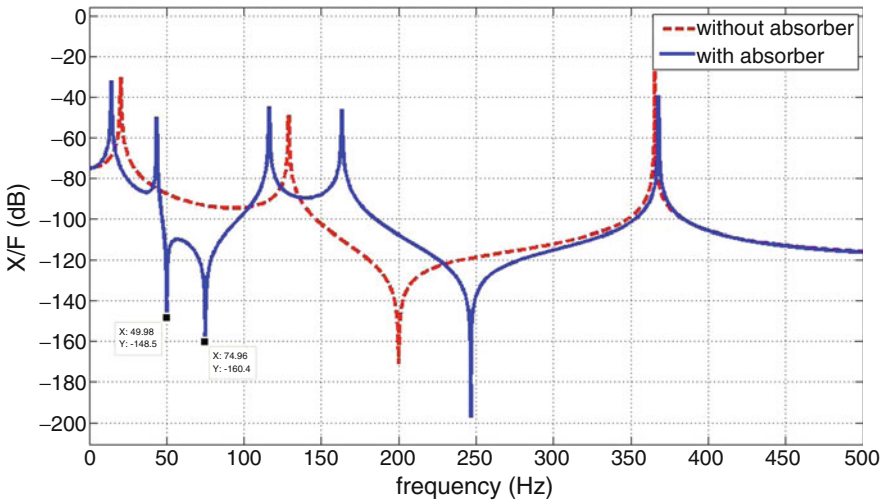

Fig. 36.3 Receptance α_{lk} with and without absorbers

36.4 Conclusions

In this paper a new method is proposed to impose node on an arbitrary point of a linear structure subjected to a multi-harmonic excitation by attaching dynamic vibration absorbers at arbitrary points, based on SMURF technique. The method calculates the mass values of the absorbers for the suggested stiffness values. The advantage of the method is

that the vibration absorbers can be designed using the experimental results from modal testing and there is no need to FE model. Also, the method is not restricted to any particular geometry or boundary conditions. A cantilever beam subjected to multi-harmonic excitations was considered as a numerical case study in a simulated test. The results show the effectiveness of method in suppressing the vibration amplitude at the desired point in the frequencies of excitations. The vibration amplitude was decreased by 100%.

References

1. Jacquot RG (1978) Optimal dynamic vibration absorbers for general beam systems. J Sound Vib 60(4):535–542
2. Ozgüven HN, Candir B (1986) Suppressing the first and second resonances of beams by dynamic vibration absorbers. J Sound Vib 111(3):377–390
3. Manikanahally DN, Crocker MJ (1991) Vibration absorbers for hysterically damped mass loaded beams. J Vib Acoust 113:116–122
4. Keltie RF, Cheng CC (1995) Vibration reduction of a mass-loaded beam. J Sound Vib 187(2):213–228
5. Alsaif K, Foda MA (2002) Vibration suppression of a beam structure by intermediate masses and springs. J Sound Vib 256(4):629–645
6. Ozer MB, Royston TJ (2004) Application of Sherman–Morrison matrix inversion formula to damped vibration absorbers attached to multi-degree of freedom systems. J Sound Vib 283(3–5):1235–1249
7. Cha PD, Pierre C (1998) Imposing nodes to the normal modes of a linear elastic structure. J Sound Vib 219(4):669–687
8. Cha PD, Zhou X (2006) Imposing points of zero displacements and zero slopes along any linear structure during harmonic excitations. J Sound Vib 297(1–2):55–71
9. Nematipoor N et al (2010) Vibration absorber design via frequency response function measurements Proceedings of the 28th IMac, a Conference on Structural Dynamics, Jacksonville, Florida USA. In: Proceedings of the 28th IMAC, Jacksonville, 12:pp 1587–1593 http://www.springerlink.com/content/k3557578t6320t76/
10. Nematipoor N et al (2010) Imposing nodes at two locations in harmonically excited structures using measured FRFs. In: Proceedings of the 17th international congress on sound and vibration, Cairo, 18–22 July 2010
11. Nematipoor N et al (2011) Imposing nodes for linear structures during harmonic excitations using SMURF method http://www.springerlink.com/content/a872040515055867/
12. Sun HL et al (2008) Application of dynamic vibration absorbers in structural vibration control under multi-frequency harmonic excitations. Appl Acoust 69:1361–1367
13. Ashory MR, Ewins DJ (1998) Generation of the whole FRF matrix from measurements on one column. In: Proceedings of the International Modal Analysis Conference IMAC (1998) SEM, Bethel, CT, United States, 2:800-814 February 1998

Chapter 37
Experimental Modal Analysis of a Full-Scale Seven-Story Shear Wall Based on Nonlinear Seismic Response

Eliyar Asgarieh and Babak Moaveni

Abstract In this study, the deterministic-stochastic subspace identification (DSI) method is used for estimating the instantaneous modal parameters of a full scale seven-story shear wall structure. Modal analysis is performed based on short time-windows of input-output data measured during different seismic base excitations on a shake table. The structure has been subject to four historical earthquakes with increasing intensities and various characteristics. At each time window, an equivalent global secant stiffness of the structure is estimated based on the hysteretic curve of base moment versus roof displacement. It is observed that the trend of identified instantaneous natural frequencies of the first vibration mode is strongly correlated with that of the square root of secant stiffness estimates. This observation encourages the use of experimental modal analysis for characterizing the stiffness behavior of nonlinear structures when subjected to nonstationary, large intensity excitations such as earthquakes.

Keywords Deterministic-stochastic subspace identification (DSI) • System identification • Structural health monitoring

37.1 Introduction

Structural health monitoring based on dynamic properties of structure has received increased attention in recent years. Modal parameters are known as the most common dynamic properties of structures, which are sensitive to damage [1, 2]. Different linear system identification methods have been successfully applied by researchers for identification of modal parameters of structures from output-only or input-output data [3–6]. Among the system identification methods, subspace system identification methods are known to be one of the most reliable methods [7, 8]. The identification methods just based on output could be subject to high errors for narrow-band non-stationary inputs. Therefore, identification methods based on input-output data are recommended when the input signal is available/measured. Most of the civil structures behave nonlinearly as they are subjected to higher amplitude excitations. Considering the nonlinearity in structures, modal parameters could be assumed as instantaneous features connected to tangent stiffness of structure at each moment instead of constant invariable features.

In this study the deterministic stochastic subspace identification (DSI) method is used for short-time/instantaneous system identification of a nonlinear structure subjected to non-stationary base excitations. A short length of data window is considered around each moment for estimation of instantaneous modal parameters at that moment. The method is performed using the input-output data from shake table test of a full-scale seven-story shear wall structure. The identified values are compared with the effective global stiffness of the structure, over the considered time window at each moment.

E. Asgarieh • B. Moaveni (✉)
Department of Civil and Environmental Engineering, Tufts University, 200 College Ave, Medford, MA, USA
e-mail: babak.moaveni@tufts.edu

J.M. Caicedo et al. (eds.), *Topics on the Dynamics of Civil Structures, Volume 1*,
Conference Proceedings of the Society for Experimental Mechanics Series 26,
DOI 10.1007/978-1-4614-2413-0_37,

37.2 Test Structure and Dynamic Tests

The test structure is a full-scale seven-story reinforced concrete shear wall, consisting of a main wall (web wall), a back wall (flange wall) perpendicular to the main wall for transversal stability, a concrete slab at each floor level, an auxiliary post-tensioned column to provide torsional stability, and four gravity columns to transfer the weight of the slabs to the shake table. Figure 37.1 shows the test structure mounted on the University of California San Diego (UCSD)-NEES shake table. More details about the test structure can be found in [9, 10]. The structure was excited by four historic earthquakes with increasing magnitude. The response of structure was measured with different types of sensors along the height of structure. The measured response data from seven longitudinal acceleration channels at each floor and the input acceleration measured at top of the shake table are used for short-time modal identification in this study.

The four earthquakes applied to the test structure are: (1) longitudinal component of the 1971 San Fernando earthquake ($M_w = 6.6$) recorded at the Van Nuys station (EQ1), (2) transversal component of the 1971 San Fernando earthquake recorded at the Van Nuys station (EQ2), (3) longitudinal component of the 1994 Northridge earthquake ($M_w = 6.7$) recorded at the Oxnard Boulevard station in Woodland Hill (EQ3), and (4) 360° component of the 1994 Northridge earthquake recorded at the Sylmar station (EQ4). Since the first earthquake does not cause any nonlinear behavior in the structure, data from only the last three tests are used for short-time system identification. Figure 37.2 shows the acceleration time histories of input base excitations measured on the shake table for EQ2, EQ3, and EQ4. It is worth noting that EQ2 and EQ3 result in similar levels of response nonlinearity in the shear wall while the nonlinearity in the response due to EQ4 is significantly larger. More details about the instrumentation and dynamic testing of the test structure can be found in [10].

37.3 Deterministic-Stochastic Subspace Identification (DSI)

The deterministic-stochastic state-space model for linear time-invariant systems can be written as

$$\begin{cases} x(k+1) = \mathbf{A}\mathbf{x}(k) + \mathbf{B}\mathbf{u}(k) + \mathbf{w}(k) \\ y(k) = \mathbf{C}\mathbf{x}(k) + \mathbf{D}\mathbf{u}(k) + \mathbf{v}(k) \end{cases} \tag{37.1}$$

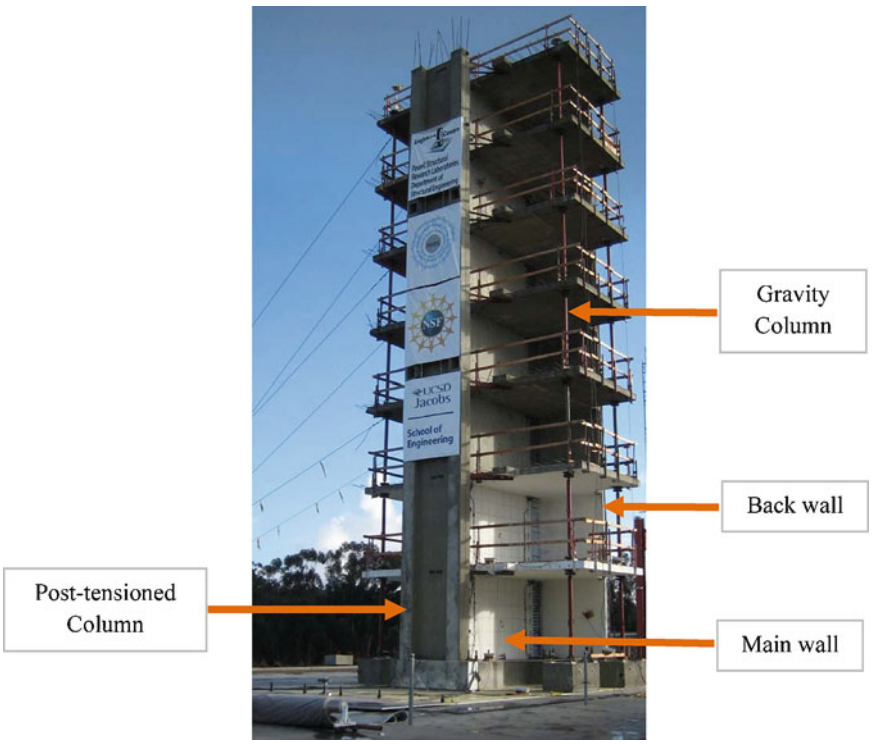

Fig. 37.1 Full-scale seven-story test structure on the UCSD-NEES shake table

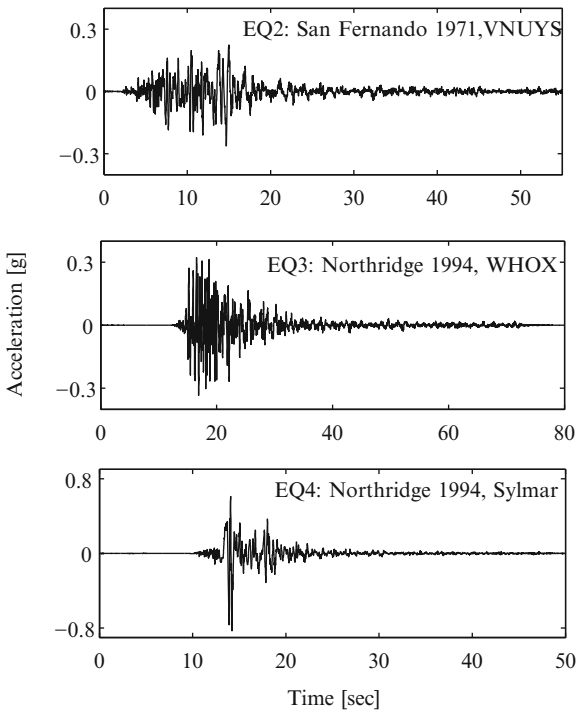

Fig. 37.2 Acceleration time histories of the three considered earthquakes measured on shake table

where **A**, **B**, **C** and **D** refer to the state-space matrices, $\mathbf{u}(k)$ and $\mathbf{y}(k)$ denote the input and output vectors, respectively, and $\mathbf{x}(k)$ is the state vector. In the deterministic-stochastic model, the process noise $\mathbf{w}(k)$ represents disturbances (small unmeasured excitations) and modeling inaccuracies, while the measurement noise $\mathbf{v}(k)$, models the sensor inaccuracies. The DSI is a linear parametric system identification method. This method uses both inputs and outputs data to fit a state-space model to the related system [7]. Since the input disturbance and measurement noise are considered explicitly in the DSI formulation, the method is robust against disturbances and noises. The method benefits from powerful numerical methods such as QR factorization, singular value decomposition, and least squares. The order of the model and the physical (as opposed to numerical/spurious) vibration modes are chosen based on stabilization diagrams.

37.4 System Identification Results

The DSI method is applied for short-time system identification of the test structure along its response time history for the three considered earthquakes (EQ2–EQ4). The sampling frequency of the data is 240 Hz. Two window lengths of 1- and 2-s are used for short-time system identifications. The sizes of Hankel matrices in 1- and 2-s window lengths are $(26 \times 8) \times 215$ and $(52 \times 8) \times 422$, respectively. The identification results for first natural frequency of test structure during the three earthquakes are shown in Fig. 37.3a. Figure 37.3b represents the square root of effective global stiffness of the structure during the three seismic tests. The effective global stiffness of the test structure at each time window is estimated as the secant stiffness of base moment versus roof displacement hysteretic curve during that time window (1- or 2-s). The base moment is estimated using the floor accelerations and their contributory masses. It is worth noting that for the considered dynamic tests, base moment versus roof displacement curves provide more clear hysteretic behavior of the structure than other types of hysteretic curves such as base shear versus roof displacement [9]. Figure 37.4 shows hysteretic curve of base moment versus roof displacement of structure during EQ2 at $t = 12$ s for a 2-s time window (i.e., $t = 11$–13 s) together with the line representing the secant stiffness at this moment.

From the Fig. 37.3, it can be observed that the natural frequency of the first mode is decreasing significantly as the energy of excitation is increasing (i.e., increasing nonlinearity). The identifications show that the first mode frequency is remarkably smaller at the end of excitation in comparison to its beginning for all three earthquakes considered. This effect is related to stiffness degradation of the structure. The effective stiffness and modal frequencies of the structure change consistently.

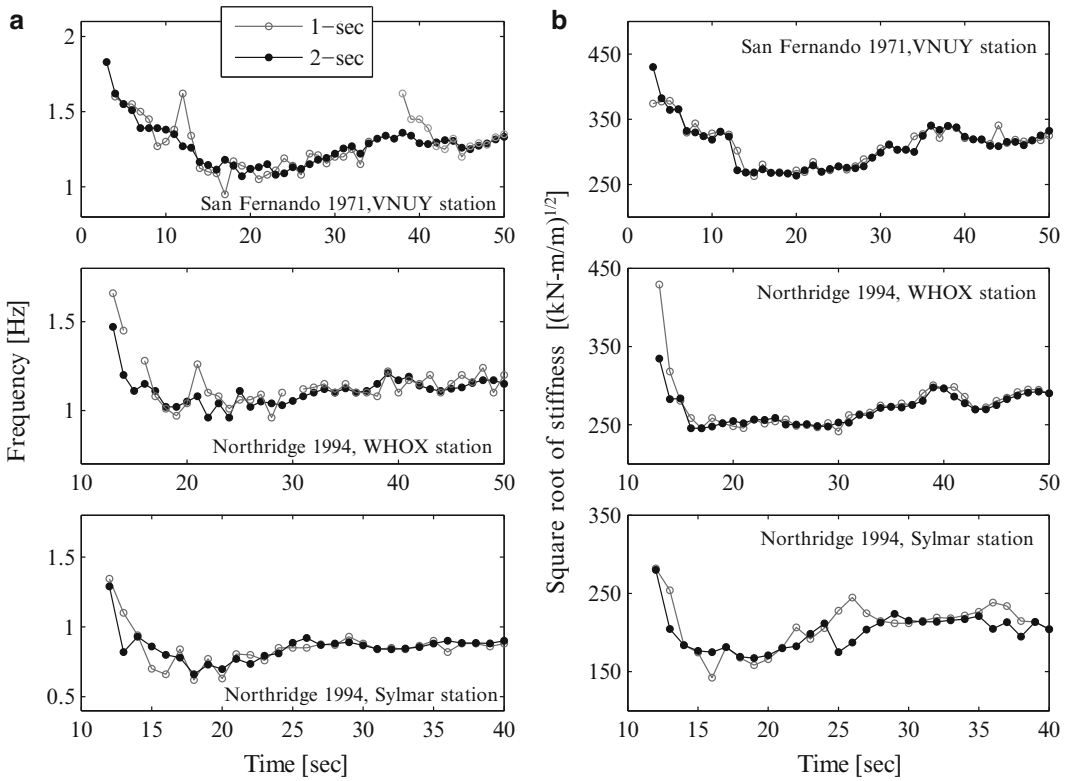

Fig. 37.3 Time histories of (**a**) instantaneous fundamental natural frequency, and (**b**) square root of an effective global stiffness measure of the test structure, estimated using 1- or 2-s data windows during the three considered

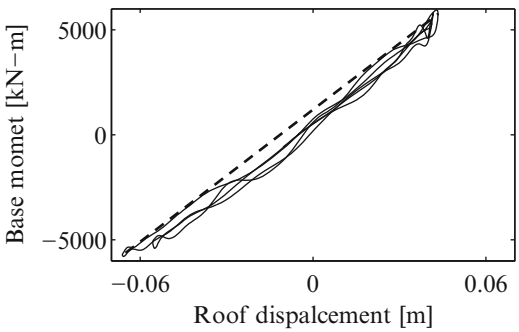

Fig. 37.4 Hysteretic curve and secant line of test structure at t = 12 s during EQ2 for a 2-s time window

Therefore, the short-time modal identification results by the DSI could be a proper indicator of changes in the tangent stiffness of the structure which can in turn be used for damage identification.

37.5 Conclusions

In this research the performance of deterministic stochastic subspace identification (DSI) method for instantaneous modal identification of nonlinear systems is evaluated. The data from shake table test of a full-scale seven-story shear wall structure is used for short-time modal identification. It is observed that short-time modal identifications by the DSI could be used to track the stiffness degradation (i.e., damage) in the structure. The results for instantaneous frequency identifications confirm

the intense decrease in stiffness at the strong motion part of the excitation and the permanent stiffness degradation. The instantaneous natural frequencies at the beginning and end of the excitation are bounded by the identified values from the ambient vibration and white noise data [10].

This study highlights the effectiveness of the DSI method for short-time (instantaneous) modal identification of nonlinear structural systems. It is expected that accurate estimates of instantaneous modal parameters can be used for characterizing the hysteretic behavior of the structures, which is the topic of an ongoing research by the authors. In addition, the instantaneous mode shapes identified using DSI for nonlinear structural systems at different levels of input energy can provide an estimate to the nonlinear normal modes [11] of the structural system.

Acknowledgements The authors would like to thank Professors Joel Conte and Jose Restrepo at UCSD for making the shake table test data available for this study. Assistance of Professors Marios Panagiotou and Ozgur Ozcelik as well as the technical staff at the Englekirk Structural Engineering Center in collecting the test data used in this study is also greatly acknowledged.

References

1. Doebling SW, Farrar CR, Prime MB (1998) A summary review of vibration-based damage identification methods. Shock Vib Dig 30 (2):91–105
2. Sohn H, Farrar CR, Hemez FM, Shunk DD, Stinemates DW, Nadler BR (2003) A review of structural health monitoring literature: 1996–2001. Los Alamos National Laboratory Report, LA-13976-MS, Los Alamos
3. Lus H, Betti R, Longman RW (2002) Obtaining refined first order predictive models of linear structural systems. Earthquake Eng Struct Dynam 31(7):1413–1440
4. Farrar CR, James GHIII (1997) System identification from ambient vibration measurements on a bridge. J Sound Vib 205(1):1–18
5. Magalhaes F, Cunha A, Caetano E, Brincker R (2009) Damping estimation using free decays and ambient vibration tests. Mech Syst Signal Process 24(5):1274–1290
6. Reynders E, Degrauwe D, De Roeck G, Magalhaes F, Caetano E (2010) Combined experimental-operational modal testing of footbridges. J Eng Mech 136(6):687–696
7. Van Overschee P, De Moore B (1996) Subspace identification for linear systems. Kluwer, Norwell
8. Peeters B, De Roeck G (1999) Reference-based stochastic subspace identification for output-only modal analysis. Mech Syst Signal Process 13(6):855–878
9. Panagiotou M, Restrepo JI, Conte JP (2011) Shake-table test of a full-scale 7-story building slice – phase I: rectangular wall. J Struct Eng 137(6):691–704
10. Moaveni B, He X, Conte JP, Restrepo JI, Panagiotou M (2011) System identification study of a seven-story full-scale building slice tested on the UCSD-NEES shake table. J Struct Eng 137(6):705–717
11. Kerschen G, Peeters M, Golinval JC, Vakakis AF (2009) Nonlinear normal modes, part I: a useful framework for the structural dynamicist. Mech Syst Signal Process 23(1):170–194

Chapter 38
Application of DDE-Model to Enhancing Seismic Response of Reinforced Concrete Frame

Chin-Hsiung Loh and Jung-Huan Li

Abstract In any assessment of the damage to a reinforced concrete structure, inelastic hysteretic behavior of structural member must be considered. In this study an advanced signal processing technique is used to investigate the physical features of an inelastic degrading hysteretic behavior of a reinforced concrete frame from its seismic response measurements. Through the singular spectrum analysis (SSA) and the nonlinear SSA (NLSSA), the original seismic response data is decomposed into independent additive components of decreasing weight which can be used for developing hysteresis loop in degrading order. The advantage of using NLSSA to extract the nonlinear feature form response data is demonstrated. Finally, the deteriorate distributed element (DDE) model is applied to simulate the damage pattern of the reinforced concrete frame with respect to each of the developed degrading hysteresis loop and to identify the degrading stiffness and equivalent damping ratio. Comparison on the physical indices between the developed DDE model and the recorded data is discussed.

Keywords Nonlinear single spectrum analysis (NLSSA) • Reinforced concrete • System identification

38.1 Introduction

Reinforced concrete structures typically exhibit nonlinear and inelastic behavior under severe dynamic loading, such as under earthquakes. Earthquake engineering considers both the expected performance of structures in an earthquake and the state of the damage after seismic events. For example, the finite element-based model updating method is a well known model-based method that can locate and quantify damage to each structural element. In practical applications, these have been characterized using indices, such as inter-story drift, other than stress. This measure generally neglects the effect of cumulative damage. The effect of accumulated damage to reinforced concrete members and structures under a seismic load is even more important than the maximum inter-story drift. In any assessment of the damage to a reinforced concrete structure, nonlinear hysteretic behavior of each member must be considered.

Hysteresis refers to the hereditary and the memory nature of an inelastic system, in which the restring force depends not only on the instantaneous deformation but also on the past history of deformation. Hysteresis is particularly important in depicting the nonlinear response of reinforced concrete. Various empirical models of restoring forces were proposed to account for the hereditary nature of inelastic systems. One of the widely accepted models is a differential model of hysteresis originally proposed by Bouc [1] and subsequently generalized by Wen [2] and other researchers. In this model, by specifying the loop parameters, it is possible to generate a large variety of hysteretic data from cyclic performance tests. A question is how the loop parameters can be selected so as to reproduce a good approximation of the measured data.

System identification offers a class of techniques for estimating the parameters of nonlinear structural systems from a set of given data. For parametric system identification method using recursive least squares, Gauss-Newton and Levenberg-Marquardt methods have been used with success if the data are not corrupted with noise [3]. The development of a stochastic algorithm, such as Extended Kalman filter, capable of identifying the loop parameters in a generalized model from noisy data, is also developed [4]. A typical feature of nonlinear vibration is that the instantaneous natural frequency and damping

C.-H. Loh (✉) • J.-H. Li
Department of Civil Engineering, National Taiwan University, Taipei 10617, Taiwan
e-mail: lohc0220@ccms.ntu.edu.tw; r98521205@ntu.edu.tw

J.M. Caicedo et al. (eds.), *Topics on the Dynamics of Civil Structures, Volume 1*,
Conference Proceedings of the Society for Experimental Mechanics Series 26,
DOI 10.1007/978-1-4614-2413-0_38,

coefficient of the system may become functions of time depending upon the type of nonlinearity. Different from the parametric identification method, time-frequency analysis of non-stationary signals have been proposed. It provides additional insight into the system dynamics compare with combined time- and frequency-domain analysis. The advantage of time-frequency decompositions is that they permit projections of the time history onto a space that allow s separation of component of the signals, which facilitates filtering in the case of multi-component signals. Methods such as Wavelet packet transform (WPT), Wigner-Ville distribution (WVD), and Empirical Mode Decomposition (EMD) etc. have been widely studied for identification of nonlinear parameters [5–7].

In this study the application of Singular Spectrum Analysis (SSA) is applied to the seismic response data of reinforced concrete frame. The SSA has a wide and multidisciplinary range of application which can also be analyzed by the familiar Principal Component Analysis (PCA); it allows a time series to be decomposed into different components, e.g. the signal itself, as well as various noise components, which can be subsequently removed from the data. In PCA, a straight-line approximation to the dataset is sought which accounts for the maximum amount of variance in the data. Instead of the straight line, a continuous curve to approximate the data can be achieved by Neural Network models. The nonlinear PCA (NLPCA) method is capable of extracting open-curve solution to approximate the data [8]. It had proposed the NLPCA algorithm by applying AANN to perform feature Extraction. Neural network theory has meanwhile allowed principal component analysis (PCA) to be generalized to the Nonlinear PCA (NLPCA) with its ability to extract closed curve solutions. For extracting close-curve solutions, NLPCA with a circular node at the bottleneck was introduced [9]. Based on NLPCA the nonlinear SSA (NLSSA) was developed [10]. The advantages of NLSSA include: (a) The SSA modes are not inefficient at modeling strongly an-harmonic oscillations, (b) Different SSA modes are associated with different time-scales, while NLSSA reveals the time-scale between which they are interaction. With the multivariate case where there is more than one time history, both acceleration and displacement will be used to represent the inelastic hysteretic behavior, the multichannel SSA (MSSA) method applied. Consider the advantages of NLSSA, the inelastic response of reinforced concrete structure (nonlinear hysteresis) subjected to earthquake loading can be investigated.

38.2 Singular Spectrum Analysis and Nonlinear SSA

38.2.1 Singular Spectrum Analysis

The Singular Spectrum Analysis (SSA) is essentially a principal component analysis in the time domain that extracts information from time series without prior knowledge of the dynamics affecting the time series [11, 12]. The method starts by constructing a data Hankel matrix from the time series itself by sliding a window that is shorter in length than the original series. Procedures for SSA are briefly described as follows:

First step: *Embedding* The *embedding* procedure maps the original time series to a sequence of multi-dimensional lagged vectors. In the embedding step, the window length L is chosen first, where $2 < L < N/2$ to embed the initial time series. The L-trajectory matrix (or simply trajectory matrix) of the series Y is defined as:

$$X = (x_{ij})_{i,j=1}^{L,K} = \begin{bmatrix} y_0 & y_1 & y_2 & \cdots & y_{K-1} \\ y_1 & y_2 & y_3 & \cdots & y_K \\ y_2 & y_3 & y_4 & \cdots & y_{K+1} \\ \vdots & \vdots & \vdots & \ddots & \vdots \\ y_{L-1} & y_L & y_{L+1} & \cdots & y_{N-1} \end{bmatrix}_{\mathrm{L\times K}} = [\mathrm{X_1\ X_2\ \cdots\ X_k}] \tag{38.1}$$

which has dimension $L \times K$. The embedding procedure forms K lagged vectors (K = N − L + 1), and

$$X_i = (y_{i-1}, y_i, ..., y_{i+L-2})^T, 1 \le i \le K, \tag{38.2}$$

For multi-channel data, y_i can be replaced by a vector form. Then the dimension of **X** will be $nL \times K$ and n is the number of channels.

Second step: *Singular value decomposition (SVD)* Conduct singular value decomposition of the trajectory matrix and represents it as a sum of rank-one bi-orthogonal elementary matrices. Define the matrix $S = XX^T$ with dimension $L \times L$. The eigenvalues of S are denoted by $\lambda_1, \lambda_2, ..., \lambda_L$ (in decreasing order of magnitude, $\lambda_1 \ge \lambda_2 \ge ...\lambda_L \ge 0$) and the eigenvalues of

S are denoted by $U_1, U_2, ..., U_L$ (the orthonormal system with $(U_i, U_j) = 0$ for $i \neq j$). Define $\mathrm{V_i} = \mathbf{X^T}\mathrm{U_i}/\sqrt{\lambda_i}$, then the SVD of the trajectory matrix can be written as:

$$\mathbf{X} = \mathbf{X_1} + \mathbf{X_2} + \cdots + \mathbf{X_d} = \sum_{\mathrm{i=1}}^{\mathrm{d}} \mathbf{X}_\mathrm{i} = \sum_{\mathrm{i=1}}^{\mathrm{d}} \sqrt{\lambda_\mathrm{i}}\mathrm{U_i}\mathrm{V_i^T} \tag{38.3}$$

$\mathrm{U_i}$ and $\mathrm{V_i}$ stand for the left and right eigenvectors of the trajectory matrix. The collection (λ_i, $\mathrm{U_i}$, $\mathrm{V_i}$) is called the *i*-th eigentriple of the matrix **X**, and $\sqrt{\lambda_\mathrm{i}}(i = 1, \ldots, \mathrm{d})$ are the singular values of the matrix **X**.

Third step: *Grouping & Diagonal averaging* It is used for smoothing a time series. It consists of approximating matrix **X** by summation of the first *r* elementary matrices and transforms each matrix of the grouped decomposition (38.3) into a new series of length N. Let **P** be an L × K matrix with elements $\mathrm{p_{ij}}$, $1 \leq \mathrm{i} \leq \mathrm{L}$, $1 \leq \mathrm{j} \leq \mathrm{K}$. We set $\mathrm{L^*}$= min (L,K), $\mathrm{K^*}$= max (L,K) . Let $\mathrm{p_{ij}^*} = \mathrm{p_{ij}}$ if $\mathrm{L} < \mathrm{K}$ and $\mathrm{p_{ij}^*} = \mathrm{p_{ji}}$ otherwise. Diagonal averaging transfers the matrix **P** to the series $g_0, g_1, \ldots g_{N-1}$ by the formula:

$$g_k = \left\{ \begin{array}{l} \frac{1}{k+1} \sum\limits_{m=1}^{k+1} p^*_{m,k-m+2} \; for \; 0 \leq k < L^* - 1 \\ \frac{1}{L^*} \sum\limits_{m=1}^{L^*} p^*_{m,k-m+2} \; for \; L^* - 1 \leq k < K^* \\ \frac{1}{N-k} \sum\limits_{m=k-K^*+2}^{N-K^*+1} p^*_{m,k-m+2} \; for \; K^* \leq k < N \end{array} \right\} \tag{38.4}$$

The first two steps together are considered as the decomposition stage of SSA and the last step form the reconstruction sage. The result of the step is a representation of the trajectory matrix as a sum of several resultant matrices. The last step transfers each resultant matrix into a time series, which is an additive component of the initial series. The corresponding operation is called diagonal averaging. It is a linear operation and maps the trajectory matrix of the initial series into the initial series itself. In this way one can obtain a decomposition of the initial series into several additive components.

38.2.2 Nonlinear Singular Spectrum Analysis (NLSSA)

The SSA method is restricted to exploiting information related to linear correlations in multivariate data to reveal interesting latent structures. However, the tools may have limited applicability when significant nonlinear correlations exist in the data. *Hsieh* et al. [13–16] describes an extension of basic SSA to a nonlinear approach that uses auto-associative neural networks (AANN) to exploit nonlinear redundancies that may exist in the time series that are not detected by the basic approaches discussed above. To analyze the nonlinear data, the NLPCA is further extended to perform nonlinear SSA: First, the SSA is applied to the data, then the leading principal components of the SSA are chosen as inputs to an NLPCA (AANN) network (with a circular node at the bottleneck), as shown in Fig. 38.1, which performs the NLSSA by nonlinearly combining all the input SSA modes into a single NLSSA mode. Through network training, the weights in the AANN can be determined. Procedures for NLSSA are briefly described as follows:

(a) *Data normalization for NLPCA* Let $F \in \Re^{\mathrm{L}\times\mathrm{K}}$ represent the matrix whose column vectors f_K are the component values of the principal components of the SSA, where L is the dimension of data and K is the number of data sets. In order to detect the percentile reduction of the component values directly, the matrix ***F*** is formed by the data that has been semi-standardized as

$$\hat{f}_{\mathrm{LK}} = \frac{f_{\mathrm{LK}} - \mu_\mathrm{L}}{\mu_\mathrm{L}} \tag{38.5}$$

where $\hat{f}_{\mathrm{LK}}$ is the non-normalized value of the L_{th} component at time $\mathrm{t_K}$ and μ_L is the mean of the row vector f_{LK}.

(b) *From NLPCA to NLSSA* Assume the SSA has been applied to the dataset, and after discarding the higher modes and data normalization, we have retained the leading PCs, $\hat{f}(t) = [\hat{f}_1, \hat{f}_2, \ldots, \hat{f}_l]$, where each variable $\hat{f}_i; (i = 1, 2, \ldots, l)$, is a time series of length K. The variables $\hat{f}$ are the inputs to a feed-forward neural network, mapping through a bottleneck to the output $\hat{f}'$.

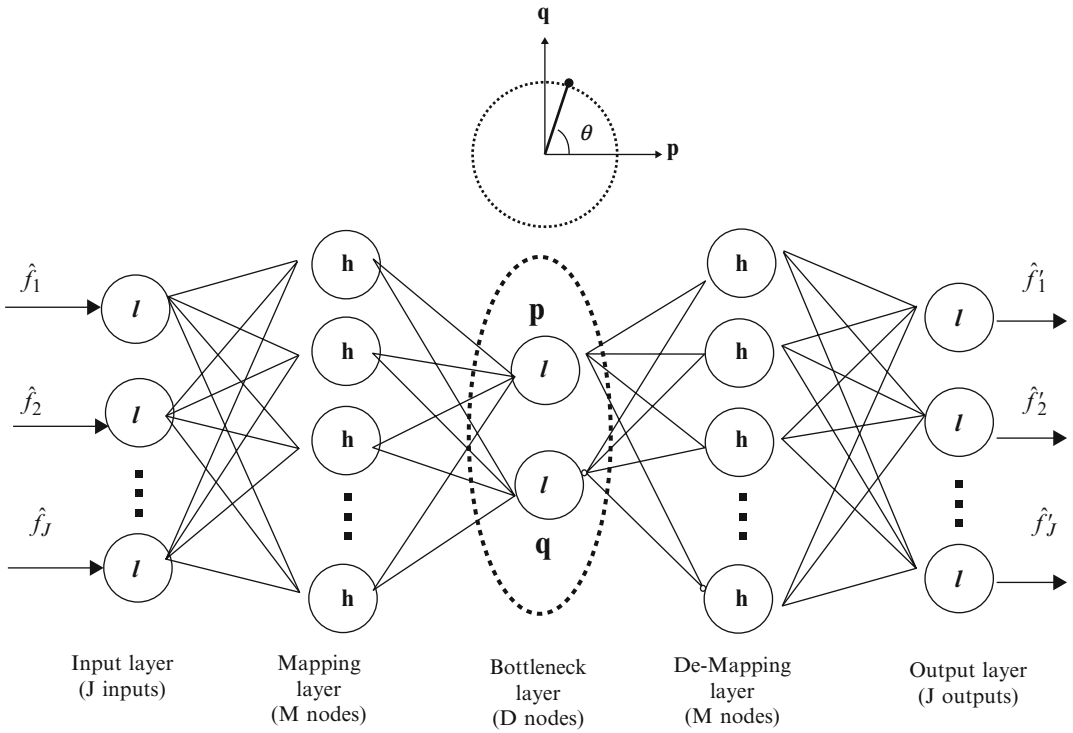

Fig. 38.1 A schematic diagram illustrated the NN model for calculating the nonlinear principal component analysis with a circular node at the bottleneck. For NLSSA, the inputs to the network are the leading principal components from SSA which serves as a pre-filter [15]

(c) *Extract single mode from NLSSA* To reconstruct the single mode from AANN, the mapping from the bottleneck layer to the decoding layer needs to be done from the following equation:

$$h_k^{(d)} = \tanh((w^{(d)}p + \tilde{w}^{(d)}q + b^{(d)})_k), \text{ with } k = 1, \ldots, M. \tag{38.6}$$

where d is bottleneck node in NLPCA,$w^{(d)}$,$\tilde{w}^{(d)}$are weight parameter vectors, and $b^{(d)}$ is the bias parameter. The bottleneck contains two neurons p and q confined to lie on a unit circle.

Finally, the network output is given by

$$\hat{f}_i' = (w^{(d)}h^{(d)} + \bar{b}^{(d)})_i \tag{38.7}$$

This nonlinear spectral technique allows the detection of highly an-harmonic oscillations. Besides, as different SSA modes are associated with different time-scales, the relations found by the NLSSA reveal the time-scales among which there are interactions.

In SSA, it is common to encounter periodic modes, each of which had to be split into a pair of modes, as the underlying PCA technique is not capable of modeling a periodic mode by a single mode (a straight line). Thus, two (or more) SSA modes can easily be combined into one NLSSA mode. Because the original input data the neural network is the result of normalized, so the output data to be done to restore

$$f_i' = \hat{f}_i' \times \mu_L + \mu_L \tag{38.8}$$

where f_i' is the restoring the signal data of the L_{th} component at time t_K and μ_L is the mean of the row vector f_{LK}, L is the component number of input or output data and K is the number of data sets. The reconstructed component 1 is the approximation of the original time series by the NLSSA mode 1. The restoring f_i' is the NLSSA mode 1 approximation for the L leading PCs. Multiplying these approximation PCs by their corresponding SSA eigenvectors, and summing over the L modes allows the reconstruction of the time series from the NLSSA mode 1. As each eigenvector contains the loading over a range of lags, each value in the reconstructed time series at time t_j also involves averaging over the contributions at t_j from various lags.

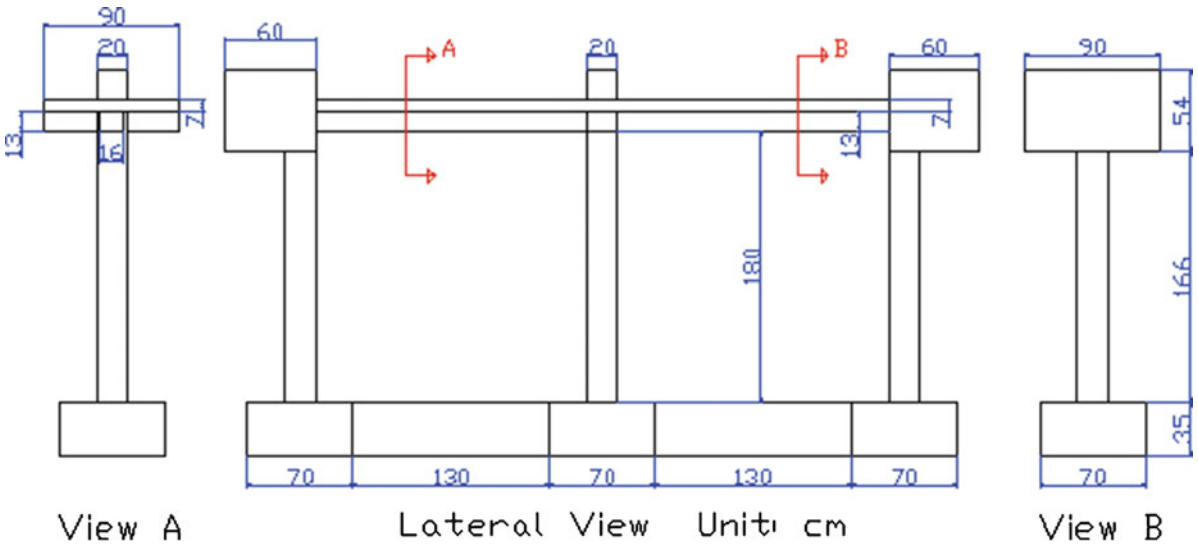

Fig. 38.2 Dimension (unit:cm) and member design detail of the test specimen RCF6

After the first NLSSA mode has been extracted, it can be subtracted from original data to get the residual, from which the SSA can also be use to find the second component and then to continue the NLSSA to extract the second NLSSA mode, and so forth to the higher modes.

38.2.3 Application of SSA and NLSSA to Seismic Response of RC Frame

Dynamic test data of a one-story two-bay reinforced concrete frame was used in this study. Figure 38.2 shows the design details of the test frame. The beam length is 2 m. The thickness of the roof plate is 7 cm. The concrete design compressive strength is 210 kg/cm^2. The design strength of steel is 4,200 kg/cm^2. The failure modes of columns and beams are designed as flexural failure. The column size is 20 $\times$ 20 cm. Eight #4 steel bars are used as longitudinal reinforcement in the middle column. Four #4 steel bars are used as longitudinal reinforcement in the side columns. #3 steel bars with 10 cm spacing are used as transverse reinforcement of all columns. The beam width is 16 cm. The beam depth is 20 cm. #3 steel bars are used as longitudinal reinforcement. #3 steel bars with 10 cm spacing are used as transverse reinforcement of the beam. The strength and stiffness of the base and base beam are designed much higher than column. Shaking table test was conducted by using input excitation level of 600 gal of the Chi-Chi earthquake data of station TCU082. Figure 38.3a shows the recorded absolute acceleration response and the relative displacement of the frame structure. The restoring force diagram (hysteretic loop) of the test specimen (RCF6) is also shown in Fig. 38.3b. The dominant frequency of the frame structure changes with respect to time during the excitation is obvious which indicated the structure has inelastic nonlinear response. To demonstrate the applicability of SSA and NLSSA, the nonlinear response of the test specimen was used. Procedures on data analysis are listed as follows;

(a) *Data pre-processing using SSA* First, SSA is applied as the de-noising process (pre-filter). The permanent deformation of the story drift was removed from the original displacement data by using the SSA (the reconstruction of first leading component was identified as the permanent deformation). Second, high frequency components of the measurements were also filtered to get the SSA-smoothed signals. In this study, 95% of the eigenvalues from singular spectrum of the data were extracted to reconstruct the response data. Comparison on the restoring force diagram between the original and the processed data is shown in Fig. 38.3c.

(b) *Multi-Dimensional SSA* Since the restoring force diagram of the RC frame was constructed by using both acceleration and displacement responses, the multi-dimensional SSA must be used [17]. To construct the data Hankel matrix, each $\mathbf{y}_i$ in (38.1) is defined as a vector which formed by both acceleration and displacement data at time $t = t_i$. Data normalization is used, as shown in (38.5), and form the data Hankel matrix for conducting SSA or Nonlinear-SSA.

(c) *SSA versus Nonlinear SSA* Both SSA and NLSSA are used to analyze the data. First, the singular spectrum of the original data was obtained with a window length L $=$ 450 (for sampling rate of 200 Hz). To reconstruct the principal component

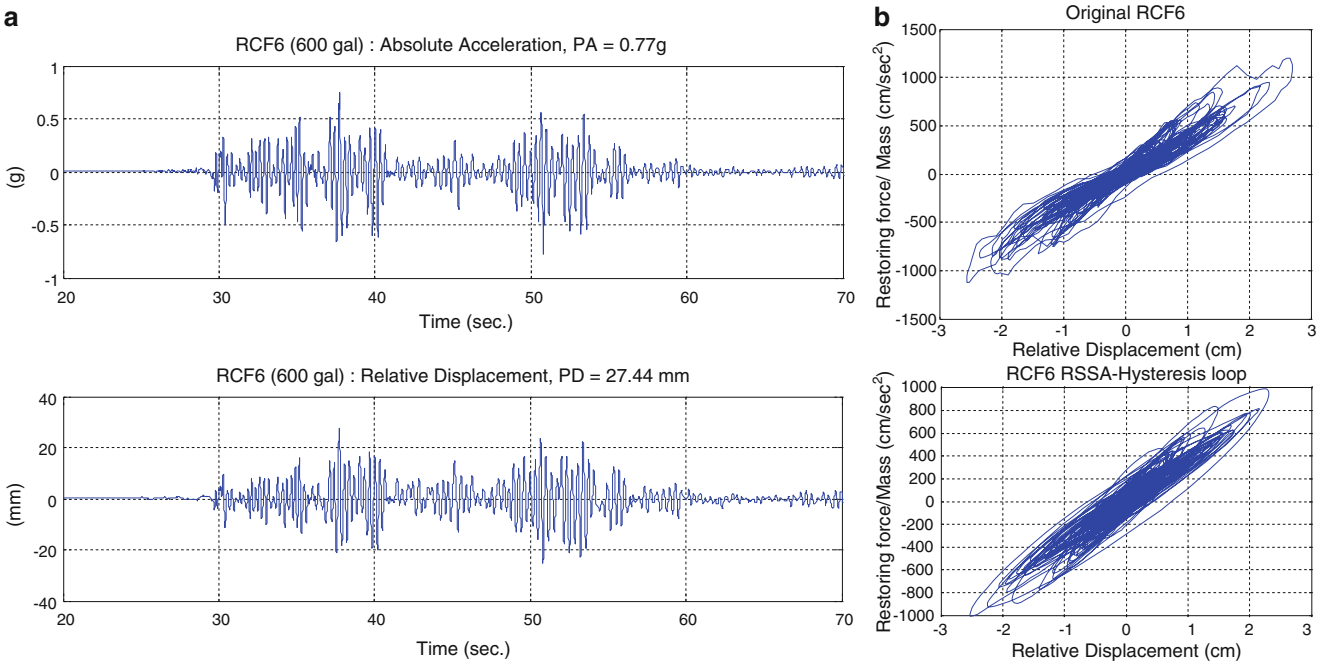

Fig. 38.3 (**a**) Recorded absolute acceleration and displacement from the top floor of the test specimen under the excitation of El Central earthquake of 600 gal. (**b**) Comparison on the restoring force diagram of the test specimen directly from the measurement and after pre-processing

using either through SSA or NLSSA depends on the distribution of eigenvalues in the singular spectrum. It had been proved that Hankel matrix embedded by a harmonic signal contains only two singular values, which represent two orthogonal bases: sine and cosine terms and the difference between the two singular values of a harmonic signal are small. For such a case SSA can be applied to extract such a harmonic signal. If a sequence of singular values is close to each other with minor difference in eigenvalues, the nonlinear-SSA needs to be applied to extract the non-linear principal component by using the individual reconstructed signal from each of the corresponding components of the sequence of singular values. Figure 38.4 shows the singular spectrum from the sequence of Multiple SSA and Nonlinear-SSA on the recorded data of specimen RCF6. The individual reconstructed waveform obtained from each analysis is also shown in this figure. Depends on the distribution of singular spectrum, one can use either MSSA or NLSSA will be applied to reconstruct the narrow-band signal.

(d) *Generate Evolutionary Restoring Force Diagram* Based on the decomposed signal from previous steps, the restoring force diagram can be constructed. From each individual reconstructed waveform, as shown in Fig. 38.4 (both acceleration and displacement), re-arranged the waveform in sequence of the signal degrading dominant frequency. Figure 38.5 shows the time histories as well as the spectrogram of the decomposed signals. Since each decomposed signal contents narrow-band frequency, therefore, the restoring force diagram from each frequency band (follow the degradation of its dominant frequency) can be developed. From each restoring force diagram the yield displacement and equivalent stiffness can be determined from each restoring force diagram, as shown in Table 38.1. Finally, to form the final system restoring force diagram, accumulation of all individual hysteretic diagrams is needed. Figure 38.6 shows the final system restoring force diagram.

38.3 System Identification Using Deteriorating Distributed Element

38.3.1 The Deteriorating-Distributed-Element Model

The Deteriorating Distributed Element model [14] consists of an ensemble of linear springs and Coulomb, arranged in parallel as show in Fig. 38.7. This model consists of four categories of elements: (1) a linear element, which is represented by a linear spring with stiffness K_e; (2) an elastic-plastic element, which consists of a linear spring with stiffness K_{ep} in series with a slip element that allows a maximum force equal to $K_{ep}X_{yep}$ (Xyep is the yielding displacement of the elastic-plastic

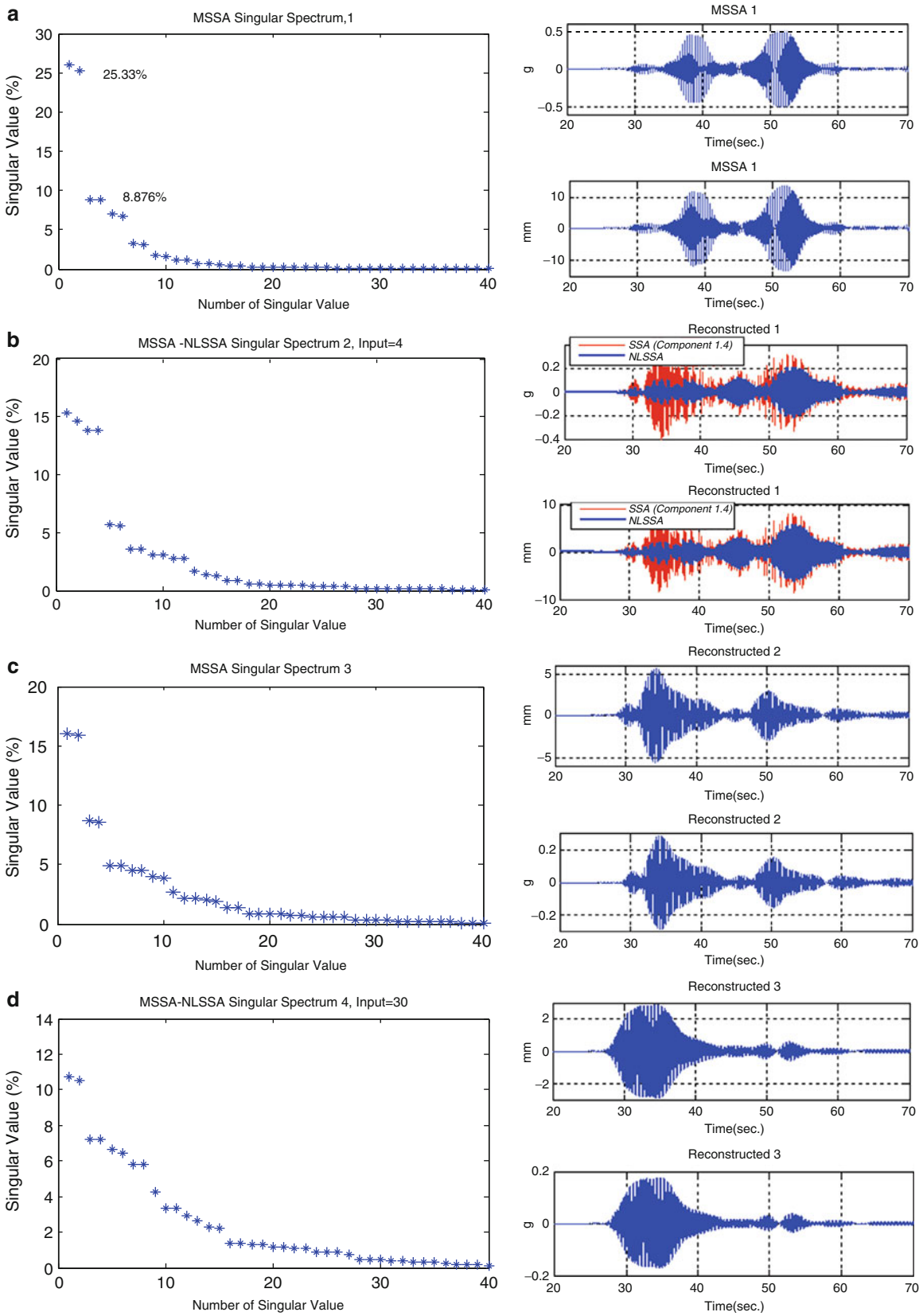

Fig. 38.4 (**a**) Singular spectrum and reconstruction obtained from the first two singular values, (**b**) Singular spectrum of the remaining signal: after step a. Reconstruction from the first four singular values using NLSSA, (**c**) Singular spectrum of the remaining signal: after step a & b. Reconstruction from the first two singular values, (**d**) Singular spectrum of the remaining signal: after step a, b & c. Reconstruction from the first 30 singular values using NLSSA, (**e**–**g**) Singular spectrum from the residual signal after NLSSA. Reconstruction from the first 30 singular values using NLSSA is also shown

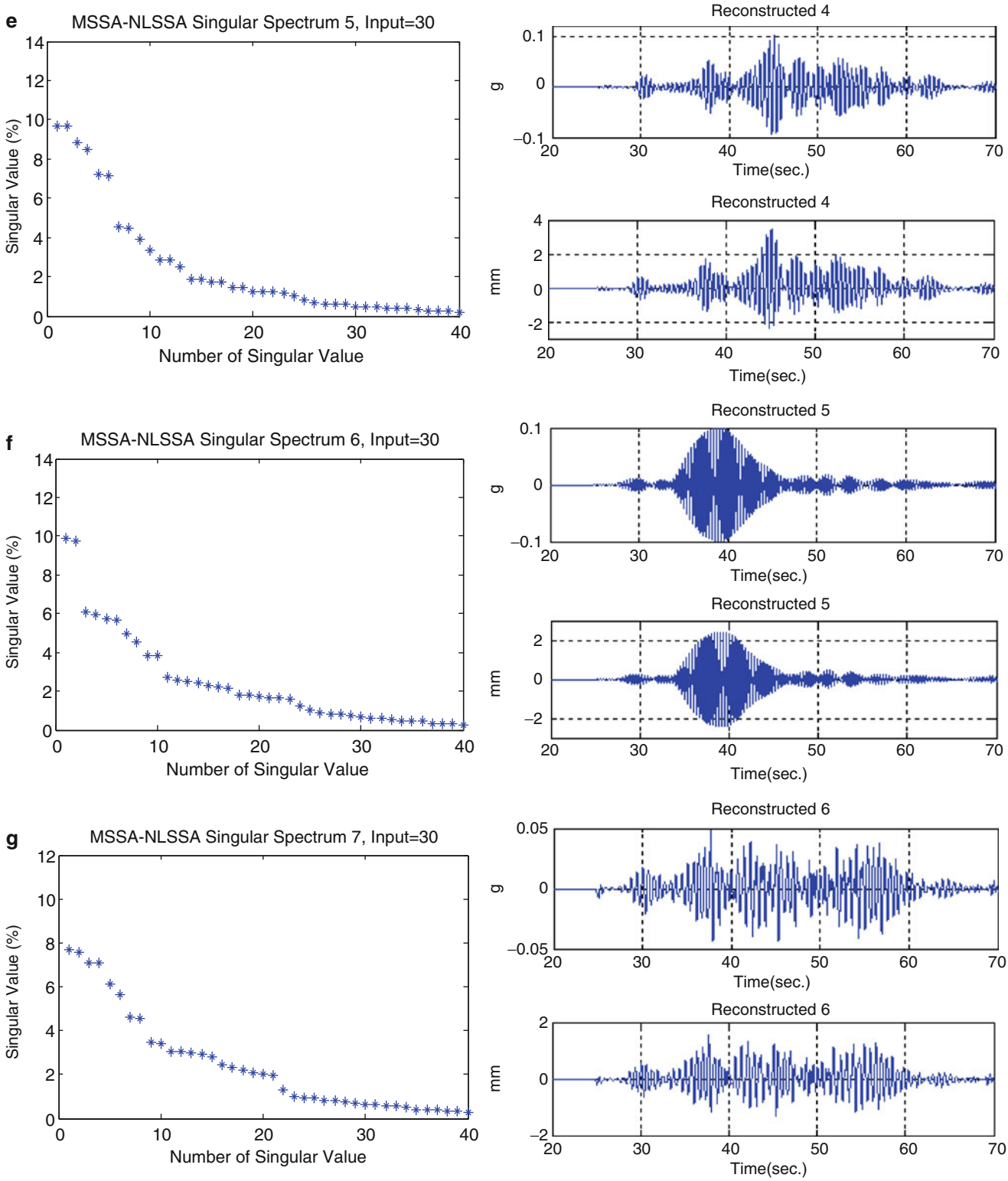

Fig. 38.4 (continued)

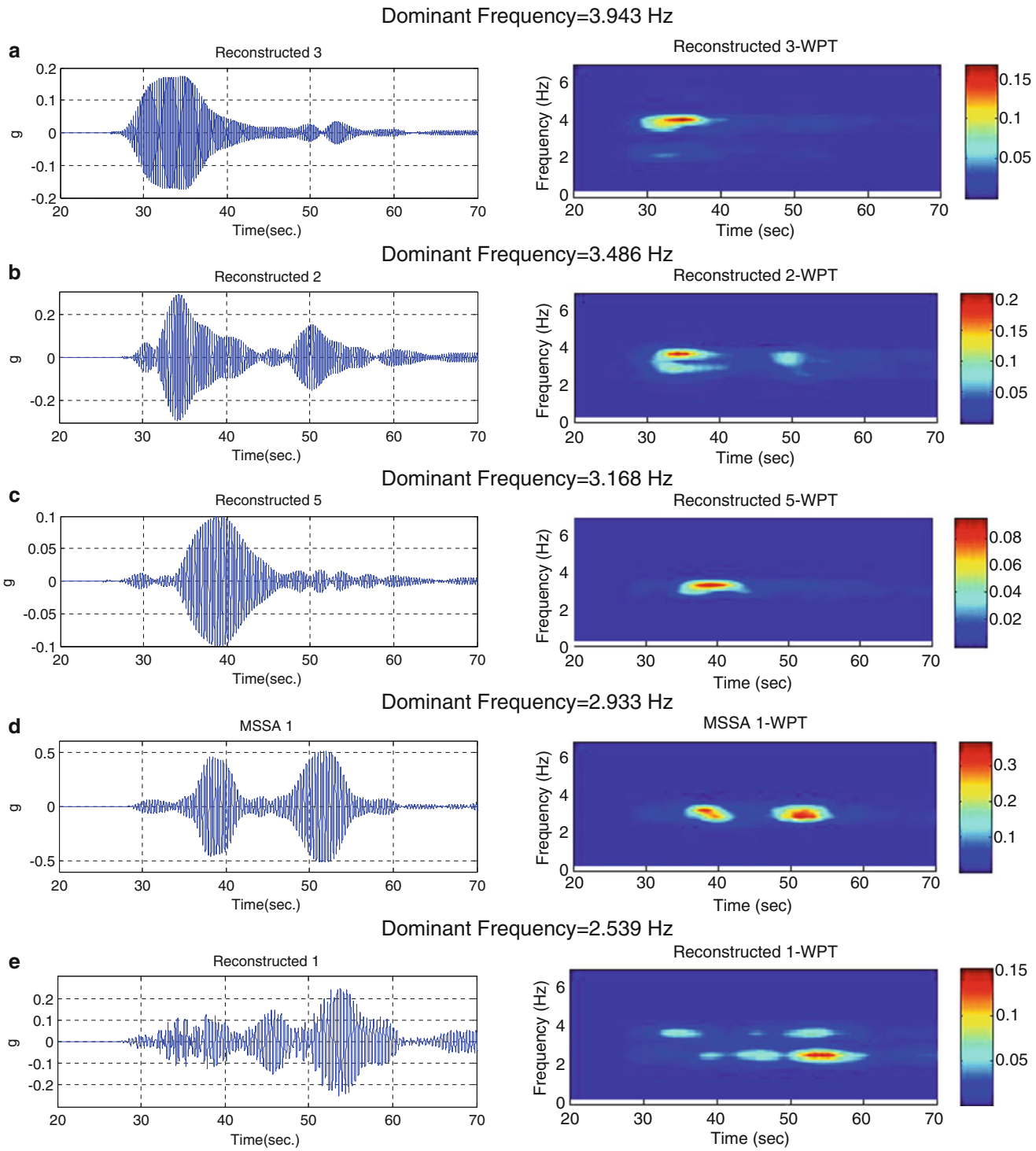

Fig. 38.5 Re-arrangement of the reconstructed acceleration time history follows in sequence of the decreasing dominant frequency of the signal. The spectrogram of each component time history is also shown

element); (3) a set of N deteriorating elements, which consist of a breaking linear spring with stiffness k_i' in series with a slip element having a yielding force of k_{ixyi}'. The deteriorating element fails (spring break) when the absolute value of the displacements exceeds a value β_{xyi}. The coefficient β may be any number greater than 1. Failure of structural element is usually assumed that the displacement reach to x_{max}, then β can be chosen from: $\beta_i \leq (x_{max}/x_{yi})$. (4) Damping element, this element can be considered as a dashpot which contributes to the restoring force with a value to $C\dot{x}$.

Table 38.1 Identified element stiffness, damping ratio and yield displacement from both decomposed signal and DDE model

RCF6	Effective stiffness (from decomposition data)	Yield displacement (cm)	Effective stiffness (from DDE model)	Equivalent damping ratio
K_1	587.086	0.287	587.086	0.0529
K_2	540.226	0.798	516.742	0.0542
K_3	507.668	0.893	507.675	0.0632
K_4	379.338	1.633	395.591	0.0708
K_5	362.043	1.951	362.063	0.0804

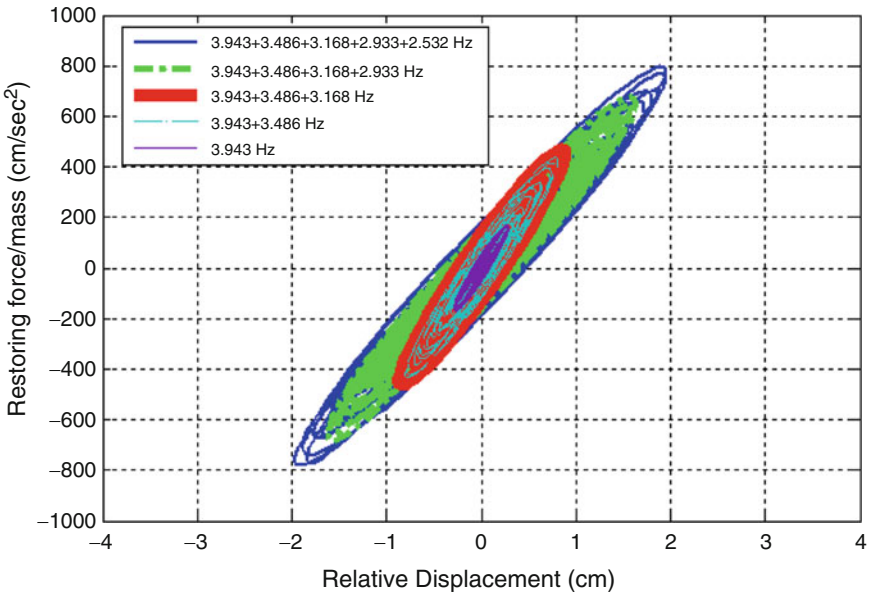

Fig. 38.6 Reconstructed system restoring force diagram through the summation of individual restoring force identified using SSA and NLSSA

Each deteriorating element is completely defined by three parameters; the spring stiffness ki′, the yielding displacement and the damping ci′. If there are N deteriorating elements, there will have 3N parameters to be determined. Now consider a beam be deformed under the action of a bending moment M, as shown in Fig. 38.6. It is assumed that the bending moment applied to the beam is resisted by a large number of axial fibers arranged in parallel, and each fiber behaves as an elastic-plastic sub-element with a yielding displacement xy. If θ is the rotation of the end planes of the beam section, the elongation of a typical fiber i will be,

$$x_i = \delta_i \theta \tag{38.9}$$

where xi is the elongation and δi is the distance between the i^{th} fiber and the neutral axis of the section. The moment of this fiber is

$$M_i = (kx_i)\ \delta_i = k\delta_i^2\ \theta = k_i^* \theta \tag{38.10}$$

where

$$k_i^* = k\delta_i^2 \tag{38.10a}$$

Let θyi be the rotation angle of the i^{th} fiber that reaches its yielding displacement xy. Then

$$\theta_{yi} = \frac{x_y}{\delta_i} \text{ and } k_i^* = k\frac{x_y^2}{\theta_{y_i}^2} \tag{38.11}$$

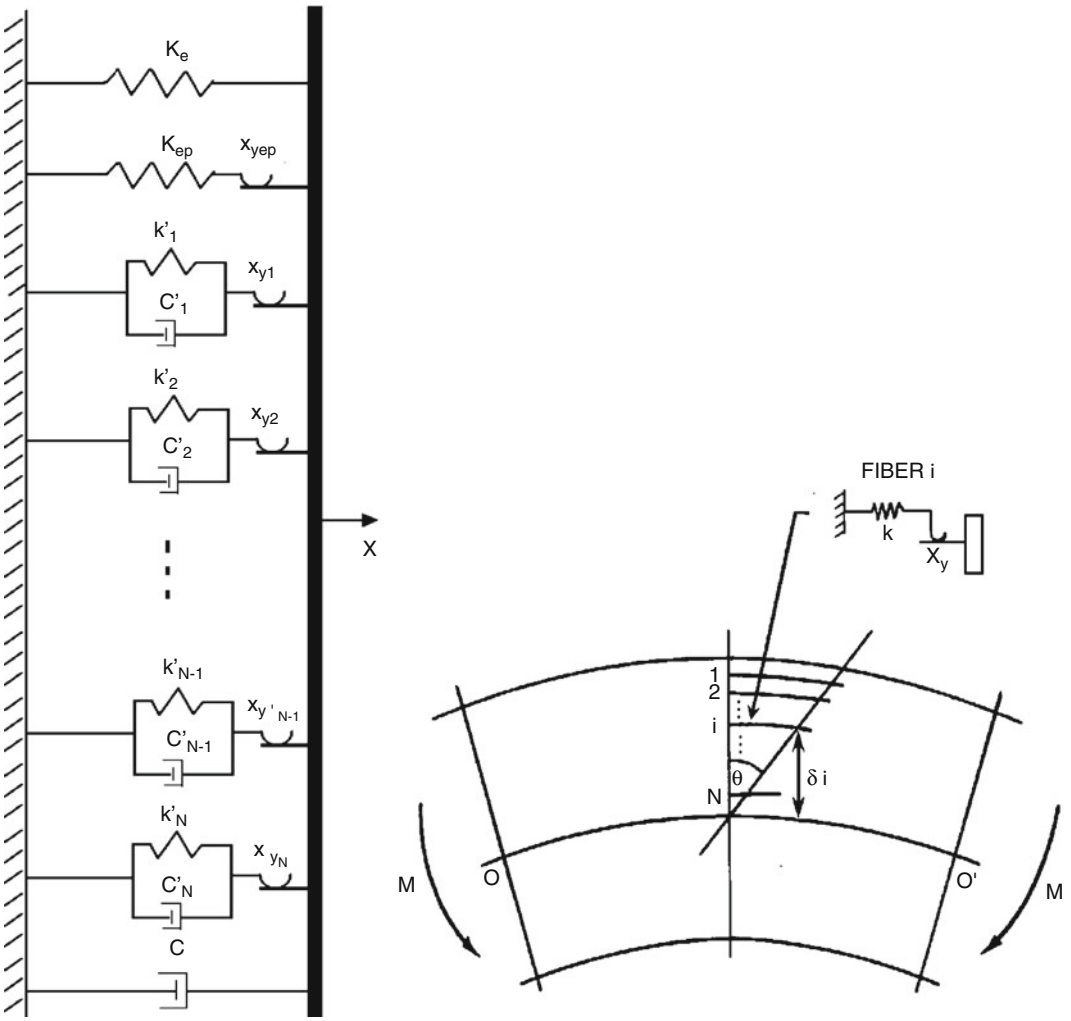

Fig. 38.7 The deteriorating distributed element (DDE) model [14]

Note that $\theta_{y1} < \theta_{y2} < \cdots < \theta_{yN}$ in Fig. 38.7. When a force F is applied in the DDE model, each deteriorating element will resist a stiffness k_i' proportional to $1/x_{yi}^2$

$$k_i' = \frac{A}{x_{y_i}^2}, i = 1, 2, \ldots, N \tag{38.12}$$

In the DDE model the deteriorating element have been arranged as $x_{y1} < x_{y2} < \cdots < x_{yN}$, and k_i' is the linear spring stiffness; xyi is the yielding displacement of the element and A is a proportionality constant that needs to be determined.

Consider a member with initial stiffness K_0 which can be related to the parameters of the DDE model by the following relationship

$$K_0 = K_e + K_{ep} + \sum_{i=1}^{N} k_i' = K_e + K_{ep} + A \sum_{i=1}^{N} \frac{1}{x_{yi}^2} \tag{38.13}$$

This equation establishes that the initial stiffness of the DDE model is equal to the summation of the contribution the elastic element, the elastic-plastic element and N deteriorating elements. Assuming then that the deteriorating elements $l+1, l+2, \ldots, N$ have not failed in the final stiffness of the system K_f, then it can be expressed as

$$K_f = K_e + K_{ep} + A \sum_{i=l+1}^{N} \frac{1}{x_{yi}^2} \tag{38.14}$$

From (38.13) and (38.14) one obtains

$$A = (K_0 - K_f) \Big/ \sum_{i=1}^{l} \frac{1}{x_{yi}^2} \tag{38.15}$$

This relationship allows A to be determined from the system effective stiffness and the yield displacement of each degradation element.

38.3.2 System Identification

Consider the seismic response of the specimen RCF6. The restoring force diagram of each individual frequency had been extracted using SSA and Nonlinear-SSA. Both effective stiffness (K), damping ratio and maximum yield displacement (x_y) from each extracted signal can also be identified using equivalent linear model, as shown in Table 38.1. A total of five stages were identified from the test data. The restoring force diagram from each stage will be used to estimate the model parameters of the DDE model. From the observation of the identified stiffness, rapid change of equivalent stiffness between K_3 and K_4, are observed from Table 38.1. It indicated two different degradation behaviors had developed in this test specimen. Therefore, two different set of the DDE parameters need to be identified instead of using one set. It is assumed that x_{y3} and x_{y5} is the maximum displacement in stage 1 and stage 2, respectively. In the beginning, the deteriorating coefficient β for these two stages are estimated:

For stage 1, since $x_{y3}/x_{y2} = 0.893/0.798 = 1.119$, it is define $\beta_1 = 1.1$, and i = 2. and for stage 2, $x_{y5}/x_{y4} = 1.951/1.633 = 1.195$, it is then defined $\beta_2 = 1.2$. In stage 1 it is assumed that element 1 and 2 are not deteriorated and in stage 2 element 3 and 4 are not deteriorated. To determine the model parameters, in step 1, based on (38.12) the initial equivalent stiffness of the model can be expressed as

$$K_1 = K_e + K_{ep} + A\sum_{1}^{2} \frac{1}{x_{yi}^2} + B\sum_{3}^{5} \frac{1}{x_{yi}^2} \tag{38.16}$$

where A and B are two parameters which can be determined from the initial stiffness of the member. Due to the sequential deteriorating of element, the second and third equivalent stiffness will be modified to the following forms

$$K_2 = K_e + K_{ep} + A\sum_{2}^{2} \frac{1}{x_{yi}^2} + B\sum_{3}^{5} \frac{1}{x_{yi}^2} \tag{38.17}$$

$$K_3 = K_e + K_{ep} + B\sum_{3}^{5} \frac{1}{x_{yi}^2} \tag{38.18}$$

Then

$$\mathrm{A} = (K_1 - K_3) \Big/ \sum_{1}^{3} 1 \Big/ x_{yi}^2 = \frac{79.418}{13.753} = 5.774 \Rightarrow k_1{}' = \frac{A}{x_{y1}^2} = 70.344, k_2{}' = \frac{A}{x_{y2}^2} = 9,067$$

From which the deteriorating element stiffness $k_1^{'}$ and $\mathrm{k}_2^{'}$ can be estimated:

$K_1'' = K_1 = 587.089$, $K_2'' = K_1 - k_1' = 516.742$, $K_3'' = K_2'' - k_2' = 507.675$. Similar approach can also be applied to determine the parameters: k_3', k_4' and k_5'. It is assumed that

$$K_3'' = K_e + K_{ep} + B\sum_{3}^{5} \frac{1}{x_{yi}^2} \tag{38.19}$$

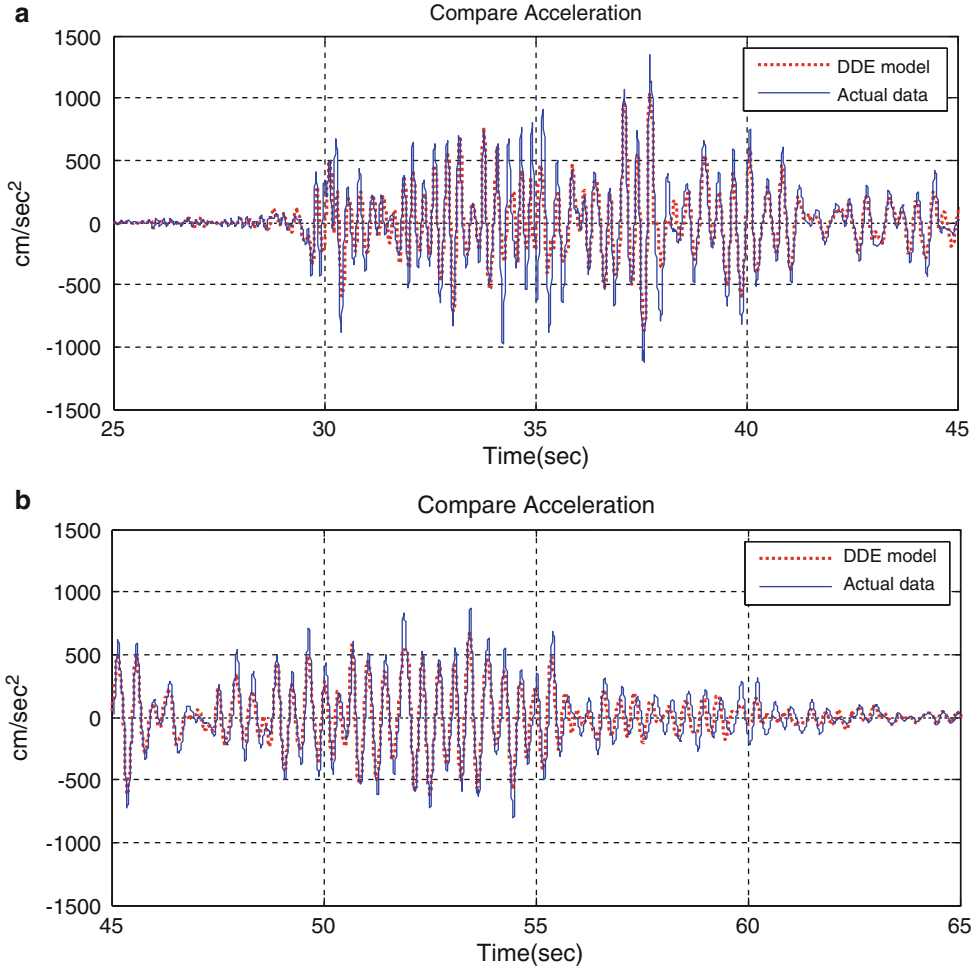

Fig. 38.8 Comparison between the simulation (using DDE model) and recorded acceleration response of RC frame

$$K_4 = K_e + K_{ep} + B\sum_{4}^{5}\frac{1}{x_{yi}^2} \tag{38.20}$$

$$K_5 = K_e + K_{ep} + B\sum_{5}^{5}\frac{1}{x_{yi}^2} \tag{38.21}$$

$$\Rightarrow \quad B = (K_5 - K''_3)\Big/\left(\sum_{3}^{4}\frac{1}{x_{yi}^2}\right) = 145.632/1.516 = 89.442$$

$$k_3^{'} = \frac{B}{x_{y3}^2} = 112.084,\ k_4' = \frac{B}{x_{y4}^2} = 33.528, k_5' = \frac{B}{x_{y5}^2} = 23.491$$

Therefore, $K_4'' = K_3'' - k_3' = 395.591,\ K_5'' = K_4'' - k_4' = 362.063$.

Based on the identified model parameters of the DDE model from the seismic response data of specimen RCF6, verification of the seismic response using the DDE model was also presented. Figure 38.8 shows the comparison on the acceleration response and the Fourier amplitude spectrum between the predict (using DDE model) and the recorded data. One may concludes that the DDE model gives a good approximation of the dynamic response of structure existing hysteretic behavior. With Multi-dimension SSA and Nonlinear-SSA the model parameters of the DDE model can be identified which capture the essential features of the nonlinear behavior of concrete structure and includes the elements to account for the energy dissipated due to hysteresis and deterioration.

38.4 Conclusions

Using complex nonlinear model to simulate the nonlinear inelastic behavior of reinforced concrete member subject to strong earthquake excitation, such as the Bouc-Wen Model, may need to identify many unknown model parameters. Besides, the mechanism of deteriorating of reinforced concrete member subjected to strong excitation cannot be clearly identified. In this study a simple deteriorating distributed element (DDE) model was used to simulate the inelastic behavior of a reinforced concrete member. To identify the time-frequency change of the sequential deteriorating element, an advanced signal processing technique is proposed to decompose the response measurements. From which the model parameters of DDE model can be identified.

For signal decomposition both Singular Spectrum Analysis (SSA) and Nonlinear SSA techniques are used in this study. SSA is a novel non-parametric technique used in the analysis of time series based on multivariate statistics. It can be applied not only to extract the tendency of the signal but can also be applied to eliminate noise effect, or to detect the singularities. In SSA approach, a time series is lagged by $1, \ldots, K$ time steps. The time series and its lagged versions can be analyzed by the familiar Principal Component Analysis (PCA). Multichannel SSA method was also applied for multivariate case where there is more than one time series. In order to extract the anharmonic signal (such as inelastic hysteretic system), the NLSSA is used where strong nonlinearity signal can be extracted. Considering the nonlinear signal of the seismic response of RC member, the used of NLSSA to extract the time-frequency signal proves to be quite successful. Combination of the decomposed signal from response measurements and implemented to the DDE model, the deteriorating behavior of the RC member can be identified.

Acknowledgements Support from National Science Council of the Republic of China, Taiwan (Contract No. NSC 99-2221-E-002 -088 -MY3) and the Research Program of National Taiwan University (Contract No. 99R80805) are acknowledged.

References

1. Bouc R (1967) Forced vibration of mechanical systems with hysteresis. In: Proceedings of the 4th international conference in nonlinear oscillation, Prague
2. Wen YK (1980) Equivalent linearization for hysteretic systems under random excitations. ASME J Appl Mech 47:150–154
3. Hagan MT, Demuth HB, Beale M (1995) Neural network design. PWS Publishing, Boston Company, Boston
4. Soderstrom T, Stoica P (1989) System identification. Prentice Hall International, London
5. Sun Z, Chang CC (2002) Structural damage assessment based on wavelet packet transform. J Struct Eng ASCE 128:1354–1361
6. Huang NE, Brenner MJ, Salvino L (2006) Hilbert Huang transform stability spectral analysis applied to flutter flight test data. J AIAA 44:772–786
7. Baum PG (2002) Time-filter Wigner transformation for use in signal analysis. Mech Syst Signal Process 16(6):955–966
8. Kramer MA (1991) Nonlinear principal component analysis using auto associative neural networks. AICHE J 37:233–243
9. Kirby MJ, Miranda R (1996) Circular nodes in neural networks. J Neural Comput 8:390–402
10. Hsieh WW, Wu A (2002) Nonlinear multichannel singular spectrum analysis of the tropical Pacific climate variability using a neural network approach. J Geophys Res-Oceans 107:1–36
11. Golyandian N, Nekrutkin V, Zhigljavsky A (2001) Analysis of time series structure: SSA and related techniques. Chapman and Hall/CRC, Boca Raton
12. Alonso FJ, Del Castillo JM, Pintado P (2005) Application of singular spectrum analysis to the smoothing of raw kinematic signals. J Biomech 38:1085–1092
13. Hsieh WW (2004) Nonlinear multivariate and time series analysis by neural network methods. Rev Geophys 42:RG1003. doi:10.1029/2002RG000112
14. Cifuentes A (1984) System identification of hysteretic structures. Ph.D. Thesis, California Institute of Technology, Pasadena
15. Hsieh WW, Wu A (2002) Nonlinear singular spectrum analysis, IEEE, Honolulu, HI, 2819–2824
16. Hsieh WW, Hamilton K (2003) Nonlinear singular spectrum analysis of the tropical stratospheric wind. QJR Meteorol Soc 129:2367–2382
17. Lisi F, Medio A, Sandri M (1994) Noise-filtering by multichannel singular system analysis. In: Working paper. Department of Economics, University of Venice

Chapter 39
Modal Parameter Variation of an Earthquake Damaged Building

Antonio A. Aguilar, Ruben L. Boroschek, and Leonardo M. Massone

Abstract On February 27, 2010 one of the largest magnitude earthquake ever registered occurred in Chile. Although, several tall buildings suffered damage without collapse, the response of these buildings, in general, has been considered a success. Several studies have been carried out to understand the seismic response of these damage buildings, in order to develop appropriate retrofit strategies. We have selected one building located in the coastal city of Viña del Mar for instrumentation. This area suffered strong shaking with peak ground acceleration close to 0.35 g and more than 180 s of motion. The structure is a residential shearwall building with 17 stories and one basement level. The main structural system was damaged at the basement and first floor levels. The main damage was concrete crushing of walls, along with longitudinal reinforcement buckling at wall boundaries and severe cracking of slabs and lintel beams. An array of 12 accelerometers was deployed in the building to evaluate its modal properties variations, recording five aftershocks. This publication presents the structural damage in the building and the preliminary system identification results from strong motion records. Variations of the modal parameters are correlated with motion amplitudes and compared with ambient vibration conditions.

Keywords SHM • Chile earthquake • Damping • System identification

Nomenclature

$\{x_k\}$	State vector on k.
$[A]$	Discrete system matrix.
$[C]$	Output matrix.
$\{w_k\}$	Process noise vector
$\{v_k\}$	Measurement noise vector.
i	i-th mode.
λ_i	Eigen value from continuous system matrix.
μ_i	Eigen value from discrete system matrix.
Δt	Sample time.
ω_i	Angular frequency.
ξ_i	Damping ratio.
$[\phi]$	Modal shape.
$[\Psi]$	Eigen vector from discrete system matrix.
$ag_j(t)$	Recorded base acceleration. Direction j.
$L_{i,j}$	Modal participation ratio for base acceleration in direction j.
$\phi_{i,p}$	Modal shape vector at position p.
$y_i(t)$	Modal response.

A.A. Aguilar • R.L. Boroschek (✉) • L.M. Massone
Civil Engineering Department, University of Chile, Blanco Encalada 2002, Santiago, Chile
e-mail: aaguilar@ing.uchile.cl; rborosch@ing.uchile.cl; lmassone@ing.uchile.cl

J.M. Caicedo et al. (eds.), *Topics on the Dynamics of Civil Structures, Volume 1*,
Conference Proceedings of the Society for Experimental Mechanics Series 26,
DOI 10.1007/978-1-4614-2413-0_39,

$a_p(t)$ Estimated acceleration of MIMO algorithm at position p.
E MIMO goodness of fit error.
α_p Weight coefficient at position p in MIMO goodness of fit error.

39.1 Introduction

The Mw 8.8 earthquake that hit Chile in 2010 caused damage in several buildings in the south-central area of the country. In particular, cities such as Concepción, Viña del Mar and Santiago, which concentrate an important part of the population, presented damage in tall buildings. There were few, but important cases, were the structure collapsed and many cases where the structure presented important structural damage. Several studies have been undertaken to increase the knowledge of building damage behavior. This study identifies the post-earthquake modal properties of a damaged building from ambient vibration, using the Stochastic Subspace Identification (SSI), and three of five seismic events recorded using a Multiple Input – Multiple Output technique (MIMO).

39.2 Building and Instrumentation Description

The building is located in the city of Viña del Mar, central Chile, which is about 340 km from the epicenter. The building, a reinforced concrete shearwall structure, has 17 stories above ground, constant in shape above the second floor, and one basement level. The typical height between floors is of 2.60, 3.20 m in the first level and 3.50 m for the basement level. Wall thickness varies between 20 and 30 cm. The ratio of wall area in one direction to plan area (wall density) varies with height. For the basement level this ratio is 2.0% in the EW direction, and 2.5% in the NS direction. Wall densities for the typical floor are 2.9% in the EW direction and 3.6% in NS direction. Floor slabs are 13 cm thick in all stories above ground level, and varies between 13 and 20 cm. A sample of the structure is shown in Figs. 39.1 and 39.2

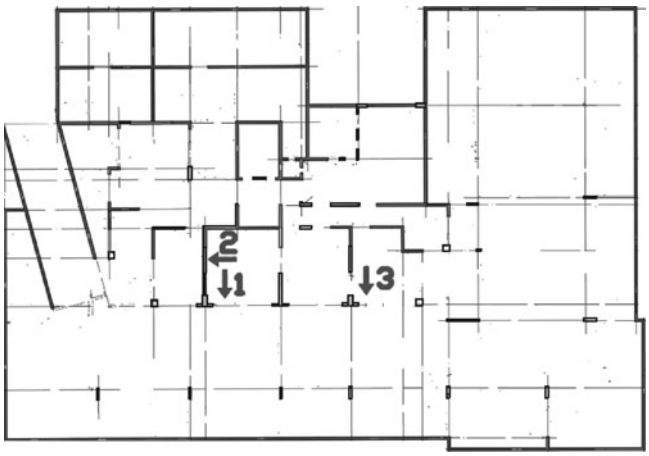

Fig. 39.1 Underground basement

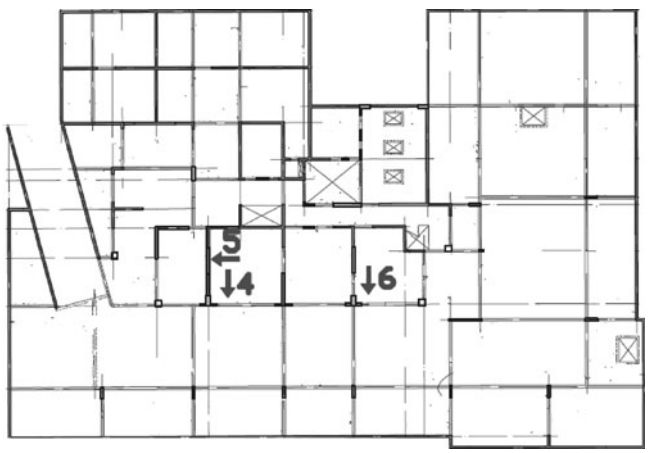

Fig. 39.2 Underground ceiling

Fig. 39.3 Seventh floor

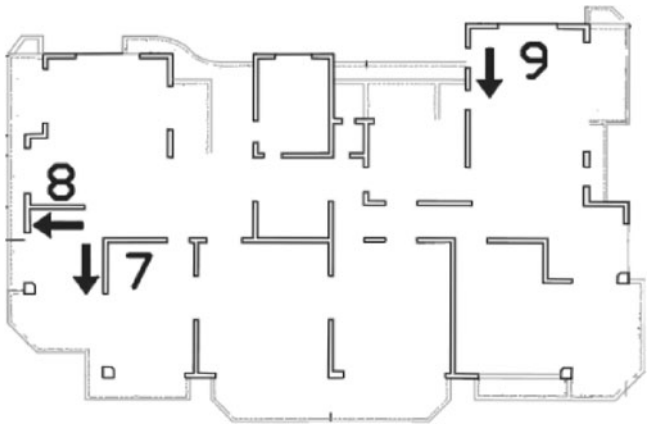

Fig. 39.4 Sixteenth floor

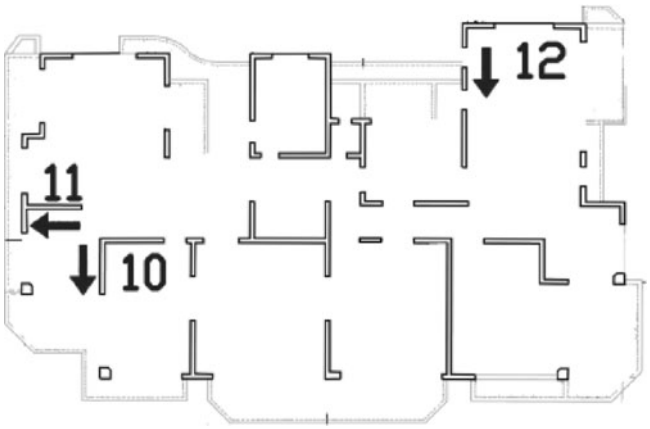

Table 39.1 Accelerometer location in structure

Signal channel Accelerometer	Measurement Direction	Level
1	N-S	Underground basement
2	E-W	Underground basement
3	N-S	Underground basement
4	N-S	First floor
5	E-W	First floor
6	N-S	First floor
7	N-S	Seventh floor
8	E-W	Seventh floor
9	N-S	Seventh floor
10	N-S	Sixteenth floor
11	E-W	Sixteenth floor
12	N-S	Sixteenth floor

An array of 12 uniaxial accelerometers was deployed in four levels of the building after the main shock and damage in the building occurred. Three accelerometers were located horizontally on the structure basement, two parallels in the NS direction and one orthogonal in the EW direction; other three sensors were located at the basement ceiling with the same configuration in accordance with basement distribution, shown in Figs. 39.1 and 39.2. The six reminder accelerometers were place at the 7th and 16th floor, as shown in Figs. 39.3 and 39.4, and as indicated in Table 39.1.

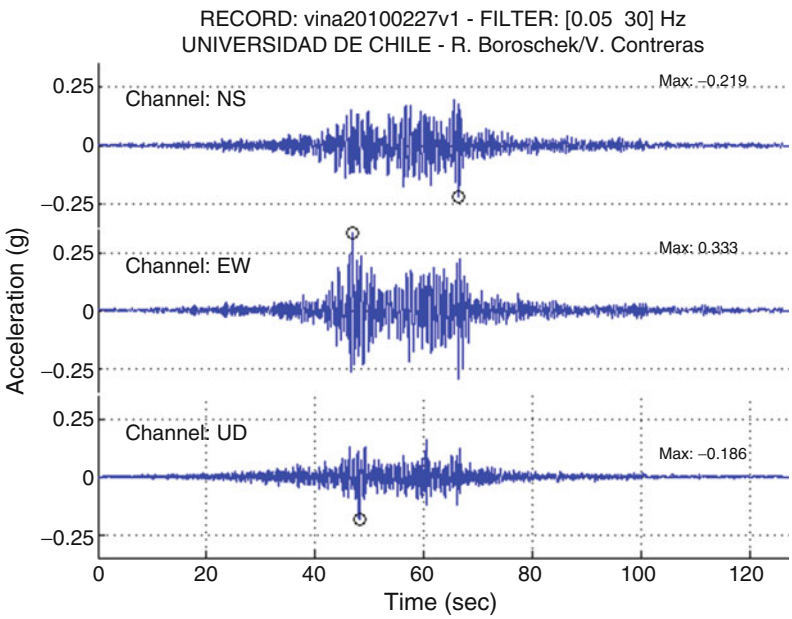

Fig. 39.5 Acceleration time series for Mw = 8.8 Chilean Earthquake – Viña del Mar station

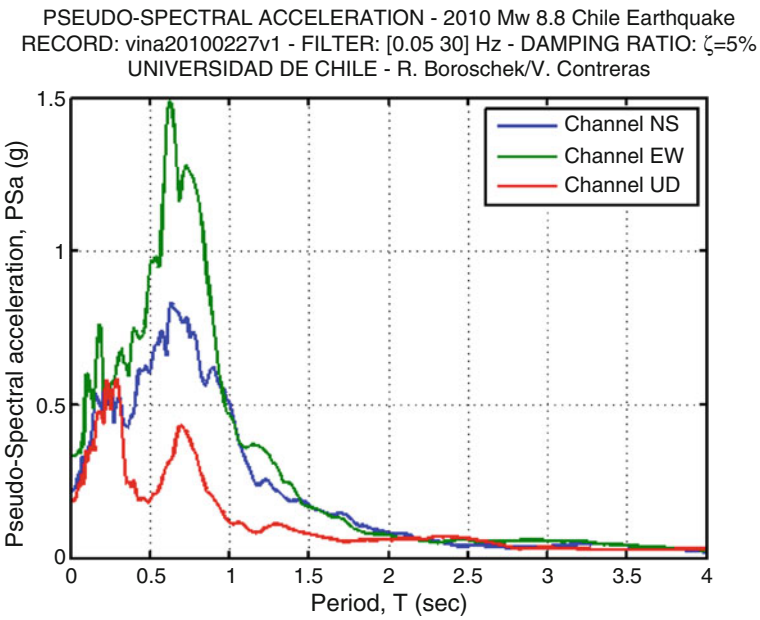

Fig. 39.6 Pseudo-spectral acceleration for 2010 Chilean Earthquake – Viña del Mar station

39.3 The 2010 Chilean Earthquake and Damage Building Status

The building was not instrumented before the Mw = 8.8 2010 Chilean Earthquake. The nearest strong motion station that recorded the main event was 1 km away from building location. The earthquake record is shown in Fig. 39.5. It shows 120 s of motion with nearly 30 s of strong shaking. The peak acceleration for NS direction was 0.219 g, for the EW direction it was of 0.333 g and for the vertical record 0.186 g. The pseudo acceleration spectrum is shown in Fig. 39.6; the maximum values are between 1 and 2 Hz. It is estimated that this strong demands severely affect to the first two natural frequency of the structure, contributing to its damage.

Fig. 39.7 Basement wall crushed at beam connection level

Fig. 39.8 Basement wall damaged

Basement and first floor walls suffered crushing of concrete due to a combination of flexure and compression, as well as, diagonal cracking associated to shear. The most important damage was concrete crushing, along with buckling of the longitudinal reinforcing bars, as shown in Figs. 39.7 and 39.8. In some cases, buckled bars were also characterized by fracture. Most of the lintel beams and slabs above ground floor of the building suffered serious damage Fig. 39.9b. There were some non-structural elements that present some damage, like partition walls.

39.4 Ambient Vibrations and Seismic Events Records

There were no seismic motions or ambient vibration records before the main shock so there is no experimental data to determine the dynamic properties for the structure in its undamaged conditions. No further damage occurred in the building during the monitoring period.

Thirteen ambient vibration records were obtained during a 3 h period. In addition, five low intensity seismic events were recorded in a period of 5 months. Details of data recorded are given in Table 39.2.

Fig. 39.9 (**a**) Buckling in longitudinal reinforcement bars first floor columns. (**b**) Lintel beam cracked

Table 39.2 Seismic events

Event	Name	Date	Local hour	Epicenter		Depth [km]	Magnitude
				Latitude	Longitude		
1	regsis0119	19-01-2011	2:20:00	−33.96	−72.453	12.9	5.4
2	regsis0126	26-01-2011	17:13:44	−31.737	−71.857	37.2	4.8
3	regsis0328	28-03-2011	3:10:41	−34.889	−71.837	45	5.7
4	regsis0331	31-03-2011	20:39:18	−34.292	−72.199	48.1	3.8
5	regsis0505	05-05-2011	10:35:34	−22.993	−70.189	46.5	3.2

For ambient vibration records modal parameters were obtained using N4SID SSI method developed by Van Overschee and De Moor [1–3]. Modal parameters from seismic records were identified using a MIMO technique, [4, 5]. The ambient vibration modal parameters are used as reference low level amplitude results. Variation of modal properties due to seismic events is determined for the strong motion vibration.

39.5 System Identification Techniques

The SSI technique developed by Van Overschee and De Moor [1–3] uses the stochastic space model, described by the equations system (39.1). This technique identifies modal properties from output only response signals.

$$\begin{aligned} \{x_{k-1}\} &= [A] \cdot \{x_k\} + \{w_k\} \\ \{y_k\} &= [C] \cdot \{x_k\} + \{v_k\} \end{aligned} \tag{39.1}$$

Equation 39.1 constitutes the basis for time-domain modal identification through ambient vibration measurements. There are several techniques and algorithms to obtain modal parameters from stochastic subspace model [1], (39.2). The mathematical background for many of such methods is similar, differing only in implementation aspects. The algorithms identify the state-space matrices $([A], [C])$ based on the measurements by robust numerical techniques, such as QR factorization, singular value decomposition (SVD), and least squares [3].

Table 39.3 Frequencies and damping ratios identified by SSI method

Frequency [Hz]	Minimum frequency [Hz]	Maximum frequency [Hz]	ξ [%]	Minimum ξ [%]	Maximum ξ [%]
0.80	0.80	0.83	1.5	0.60	3.20
0.82	0.81	0.83	1.2	0.90	1.90
1.04	1.04	1.06	1.9	1.20	3.30
3.11	3.10	3.13	1.0	0.90	1.90
3.67	3.64	3.71	2.3	1.50	3.90
4.19	4.07	4.23	2.3	1.40	2.50

Once the mathematical description of the structure is found, modal parameters such as frequency,ω_i damping ratio ξ_i and operational mode shapes,$[\phi]$are determined as:

$$\lambda_i = \frac{\ln(\mu_i)}{\Delta t} \qquad \omega_i = |\lambda_i| = \sqrt{\lambda_i - \lambda_i^*} \qquad \xi i = \frac{real(\lambda_i)}{|\lambda_i|} \qquad [\phi] = [C] \cdot [\Psi] \tag{39.2}$$

The MIMO system identification technique [6, 7], is based mainly on the dynamic modal equilibrium equation (39.3) and (39.4). This is an algorithm that searches for the optimal combination of parameters that best fits the measured response of the structure. There are other non-recursive techniques to identify modal parameters; nevertheless in this study this procedure was used because of the possibilities to control the identification procedure through bounding parameters and error levels.

$$\ddot{y}_j(t) + 2 \cdot \omega_j \cdot \beta_j \cdot \dot{y}_j(t) + \omega_j^2 \cdot y_j(t) = \sum_{i=1}^{N} L_{j,i} \cdot ag_i(t) \tag{39.3}$$

$$a_p(t) = \sum_{j=1}^{N} \phi_{j,p} \cdot \ddot{y}_j(t) \tag{39.4}$$

$$E = \frac{\sqrt{\sum_p \alpha_p \cdot \sum_t \left(a_{0,p}(t) - a_p(t)\right)^2}}{\sum_p \alpha_p \cdot \sum_t \left(a_{0,p}(t)\right)^2} \tag{39.5}$$

The target function of the optimization problem, E, indicated in (39.5), is a weighted least-square error between $a_{0,p}(t)$ and $a_p(t)$, where coefficients α_p controls the importance of each channel of the response record in the modal identification process.

The iterative algorithm starts the identification process using only the modes with the highest response participation. In each iteration, a new group of modes is added to the process. At the end, only the modes with most contribution to reduce the MIMO goodness of fit error, E, are kept.

39.6 Identified Modal Parameters

The modal parameters of the building due to ambient vibration for 11 consecutive 15 min non overlapping windows (3 h) are shown in Table 39.3. Frequencies remain relatively constant during the recorded time period. Important damping ratio variability is observed despite the fact that records were taken in three continuous hours. Variations are considered consistent with method used and nonlinearity of the damage structure. A typical stability diagram is shown in Fig. 39.10. All diagrams give very noisy results especially for first frequencies due to resolution problems trying to monitor ambient and seismic vibrations, Final results are obtained from average of values from all analyzed windows. Modal shapes obtained using MACEC v.3.0 [8], for each modal frequency is shown in Figs. 39.11, 39.12, 39.13, 39.14, 39.15 and 39.16. Important coupling of translational and rotational components are observed.

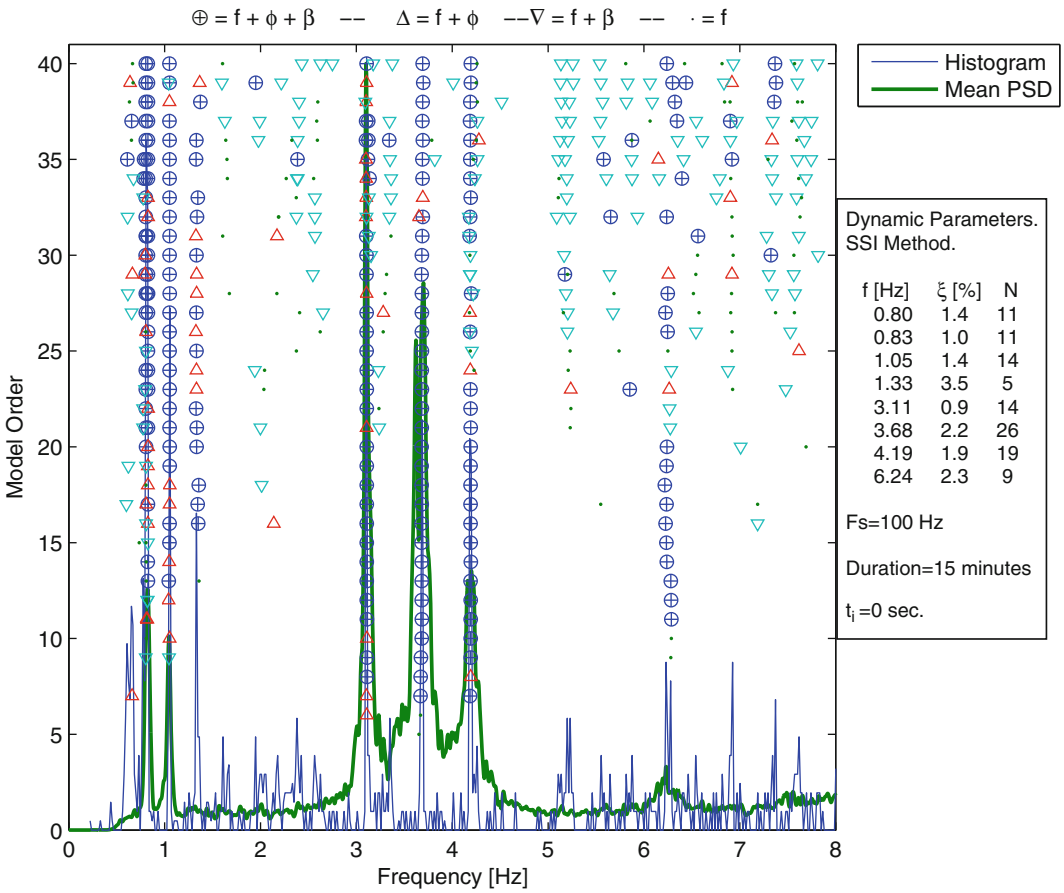

Fig. 39.10 Stabilization diagram

Fig. 39.11 First operational shape

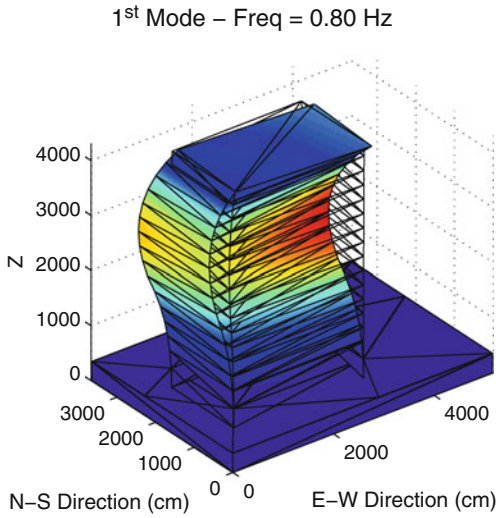

The modal shapes reflect a coupling between translational and torsional modal shapes in at least the first two natural frequencies. There is a nearly pure torsional modal shape, corresponding to fourth mode, at 3.11 Hz.

MIMO identification was applied to the strong part of the shaking of each record set. Strong shaking was determined using the Husid Intensity plot for 90% of total energy.

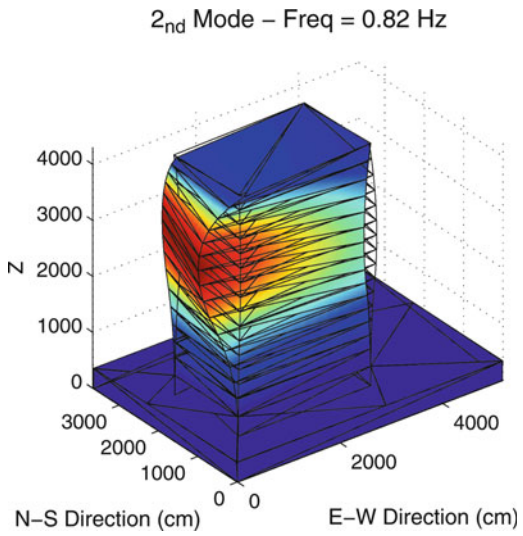

Fig. 39.12 Second operational shape

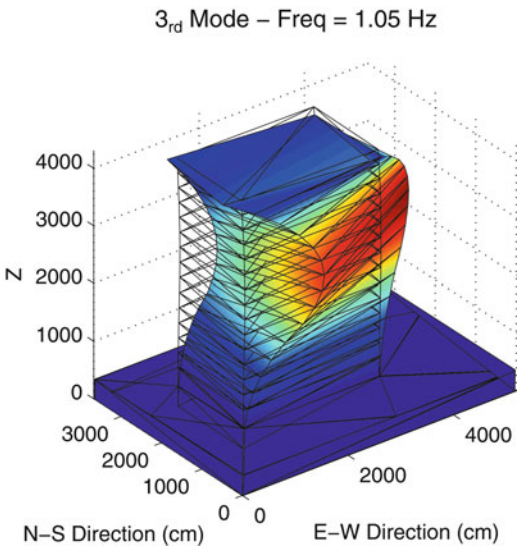

Fig. 39.13 Third operational shape

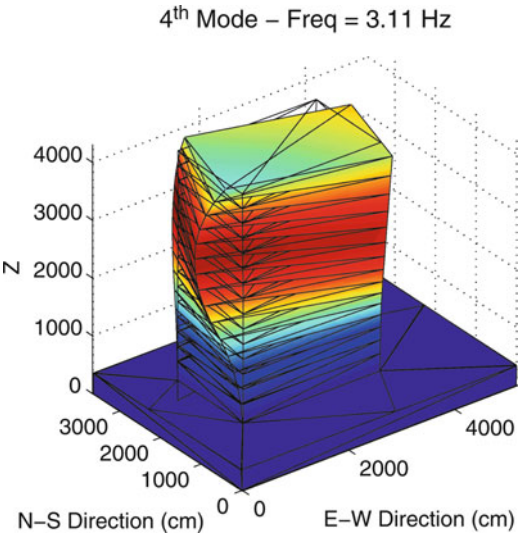

Fig. 39.14 Fourth operational shape

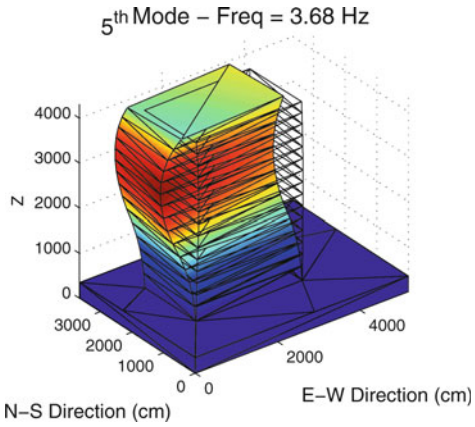

Fig. 39.15 Fifth operational shape

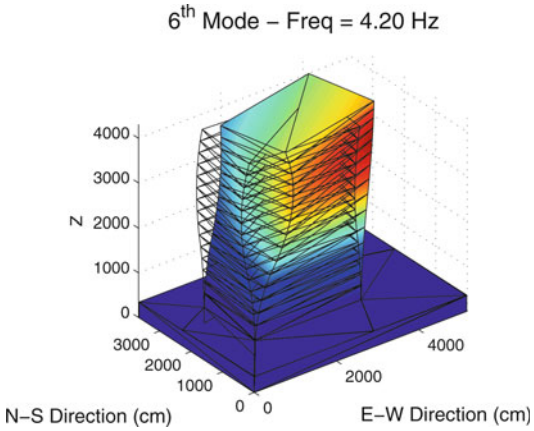

Fig. 39.16 Sixth operational shape

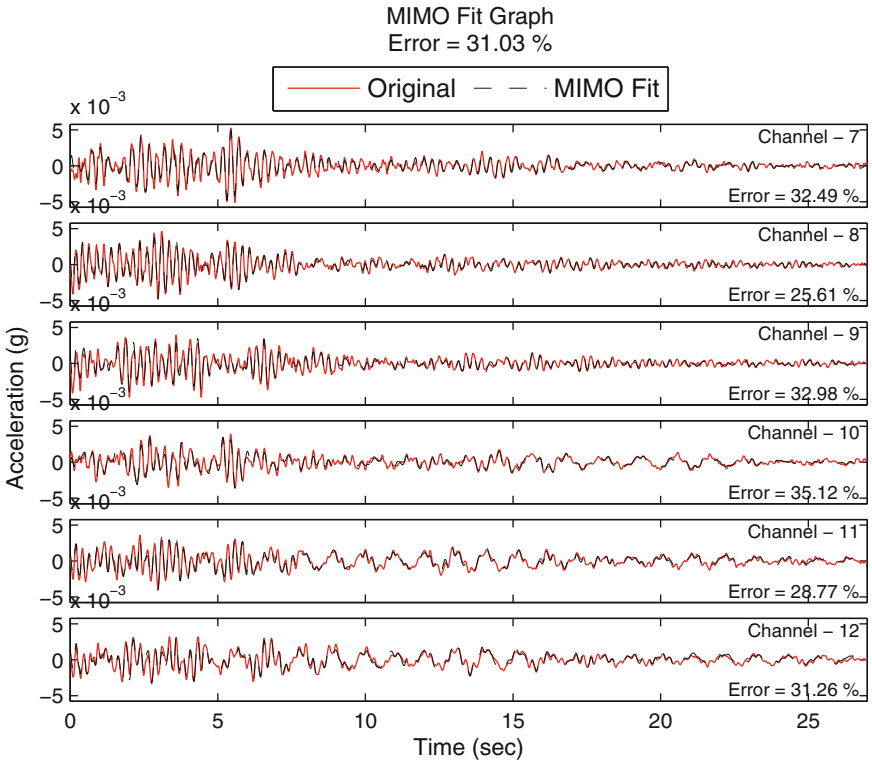

Fig. 39.17 MIMO fit for regsis0126

Table 39.4 Modal parameters – regsis0119. SSI method versus MIMO algorithm identification

regsis0119					
Global error = 40.2%					
AI = 1.7E-4 m/s					
ξ_{SSI} %	ξ_{MIMO} %	Relative difference %	f_{SSI} [Hz]	f_{MIMO} [Hz]	Relative difference %
1.5	6.1	309	0.8	0.68	−14
1.2	1.6	34	0.82	0.72	−12
1.9	4.3	128	1.05	0.90	−14
1	3.3	231	3.11	2.76	−11
2.3	2.9	26	3.68	3.40	−8

Table 39.5 Modal parameters – regsis0126. SSI method versus MIMO algorithm identification

regsis0126 – global error = 31.0%					
AI = 4.1E-6 m/s					
ξ_{SSI} %	ξ_{MIMO} %	Relative difference %	f_{SSI} [Hz]	f_{MIMO} [Hz]	Relative difference %
1.5	2.1	37	0.8	0.8	−4
1.2	2.7	126	0.82	0.7	−19
1.9	2.4	27	1.05	1.0	−6
1	2.0	97	3.11	3.0	−5
2.3	1.6	−30	3.68	3.6	−2

Table 39.6 Modal parameters – regsis0328. SSI method versus MIMO algorithm identification

regsis0328 – global error = 32.0%					
AI = 5.0E-5 m/s					
ξ_{SSI} %	ξ_{MIMO} %	Relative difference %	f_{SSI} [Hz]	f_{MIMO} [Hz]	Relative difference %
1.5	5.0	235	0.8	0.70	−12
1.2	2.7	126	0.82	0.70	−15
1.9	4.0	108	1.05	0.90	−14
1	2.6	164	3.11	2.79	−10
2.3	2.1	−8	3.68	3.44	−6

Table 39.7 Modal parameters – regsis0331. SSI method versus MIMO algorithm identification

regsis0331 – global error = 40.6%					
AI = 1.8E-6 m/s					
ξ_{SSI} %	ξ_{MIMO} %	Relative difference %	f_{SSI} [Hz]	f_{MIMO} [Hz]	Relative difference %
1.5	5.0	235	0.8	0.70	−12%
1.2	2.7	126	0.82	0.70	−15%
1.9	4.0	108	1.05	0.90	−14%
1	2.6	164	3.11	2.79	−10%
2.3	2.1	−8	3.68	3.44	−6%

Adjustment of equivalent linear models gives different global errors for each seismic record processed. The best fit of equivalent viscoelastic modal parameters was given by regsis0126 analysis. In this case, each channel was fitted with an error less than 35%, as it can be observed in Fig. 39.17.

MIMO identified properties are later compared with ambient vibration values using (39.6). This comparison is presented in Tables 39.4, 39.5, 39.6, 39.7 and 39.8.

Table 39.8 Modal parameters – regsis0505. SSI method versus MIMO algorithm identification

regsis0505 – global error = 37.8%					
AI = 4.1E-6 m/s					
ξ_{SSI} %	ξ_{MIMO} %	Relative difference %	f_{SSI} [Hz]	f_{MIMO} [Hz]	Relative difference %
1.5	0.7	−56	0.8	0.58	−27
1.2	2.2	79	0.82	0.73	−10
1.9	3.5	84	1.05	0.93	−11
1	2.1	111	3.11	2.91	−6
2.3	1.6	−31	3.68	3.50	−5

$$\frac{X_{MIMO} - X_{SSI}}{X_{SSI}} \cdot 100\% \tag{39.6}$$

39.7 Conclusion

In this study, a 17 story reinforced concrete shearwall building was analyzed to determine the variation of modal properties from ambient and seismic vibrations. Six frequencies and damping ratios were identified from ambient vibrations using the SSI method. Modal frequencies remain relatively constant during ambient vibration measurement period. Modal damping ratios show a high variance that raises more than 60% in many cases. Mode shapes show coupling between translational and torsional modal shapes in first two natural frequencies.

For each seismic event identified modal properties gives lower frequencies than those determine from ambient vibrations, as expected considering that the structural stiffness decrease with increasing motions. Modal damping ratios show high variances when compared to the SSI results. Further analysis of the data is underway. The retrofitted building will be monitored and compared with parameters identified in its damage stage.

References

1. Van Overschee P, De Moor B (1993) Subspace algorithms for the stochastic identification problem. Automatica 29(3):649–660
2. Van Overschee P, De Moor B (1994) N4SID: subspace algorithms for the identification of combined deterministic-stochastic systems. Automatica 30(1):75–93. Special issue on Statistical signal processing and control
3. Van Overschee P, De Moor B (1996) Subspace identification for linear systems: theory-implementation- applications. Kluwer, Dordrecht
4. Boroschek R, Carreno R (2011) Modal parameters variation due to earthquake of different intensities. In: XXIX IMAC conference and exposition on structural dynamics, Society for Experimental, U.S.
5. Carreno R (2009) Variation of dynamic properties of Chilean chamber of construction building: seismic case. Civil Engineering Thesis, University of Chile, Chile
6. Beck JL (1978) Determining models of structures from earthquake records. Report EERL 78-01, Caltech, Pasadena
7. Mau ST, Li Y (1991) A case study of MIMO system identification applied to building seismic records. Earthquake Eng Struct Dynam 20:1045–1064
8. Reynders E, Schevenel M, De Roeck G (2008) MACEC: a Matlab toolbox for experimental and operational modal analysis. User manual, Katholieke Universiteit Leuven

Chapter 40
Modal Analysis of the Palazzo Lombardia Tower in Milano

A. Cigada, E. Mola, F. Mola, G. Stella, and M. Vanali

Abstract The 'Palazzo Lombardia' Tower, located at the heart of the city of Milan, Italy, has been recently completed. The new building, 161.30 m high, is currently the tallest in Italy, and one of the strongest features in the city skyline of the for many years to come.

Given the strategic importance and the strong impact of the new building, it was decided to complete the final testing with a series of dynamic excitation tests, with special emphasis on the Tower. It was possible to extract its basic modal features and then to compare them to the numerical simulation predictions provided by the same finite element numerical analysis used for design. This offered the chance to start an important and interesting model updating procedure, taking benefit from both static and dynamic measurements, these latter having added significant details.

The Mechanical Engineering Department of Politecnico di Milano was in charge of the design and execution of the tests. ECSD and CAD Data Consult took part in the design of the experiments and the model updating procedure.

The tests provided an experimental verification of the modeling assumptions accuracy and of the robustness and reliability of the FE model in predicting the structure behavior as from design; on the other hand, the comparison between tests and predictions was meant as a tool for early detection of any possible construction inaccuracies or unexpected modifications with respect to the design statements. Finally, the experimental validation of the Tower FE model was meant as the initial part of an intended continuous monitoring activity. The present paper describes the main structural features of the 'Palazzo Lombardia' Tower and those of the experimental tests. Also, the FE model is presented and the comparison between the numerically predicted and the experimentally derived modal properties is discussed.

Keywords Tall buildings • Numerical analysis • Dynamic tests • Modal analysis • Reinforced concrete structures • Monitoring

40.1 Introduction

The project for 'Altra Sede', meaning the new seat for the offices of Lombardia Region, located in Milano, is one of the most significant in the Italian panorama of the last few decades, setting the record of the tallest building in Italy, at 161.30 m.

The building, now officially called 'Palazzo Lombardia', after the citizens themselves chose the new name by voting online, is destined to strongly mark Milan's skyline for the years to come.

A. Cigada
Dipartimento di Meccanica, Politecnico di Milano, Via La Masa, 1, 20156 Milan, Italy

E. Mola • F. Mola
ECSD S.r.l, Milan, Italy

G. Stella
CAD Data Consult, Milan, Italy

M. Vanali (✉)
Dipartimento di Ingegneria Industriale, Università di Parma, Parma, Italy
e-mail: marcello.vanali@polimi.it

J.M. Caicedo et al. (eds.), *Topics on the Dynamics of Civil Structures, Volume 1*,
Conference Proceedings of the Society for Experimental Mechanics Series 26,
DOI 10.1007/978-1-4614-2413-0_40,

Fig. 40.1 Palazzo Lombardia: the whole complex

The complex is made up of five lower buildings (about 40 m high, called Cores 2, 3, 4, 5 and 6), surrounding the high-rise Tower (Core 1), which scored the already mentioned height record in Italy. The complex's sinuous interweaving strands recall the mountains, valleys, and rivers of the Lombardia region. The curvilinear forms largely used in the architectural design, and clearly visible in the facades of all the buildings, are adaptable to changing functional requirements and are receptive to the region's evolving organizational structure.

The curvilinear shapes of the buildings, while having a very strong aesthetical impact, are also strongly reflected in the irregular plan-wise configuration of the complex, which, at its center, defines an inner covered public 'plaza', having an area of about 4,200 m^2, covered by a steel truss system supporting transparent Texlon ETFE (ethylene-co-tetrafluoroethylene) cushions. In Fig. 40.1, the six buildings, or Cores (1–6) making up the complex are visible in a picture taken at the end of the construction phase, in 2010.

The structural system is entirely made of reinforced concrete load bearing elements, except for the Auditorium area in Core 4 and the 'Velarium' on top of Core 1, a three-storey high belvedere area to be used for official public purposes and rented for private events. For these two parts structural steel was employed.

Due to the strategic importance of the building, a detailed analysis of the dynamic behavior was requested to assess the structural response to earthquakes, also according to the Italian law on building earthquake performances, and to prevent any possible vibration serviceability issue [1, 2]. To this aim a numerical FE model was implemented for the most sensible building part, the tower, and then validated against a series of experimental tests. In this paper the model results and the experimental validation are presented together. Then a comparison will be performed between the numerical forecast and the real structure response. At first the structure itself is described and some of the design choices are explained. Then the FE model in introduced together with the model parameter choice description. Following this the experimental set-up and the experimental tests are presented and then a final comparison with the FE model results is shown.

The results shown in the paper set the basis for the future health monitoring of the building which will also be based on the dynamic behavior evaluation, among others.

40.2 Description of the Structure and Design Choices

A thorough description of the structural features of the complex and a discussion of the reasons behind the basic conceptual design choices are provided in [3]. In the present paper, only a few highlights, most of them regarding the Tower (Core 1) are reported, with the purpose of better clarifying the modeling assumptions enforced in the implementation of the finite element model of Core 1.

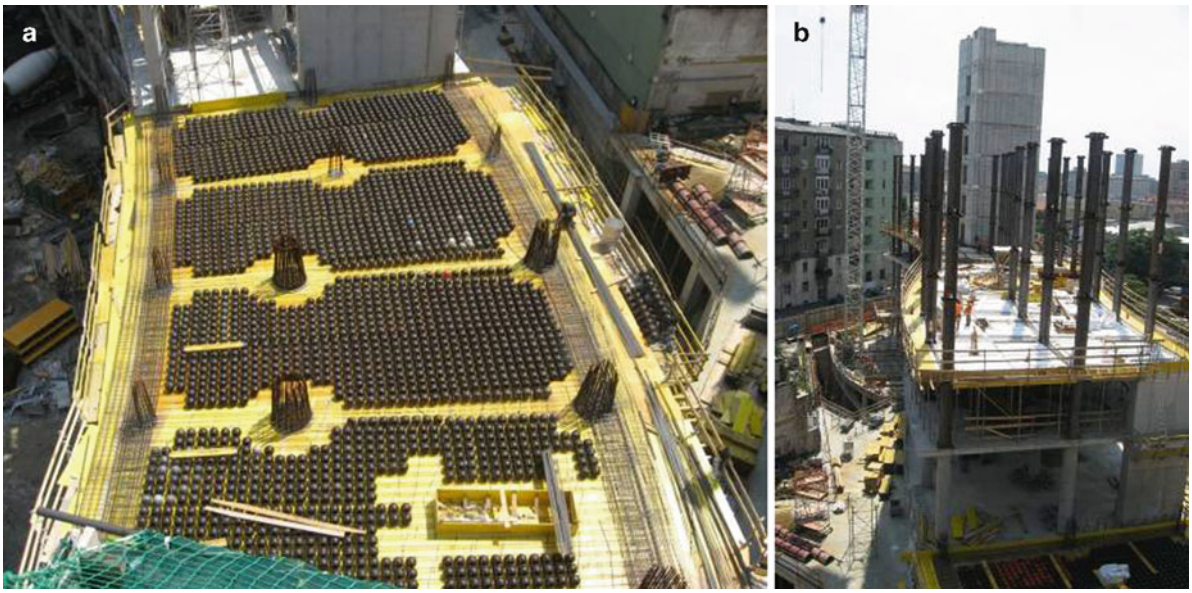

Fig. 40.2 Structural details: (**a**) 'bubbledecks' in Core 1, (**b**) steel encasing for columns of Core 1

The load bearing elements of Core 1 are entirely made of reinforced concrete: the lateral load bearing capacity is fully provided by a central stairways core, whereas the vertical structural elements are circular columns with varying cross sections, with diameters ranging between 120 and 65 cm.

The slabs are different along the height of the building: the underground floors are interconnected with those of the lower Cores, while starting from the ground floor, and up to the top slab of the lower buildings (i.e. at a height of about 40 m), the slab surface is larger than that of the upper storeys, rising to the top.

The slabs of Core 1 starting from the ground floor are 35 cm thick, fully bi-directional reinforced concrete structural systems once referred to as 'bubbledecks', since the reduction of weight is obtained by inserting high density polyethylene (PEHD) spheres with a diameter of 270 mm in the slab, holding them into place during casting by means of retaining rebar cages, in addition to the usual bi-directional structural rebar layers. The use of this construction technology generated two advantages from a structural point of view, in particular improving the seismic response, since these bi-directional slabs weigh up to 20% less than their fully cast-in-situ counterparts.

The structural system achieved by means of steel encasing for the vertical elements and light weight 'bubbledeck' slabs exhibits the behavior of a continuous plate on point supports (the columns) and continuous support (the walls of the core). The encasing elements were thus holed so that slab rebar and concrete could pass through, thus making the column-to-slab joints completely effective in bearing lateral load induced moments. The slabs and columns are represented in Fig. 40.2a, b respectively.

The peculiar features of the slab-to-column joints were an aspect of interest and investigation when the finite element model was implemented, as detailed in the following paragraph.

Another significant feature affecting the global modal properties of the structure and, as a consequence, of the finite element model, remains in the foundations.

The foundation of Core 1 is made of a slab with a thickness ranging between 2 and 4 m. Under the slab, the ground was injected with compacting grout columns, having a diameter of 1.5 m, spacing between 3 and 4 m, and depth between 14 and 22 m. Self compacting concrete was used to cast the lower layer of the slab, due to the strong rebar congestion, then normal concrete was used for the remaining depth. The two layers were interconnected by means of vertical steel bars purposely distributed in the slab. All the steel bars were joined by means of steel couplers.

The foundation slab was initially analyzed as a plate on an elastic surface, according to Winkler's model, for pre-dimensioning purposes. Structural analysis was carried out on a 3D shell element model representing the slab, with different subgrade coefficient values, ranging between 0.5×10^{-3} and 2.5×10^{-3} N/mm^3.

In Fig. 40.3, the soil pressure resulting from the analysis is represented. The highest values of such pressure, about 0.5 MPa, are distributed in the central part of the slabs, below Core 1, which led to increase the slab thickness in this area, so that differential displacements between the foundation of the inner core of the tower and those of the columns could be limited.

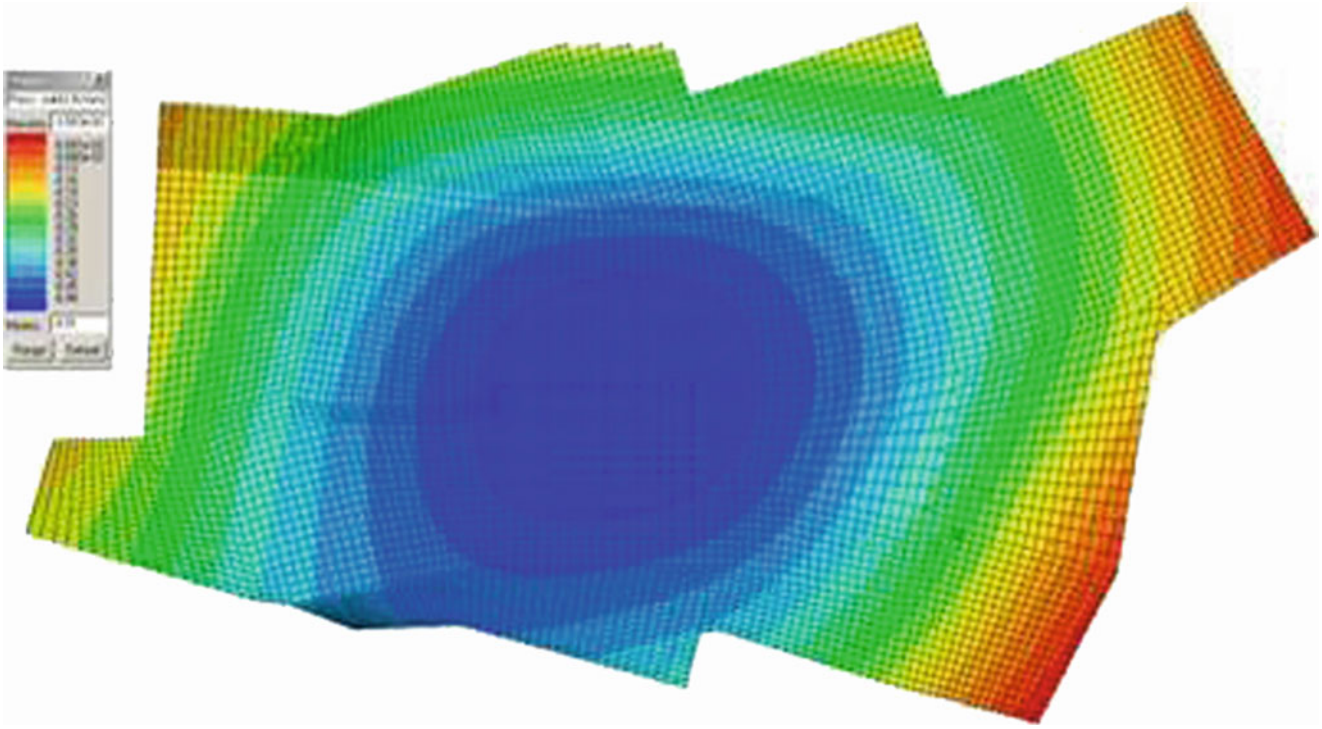

Fig. 40.3 Foundation slab analysis: distribution of soil pressure

When implementing the global finite element model, the foundation slab was included and different subgrade coefficient values were assumed in the model, to test the sensitivity of the final results to this parameter. The stiffness of the foundation was exactly computed and its restraining effects on the global structural models were thus accounted for, as detailed in the following.

40.3 The Finite Element Model: Features and Analysis

A finite element model of Core 1 was implemented, using GT STRUDL® [4] a commercial software for structural analysis, to run both static and dynamic analyses.

The static analyses allowed for the validation of the conceptual design and the dimensioning of the structural elements; also, optimization of the structural elements' performance, both in the service limit state and at ultimate, was pursued by means of refined analyses.

Given the inherent flexibility of the structure, whose first modal period is well in the tail section of the EC8 type design spectrum, and, on the other hand, given the very wide surfaces exposed to wind pressure, static analyses confirmed that the heaviest loading condition for lateral load bearing capacity was due to wind, so that, for dimensioning purposes, the strongest wind in the exercise limit state was used.

In order to derive the modal features of the structure, a linear dynamic modal analysis was then carried out. The main purpose of the analysis was to provide accurate numerical predictions of the modal response of the building, which would be compared to the series of dynamic excitation tests described in the present paper, which were meant as a pre-requisite for its final validation, as mentioned above

The global finite element model was implemented assuming the design properties of materials and of the ground and accurately describing both the global geometry and the local features peculiar of the different structural elements. The high level of accuracy required in the numerical analyses and the remarkable dimensions of the building itself led to the development of a quite complex model, whose main features are:

52,757 6-degrees-of-freedom joints, for a total of 316,542 dofs
53,910 shell elements + 9,088 linear element (beams and columns)

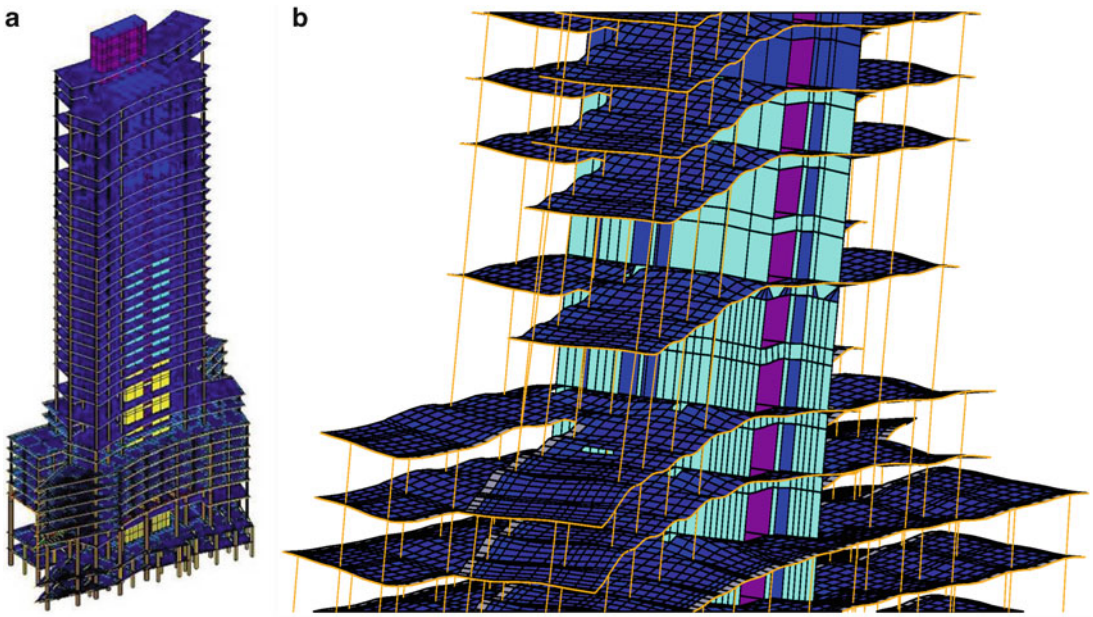

Fig. 40.4 Finite element model in GT Strudl – (**a**) global view and (**b**) close-up (of earthquake loading induced deformed shape)

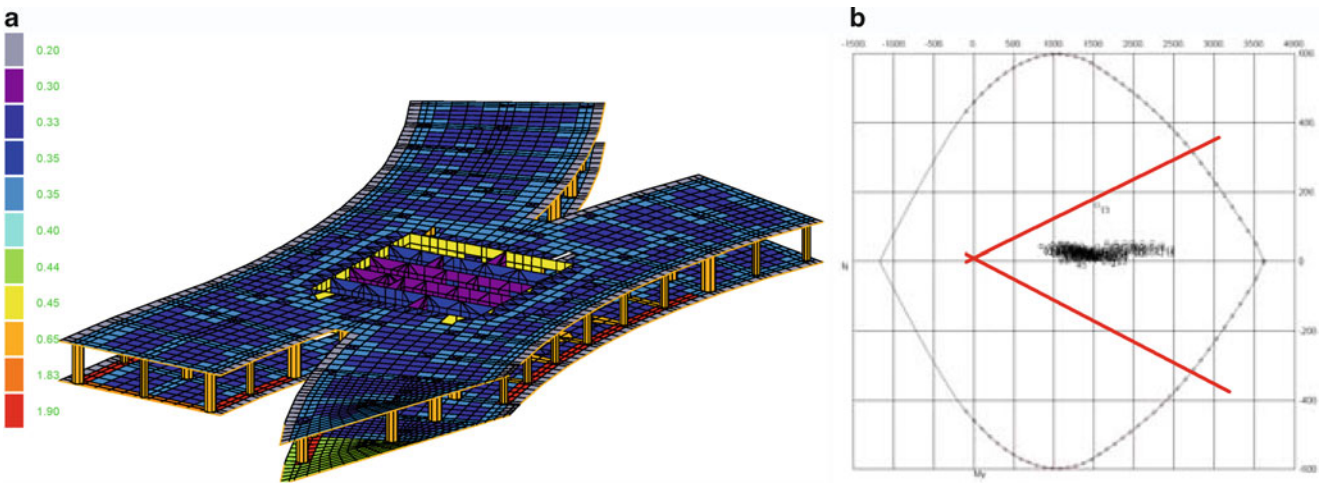

Fig. 40.5 Finite element model – examples of output: (**a**) slab stress distribution and (**b**) column limit state verification

77,171 load types, divided in 27 basic loading conditions and five loading combinations: assigning the different loads to separate loading conditions was a pre-requisite to be able to effectively reproduce the real mass distribution of the structure in the various construction and service life conditions

It was deemed important to properly model the slab-to-column connections and, in general to replicate, in the closest possible way, the behaviour of the slabs of the Tower; for this reason, the so-called 'bubble slabs' described in the previous paragraph (i.e. cast-in-situ RC slabs lightened by means of polyethylene spheres) were modelled by means of shell elements with an equivalent thickness to provide the correct flexural stiffness. These areas are highlighted in a different color in the pictures of the model, Figs. 40.4a, b and 40.5a.

Since the effective stiffness of the slab-column joints remarkably affects the relative structural deformation distribution between slab and columns, thus modifying the modal analysis results, in order to investigate the sensitivity of the modal properties to the effective stiffness distribution in slabs, two different meshing options were implemented. The first mesh did

not take into account the stiffening effect of the columns' effective cross sections on the joints of the slabs mesh; the second meshing option did take into account the presence of the columns' cross sections by means of an additional infinitely rigid constraint imposed to the joints of the mesh where each columns was present and in its immediate vicinity.

Modal dynamic analyses were carried out assuming a linear elastic behaviour of materials, since it was expected that the experimental excitation provided to the structure during the tests would have to be well in the elastic range of the response, being produced by the wind or by fit-to-the-purpose exciters.

It is well known that modal properties depend on the actual material properties: in particular, the actual elastic modulus of concrete, which is used to determine the stiffness matrix, depends in turn on the concrete class and its characteristic strength.

For this reason, when using the nominal design properties of materials in the finite element model, a margin of error comes from the gap between the actual material properties and the nominal ones. In the case of Core 1, the results of the compressive strength tests on cubes extracted during construction were available; a mean value of the compressive strength was thus derived for the different structural elements and, from this, by applying the Model Code 90 [5] formulation (40.1), the corresponding elastic modulus was computed:

$$\text{with} \qquad \beta_E(t') = \left\{ e^{\left[s\cdot\left(1-\sqrt{28/t'}\right)\right]} \right\}^{\frac{1}{2}} \qquad \begin{aligned} E_c(t') &= \beta_E(t') \cdot E_{c,28}, \\ E_{c28} &= 2.15 \cdot 10^4 \cdot \left(\frac{f_{cm}}{10}\right)^{\frac{1}{3}} \end{aligned} \tag{40.1}$$

Two different modelling assumptions were then made, in order to investigate the sensitivity of the modal properties to a change in the material properties: at first, the design properties of all the employed materials were implemented in the model; then, the actual elastic moduli derived from the experimental compressive strength were implemented for each class or group of elements. The results proved that the sensitivity of the first eigenfrequencies and eigenvectors to this parameter was much lower than that due to the mesh refinement; it was thus decided to assume the design properties of materials in all the subsequent analyses.

Modal frequencies and modal shapes not only depend on the stiffness distribution (both of cross section inertiae and elastic modulus) but also on the actual mass distribution – both the structural masses and those of the loads that were already present when the tests were carried out, these latter assumed to be just a fraction of the design loads. Since the experimental dynamic excitation tests were run at the end of construction, but before the whole static permanent loading was put in place, it was necessary to make a computation of the actual masses present on the structure when the tests were run. For the final simulations it was thus assumed that a fraction of 20% of the permanent loading would be present.

Finally, as for the foundation properties, a subgrade coefficient value of 2.0×10^{-3} N/mm^3 was assumed; this was the design value used in the pre-dimensioning analyses run separately on the foundations alone, and it proved to be the value of this parameter providing the modal response that best matched the experimentally derived one.

The GT STRUDL® software, one of the longest established structural analysis software currently available, couples high reliability of results with highly reduced computational times: the total computational time for the modal analyses of the Tower model is 5 min if the optimized processor is employed and of 12 min if the standard processor is used.

40.4 The Experimental Tests: Features and Results

Dynamic testing is considered more and more important as a valuable tool providing a validation to refine and eventually update numerical simulation models and giving information about the response to an external stimulus like the wind or an earthquake.

For example, very often it happens that static numerical models need a further refinement step, to account for dynamic features. Mass distribution and stiffness are given at certain uncertainty levels, as discussed above in the case of Core 1, and, even worst, damping coefficients are hard to be estimated theoretically and sometimes affected by strong non linear structural behaviours. A check on both static and dynamic behavior can help narrowing this uncertainty. A further goal which is growing in importance, is trying to lay down the basis for a proper permanent monitoring [6]. In the case of 'Palazzo Lombardia', given its importance, a series of dynamic excitation tests were deemed a mandatory pre-requisite for the final design validation.

Fig. 40.6 view of the pre-test operational set-up on the building

40.5 Test Set-Up and First Operational Modal Analysis Results

The main problems in testing a skyscraper are a proper forecast of the mode shapes, to fix sensors in the right positions and the certainty to have a proper input to excite the structure.

The main global behaviour of Core 1 is that of a cantilever beam, at least in a first approximation approach: as mentioned above, the well distributed lateral load resisting elements and the regular plan-wise configuration made it easier to predict a regular and mostly uncoupled modal response. In fact, the numerical model provided an initial approximation of the expected vibration modes and frequencies that could reasonably be assumed as a confirmation of this behaviour. To further confirm these assumptions a short pre-test exploiting ambient vibrations was designed and executed. The idea was to exploit Operational Modal Analysis [7, 8, 11] approaches to get a first experimental estimate of the natural frequencies and a rough idea of the associated mode shapes.

Three acceleration measurement positions have been chosen, at the Tower 38th floor. Low noise Seismic Piezo accelerometers have been used, taking care of the conditioning unit too, in order to assure a flat frequency response even in the 0.1–0.5 Hz region, being 0.1 Hz the lowest frequency measurable by the selected sensors.

A picture of a part of the installed measurement system for the operational pre-test is shown in Fig. 40.6 (data collection unit and some accelerometers during the calibration phase).

The first test has exploited ambient excitation for 1 week, accepting wind and traffic as the unknown input. Apart from gauging the structural sensitivity to this excitation, this test has also allowed for a first check about the identification of the first natural frequencies and the related mode shapes: even if the signal to noise ratio is less favorable in this kind of tests, acquisition through the whole week has allowed for an improvement in the output signals, thanks to continuous averaging, especially selecting the periods with higher and stationary vibration levels. Figure 40.7 provides one the output from these tests, in terms the power spectral density (PSD) averaged on a 24 h time window, for the measurement points on the 38th floor.

Three main peaks are well evident in the lowest frequency range: the 0.33 Hz mode shows all the weak axis sensitive accelerometers measuring the same amplitude, justifying a flexural mode; the same applies to the 0.42 Hz mode, just exchanging the weak axis with the strong axis. The third peak, at 0.65 Hz exhibits higher amplitudes as the distance from the main core increases, and this is compatible with a torsion. Any contribution at higher frequencies is not so easily detectable, having peaks close to the transducers noise floor: ambient excitation cannot input enough energy to excite higher modes. A summary of the operational identified values for the first three vibration modes is given in Table 40.1.

It must be noted that the estimated damping values showed a higher spread, being a function of the considered time frame within the testing week, which is also confirmed by literature results. Modal parameters of this kind of structures are influenced by temperature, vibration levels and load conditions [9].

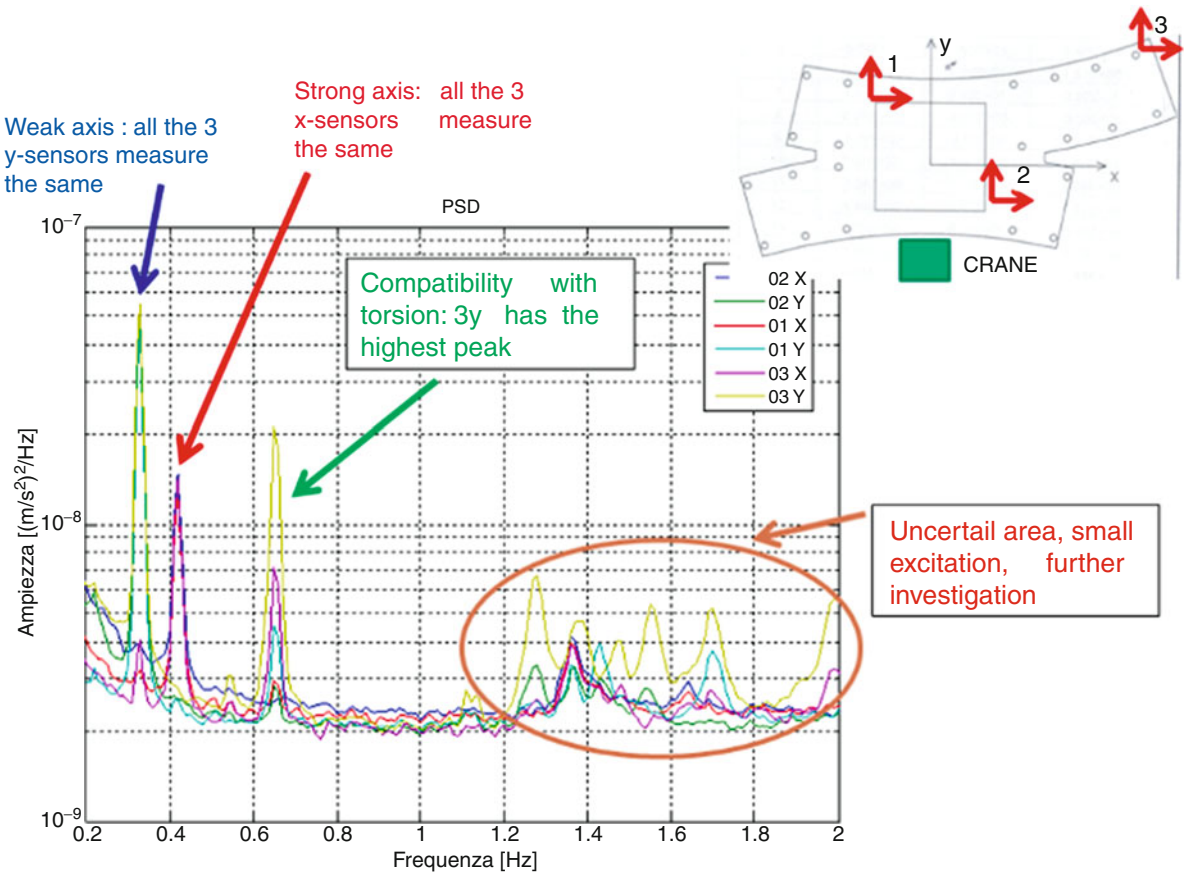

Fig. 40.7 Measured accelerations PSD at floor 38 – operational modal analysis test

Table 40.1 Identified modal frequencies and damping for the first three modes via operational modal analysis

Mode number	Frequency [Hz]	Estimated damping [% rc]
1	0.33	1.8
2	0.42	2.2
3	0.65	1.6

40.6 Forced Vibration Test Set-Up

On the basis of the model assumptions and the first operational results, the location of the forced test sensors was decided and the expected range of potential resonance frequencies was defined; moreover, fixing a rough damping estimate, from the numerical modal analysis a first approximation about the needed input to produce a measurable output was derived. This time the sensors were located on three different floor levels, the 21st, the 32nd and the top floor, the 38th, considered enough to identify the first vibration mode shapes (Fig. 40.8). Each floor has been instrumented as shown in Fig. 40.9, with two orthogonal axis accelerometers in the horizontal plane, capable to identify flexural modes (strong and weak axis) and torsion modes.

Concerning forced tests, one of the most important issues when dealing with large structures, having low natural frequencies, is giving an adequate energy input in order to guarantee a coherent structural response. It is well known how inertial exciters have problems in producing a meaningful force at low frequencies. The inertia force is the product between mass and acceleration; assuming that a sine function is used as input, it follows that acceleration is low at low frequencies, as the peak acceleration is the displacement peak amplitude multiplied by the circular frequency squared. It comes out that high energies at low frequencies are possible to be provided only with long strokes and big masses; moreover, all the available energy must be provided at a single frequency, pushing toward the use of a stepped sine signal test design.

To fulfil these requirements, a linear motor specifically adapted for the tests was lifted on top of Core 1 (floor 38), allowing to move up to 1,000 kg in the frequency range of interest, with a stroke close to 2 m: no other traditional means can provide the same performances. Figure 40.10 shows the linear motor installed on floor 38.

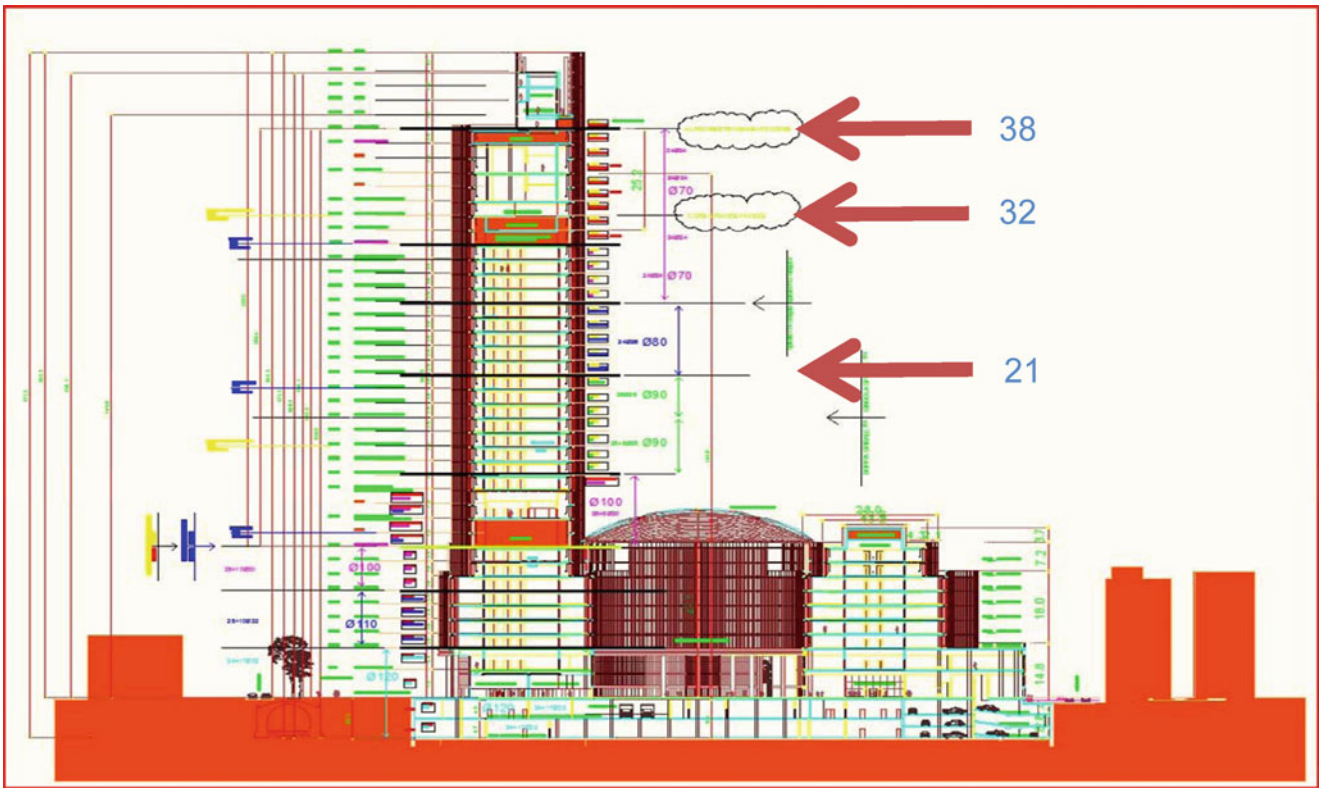

Fig. 40.8 Location of accelerometers on the different floors

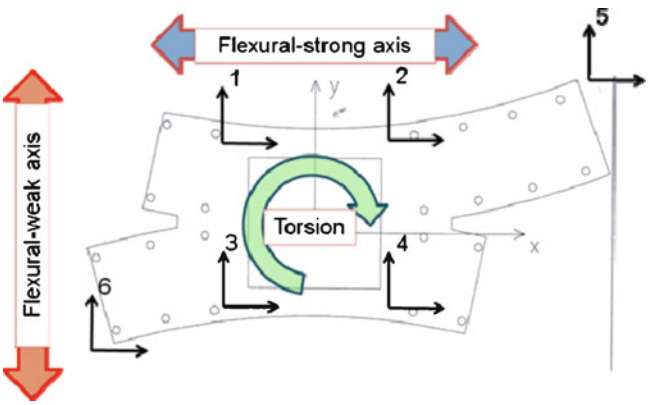

Fig. 40.9 Instrumented floors plan

The use of such a device allowed also a complete control on the input force, as frequency and stroke could be controlled and changed at each step of the analysis. A constant force has been applied at all frequencies of interest.

As previously stated tests were carried out using a stepped sine excitation with a frequency resolution of 0.01–0.005 Hz, changed accordingly to the known resonance positions (higher resolution close to resonance). The use of a stepped sine excitation allowed to test the structure under steady state conditions, therefore assuring maximum repeatability of the test results. Test was repeated twice Forcing the structure in two orthogonal directions in order to excite both flexural modes.

Measurements have been analyzed through a synchronous approach, in order to reduce spectral leakage. An example of the identified frequency response function is given in Fig. 40.11 in terms of amplitude and phase vs. frequency, for the accelerations measured at floor 38. Positions refers to the points in Fig. 40.8.

As can be seen in Fig. 40.11, the peaks identified via operational modal analysis are still present in the Frequency response function, moreover some resonances are evidenced in the area 1.2–1.5 Hz.

Fig. 40.10 Linear motor at floor 38 axis

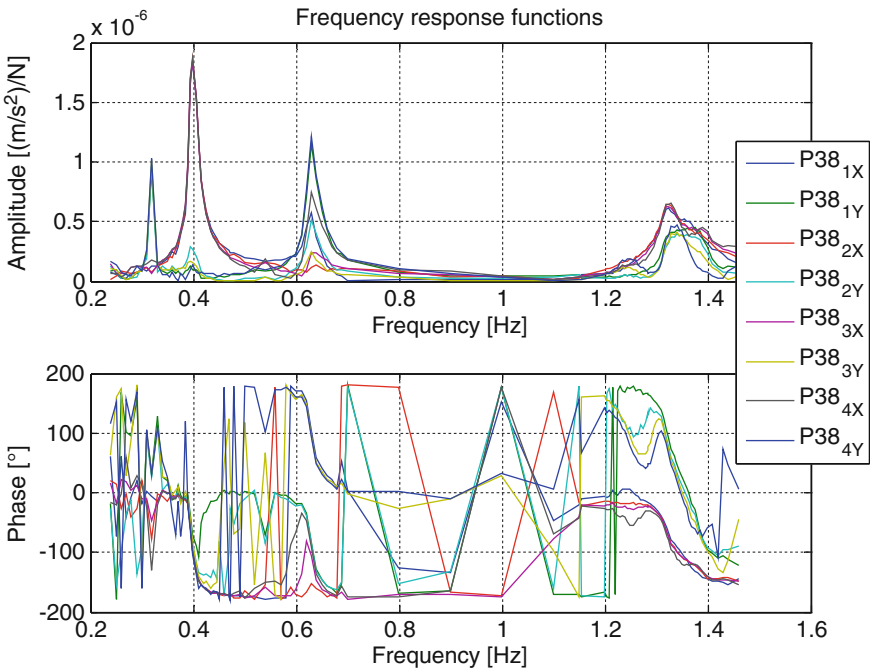

Fig. 40.11 Frequency response function measured on floor 28. Forcing in the flexural strong axis direction

Table 40.2 Identified vibration modes from the forced testing (mode 3 has been identified in both forcing directions.

	Mode 1	Mode 2	Mode 3	Mode 3	Modo 4	Modo 5
Freq [Hz]	0.32	0.4	0.63	0.63	1.25	1.35
Damping [%rc]	1.19	1.47	1.49	1.43	1.46	1.28

All the computed frequency response functions have been processed with the Least Square Frequency domain method [10] in order to extract the relevant modal parameters. A summary of the identified modes in terms of frequency and damping in given in Table 40.2. Mode number 3 appears two times as it has been identified during testing along both the strong and the weak flexural direction.

The identified damping values are compatible to what was expected from literature [8, 9] considering the low vibration amplitude: on one side this guarantees that the linear response field is not exceeded, but this also means accepting an

Table 40.3 Comparison between numerical analysis and experimental results: modal frequencies, no rigid joints

No slab-to-column joint constraint					
With foundation mass			Weight = 109,533 T		
	Freq. cyc/s		Ratio	Ratio	Gap
MODE	Meas.	Num.	Meas/num	Num/meas	%
1	0.32	0.32	0.97	1.01	−0.93
2	0.40	0.37	1.04	0.92	7.60
3	0.63	0.55	1.13	0.87	13.22
4	1.25	1.09	1.13	0.87	12.83
5	1.35	1.19	1.11	0.89	11.42

Table 40.4 Comparison between numerical analysis and experimental results: modal frequencies, rigid joints

Constrained slab-to-column joints					
With foundation mass			Weight = 109,533 T		
	Freq. cyc/s		Ratio	Ratio	Gap
Mode	Meas.	Num.	Meas/num	Num/meas	%
1	0.32	0.34	0.95	1.05	−5.1
2	0.40	0.40	0.99	1.01	−1.0
3	0.63	0.57	1.11	0.90	10.0
4	1.25	1.12	1.11	0.90	10.2
5	1.35	1.24	1.08	0.92	7.5

increased sensitivity of the measures to any kind of random disturb. The values are slightly less than those obtained from operational modal analysis (Table 40.1), but this can be due to the better signal to noise ratio of the forced testing.

The identified mode shapes are those expected from a cantilever beam behavior and this aspect will be discussed in the next session on numerical-experimental comparison.

40.7 Comparison and Discussion

The comparison between experimentally and numerically derived modal frequencies yielded good results, due to a number of reasons, mostly but not only related to the structural configuration.

From the structural design point of view, the basic conceptual design configuration of the structure is based on the optimization of the stiffness ratio of the core vs. that of the columns and on the reduction of differential lateral and vertical displacements of columns and core.

The dynamic behaviour of the structure is thus characterized by the first two modal shapes being almost totally uncoupled inflections along the two main stiffness axes, with no major torsional effects affecting the modal response and significant torsional effects being present only at higher modes.

Also, the very strict quality control procedure carried out on both the materials and the construction methods guaranteed that the mechanical properties assumed in the design and modelling phase would be the same in the 'as built' structure, meaning that the estimate of the structural stiffness made by the software, based on nominal material properties, would be very accurate and that, as a consequence, the estimate of the modal properties would be equally good.

From the numerical point of view, the model that took into account the stiffening effects of the columns on the slab elements gave a better prediction of the modal frequencies, but both of them matched the measured values extremely well. In Table 40.1 and Fig. 40.10, it can be seen that the 'rigid-joints' model, as expected, improves the predicted frequencies, particularly in the weak direction (i.e. the second vibration mode). In both cases, though, the ratio of numerical vs. experimental frequencies is in a range less than 10% for the first five modes (down to less than 5% for the first two modes), which is extremely good, and particularly impressive for a model with this complexity and such a high number of degrees of freedom.

As for the modal shapes, one of which is plotted in Fig. 40.4b, the eigen vectors exhibit full compatibility with the measured accelerations at the floors, in direction, proportion and sign, which confirms a modal response dominated by the cantilever flexural mode along the weak axis (Mode 1, with almost 50% normalized participation factor), followed by a cantilever flexural mode along the strong axis (Mode 2, 42% normalized participation factor) and showing torsional effects only at higher modes (for example Mode 4, involving both X and Y directions with the same normalized participation factor, much lower than the first two) (Tables 40.3 and 40.4, Fig. 40.12).

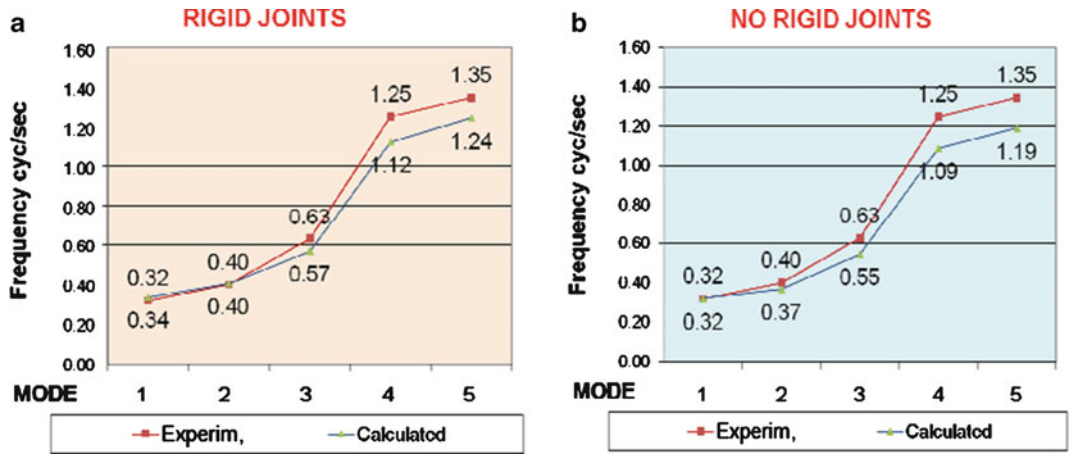

Fig. 40.12 Comparison between numerical and experimental modal frequencies (modes 1–5): (**a**) rigid joints; (**b**) no rigid joints

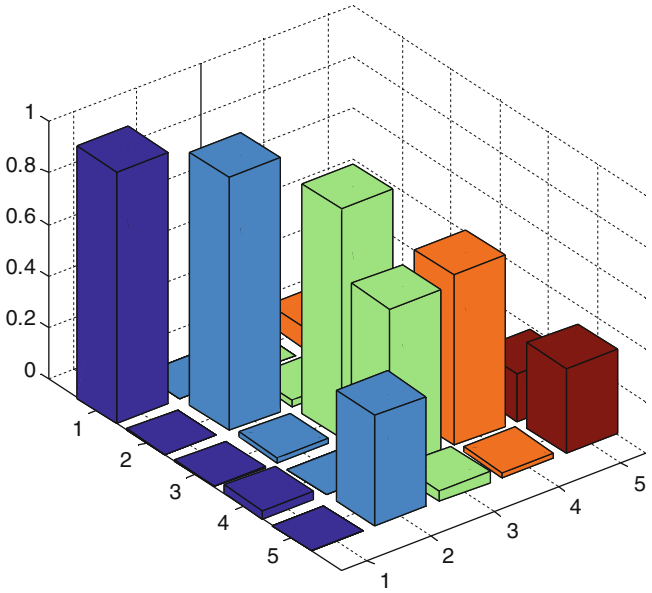

Fig. 40.13 MAC matrix between experimental and numerical mode shapes for the first five modes

Concerning the obtained mode shapes a modal assurance criterion (MAC) analysis has been carried out between the obtained numerical mode shapes and the correspondent experimental ones.

The result of this analysis are given in Fig. 40.13.

As it can be seen in Fig. 40.13 the MAC coefficient is very good for the first three modes, indicating a high correlation degree between the experimental and numerical mode shapes. Concerning mode 4 the degree of correlation is lower and some extra diagonal elements have values different from zero. The lower diagonal value is probably due to the lower vibration levels achieved for this mode, see Fig. 40.11, and the extra diagonal values are due to the reduced number of points used in the measurement mesh for this mode, that may lead to high correlation between different mode shapes. MAC for mode 5 is quite low, but if Fig. 40.11 is looked at, this mode is not clearly defined in the transfer function and this causes a higher uncertainty in the modal residue identification.

40.8 Conclusions

This work described the numerical modelling of the 'Palazzo Lombardia' and the experimental testing carried out to validate the model.

At first a description of the building has been given focussing on the strategic choices carried out during the design phase, and used as a base in developing the numerical model. Then the numerical model has been described and finally the experimental campaign that has been planned and carried out has been presented.

The set of dynamic excitation tests carried out on 'Palazzo Lombardia' proved to be an effective and reliable tool to validate the finite element modeling assumptions and the basic conceptual choices enforced in the design phase.

The structural system exhibited a good response to dynamic excitation, governed by mostly uncoupled flexural deflection vibration modes, associated to low frequencies, making it less sensitive to potential earthquake excitations.

The global numerical analysis model implemented in GT STRUDL proved to be well tuned, as for the basic parameters and assumptions and able to derive the modal properties of the structure with good accuracy. The experimental tests were also an additional method to enforce a final quality control on the materials and the construction method: they highlighted a good correspondence between the 'as-designed' structure and the 'as-built' one.

The numerical analysis model, thus experimentally validated, can now be used as the basis for the planned continuous monitoring activity on the Tower.

Acknowledgements 'Palazzo Lombardia':
Owner: Regione Lombardia
Architectural Design: Pei Cobb Freed and Partners Architects (USA) with Caputo Partnership (ITA) and Sistema Duemila (ITA) – Architectural Project Supervisor: Arch. Henry N. Cobb
Structural Design: Prof. Ing. Franco Mola – ECSD Srl – Engineering Consulting and Structural Design, Milano (ITA)
Construction Supervisor: Infrastrutture Lombarde Spa
General Contractor: Consorzio Torre Spa
Leading Contractor: Impregilo Spa – President and General Manager: Ing. Gaetano Salonia
Site Technical Manager: Ing. Vinicio Scerri
Construction Site General Manager and Safety Supervisor: Ing. Guglielmo Fariello

References

1. ISO 10137
2. EUROCODE EN 1990
3. Mola F (2010) The 'Altra Sede' building for the Regione Lombardia in Milan: conceptual design and technological features of the tallest building in Italy. In: Proceedings of the IABSE Symposium 2010, Venice, 24–27 Sept 2010 (to be published)
4. GT STRUDL structural analysis software, v.30, by Georgia Tech CASE Center, Georgia Institute of Technology, Atlanta, Georgia, http://www.gtstrudl.gatech.edu/, 2009
5. CEB/FIP, Bulletin d'information n.215 (Model Code 90) – structural effects of time dependent behaviour of concrete (1993)
6. Cigada A, Moschioni G, Vanali M, Caprioli A (2010) The measurement network of the san Siro Meazza stadium in Milan: origin and implementation of a new data acquisition strategy for structural health monitoring. Exp Tech 34:70–81
7. Ewins J (2001) Modal testing: Theory, practice and application, 2nd ed., Taylor and Francis Group, London
8. Farrar CR (1997) System identification from ambient vibration measurements on a bridge. J Sound Vib 205(1):1–18
9. Cornwell PJ, Farrar CR, Doebling SW, Sohn H (1999) Environmental variability of modal properties. Exp Tech Nov/Dec:45–48
10. Peeters B, Van der Auweraer H, Guillaume P, Leuridan J (2004) The PolyMAX frequency-domain method: a new standard for modal parameter estimation? Shock Vib 11(3–4):395–409. IOS Press, ISSN 1070-9622 (Print) 1875-9203 (Online)
11. Mohanty P, Rixen DJ (2004) Operational modal analysis in the presence of harmonic excitation. J Sound Vib 270(1–2):93–109

Chapter 41
Impact of Nonstructural Components on Modal Response and Structural Damping

A. Devin and P.J. Fanning

Abstract Damping in a building has significant impact on the amplitude of structural response. The trend towards lighter primary and secondary structural elements in modern buildings has led to structures being more susceptible to vibration. The level of vibration is largely dependent on the structure's total damping, which includes structural and non-structural damping along with other factors. This paper discusses the effect of non-structural elements, on the damping characteristics of a four storey reinforced concrete structure. The dynamic properties of the test structure considered, a new build on the campus of University College Dublin, were determined by post-processing ambient and forced vibration response data measured in-situ on the first floor at various stages of construction, including prior to and post installation of non-structural elements. Post-processing of measured ambient responses was undertaken using a combination of Operational Modal Analysis (OMA) and Frequency Domain Decomposition (FDD) techniques. Three methods to calculate the damping ratio of the structure are discussed, including one in the time domain, Logarithmic Decrement and two in the frequency domain, Half-Power Bandwidth method and Enhanced Frequency Domain Decomposition (EFDD). The level of damping was found to vary as the structure evolved to completion with the highest damping values occurring at completion.

Keywords Nonstructural components • Damping ratio • EFDD • Dynamic response

41.1 Introduction

Damping in buildings has a significant effect on structural dynamic response. With the advancements in construction technology, a trend has emerged toward lighter primary and secondary elements in modern buildings. Such developments in structural engineering have led to structures which can be more susceptible to vibration if mitigation measures have not been incorporated at the design stage. This has been further compounded by a trend toward open-plan floor structures and 'electronic' offices [1] which result in much less live load on the floor reducing the structure's damping capability [2]. The combination of these factors has led to a higher number of troublesome floors. The estimation of damping within a structure at the design stage is a complex exercise particularly due to the fact that there are a number of sources within the structure which contribute to the overall energy dissipation capability [3].

Such sources include:

1. Primary structural elements.
2. Secondary structural elements.
3. Boundary damping due to the dissipation between interfaces or joints in the structure.
4. Furniture, fittings and finishes.

Unlike other structural properties, such as mass and stiffness, damping cannot be directly related to construction materials or structure configuration, therefore a uniform model to estimate structural damping is not possible. Hence codes and guidelines contain recommended values for various types of structures. Recommended values of damping ratio for a concrete

A. Devin (✉) • P.J. Fanning
School of Civil, Structural and Environmental Engineering, University College Dublin, Dublin 4, Ireland
e-mail: austin.devin@ucd.ie

J.M. Caicedo et al. (eds.), *Topics on the Dynamics of Civil Structures, Volume 1*,
Conference Proceedings of the Society for Experimental Mechanics Series 26,
DOI 10.1007/978-1-4614-2413-0_41,

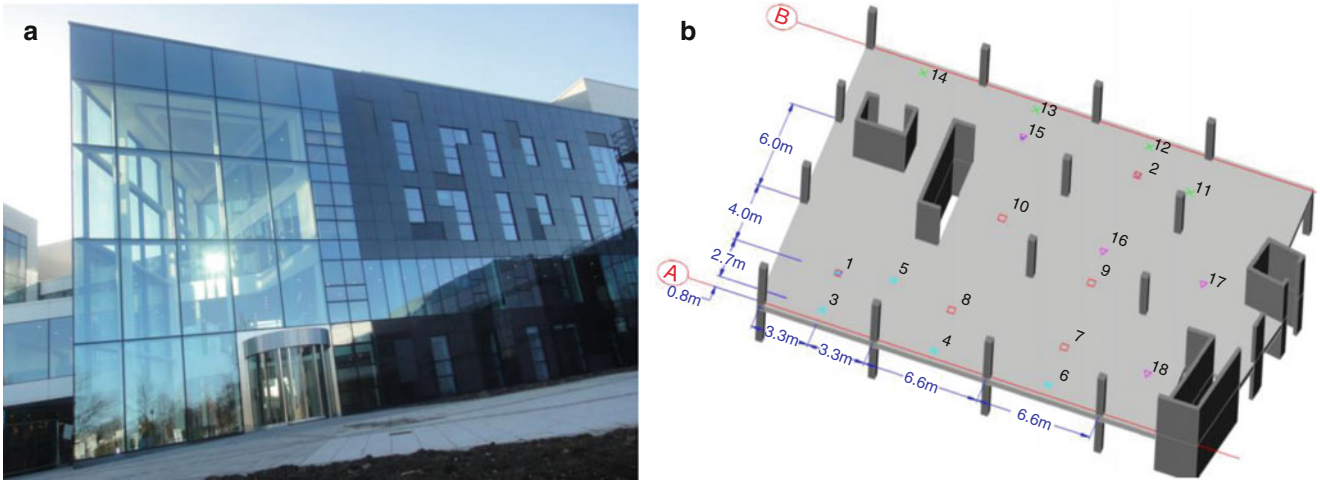

Fig. 41.1 (**a**) The completed Charles Institute. (**b**) Sensor locations: 1–18

structure according to "Design Criterion for Vibrations due to walking" [4] vary from 2–3% for bare concrete to 5–8% for an office with full-height partitions. Others sources [5] recommend a method of adding the damping from various components, such as structural material, furniture and finishes. Such an equation means that concrete can have a minimum damping ratio of 2%, with additional percentages added for the amount of furniture and types of finishes. For example an open plan concrete office building, with full-height partitions and suspended ceilings would have an estimated damping ratio of 4%.

While such methods of estimation may give an approximation of damping ratios that can be expected from finished structures; it is by no way an accurate tool and should only be utilised used as guide. Currently there is no reliable method of accurately predicting the damping ratio of an in-service structure without carrying out full scale experimental testing. Kim et al. [6] evaluated the dynamic properties of a tall residential building and concluded that damping could be significantly underestimated at the design stage and the only way to accurately estimate damping was to consider factors which are generally overlooked such as non-structural elements.

Butterworth et al. [7] carried out full-scale forced vibration testing on a 11-storey reinforced concrete shear-core office building. Both Half-power Bandwidth and Logarithmic Decrement methods were utilised to estimate the damping ratio of the structure. It was found that the equivalent viscous damping ratio varied from 1.5% to 4.6% for the first four natural frequencies of the structure.

Satake et al. [8] used a database of full-scale damping ratio data collected by the Damping Evaluation Committee of the Architectural Institute in Japan to investigate how various parameters affect the damping ratios of structures. These parameters included foundation type, building use and amplitude dependence. It was concluded that hotels and apartments generally have larger damping ratios than other buildings, as they tend to have a higher number of non-structural partitions. It was also concluded that damping ratios are also more widely scattered than natural frequencies of buildings indicating that damping exhibits a higher level of uncertainty compared to other dynamic properties.

This paper will investigate experimentally the contribution of non-structural components specifically to the damping, for a new build structure located on the UCD campus, using three different methods for calculating damping from acceleration time history responses.

41.2 Test Structure: Charles Institute

The Charles Institute on the University College Dublin (UCD) campus in Ireland is a four storey reinforced concrete frame office building shown in Fig. 41.1a. Structurally it consists of two-way spanning flat slabs, 0.3 m thick, supported on 0.4 m square columns positioned on a 7.5 × 6.6 m grid. The lateral load resisting system is made up of a number of reinforced concrete stairwells, lift cores and service ducts with wall thicknesses of 0.2 m. Each floor level is divided into laboratories and office accommodation using light-weight non-structural partitions.

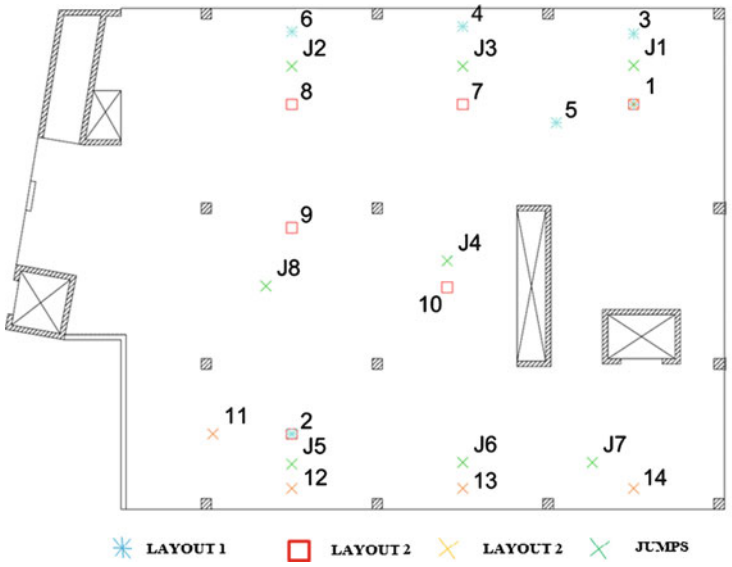

Test	Layout	Jump Location	Sensor(s) excited
2	1	1	1
			3
			5
3	1	2	6
5	2	2	8
6	2	3	7
7	2	8	9
8	2	4	10
10	3	5	2
			12
11	3	6	13
12	3	7	14

Fig. 41.2 Sensor locations for jump excitation of the slab

The selection of sensor locations for the recording of the vertical response of the first floor slab, numbered 1–18 in Fig. 41.1b, was aided by a preliminary FE model so that a broad range of relevant mode shapes could be identified. Test visits, TV1 to TV3, were made at three different stages of construction:

TV1: At the completion of the reinforced concrete frame.
TV2: Once cladding elements were added to two sides of the frame along gridlines A and B as shown in Fig. 41.2.
TV3: At building completion; ready for occupation.

41.3 Experimental Procedure

Ambient and human-induced vibration responses were recorded [9]. The human-induced vibration comprised of a person jumping on the spot for 30 s with a subsequent period of free response to allow the energy of the jump excitation to dissipate. The location of the forced vibration was selected by analysing the mode shapes extracted from the preliminary FE model of the floor slab. Each jump location was positioned to excite a certain mode of the slab. When possible for sufficient excitation of the mode in question, the jump location was placed at the location of maximum displacement for that given mode shape. However for certain jump locations the ideal location was blocked or inaccessible due to non-structural components upon the building's completion; so the nearest possible location was selected. Three sensor layouts and eight jump locations for the jump excitation tests as was used for analysis of the first floor are shown in Fig. 41.2. Six sensors were used for each layout with sensors 1 and 2 as stationary reference sensors.

Each data set recorded was detrended using a linear baseline correction and cosine tapered to avoid data leakage. Next the data was filtered using a low pass filter with an upper bound limit of 40 Hz, to enhance the clarity of the natural frequencies of the concrete slab. This processed acceleration time history data was then used to calculate the damping ratio of the slab for the jump excitation data sets. The data sets were converted to the frequency domain using Frequency Domain Decomposition (FDD) [10].

It was found from the ambient vibration data that the natural frequencies of the slab occur in the range of 9–30 Hz [9]. The natural frequency of the slab increases from TV1 to TV2. This occurs due to the partial completion of the facade along gridlines A and B (Fig. 41.1b). The evolution between TV2 and TV3 is more complex due to both the completion of the building's facade and internal partitions as well as the inclusion of furniture and laboratory fixings. Figure 41.3 below illustrates the singular value plot for the human-induced excitation testing undertaken for test 2 carried out for the three test visits.

Three methods to calculate the damping ratio of the slab were then investigated, these included:

1. Logarithmic Decrement Method
2. Half-power Bandwidth Method
3. Enhanced Frequency Domain Decomposition (EFDD)

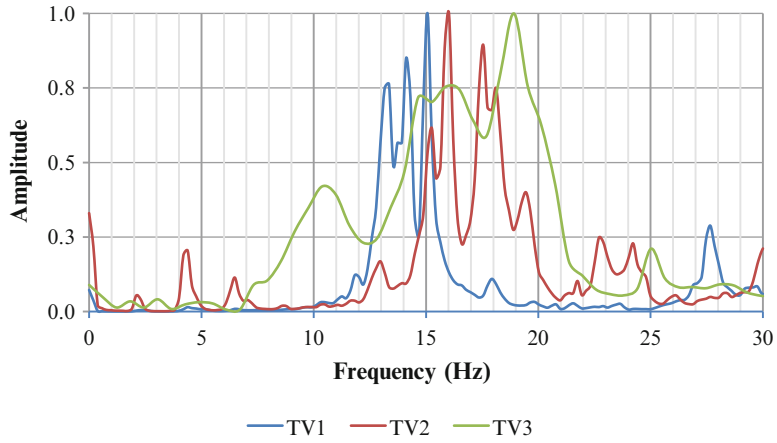

Fig. 41.3 Singular value plot for human-induced excitation during test 2 for TV1, TV2 and TV3

41.4 Calculation of Damping Ratios

41.4.1 Logarithmic Decrement Method

The Logarithmic Decrement (δ) is used to calculate the damping ratio of a structural system in the time domain. Logarithmic Decrement comprises of the natural log of the ratio between the amplitudes of any two closely adjacent peaks of an acceleration time history calculated using (41.1) and the damping ratio is subsequently calculated using (41.2):

$$\delta = \frac{1}{n} \ln \frac{x_0}{x_n} \tag{41.1}$$

$$\zeta = \frac{1}{\sqrt{1 + \left(\frac{2\pi}{\delta}\right)^2}} \tag{41.2}$$

This method was used on the acceleration excitation response from the jump excitation tests. This was carried out for a number of different jump excitations for each test setup. Damping ratios were calculated from time histories recorded on sensors located adjacent to jump locations.

It should be noted that as the Logarithmic Decrement method tends to overestimate damping due to the fact it not only measures energy dissipation but also the transmission of vibrational energy due to other structural components [2]. Furthermore the damping derived in this way should be considered as global rather than modal damping as the time history response would be expected to include contributions from multiple modes.

41.4.2 Half-Power Bandwidth Method

The shape of the peaks of any acceleration response plotted in the frequency domain is governed by the magnitude of damping available within the system; specifically the bandwidth, which is the difference between two frequencies corresponding to the same response amplitude [10]. Therefore by measuring the difference in frequency between either side of a peak for a given frequency, the damping ratio of the system at that given natural frequency can be estimated. For convenience the frequency values are usually calculated at $1/\sqrt{2}$ of the peak amplitude (E_0). The frequency values at $E_0//\sqrt{2}$ are also known as the half-power points. The damping ratio of the system is then calculated using (41.3) as shown. Figure 41.4 highlights how f_1 and f_2 are estimated from the frequency curve.

$$2\zeta = \frac{f_2 - f_1}{f_0} \tag{41.3}$$

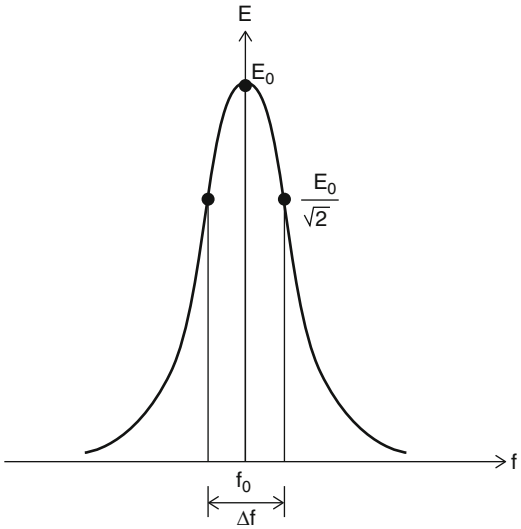

Fig. 41.4 Method to calculate f_1 and f_2 Half-power values for the Half-power Bandwidth method

41.4.3 Enhanced Frequency Domain Decomposition (EFDD)

EFDD is an advancement of the original Frequency Domain Decomposition method, explained in detail by Brincker et al. in [11], so modal damping can be estimated from the Singular Value plots produced from recorded acceleration time history data sets. This is completed by decomposing the power spectral density matrix into a set of individual single degree of freedom auto spectral density functions which are then transformed back to the time domain where curve fitting can be used to estimate the modal damping for any given frequency [12]. Like the Half-power Bandwidth method the damping values determined are modal damping values associated with particular frequencies of vibration.

41.5 Discussion of Results

41.5.1 Logarithmic Decrement Method

Damping ratios calculated using the Logarithmic Decrement method are compared for each jump test in Fig. 41.5. Damping ratios ranged from 2.3% to 5.9% for TV1, 2.5% to 6.1% for TV2 and 3.5% to 9.7% for TV3. This shows a stepped increase for the majority of tests from TV1 to TV3 as non-structural components are added to the structure. This indicates that the inclusion of non-structural components increases energy dissipation within the structure; in turn increasing the damping ratio.

Tests 7 and 8 have the highest damping ratios for the final visit TV3. This is believed to be due to this jump being located in the centre of the slab, hence there was at least one bay either side in each direction. This meant that more of the slab and columns could be utilised to dissipate energy excited in the slab. For a number of tests the damping ratio for TV2 was in fact lower than that of TV1. This decrease could be attributed to the removal of a scaffolding staircase and loading bay from the perimeter of the structure between TV1 and TV2.

41.5.2 Half-Power Bandwidth Method

Damping ratios ranged from 1.1% to 2.9% for TV1, 1.4% to 3.2% in TV2 and 1.2% to 8% for TV3 when calculated using the Half-power Bandwidth method. Similar to the Logarithmic Decrement method damping ratios generally increased from TV1 to TV3. There were some tests however where the damping ratio in TV2 was lower than TV1. As previously surmised this was believed to be due to the removal of the scaffolding towers used as a loading bay and staircase between these test visits.

Table 41.1 summarises the modal damping for each of the natural frequencies excited by the forced vibration during test 2. While the first natural frequency excited increases from 13.4 to 15 Hz between TV1 and TV2. The damping ratio decreases by more than half from 3.3% to 1.5% between these visits. This change in natural frequency can be related to the

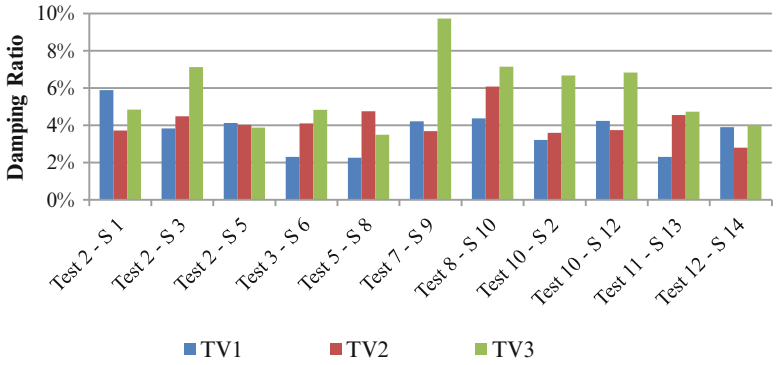

Fig. 41.5 Comparison of damping ratios for each test during the three test visits

Table 41.1 Modal damping ratios calculated for test 2 using the Half-power Bandwidth method

TV1		TV2		TV3	
Nat. frequency (Hz)	Damping ratio (%)	Nat. frequency (Hz)	Damping ratio (%)	Nat. frequency (Hz)	Damping ratio (%)
13.4	3.3	15.3	1.5	10.4	9.6
14.1	2.3	16.0	1.3	16.5	10.2

Table 41.2 Modal damping ratios calculated for test 2 using the EFDD method

TV1		TV2		TV3	
Nat. frequency (Hz)	Damping ratio (%)	Nat. frequency (Hz)	Damping ratio (%)	Nat. frequency (Hz)	Damping ratio (%)
13.4	2.6	15.3	1.3	10.4	5.9
14.1	2.4	16.0	1.5	16.5	4.0

addition of cladding panels on two sides of the structure which stiffened the edges of the slab, thus increasing its natural frequency. While the removal of scaffolding from the structure results in reduced damping. However from TV2 to TV3 the natural frequency decreases to 10.4 Hz and the damping ratio increases to almost 10% of critical damping. It is possible that this significant increase in the damping ratio is due to the addition of furniture and fittings to the building, such as floor coverings, as well as desks and chairs which would increase the dissipation of energy in the structure. The decrease in natural frequency is attributed to the structure being fully kitted out internally, for example Furniture would increase the total structural mass with little increase in stiffness, thereby causing a decrease in natural frequency. For the second mode excited during Test 2 a similar pattern was observed for modal damping between TV1 and TV3.

41.5.3 Enhanced Frequency Domain Decomposition (EFDD)

The damping ratios calculated using EFDD ranged from 1.0% to 2.7% for TV1, 1.1% to 2.4% for TV2 and 2.4% to 4.9% in TV3. As with the previous methods, generally damping ratios increase from TV1 to TV3. Indicating that the addition of non-structural elements has the effect of increasing modal damping.

The natural frequencies and damping ratios extracted from test 2 during TV1 to TV3 are shown in Table 41.2. The damping ratios for test 2 follow a similar pattern to the values calculated using the Half-power Bandwidth method, with the ratio decreasing from TV1 to TV2 and increasing to its maximum value in TV3. These changes in damping ratio were expected due to the evolution of the structure from visit to visit. However it is interesting to note that the damping ratio for TV3 is much lower when calculated using the EFDD method, almost half the value calculated using the Half-power Bandwidth method.

41.5.4 Comparison of Damping Ratios Calculated

Whilst there is some variability between damping values determined using different predictive methods, all methods indicate that the amount of damping increases from TV1 to TV3.

For TV1 damping values varied between 4% and 6% using the Logarithmic Decrement method and 2.3% and 3.3% for the other two techniques. The Logarithmic Decrement method results in a global damping measure derived from multiple modes, that may have been excited, while the Half-power Bandwidth and EFDD methods produce individual modal damping values. The contribution of multiple modes in the Logarithmic Decrement method thus results in a higher value.

Comparing the two modal damping methods results in similar damping values for TV1 and TV2. However the Half-power Bandwidth method almost twice as high as those identified using EFDD. The values of 9.6–10.2% seem high given levels reported in the literature. The Half-power Bandwidth method involves direct estimation of the damping ratio from the singular value plot while EFDD involves the generation of a time domain response from a singular value plot. Hence the Half-power Bandwidth method will suffer more, in terms of accuracy, that the EFDD method from low frequency resolution in the singular value plot.

41.6 Conclusion

Forced vibrations, carried out using human-induced vibrations, were recorded at the newly constructed Charles Institute on the University College Dublin campus at three stages of construction varying from a completed bare structural frame and progressing towards a fully completed building ready for occupation to investigate the impact of non-structural components on the damping of the first floor concrete slab.

The following conclusions are drawn:

- Damping is difficult to measure precisely and repeatability.
- The level of damping inherent to a structure evolves during construction and where accurate measures of damping are required for a particular structure it is recommended that testing be undertaken on completion of structural work and fittings, finishes and furnishing of the building interior.
- Recommendations in the literature of 2–3% damping for a bare frame structure and 4–8% damping for a finished structure appear sensible.

Acknowledgements The authors wish to express their gratitude to the Irish Research Council for Science, Engineering and Technology for their financial support and WALLS Construction for access to the Charles Institute for the purpose of response measurements.

References

1. Reynolds P, Diaz I, Nyawako D (2009) Vibration testing and active control of an office floor. In: 27th international modal analysis conference, Orlando
2. Murray T (2001) Tips for avoiding office building floor vibrations. Modern Steel Construct 41:24–33
3. Kijewski-Correa T (2003) Full-scale measurement and system identification: a time-frequency perspective. Thesis, Notre Dame
4. Allen D, Murray T (1993) Design criterion for vibrations due to walking. Eng J, American Institute of Steel Construction, Fourth Quarter, pp 117–129
5. ArcelorMittal (1995) Design guide for floor vibrations. AccelorMittal, Luxembourg (Nov 2008)
6. Kim J, Kim D, Kim S (2008) Evaluations of the dynamic properties for a residential tall building in Korea. In: CTBUH 8th world congress, Dubai
7. Butterworth J, Lee J, Davidson B (2004) Experimental determination of modal damping from full scale testing. In: 13th world conference on earthquake engineering, Vancouver, Paper No. 310
8. Satake N, Suda K, Arakawa T, Sasaki A, Tamura Y (2003) Damping evaluation using full-scale data of buildings in Japan. J Struct Eng ASCE 129:471–477
9. Devin A, Fanning P (2011) Non-load bearing elements and their contribution to a structure's dynamic response. Experimental Vibration Analysis for Civil Engineering Structures (EVACES 2011), Lake Como, Italy
10. Brincker R, Zhang L, Andersen P (2001) Modal identification of output-only systems using frequency domain decomposition. Smart Mater Struct 10:441–445
11. Paz M, Leigh W (2004) Structural dynamics – theory and computation, 5th edn. Kluwer, Boston
12. Brincker R, Ventura C, Andersen P (2001) Damping estimation by frequency domain decomposition. In: 19th international modal analysis conference (IMAC), Kissimmee, FA, pp 141–146

Chapter 42
Use of Family of Models for Performance Predictions and Decision Making

H. Burak Gokce, F. Necati Catbas, and Dan M. Frangopol

Abstract The issue about performance prediction is the need of a well representative model which can be analytical or mathematical due to non-availability of the future data. Analytical or mathematical models can be identified with the help of current data coming from structural health monitoring (SHM) systems and these models can be used for future performance predictions by incorporating uncertainties coming from modeling and monitoring data. In this study, a well calibrated finite element model (FEM) of a real life structure, which is accepted as the parent model of the family models, is introduced. Based on this model, offspring models, which include the modeling and measurement uncertainties are generated. In the offspring generation process uncertainties such as boundary conditions, loads, geometric and mechanical properties of the elements are defined with distributions. After the generation process, offspring models are analyzed and set of results are obtained for a family of models. These results are used for structural reliability calculations in the performance prediction part of the paper. At this point, the other important considerations such as system model definition and correlation of the components for the system reliability approach are also taken into account. Finally, future performances in the case of instantaneous or continuous structural changes are considered for structural system reliability prediction, which is critical for decision making about future performance of the structure, by incorporating uncertainties from measurement through modeling on the movable bridge.

Keywords FEM • SHM • Movable bridge • Uncertainty • Reliability • Load rating • Prediction • Structural identification

Nomenclature

C(t)	Corrosion penetration rate
A	Statistical random variable
B	Statistical random variable
$\Delta_{increase}$	Expected 75 year maximum traffic load
$\mu_{traffic}$	Mean of the current traffic load
$\sigma_{traffic}$	Standard deviation of the current traffic load
g	Limit state function
ε_{yield}	Yielding strain

H.B. Gokce • F.N. Catbas (✉)
Civil, Environmental and Construction Department, University of Central Florida, Orlando, FL 32816, USA
e-mail: hgokce@mail.ucf.edu; catbas@ucf.edu

D.M. Frangopol
Department of Civil and Environmental Engineering, ATLSS Center, Lehigh University, Bethlehem, PA 18015-4729, USA
e-mail: dan.frangopol@lehigh.edu

J.M. Caicedo et al. (eds.), *Topics on the Dynamics of Civil Structures, Volume 1*,
Conference Proceedings of the Society for Experimental Mechanics Series 26,
DOI 10.1007/978-1-4614-2413-0_42,

$\varepsilon_{offspring\_DeadLoad}$	Dead load strain coming from offspring models
$\varepsilon_{offspring\_TrafficLoad}$	Traffic load strain coming from offspring models
$\varepsilon_{SHM\_TrafficLoad}$	Traffic load strain coming from SHM data
$\varepsilon_{SHM\_TempCycle}$	Temperature induced strain coming from SHM data
RTA	River transit bus
FT	Fire truck
EN	East North
WS	West South

42.1 Introduction

SHM applications to civil infrastructures can provide various measurements and these are used for model updating/calibration studies where the goal is to fine-tune the model parameters such that measured data and predicted values would match. In the literature, SHM data based structural identification can be seen by using the vibration measurements [1–3] as well as by using the static measurements [4–6]. In both groups different error optimization techniques are developed to minimize the difference between the measured and predicted values.

The uncertainty types and sources were closely investigated in recent years [7–9] and it is accepted that the presence of the uncertainties in the measurement and modeling is inevitable but these can be reduced with improved knowledge. In structural identification applications, which involve both measurement and modeling procedures, will directly affected by the uncertainties. Therefore, it is not reasonable to use single FEM. Using a single calibrated FEM that can predict accurately might identify the wrong model.

42.1.1 Objective and Scope

According to the authors, conducting field measurements along with parameter identification and establishing the decision making needs, family of models approach should be investigated carefully for predicting the performance of real life structures such as bridges. The consideration here is the evaluation of the limitations and the adequacy of a calibrated model before leveraging it for decision-making such as load rating and reliability of the structural system for the remainder of its service life. The uncertainty in the data collected by means of intermittent testing or monitoring, limitations of the models, non-stationary nature of behavior need to be considered and those can be represented by a family of models as described as parent and off-spring models that incorporate uncertainties.

This study proposes an SHM data based family of models integrative approach to predict the system reliability of a movable bridge more accurately for decision making. For the system reliability approach, the movable bridge is modeled with different system configurations and the analyses are conducted based on SHM data, which provides the extreme traffic stresses, temperature cycles and correlation of the random variables, and based on family of model simulations in which a traffic flow is generated with different vehicles. To cover the movable bridge issues, time dependent deterioration models that include corrosion of the girders, along with a live load increase model over time is investigated on behalf of future predictions by considering uncertainty on the movable bridge. The methodology of the paper is summarized in Fig. 42.1.

42.2 Sunrise Boulevard Bridge (SBB)

Sunrise Boulevard Bridge (SBB), which was constructed in 1989 in Ft. Lauderdale, FL, has double leaf bascule leaves with a total span length of 35.7 m and a width of 16.3 m, carrying three traffic lanes (Fig. 42.2). The bridge can be opened every 30 min when requested. Depending on the boat traffic, the bridge opens usually about 10–15 times a day. The selected representative movable span is the west-bound span of two parallel spans on Sunrise Boulevard.

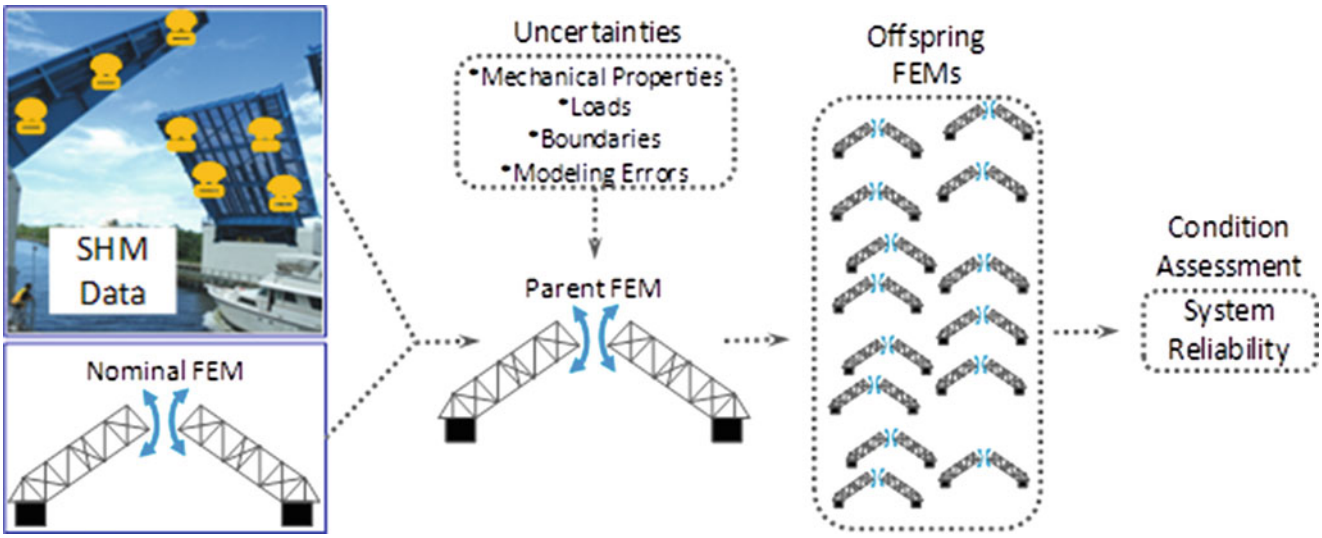

Fig. 42.1 Methodology of the paper

Fig. 42.2 Sunrise Boulevard Bridge (SBB)

42.2.1 Monitoring System

Monitoring system of SBB consists of 160 sensors which are distributed on structural, mechanical and electrical components of the movable bridge. The instrumentation plan is designed based on historical analysis of inspection reports, condition states, critical components and failure modes. Instrumentation includes strain gages distributed along the main girders, approximately at each one-third of the span length. Strain gages will reveal the performance of the girder, which is often subject to heavy truck traffic. Strain data are monitored continuously to detect both the level and distribution of stress on the girder, as well as any changes in the performance due to overloading or time-dependent deterioration effects like corrosion. More details about the monitoring system can be found in [10].

Fig. 42.3 Parent FEM of SBB and location nomenclatures

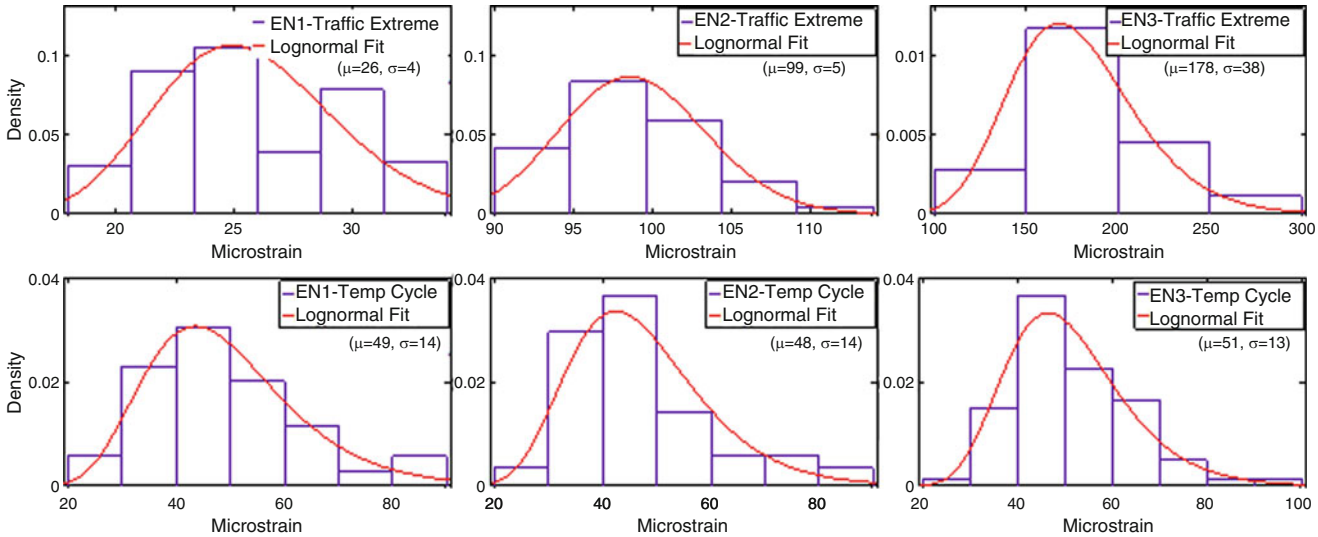

Fig. 42.4 Typical traffic and temperature induced strain histograms coming from SHM data

42.2.2 Parent Finite Element Model (FEM)

Construction plans and details of the SBB were closely studied to ensure a proper modeling of the superstructure. There are a few main components of the bridge superstructure that are critical to accurately model the local behavior of the deck and secondary beams as well as the global behavior. The first main component of the bridge was the main girders where boundary conditions were imposed at the trunnion and live load shoe locations. The second main component of the system to be created was the floor beams, sidewalk brackets, and diagonal bracing which were composed of frame elements. These elements were connected to main girders and each other with rigid links at the centroids. Once all secondary beams were created, the deck of the bridge was constructed. The deck was modeled using four-node quadrilateral shell elements and connected to the main girders and secondary beams using rigid links. Finally, solid elements were created to model the concrete counterweight. More details about calibrated parent FEM (Fig. 42.3) can be found in [11].

It should be noted that this study focuses on the 3 months monitored data from the bottom flanges of main girders' high and low speed strain gages. The nomenclature for strain gages are given in Fig. 42.3 whereas the corresponding 3 month traffic strain and temperature cycle histograms coming from the real data are given in Fig. 42.4. In this figure, extreme traffic strain histograms for East-North (EN) whereas temperature induced strain cycle histograms for West-North (WN) and fitted lognormal distributions are shown.

42.2.3 Uncertainties

The two types of uncertainty are the aleatory uncertainty, which is associated with the randomness, and the epistemic uncertainty, which is associated with imperfect knowledge due to lack of data or crude models [7]. The main difference

Table 42.1 Statistical parameters

	Uncertainty (%)	Distribution
Moment of inertia (I)	18	Normal
Modulus of elasticity (E)	10	Lognormal
Dead load (D)	10	Normal
Live load (P)	18	Normal
Spring constant (k)	10	Normal
Yield stress (Fy)	10	Lognormal
DAQ and sensor (η)	2	Uniform

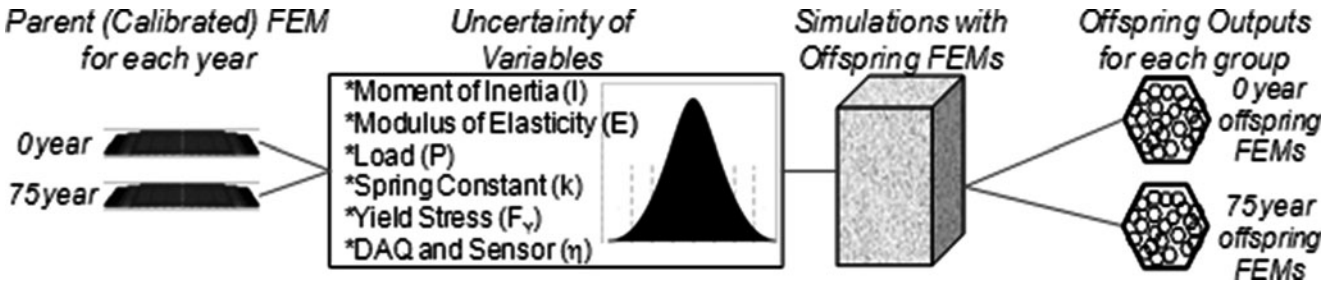

Fig. 42.5 Incorporating uncertainty of variables into the parents to generate offspring FEMs

between these two types is the epistemic uncertainty can be identified by incorporating these uncertainties into models and with this incorporation use of family of models become more critical.

In this study, sources of uncertainties (Table 42.1) are classified into three different groups: (1) Modeling uncertainties: boundary conditions, material properties, section properties, loads, deterioration and damage (2) Measurement uncertainties: data acquisition accuracy, sensor resolution and field test design (3) Data post-processing uncertainties: failure modes, correlation and assumed distributions. Offspring FEMs, which will be described in the next section, are generated by incorporating these uncertainties into parent FEMs

42.2.4 Offspring FEMs

A total of 10,000 offspring FEMs are to be created for each parent FEM. In each group of offspring FEMs, variables such as mechanical properties, loads, and boundary conditions are manipulated based on the uncertainty distributions given in Table 42.1 to create numbers of offsprings from each parent FEM. This manipulation is accomplished by a created visual basic (VBA) code that randomly changes the variables with the defined distributions in the text files of the parent FEMs. Moreover, the analysis of the offspring FEMs are completed with a created batch file that automatically opens and analyzes the model then saves the outputs in a defined format under defined loads for interested locations. Offspring FEM generation process is summarized in Fig. 42.5.

42.2.5 Deterioration and Traffic Increase

As mentioned earlier, movable bridges undergo certain deterioration effects due to normal aging and overloads. For maintenance operations and bridge safety, it is crucial to estimate the future condition of bridges. Corrosion penetration and associated section loss can be considered as the main factor in capacity degradation over the lifetime of the bridge. Section loss due to corrosion is a major cause of deterioration for steel profiles, especially at locations closer to salt water and

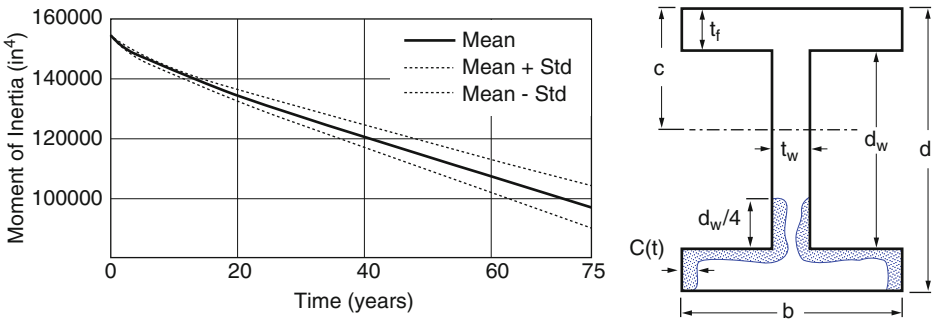

Fig. 42.6 Corrosion penetration model, moment of inertia and section modulus change over time for WS3 section

with high humidity. The following corrosion penetration model is used in the family of model application to define the degradation effect over time:

$$C(t) = A \times t^{B} \tag{42.1}$$

where *C(t)* is the corrosion penetration depth in 10^{-6} m, t is time in years, and *A* and *B* are statistical random variables given by [12]. The corrosion penetration is assumed to be following the pattern shown in Fig. 42.6. According to this pattern, due to pooling, the corrosion progresses along the top surface of the bottom flange and ¼ of the depth of the web. Based on the corrosion penetration function and the corrosion pattern, loss of section can be calculated. Mean value and standard deviation for the moment of inertia and section modulus are evaluated with respect to time for all girder members of the parent FEM and in Fig. 42.6, these changes are shown for WS3 section. Finally, the long-term deterioration effects due to corrosion are modeled as statistical variables. The parent FEM discussed above is selected to represent the current condition (0 year) of the SBB. By considering the time dependent corrosion models, another parent FEMs is created to represent the condition of SBB for 75 years.

For the future model (75 years), a traffic load increase over time is also considered based on the following equation given by [13]:

$$\Delta_{increase} = \mu_{traffic} + 5.33 \times \sigma_{traffic} \tag{42.2}$$

where "$\Delta_{increase}$" is the expected 75 year maximum traffic load, "$\mu_{traffic}$" and "$\sigma_{traffic}$" are the mean and the standard deviation of the current traffic load based on the 3 months daily maximum data, respectively.

42.2.6 Traffic Loads on FEMs

The parent FEM of SBB is loaded with a total of 14 vehicles which consist of the River Transit Buses (RTAs) and Fire Trucks (FTs) in the right and left lanes for the system reliability evaluation (Fig. 42.7). The idea behind the loading numbers of heavy vehicles is to create traffic flows from the offspring FEMs. With the help of programming, the traffic flow is generated from the offspring outputs.

As mentioned earlier, 14 different heavy vehicles (RTA and FT) are loaded in each offspring model and a traffic flow is generated for each family of model with an artificially intelligent random selection process based on the following probabilistic assumptions: (1) In 60% of the situations, only one vehicle will be on one lane. For example, there are 14 pre-defined spots, which cover almost all of the locations in right and left lane, and randomly one of the vehicles (RTA or FT) will be on one of these spots. (2) In 30% of the situations, which yields 3,000 out of 10,000 simulations, two vehicles will be on two different lanes. (3) In 10% of the situations two vehicles will be on the same lane. The distributions are obtained to calculate the system reliability, and can be seen for WN and ES main girder locations for Year 0 in Fig. 42.8. For all of the locations, it is seen that the best distribution fit is chosen as Generalized Extreme Value (GEV) distribution which are used in the system reliability calculations.

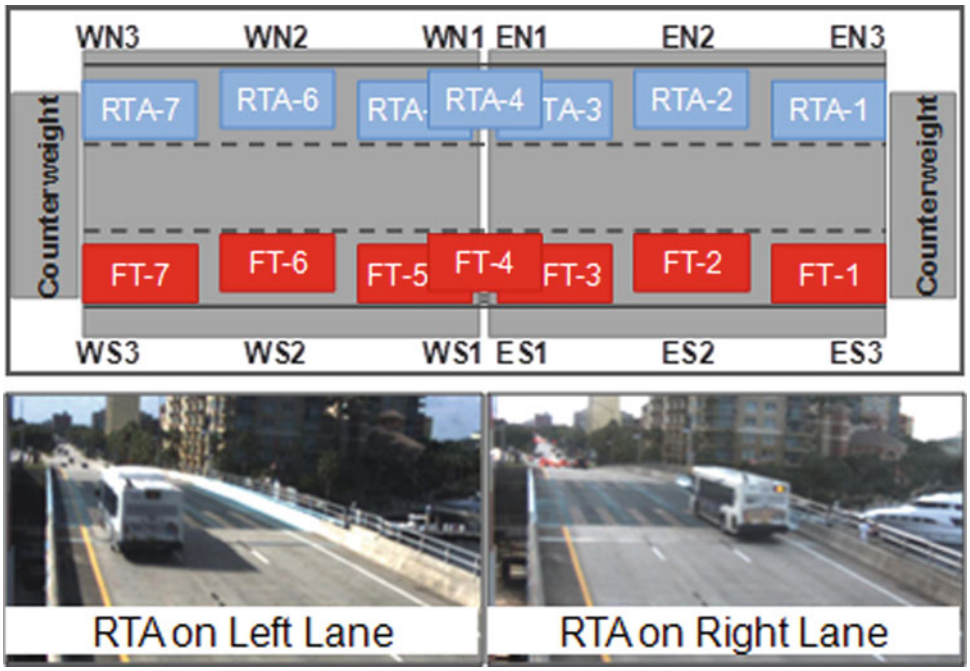

Fig. 42.7 FEM loading locations for identified heavy vehicles (RTA and FT)

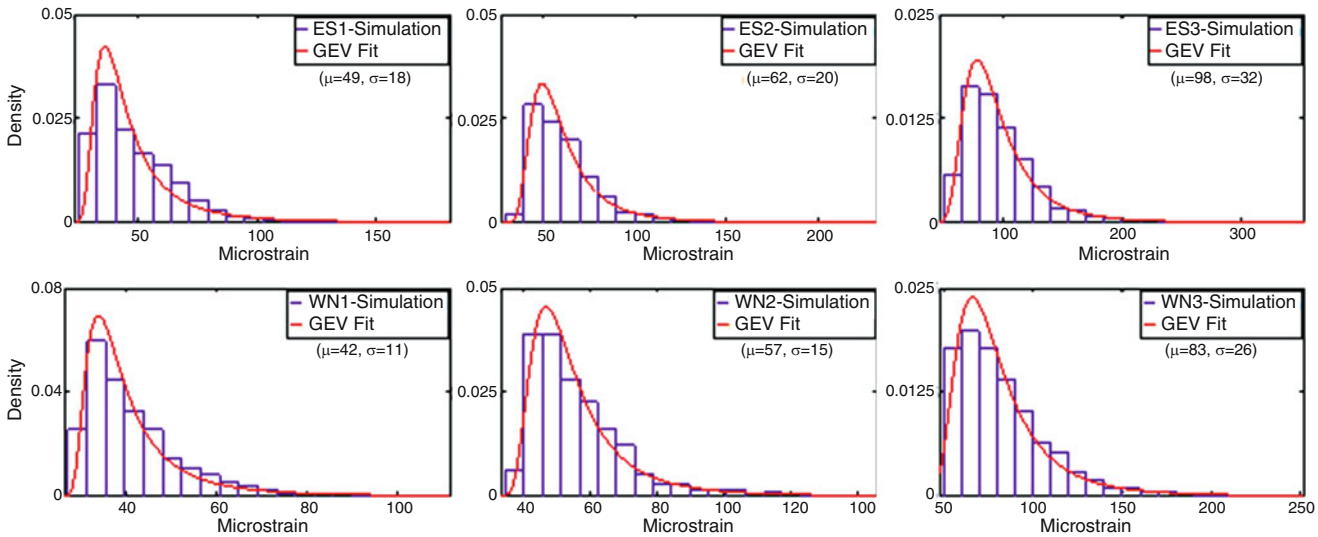

Fig. 42.8 Representative offspring output histograms coming from the generated traffic flow for WN and ES main girder locations for Year 0

42.3 System Reliability

The bridge performance metric demonstrated in this study is the reliability index that can be defined as probabilistic modeling of capacities and demands under a given limit state. Prior to applying the system reliability approach, the limit state functions for the components are defined; the correlation between responses of different components and the system models are generated. In this study, SBB is analyzed with respect to yield strain of 12 different failure modes. SBB component reliabilities are obtained mostly from SHM data by using the following limit state function:

$$g = (0.9 \times \varepsilon_{yield}) - \varepsilon_{Offsprings\_DeadLoad} - \varepsilon_{Offsprings\_TrafficLoad} - \varepsilon_{SHM\_TrafficLoad} - \varepsilon_{SHM\_TempCycle} \quad (42.3)$$

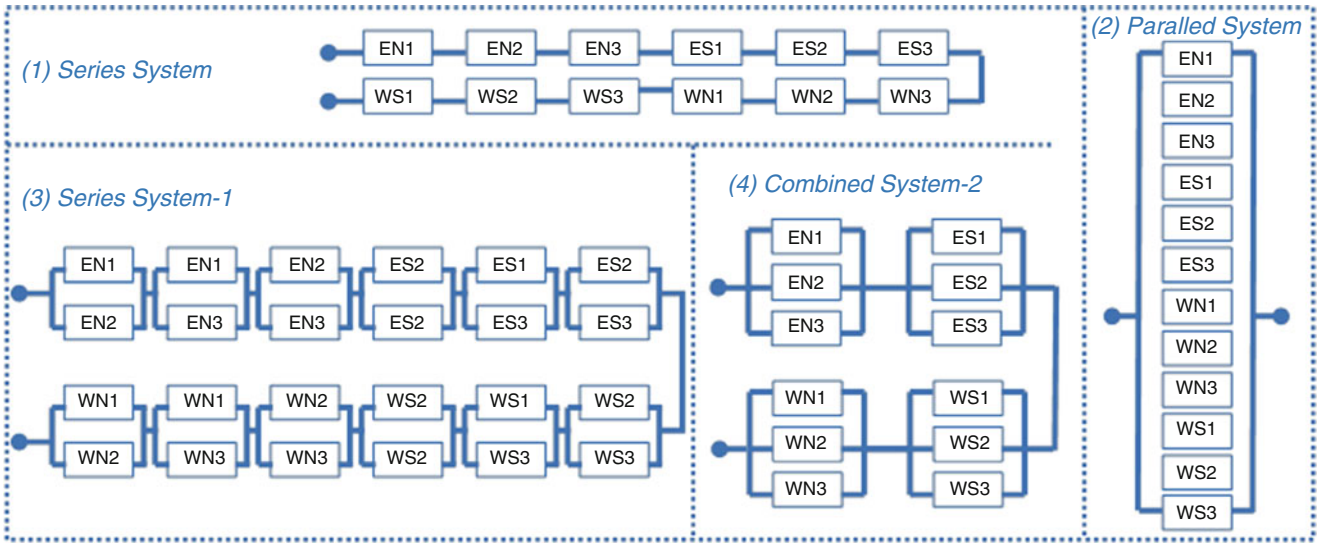

Fig. 42.9 Series, parallel and combined system models for SBB

Table 42.2 System reliability indices for series, parallel and combined system models for different correlation values

Time	System type	Corr = 0	Corr = 0.5	Corr = 1
0	Series	4.5	4.5	4.6
	Parallel	10.0	10.0	10.0
	Combined-1	9.1	7.8	7.6
	Combined-2	10.0	9.9	8.9
75 years	Series	1.0	1.1	1.3
	Parallel	10.0	10.0	8.8
	Combined-1	5.3	4.8	4.7
	Combined-2	9.2	7.3	6.8

The given limit state function consists of the capacity and demands. For the strain capacity, a multiplier 0.9 is assumed for the given limit state to be within linear range. On the other hand, demand has different components such as dead load and traffic load obtained from off-spring FEMs, SHM based extreme traffic strains and SHM based temperature induced strain cycles. For the sake of brevity, component reliability results are not presented in this paper. Based on the component reliabilities system reliability indexes are obtained by considering different system models and different correlations of components. More details about calculation of system reliability index can be found in [14].

The probability of failure of any system depends also on the correlation among the safety margins of the components. The two extreme cases are: (a) perfectly correlated safety margins, and (b) independent safety margins. Detailed investigation of individual correlation will be reported in future studies. For the sake of better illustration the upper and lower bounds of the reliability, correlation factors of 0, 0.5 and 1.0 are used for the evaluation of different systems.

Four different system models (Fig. 42.9) are generated to cover possible failure modes of the SBB as follows: (1) Series system: Failure of any component will fail the system, (2) Parallel system: Failure of all components will fail the system, (3) Combined System 1: Failure of any two main girder components will fail the system and (4) Combined System 2: Failure of all components any main girder will fail the system.

The reliability analysis of the bridge was conducted by using the reliability software RELSYS [15]. RELSYS can compute reliability of generic series/parallel systems other than single components. In order to compute system reliability, RELSYS needs to reduce the systems to one equivalent component by solving the parallel components first and then the series components. System reliability results for deterioration over time are summarized for different system models in Table 42.2.

For a series system, the system safety is maximum when components are perfectly correlated and minimum when they are independent. For a parallel system, the system safety is maximum when components are independent and minimum when they are perfectly correlated. As a result, the upper reliability bound is the parallel configuration of the system with zero correlation variables and the lower bound is the series configuration with zero correlation. In these system reliability

calculations, failure modes with very high reliabilities (e.g., $\beta > 10.0$) are taken as 10. The bridge system reliability bounds for current year ($t = 0$) are found between 4.5 and 10.0 and for 75 years are found between 1.0 and 10. These results show that the system configuration of the structure and the correlation structure are important factors for system reliability calculations. In this particular case, the worst case scenario of zero correlation of random variables for a series system is illustrated as the lower system reliability bound.

42.4 Summary and Conclusions

In this paper, a structural identification implementation by means of a family of calibrated models for system reliability prediction with the consideration of uncertainties is presented. The model family incorporates the parent and the off-springs. The main points and conclusions from this study are: (1) A single FEM that is calibrated using a set of data may reproduce that data set accurately within acceptable numerical limits, however, another prediction might not be accurate as a result of uncertainties in data, model and non-stationarity, non-linearity of real-life structures. (2) As a demonstration, a real life movable bridge performance is evaluated for a 75-year period with the inclusion of deterioration (corrosion of steel members). (3) The system reliability of the bridge is considered by using five different system models. Perfectly correlated safety margins (correlation is one), partial correlation (correlation is 0.5), and independent safety margins (correlation is zero) are considered and the reliability of the system is predicted within bounds over a period of time. A careful selection of the system model and the use of monitoring based correlation among the safety margins of different components can be used for performance predictions as well.

Acknowledgements The research project described in this paper is supported by the Florida Department of Transportation (FDOT) Contract # BD548/RPWO 23 and Federal Highway Administration (FHWA) Cooperative Agreement Award DTFH61-07-H-00040. The authors would like to thank Mr. Marcus Ansley, P.E., the Head of Structures Research at FDOT for his support and guidance throughout the project. The writers also greatly appreciate the valuable feedback provided by Mr. Alberto Sardinas at FDOT District 4, who has shared his experience. The authors would like to express their profound gratitude to Dr. Hamid Ghasemi of FHWA for his support of this research. The support of both agencies and their engineers is greatly recognized and appreciated. The authors would also like to acknowledge the following for their contributions of several other colleagues and students. The opinions, findings, and conclusions expressed in this publication are those of the authors and do not necessarily reflect the views of the sponsoring organizations.

References

1. Sohn H et al (2001) Structural health monitoring using statistical pattern recognition techniques. J Dynam Syst Meas Control ASME 123:706–711
2. Brownjohn JMW et al (2003) Assessment of highway bridge upgrading by dynamic testing and finite-element model updating. J Bridg Eng ASCE 8(3):162–172
3. Gul M, Catbas FN (2008) Ambient vibration data analysis for structural identification and global condition assessment. J Eng Mech 134 (8):650–662
4. Reich GW, Park KC (2001) A theory for strain-based structural system identification. J Appl Mech 68(4):521–527
5. Sanayei M et al (2006) Damage localization and finite-element model updating using multiresponse NDT data. J Bridg Eng 11(6):688–698
6. Bell ES et al (2007) Multiresponse parameter estimation for finite-element model updating using nondestructive test data. J Struct Eng 133 (8):1067–1079
7. Ang AHS, De Leon D (2005) Modeling and analysis of uncertainties for risk-Informed decisions in infrastructures engineering. Struct Infrastruct Eng 1(1):19–31
8. Moon FL, Aktan AE (2006) Impacts of epistemic uncertainty on structural identification of constructed systems. Shock Vib Dig 38(5):399–420
9. Catbas FN, Susoy M, Frangopol DM (2008) Structural health monitoring and reliability estimation: long span truss bridge application with environmental monitoring data. Eng Struct 30(9):2347–2359
10. Catbas FN, et al (2010) Long term bridge maintenance monitoring demonstration on a movable bridge. A framework for structural health monitoring of movable bridges, Florida Department of Transportation (FDOT)
11. Catbas FN, et al (2011) Movable bridges: condition, modeling and damage simulations. In: Proceedings of the ICE – bridge engineering (accepted)
12. Albrecht P, Naeemi AH (1984) Performance of weathering steel in bridges. Transportation Research Board, Washington, DC
13. Nowak AS (1999) Calibration of LRFD bridge design code. NCHRP Report 368: Washington, DC
14. Ang AH-S, Tang WH (1984) Probability concepts in engineering planning and design, IIth edn. Wiley, New York
15. Estes AC, Frangopol DM (1998) RELSYS: a computer program for structural system reliability analysis. J Struct Eng Mech 6(8):901–919

Chapter 43
Vibration Characteristics of Foundation and Free-Field Motions of Instrumented Buildings During Earthquakes

Bishnu H. Pandey, Carlos E. Ventura, and W.D. Liam Finn

Abstract Soil-foundation-structure interaction during earthquakes is characterized by several important aspects, including the variation between the free-field and foundation-level ground motions. This variation is primarily attributed to the kinematic interaction between soil and stiff foundation slabs and embedment effects. This paper presents the results of a study of 22 instrumented buildings in California, which have records from both at the foundation level and at a nearby free-field site. A total of 215 earthquake records of sensor located in the free-field site, basement-slab and ground floor have been analyzed and compared. Comparison of dynamic characteristics of free-field site and foundation motions in those buildings provide confirmation of reduced foundation motion by interaction of foundation and soil. It is consistently observed that the effect is pronounced in the high frequency ranges. A comparative analysis of power spectral density functions of corresponding records and associated coherence, phase shift and transfer function between them is also presented and discussed. These observations are contrasted with state-of-practice analytical models suggested by other researchers.

Keywords Soil-structure-interaction • Base slab averaging • Instrumented buildings • Slab foundation • Wave passage

43.1 Introduction

The characteristics of the recorded motions from a single earthquake at free-field and foundation are observed to be different. This deviation is attributed to soil-foundation-structure interaction (SFSI) effects during earthquake shaking. The SFSI effects can be broadly categorized into two types (1) inertial effect and (2) kinematic effect. The inertial interaction effect is due to mass inertia of the structure and foundation system to the shaking may give rise to lateral displacement and rocking of foundation. This effect is concentrated in a narrow frequency range around first-mode frequency for translational motions [1]. Inertial effects at higher-modal frequencies are generally found small. The direct effects of the inertial interaction is period shifting of the structural system and increase in foundation damping. The kinematic interaction effect refers to averaging effect of massless rigid body rested upon or in site subjected to seismic wave field. Due to this kinematic interaction, the translation motion of wave is attenuated in high frequency range and rotational motions are introduced. This study is focused in investigating the variation of motions between free-fields and shallow foundations primarily by taking the account of parameters that are associated with kinematic effects.

The kinematic interaction that causes deviation of foundation motion from free-field arises from base slab averaging and embedment effects. The variable motions in a large area of incident wave field under the base slab of foundation get averaged when wave hit the rigid slab. The resulting motion will be less than the localized maxima that would have occurred in the free-field. Hence, the higher the incoherence of the wave motion, the larger will be the kinematic effect as averaging effect will be higher in such cases. Similar effect occurs for inclined waves. The averaging effect from incoherent or inclined waves will be higher with the larger size of the foundation. The kinematic effect is observed to be significant in the higher range of frequency of the motion because in high frequency motion, relative size of the foundation in comparison with wave length will be higher and the effect is pronounced. The reduction of motion due to embedment effect is simply attributed to lower ground motion observed as depth increases.

B.H. Pandey (✉) • C.E. Ventura • W.D.L. Finn
University of British Columbia, 6250 Applied Science Lane, Vancouver, BC V6T 1Z4, Canada
e-mail: bishnu@interchange.ubc.ca

J.M. Caicedo et al. (eds.), *Topics on the Dynamics of Civil Structures, Volume 1*,
Conference Proceedings of the Society for Experimental Mechanics Series 26,
DOI 10.1007/978-1-4614-2413-0_43,

In conventional seismic design practice, it is assumed that base of the structure experiences the free-field ground motion. The structure is assumed to be fixed at the base and the analysis is carried out considering only target structure subjected to free-field input motion at the base with no regards of supporting soil. Until recently, most of codes were silent on the issue and some addressed the issue of SFSI but mostly limited to inertial effects that result into change in fundamental period and damping of the system. The ATC-40[2] and FEMA-356[3] addressed the flexible foundation effects; Eurocode-8 [4] recognizes the kinematic effects but restricted to pile foundation. Recently, FEMA- 440 [5] gives guidelines on including SSI effects in nonlinear inelastic analysis. The basis of treatment of kinematic effect in FEMA-440 is based on work by Kim and Stewart [1] who calibrated the model proposed by Veletsos et al. [6] on the basis of recordings of instrumented buildings. The simplified model accounts the spatial variation of the incident waves and gives reduced seismic demand at the base based on averaging the wave effect over the foundation area. While reduction in the motion is observed at the base in several buildings, there are observations in other buildings where foundation motions are amplified considerably increasing the seismic demand [7].

We studied 22 CSMIP instrumented building which have records both in foundation and nearby free-field site. In this study, we focused on the kinematic interaction between soil and stiff foundation slabs as this is regarded as the contributing phenomena of motion variation between free-field and foundation. Some observations are contrasted with state-of-practice analytical models suggested by other researchers.

43.2 Recorded Motions at Instrumented Buildings

43.2.1 Processing of Records

For this study, earthquake records were collected from sites of instrumented buildings in California using earthquake data base of CSMIP, PEER, USGS and COSMOS. The instrumented building sites should have records at the foundations and nearby free-fields at a distance of less than 500 m. Table 43.1 provides list of buildings selected and details of the record including peak acceleration at each component. If there is more than one sensor available at foundation level, the sensor which corresponds with sensor at free-field most closely is chosen for comparison of of the vibration characteristics.

Free-field records were checked and corrected for compatibility in direction with corresponding records at foundation if reference axis is different than that of building. Each motion selected for the study is then processed in Seismosignal for filtering and baseline correction. Frequency filtering was carried out in most of the records, which are found uncorrected. A Butterworth fourth order infinite-impulse-response (IIR) filter was used for band pass filtering with frequency range of 0.1–25 Hz to pass. In a few cases, Chebsev filter with higher order filter gain configuration was also used to get expected trend in time history, particularly in displacement history.

43.2.2 Spectral Analysis

Spectral acceleration, spectral velocity and spectral displacement of records at free-field and foundation base were developed for 5% damping and comparisons were made for a period of 0–4 s. Power Spectral Density (PSD), which shows the strength of signal in frequency domain, was developed for records at free-field and foundation of each targeted buildings. In order to develop PSD, the acceleration time history records are further modified with zero padding at the end to make the length of record equals to a number in the power of 2 higher than 1.5 times of original length of record. The PSDs were estimated by Welch's averaged modified accelerogram method with Hamming window with section of one-fourth length of accelerogram used with 2% overlap. The outcome of PSD is smoothened by moving average with span of three points.

The records at free-field and foundation from the same earthquake events were checked for their coherence by means of magnitude squared coherence given by

$$\gamma_{xy}^2 = \frac{\left|(S_{xy})\right|^2}{(S_{xx}S_{yy})} \tag{43.1}$$

where S_{xy} is cross spectrum of two records measured and S_{xx} and S_{yy} are their PSD functions.

Table 43.1 Instrumented buildings selected for the study

No.	Building	Earthquake (epicentral distance in Km)	Free-field peak ground acceleration (gal)			Foundation level peak acceleration (gal)			Free-field distance from bldg. (m)
			EW	NS	Vert.	EW	NS	Vert.	
1	Rancho Cucamonga 4 st. Justice Cntr.	LD (106.0)	65.47	107.4	41.8	67.34	98.9	47.14	100.0
		NR(90.0)	38.33	63.16	31.1	37.4	36.26	25.7	
		PS(90.1)	15.7	7.86	–	12.7	13.36	–	
		UL(12.1)	214.18	248.24	4.13	104.56	119.48	4.03	
		WT(47.0)	34.47	36.79	25.67	25.44	20.48	19.32	
2	Pomona – 2-st. Commercial Bldg.	UL(9.9)	187.05	168.54	83.64	116.63	24.08	76.08	87.0
		WT(30.0)	42.96	52.17	–	42.02	47.81	–	
3	Los Angeles – 7-st. Univ. Hospital	LD(163.0)	40.05	48.89	–	24.72	38.88	–	104.0
		NR(36.0)	222.36	477.91	15.45	160.04	379.03	82.35	
4	Santa Cruz 5- st. Govt office Bldg.	GL(37.5)	27.44	33.48	21.17	14.6	21.12	7.84	105.0
5	Richmond – 3-story Govt Office Bldg.	LP(108.0)	132.42	109.36	32.97	97.63	128.56	31.62	200.0
6	Los Angeles – 14-st. Hollywood Storage	NR(23.0)	234.11	352.88	103.99	191.47	277.33	82.46	
		WT(25.0)	–	200.29	–	–	114.4	–	
7	Los Angeles – 15-st. Govt Office Bldg	LD(168.0)	30.85	30.63	16.75	30.69	29.28	14.08	
		NR(32.0)	127.47	197.41	96.2	129.34	198.19	65.6	
8	Seal beach 8 story Office Bldg.	LD(160.0)	43.93	40.82	17.11	45.59	37.33	14.48	139.0
		NR(66.0)	77.61	65.82	33.46	79.02	55.56	22.2	
9	El Centro- 6-st Imperial Co. Services bldg.	IP (28.4)	38.62	234.50	233.88	342.06	294.79	150.16	105.0
10	Newport Beach – 11-st. Hospital	NR(86.0)	101.59	82.7	19.98	75.43	52.11	30.69	105.0
11	Long Beach – 7-st. Office Bldg.	NR(36.0)	65.02	55.01	23.39	65.58	44.44	18.05	60.0
12	San Bernardino – 9-st. Commercial Bldg.	LD(80.0)	90.78	83.86	57.77	76.95	80.58	38.36	400.0
13	San Bernardino – 3-st. 0ffice Bldg .	LD(80.0)	76.29	85.26	52.39	127.49	79.93	56.07	300.0
14	Los Angeles – 7-st. UCLA MathSc. Bldg .	NR(18.0)	47.77	431.96	269.42	226.84	280.05	198.5	
15	Sylmar – 6-st. County Hospital	NR(16.0)	581.61	804.86	449.16	701.22	444.34	338.17	140.0
		WT(45.0)	51.54	55.5	38.077	54.38	52.29	46.57	
16	Lancaster – 3-st. Office Bldg	WT(70.0)	59.22	61.42	23.80	62.20	50.37	15.59	75.0
17	Los Angeles – 2-story Fire Command Cntr.	LD(161.0)	52.17	55.28	29.42	50.97	52.02	20.82	30.0
		NR(38.0)	257.98	331.27	131.94	209.94	166.78	109.85	
		SM(28.0)	113.4	96.59	54.76	74.08	75.97	44.38	
18	Park field – 1-st. School Bldg.	PF7(4.7)	16.27	13.98	–	11.54	14.03	–	250.0
19	Templeton 1-st Hospital	PF5(46.7)	10.35	18.57	3.95	9.66	10.75	4.05	60.0
20	King City – 2-st. Hospital	PF4(80.9)	47.44	39.44	47.55	28.45	30.72	30.09	280.0
21	Hollister – 1-story Warehouse	LP(48.0)	179.2	370.89	190.19	226.89	368.81	161.52	120.0
22	San Jose – 3-story Office Bldg	AR(24.5)	35.24	46.04	26.17	17.53	24.93	12.93	155.0
		LP(21.0)	–	286.65	209.61	–	154.92	115.76	

LD Lander earthquake (1992), *NR* Northridge earthquake (1994), *PS* Palmspring earthquake (1986), *UL* Upland earthquake (1990), *WT* Whittier earthquake (1987), *GL* Gillory earthquake (2002), *IP* Imperial Valley earthquake (1989), *LP* LomaPrieta earthquake (1989), *PF7* Parkfield earthquake (2007), *AR* Alumrock earthquake (2007), *PF4* Parkfield earthquake (2004), *PF5* Parkfield earthquake (2005), *SM* Sierramadre earthquake (1991)

The higher the value of coherence, with maximum of 1, at given frequency indicates that the two records are highly correlated at that frequency. The length of window, overlaps, moving average section and length of FFT points are similar to that used for estimating PSD functions.

The change in signal (acceleration) between free-field and foundation is represented by transfer function between two records. The transfer function, *Tf,* is given by:

$$Tf = \frac{S_{xy}}{S_{yy}} \tag{43.2}$$

Figure 43.1 presents the case of response spectra of acceleration, velocity and displacement from Upland Earthquake records in Pamona 2-story Commercial Building in north south direction. The basement record shows reduction in spectral acceleration at basement compared to free-field in short period range. The spectral velocity and displacement, however, do not show the significant change. Figure 43.2 illustrates power spectral density of basement and free-field records as well as

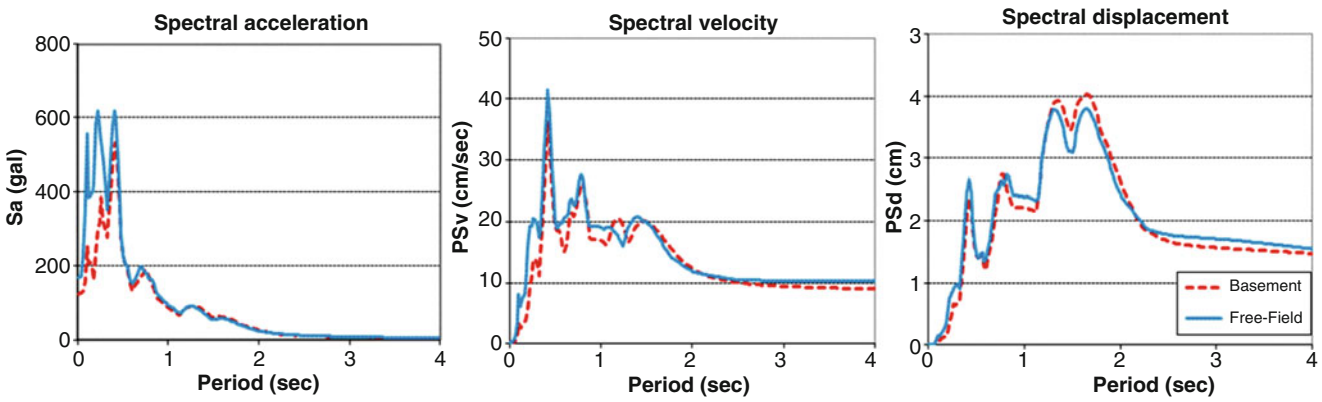

Fig. 43.1 Spectral acceleration, velocity and displacement of motions at basement and free-field of Pomona 2-story Commercial Building in Upland 1990 earthquake in north south direction

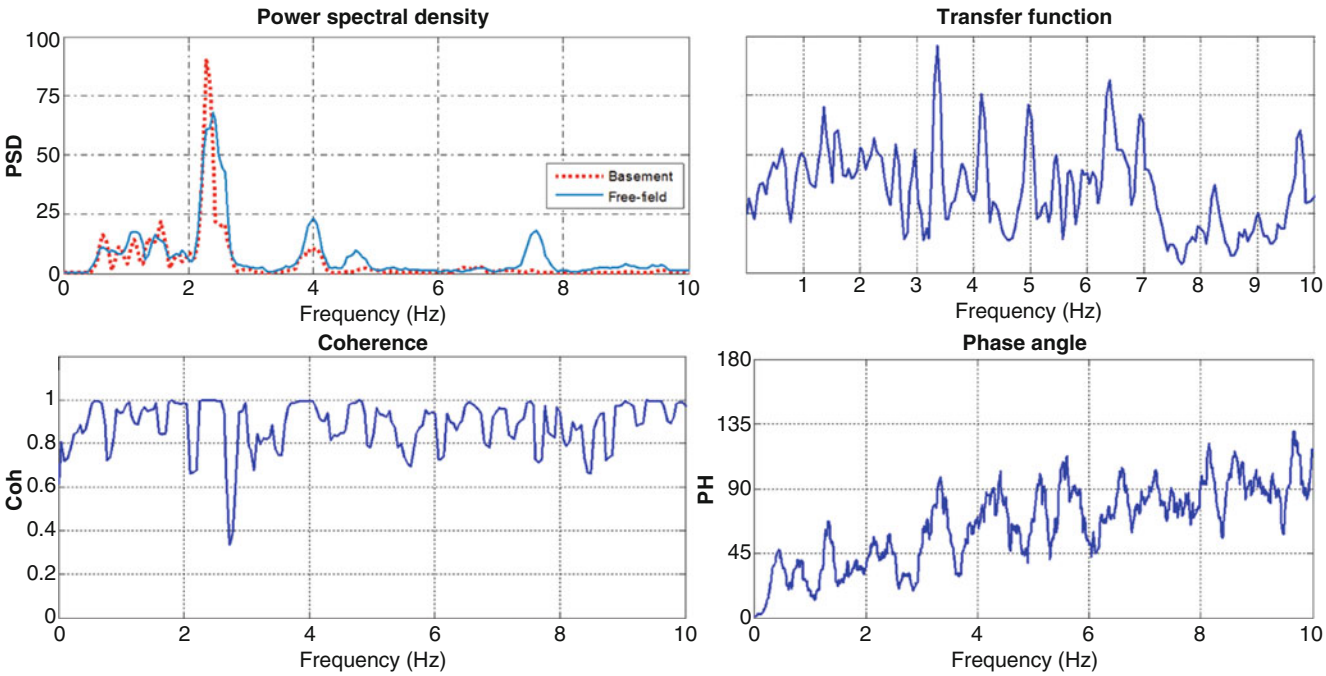

Fig. 43.2 Power spectral density function, coherence, transfer function and phase shift between records at free-field and basement of Pomona 2-story Commercial Building in Upland 1990 earthquake in north–south direction

coherence, transfer function and phase sift between the records observed in the same earthquake. The basement record has very low PSD value and does not have peaks as free-field record has in high frequency range suggesting that the motion in building–soil system has been damped. Two motions are coherent in the range where PSD curves have their peak. The transfer function also shows reduction in motion high frequency range. This is well in agreement with base slab averaging model [7].

43.2.3 Free-Field and Foundation Motions

Out of 98 pairs of records of instrumented buildings with foundation with rigid slab or interconnected strip footing resting on ground (shallow foundations with no basement), two-thirds of the records in buildings with surface foundations showed a reduction in motion at the foundation level and rest one-third of the records showed amplifications in peak acceleration or spectral accelerations.

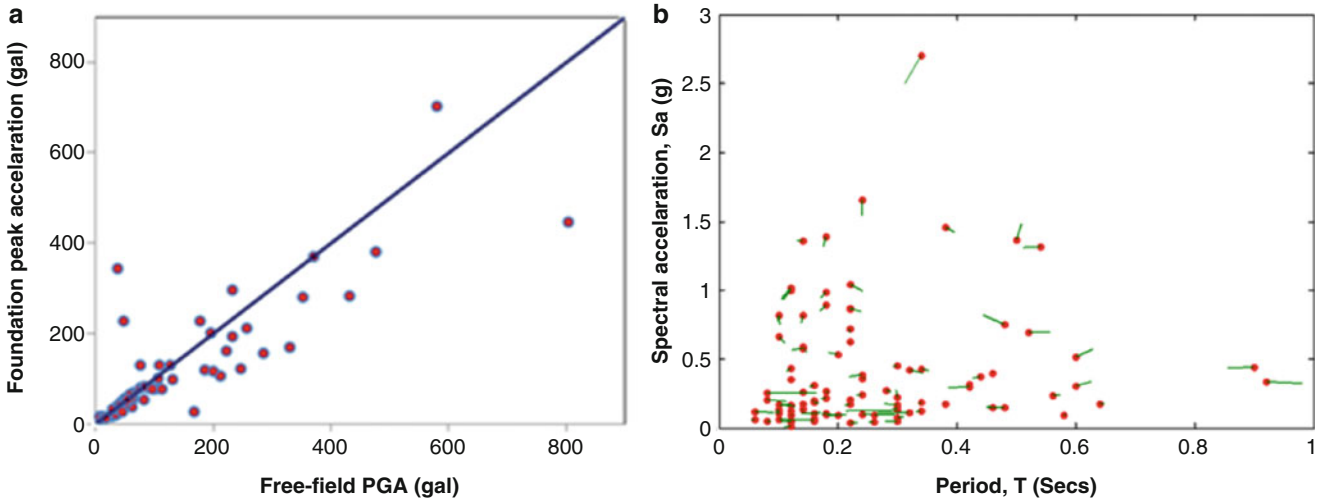

Fig. 43.3 (**a**) Foundation peak acceleration in relation to free-field peak ground acceleration (**b**) Maximum spectral acceleration at free-field and corresponding shifts at building foundation

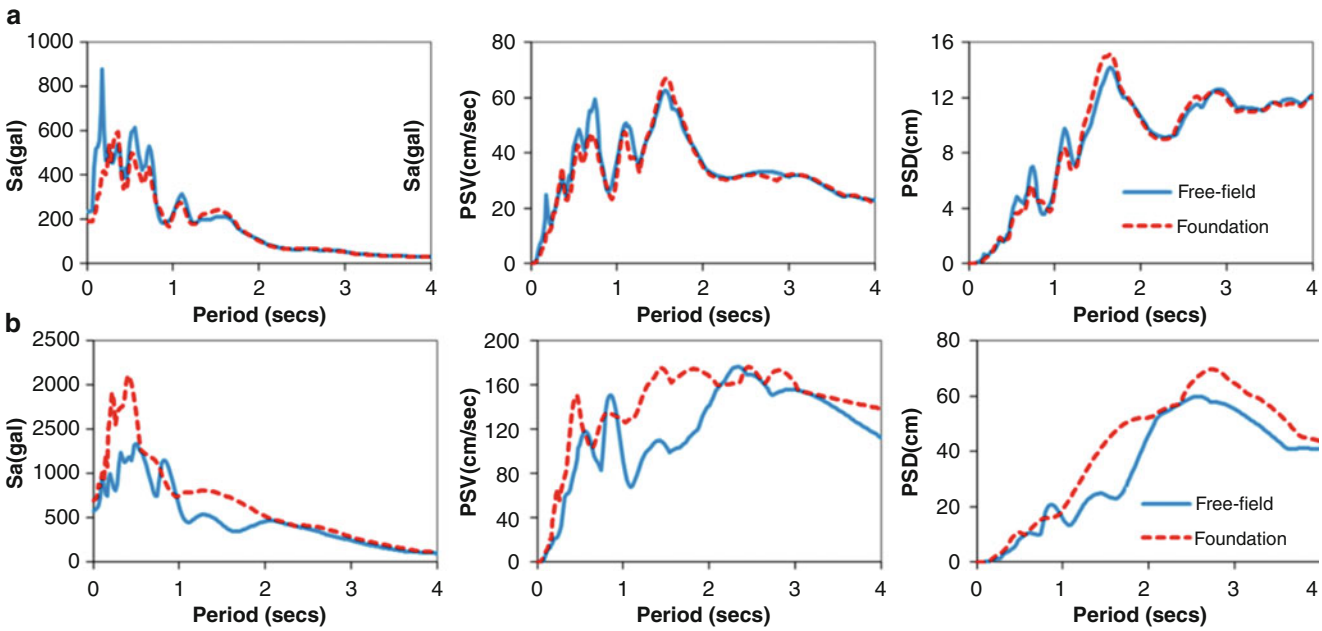

Fig. 43.4 Spectral accelerations, velocities and displacements of motions at free-field and foundation (**a**) Hollywood Storage Building (**b**) Sylmar Hospital Building for the 1994 Northridge earthquake in east west direction

The variations of the foundation motion relative to the free-field motion are observed in instrumented buildings with attenuation and amplification in some cases. Figure 43.3a shows the foundation motion in relation to free-field peak ground acceleration. While most of the pairs of the records show reduction, there are some buildings which clearly get motion amplified at their bases.

Figure 43.3b shows the variation in maximum spectral acceleration of the motion from free-field to building foundation. The circles plot the maximum spectral value at free-field at respective period and the line attached to them show the shift in time period maximum spectral value at the foundation. From the observed data in peak spectral acceleration does not provide clear trend in reduction or amplification. Similarly, there is no definite shifting of period at the peak.

Figure 43.4a, b shows 5% damping response spectra for acceleration, velocity and displacement of foundation and free-field records observed in 14-story Hollywood Storage Building and 6-story Sylmar Hospital Building respectively in 1994 Northridge Earthquake. The PSDs and transfer functions between them are illustrated in Fig. 43.5a, b.

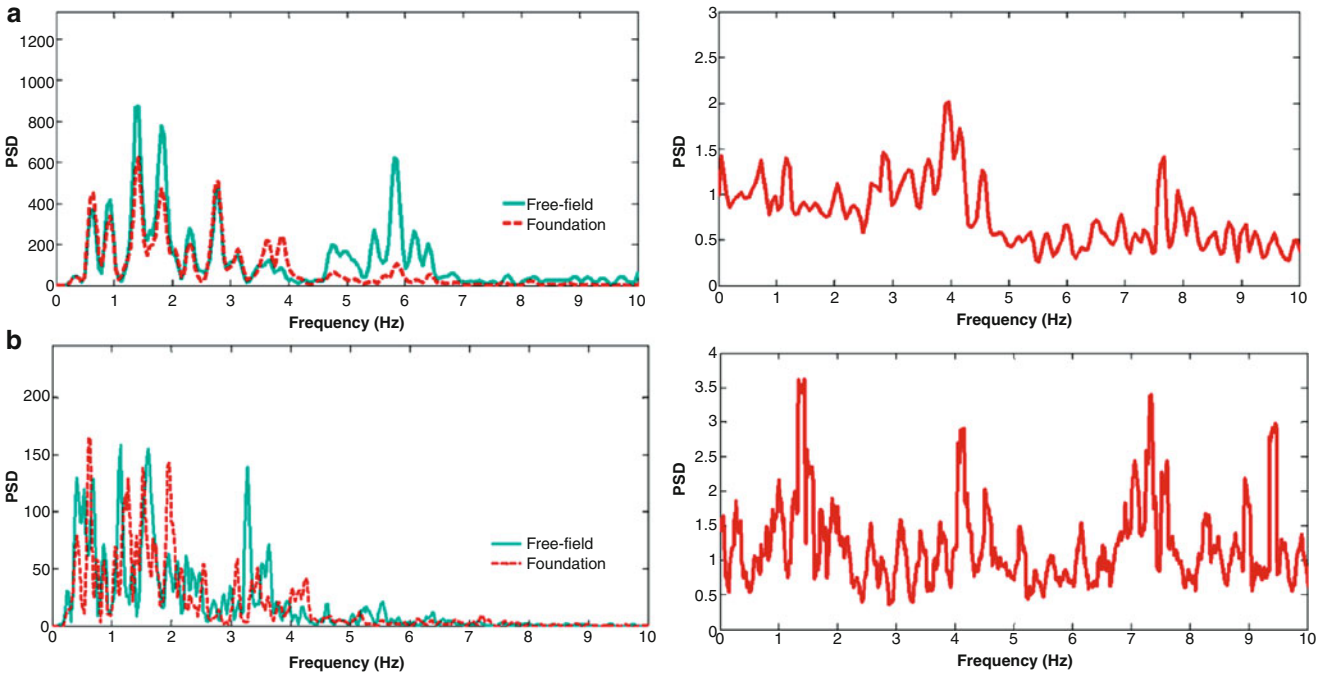

Fig. 43.5 Power spectral density functions (PSD) and transfer functions (TF) between records at free-field and basement of (**a**) Hollywood Storage Building (**b**) Sylmer Hospital Building for the 1994 Northridge earthquake in east west direction

In Hollywood Storage Building, the spectral acceleration reduced at the foundation level. The spectral velocity and displacement do not vary significantly. The reduction in the motion is mainly in short period ranges where acceleration has higher sensitivity. The motions at the base and free-field have peaks around same frequencies (Fig. 43.5a) which suggest that this is no significant shift in period. The transfer function between foundation and free-field in the figure shows that reduction in motion occurs for a frequency range higher than 4 Hz which coincides with very low power spectral density for foundation motion. This implies that the significance of the attenuation at the foundation is low in terms of its energy. In Sylmar Hospital Building, the foundation motion got amplified in a period range up 0.7 s (Fig. 43.4b). Similar trend is observed in velocity and displacement spectra in longer period. The PSD and TF between motion at foundation and free-field show that the amplification is not limited to lower modes of vibration. The periods of the motions are not in the phase.

43.3 Comparative Analysis on Variation of Motion

43.3.1 FEMA Provision on Kinematic SSI Effect in Buildings with Shallow Foundation

It appears to be generally accepted that large foundation slabs reduce the free-field ground motions for period up to 0.5 s. FEMA-440 [5] has developed reduction factors for spectral values due to the action of foundation slab for slab foundation with shallow embedment. As discussed in earlier sections, one-thirds of records at foundation slab are amplified from corresponding free-fields. The fact that the 30% of cases we investigated showed significant increases in slab motion suggests that we cannot rely on reduction of motion in all cases of shallow foundation.

In FEMA-440, it is suggested that the foundation input motion is obtained by applying the period dependent reduction factor as shown in Fig. 43.6 to the code spectrum. Reduction factor for response spectra are obtained from the transfer function for corresponding periods obtained by applying procedure suggested by Kim and Stewart [1] for shallow foundation.

Figure 43.7 shows the comparison of estimated foundation motions with observed motions in three instrumented buildings. Figure 43.7a shows the case of Hollywood Storage Building for Northridge Earthquake in north south direction. The motion at the foundation is reduced compared to free-field which FEMA also predicts. The reduction is, however, underestimated by the FEMA. Figure 43.7b is the case of Los Angeles 15-story Building where foundation is amplified in

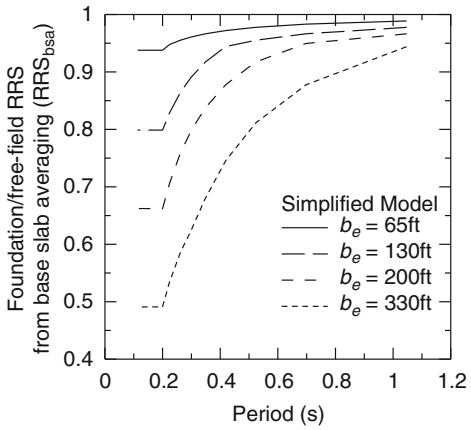

Fig. 43.6 Spectral reduction from base slab averaging (RRSbsa) as a function of period in FEMA-440

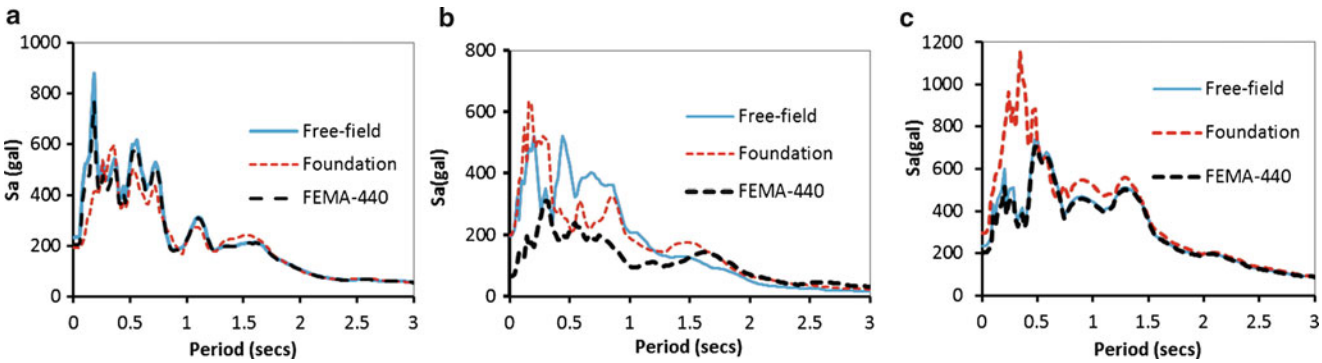

Fig. 43.7 Comparisons of foundation response spectra as per FEMA-440 with observed records in (**a**) Hollywood Storage Building (**b**) Los Angeles Office Building (**c**) El Centro Imperial Co. Service Building

short period and attenuated in the period range longer than 0.5 s in Northridge Earthquake. The FEMA does not provide the comparable estimate over large range. In the case of El Centro Imperial County Service Building where foundation motion get amplified in Imperial Valley Earthquake, FEMA estimation goes far from the reality (Fig. 43.7c). These comparisons suggest that the basis of the FEMA provisions needs to be reviewed.

43.3.2 Spatial Incoherency Model of Base Slab Averaging

The FEMA provisions for reduction of motion by base slab averaging are established based on the work of Kim and Stewart [1] and Veletsos et al. [6, 8] on spatial incoherency. The model proposed by Veletsos et al. for the transmissibility function that depends on foundation dimension, motion frequency soil shear wave velocity and incoherency parameter always gives attenuation of the motion from free-field to foundation slab (Fig. 43.8).

Incoherency parameter used in the model was later calibrated by Kim and Stewart [1] for soil shear wave velocity based on data of seismic records in instrumented buildings with shallow foundations. Transmissibility function is applied to free-field ground motion to get the foundation input motion (FIM) that can be applied for the subsequent analysis of the building system. Rigid base foundation slab and vertically propagating incoherent incident wave field were the assumed conditions in the process of calibration of incoherency parameter. The procedure is based on assumption that variation of ground motion between two points can be characterized by the spatial incoherency.

We carried out a comparative study of Kim and Stewart procedure against recorded motions in instrumented buildings with shallow foundations. It was observed that the result gives approximation in selected buildings where significant reduction is observed but the model does not capture the variation in other buildings, particularly where amplifications have been observed.

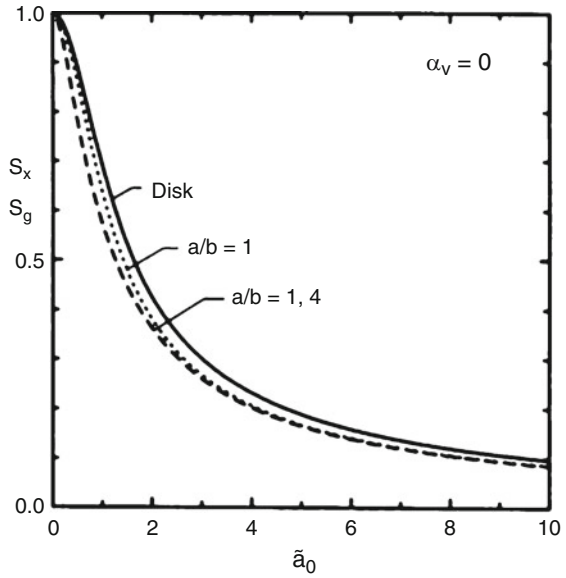

Fig. 43.8 Transmissibility function between free-field and foundation motion for vertically incoherent waves [6]

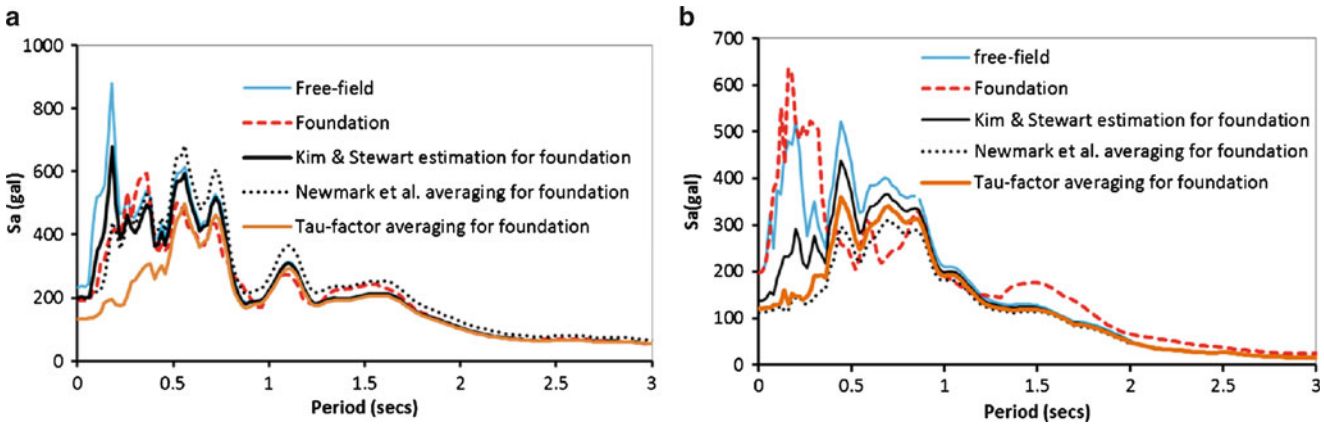

Fig. 43.9 Comparisons of foundation response spectra obtained by various methods for (**a**) Hollywood Storage Building (**b**) Los Angeles Office Building

43.3.3 Averaging Techniques

Newmark et al. [9] proposed the numerical averaging procedure to produce modified motion over the foundation slab from free-field. The technique is based on the concept that the averaging of motion happens over a time delay in excitation to parts of foundation caused by the horizontally propagating waves that impinge first on one side of the building foundation and moves to the other side. The averaging is done in effect of transit interval and moved along the acceleration time history.

For a rigid foundation, the kinematic effect in translational motion is quantified by Clough and Penzin [10] in terms of 'Tau-effect'. If the rigid foundation has dimension equal or more than apparent wave length in frequency range of interest, the motion at the base of foundation will be the average of the free-field motion over the foundation area. For one dimensional horizontal wave propagation, they proposed that the modified translational motion is obtained by Fourier transforming the free-field acceleration and multiplying the amplitude by a complex quantity called 'Tau-factor' and performing inverse fourier transformation to get the modified acceleration. The transfer function is always less than unity and hence this method cannot capture the amplification of the motions at the base that were observed in some of the instrumented buildings.

The techniques to estimate foundation slab motion describe above were applied were applied in Hollywood Storage Building (Fig. 43.9a) and Los Angeles Office Building (Fig. 43.9b) for Northridge Earthquake. The averaging technique

proposed by Newmark et al. has a good estimate in short period range in Hollywood Storage Building. However, it overestimates the motion in medium period range. Kim and Stewart model and 'Tau-factor' technique are not in good agreement in short period range as the former overestimates and later underestimates the foundation motion. In the case of Los Angeles Building where foundation motion is amplified in short period range, none of the above method gives good estimations. This is obvious for Kim and Stewart method and 'Tau-factor' technique as their transfer function always give reduction only. In principle, amplification is possible in the numerical averaging technique proposed by Newmark et al., which however could not capture the motion in short period range.

43.4 Conclusions

The basis of all methods described above proposed for quantifying the variation of motion between foundation base and nearby free-field is the averaging effect of wave passage over the foundation area. They assume either horizontal or vertical wave propagation. Except averaging of wave field by rigid mass, there is no account of interaction that may happen through wave reflection by the foundation slab and progressively stiffer layers of the underneath soil. Also, the inertial interaction between mass of soil and building in non-linear range could contribute significantly not only to the period shifting and damping of the system but also to the variation of motion amplitude. Although separating kinematic effect and inertial effect would simplify the problem, this approach may not capture the total interaction happenings between soil and structure.

The FEMA approach which accounts only reduction of motion at the foundation needs to be closely reviewed from all aspects including the basis of averaging model it used. A clear picture of the mechanics of interaction should be established, which would justify the variation of motion, both with amplification and de-amplification. The case of amplification is more important considering the fact that the analysis using the current procedure could significantly underestimate the demand to the structure.

References

1. Kim S, Stewart JP (2003) Kinematic soil-structure interaction from strong motion recordings. J Geotech Geoenv Eng 129:323–335
2. ATC-40 (1996) Seismic evaluation and retrofit of concrete building. ATC-40, Redwood City
3. FEMA-356 (2000) NEHRP guidelines for the seismic rehabilitation of buildings. Report No. FEMA-356. Federal Emergency Management Agency, Washington DC
4. EC8 (2000) Design provisions for earthquake resistance of structures, part 5: foundations, retaining structures and geotechnical aspects. EN 1998-2005. European committee for standardization, Brussels
5. ATC (2005) Improvement of nonlinear static seismic analysis procedures. Report No. FEMA-440. Federal Emergency Management Agency, Washington, DC
6. Veletsos AP, Prasad AM, Wu WH (1997) Transfer functions for rigid rectangular foundations. J Earthquake Eng Struct Dynam 26:5–17
7. Poland C, Sun J, Meija L (2000) Quantifying the effect of soil-structure interaction for use in building design. Data Utilization Report CSMIP/00-02. California Department of Conservation, California
8. Veletsos AP, Prasad AM (1989) Seismic interaction of structures and soils; stochastic approach. J Struct Eng 115:935–956
9. Newmark M, Hall WJ, Morgan JR (1977) Comparison of building response and free-field motion in earthquakes. In: Proceedings of the 6th world conference on earthquake engineering, New Delhi, India, pp 972–978
10. Clough RW, Penzien J (1995) Dynamics of structures, 3rd edn. Computers and Structures, Inc., Berkeley, CA (USA)

Chapter 44
Modified Ibrahim Time Domain Method for Identification of Closely Spaced Modes: Experimental Results

A. Malekjafarian, R. Brincker, M.R. Ashory, and M.M. Khatibi

Abstract Traditional Experimental Modal Analysis (EMA) is generally known as a standard tool to identify the dynamic signature of structures. Frequency domain methods are most based on Fourier analysis which transforms the time data to the frequency data. The methods such as: Ibrahim time domain (ITD) method, the least-squares complex exponential (LSCE) method and the Eigen realization algorithm (ERA), are the well-known methods in time domain that require free decay responses or Impulse Response Function (IRF) of the structures. It is often claimed that ITD does not work well in case of closely spaced modes because the method is SIMO, whereas the other mentioned techniques that are known to be MIMO are claimed to work well also in case of closely spaced modes. In this paper, a modified ITD is proposed using Hankel matrix averaging for identification of closely spaced modes. The traditional ITD method is investigated under the presence of closely spaced modes and is compared to a modified formulation of the ITD that can take advantage of multiple input loadings. It is shown that the results of the traditional ITD has been improved using the modified ITD in identification of closely spaced modes. To validate the proposed method, an experimental case study with closely spaced modes in a gear box shaft is considered.

44.1 Introduction

The dynamic analysis is necessary in the design, manufacturing and maintenance of structures. Numerical models such as finite element models are not accurate and in the most practical cases there is no reliable analytical solution. Therefore, modal testing is used as an experimental tool to obtain properties of the structure which reduces the problem to estimation of modal parameters including natural frequencies, mode shapes and damping ratios. Modal testing methods are divided in two main categories; frequency domain methods and time domain methods. Fast Fourier Transform often is used in frequency domain methods and the modal parameters of the structure are identified in frequency domain. But in time domain, the measured time signals are used more directly. Therefore, problems related with the Fourier transform, such as leakage is prevented.

In output-only modal analysis, frequency domain methods are normally based on spectral density functions or power spectral densities as they are also called. On the other hand, the time domain methods are often based on impulse response functions (this assumes traditional modal testing where the input is known), free decays responses where the structure is actually excited to perform free decays, or methods where pseudo free decays found by some kind of signal processing like random decrement functions or correlation functions are used.

Complex Exponential algorithm is one of the earliest modal analysis methods in time domain. CE was improved by least square solution in [1] and called Least Square Complex Exponential (LSCE) method. Ibrahim Time Domain (ITD) method first was proposed for SIMO systems in [2]. Fukuzono developed the ITD method for MIMO systems in [3].

A. Malekjafarian (✉) • M.R. Ashory • M.M. Khatibi
School of Mechanical Engineering, Semnan University, P.O.Box:35195-363, Semnan, Iran
e-mail: a.malekjafarian@gmail.com

R. Brincker
Aarhus School of Engineering, Aarhus University, Ny Munkegade 120, Building 1521, Aarhus 8000, Denmark

J.M. Caicedo et al. (eds.), *Topics on the Dynamics of Civil Structures, Volume 1*,
Conference Proceedings of the Society for Experimental Mechanics Series 26,
DOI 10.1007/978-1-4614-2413-0_44,

Ibrahim suggested a double least square solution for ITD method in [4]. The LSCE method was developed for MIMO systems in Polyreference Complex Exponential (PRCE) by Vold in [5]. State space modelling that is commonly used in control engineering was used in the Eigensystem Realization Algorithm (ERA) by [6]. Correlation of the TRF was used in an improved version of PRCE that called Improved Polyreference technique (IPCE) to decrease the influence of noise in the results by [7]. Data correlation that reduces the order of the model to be identified was used in ERA/DC by Juang [8] and accuracy of the identification was developed. Natural Excitation Technique (NExT) was proposed in [9] to do modal parameter identification from output-only data or measured responses without knowledge of input forces. Correlation functions of the random responses of the structure that is excited by natural excitation were used in NExT. All of the MIMO time domain methods that were mentioned before can be used as NExT. It means these time domain methods can be used not only as conventional modal analysis, but also can be used as operational modal analysis (OMA) methods using for instance correlation function instead of physical free decays. A unified two-stage modal identification approach in time domain is proposed during a revisit to modal identification methods in [10].

Structures with some degree of symmetry such as: circular plates, gears or bladed-discs, usually have two modes with the same frequency or close natural frequencies. These modes are known as closely spaced modes. From an experimental point of view, closely spaced modes are two close modes that in application of modal identification methods are sometimes identified as one single mode instead of two closely spaced modes.

There are some limitations when the structure has closely spaced modes. Therefore, the identification methods which can separate the close modes are more useful. The parameters of amount of interaction of two close modes in each other are investigated in [11] and [12]. Circle-fitting and Inverse methods are SDOF methods that can be used for identification of close modes [11]. RFP method is also a SISO method that can be used for closely spaced modes. GRFP and Global are SIMO methods and Spectral is MIMO methods for identification of closely spaced modes of the structure which are presented in Chap. 5 in [11]. GRF method is an extension of RFP method, but is more sensitive to the selected frequency range that cause to decrease its ability in identification of closely spaced modes in compared with RFP method.

Spectral method was presented in [13]. Spectral method is applicable for theoretical data but its results not acceptable for real structures. Generally, error of Spectral, Global and GRFP methods in natural frequencies, and phase angles are acceptable, but in estimation of damping ratios and modal constants do not give accurate results.

CMIF method uses singular value decomposition for estimation of modal parameters and it is capable to identify closely spaced modes [14]. FDD method is a frequency domain output-only method that first presented in [15]. In FDD method, spectral density matrix is decomposed to SDOFs systems that can identify closely spaced modes.

It is well known, that ITD, as it is a SIMO method in its traditional formulation, has problems identifying closely spaced modes. The traditional ITD can in fact be formulated as a MIMO method as proposed by Zhang [10], however this requires a total reformulation of the traditional ITD method.

In the paper it is shown, that the traditional ITD method with very small changes can be formulated as an MIMO technique, and the traditional ITD and the modified ITD is compared concerning their capability of identifying closely spaced modes. This investigation is performed on experimental data from a gear box shaft. In order to ensure from existing closely spaced modes in the experimental case, FEM model of the structure is considered using ANSYS software. Conventional modal testing using FRFs, traditional ITD and modified ITD are applied on the measured data. It is shown the modified ITD can detect the close modes, but traditional ITD can not show the close modes.

44.2 Theory

44.2.1 Traditional Ibrahim Time Domain (ITD) Method

Ibrahim Time Domain method which is called ITD method uses time function data to estimate modal parameters. An eigenvalue problem is constructed from the time function data and by solving the eigenvalue problem, the natural frequencies, damping ratios and mode shapes are estimated. The time functions are either free decays from the structure, pseudo free decays as mentioned above or impulse response functions which are obtained from the inverse of the FRFs can be used in the ITD method. In the following short introduction to the ITD method is given in a modern formulation.

Any free response of the structure can be expressed as a linear combinations of modes:

$$\mathbf{y}(t) = \mathbf{y}(k\Delta t) = \psi_1 e^{\lambda_1 k\Delta t} + \psi_2 e^{\lambda_2 k\Delta t} + \ldots = \psi_1 \mu_1^k + \psi_1 \mu_1^k \ldots \tag{44.1}$$

A matrix of sampled free vibration response can be formed as:

$$\mathbf{Y} = \begin{bmatrix} y(1) & y(2) & y(3) & \cdots \\ y(2) & y(3) & y(4) & \cdots \\ y(3) & y(4) & y(5) & \cdots \\ y(4) & y(5) & y(6) & \cdots \end{bmatrix} \tag{44.2}$$

which $y(k)$ includes the response of the structure at kth time sample. This matrix is based on row shift and is called a block Hankel matrix since the blocks (the response vector) is constant along the anti diagonals.

By inspection of (44.1, 44.2) can be rewritten as:

$$\mathbf{Y} = [\psi_1 \quad \psi_2 \cdots] \begin{bmatrix} \mu_1^0 & \mu_1^1 & \cdots \\ \mu_2^0 & \mu_2^1 & \\ \vdots & & \ddots \end{bmatrix} = \Psi\Lambda \tag{44.3}$$

By dividing the Hankel matrix to two parts, $\mathbf{Y}_1$ and $\mathbf{Y}_2$ are formed as:

$$\mathbf{Y}_1 = \begin{bmatrix} \mathbf{y}(1) & \mathbf{y}(2) & \cdots \\ \mathbf{y}(2) & \mathbf{y}(3) & \cdots \end{bmatrix}; \quad \mathbf{Y}_2 = \begin{bmatrix} \mathbf{y}(3) & \mathbf{y}(4) & \cdots \\ \mathbf{y}(4) & \mathbf{y}(5) & \cdots \end{bmatrix} \tag{44.4}$$

If (44.1) is considered, (44.4) can be written as:

$$\mathbf{Y}_1 = \begin{bmatrix} \psi_1 & \psi_1 & \cdots \\ \mu_1\psi_1 & \mu_1\psi_1 & \cdots \end{bmatrix} \Lambda = \Psi_1\Lambda \tag{44.5}$$

$$\mathbf{Y}_2 = \begin{bmatrix} \psi_1 & \psi_1 & \cdots \\ \mu_1\psi_1 & \mu_1\psi_1 & \cdots \end{bmatrix} \begin{bmatrix} \mu_1^2 & 0 & \cdots \\ 0 & \mu_1^2 & \\ \vdots & & \ddots \end{bmatrix} \Lambda = \Psi_1\mathbf{M}\Lambda \tag{44.6}$$

From (44.5) and (44.6) we derive the equation where Λ has been eliminated

$$\Psi_1^{-1}\mathbf{Y}_1 = \mathbf{M}^{-1}\Psi_1^{-1}\mathbf{Y}_2 \tag{44.7}$$

Now, multiplying with $\mathbf{Y}_1^T$ from the right, we obtain the square and normally full rank matrix $\mathbf{Y}_1\mathbf{Y}_1^T$ on the left side that can be inverted, and thus we obtain:

$$\Psi_1^{-1} = \mathbf{M}^{-1}\Psi_1^{-1}\mathbf{Y}_2\mathbf{Y}_1^T(\mathbf{Y}_1\mathbf{Y}_1^T)^{-1} \tag{44.8}$$

Then matrix $\mathbf{A}_1$ can be found from (44.8) as:

$$\mathbf{A}_1 = \Psi_1\mathbf{M}\Psi_1^{-1}; \quad \mathbf{A}_1 = \mathbf{Y}_2\mathbf{Y}_1^T(\mathbf{Y}_1\mathbf{Y}_1^T)^{-1} \tag{44.9}$$

Thus the eigenvectors and eigenvalues can be found by performing an eigenvalue decomposition of the matrix $\mathbf{A}_1$. As we see from (44.6), the matrix a can also be found by the alternative least square estimate:

$$\mathbf{A}_2 = \mathbf{Y}_2\mathbf{Y}_2^T(\mathbf{Y}_1\mathbf{Y}_2^T)^{-1} \tag{44.10}$$

It is well known that both estimates for the **A**-matrix are biased, and that a average estimate is often used instead and referred to as the unbiased estimate (or double least square) estimate:

$$\mathbf{A} = (\mathbf{A}_1 + \mathbf{A}_2)/2 \tag{44.11}$$

44.2.2 Modified Ibrahim Time Domain Method for Closely Spaced Modes

In case of two repeated poles, the response from (44.1) has rank one, thus also the derived matrices $\mathbf{Y}_1$, $\mathbf{Y}_2$ and $\mathbf{A}$ has rank one. Taking the time function to be any linear combination of two different free responses will result in a rank one response and thus the derived matrices will be limited to rank one. Now, taking two different free decays $\mathbf{y}_1(t)$ and $\mathbf{y}_2(t)$, the corresponding Hankel matrices can be built as:

$$\mathbf{Y}_{11} = \begin{bmatrix} \mathbf{y}_1(1) & \mathbf{y}_1(2) & \cdots \\ \mathbf{y}_1(2) & \mathbf{y}_1(3) & \cdots \end{bmatrix}; \quad \mathbf{Y}_{12} = \begin{bmatrix} \mathbf{y}_1(3) & \mathbf{y}_1(4) & \cdots \\ \mathbf{y}_1(4) & \mathbf{y}_1(5) & \cdots \end{bmatrix} \tag{44.12}$$

$$\mathbf{Y}_{21} = \begin{bmatrix} \mathbf{y}_2(1) & \mathbf{y}_2(2) & \cdots \\ \mathbf{y}_2(2) & \mathbf{y}_2(3) & \cdots \end{bmatrix}; \quad \mathbf{Y}_{22} = \begin{bmatrix} \mathbf{y}_2(3) & \mathbf{y}_2(4) & \cdots \\ \mathbf{y}_2(4) & \mathbf{y}_2(5) & \cdots \end{bmatrix} \tag{44.13}$$

And the corresponding $\mathbf{A}$ matrices can be formed as:

$$\mathbf{A}_{11} = \mathbf{Y}_{12}\mathbf{Y}_{11}^T(\mathbf{Y}_{11}\mathbf{Y}_{11}^T)^{-1}; \quad \mathbf{A}_{12} = \mathbf{Y}_{12}\mathbf{Y}_{12}^T(\mathbf{Y}_{11}\mathbf{Y}_{12}^T)^{-1} \tag{44.14}$$

$$\mathbf{A}_{21} = \mathbf{Y}_{22}\mathbf{Y}_{21}^T(\mathbf{Y}_{21}\mathbf{Y}_{21}^T)^{-1}; \quad \mathbf{A}_{22} = \mathbf{Y}_{22}\mathbf{Y}_{22}^T(\mathbf{Y}_{21}\mathbf{Y}_{22}^T)^{-1} \tag{44.15}$$

The $\mathbf{A}_1$ matrix can now be defined as:

$$\mathbf{A}_1' = (\mathbf{A}_{11} + \mathbf{A}_{21})/2 \tag{44.16}$$

$$\mathbf{A}_2' = (\mathbf{A}_{12} + \mathbf{A}_{22})/2 \tag{44.17}$$

Both of (44.16) and (44.17) having full rank. Finally the generalized unbiased estimate of the $\mathbf{A}$-matrix with full rank is:

$$\mathbf{A} = (\mathbf{A}_1' + \mathbf{A}_2')/2 = (\mathbf{A}_{11} + \mathbf{A}_{12} + \mathbf{A}_{21} + \mathbf{A}_{22})/4 \tag{44.18}$$

44.3 Experimental Case Study

44.3.1 Finite Element Model

As a case with a degree of symmetry, a gearbox shaft was considered (Fig. 44.1). The FEM model of shaft was built using eight node elements of ANSYS software (Fig. 44.2). Then, the natural frequencies and mode shapes were obtained.

Table 44.1 shows the first three natural frequencies of shaft. The first two modes are close together, presenting the double modes. Figure 44.3 illustrates the first and second mode shapes of shaft.

It is shown that the double modes of structure were detected using FEM.

Fig. 44.1 Gearbox shaft

Fig. 44.2 FEM model of the gearbox shaft

Table 44.1 FEM natural frequencies

No. of mode	1	2	3
FEM natural frequency (Hz)	2,480.4	2,484.0	6,127.2

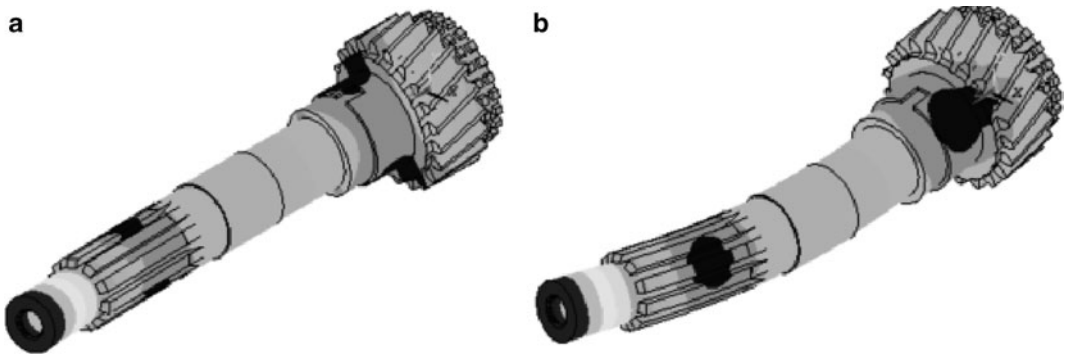

Fig. 44.3 (**a**) The first mode shape, (**b**) the second mode shape

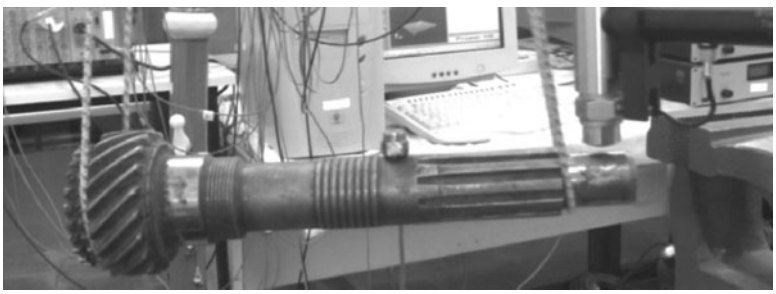

Fig. 44.4 Test setup for experimental modal analysis

44.3.2 Conventional Modal Testing Using FRFs

The conventional modal analysis was conducted on the shaft using an accelerometer type A123E and a force transducer type 8200 and a charge amplifier type 2647A. A 3560D analyser was used to extract the measured FRFs. The shaft was modelled by exciting the structure at six points in the hammer test as shown in Fig. 44.4.

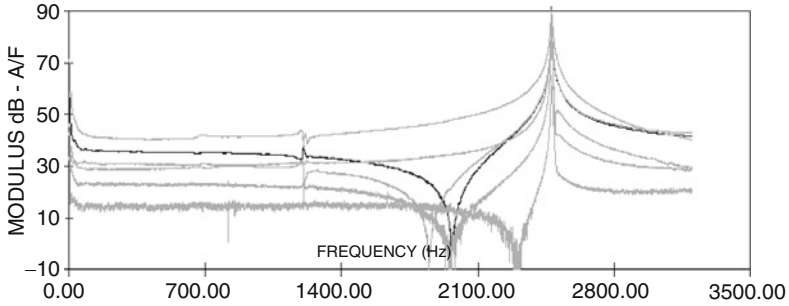

Fig. 44.5 Frequency response functions (FRFs) from modal analysis

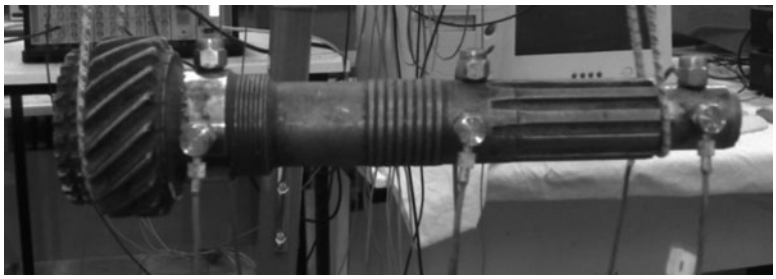

Fig. 44.6 Test setup for ITD

Table 44.2 Natural frequencies from FDD method

No. of mode	1	2
Traditional ITD natural frequency (Hz)	2,436	–
Modified ITD natural frequency (Hz)	2,436	2,438

The frequency range of measurement was 0–3,000 Hz. The measured FRFs show only one mode at 2,478 Hz and the double modes can not be recognized from the results at this frequency (Fig. 44.5).

44.3.3 Modified ITD and Traditional ITD

The shaft was tested using six accelerometers installed at six points of shaft as shown in Fig. 44.6.

In order to have free decays from the test, the shaft was excited at one point by a hammer and the free decays responses were measured. As the modified ITD needs two free decays with different initial conditions, the shaft was excited again with a hammer in a different point, therefore double modes are excited and can be detected. This is not usually the case in conventional modal testing in which the structure is excited at one point and one direction. The traditional ITD and modified ITD methods were applied on the measured data to obtain the double modes of the structure. The obtained results are given in Table 44.2.

The double modes were detected from the modified ITD, while traditional ITD was not able to detect the double mode of the structure. This is due to the nature of modified ITD which can separate the double modes from multiple free decays.

44.4 Conclusion

The classical Ibrahim time domain method has been reviewed and slightly modified in order to be able to provide full rank system matrices in case of closely spaced modes. The classical and modified ITD has been compared, and it as expected, in case of closely spaced modes, classical ITD has some problems performing well, whereas the modified ITD shows a better performance in identifying the closely spaced modes. In order to validate the method, an experimental case study of a gear box shaft was tested in conventional modal testing using FRFs, traditional ITD method and modified ITD method. It is shown closely spaced modes were not detected from FRFs and traditional ITD, while modified ITD detected it properly.

References

1. Brown DL et al (1979) Parameter estimation techniques for modal analysis, SAE Paper No. 790221
2. Ibrahim SR, Mikulcik EC (1977) A method for the direct identification of vibration parameters from the free response. Shock Vib Bull 147:183–198
3. Fukuzono K (1986) Investigation of multiple reference Ibrahim time domain modal parameter estimation technique. M.S. Thesis, Department of Mechanical and Industry Engineering, University of Cincinnati
4. Ibrahim SR (1986) Double least squares approach for use in structural modal identification. AIAA J 24(3):499–503
5. Vold H et al (1982) A multi-input modal estimation algorithm for mini-computers. SAE Paper No. 820194
6. Juang J-N, Pappa R (1984) An eigensystem realization algorithm (ERA) for modal parameter identification. In: NASA/JPL workshop on identification and control of flexible space structures, Pasadena
7. Zhang L-M, Yao Y-X, Lu M-F (1987) An improved time domain polyreference method for modal identification. Mech Syst Signal Process 1(4):399–413
8. Juang J-N, Cooper JE, Wright JR (1988) An eigensystem realization algorithm using data correlation (ERA/DC) for modal parameter identification. Contr Theor Adv Tech 4(1):5–14
9. James GH, Carne TG, Lauffer JP, Nard,AR (1992) Modal testing using natural excitation. In: Proceedings of the 10-th IMAC, Sandiago, 3–7 Feb 1992
10. Zhang L, Brincker L, Andersen P (2002) An unified approach for two-stage time domain modal identification. In: Proceedings of the international conference on structural dynamics modelling, Portugal
11. Maia NMM (1988) Extraction of valid modal properties from measured data in structural vibrations. Ph.D. Thesis, Imperial College, Department of Mechanical Engineering, London
12. IX541 – Maia, NM M (1985) Interference criteria in modal identification. M.Sc. Thesis, Technical University of Lisbon, Portuguese
13. Klosterman A (1971)On the experimental determination and use of modal representation of dynamic characteristics. Ph.D. Thesis, University of Cincinnati
14. Ewins DJ (2000) Modal testing: theory, practice and application, 2nd edn. Research Studies Press, Baldock
15. Brincker R, Zhang L, Andersen P (2000) Modal identification from ambient responses using frequency domain decomposition. In: Proceedings of the 18th international modal analysis conference (IMAC-XXI), pp 625–630